FOURTH EDITION

Chemical Oceanography

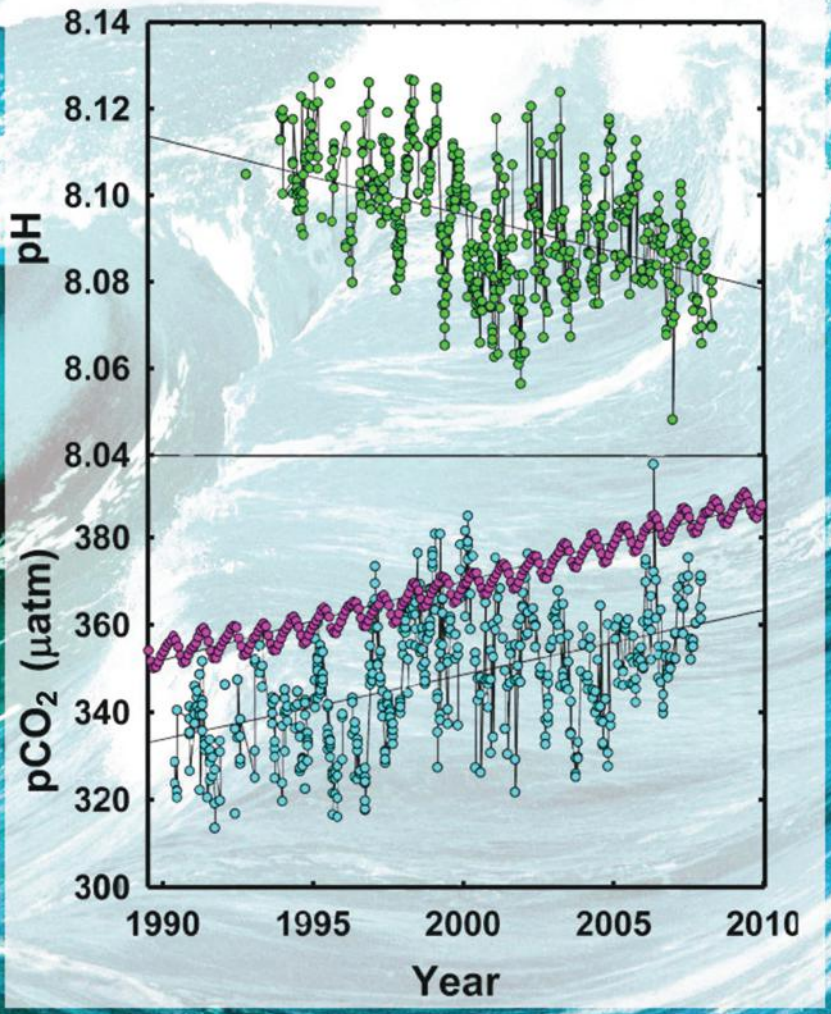

Frank J. Millero

CRC Press
Taylor & Francis Group

FOURTH EDITION

Chemical Oceanography

FOURTH EDITION

Chemical Oceanography

Frank J. Millero

CRC Press
Taylor & Francis Group
Boca Raton London New York

CRC Press is an imprint of the
Taylor & Francis Group, an **informa** business

CRC Press
Taylor & Francis Group
6000 Broken Sound Parkway NW, Suite 300
Boca Raton, FL 33487-2742

Version Date: 20130408

International Standard Book Number-13: 978-1-4665-1255-9 (eBook - PDF)

Contents

Preface to the First Edition

This book is the result of a course that I have taught over the last 20 years at the University of Miami. Shortly after I arrived in Miami in 1966 from a short stint in industry, I was asked to teach a graduate course in chemical oceanography. At the time I knew little about the oceans and found it necessary to do a lot of reading. Luckily J. P. Riley and G. Skirrow (1965) had just edited a two-volume book on chemical oceanography. The book contained chapters written by a number of authors that described the basic areas of the field. I used these volumes as a source for my first course and the present book is patterned after these volumes. My early reading included the classical text *The Oceans* by Sverdrup, Johnson, and Fleming and the book *Oceanography* edited by M. Sears (1961). I used the text *Marine Chemistry* by Horne (1969), and the text *Introduction to Marine Chemistry* by Riley and Chester (1971) for some time, but they became outdated. The volumes of *The Sea: Ideas and Observations*, edited by Hill and others (1963, 1974, 1977) were used as a source of supplemental material. The second edition of *Chemical Oceanography* by Riley and Skirrow (1975) and later volumes by Riley and Chester (1976, 1978, 1983) and by Riley (1989) are still used to keep the course up to date.

In 1980 I started teaching an undergraduate course in chemical oceanography and found the need for a textbook. The text *Chemical Oceanography* by Broecker (1971) was used for a time, but it did not cover the classical areas that were more familiar to me. The more recent *Tracers in the Sea* by Broecker and Peng (1982) was better, but the undergraduate students found it difficult to follow. Although graduate students can probe the volumes of *Chemical Oceanography* and current literature references, undergraduate students need a more fundamental approach to the field. The present text is my attempt to put together my views of the field. It is largely descriptive and is biased by my strong mechanistic feelings as a physical chemist. Since it is meant to be an undergraduate text, I have not given all the original references. I have mentioned by name many of my colleagues who have contributed to the field—I apologize for any omissions. Since my background and interests in organic chemistry are rather meager, I asked May Sohn to join me as co-author. She has been very helpful in correcting some of my mistakes and wrote the chapter on organic chemistry.

As with most endeavors, I owe thanks to a number of people: my many students, both graduate and undergraduate who have struggled through my courses; Mrs. Rita Marvez who has typed and re-typed the many drafts of this book; Mrs. Sara Sotolongo who has drawn many of the figures; and Kara Kern, who carefully proofed the final copy. The support of my research from the National Science Foundation and the Office of Naval Research should also be acknowledged. These agencies provided me with research funds to probe the thermodynamics and kinetics of processes occurring in the oceans.

I am sure the book has some flaws, but I hope it will prove useful to those wishing to get an introduction to the field of chemical oceanography. Some of the books that have shaped my views of the field are given below.

The Oceans, H. U. Sverdrup, M. W. Johnson, and R. H. Fleming, Prentice-Hall, Englewood Cliffs, New Jersey (1942).

The Chemistry and Fertility of Seawater, H. W. Harvey, Cambridge University Press, London (1955).

Oceanography, M. Sears, Ed., Pub 67, A.A.A.S., Washington, D.C. (1961).

The Sea: Ideas and Observations, M. N. Hill, Ed., Vol. 2, John Wiley & Sons, New York (1963).

The Sea: Ideas and Observations, E. D. Goldberg, Ed., Vol. 5, John Wiley & Sons, New York (1974).
The Sea: Ideas and Observations, E. D. Goldberg, I. N. McCave, J. J. O'Brien, and J. H. Steel, Eds., Vol. 6, John Wiley & Sons, New York (1977).
Marine Chemistry, R. A. Horne, Wiley-Interscience, New York (1969).
Introduction to Marine Chemistry, J. P. Riley and R. Chester, Academic Press, New York (1971).
Chemical Oceanography, W. S. Broecker, Harcourt, Brace and Jovanovich Inc., New York (1971).
Chemical Oceanography, J. P. Riley and G. Skirrow, Vols. 1 and 2, 1st ed., Academic Press, New York (1965).
Chemical Oceanography, J. P. Riley and G. Skirrow, Vols. 1 to 4, 2nd ed., Academic Press, New York (1975).
Chemical Oceanography, J. P. Riley and R. Chester, Vols. 5 and 6, 2nd ed., Academic Press, New York (1976).
Chemical Oceanography, J. P. Riley and R. Chester, Vol. 7, 2nd ed., Academic Press, New York (1978).
Chemical Oceanography, J. P. Riley and R. Chester, Vol. 8, 2nd ed., Academic Press, New York (1983).
Chemical Oceanography, J. P. Riley, Vols. 9 and 10, 2nd ed., Academic Press, New York (1989).
Tracers in the Sea, W. S. Broecker and T. H. Peng, Eldigio Press, Palisades, NY (1982).

Preface to the Second Edition

In 1992 the first edition of this book was published as a result of my teaching a course in chemical oceanography at the University of Miami over the last 25 years. This edition is an updated version of this book which I hope is improved due to the comments of undergraduate and graduate students that have struggled through my first attempt. I have deleted the chapter on organic chemistry largely due to my ignorance of this field and the problems my students had getting through this area. I discuss the organic compounds that are related to primary production in a separate chapter. This chapter also includes a discussion on the iron hypothesis that has been examined in recent years. The other chapters have been updated as new areas have been discussed in the literature. As with the first edition of the book, it is meant to be used as an upper level undergraduate course or a first year graduate course in chemical oceanography. At the graduate level it can be supplemented with the volumes of *Chemical Oceanography* and current literature references. It remains biased with my views of the field. It is largely descriptive and is biased by my strong mechanistic feelings as a physical chemist. Since it is meant to be an undergraduate text, I have not given all the original references. I have mentioned by name many of those colleagues of mine that have contributed to the field— I apologize for any omissions.

As with most endeavors, I owe thanks to a number of people: my many students, both graduate and undergraduate, who have struggled through my courses; Mrs. Sara Sotolongo, Elizabeth Degler, Meridith Galanter, and Danny Madina who have drawn many of the figures; and Gay Ingram for proofing the book. The support of the National Science Foundation and the Office of Naval Research of my research work should also be acknowledged. These agencies provided me with research funds to probe the thermodynamics and kinetics of processes occurring in the oceans.

I am sure the book still has some flaws, but I hope it will prove useful to those wishing to get an introduction to the field of chemical oceanography.

Preface to the Third Edition

This third edition of the book has been updated based on recent literature. It is still based on undergraduate and graduate courses I have taught for the past 39 years at the University of Miami. Over the past 10 years a number of large-scale oceanographic programs have been completed. These programs have examined the physical, chemical, and biological systems in the oceans. These include the Joint Global Ocean Flux Study (JGOFS) and the World Ocean Climate Experiment (WOCE). These studies have provided a wealth of maps and sections of properties of the oceans and are available on the web. Some of the sections for nutrients and carbonate parameters have been given. A number of iron addition experiments have been made in the southern ocean in recent years (SOIREE, Southern Ocean Iron RElease Experiment, EisenEx, "Iron" Experiment, and the SOFEX, Southern Ocean Iron Experiment). These studies have led to a vast amount of new data that have been used to examine the biogeochemical processes occurring in the oceans. In the new revision, I have attempted to discuss some of this latest material. The section of the book on the carbonate system in the oceans has been expanded to examine the input of fossil fuel CO_2 into the oceans and the effect it will have on the pH of the world oceans.

As with earlier editions of the book, several students and coworkers have helped to redo a number of the figures and proof the text. Much of this was done by Mr. Taylor Graham, who has been with my group as an undergraduate from the University of Miami and has stayed on as a research assistant before he enters graduate school. I also wish to acknowledge the help of Gay Ingram, my secretary, as well as my student Hector Bustos Serrano, who did some proofreading of the book. A number of readers have sent me corrections for typos in the last edition. I have attempted to correct all of these errors as well as others pointed out by my students taking my undergraduate class in chemical oceanography. Over the years much of the content of the book has been put into PowerPoint presentations. I hope to make these presentations available to those using the book as a text. I also have a number of Quick Basic programs that can be used to calculate the properties of seawater, carbonate parameters, and the speciation of metals in natural waters that are available upon request.

Preface to the Fourth Edition

This fourth edition of the book has been updated based on recent literature. It is still based on undergraduate and graduate courses I have taught for the past 45 years at the University of Miami. Over the past 10 years a number of new large-scale oceanographic programs have been initiated. This includes The Climate Variability Program (CLIVAR) and the recent initiation of the Geochemical Trace Metal Program (GEOTRACES). This program is aimed at understanding the biogeochemical cycles of trace elements in the oceans. The initial studies have already shown the input of Fe and Pb from hydrothermal vents and the redox behavior of metals in low oxygen waters. These recent and future studies will produce a wealth of information on the biogeochemistry of the world oceans. The increasing CO_2 in the atmosphere from the burning of fossil fuels continues to affect the atmosphere and the oceans. The increased temperature of surface waters is causing stratification in the oceans. This has led to areas of low oxygen regions in coastal waters. Each year oceanographers contribute to the expanding knowledge of the oceans. I have tried to build and update this introduction to *Chemical Oceanography* with new understanding and concepts. The dissolution of CO_2 in the waters is lowering the pH (called ocean acidification). This lower pH will affect calcifiers in the oceans and biogeochemical processes such as equilibrium and rates of reactions. New research in the field of ocean acidification has been added as well as information on the new standards developed by the SCOR/IAPSO working group to describe the properties of seawater for researchers to report their measurements. Standardization of measurements in the literature leads to a clearer understanding and less confusion in reporting the processes in the oceans. More research will come over the next ten years and I will try to add any new and exciting changes in the oceans in my PowerPoint Lecture that I update each year. I hope the new edition covers some of the areas that were missing and gives a reasonable review of the basic concepts of the field.

There are a number of graduate and undergraduate students that have contributed to the updating of this book. This summer I was fortunate to have Sara Denka, a junior majoring in marine science/biology at the University of Miami, assist me in editing this fourth edition of *Chemical Oceanography*. She took my undergraduate course and was familiar with the content of the earlier version. From 2005-2012, my Ph.D. students Yanxin Luo, William Hiscock, Mareva Chanson, John Michael Trapp, Hector Bustos Serrano, Jason Waters, Ryan Woosley, Benjamin Ditrolio, and Carmen Rodriguez provided additional comments and corrections to the text. Gay Ingram, my right hand, has also edited the various versions of my papers and books over the years.

The continual support of the National Science Foundation and the National Oceanographic and Atmospheric Administration provided the research funds for our work. Without the financial backing from these two U.S. government agencies our research would be seriously curtailed. We thank them for their interest in the common good and advancement of scientific knowledge.

About the Author

Dr. Frank J. Millero was born in Greenville, Pennsylvania, in 1939. He received his B.S. (1961) from Ohio State University and his M.S. (1964) and Ph.D. (1965) from Carnegie-Mellon University in physical chemistry. After a brief interval in industry, he came to the Rosenstiel School of the University of Miami in 1966. He has been a professor in marine and physical chemistry since that time. During 1986 to 2006 he was the Associate Dean of Academic Affairs and Research at the school. His research focuses on the application of physical chemical principles to natural waters. He uses chemical models to understand how ionic interactions affect the thermodynamics and kinetics of processes occurring in the oceans. These studies have resulted in numerous research cruises in the Indian, Pacific, Atlantic, and Southern oceans and the Arabian Sea. Millero's research group is presently studying the carbonate system in the world oceans as part of the CLIVAR (Climate Variability) project to determine the changes in the flux of CO_2 across the air–sea interface in the oceans and ocean acidification. Over the years, he has received a number of awards for his teaching and research accomplishments. These include the Office of Naval Research Educator Award (1991-1995), Sigma Xi Professor of the Year (1989), Florida Academy of Science Medal (1991), Sigma Xi Professor of the Year (1989), Florida Academy of Science Medal (1991), and a Gold Medal from Rudjer Boskovic Institute, Zabreb, Croatia, in recognition of contributions to marine chemistry (1988). He was selected as a member of his Warren, Ohio, High School Distinguished Alumni Hall of Fame and won the Carnegie Mellon Distinguished Achievement Award (2003). He received the Distinguished Faculty Scholar Award from the University of Miami (1966). In 2011 Millero received the Geochemical Society Victor Moritz Goldschmidt Award for distinguished research in geochemistry and the Florida Award (Florida section of the American Chemical Society (FLACS). He is a Fellow of the 1) American Geophysical Union (1999); 2) Geochemical Society and the European Association for Geochemistry (2000); and 3) American Association for the Advancement of Science (2009).

He has served on the National Academy of Sciences Ocean Science Board (1981–1983) and is a member of a number of chemical and oceanographic societies. He also served on the National Academies Committee on the Development of an Integrated Science Strategy for Ocean Acidification Monitoring, Research and Impacts Assessment (2009-10). In addition, he serves as an associate editor for a number of journals and is presently editor-in-chief of *Marine Chemistry*. Professor Millero has authored more than 550 juried publications in 75 different journals and numerous book chapters and has published two major books on marine chemistry.

At the university he has taught courses in chemical oceanography and marine physical chemistry at the graduate and undergraduate level for 45 years. He is proud to have published papers with 8 high school students, 21 undergraduate students, and 43 graduate students over the years. Many have become successful chemists, engineers, and other professionals.

1

Descriptive Oceanography

1.1 Introduction

Before we discuss the chemistry of the oceans, it is useful to review some descriptive features of the oceans. Oceanography is the scientific study of the oceans and can be divided into four major areas:

1. Physical oceanography: the study of the physics of the oceans and their interactions with the atmosphere
2. Biological oceanography: the study of the biology of the oceans
3. Geological oceanography: the study of the geology and geophysics of the oceans
4. Chemical oceanography: the study of the chemistry of the oceans

The basic goal of oceanography is to obtain a clear and systematic description of the oceans. It is hoped that an increased knowledge of the oceans will lead to a better understanding of how they control the climate of the earth and how they can be used as a source of food, chemicals, and energy.

The goal of the physical oceanographer is to obtain a systematic and quantitative description of ocean waters and their movements. The ocean currents circulate continuously with small-scale variations from tides and waves generated by winds and earthquakes. This physical study of the oceans has been examined by

1. The descriptive approach: Observations are made of specific features and reduced to a single characterization of the general features.
2. The dynamic approach: The known laws of physics are applied to the oceans. An attempt is made to solve the mathematical equations for the motion of a body acted on by forces.

This chapter gives a brief review of descriptive physical oceanography of the oceans. It is important to understand these descriptive features since the movement of ocean waters affects the biogeochemical processes that occur in the oceans. Much of the material covered in the earlier editions of the book was taken from books by Pickard and Emery (1982), Dietrich et al. (1980), and Tchernia (1980). Lynne Tally, George Pickard, and Wilmer Emery and James Smith (2011) have written a sixth edition of the earlier Pickard and Emery (1982) book. It is up to date and should be referred to for further details.

The field of physical oceanography has expanded in recent years due to a number of large-scale research programs, including the following:

1. The Geochemical Oceans Sections Study (GEOSECS) from 1970 to 1980
2. The World Ocean Circulation Experiment (WOCE) from 1990 to 2000
3. The Climate Variability and Predictability (CLIVAR) project from 2001 to the present

Early theoretical studies of surface tides were made by Newton and Laplace and of waves by Gerstner and Stokes. The Scandinavian meteorologists Bjerknes, Ekman, and Helland-Hansen developed the field of dynamic oceanography. Recent studies have examined coastal processes, western boundary currents (such as the Gulf Stream), and small-scale fluctuations, eddies or rings, bottom water movement, and the use of tracers to study large-scale mixing processes. Currently, physical and chemical oceanographers are participating in CLIVAR. This study is a continuation of the WOCE program. This global study includes a reoccupation of some of the long lines that were studied as part of the Joint Global Ocean Flux Study (JGOFS) and Ocean–Atmosphere Carbon Exchange Study (OACES) CO_2 programs, which are discussed further elsewhere in this book. Future oceanography will have a strong component dealing with satellites and remote sensing techniques utilizing moored arrays of instruments in the oceans. This global ocean observing system (GOOS) will be concerned with making continuous physical and chemical measurements of the global ocean. It should also be pointed out that a new International Study of Marine Biogeochemical Cycles of Trace Elements and Their Isotopes has been initiated. It is called GEOTRACES. These studies should provide a wealth of information on the effect that trace metals have on biogeochemical processes in the oceans.

1.2 Physical Characteristics of the Oceans

Some general physical features of the oceans to keep in mind are the following:

1. Of the earth's surface, 71% is covered by the oceans (361×10^6 km^2).
2. The deepest trench is 11,022 m (Mariana); the highest mountain on land is 8848 m (Mt. Everest).
3. The Southern Hemisphere has the largest percentage of water (80.9%) in the oceans.
4. The world oceans are made up of 50% Pacific, 29% Atlantic, and 21% Indian Oceans by volume.
5. The major depth zone of the ocean (74%) lies between 3 and 6 km.
6. Of ocean waters, 50% have a temperature range between 1.3 and 3.8°C and salinity (grams of salt in 1 kg of seawater) between 34.6 and 34.8.
7. The mean depth of the oceans is 3.7 km; the mean temperature is 3.5°C, and the mean salinity is 34.7.

The major features of the ocean floor are shown in Figure 1.1. Continental margins show a wide range of unique features, and a number of studies have been conducted of seamounts that occur in deep-sea basins. The detailed structure has been examined for the midocean ridge systems (see Figure 1.2).

The **shore** is the part of the land mass close to the sea that has been modified by the sea. The continental shelf is seaward from the shore and has a gradient or slope of 1 to

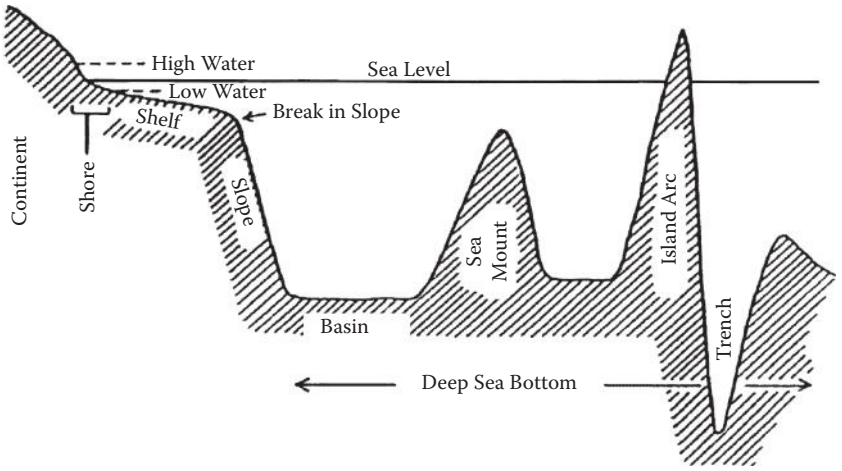

FIGURE 1.1
Structure of the ocean floor.

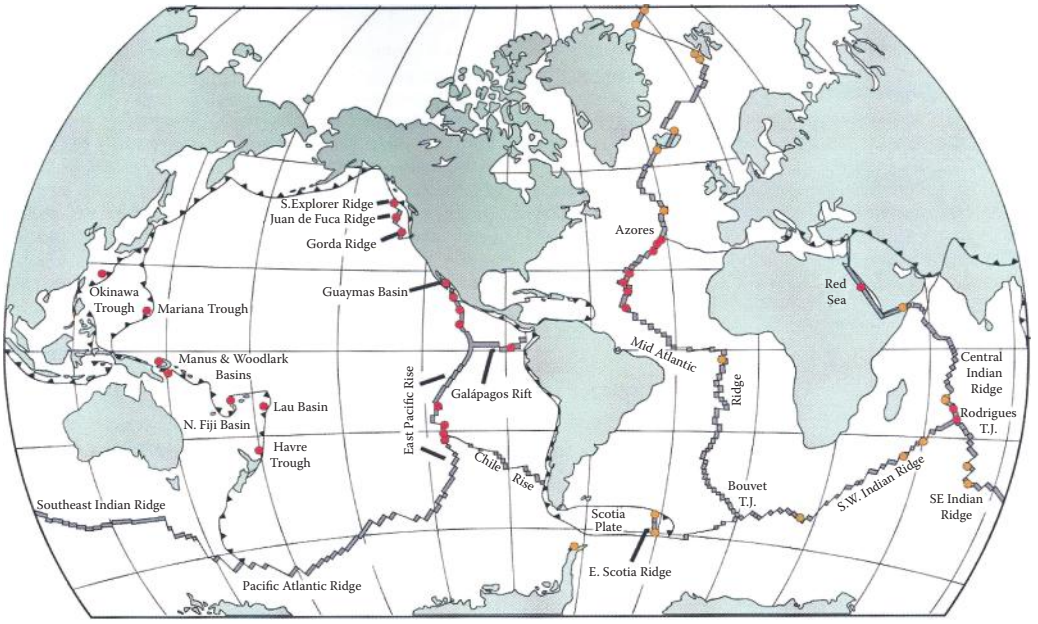

Locations of known hydrothermal activity along the global mid-ocean ridge system
● = Known active sites ● = Active sites indicated by midwater chemical anomalies

FIGURE 1.2
Active ridge systems in the oceans.

500 and an average width of 65 km. The **break in slope** is the outer limit of the shelf and has a slope of about 1 to 20 and an average depth of 130 m. The **continental slope** is about 4000 m from the shelf to the deep-sea bottom. In some places, it extends as much as 9000 m vertically over a relatively short horizontal distance (e.g., off the western coast of America). The **deep-sea bottom** represents the most extensive topographic area (76% of ocean basins)

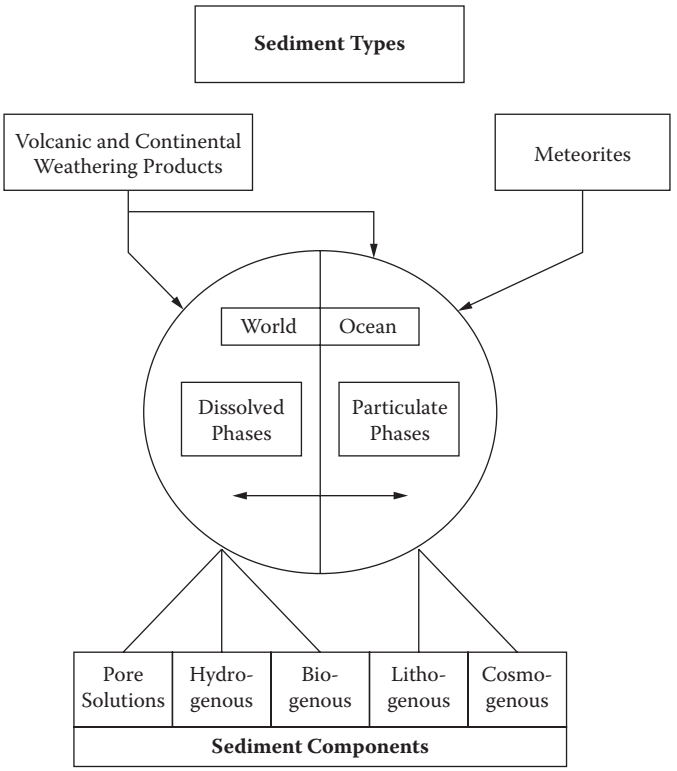

FIGURE 1.3
Types of ocean sediments.

and has a depth between 3 and 6 km. This area is not completely flat but is characterized by welts, furrows, swells, and basins.

The bottom sediments contain material both formed in the sea (pelagic) and brought from the land by rivers and the atmosphere (nonpelagic). The components of sediments can be divided into a detrital fraction transported as a solid and a nondetrital, or authigenic, fraction transported as dissolved matter. Sediments can be divided into four types (see Figure 1.3):

1. Hydrogenous: formed by reactions (precipitation and adsorption) in the water
2. Biogenous: produced by living organisms from the parts of shells and skeletons
3. Lithogenous: produced from the weathering of the earth's surface and transported by rivers and winds to the oceans
4. Cosmogenous: produced from extraterrestrial sources

Examples of the various types include

1. Hydrogenous: aragonite ($CaSO_3$) in the form of "whitings" on the Bahama Banks; manganese (MnO_2) nodules in the deep Pacific; iron hydroxides (Fe_2O_3); sulfates ($CaSO_4$); and phosphates, $Ca_3(PO_4)_2$
2. Biogenous: calcite ($CaCO_3$) from foraminifera and cocoliths, aragonite from pteropods, silica (SiO_2) from radiolarians and diatoms

3. Lithogenous: clay minerals (Al silicates) and quartz (SiO_2) as rock fragments transported by wind, rivers, glacial waters, and volcanic sources
4. Cosmogenous: ferric meteorites (Fe_2O_3) from outer space

1.3 Distribution of Temperature and Salinity for Ocean Waters

Much of our descriptive knowledge of the physics of the oceans comes from an examination of the properties of seawater from place to place. Our knowledge of the distribution of various properties comes from the collection of measurements made at oceanographic or hydrographic stations. Properties such as temperature, salinity (the grams of sea salt in 1 kg of seawater), and the concentration of oxygen, nutrients, and so on are measured as a function of depth. These measurements at a given station are plotted as a function of the depth (which can be related to the pressure, 10 m ~ 1 bar) and are called a vertical profile. Profiles from a string of stations can be combined to form a vertical section. The common values of a given property are connected to give a contour of the property of interest as a function of depth and distance. Similar contours of common properties can be made of surface waters and waters at a fixed depth (e.g., 4000 m). The contour lines can be used to elucidate the horizontal and vertical flow of waters from sinking, upwelling, mixing, precipitation, freezing, and so on. The basic assumption is that ocean waters within a given region have similar average properties over time. The variation with time, or temporal variability, can be observed from anchor stations, fixed buoys, floating instrument packages, and, for surface waters, from satellites.

The vertical distribution of the density of seawater controls vertical mixing in the oceans. Since the density of seawater is directly related to the temperature and salinity of ocean waters, it is useful to examine the typical distributions of these properties. The distribution of temperatures of ocean waters is zonal, with lines of constant temperature (isotherms) (see Figure 1.4). Near the western coast of both South America and Africa, however, the surface waters have lower temperatures because of upwelling. Open ocean

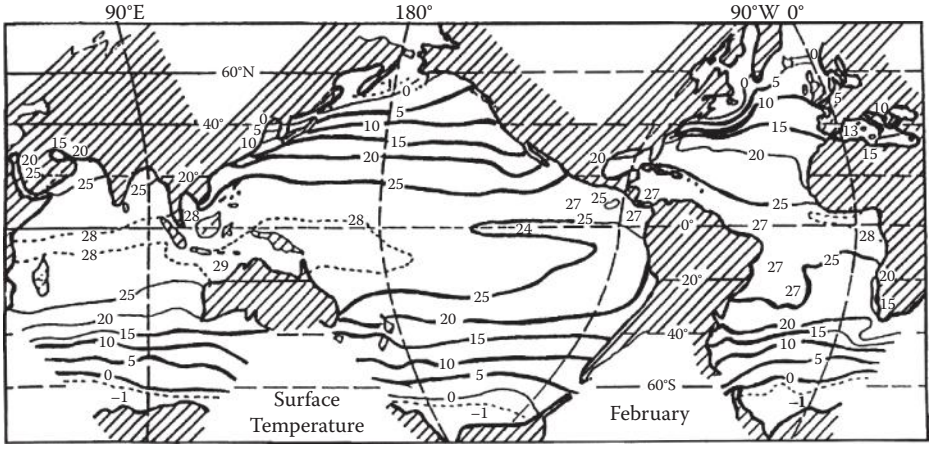

FIGURE 1.4
Temperature of ocean surface waters.

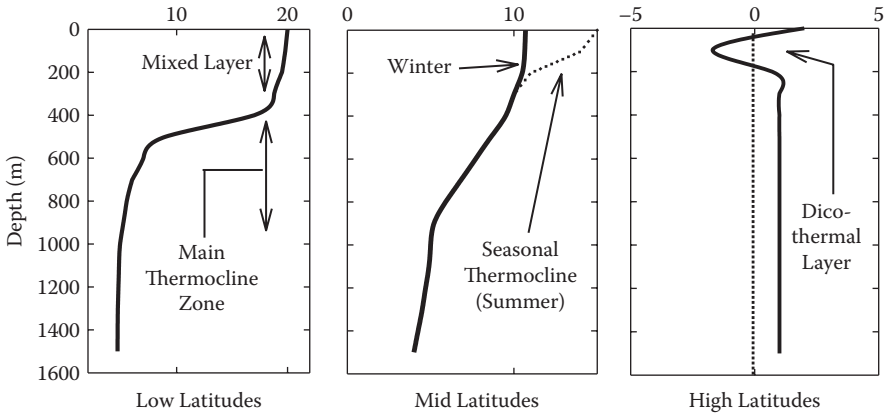

FIGURE 1.5
Typical temperature profiles in the ocean.

waters vary from –2°C (close to the freezing point) in polar regions to 28°C near the equator, although the temperature in confined areas can be as high as 40°C. The annual variations of temperature are about 2°C at the equator and poles, 8°C at 40° N or S, and as high as 15°C in coastal surface waters. The diurnal temperature variations are about 0.3°C in the open oceans and 2 to 3°C in shallow waters.

Typical temperature profiles are shown in Figure 1.5. Below the surface, the water can be divided into three zones. The upper zone, from 5 to 200 m, has similar temperatures to surface waters. Below this mixed layer, from 200 to 1000 m, the temperature decreases rapidly with depth (the zone with the maximum decrease is called the *thermocline*). In the deep zone, the temperature changes slowly with depth. In low-latitude waters, the surface mixed-layer temperatures will be about 20°C. The deep waters in this region will have temperatures between 5 and 2°C and be separated from the mixed layer by a permanent thermocline. In midlatitudes, the surface mixed layer will be about 15°C in the summer and will decrease to about 5 to 10°C in the winter. This change in temperature results in a seasonal thermocline in the summer months that disappears in the winter. This growth and decay of the thermocline is shown in Figure 1.6. The near-vertical distribution of temperature in the winter results in the mixing of the waters to a great depth and the replenishment of nutrients to the surface waters.

In high latitudes, the surface temperatures are much lower. The main thermocline may not be present, and only a seasonal thermocline may occur. Between 50 and 100 m, a dicothermal layer can develop. This layer of cold water at –1.6°C is sandwiched between the warmer surface and deep waters. The stability is maintained by an increase of salinity with depth through the layer.

The temperature of deep waters decreases to a depth of about 3000 m; in deep trenches, however, the *in situ* temperature increases slowly with depth owing to the effect of an increase in pressure. If seawater of S = 35 and t = 5°C were lowered to 4000 m adiabatically (not allowing heat to exchange with the surrounding water), the temperature would increase to 5.45°C from compression. An appropriate decrease in temperature of 0.45°C would occur if the waters were brought from 4000 m to the surface because of expansion. The potential or adiabatic temperature Θ is defined as the temperature of the water after it has been corrected for the adiabatic effect (5°C in the example). The *in situ* temperature at great depths in the oceans is higher than the potential temperature. An example of the

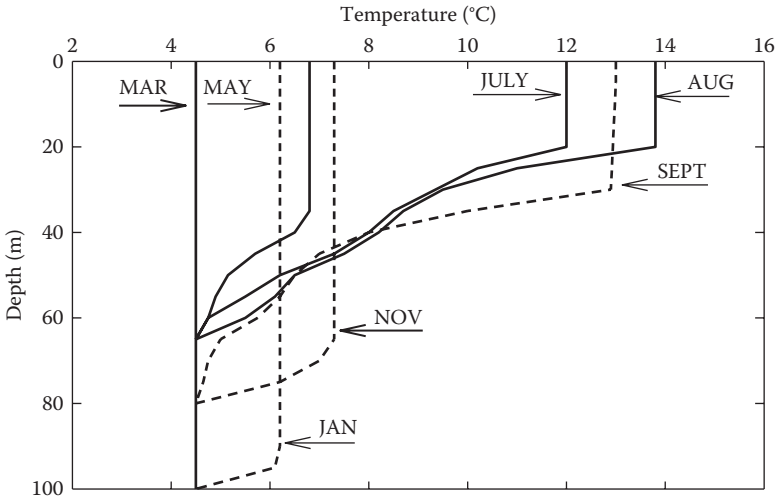

FIGURE 1.6
Growth and decay of the thermocline.

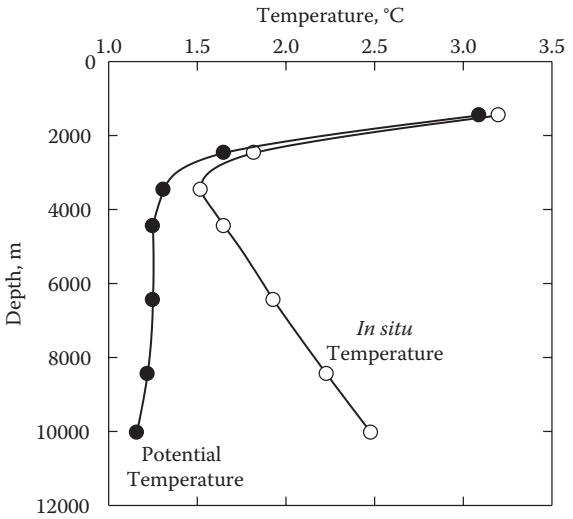

FIGURE 1.7
In situ and potential temperature in a deep-sea trench.

importance of potential temperature is shown for the temperature data in the Mindanao Trench (Figure 1.7). The *in situ* temperature (Table 1.1) of the deep waters is 2°C, which is higher than the waters above the trench. This leads to the calculated deep densities being higher than the waters above the trench. This is an unstable density structure and would result in the uplifting of these waters. The potential temperatures, however, show a smooth decrease with depth, and the densities increase slowly with depth, as expected for a stable water column.

TABLE 1.1

In situ and Potential Temperature in the Mindanao Trench

Depth	Salinity	Temp. (°C) *in situ*	Density (°C) Θ	σ_T	σ_Θ
1455	34.58	3.20	3.09	27.55	27.56
2470	34.64	1.82	1.65	27.72	27.73
3470	34.67	1.52	1.31	27.76	27.78
4450	34.67	1.65	1.25	27.76	27.78
6450	34.67	1.93	1.25	27.74	27.79
8450	34.69	2.23	1.22	27.72	27.79
10035	34.67	2.48	1.16	27.69	27.79

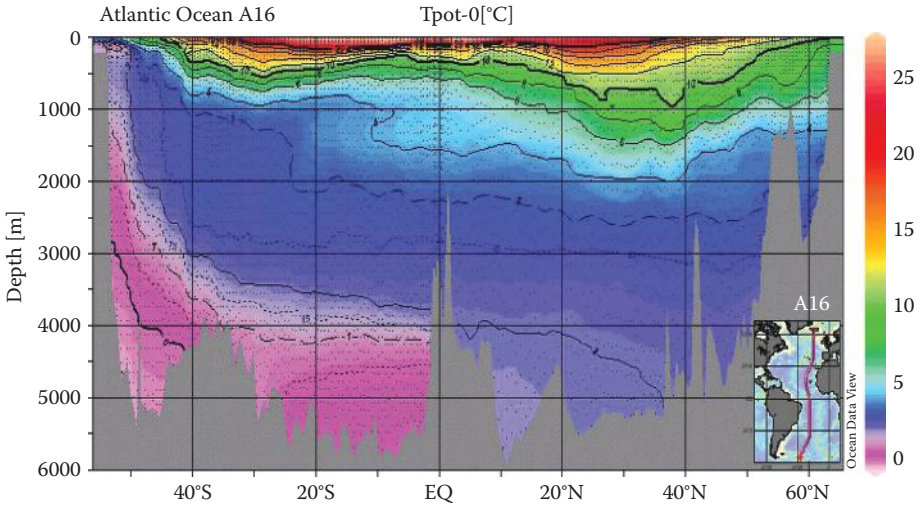

FIGURE 1.8
North-south section of potential temperature in Atlantic Ocean.

By connecting the constant temperature of various profiles (isotherms), it is possible to produce temperature sections for the major ocean basins. The resulting sections for the Atlantic, Pacific, and Indian Oceans are shown in Figure 1.8 to Figure 1.10, respectively.

The deep waters have similar temperatures (~2°C), while the surface waters show a great deal of structure. The convergence zones are clearly demonstrated in the South Atlantic, Pacific, and Indian Oceans. The upwelling in the equatorial regions on the coasts of Africa and South America bring cold, nutrient-rich waters to the surface.

A new satellite called *Aquarius* is making continuous measurements of the surface salinity of ocean waters. The initial results are shown in Figure 1.11. These surface values are affected by physical processes occurring in the waters.

The salinity will increase as a result of evaporation and freezing and decrease as a result of rain, river runoff, and the melting of ice. The difference between the evaporation and precipitation occurring at different latitudes controls the surface salinities. This is demonstrated in Figure 1.12. The decrease in the surface salinities near the equator are caused by greater precipitation, while the increase in the midlatitudes (30° N and S) is caused

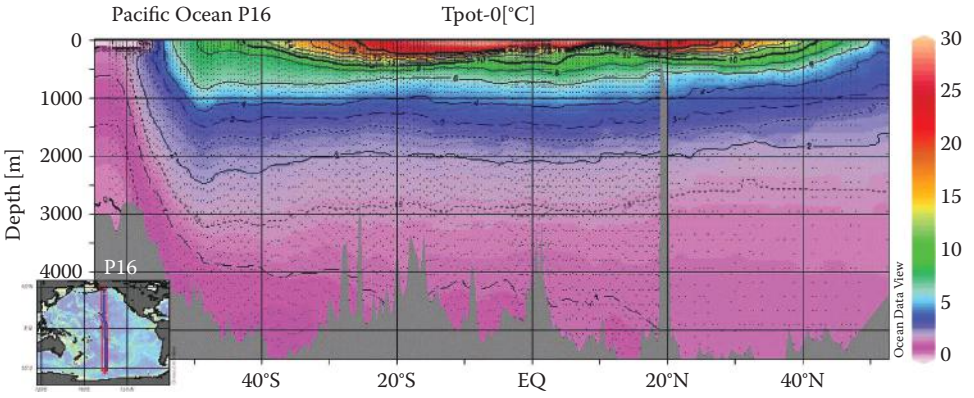

FIGURE 1.9
North-south section of potential temperature in Pacific Ocean.

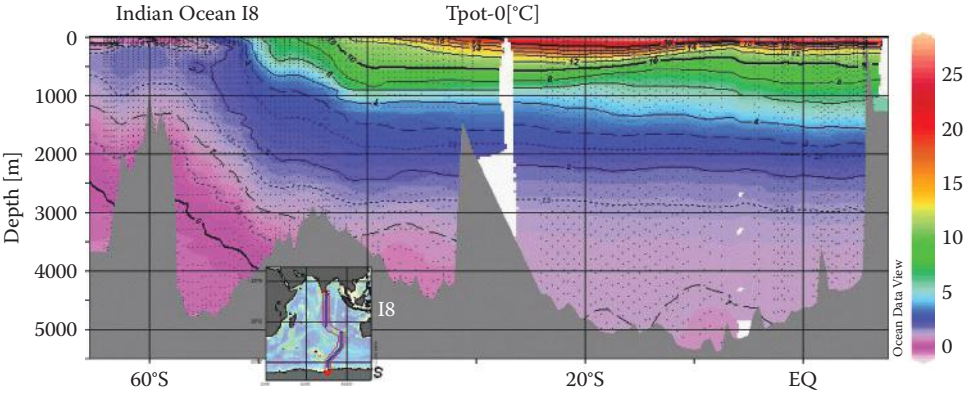

FIGURE 1.10
North-south section of potential temperature in Indian Ocean.

by higher rates of evaporation. The annual variation of salinity in the open oceans is 0.5, while the values range from S = 33 to 37. Higher values occur in regions of high evaporation such as the Mediterranean (S = 39) and Red Seas (S = 41). Values as high as S = 300 can be attained in closed lagoons during the summer in arid areas. The salinity of the North Atlantic surface waters is higher (S = 37.3) than North Pacific waters (S = 35.5).

The higher salinity of the North Atlantic surface waters is important because it leads to a higher density when the waters are colder. This in turn leads to the formation of deep waters in the North Atlantic, but not in the North Pacific. The late Bruce Warren (Woods Hole Oceanographic Institution) gave a clever answer to why the North Atlantic waters have a higher salinity than the North Pacific. The higher salinity exists because evaporation rates are about twice as high in the North Atlantic. This overcomes the higher river input into the Atlantic. The precipitation in both oceans is about the same. The lower evaporation rates in the North Pacific are due to the lower surface temperature. Cold waters have a lower specific humidity, which reduces the evaporation. This thermal effect is due to differences in the winds in the two oceans. In the Pacific, the maximum westerlies of the

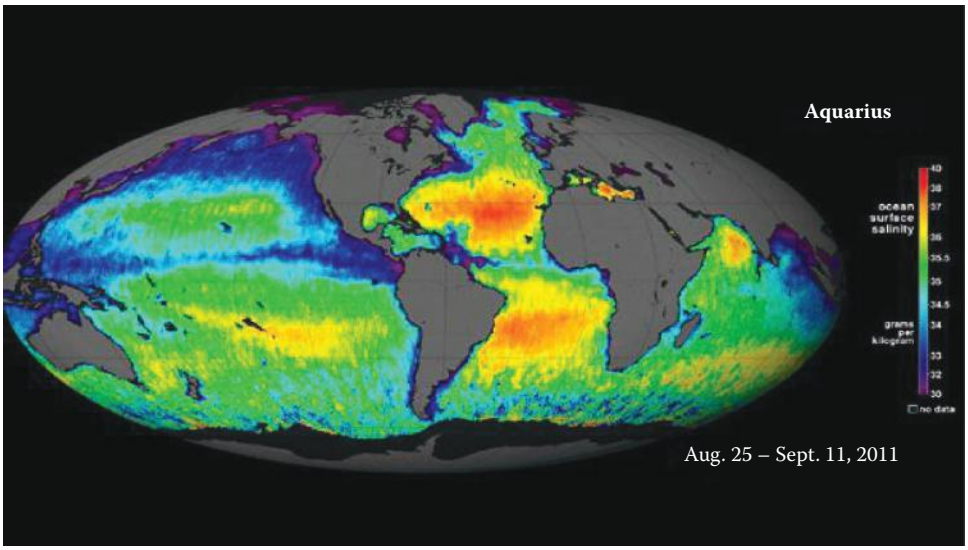

FIGURE 1.11
Salinity of ocean surface waters from satellite.

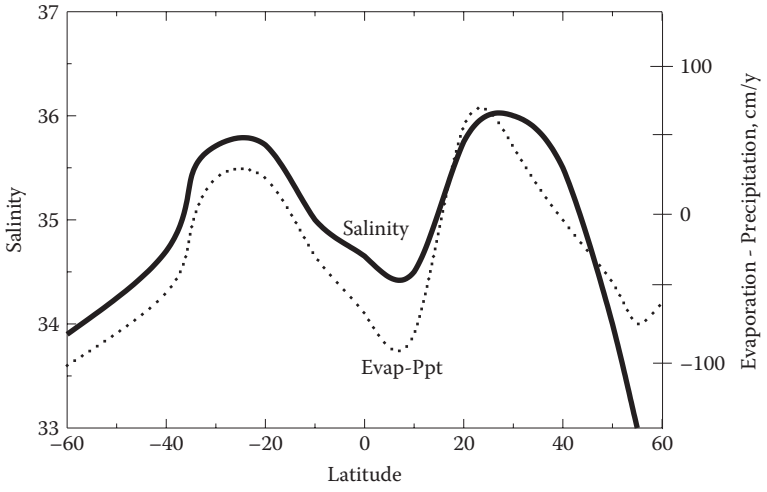

FIGURE 1.12
Surface salinity compared to evaporation minus precipitation (cm yr^{-1}).

wind field are further south. This limits the effectiveness of the winds to transfer warm subtropical water to the North. This may be a response to large-scale factors. The density of the North Pacific is thus reduced by lower evaporation at the lower temperatures. The inflow of water into the North Pacific matches the Ekman-induced upwelling in the subpolar gyre. The surface waters of the Pacific have a lower density because of the decrease in salinity caused by lower evaporation. In the North Atlantic, the densities are higher because of the increase in evaporation. This allows for deep-water formation.

Recent studies have suggested that a number of areas of the world ocean have higher or lower salinity due to evaporation and precipitation. Measurements with 3500 Argo floats

in the oceans over 50 yr indicated that this water cycle has increased by 4%, apparently due to surface warming of 0.5°C. This 8% increase/degree of warming is the expected rate on the amount of moisture the atmosphere can hold (Durack et al., 2012). The expected increase in temperature of 2 to 3°C will probably continue the process in the oceans and on land.

The typical vertical distributions of salinity in the Atlantic, Pacific, and tropics are shown in Figure 1.13. There is a marked salinity minimum at 600 to 1000 m in the Atlantic.

This is due to the movement of subantarctic intermediate water to the north. The maximum near 100 to 200 m in the tropics is close to the top of the thermocline. It results from water sinking at the tropical salinity maximum and flowing toward the equator. In high latitudes, the surface salinity values are low owing to the melting of ice. The salinity generally increases with depth to 2000 m with no subsurface maximum. In low and midlatitudes, the surface salinities are higher because evaporation is greater than rainfall. In coastal waters with river runoff, there is a strong, rapid increase in salinity (halocline) between the fresh river water and deep saline water. The salinity of deep water below 4000 m is quite uniform (34.6 to 34.9), while the temperature ranges from –1 to 2°C.

Sections of salinity for the Atlantic, Pacific, and Indian Oceans are shown in Figure 1.14 to Figure 1.16, respectively. The sections are in the intermediate waters (400 to 1500 m).

The Atlantic waters show the southern movement of North Atlantic deep water and the remaining core of high-salt water between 20° N and 30° N that may be caused by the input of Mediterranean waters. The North Pacific waters show the southern movement of subarctic intermediate water but no formation of deep water. In the Indian Ocean, no cold, deep waters are formed in the north because of the Asian land mass. Salty intermediate waters, however, are formed from the high-salinity waters coming from the Red Sea. A summary of the temperature and salinity of the world ocean waters is shown in Figure 1.17.

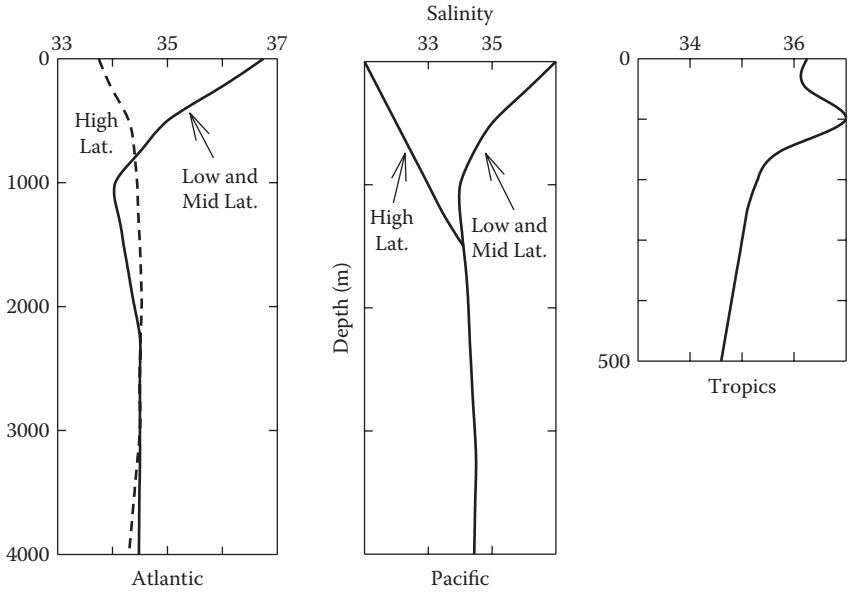

FIGURE 1.13
Typical salinity profiles in the ocean.

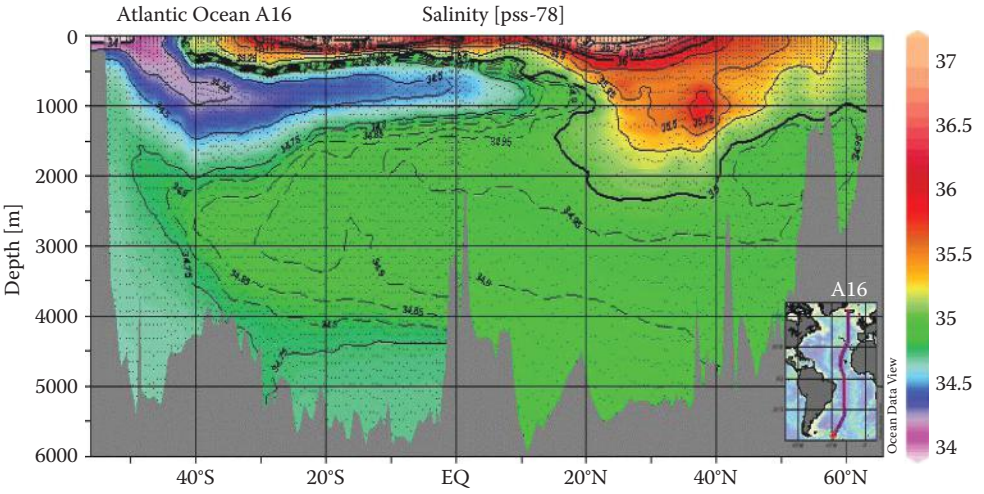

FIGURE 1.14
North-south section of salinity in Atlantic Ocean.

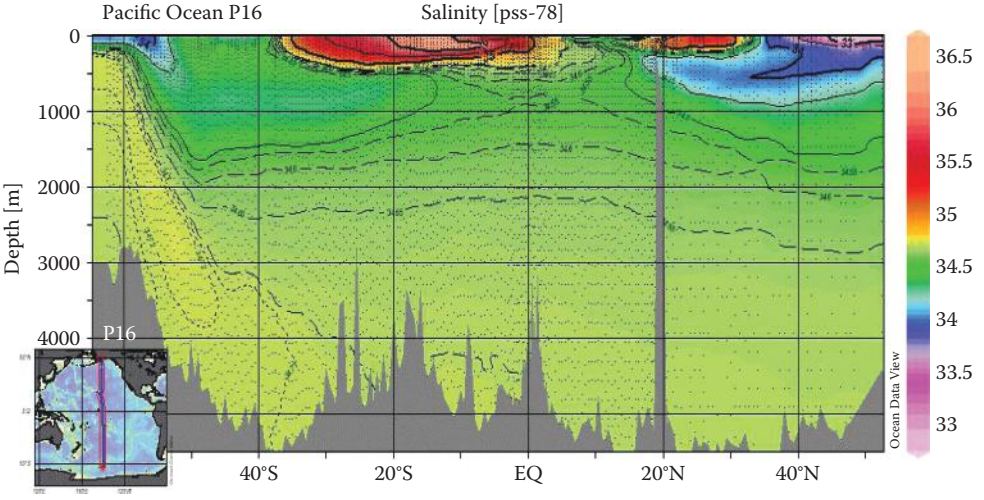

FIGURE 1.15
North-south section of salinity in Pacific Ocean.

The temperature and salinity of ocean waters control the density. The change in the density with depth is important because it determines the water's static stability. When the stability is high, vertical mixing is minimized. The density of ocean waters is normally characterized by the symbol σ_T, which is called sigma-T. This quantity is related to the density (ρ, kg m^{-3}) of seawater by

$$\sigma_T = (\rho - 1)\, 10^3 \tag{1.1}$$

The density of seawater as a function of salinity S and temperature T (°C) and pressure (P, bar) can be calculated from the international equation of state (Millero and Poisson, 1981; Millero et al., 1980) given in Table 1.2. More is said about the new Thermodynamic

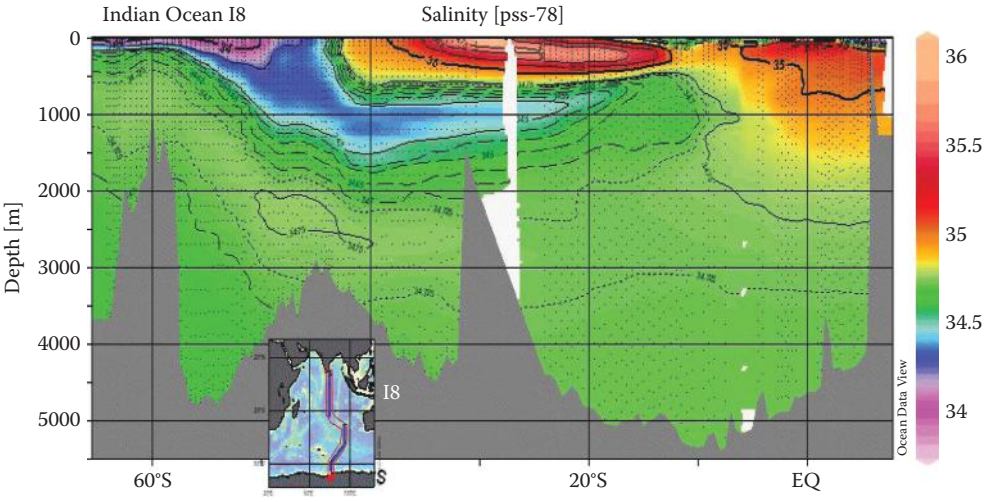

FIGURE 1.16
North-south section of salinity in Indian Ocean.

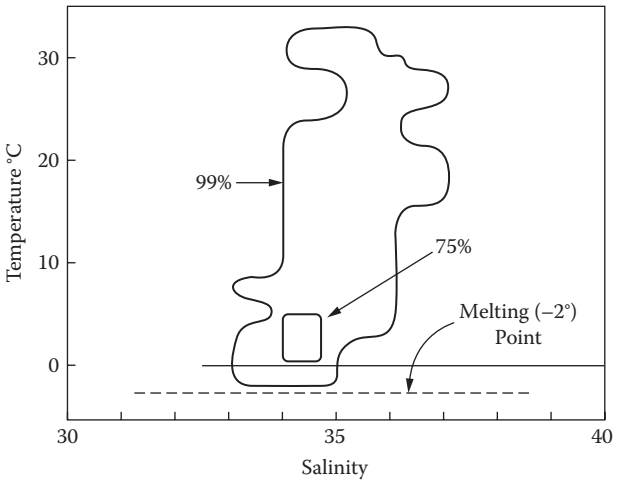

FIGURE 1.17
Temperature versus salinity for ocean waters.

Equation of Seawater 2010 (TEOS-10) in Chapter 2. A typical sigma-T profile is shown in Figure 1.18. The density normally increases with increasing depth. Minimum energy is obtained when the less-dense water is at the surface. The density of surface waters shown in Figure 1.19 is strongly affected by temperature, except in polar regions, where salinity becomes important.

In coastal waters, fjords, and estuaries, salinity often controls the density at all depths. It should be pointed out that a reasonable estimate of the density of rivers and lakes can be made from the seawater equation of state at the same salinity (Millero, 2000b). Deep waters in the oceans will have a higher density than the value calculated from the conductivity salinity because of the added nutrients and carbonate from the oxidation of

TABLE 1.2

The 1980 International Equation of State for Seawater ($m^3\ kg^{-1}$)

$$v^P = v^0(1 - P/K)$$
$$\rho^P = \rho^0[1/(1 - P/K)]$$

Where

$$\rho 0 = 999.842594 + 6.793952 \times 10\text{-}2\ t - 9.095290 \times 10^{-3}\ t^2 + 1.001685 \times 10^{-4} t^3 - 1.120083 \times 10^{-6}\ t^4 + 6.536336 \times 10^{-9}\ t^5 + (8.24493 \times 10^{-1} - 4.0899 \times 10^{-3}\ t + 7.6438 \times 10^{-5}\ t^2 - 8.2467 \times 10^{-7}\ t^3 + 5.3875 \times 10^{-9}\ t^4)\ S + (-5.72466 \times 10^{-3} + 1.0227 \times 10^{-4}\ t - 1.6546 \times 10^{-6}\ t^2)\ S^{1.5} + 4.8314 \times 10^{-4}\ S^2$$

$$K = 19652.21 + 148.4206\ t - 2.327105\ t^2 + 1.360477 \times 10^{-2}\ t^3 - 5.155288 \times 10^{-5}\ t^4 + S(54.6746 - 0.603459\ t + 1.09987 \times 10^{-2}\ t^2 - 6.1670 \times 10^{-5}\ t^3) - S^{1.5}\ (7.944 \times 10^{-2} + 1.6483 \times 10^{-2}\ t - 5.3009 \times 10^{-4}\ t^2) + P\ [3.239908 + 1.43713 \times 10^{-3}\ t + 1.16082 \times 10^{-4}\ t^2 - 5.77905 \times 10^{-7}\ t^3 + S\ (2.2838 \times 10^{-3} - 1.0981 \times 10^{-5}\ t - 1.6078 \times 10^{-6}\ t^2) + S^{1.5}\ (1.91075 \times 10^{-4})] + P^2\ [8.50935 \times 10^{-5} - 6.12293 \times 10^{-6}\ t + 5.2787 \times 10^{-8}\ t^2 + S\ (-9.9348 \times 10^{-7} + 2.0816 \times 10^{-8}\ t + 9.1697 \times 10^{-10}\ t^2)]$$

Check values:	S	t	P	v($m^3\ kg^{-1}$)	K(b)
	35	5°C	0 b	1,027.67547	22,185.93358
			1,000	1,069.48914	25,577.49819

Source: Millero, F.J., *Deep-Sea Res.*, **27**, 255, 1980; Millero, F.J., and Poisson, A., *Deep-Sea Res.*, **28**, 625, 1981.
Note: ρ is the density and K the secant bulk modulus, S is practical salinity, and $v = 1/\rho$ is the specific volume. The superscript 0 is for water and P is for pressure in bar.

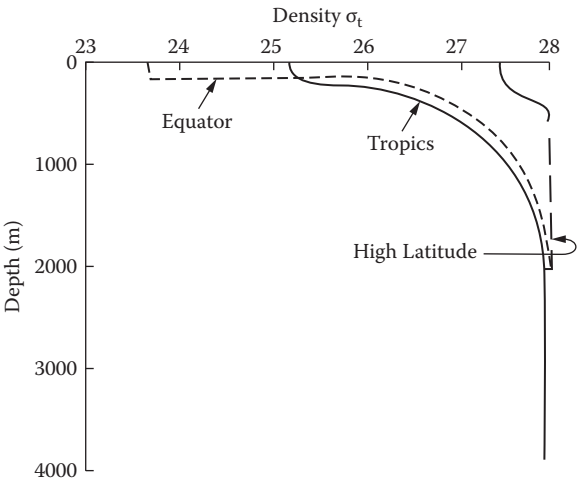

FIGURE 1.18
Typical sigma-T profiles in the ocean.

plant material and the dissolution of $CaCO_3$ (Millero, 2000a). In equatorial and tropical regions, there is a shallow upper layer of nearly uniform density, then a layer where the density increases rapidly. This depth region is called the *pycnocline*. Below this region, the density increases slowly with depth. Most deep waters have a σ_T near 27.9. At higher latitudes, the surface values of $\sigma_T = 27$, so that the increase of density with increasing depth is much smaller. For deep ocean waters the values of σ_T at the adiabatic temperature should be used to examine the stability of deep waters (i.e., σ_T, Θ).

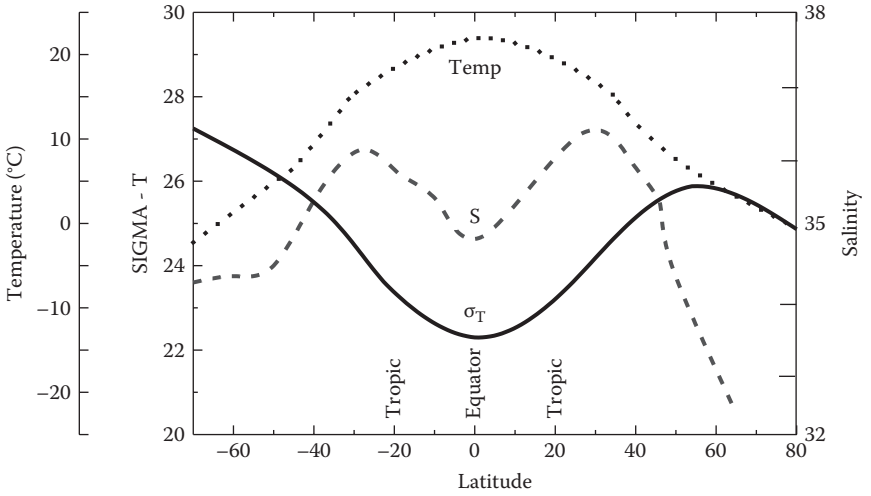

FIGURE 1.19
Comparison of sigma-T to temperature and salinity for surface waters.

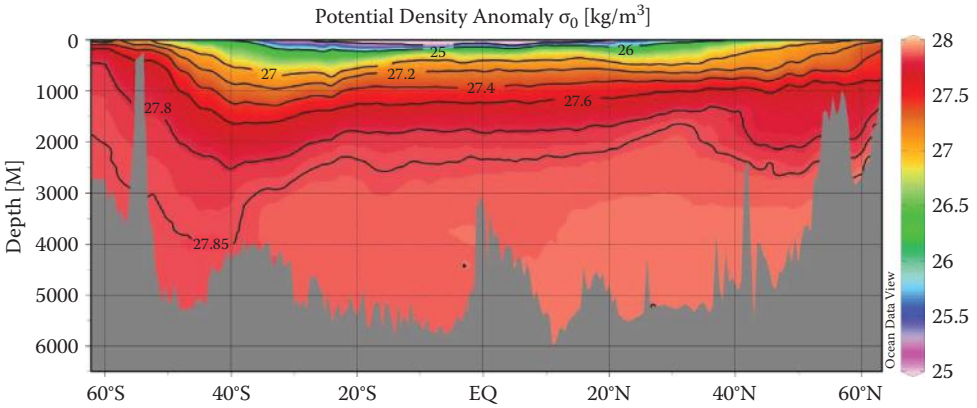

FIGURE 1.20
North-south section of sigma-T in the Atlantic Ocean.

The geographic distribution of density for the Atlantic in a north-south section is shown in Figure 1.20. The upper layers tend to be concave upward, showing an increase from the equator to the pole. Below 2000 m, the values of σ_T range from 27.6 to 27.9 for most deep waters. It should be pointed out that the flow of ocean waters tends to follow constant-density surfaces. One can frequently trace the origin of deep waters to the region of formation at the surface.

Although the densities of water masses can be arrived at by a number of possible combinations of S and T, one finds that only a limited number occur in different regions. Thus, it is possible to recognize a water mass by its characteristic combination of water properties. By plotting temperature against salinity (T-S plots) for individual oceanographic stations, it is possible to develop a characteristic diagram. The T-S relation for the major ocean waters is shown in Figure 1.21. It is not necessary to plot density on this

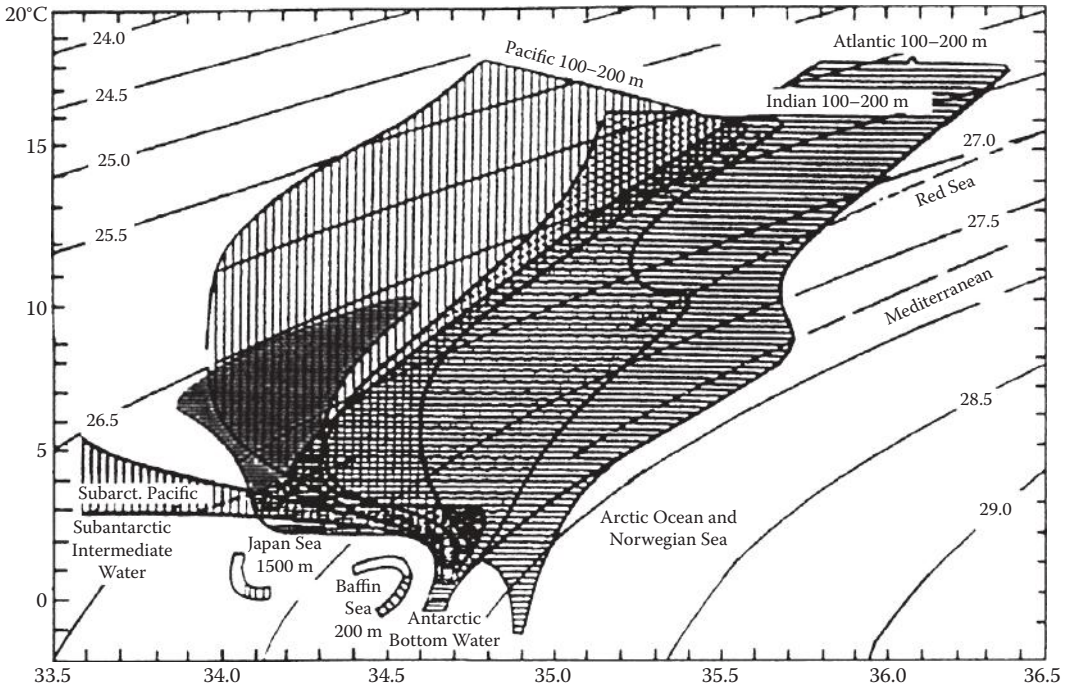

FIGURE 1.21
Temperature salinity (T-S) diagram for waters of the ocean.

diagram since it depends on T and S. Each point on this diagram corresponds to a particular combination of T and S and a given density.

The same density, however, can be attained by different combinations of T and S. These combinations lie on a smooth curve on the T-S diagram and can be shown as the dotted lines shown in Figure 1.21. When a T-S diagram is discussed, a water type is represented by a point and a water mass by a line. These are ideal definitions, and the actual data show some scatter. Climatic processes at the surface form water types, and water mass results from the mixing of two or more water types. Since surface waters are not normally conservative, they are omitted from T-S diagrams. The T-S diagrams have two disadvantages: (a) They give a poor indication of the distribution with depth of the water property because depth along a T-S diagram is not linear; (b) they give no indication of the spatial distribution of water properties. This is more clearly demonstrated using vertical or horizontal sections.

It is also possible to consider the volume of ocean waters with given properties of T and S. Montgomery was the first to suggest that T-S-V diagrams could be useful. A three-dimensional T-S-V diagram for the waters of the ocean is shown in Figure 1.22.

1.4 Circulation and Water Masses of the Oceans

The energy from the sun is responsible for the circulation of ocean waters. This circulation can be divided into two types:

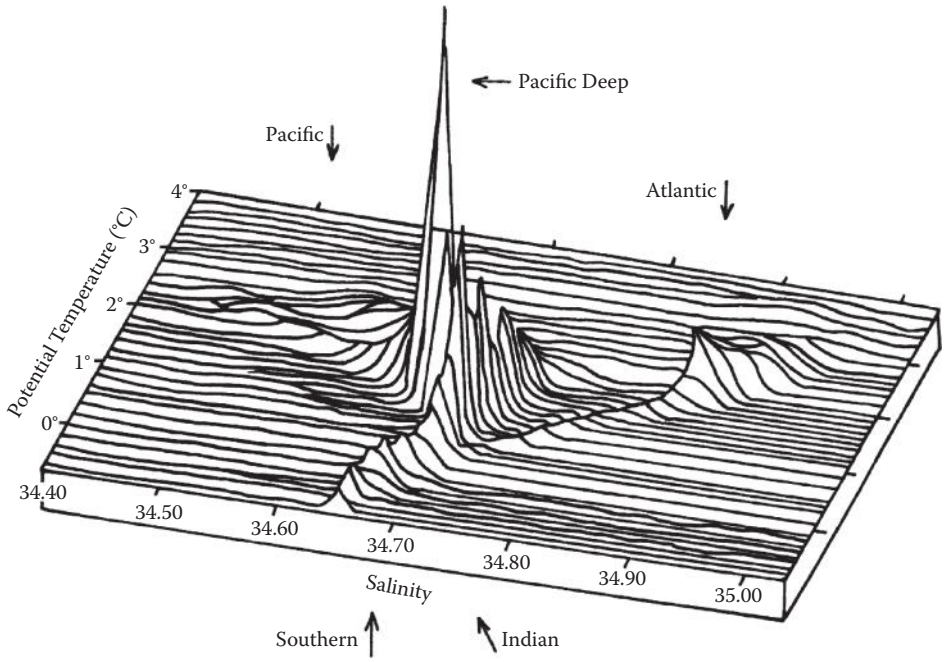

FIGURE 1.22
Three-dimensional distribution of ocean waters as function of potential temperature and salinity.

1. **Wind-driven circulation** is caused by the wind blowing over the surface waters. This affects the upper few hundred meters of the oceans, yielding primarily horizontal circulation.
2. **Thermohaline circulation** is caused by the movement of water because of density differences caused by changes in temperature and salinity. This leads to deep-sea and vertical circulation.

The processes that result in mixing are eddy diffusion, caused by concentration gradients, and advection, caused by currents. The pycnocline acts as a barrier to thermohaline mixing in the oceans.

The surface circulation of waters in the various oceans is similar and caused by the distribution of the major winds shown in Figure 1.23.

The trade winds and the westerlies combine to lead to a clockwise gyre in the Northern Hemisphere and a counterclockwise gyre in the Southern Hemisphere (see Figure 1.24).

In the Northern Hemisphere, the waters have a right-hand component because of the spinning of the earth. This so-called Coriolis effect has a left-hand component in the Southern Hemisphere. In the North Atlantic and the Pacific, the currents are narrower and faster on the western side of each ocean. This westward intensification results in the Gulf Stream in the North Atlantic and the Kuroshio Current in the North Pacific. When the trade winds from the north or south cross the equator, the Coriolis effect causes a countercurrent in a direction opposite to that of the major gyres. The surface currents of the oceans are divided into a number of separate currents.

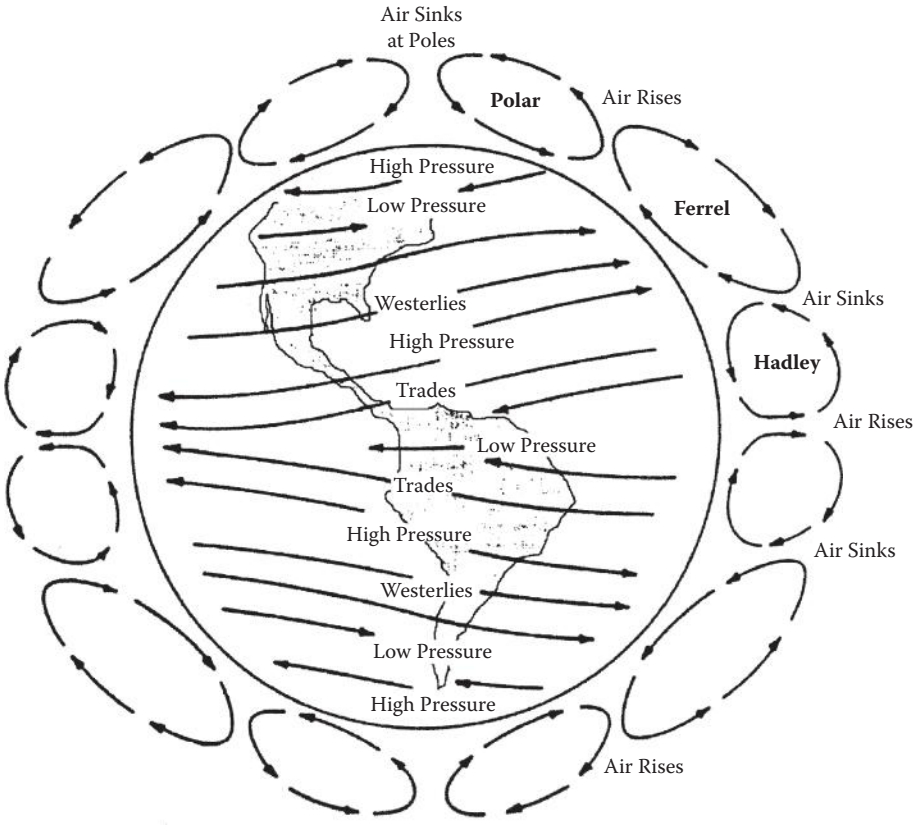

FIGURE 1.23
The major wind systems of the earth.

1.4.1 Atlantic Ocean Waters

As shown in Figure 1.25, the upper water circulation of the Atlantic Ocean consists of two gyres: (a) a clockwise gyre in the north and (b) a counterclockwise gyre in the south. In the north, the gyre starts with the North Equatorial Current that is driven by the northeastern trade winds. It is joined by the South Equatorial Current and becomes the Antilles Current off the West Indies. The Florida Current comes from waters that go through the Yucatan and Gulf of Mexico (called the Gulf of Mexico Loop Current) and escapes between Florida and Cuba into the Atlantic. The Gulf Stream is the northern extension of the Florida Current, which joins with the Antilles Current. The flow of the Florida Current waters is about 26×10^6 m^3 s^{-1} (26 Sv [Sverdrups]). The Antilles Current has a flow rate of about 12 Sv, and the flow rate of the Gulf Stream off the Chesapeake Bay is about 80 Sv. The North Atlantic Current is a continuation of the Gulf Stream. The Labrador Current waters flow south out of the Labrador Sea. This cold, low-salinity water mixes with the warm Gulf Stream water, causing a complicated mixing regime. Part of the North Atlantic Current continues toward the Arctic and becomes the Norwegian Current. The remainder goes south to complete the gyre. The waters flowing off the coast of Africa are called the Canary Current.

In the South Atlantic, the counterclockwise gyre starts near the equator because of the stress of the southeast trade winds, causing the South Equatorial Current to move toward

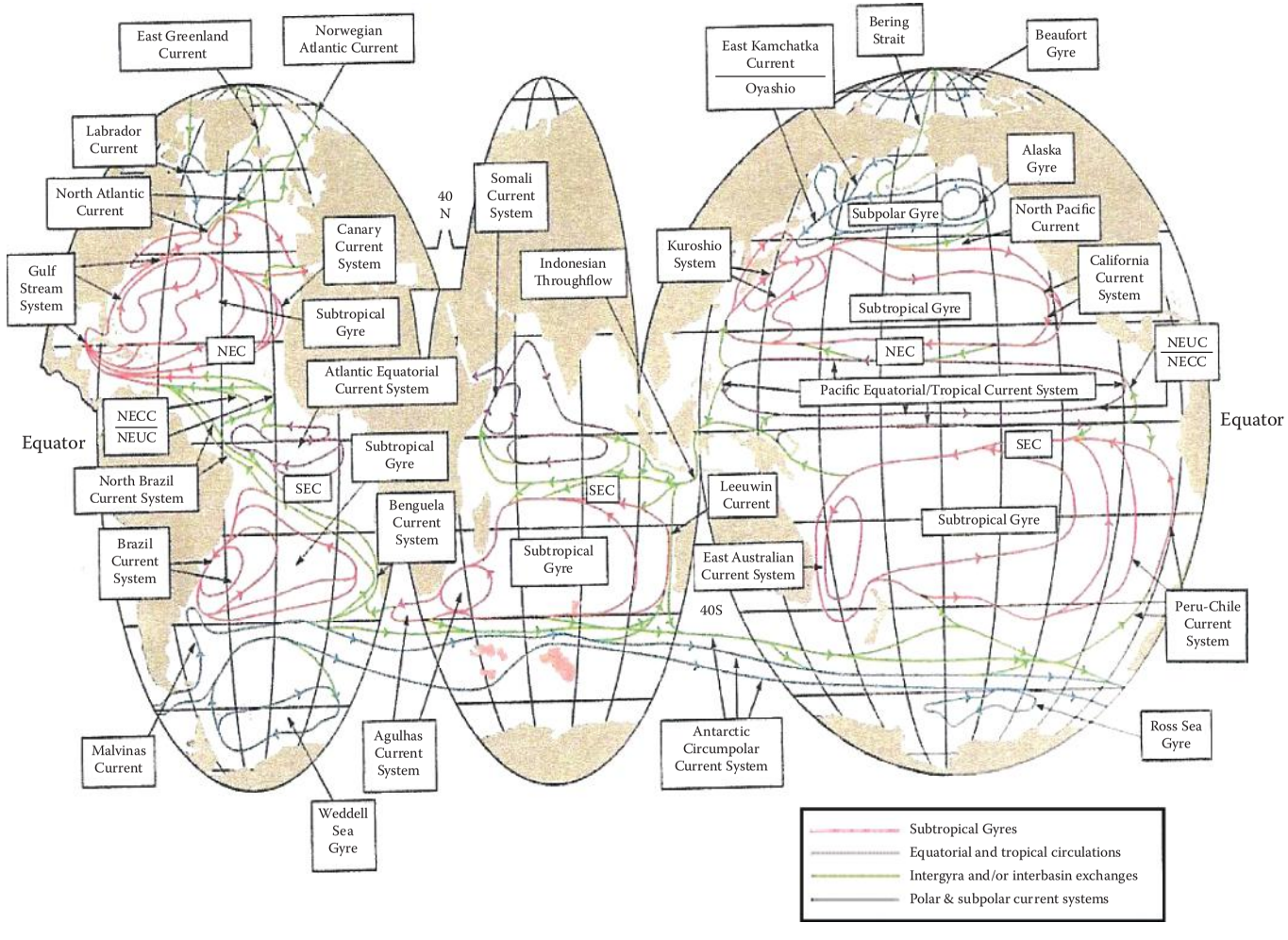

FIGURE 1.24
The surface currents of the oceans.

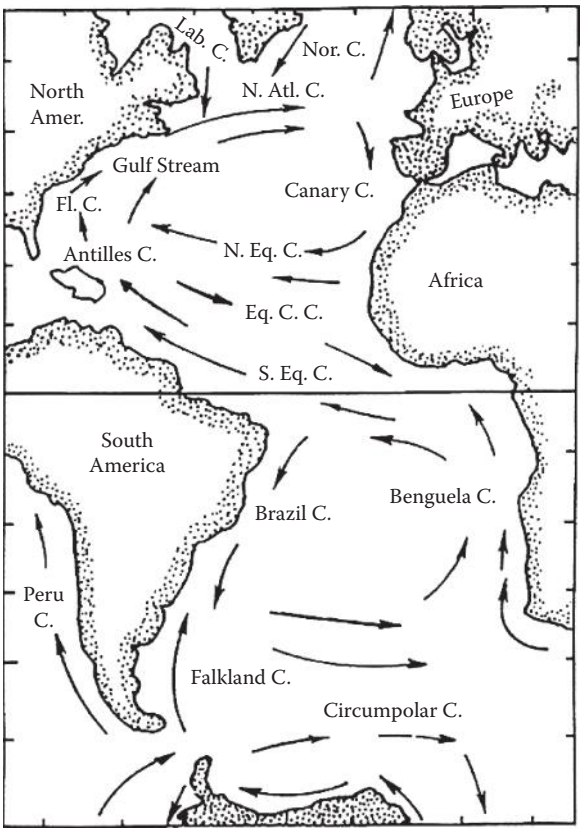

FIGURE 1.25
The surface currents of the Atlantic Ocean.

Central America. Part goes north and part goes south. The southern component is called the Brazil Current. This current turns east at the subtropical convergence and becomes part of the Circumpolar Current. It turns north off the coast of Africa and becomes the Benguela Current. The Brazil Current is warm and salty water, while the Circumpolar Current is cold and less saline. The Falkland Current flows north from the Drake Passage up the coast of South America. It separates the Brazil Current from the coast to about 25° S.

One of the most studied currents in the Atlantic is the Gulf Stream. Studies have been made on the formation of Gulf Stream rings. These rings are formed from the meandering of the Gulf Stream (see Figure 1.26). Two types of rings are formed: cold core rings and warm core rings. The cold core rings are formed from the waters north of the Gulf Stream. This colder slope water forms a counterclockwise gyre that moves to the south. These rings (The Ring Group, 1981) can exist for 2 to 4 yr but usually rejoin the Gulf Stream after 6 to 12 months. The warm core rings are formed from the closure of a ring of warm Sargasso Sea water. This clockwise gyre of warm water moves toward the north.

The cold core rings are rich in nutrients and support increased productivity in these waters. The temperature structure of a typical ring is shown in Figure 1.27. The cold, nutrient-rich waters are brought toward the surface as a result of the circulation. This increase in nutrients results in the productivity of plankton in the rings. By using satellite images (Figure 1.28), it is possible to study the formation and destruction of rings by

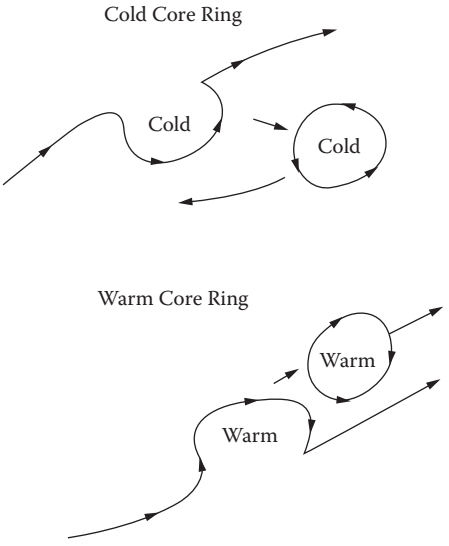

FIGURE 1.26
The formation of Gulf Stream rings.

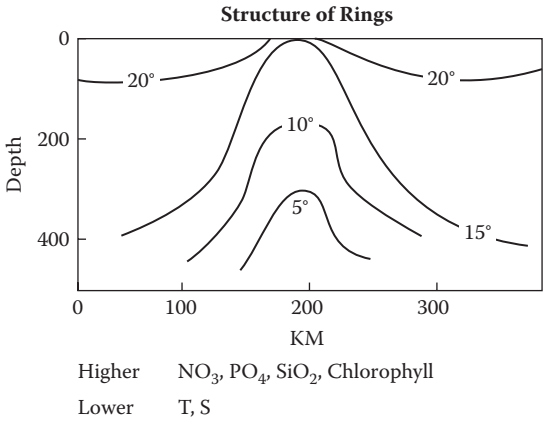

FIGURE 1.27
The temperature of a Gulf Stream ring.

remote sensing techniques. This satellite information is also very useful in positioning ships in a ring and tracking a ring as a function of time. More recently, these satellite images have been used to locate fronts that may be areas of high concentrations of fish.

The water masses in the Atlantic have been studied for some time. Two expeditions, the Meteor in 1925–1927 and the International Geophysical Year in 1957–1958, supplied the earlier data, while more recently, the GEOSECS, TTO (Transient Tracer in the Oceans), and WOCE programs have provided physical and chemical data for the Atlantic. The T-S diagram for water masses in the Atlantic is given in Figure 1.29. The upper waters below the surface are called Atlantic central waters. They extend to depths of 300 m on either side of the equator and deepen to 600 to 900 m at midlatitudes. These waters are thought to be formed by the sinking of waters on the equatorward side of the subtropical convergence. The cooler, less-saline water sinks at higher latitudes. The more saline, warmer

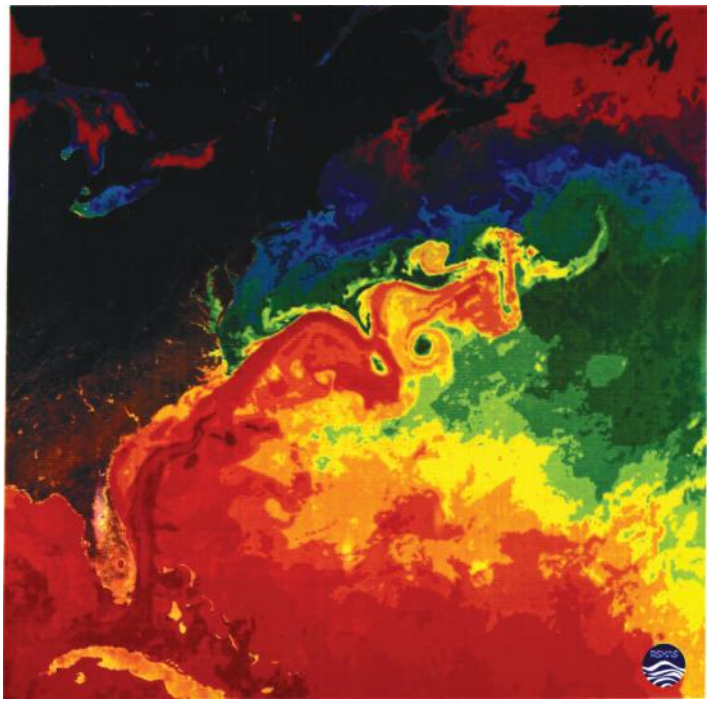

FIGURE 1.28
Satellite photograph of the temperature structure of the Gulf Stream.

water sinks at lower latitudes and flows toward the equator. In the South Atlantic, the central water terminates at a depth where it merges with the Antarctic intermediate water. In the North Atlantic, the Arctic intermediate water is not as dominant. The Atlantic central water merges into this Arctic water at high latitudes in the North Atlantic and into Mediterranean water at low latitudes. The effect of the Mediterranean water can be demonstrated by examining the horizontal section of salinity at a depth of 1000 m (Figure 1.29).

The temperature (Figure 1.8) and salinity (Figure 1.14) sections for the Atlantic shown previously (as well as the O_2 section to be shown in Chapter 6) demonstrate that the great bulk of Atlantic water is deep water. The major source of this North Atlantic deep water is the Norwegian Sea. This water flows over the sills between Scotland, Iceland, and Greenland and sinks into the deep Atlantic. This flow is not continuous but occurs in pulses. The salinity is 34.9, and the temperature is between 2 and 3°C for most of the North Atlantic deep waters.

The bottom waters in the western and eastern basins of the South Atlantic are different because of the separation of the Mid-Atlantic Ridge. On the western side, the bottom water has temperatures down to 0.4°C, while on the eastern side the minimum is 2.4°C. The bottom waters are prevented from flowing into the eastern basin by the Walfish Ridge, which has a sill depth of 3500 m. The salinity difference is not as dramatic (34.7 on the west and 34.9 on the east).

Earlier tritium measurements by Ostlund and coworkers in Miami have clearly demonstrated the speed of the formation of North Atlantic deep waters. Their results for tritium in the North Atlantic obtained from the earlier GEOSECS and TTO studies are shown in Figure 1.30. The measurements show the deep southward penetration of tritium, which

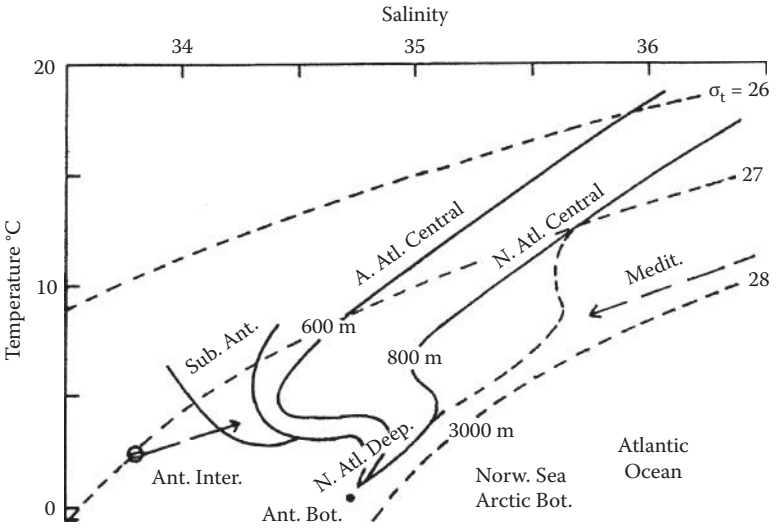

FIGURE 1.29
The T-S diagram for the Atlantic Ocean.

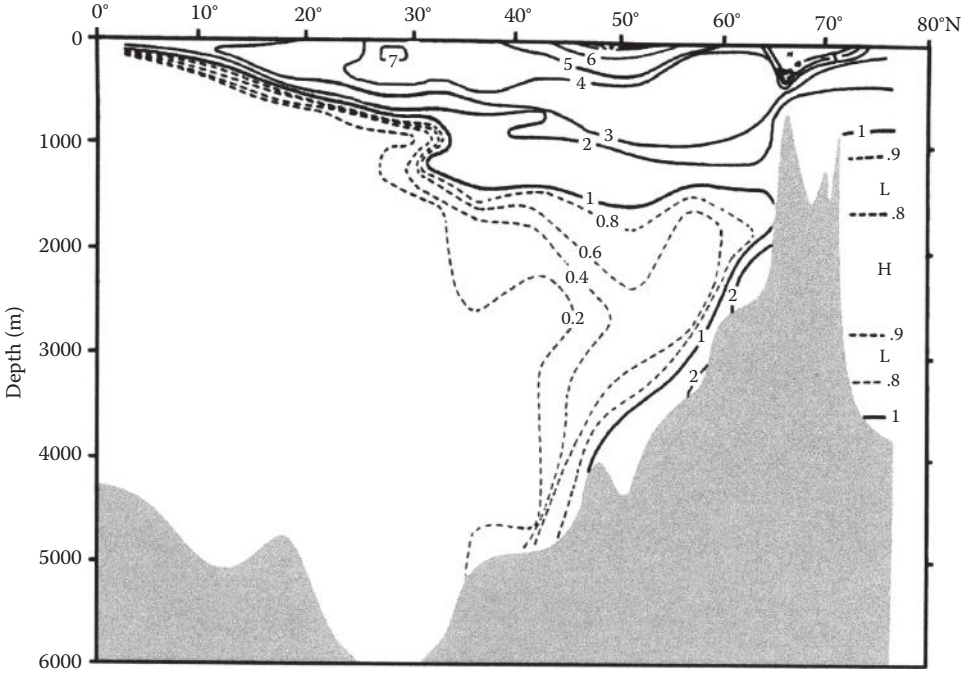

FIGURE 1.30
North-south section of tritium in the Atlantic Ocean.

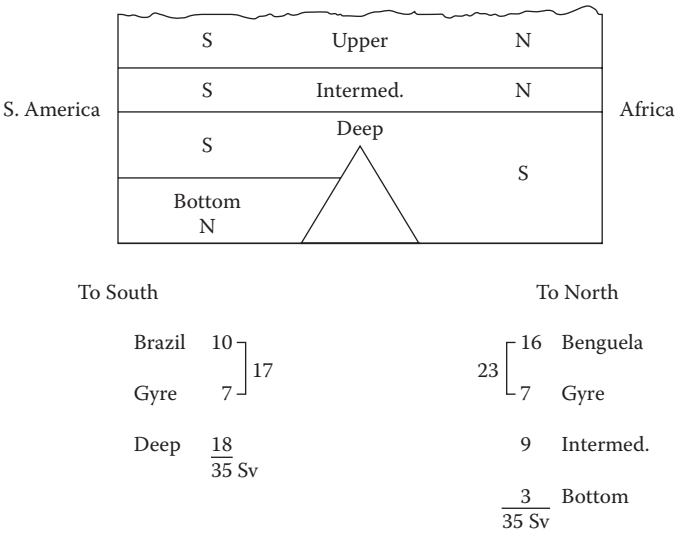

FIGURE 1.31
The balance of water masses in the South Atlantic.

has a half-life $t_{1/2}$ of 12 yr and entered the North Atlantic waters after the 1960 atomic bomb tests. The TTO measurement made about 10 yr after the GEOSECS work shows the further movement of North Atlantic deep waters.

A summary of the balance of water masses for the South Atlantic is shown in Figure 1.31. The southward flow consists of 17 Sv of surface waters and 18 Sv of deep waters. The northward flow consists of 23 Sv of upper gyre waters, 9 Sv of Antarctic intermediate waters, and 3 Sv of Antarctic bottom waters.

Another feature of the circulation of the Atlantic waters that should be mentioned is the vertical circulation in the equatorial regions (shown in Figure 1.32). There is a general upwelling that is revealed in the profiles of salinity and temperature described previously. These features bring cold, nutrient-rich waters near the surface and support primary productivity near the equator. Studies have also examined the countercurrents near the equatorial regions. More will be said about this when discussing the Pacific Ocean waters.

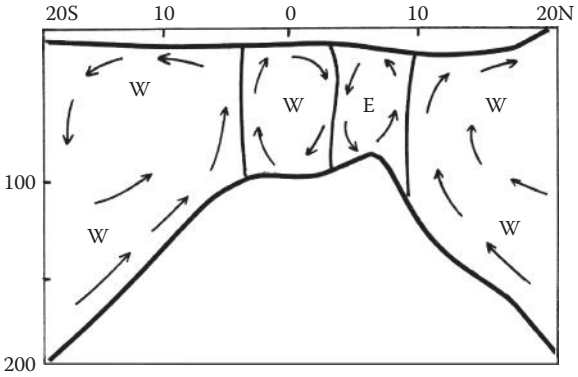

FIGURE 1.32
Vertical circulation in the Equatorial Atlantic.

1.4.2 Southern Ocean Waters

Surface water circulation in the southern oceans is controlled by the circumpolar and polar gyres, which are driven, respectively, by the west wind drift (clockwise) and east wind drift (counterclockwise) (see Figure 1.33). The surface circulation is strongly affected by a number of convergence zones, shown in Figure 1.34. Going north from Antarctica, the surface sea temperature increases slowly until a region is reached, where it rapidly increases by 2 to 3°C. This convergence zone is called the *Antarctic convergence*. This zone occurs at about 50° S in the Atlantic and Indian Oceans and 60° S in the Pacific Ocean. The region from the continent to the Antarctic convergence is called the Antarctic zone. The surface temperatures of waters in this zone are –2 to 1°C in the winter and –1 to 4°C in the summer. Salinities are less than 34.5 because of the melting of ice and because the colder surface waters moving north sink in this region and continue to flow north. This water mass is called the Antarctic intermediate water and mixes with the North Atlantic deep water as it moves north. It is about 500 m thick and has a temperature of 2°C and salinity of 33.8. It has a σ_T of 27.0 and forms a low-salinity tongue with its center at 800 to 1000 m at 40° N. It also has a high O_2 concentration (220 to 300 μM) when it leaves the surface.

North of the Antarctic convergence, the temperature rises slowly to a region where it rapidly rises by about 4°C with a salinity increase of 0.5. This region is called the subtropical convergence. It occurs at about 40° around most of the Antarctic, but it is poorly defined in the eastern South Pacific. The area between the Antarctic and subtropical convergence is called the subantarctic zone. It has surface temperatures of 4 to 10°C in the winter and up to 14°C in the summer. The salinity is 33.9 to 34.9 in the winter and as low as 33 in the summer when the ice melts. The strong circumpolar current has a northern component because of the Coriolis force (from the rotation of the earth). The speed of this current

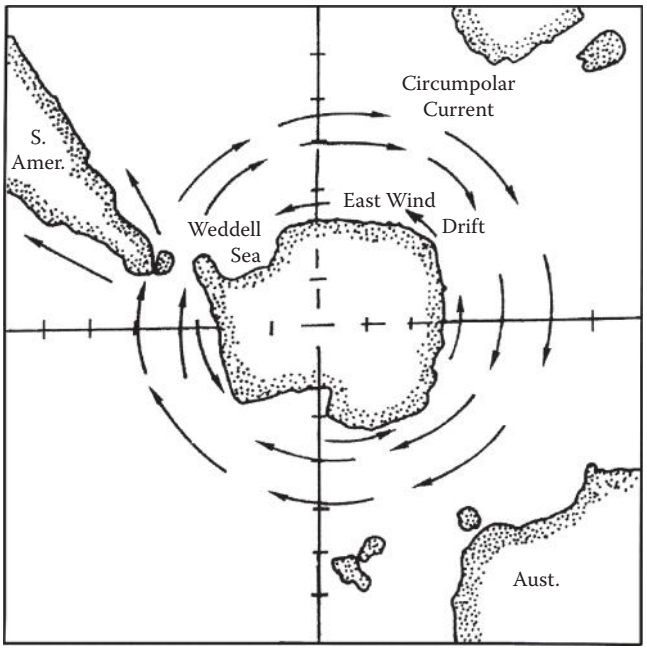

FIGURE 1.33
The surface currents of the Southern Ocean.

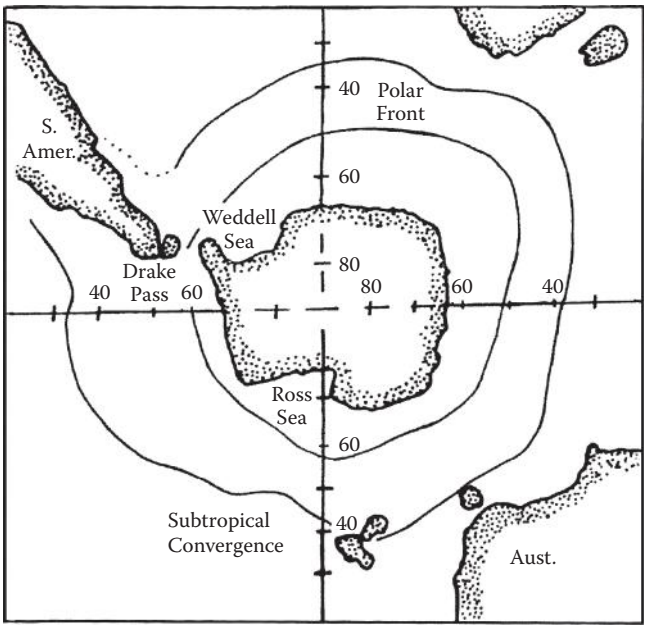

FIGURE 1.34
The convergence zones of the Southern Ocean.

varies from 4 cm s^{-1} in the Antarctic zone to 15 cm s^{-1} north of the Antarctic convergence. It has the largest volume flow of all the water masses (150 to 190 Sv). A sketch of the water masses in the southern oceans is shown in Figure 1.35. The circumpolar water extends from the surface to 400 m. At 400 m, it has a temperature of 2.5°C and a temperature of 0°C at the bottom. The salinity is 34.7 for the circumpolar water. It is made up of North Atlantic deep water with some mixing with surface and intermediate waters.

Antarctic bottom water is formed in the Weddell and Ross Seas. It is a mixture of circumpolar water and shelf water (t = –1.9°C, the freezing point of seawater; S = 34.6; σ_T = 27.9, the highest value in the Southern Ocean). The bottom water is formed at a high density (σ_T = 27.9) and flows down the continental slope northward in the Atlantic, Indian, and Pacific Oceans. As it moves north, it mixes with deep water, and the temperature rises to 1.5°C and the salinity goes from 34.7 to 34.8.

As mentioned, Antarctic intermediate water forms at the Antarctic convergence. It includes Antarctic surface water and circumpolar water. It moves north in the Atlantic, Indian, and Pacific Oceans, mixing with deep waters and surface waters. The deep water in the Southern Ocean comes from the North Atlantic deep water, which is circulated as part of the circumpolar current. It moves toward the north in the Indian and Pacific Oceans and lies between 1500 and 3000 m in the subantarctic region (t = 2 to 3°C and S = 34.6 to 34.8). This "warm" deep water is sandwiched between the colder intermediate and bottom waters. The North Atlantic origin of deep waters was suggested by earlier oceanographers to be due to the similarities in their temperature and salinity (t ~ 2°C and S = 34.9). These waters lose O_2 and gain nutrients as they make their tour from the North Atlantic to the North Pacific.

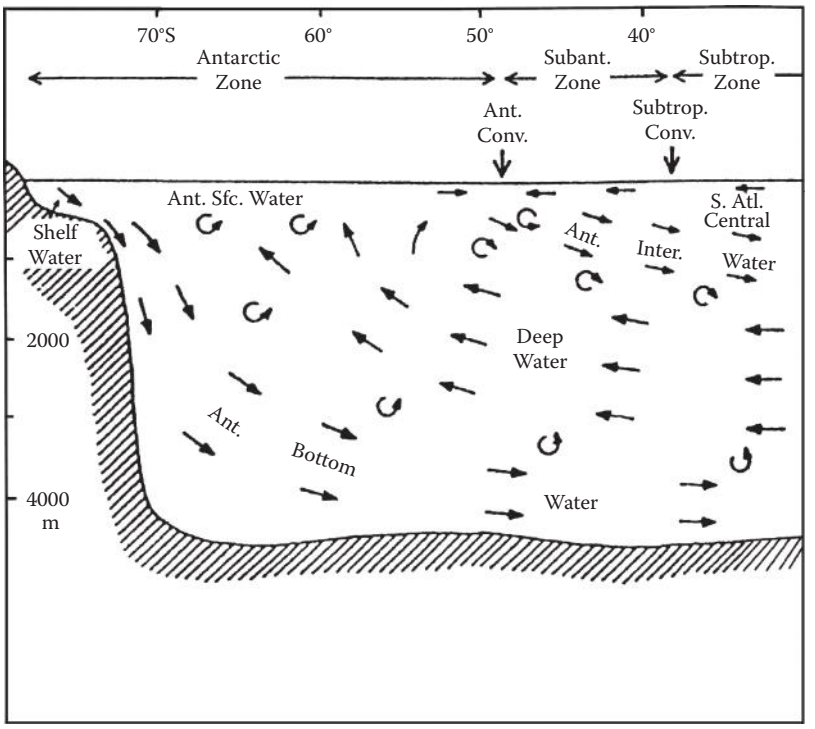

FIGURE 1.35
South-north section of water masses in the Southern Ocean.

1.4.3 Pacific Ocean Waters

Surface water circulation in the Pacific is similar to the Atlantic (see Figure 1.36). In the North Pacific, there is a clockwise gyre, and in the South Pacific, there is a counterclockwise gyre. The equatorial currents are more distinguishable in the Pacific because of its larger size. The North and South Equatorial Currents flow toward the west and represent parts of the two major gyres. Both are driven by the trade winds. The North and South Equatorial Countercurrents flow toward the east. The North Equatorial Current has surface speeds of 25 to 30 cm s^{-1} and volume flows of 45 Sv. The Equatorial Countercurrent has speeds of 35 to 60 cm s^{-1} except in the spring (March and April), when it decreases to 20 cm s^{-1}. The countercurrents extend to depths of 1500 m and have volume transports as high as 60 Sv. At the equator, there is an undercurrent called the Cromwell Current, which is below the sea surface (200 m in the west to 40 m in the east). It is only 0.2 km thick but 300 km wide and has a length of 14,000 km. The speeds are up to 170 cm s^{-1}, and the maximum volume transports are 70 Sv (the average is 40 Sv). This current was discovered by Buchanan in 1886 during the *Challenger* expedition but was forgotten until rediscovered by Cromwell, Montgomery, and Stroup in 1952.

No major transport of water from the South to North Pacific Ocean occurs near the equator in the Pacific. The North Pacific does have a strong western boundary current like the Atlantic. It is called the Kuroshio Current and Extension. Its volume flow is about 65 Sv. It also meanders like the Gulf Stream, and eddies or rings are formed. The California Current

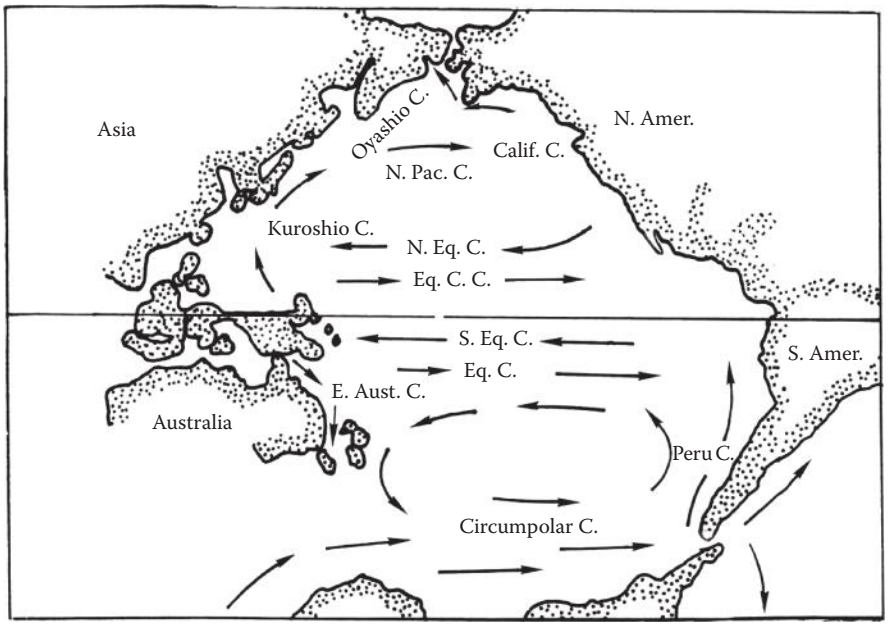

FIGURE 1.36
The surface currents of the Pacific Ocean.

in the North and Peru or Humboldt Current in the South Pacific results in upwelling along the coasts. Both currents bring cold water toward equatorial regions and influence the climate in these areas. The Peru Current turns west between January and March at a few degrees south of the equator. The North Equatorial Countercurrent follows it south and brings warm water near the coast. This phenomenon is called "El Nino" because it occurs near Christmas. This increase in temperature kills fish and increases the evaporation from the ocean and precipitation on the land, resulting in floods. In recent years, a number of studies have been made on El Nino in attempts to predict its behavior caused by processes occurring in the Eastern Pacific.

The water masses in the Pacific are more complicated than the Atlantic because of its size. The salinity of surface waters shows a maximum in the tropics like the Atlantic, but the values in the North Pacific are lower than in the North Atlantic. The salinities in the South Pacific are greater than in the North Pacific but less than the South Atlantic. As discussed, this is related to the high evaporation rates in the Atlantic. The surface temperatures of the Pacific waters are highest near the equator and in the western basin due to the circulation from the North and South Equatorial Currents. The lower temperatures off the coast of Peru are due to the upwelling. The winds off the coast move the surface water off the shelf, and they are replaced with cold, nutrient-rich intermediate waters (~500 m). The waters between 100 and 800 m in the Pacific are called central waters.

The waters between 20° N to 10° N are the most saline waters in the Pacific. The surface waters are separated from the Pacific equatorial waters by a strong thermocline. Vertical transport is prohibited; the discontinuation layer is 150 to 200 m in the west and 50 m or less in the east. It can reach the surface off the west coast of Central America (called the Costa Rican thermal dome). A salinity maximum occurs in the equatorial waters as with the Atlantic. At about 800 m, the salinity goes through a minimum because of the flow,

south, of Arctic intermediate waters and the flow, north, of Antarctic intermediate waters. The Pacific subarctic waters (S = 33.5 to 34.5 and t = 2 to 4°C) are more extensive than the Atlantic subarctic waters. They are formed at the subarctic convergence (western Pacific) between the more saline Kuroshio Extension and the cold Oyashio Current waters.

The Antarctic intermediate waters in the Pacific (t = 2.2°C and S = 33.8) form at the Antarctic convergence. It is limited in its northern extension by the Pacific equatorial waters. In the Atlantic, the equatorial waters are not as clearly defined, and the intermediate waters go across the equator. The North Pacific intermediate waters are delineated by a salinity minimum at 800 m in the west and 300 m in the east. These waters appear to circulate in a clockwise gyre similar to surface waters. The high O_2 values indicate that the waters are replenished with surface waters. Reid (1973) has pointed out, however, that the density of these waters differs from those at the surface. He thus concluded that these intermediate waters attain their properties below the surface.

The deep Pacific waters (2000 m to the bottom) have temperatures of 1.1 to 2.2°C and salinity of 34.65 to 34.75. The salinity increases or remains constant with depth, unlike the Atlantic, where a salinity maximum is observed. The reason for the uniformity is that no deep water is formed in the North Pacific; it is a sink for North Atlantic (and other) deep waters. In the South Pacific, bottom waters are supplied from the Antarctic circumpolar waters. The temperature of these bottom waters increases from 0.9°C in the Antarctic to 1.5°C in the North Pacific. This is thought to be due to heat flow from the interior of the earth. The deep and bottom water movements in the Pacific are very slow, and only a little exchange occurs between the South and North Pacific. The deep waters of the Pacific and Indian Oceans have similar properties (t = 1.5°C and S = 34.7) and form the largest water mass of the world oceans, called oceanic or common water. It is largely a mixture formed from North Atlantic deep water and Antarctic bottom waters. As will be discussed, the deep Pacific waters have much lower O_2 and higher nutrients than deep Atlantic waters. This is due to the waters being older and due to the high productivity of some of the surface waters. The Pacific has no source of high-salinity water like the Mediterranean in the Atlantic and the Red Sea in the Indian Ocean.

The T-S diagrams for the major water masses in the Pacific are shown in Figure 1.37. The water masses are more complicated than in the Atlantic because of the size of the Pacific. The upper water masses below the surface have a variety of properties. Between 100 to 800 m, the North and South Pacific waters and the Pacific equatorial water masses dominate. The equatorial water extends over the entire ocean and has a very uniform T-S relationship. The surface waters are separated from the equatorial waters by a strong thermocline that inhibits the vertical transfer of waters. The depth of the discontinuity layer decreases from 150 to 200 m in the west to 50 m or less in the east. The layer sometimes reaches the surface near the American coast and is called the Costa Rican thermal dome.

The equatorial undercurrent in the Pacific, called the Cromwell Current, has been studied for some time. Its rediscovery by Cromwell, Montgomery, and Stroup in 1954 caused a great deal of excitement because it had not been predicted by theory. The current was discovered by tracking drogues that were released at different depths. The submerged current was observed as a narrow undercurrent above the thermocline. The technique was similar to the methods used by Buchanan in the nineteenth century to study the Atlantic undercurrent. The velocity of the eastward flow reaches speeds as high as 120 cm s^{-1}, and transport is about 40 Sv. The South Equatorial Current flows above the undercurrent and separates it from the surface countercurrents to the north and south. It should be pointed out that the vertical circulation in the equatorial Pacific is similar to the Atlantic.

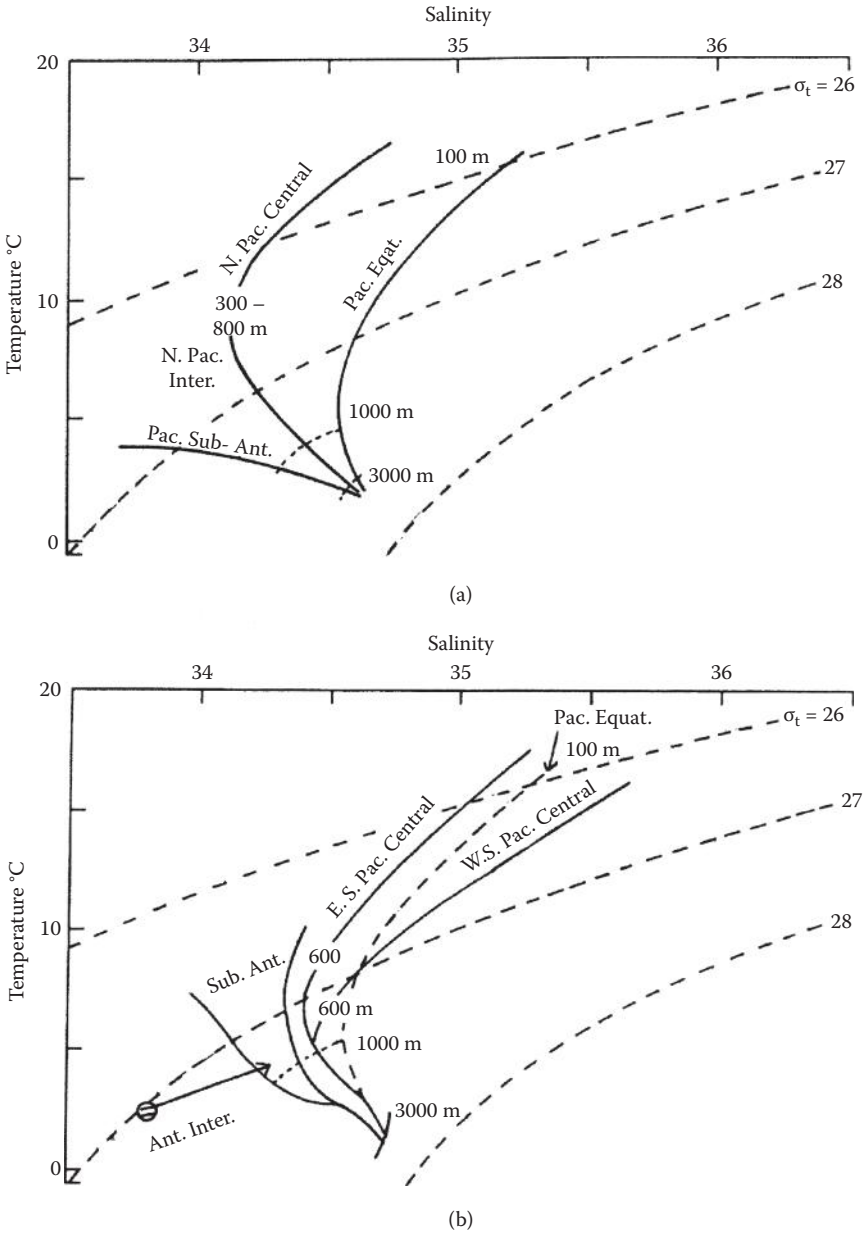

FIGURE 1.37
The T-S diagram for the (a) North and (b) South Pacific Ocean.

1.4.4 Indian Ocean

The surface currents in the Indian Ocean are shown in Figure 1.38. The Indian differs from the Atlantic and Pacific in its limited northern extent because of the Asian land mass. The subtropical convergence at 40° S is considered to be the southern boundary of the Indian Ocean. In the South Indian Ocean, the counterclockwise gyre is similar to the South Atlantic and Pacific Oceans. It is bound on the south by the Polar Current. Part of

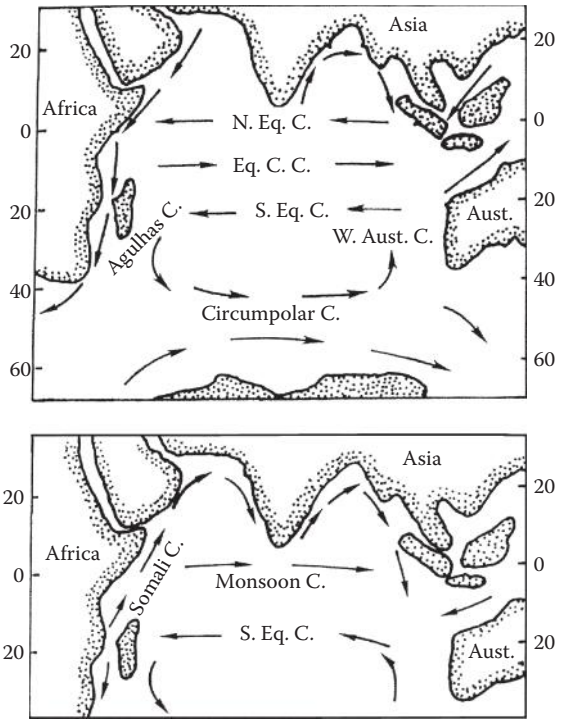

FIGURE 1.38
The surface currents of the Indian Ocean. The top figure is for conditions between November and March, and the bottom figure is for conditions between May and September.

this current flows north along the western coast of Australia and is augmented by a coastal current that flows toward the west along the south of Australia. Part of this current flows west and becomes the South Equatorial Current. The southward current along the south coast of Africa is called the Agulhas Current and completes the gyre. Part of this current flows west into the Atlantic to form the Benguela Current.

The equatorial current systems in the Indian Ocean differ from the Atlantic and Pacific because of seasonal changes in the winds. From November to March, the winds and currents are similar to the other oceans except that they are further south. The South Equatorial Current (20° S to 8° S) flows west throughout the year. The Equatorial Countercurrent (8° S to 2° S) flows toward the west. The North Equatorial Current (2° S to 10° N) flows to the east and is maintained by the northeastern trade winds.

In April, the winds change, and from May to September, the northeastern trade winds are replaced by winds from the southwest called the southwestern monsoon winds. These are really a continuation across the equator of the southeastern trade winds. The North Equatorial Current is replaced by a Southwest Monsoon Current. The Equatorial Countercurrent also disappears or becomes indistinguishable from the Monsoon Current. During the monsoon period, the South Equatorial Current turns north, supplying the Somali Current, which flows north along the eastern coast of Africa.

The temperature and salinity of waters near the equator in the Indian Ocean are similar to those in the Atlantic and Pacific. Waters in the Bay of Bengal have lower salinities (31 to 34) because of river runoff, particularly during the monsoon season. Waters in the Arabian Sea have a high salinity (36.5) because of evaporation. The T-S diagrams of the major water masses

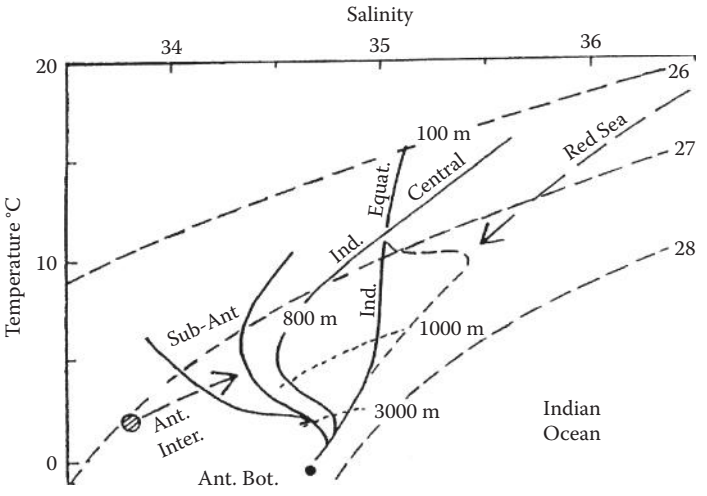

FIGURE 1.39
The T-S diagrams for the Indian Ocean.

in the Indian Ocean are shown in Figure 1.39. The equatorial waters have a salinity of 34.9 to 35.2 and are located north of 10° N at a depth of 100 to 2000 m. The central waters are similar to South Atlantic central waters (800 to 1000 m). The Antarctic intermediate waters are characterized by the usual salinity minimum. They are formed at the Antarctic convergence as in the Atlantic and Pacific. The deep waters in the Indian Ocean have temperatures of 1 to 3°C and salinity of 34.6 to 34.8. This deep water has properties similar to the Pacific deep waters and is the remnant of North Atlantic deep water. The Antarctic bottom water in the South Indian Ocean has properties similar to the bottom waters formed in the Atlantic and Pacific.

In the northern and western Indian Ocean, a warm saline water mass flows out of the Red Sea to a depth of 1000 to 1500 m. The sill depth of the Red Sea is about 125 m. Since evaporation exceeds precipitation in the Red Sea and there is little river runoff, the salinity becomes very high (42.5), as does the temperature. This salty water sinks and flows out of the Red Sea across the sill. The water that leaves the Red Sea has different properties than deep Red Sea waters. Inside the sill, the temperature is 24°C, and salinity is 39.8; outside the sill, the temperature is 15°C, and salinity is 36. Surface inflow occurs similar to the Mediterranean Sea.

1.4.5 Arctic and Adjacent Seas

The surface circulation in the Arctic and adjacent seas is shown in Figure 1.40. The Norwegian Current is a continuation of the North Atlantic current that turns north and flows into the Norwegian Sea. The East Greenland Current flows southwestward along the Greenland coast. It is composed of waters from the Arctic Sea, with some mixing with Norwegian Current waters. The speed of the current is about 30 cm s^{-1}. The ridge from Greenland to Scotland is 1000 m and prevents deeper Atlantic water from entering the Norwegian and Arctic Seas. The East Greenland Current carries ice from the Arctic into the North Atlantic.

In the Norwegian and Greenland Seas, the surface waters consist of the Greenland gyre (above 1500 m, t = –1.1 to –1.7°C and S = 34.86 to 34.90; below this depth, S = 34.92 and t <1.1°C). The deep waters of the Norwegian gyre have the same salinity, but the

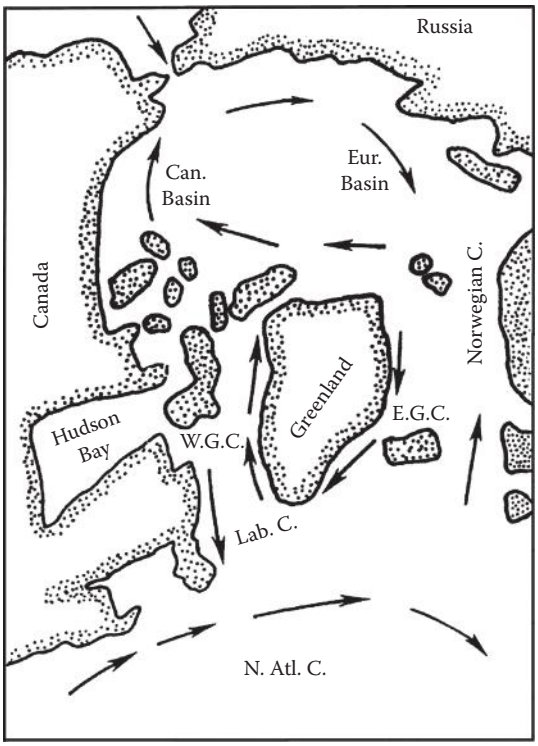

FIGURE 1.40
The surface currents of the Arctic Sea.

temperatures are greater than –0.95°C (similar to the bottom water of the Arctic basin). The Norwegian Sea thus forms a barrier to the passage of the colder Greenland gyre water. The deep waters of both seas have high O_2 concentrations, indicating that their formation takes place by the cooling and sinking of winter waters.

The West Greenland Current is the result of East Greenland Current water that flows around the tip of Greenland into the Labrador Sea. The Baffin Land Bay Current flows southward and becomes the Labrador Current, which flows into the Atlantic. It has a low salinity (30 to 34) and a low temperature (less than 0°C). The volume flow of the Labrador Current has been estimated to be 5.6 Sv. This can be compared to the East Greenland Current with a flow of 7.5 Sv. The difference (1.9 Sv) is the estimate of outflow as deep water into the Atlantic.

The Arctic Sea is divided into two basins separated by the Lomonosov ridge between Greenland and Siberia. The Canadian basin has a maximum depth of 3800 m, while the Eurasian basin has a maximum depth of 4200 m. The sill depth separating the basins is 1200 to 1400 m, and the main connection of the Eurasian basin with the Atlantic is through Greenland and Spitzbergen, which has a sill depth of 1500 m. The Bering Strait has a sill depth of 50 m; thus, the Canadian basin has little exchange with the North Pacific. The upper circulation of waters in the Arctic was obtained from the early records of ships held in ice. The clockwise circulation in the Canadian basin leads out to the East Greenland Current. This is augmented by the counterclockwise circulation in the Eurasian basin.

The water masses in the Arctic include the surface, or Arctic, water (0 to 200 m), Atlantic water (200 to 900 m), and bottom water (900 to bottom). The density is largely determined by the salinity. Plots of salinity and temperature in the two basins are shown in Figure 1.41.

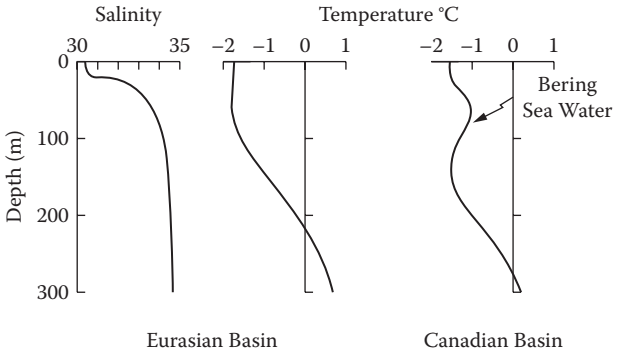

FIGURE 1.41
Typical temperature and salinity profiles for the Arctic Sea.

The surface salinity varies from 28 to 34 and is strongly influenced by melting and freezing. The temperature thus remains near the freezing point (–1.5°C at S = 28 to –1.8°C at S = 33.5). Seasonal variations (±2 in salinity and ±0.2°C in temperature) are limited to the surface waters. The subsurface is isothermal but has a strong halocline between 25 to 100 m. Below 100 m, the temperature increases greatly. The subsurface water is thought to be maintained by horizontal advection from the Eurasian shelf. This process is similar to the flow that occurs in an estuary where freshwater (from river runoff from Siberia) flows over saline water (Atlantic water). The Canadian basin water also shows a halocline. The temperature, however, goes through a maximum at 75 to 100 m. This maximum is attributed to Bering Sea water coming into the Arctic through the Bering Strait. It is warmer and denser because of its higher salinity. This is one of the few examples of a subsurface maximum in temperature that occurs in the oceans.

The lower-layer water (200 to 900 m) is a mixture of subsurface Arctic water and Atlantic water (t = 3.0°C and S = 34.8 to 35.1). It becomes the deep Arctic water (t = 0.4°C and S = 34.85 to 35.00). The circulation of this deep water is counterclockwise (opposite to the Arctic surface waters). The Arctic bottom water (900 m to the bottom) makes up 60% of the volume of the Arctic Sea. It has a salinity of 34.90 to 34.99 and a minimum temperature of –0.8°C in the Eurasian basin and –0.4°C in the Canadian basin. This bottom water originates in the Norwegian Sea. The higher-temperature water in the Eurasian basin cannot enter the Canadian basin because of the Lomonosov ridge.

Ostlund and coworkers (Miami) have studied the deep-water exchange in the Arctic Sea. They found that the deep-water exchange in the Eurasian basin is between 10 and 100 yr, while it is about 700 yr in the Canadian basin. Less than 10 to 15% of the deep waters originate from the shelves.

The polar ice cap covers 70% of the Arctic Sea. It is always present and extends from the pole to about the 1000-m isobath. Some of the ice melts in the summer, and the thickness decreases to a few meters. Open spaces called polynyas may form, and ridges (rafting) occur in the fall. In the winter, the thickness is about 3 m, with hummocks that increase to a height of 10 m above sea level and up to 40 m below sea level. The polar cap ice is not always the same; up to one-third is carried away by the East Greenland Current. Pack ice covers about 25% of the arctic area outside the polar cap. It is lighter than cap ice and is carried further south than polar cap ice. This ice floe causes problems for navigation. Ice that forms out from shore is called fast ice. It normally breaks up and melts in the summer. Icebergs are pieces of glaciers that come from the western coast of Greenland. It is different

from pack ice and can extend to 70 m above sea level (as much as 500 m long). The volume below sea level varies from 1:1 to 7:1 depending on its shape. The drift of icebergs is influenced by water currents, while pack ice is influenced by winds. The pack ice moves to the right in the Northern Hemisphere because of the Coriolis force. This was known by sailors long before it was noted by Nansen or suggested by Ekman.

1.4.6 Closed Basins

1.4.6.1 Mediterranean Sea

The Mediterranean Sea is divided into a western and eastern basin separated by a sill of 400 m that extends from Sicily to North Africa. The maximum depths are 3400 m in the western basin and 4200 m in the eastern basin. The sill depth between the Mediterranean and the Atlantic is 330 m. The Mediterranean Sea is an example of a closed basin that has a higher rate of evaporation than the rate of precipitation and an input of river water. This results in high salinities (S = 39) being formed in the surface layers. These waters sink in the winter and form saline deep waters. Off the coast of Turkey, lavantine intermediate waters are formed with a temperature of 15°C and salinity of 39.1. These waters flow toward the west at 200 to 600 m and out through the Strait of Gibraltar into the Atlantic. The Mediterranean water that flows into the Atlantic has a temperature of 13°C and salinity of 37.3 from mixing with the incoming Atlantic waters. The deep and bottom waters are formed during the winter off the Riviera in the western basin (t = 12.6°C and S = 38.4) and in the South Adriatic Sea in the eastern basin (t = 13.3°C and S = 38.65). Since the deep waters are replenished, they have high concentrations of oxygen.

1.4.6.2 Red Sea

The average depth of the Red Sea is 1000 m, with a maximum depth of 2200 m. The sea is separated from the Indian Ocean by a sill of 100 m depth. Because of the very dry climate, evaporation exceeds precipitation by about 200 cm yr^{-1}. There is no river runoff into the Red Sea. This leads to salinities as high as 42.5, combined with temperatures of 30°C in the summer and 18°C in the winter. The deep water below the sill depth has a uniform temperature and salinity (t = 21.7°C and S = 40.6). This water is formed in the winter in the north. The intermediate water that flows out over the sill starts with a temperature of 25°C and salinity of 39.8 and becomes 15°C and 36 salinity outside the sill. This subsurface flow is compensated by a surface inflow of Indian Ocean water. This is similar to the Mediterranean Sea. The Red Sea water that flows over the sill can be identified in the northern Indian Ocean. In the northern Red Sea, hot brine pools were discovered in some deep trenches. Temperatures of 58°C and salinities of 320 have been found. The compositions of the solutions indicate that the brines were formed by hot seawaters dissolving evaporite deposits.

1.4.6.3 Estuaries

Conditions in coastal waters of the ocean are quite different in many ways from those in the open oceans. Variations with location and time are generally larger. These differences are caused by river runoff, tidal currents, and the effects of coastal boundaries on circulation. Tidal currents twice a day change the volume of water in a harbor or bay and promote vertical mixing. This breaks down any stratification in the water and can cause

a resuspension of river sediments. River runoff reduces the salinity of the surface waters. The runoff normally has seasonal fluctuations that frequently follow the local precipitation or the summer melt of snowfields and glaciers. Most of the extreme conditions in coastal waters occur in or near river mouths or in estuaries.

Estuary can have a wide range of meanings in oceanography. The simple definition is the tidal region at the mouth of a large river. Pritchard's definition is "a semi-enclosed body of coastal water having a free connection with the sea" and containing a measurable amount of sea salt. One can classify an estuary into two major types (Pickard and Emery, 1982):

1. A **positive estuary,** where the salinity is less than the ocean because precipitation and river runoff are greater than evaporation (e.g., the Baltic Sea)
2. A **negative estuary,** where the salinity is greater than the ocean because of evaporation greater than precipitation and river runoff (e.g., the Red and Mediterranean Seas)

It is also possible to define an estuary in terms of its shape. Three such divisions are as follows:

1. A **coastal plain estuary** that results from land subsidence or a rise of sea level flooding a river valley (e.g., the St. Lawrence and Chesapeake Bay)
2. A **deep basin estuary** that has a sill toward the sea that is shallower than the basin and the outside seas (e.g., fjords of Norway and Canada)
3. A **bar build estuary** that has a narrow channel between the shore and a bar built up nearby by waves and sedimentation (e.g., Mexican lagoons)

Finally, it is possible to classify an estuary based on the distribution of the water properties. Four such types are shown in Figure 1.42:

1. A **vertically mixed estuary** is a shallow basin where the water is well mixed. This leads to a similar salinity from the surface to the bottom at any particular place along the estuary. The salinity increases as the estuary flows from the head to the mouth. The Severn River in England is an example of this type of estuary.
2. A **slightly stratified estuary** is also shallow, with the salinity increasing from the head to the mouth. The water, however, is in two layers. The upper layer is a little less saline than the deep layer. There is a net seaward flow in the upper layer and an inward flow in the deep layer. Vertical mixing of the two layers results in the increase of salinity from the head to mouth in both layers. The James River in the Chesapeake Bay is an example of this type of estuary.
3. The **highly stratified estuary** is typical for fjords. The upper layer increases in salinity from zero at the head to a value close to seawater at the mouth. The deep water has an almost uniform salinity. There is a net outflow in the surface layer and inflow in the deeper water. A very strong halocline exists between the two layers. There is normally some vertical mixing between the two layers. The depth of the interface is substantially the same throughout the estuary. The circulation in this type of estuary is dependent on the sill depth, the river runoff, and the outside water density distribution. If the sill depth is too shallow, the inflow of deep saline water will not occur. This leads to the bottom waters becoming stagnant and perhaps devoid of oxygen. This situation occurs in Norwegian fjords but not all deep basin estuaries. The rate of renewal is affected by the river runoff and outside density structure (both of which can be seasonal).

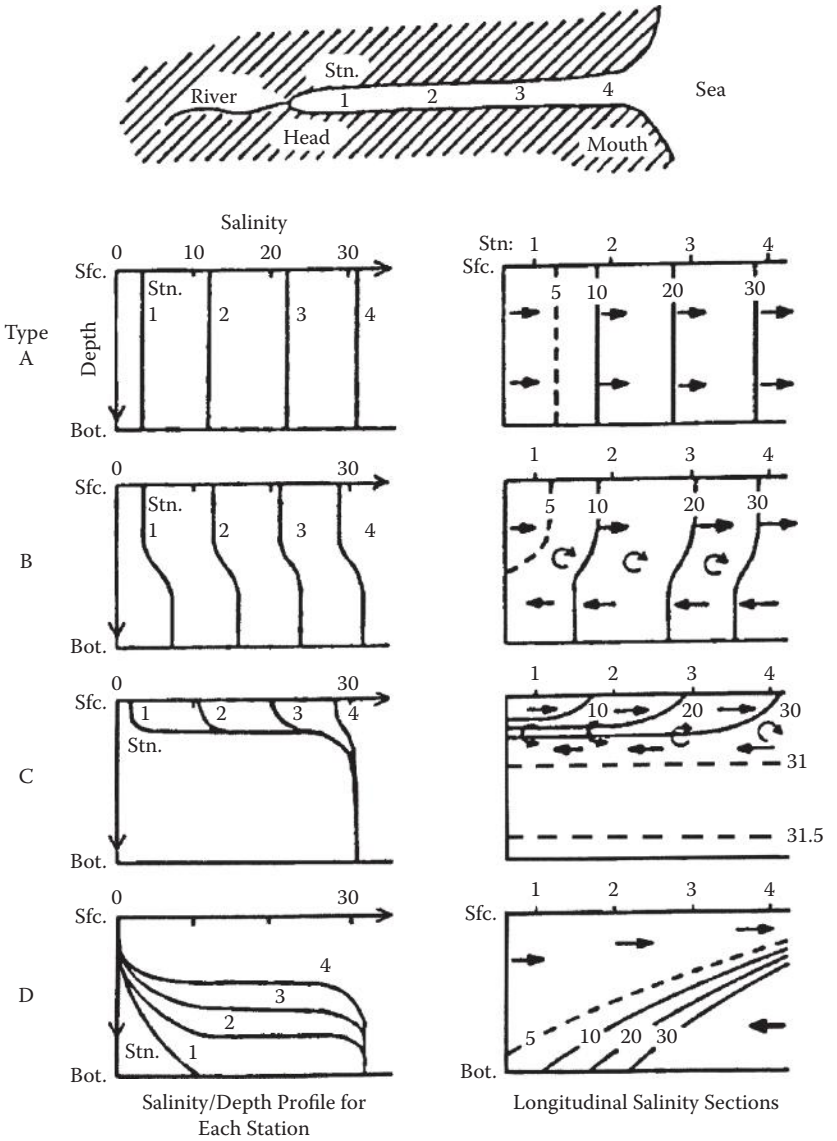

FIGURE 1.42
The salinity/depth profiles and sections for types of estuaries (A) vertically mixed; (B) slightly stratified; (C) highly stratified; (D) salt wedge.

4. The **salt wedge estuary** is named after its salinity structure. The saline water intrudes from the sea as a wedge below the river water. This situation occurs for rivers with a large-volume transport, such as the Mississippi or Fraser Rivers. The wedge is really very thin so that the isohalines are almost horizontal. There is a strong horizontal gradient of salinity at the bottom as in the slightly stratified estuary and a strong vertical gradient. The surface waters are largely fresh because of the strong river outflow.

This brief survey provides a discussion of descriptive aspects of estuarine systems. More is said about the chemistry of estuaries in the next chapter.

1.5 Use of Chemical Tracers in Oceanography

Oceanographers have used various chemical tracers to determine the mixing times of the water masses in surface and deep ocean waters. They have used tracers such as

1. Conservative tracers (T and S)
2. Isotopic tracers
   a. Stable isotopes (^{13}C, ^{15}N, ^{18}O)
   b. Radioisotopes (^{222}Rn, ^{228}Rn)
   c. Cosmic ray-produced nuclides (^{14}C)
   d. Anthropogenic nuclides (^{14}C, tritium, ^{3}H)
3. Transient tracers (time-varying sources or sinks)
   a. Chlorofluorocarbons (CFCs)
   b. Carbon-14 (^{14}C)
   c. Tritium (^{3}H)
4. Deliberate tracers
   a. Sulfur hexafluoride (SF_6)
   b. Fluorescent dyes

Most of the studies have been made using transient tracers such as CFCs and radioactive elements such as carbon-14 and tritium. They are useful as water mass tracers and for putting timescales on oceanographic processes. The detonation of nuclear weapons during the late 1950s and early 1960s produced radioisotopes of carbon and hydrogen (Figure 1.43). These elements were deposited on the surface of the oceans and were gradually mixed into the deep waters. By following these compounds with time, oceanographers have been able to obtain a better understanding of the circulation of the oceans. The inputs of these compounds into the atmosphere are reasonably well known (Figure 1.44).

1.5.1 Carbon-14

Radiocarbon (^{14}C) is being produced in the atmosphere. The protons in cosmic rays shatter the nucleus of atmospheric atoms and fragment some of them, releasing neutrons. Some of these neutrons enter the nucleus of ^{14}N, knocking out a proton, resulting in the formation of ^{14}C. The number of nucleons (protons plus neutrons) is the same, but one neutron has been substituted for a proton. Carbon-14 is radioactive and ejects an electron (beta particle) and becomes a nitrogen-14 atom. The low-level counting of the beta particle emitted is how one determines the concentration of ^{14}C in natural waters. The change in the concentration of the number of molecules of ^{14}C (N) can be determined from

$$N = N_0 e^{-\lambda t} \tag{1.2}$$

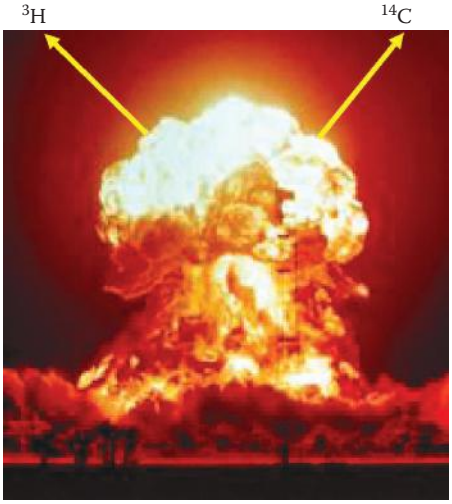

FIGURE 1.43
Production of carbon-14 and tritium in an atomic bomb.

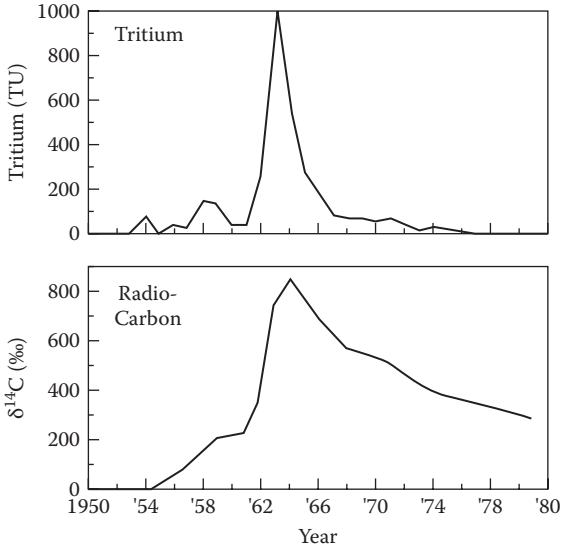

FIGURE 1.44
The input of carbon-14 and tritium into the atmosphere from bomb tests.

where N_0 is the initial concentration, and $\lambda = 1.22 \times 10^{-4}$ yr^{-1}. The amount of ^{14}C being generated over thousands of years to the surface of the earth is constant. It is disappearing by radioactive decay at the same rate as it is being produced by cosmic rays. During the nuclear weapons tests, large amounts of ^{14}C were produced and added to the amount formed naturally.

Since the half-life ($t_{1/2} = \ln 2/\lambda = 5700$ yr) and the lifetime ($\tau = 1/\lambda = 8200$ yr) for the decay of ^{14}C to ^{14}N are the same order as the mixing times of the oceans and its mixing with ordinary carbon (^{12}C) is not complete, it has become an important and valuable tool

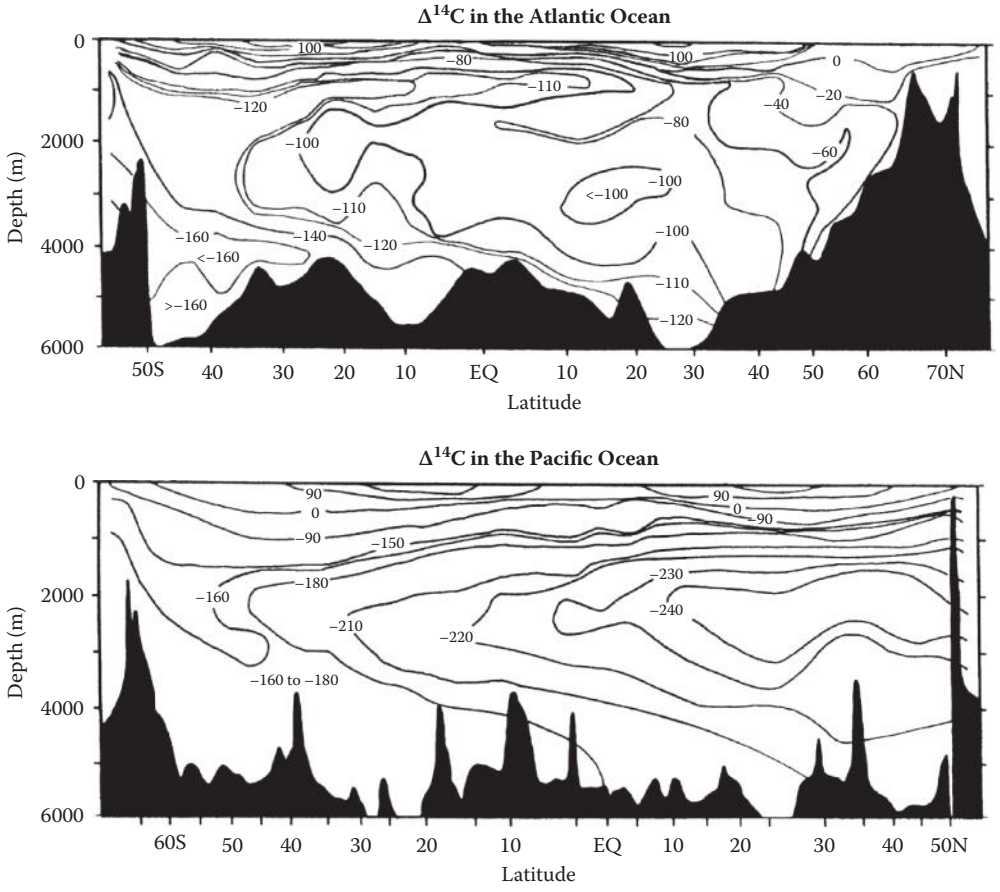

FIGURE 1.45
Section of $\Delta^{14}C$ in the Atlantic Ocean and the Pacific Ocean.

in oceanography and other fields. The slow mixing of ^{14}C over its lifetime with normal carbon will lead to lower concentrations in the older ocean waters. Thus, the atmosphere will have the highest ratios of $^{14}C/C$, and the deep North Pacific will have the lowest ratios of $^{14}C/C$. Sections of the $\Delta^{14}C = (^{14}C/C - 1)\ 1000$ (‰) in the Atlantic and Pacific Oceans are shown in Figure 1.45.

1.5.2 Tritium and Helium-3

Tritium (^3H or T) is a radioactive isotope of hydrogen. It has a half-life of 12.4 yr. It is introduced into the surface of the oceans as water (HTO) from both natural input and nuclear weapons tests in the late 1950s and early 1960s. One of the reactions that leads to tritium in the atmosphere is

$$^{14}N + n \Rightarrow {}^3H + {}^{12}C \tag{1.3}$$

The radioactive decay of tritium is by the reaction

$$^3H \Rightarrow {}^3He + e^- \tag{1.4}$$

where e^- is an electron or beta particle, and ^3He is helium-3. Tritium is measured by low-level beta counting or detecting the daughter ^3He product using a mass spectrophotometer. The first method has a detection limit of 0.05 TU (1 tritium unit equals a $^3H/^1H$ ratio of 10^{-18}), while the second method, which involves the measurement of the ratio of $T/^3He$, has a detection limit of 0.003 TU. This ratio is measured after the sample is stored for about 6 months. When both tritium and helium-3 are measured, it is possible to estimate the isolation time of a water parcel (similar to the ^{14}C method). The time can be determined from the $^3He/T$ ratio by

$$t = (12.4)\ln[(^3He/^3H) + 1)] \tag{1.5}$$

It is necessary to correct for the presence of any primordial ^3He when using this equation. It should also be noted that the mixing effects are not linear due to the exponential relationship between ^3He and ^3H. Thus, the resulting age of the mixture of two water masses will not be the arithmetic mean of the two end members. This can be illustrated in the following example of mixing component A and B:

Component	A	B	1/2(A + B)
TU	6.0	0.5	3.25
^3He (%)	3.5	1.8	2.6
Age (yr)	2.1	10.2	2.8

The actual age of the final mixture A plus B is 7.8 yr not 2.8 yr.

Typical profiles of tritium in the North Atlantic and Pacific in the 1970s are shown in Figure 1.46. In the Pacific, the surface values were about 4 TU, decreasing sharply with depth, and were below the detection limit below 800 m. By contrast, the surface waters in the North Atlantic were much higher (12 TU) and had measurable values in deep waters (2 TU). The sections of tritium in the North Atlantic were shown earlier (Figure 1.30). A more colorful section of tritium in the North Atlantic is shown in

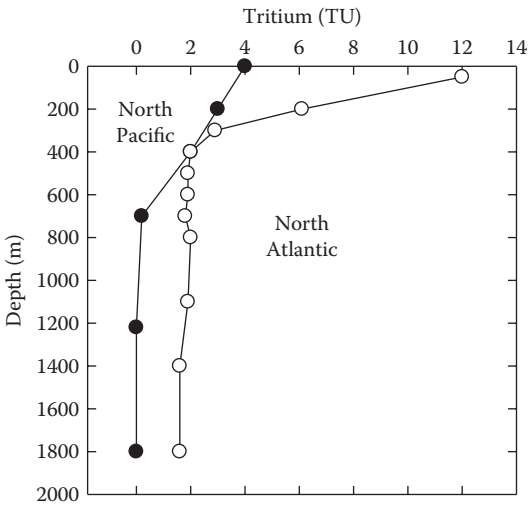

FIGURE 1.46
Typical profile of tritium in the North Atlantic and Pacific Ocean.

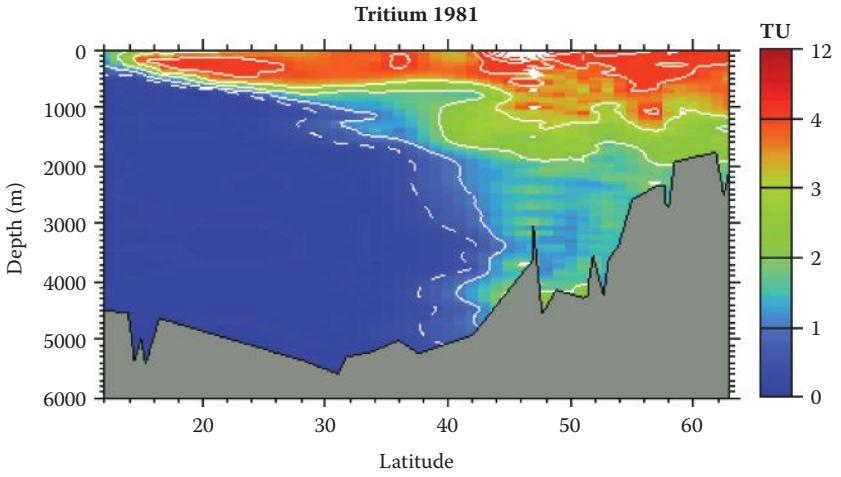

FIGURE 1.47
Section of tritium in the Atlantic Ocean.

Figure 1.47. At the time of these measurements, it was quite surprising to see measurable amounts of tritium in bottom waters as far south as 40° N in the Atlantic (since it was only 20 yr after the bomb tests). The present tritium concentrations are now below the detection limit in ocean waters. Thus, most studies examined the decay of low levels of tritium to helium-3.

^{3}He has four sources to the oceans: the atmosphere, decay of tritium in the upper layer of the oceans, terrestrial primordial input from the interior of the earth (including hydrothermal vents), and radiogenic decay from the sediments. The two naturally occurring isotopes are ^{3}He and ^{4}He and are measured together as a ratio to give us a clue of their sources. Helium is present in the atmosphere at a level of 5.2 ppm and represents a steady-state balance between the flux from the earth into the atmosphere and escape into space. The ratio of ^{3}He/^{4}He is 1.38 10^{-6} in the atmosphere (Clark, Beg, and Craig, 1969), which is assumed to be the equilibrium ratio of the He that enters the surface waters of the oceans. The tritium decay into ^{3}He in waters above the thermocline is the major factor that leads to changes in the ^{3}He/^{4}He in surface waters. In deep waters, especially in the Pacific, the flux of helium from ridge crests and hydrothermal fluids has ^{3}He/^{4}He ratios 10 times the atmospheric value. This increase in the ratio in deep waters can be used as a tracer of deep waters and hydrothermal vent fluids. The He that comes from the sediments, due to the radioactive alpha decay of mostly U and Th, increases the concentration of ^{4}He and causes a decrease in the ^{3}He/^{4}He ratio. The input of ^{3}He and ^{3}H from the interior to the deep waters of the Pacific Ocean is demonstrated in Figure 1.48.

1.5.3 Chlorofluorocarbons

The CFCs (freons) have been widely used as refrigerants, aerosol propellants, foam-blowing agents, and solvents (Fine, 2011). These compounds have a low toxicity and are not very reactive. Production of F-11 (trichlorofluoromethane) and F-12 (dichlorofluoromethane) began in the 1930s. In recent years, the industrial production of these compounds has grown. The release of CFCs to the environment differs according to their use. Aerosol propellants are released immediately, while the release of refrigerants may take up to 10 yr.

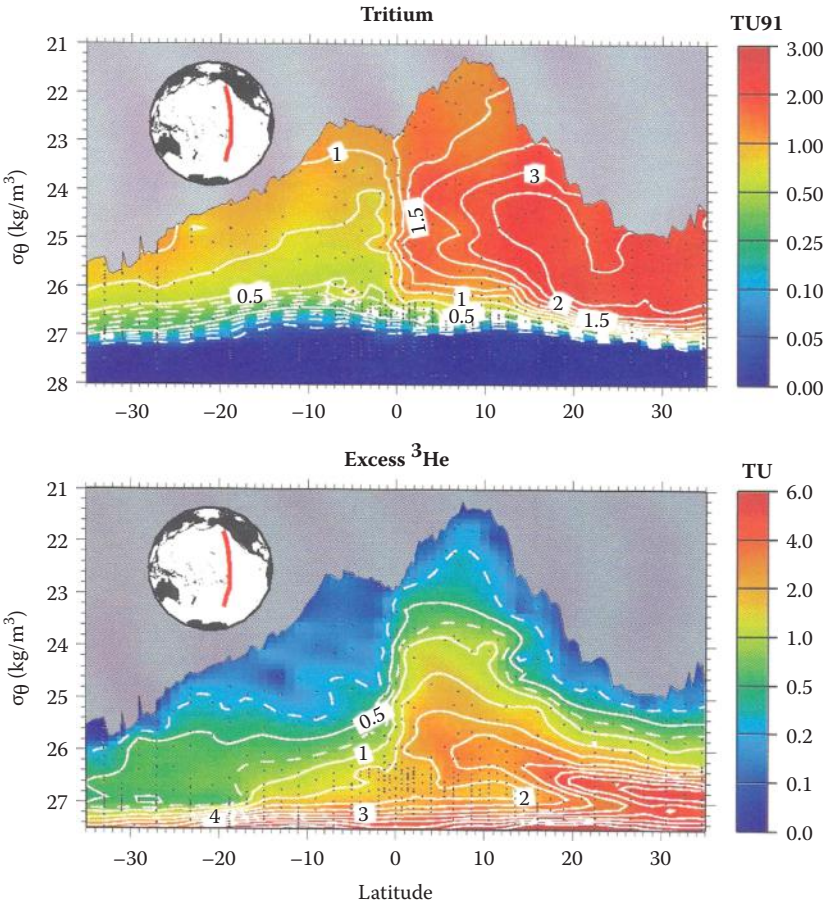

FIGURE 1.48
Section of tritium in the Pacific Ocean.

Since the mid-1970s, the ratio of F-11/F-12 in the atmosphere has remained nearly constant (see Figure 1.49).

In more recent years, these amounts have leveled off and will decrease in the future. Since these compounds have a long lifetime (75–100 yr) in the atmosphere, they can be widely dispersed in the environment. As will be discussed further, their movement into the stratosphere can lead to the destruction of ozone (Chapter 5). Much of these compounds can be rained out and deposited on the surface of the oceans. This serves as a dye that can be used to examine the movement of surface waters into the deep. The development of sensitive electron-capture gas chromatography by Lovelock, Maggs, and Wade (1973) has led to the measurement of CFCs in ocean waters as a function of time and location. At present, it is possible to detect 5×10^{-15} mol kg^{-1} (5 fM) in a 30-cm^3 sample of seawater. The concentrations in surface waters are about three times higher than the detection limit. At these levels, one must be careful to avoid sample contamination. The inputs of CFCs to the atmosphere have been modeled based on production records with corrections for losses due to photolysis in the stratosphere. Most (90%) of the release has occurred in the Northern Hemisphere. Due to the long lifetime and the rapid latitudinal mixing of the lower atmosphere (2 yr) these compounds are relatively uniformly distributed in the troposphere.

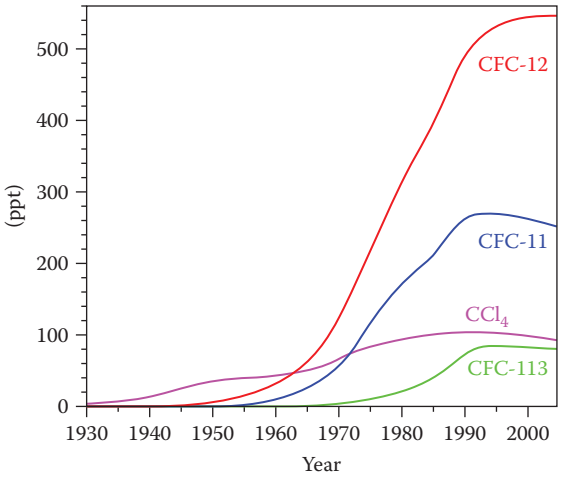

FIGURE 1.49
Input of CFC-11 and CFC-12 into the Northern Hemisphere atmosphere.

The Montreal Accord, signed in 1988 by most nations, has led to a 50% decrease in the use of CFCs; however, the concentrations are not expected to dramatically decrease for some time. The rate of decrease is about 1% per year by stratospheric photolysis; thus, CFCs will remain in the environment for a number of years.

At equilibrium, the concentration of the gaseous CFCs in ocean waters is a function of temperature and salinity (Bullister and Weiss, 1988). From the surface, these compounds can be mixed downward into the water column. From models for the input functions, one can determine the rates of these mixing and circulation processes. Since the lifetime of the CFCs is limited, they can only be used to examine waters that have been in contact with the atmosphere on timescales of months to decades. A section of the concentration of CFC-11 and CFC-12 in North Atlantic waters is shown in Figure 1.50 (Bullister, 1989).

The sections from Iceland to the coast of Brazil clearly demonstrate the formation and penetration of North Atlantic deep water. The values for the surface waters are within a few percent of the saturated concentrations. The solubility is higher in the colder waters. The overflow of cold, dense deep water from the Iceland-Scotland Ridge can be detected to 2000 m. The high concentrations in the deep western boundary current can be traced southward in the western basin of the North Atlantic for thousands of kilometers. The waters south of 20° N below 500 m have undetectable concentrations of any CFCs. Unlike the bomb, produced tracers of the CFC have a similar input function in the Northern and Southern Hemispheres. They can thus be used as tracers of the ventilation of intermediate and deep waters in waters throughout the world. A number of the CFCs may prove useful as time-dependent tracers. The ratio of the concentration of CFC-11/CFC-12 in the water can be compared with the values in the past atmosphere to determine an approximate date of equilibrium or the age of the water. If the water mass was in equilibrium with the atmosphere and mixed with CFC free water, then the age will be the true age. In recent years, new CFCs such as CFC-113 (CCl_2FCClF_2) and carbon tetrachloride (CCl_4) have extended the timescale of dating the waters in both directions. These tracers will become increasingly more important as the concentrations of CFC-11 and CFC-12 decrease and are phased out. The total inventory of CFCs in the world oceans is shown in Figure 1.51. The largest inventory of CFCs is in the North Atlantic. As will be shown, this is similar to the inventory of

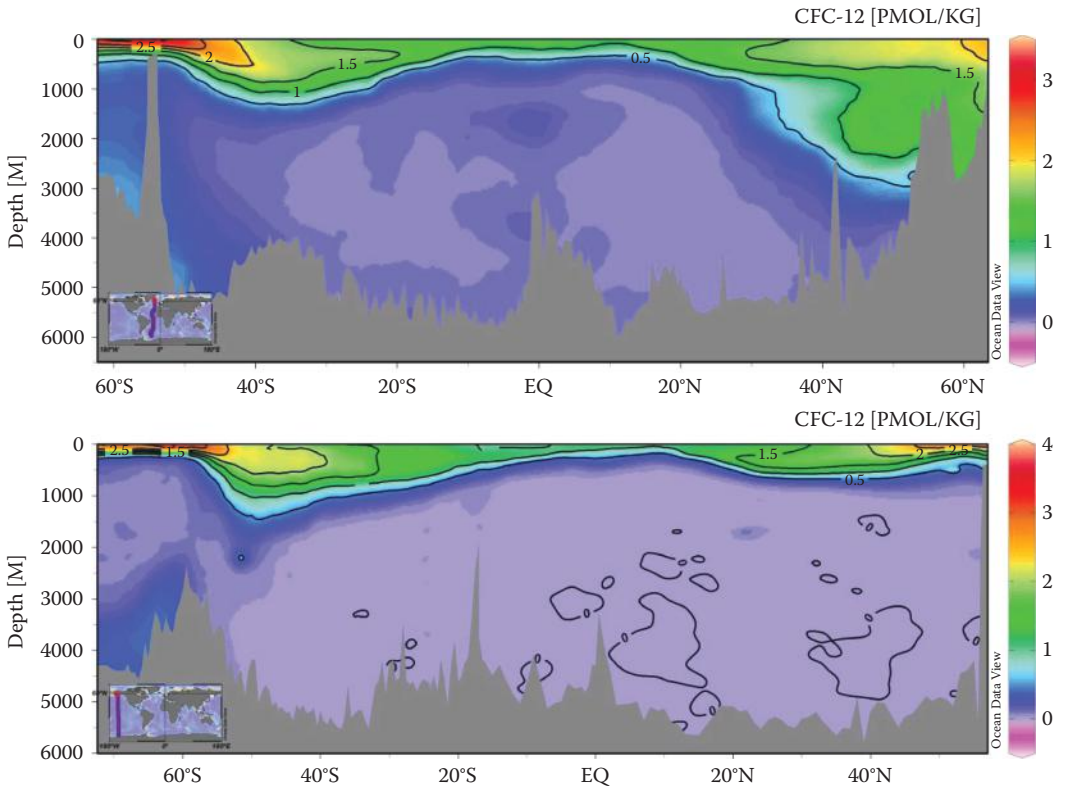

FIGURE 1.50
Section of F-12 and F-11 in the North Atlantic Ocean.

anthropogenic produced CO_2 in the world ocean. The measurements of the CFCs made during the global survey of the WOCE and CLIVAR programs will lead to a tracer field that can be used to evaluate global models and will improve our understanding of the rates and pathways of ocean circulation and the response to changes in the global climate.

1.5.4 The Age of Water Masses

A summary of the major water masses in the world ocean is given in Figures 1.52, 1.53, and 1.54. These figures are based on the water properties of the ocean waters. For a number of years, many workers have attempted to estimate the age of the deep-water masses in the world oceans using transient tracers like ^{14}C. The difference in concentration of ^{14}C in various reservoirs allows one to establish the rate of mixing across the thermocline and between various water masses. In the simplest case, the ocean can be considered to be made of two boxes (a surface box and a deep box). Three substances must be conserved between these boxes (water, C, and ^{14}C). It is also assumed that the sizes and carbon contents are constant with time. Because ^{14}C is decaying with time, its distribution between the surface and deep boxes depends on the mixing. This leads to three equations. The rates R are given by (Broecker and Peng, 1982)

$$R_{up} = R_{down} = R_{mix} \tag{1.6}$$

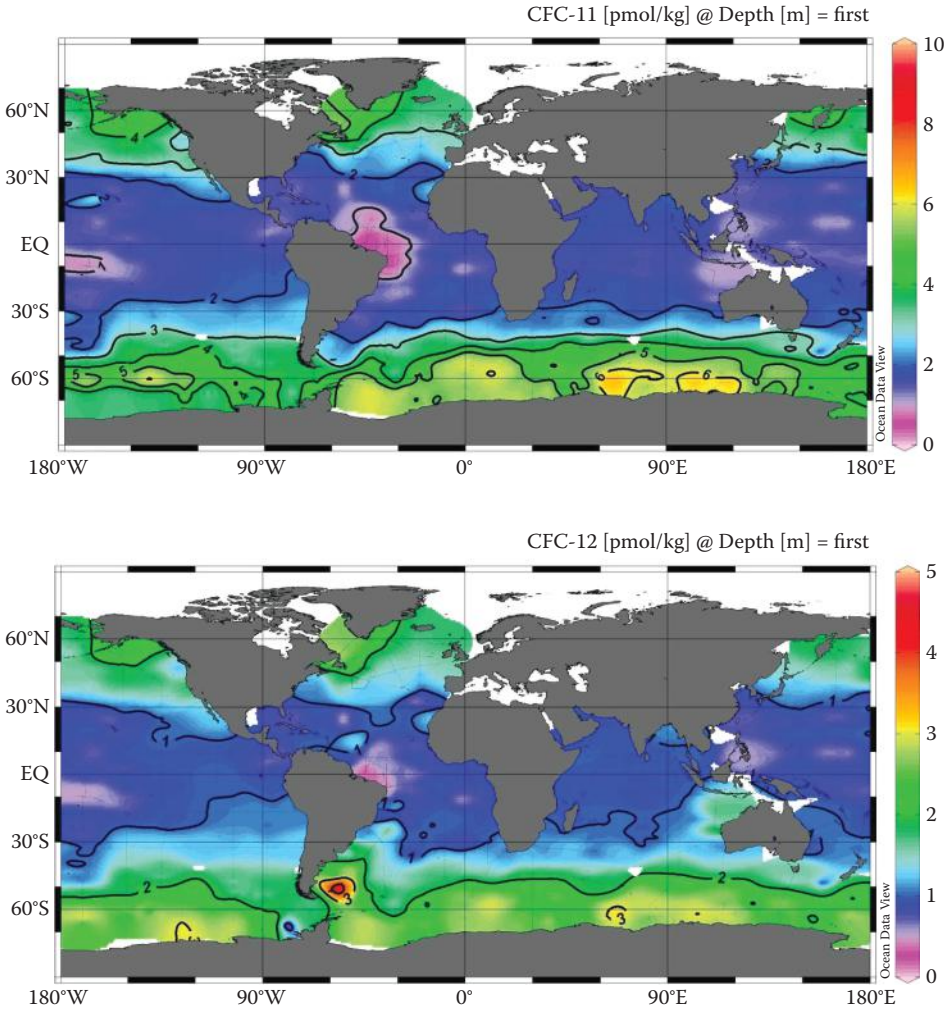

FIGURE 1.51
The surface values of CFCs in the world ocean.

The equation for ordinary carbon is given by

$$R_{mix}\, C_{deep} = R_{mix}\, C_{surface} + B \tag{1.7}$$

where B is the amount of carbon added to the reservoir due to the destruction of organic particles falling from the surface. The third equation is given by

$$R_{mix}\, C_{surface}\, (^{14}C/C)_{surface} + B\, (^{14}C/C)_{surface} = R_{mix}\, C_{deep}\, (^{14}C/C)_{deep} + V_{deep}\, C_{deep}\, (^{14}C/C)\, \lambda \tag{1.8}$$

where λ is the fraction of ^{14}C decaying each year, V_{deep} is the volume of deep water, and $B = V_{deep}\, (C_{deep} - C_{surface})$. Combining these equations and solving for R_{mix} gives

$$R_{mix} = (\lambda\, h\, A)/\{[(^{14}C/C)_{surface}/(^{14}C/C)_{deep} - 1]\} \tag{1.9}$$

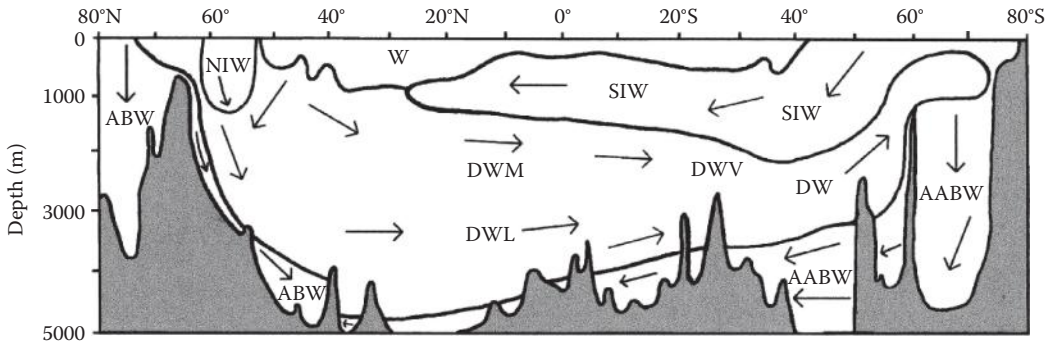

FIGURE 1.52
Characteristic water masses in the Atlantic Ocean. W = warm water sphere; NIW = subarctic intermediate water; SIW = subantarctic intermediate water; DW = deep water; DWU = deep water, upper; DWM = deep water, middle; DWL = deep water, lower; ABW = Arctic bottom water; AABW = Antarctic bottom water.

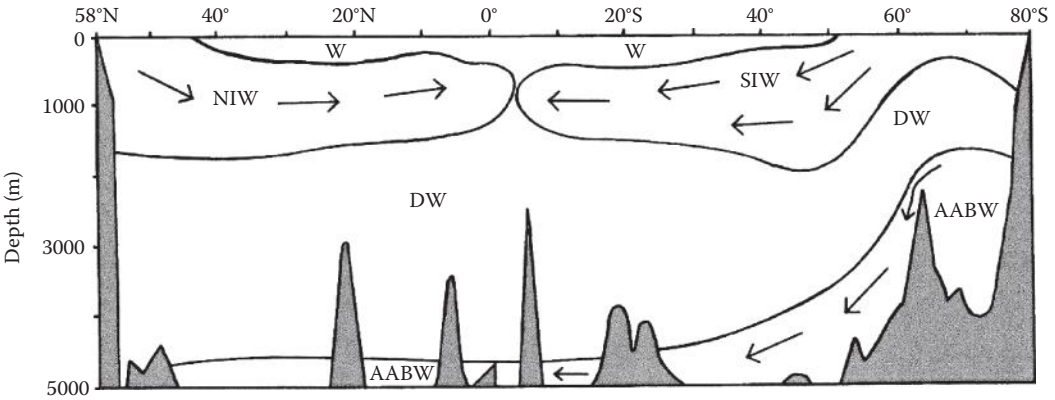

FIGURE 1.53
Characteristic water masses in the Pacific Ocean. W = warm water sphere; NIW = subarctic intermediate water; SIW = subantarctic intermediate water; DW = deep water; AABW = Antarctic bottom water.

where h is the average height of the water column (3200 m), and A is the area of the ocean ($3.23\ 10^8$ km^2) (V_{deep} = h A). The values of $(^{14}C/C)_{Atlantic}/(^{14}C/C)_{Pacific} = 1.20 \pm 0.03$ can be used to estimate the ventilation time of deep Pacific water:

$$t = V_{deep}/R_{mix} = [(^{14}C/C)_{surface}/(^{14}C/C)_{deep} - 1]\ \lambda \qquad (1.10)$$

Using $\lambda = 8200$ yr, one obtains a mean residence time of about 1600 ± 250 years.

More recent studies have divided the oceans into a number of boxes in an attempt to determine the age of the different water masses. A sketch of the box model with the values for the estimated rates of exchange is shown in Figure 1.55. The ^{14}C work from the GEOSECS program has been used to give us a look at the deep-water circulation in the world oceans (Stuiver, Quay, and Ostlund, 1983). Most of the deep-water formation takes place in the North Atlantic. The average residence time for water in the North Atlantic is about 246 yr, which is the youngest of the oceans. The major source of this North Atlantic deep water is from the Norwegian Sea. This deep water flows over the

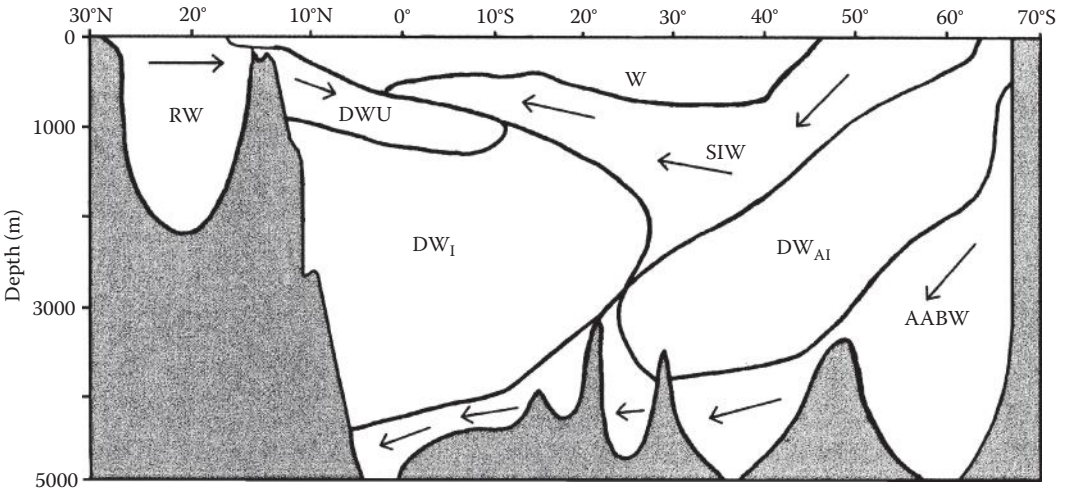

FIGURE 1.54
Characteristic water masses in the Indian Ocean. W = warm water sphere; RW = Red Sea water; DWU = deep-water, upper; SIW = subantarctic intermediate water; DW_I = deep water, Indian; DW_{AI} = deep water, Atlantic–Indian; AABW = Antarctic bottom water.

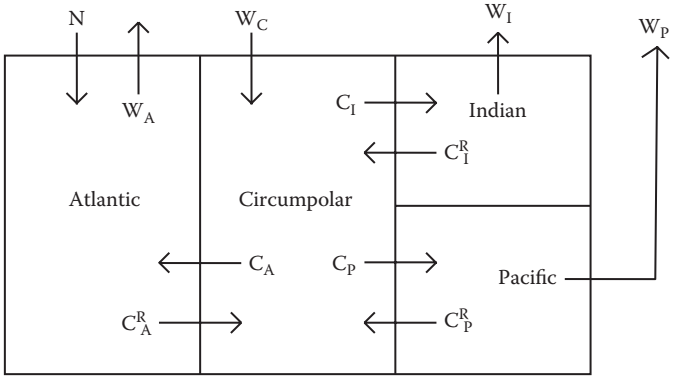

Legend	Various Waters	Volume
N	North Atlantic water formation	14 Sv
W_A	Atlantic upwelling rates	10
C_A	Transport rate from Circumpolar to Atlantic	7
C_A^R	Transport rate from Atlantic to Circumpolar	11
$C_I - C_I^R$	Net transport from Circumpolar to Indian	20
$C_P - C_P^R$	Net transport from Circumpolar to Pacific	29
W_C	Bottom water formed in Circumpolar	41
W_I	Indian Ocean upwelling	20
W_P	Pacific Ocean upwelling	25

FIGURE 1.55
Box model for the deep-water circulation of the world ocean water.

sills between Greenland and Iceland. The temperature and salinity of this water are, respectively, 2°C and 35.0. This water flows to the south and, after mixing with bottom waters, flows into the South Pacific and South Indian Oceans. It is thus the major water mass of deep-ocean basins. From ^{14}C data, estimates have been made of the time it takes for these waters to make a complete cycle. These estimates were given by Stuiver, Quay, and Ostlund (1983). The estimates came from using a simple box model to account for the ^{14}C measurements. The net flow of the water from the Atlantic to the Circumpolar is 4 Sv, while the net flow from the Circumpolar to the Indian is 20 Sv and to the Pacific is 25 Sv. The upwelling in the Atlantic (10 Sv), Indian (20 Sv), and Pacific (25 Sv) are balanced by the downwelling of North Atlantic waters (14 Sv) and Antarctic bottom water formed in the Circumpolar region (41 Sv). The 550-yr estimate for the replacement time for deep Pacific waters is much shorter than earlier estimates (1000 to 1500 yr) made using simpler box models.

The movement of waters in the oceans with time in recent years has been depicted as a great "conveyor belt" (Broecker, 1991), which is shown in Figure 1.56. It is frequently used as a logo for global change research.

Although it was designed as a simple representation of the ocean circulation, it has been quite useful in showing the linkages of the ocean circulation with the earth's climate system. As discussed, the belt is driven by the increase in the salinity of surface waters as they move to the North Atlantic and the net transport of water from the Atlantic to the Pacific. The resultant heat in the North Atlantic results in the relatively warm winters in Europe. Through the ages and perhaps in the future, this conveyor belt has been shut down (the cold condition in the Young Dryas). The complications of this system and its control on climate make it difficult to predict the effect of humans on the future climate of the earth. More recently, workers have added more details on the overturning circulation of the world oceans (Figure 1.57).

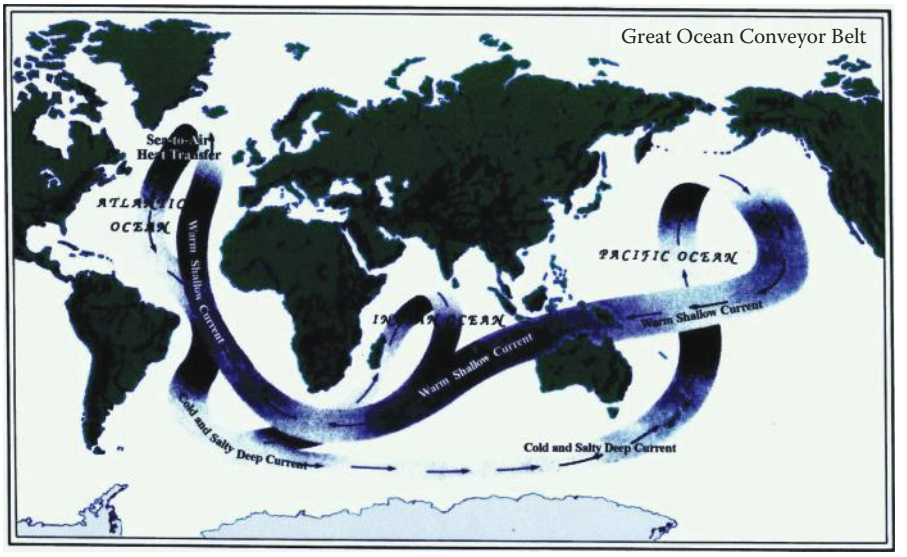

FIGURE 1.56
The "conveyor belt" movement of water in the world Ocean.

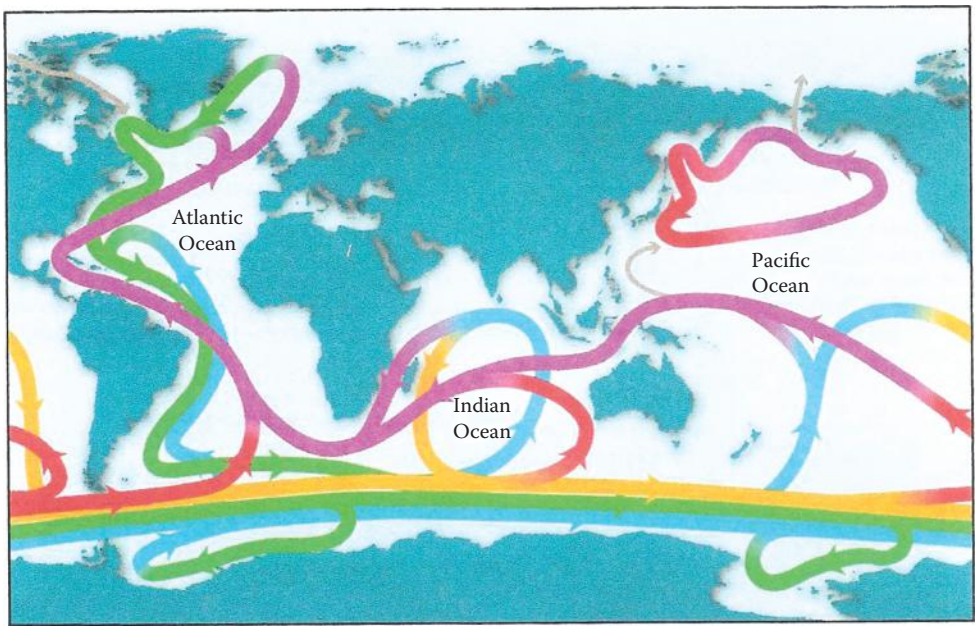

FIGURE 1.57
The overturning circulation of the world ocean.

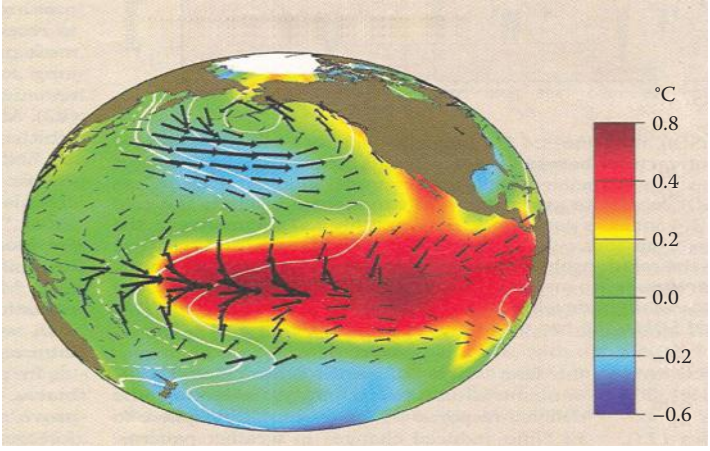

FIGURE 1.58
The El Nino Southern Oscillation.

In recent years, a number of workers have examined the North Atlantic Oscillation (NAO) and Pacific Decadal Oscillation (PDO) climate anomalies. The SAO index (Figure 1.58) is represented by the difference in the measured sea-level pressure between the Iceland low and Portugal during the winter season. The low-frequency component of this difference gives positive states and correlates with wintertime changes of temperature, precipitation,

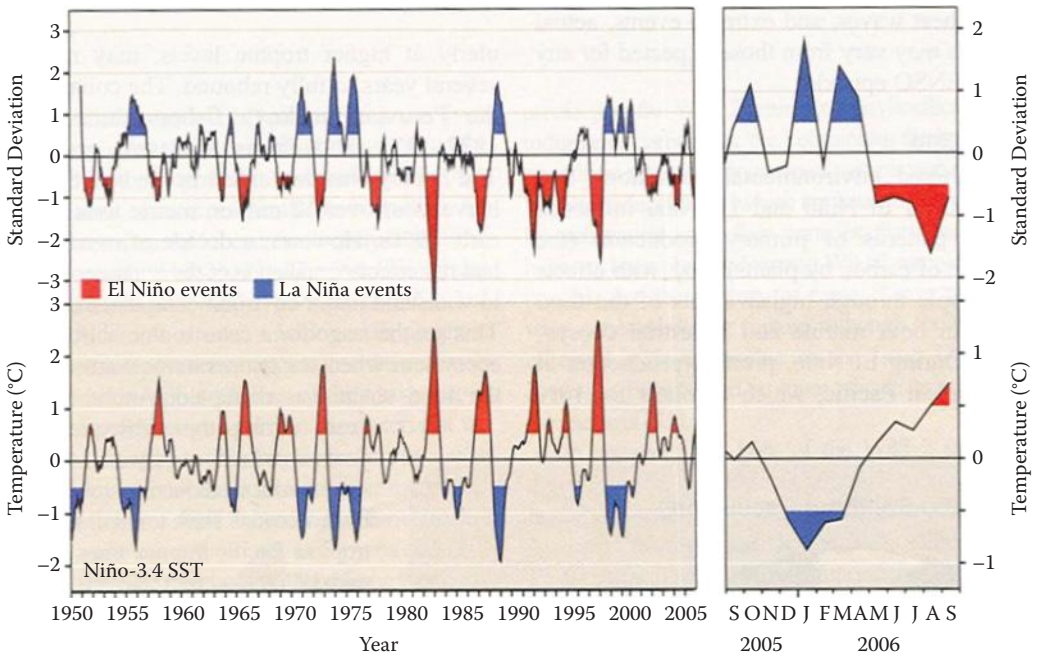

FIGURE 1.59
The Southern Oscillation Index (SOI) in the Pacific Ocean.

and storms in the North Atlantic. The PDO is related to surface temperature anomalies in the Pacific. The warm or positive phase has high sea surface temperatures in the Eastern Equatorial Pacific and cold waters in the northern Pacific. Anomalies are also observed in the sea-level pressures. The values in the east are lower than in the west. The warm waters in the east lead to the so-called El Niño (Figure 1.59) and when in reverse lead to the La Niña. These warm waters lead to higher precipitation on the coast of South America and prevent the upwelling of nutrient-rich waters that support the fisheries in the region. Other effects thought to be affected by the NAO are (McPhaden et al., 2006)

1. Patterns of primary production
2. Food chains, fisheries
3. Patterns of hurricanes
4. Climate patterns (rain, snow)
5. Bleaching of coral reefs
6. Agriculture in the United States and elsewhere
7. Drought in Australia
8. Increased diseases (malaria, cholera, etc.)

Future work will continue to be concentrated on the coupling between the atmosphere and ocean and the effect on the climate.

References and Further Reading

Descriptive Oceanography

Bowden, K.F., Oceanic and estuarine mixing processes, Chapter 1, *Chemical Oceanography,* Vol. 1, 2nd ed., Riley, J.P., and Skirrow, G., Eds., Academic Press, New York, 1–41 (1975).
Deacon, D., *Scientist and the Sea 1650–1900,* Academic Press, New York (1971).
Dietrich, G., Kalle, K., Krauss, W., and Siedler, G., *General Oceanography,* 2nd ed., Wiley, New York (1980).
McPhaden, M.J. et al., ENSO as an integrating concept in earth science, *Science* 324, 1740–1745 (2006).
Millero, F.J., A new high pressure equation of state for seawater, *Deep-Sea Res.,* 27, 255 (1980).
Millero, F.J., Effect of changes in the composition of seawater on the density–salinity relationship, *Deep-Sea Res. I,* 47, 1583 (2000a).
Millero, F.J., The equation of state of lake waters, *Aquatic Geochem.,* 6, 1 (2000b).
Millero, F.J., and Poisson, A., International one-atmosphere equation of state of seawater, *Deep-Sea Res.,* 28, 625 (1981).
Neumann, G., *Ocean Currents,* Elsevier, New York (1968).
Pickard, G.L. and Emery, W.J., *Descriptive Physical Oceanography*, Pergamon Press, Oxford , 4th Ed. (1982).
Reid, J.L., The shallow salinity minima of the Pacific Ocean, *Deep-Sea Res.*, 10, 51–68.
The Rings Group, Gulf Stream cold-core rings: their physics, chemistry and biology, *Science,* 211, 1091 (1981).
Talley, L.D., et al., *Descriptive Physical Oceanography: An Introduction*, 6th ed., Elsevier, New York (2011).
Tchernia, P., *Descriptive Regional Oceanography,* Pergamon Press, New York (1980).

Carbon-14

Broecker, W.S., *Chemical Oceanography,* Harcourt Brace Jovanovich, New York (1974).
Broecker, W.S., and Peng, T.H., *Tracers in the Sea,* Columbia University Press, New York (1982).
Campbell, J.A., The Geochemical Ocean Sections Study–GEOSECS, Chapter 44, *Chemical Oceanography,* Vol. 8, 2nd ed., Riley, J.P., and Chester, R., Eds., Academic Press, New York, 89–155 (1983).

Tritium

Ostlund, H.G., and Brescher, R., *GEOSECS Tritium*, Tritium Laboratory Data Report No. 12, Rosenstiel School, University of Miami (1982).
Roether, W., On oceanic boundary conditions from tritium, on tritiumgenic ^{3}He, and on ^{3}H/^{3}He concept, *Oceanic Circulation Models: Combining Data and Dynamics,* Anderson, D.L.T., and Willebrand, J., Eds., New York, 378–409 (1989).

Helium-3

Campbell, J.A., The Geochemical Ocean Sections Study-GEOSECS, Chapter 44, *Chemical Oceanography,* Vol. 8, 2nd ed., Riley, J.P., and Chester, R., Eds., Academic Press, New York, 89–155 (1983).
Clark, W., Beg, M.A., and Craig, H., Excess ^{3}He in the sea: evidence for terrestrial primordial helium, *Earth Planet., Sci. Lett.*, 6, 213 (1969).
Roether, W., On oceanic boundary conditions from tritium, on tritiumgenic ^{3}He, and on ^{3}H/^{3}He concept, *Oceanic Circulation Models: Combining Data and Dynamics,* Anderson, D.L.T., and Willebrand, J., Eds., New York, 378–409 (1989).

Chlorofluorocarbons

Bullister, J.L., Chlorofluorocarbons as time dependent tracers in the oceans, *Oceanography,* 2, 12–17 (1989).

Bullister, J.L., and Weiss, R.F., Determination of CCl_3F and CCl_2F_2 in seawater and air, *Deep-Sea Res.,* 35, 839 (1988).

Fine, R., Observations of CFCs and SF6 as ocean tracers, *Annu. Rev. Mar. Sci*, 7.1–7.23 (2011).

Lovelock, J.E., Maggs, R.J., and Wade, R.J., Halogenated hydrocarbons in and over the Atlantic, *Nature,* 241, 194 (1973).

Warner, M.J., and Weiss, R.F., Solubilities of chlorofluorocarbons 11 and 12 in water and seawater, *Deep-Sea Res.,* 32, 1485 (1985).

Age of Water Masses

Broecker, W.S., The ocean conveyor belt, *Oceanography,* 4, 79 (1991).

Broecker, W.S., and Peng, T.H., *Tracers in the Sea,* Columbia University Press, New York (1982).

Stuiver, M., Quay, P.D., and Ostlund, H.G., Abyssal water carbon-14 distribution and the age of the world oceans, *Science,* 219, 849 (1983).

2

Composition of the Major Components of Seawater

2.1 Introduction

Seawater is composed of a number of different components that can be divided into the following phases:

1. **Solids** (material that does not pass through a 0.45-μm filter)
   a. Particulate organic material (plant detritus)
   b. Particulate inorganic material (minerals)
2. **Gases**
   a. Conservative (N_2, Ar, Xe)
   b. Nonconservative (O_2 and CO_2)
3. **Colloids** (passes through a 0.45-μm filter but is not dissolved)
   a. Organic (complex sugars)
   b. Inorganic (iron hydroxides)
4. **Dissolved solutes**
   a. Inorganic solutes
      1. Major (>1 ppm)
      2. Minor (<1 ppm)
   b. Organic solutes

It should be pointed out that the separation of the phase of an element between solid, colloidal, and dissolved is operational and dependent upon the separation method used. Figure 2.1 demonstrates how the sizes of some solutes are related to the methods used to separate the phases. This chapter discusses the various dissolved major components of seawater. It examines the concentration of the major components in seawater and the processes that can cause them to vary from place to place.

The earliest chemical analysis of seawater was made by Bergman in 1779. Since that time, many workers have determined one or more elements in various ocean waters. Marcet in 1819 was the first to suggest that the relative composition of sea salt is nearly constant. Marcet analyzed water samples from the Arctic, Atlantic, Mediterranean, Black, Baltic, China, and White Seas. Although his techniques were rather crude and the atomic weights were only approximately known, his conclusions are correct: "All the species of seawater contain the same ingredients all over the world, these bearing very nearly the same proportion to each other, so that they differ only as to the total amount of their saline contents"

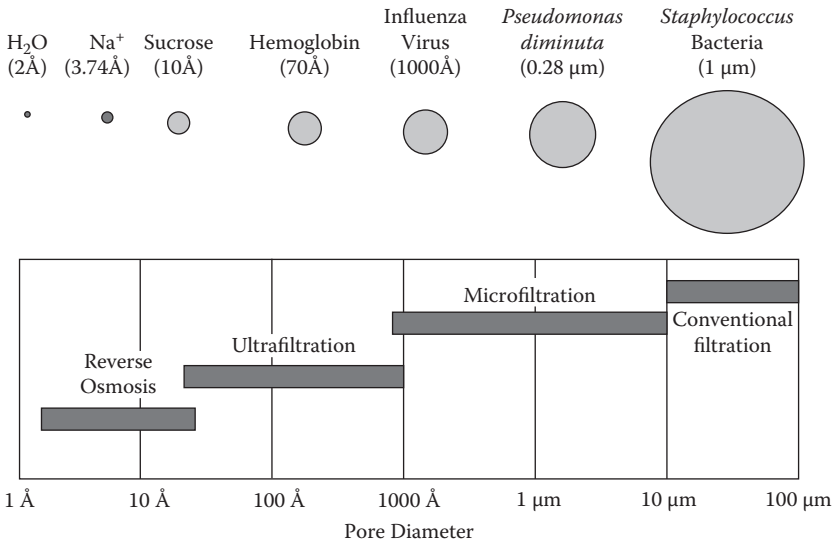

FIGURE 2.1
A comparison of the pore size of filtration to the size of solutes.

(Riley and Chester, 1971). Dana Kester (University of Rhode Island) called this simple suggestion the first law of chemical oceanography. Other earlier workers analyzed seawaters.

The first extensive investigations of the major inorganic components of seawater were made by Forchhammer in 1865. He determined the concentrations of Cl^-, SO_4^{2-}, Mg^{2+}, Ca^{2+}, and K^+ directly and Na^+ by difference. He made these measurements on several hundred surface waters from all parts of the world. He noted that the ratios of the major constituents (greater than 1 ppm by weight) were nearly constant, with only very slight variations. These major dissolved components make up 99.9% of the soluble ionic species of seawater. His results have been criticized on the grounds that he used only surface samples and that his analytical methods were inaccurate. In 1884, Dittmar analyzed 70 seawater samples collected at various depths for the major oceans during the cruise of the H.M.S. *Challenger* (1873–1876). Although his results are not as extensive as one might wish and the samples were stored for as long as 2 yr, he did adopt analytical techniques that are still used today. He also checked his experimental techniques on synthetic samples to examine the reliability of his measurements. His results agreed fairly well with the work of Forchhammer. He did find small variations in Mg^{2+}, K^+, SO_4^{2-}, Ca^{2+}, and Na^+. He found the values of Ca^{2+} for deep waters to be 0.3% higher than surface waters, which was five times higher than the analytical error. The results of Dittmar were recalculated in 1940 by Lyman and Fleming using modern atomic weights.

Since the work of Dittmar, many workers have studied the composition of natural waters. In 1965, Culkin made a thorough review of all the measurements made on the major components of seawater since the work of Dittmar. About the same time as this review appeared, an extensive study of the major components was being carried out by Cox, Culkin, and Riley (1967; Culkin, 1965; Culkin and Cox, 1966; Morris and Riley, 1966; Riley and Tongudai, 1967) as part of an international study of the salinity of seawater. Since the relative composition of ocean waters is nearly constant, it is possible to characterize the composition by measuring only one component that is easy to measure and is

conservative in its behavior. A conservative component of seawater is one that is unreactive and for which the changes from place to place are due to the addition or loss of water. The constituent originally selected to characterize a given sample of seawater or other natural waters was the chlorinity, Cl(‰). The chlorinity was originally defined as the chlorine equivalent to the total halide concentration in parts per thousand by weight (grams of Cl/kilogram of seawater) measured by titration with $AgNO_3$. Since changes can occur in the atomic weights of Ag and Cl, chlorinity was redefined in 1937 by Jacobsen and Knudsen: "The chlorinity is the mass in grams of pure silver necessary to precipitate the halogens in 328.5233 grams of seawater" (Riley and Chester, 1971). This definition gives the value of Cl(‰) as 0.3285233 Ag(‰), where Ag(‰) is the grams of silver per kilogram of seawater. The 1992 atomic weights yield ATW(Cl)/ATW(Ag) = 35.4527/107.8682 = 0.328667. Thus, the true chlorinity or chlorinity equivalent is equal to 0.328667/0.3285233 = 1.00044 times the Cl(‰).

2.2 The Concept of Salinity

Salinity was originally conceived as a measure of the mass of dissolved salts in a given mass of seawater (the weight fraction). The experimental determination of the salt content of seawater by drying and weighing presents some difficulties. At the temperatures necessary to drive off the last traces of H_2O, the bicarbonates and carbonates are decomposed to oxides (MO_2, where M = Na or K).

$$2HCO_3^- \rightarrow [MO_2] + H_2O + 2CO_2 \tag{2.1}$$

$$CO_3^{2-} \rightarrow [MO_2] + CO_2 \tag{2.2}$$

Br_2, some Cl_2 gas, and $B(OH)_3$ are also vaporized. For example, heating $MgCl_2$ solutions to dryness yields HCl gas. The Cl_2 and Br_2 lost can be determined by titrating with $AgNO_3$ before and after heating. Earlier workers (Marcet, Forchhammer, and Dittmar) found difficulty in determining the salinity by evaporation. A complete chemical analysis of seawater is the only reliable way to determine the true or absolute salinity of seawater (S_A, in parts per thousand). This method, however, is time consuming for routine studies and has a large uncertainty. The earlier studies are summarized in Table 2.1.

My earlier analysis (Millero, 2006) of the major components of seawater gives S_A = 35.1705, which is slightly higher than the Lyman and Fleming estimates using the earlier

TABLE 2.1

Estimate of S_A in Seawater from Composition Studies of the Major Components of Seawater by Various Workers at Cl(‰) = 19.274

Reference	Equation	S_A
Forchhammer (1865)	S_A = 1.812 Cl(‰)	35.11 g/kg
Dittmar (1884)	S_A = 1.806 Cl(‰)	34.98 g/kg
Lyman and Fleming (1940)	S_A = 1.8148 Cl(‰)	35.160 g/kg
Millero (2006)	S_A = 1.8154 Cl(‰)	35.1705 g/kg
Millero et al. (2008)	S_A = 1.81505 Cl(‰)	35.165 04 g/kg

TABLE 2.2

Calculation of Salinity for Average Seawater from Composition Data

Before Evaporation		**After Evaporation**		
Grams HCO_{3-}	0.1048	Grams	0.0134	
Grams CO_3^{2-}	0.0143	Grams	0.0004	
Grams CO_2	0.0004	Grams	0.0000	
Grams Br^-	0.0673	Grams Cl	0.0298	
	0.1869		0.0436	
Grams of salt loss from HCO_3^- CO_3^{2-} and Br^-; 0.1869 – 0.0436				= 0.1432
Grams of $B(OH)_3$ lost				= 0.0274
Total salts lost				= 0.1706

measurements. Recently, Millero et al. (2008) reexamined the composition of seawater and gave a value of 35.165 g/kg, which is in good agreement with the Lyman and Fleming (1940) estimate. This estimate is in reasonable agreement with the estimate made for the loss of salts when seawater is evaporated (Table 2.2) of 0.1706 g/kg.

In 1899, the International Council for the Exploration of the Sea (ICES) named Knudsen as chairman of a commission appointed to examine the definition of the salinity and density of seawater. Based on an evaporation method, Forch, Knudsen, and Sorensen defined the salinity as "the weight in grams of dissolved inorganic salts in one kilogram of seawater, when all bromides and iodides are replaced by an equivalent quantity of chlorides, and all the carbonates are replaced by an equivalent quantity of oxides" (Riley and Chester, 1971) The sample is dried to constant weight at 480°C. The Cl and Br lost are allowed for by adding a weight of Cl equivalent to the loss during drying. Salinity is thus the weight of dissolved solids minus the weight loss of HCO_3^- and CO_3^{2-} and minus the difference between Br_2 and its equivalent Cl_2. The determination has rarely been used because the method is too difficult for routine work. One can prevent the loss of HCl by adding NaF before evaporation. Morris and Riley (1964) made further improvements to the evaporation technique. Based on the assumption that the relative composition of seawater was constant, the commission defined chlorinity (given previously) and suggested that it could be used as a measure of salinity. Measurements of the chlorinity and evaporation salinity were made on nine samples of seawater (two from the Baltic, two from the Atlantic, four from intermediate Baltic–North Sea waters, and a Red Sea water). The results were found to fit the equation

$$S(‰) = 1.805\ Cl(‰) + 0.030 \tag{2.3}$$

The standard deviation was 0.01‰, and the largest deviation was 0.022‰. This formula was used in oceanography for about 65 years. As discussed previously, this definition is based on the 1902 atomic weights. The commission specified that titration results should be determined by using tables produced using Copenhagen "normal" seawater as a standard. To free chlorinity from its dependence on normal seawater stored in Copenhagen, the new definition of chlorinity was given in 1937. This definition is still used, although standard seawater, once called Copenhagen seawater, of known salinity is now provided by the Institute of Ocean Sciences (IOC) in Wormley, England.

One of the problems with this salinity–chlorinity relationship is that when Cl(‰) is 0, the value of salinity is 0.03‰. The low-salinity samples came from the Baltic, where the river waters have little chloride. As will be discussed, the form of the Knudsen

equation is quite general for a given estuarine system formed by mixing river water with seawater. Both the intercept and slope vary from location to location and from time to time.

With the development of precise conductivity bridges in the 1950s, it became possible to determine conductivity salinities to ±0.003‰. In 1961, nonthermostated commercial conductivity bridges became available. All these bridges gave conductivity ratios between the sample and standard seawater ($R = C_{sample}/C_{std}$) and used standard seawater to calibrate the bridges. Although standard seawater was calibrated for chlorinity, it was not meant to be a standard for conductivity. At about the same time, the old definition of salinity came under question because of the uncertain accuracy and small number of samples used. The Joint Panel for Oceanographic Tables and Standards (JPOTS), sponsored by UNESCO (United Nations Educational, Scientific, and Cultural Organization), ICES, IAPSO (International Association of Physical Sciences of Ocean), and SCOR (Scientific Committee on Oceanic Research), was appointed to develop a conductivity standard for salinity.

Samples were collected from around the world. These samples were analyzed for their chemical composition, chlorinity, and conductivity ratios. The JPOTS panel decided to revise the old relationship between salinity and chlorinity using Equation 2.4, which is equivalent to the original Knudsen definition at S = 35 or Cl = 19.374. Near S = 35, the two equations are identical; however, at S = 32 or 38, the difference is 0.003‰.

$$S(‰) = 1.80655\ Cl(‰) \tag{2.4}$$

Cox, Culkin, and Riley (1967) developed a relationship between the conductivity ratio at 15°C [$R_{15} = C_{15}(\text{sample})/C_{15}(\text{std seawater})$] and the chlorinity of samples collected throughout the world. Samples from deeper than 200 m were deleted (due to the Ca^{2+} affecting the R_{15}). Since most of the deep samples had S of 34.8, a discontinuity occurred when the results were deleted. The polynomial was adjusted by adding 0.0018 to make S = 35 and R = 1.0. The Cl(‰) as a function of R_{15} was converted to salinity using Cl = S/1.80655. The resultant equation was

$$S(‰) = -0.08996 + 28.2970R_{15} + 12.80832R_{15}^2 - 10.67869R_{15}^3 + 5.98624R_{15}^4 - 1.32311R_{15}^5 \tag{2.5}$$

Unfortunately, this relationship was referred to as the new definition of salinity, while in fact this polynomial merely expresses Cl in terms of R_{15} and is strictly valid at S of 35, which is equivalent to the old definition.

About the same time (1969) as the various organizations recommended the acceptance of the so-called redefinition of salinity, *in situ* salinometers became commercially available. Since the new definition only went to 10°C, it became necessary to use either extrapolated values or equations based on the dilution of seawater with pure water. Many workers attempted to use equations that joined these two methods.

Our laboratory examined many samples of standard seawater bottled from 1962 to 1975 for conductivity, salinity, and density. All the conductance measurements were made relative to the same standard seawater (P_{64} – 1973). Our results were in good agreement (±0.0012 average deviation) with measurements made by Poisson (University of Paris). The differences ranged from –0.002 to 0.008. The maximum spread of 0.0098 in salinity represents the maximum error one would obtain in using the various standard seawater samples. No systematic correlations of the differences were found with the age of the standard. These results pointed out the need to characterize the conductivity of seawater relative to a KCl standard. To examine the causes of these differences, we measured the

relative densities of the same samples. These results were then compared to the calculated values obtained using conductivity and chlorinity-derived salinities. The differences had a mean of $\pm 2 \times 10^{-6}$ g cm^{-3} (2 ppm) and showed no measurable differences in using S or Cl. Thus, the myth that conductivity salinities are better than chlorinity-derived salinities for determining density does not hold true for seawater collected in the North Atlantic over a period of 38 years.

One sample had densities 35 to 40×10^{-6} g cm^{-3} that was higher than the other samples. This was due to the dissolution of SiO_2 that occurred during closing of the sample or during storage. In general, these results indicate that standard seawater can be used as a conductivity and density standard to ±0.002 in S and $\pm 2 \times 10^{-6}$ g cm^{-3} in density.

In 1975, the JPOTS committee that had been considering a new equation of state of seawater suggested that a background paper be prepared on the salinity method (Lewis, 1978). It was concluded that a revision was needed in the definition of salinity, and the committee recommended the practical salinity scale of 1978. This new scale breaks the Cl–S relationship in favor of a salinity–conductivity ratio relationship. All waters with the same conductivity ratio have the same salinity (even though the composition may differ). Since salinity is normally used to determine a physical property like density, this was thought to be the best method for determining the effect of changes in ionic composition. This is not always the case since nonelectrolytes like SiO_2 are not detected by conductivity. More is said about this in further discussion.

A standard seawater of practical salinity of 35.000 (no units or ‰ are needed) has, by definition, a conductivity ratio of 1.0 at 15°C with a KCl solution containing a mass of 32.4356 g of KCl in a mass of 1 kg of solution. This value was determined as an average of three independent laboratory studies. The salinity dependence of the conductivity ratio was determined by measuring the conductivity (C) ratio at various temperatures of S = 35.000 seawater weight evaporated or diluted with water. The final equation is given by

$$S = a_0 + a_1 R_T^{1/2} + a_2 R_T + a_3 R_T^{3/2} + a_4 R_T^2 + a_5 R_T^{5/2} + \Delta S \tag{2.6}$$

where

$$\Delta S = [(t-15)/(1+k(t-15))](b_0 + b_1 R_T^{1/2} + b_2 R_T + b_3 R_T^{3/2} + b_4 R_T^2 + b_5 R_T^{5/2}) \tag{2.7}$$

$a_0 = 0.0080$	$b_0 = 0.0005$	
$a_1 = -0.1692$	$b_1 = -0.0056$	$k = 0.0162$
$a_2 = 25.3851$	$b_2 = -0.0066$	
$a_3 = 14.0941$	$b_3 = -0.0375$	
$a_4 = -7.0261$	$b_4 = 0.0636$	
$a_5 = 2.7081$	$b_5 = -0.0144$	
$\sum a_i = 35.000$	$\sum b_i = 0.0000$	

and $R_T = C(S, t, 0)/C(35, t, 0)$ at atmospheric pressure (p = 0).

As part of this new practical salinity scale, equations were given to reduce *in situ* conductivity, temperature, and depth (pressure) measurements to salinity. These measurements give a conductivity ratio:

$$R = C(S, t, P)/C(35, 15, 0) \tag{2.8}$$

$$R = \{C(S, t, P)/C(S, t, 0)\}\{C(S, t, 0)/C(35, t, 0)\}\{C(35, t, 0)/C(35, 15, 0)\} \tag{2.9}$$

$$R = R_P \cdot R_T \cdot r_T \tag{2.10}$$

The desired R_T is determined from $R_T = R/r_T(1 + \alpha)$, where $R_P = (1 + \alpha)$ and

$$\alpha = \frac{A_1P + A_2P^2 + A_3P^3}{(1 + B_1t + B_2t^2 + B_3R + B_4tR)} \tag{2.11}$$

$$A_1 = 2.070 \times 10^{-5} \qquad B_1 = 3.426 \times 10^{-2}$$

$$A_2 = -6.370 \times 10^{-10} \qquad B_2 = 4.464 \times 10^{-4}$$

$$A_3 = 3.989 \times 10^{-15} \qquad B_3 = 4.215 \times 10^{-1}$$

$$B_4 = -3.107 \times 10^{-3}$$

The value of r_T is given by

$$r_T = c_0 + c_1\, t + c_2\, t^2 + c_3\, t^3 + c_4\, t^4 \tag{2.12}$$

where

$c_0 = 6.7660 \times 10^{-1}$
$c_1 = 2.00564 \times 10^{-2}$
$c_2 = 1.104259 \times 10^{-4}$
$c_3 = -6.9698 \times 10^{-7}$
$c_4 = 1.0031 \times 10^{-9}$

It should be pointed out that all of the conductivity and other thermodynamic measurements of seawater were made with a known chlorinity. The equations have been converted to practical salinity using Equation 2.4. The practical salinity is valid from 2 to 42. Extensions to lower salinities are also available (Hill et al., 1986). For waters with salinities above 42, one can estimate practical salinity by diluting a sample by weight and determining the conductivity salinity.

The concept of absolute salinity S_A or true salinity S_T was discussed in our previous work. It was suggested that the density as well as most dilute other natural waters have the same values as seawater at the same absolute salinity. This has been demonstrated for a number of rivers, lakes, and estuarine waters. As part of the development of a new equation of state for seawater (Thermodynamic Equation of Seawater, TEOS-10, 2010), the composition of seawater was reexamined. The results, which are discussed elsewhere in this book, let the definition of the reference salinity b

$$S_R = (35.16504/35)\ \text{g kg}^{-1}\ S_P \tag{2.13}$$

where S_P is the practical salinity. The value of S_R provides the best estimate of the absolute salinity of standard seawater that was used in measuring the physical properties of seawater. The values of S_R are used as a concentration variable for all the physical and thermodynamic properties of seawater. This provides a salinity standard that can be used to examine the changes in the physical properties of seawater over time and a theoretical model for electrolyte mixtures.

The composition of seawater is not constant. It varies from place to place due to the addition of nutrients from the breakdown of plants and the precipitation and dissolution of $CaCO_3$. This was first pointed out by Brewer and Bradshaw (1975). They suggested that these changes in composition can change the density of deep waters and affect the density–conductivity relationship of seawater. This paper led to the examination of the density–salinity relationship of waters collected around the world by my group. The changes in the absolute salinity δS_A were given by

$$\delta S_A = S_A - S_R \tag{2.14}$$

The value of δS_A is estimated from the difference between the measured densities and the values determined from the equation of state of seawater as a function of salinity and temperature ($\Delta\rho$) using

$$\delta S_A = \Delta\rho/0.7519 \text{ kg m}^{-1}/(\text{g kg}^{-1}) \tag{2.15}$$

The values of δS_A were found to be linear functions of the concentration of SiO_2 (see Figure 2.2).

As shown in Figures 2.3 and 2.4, most of the large changes in δS_A were found in the deep waters of the Pacific Ocean.

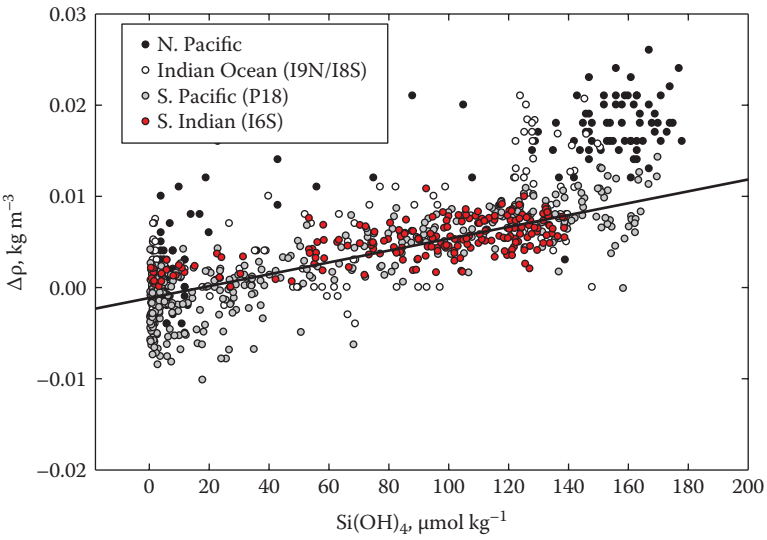

FIGURE 2.2
The changes in relative density of seawaters as a function of SiO_2 in ocean waters.

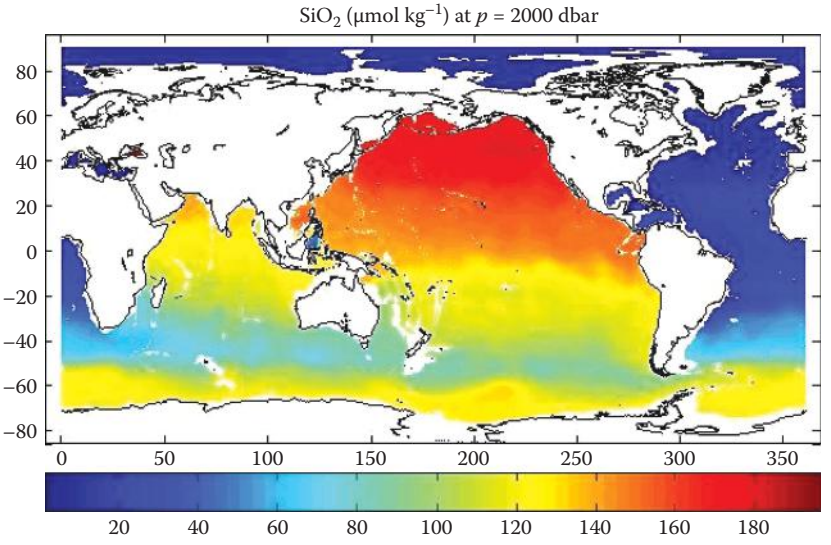

FIGURE 2.3
The changes in salinity of waters as a function of SiO_2 in ocean waters.

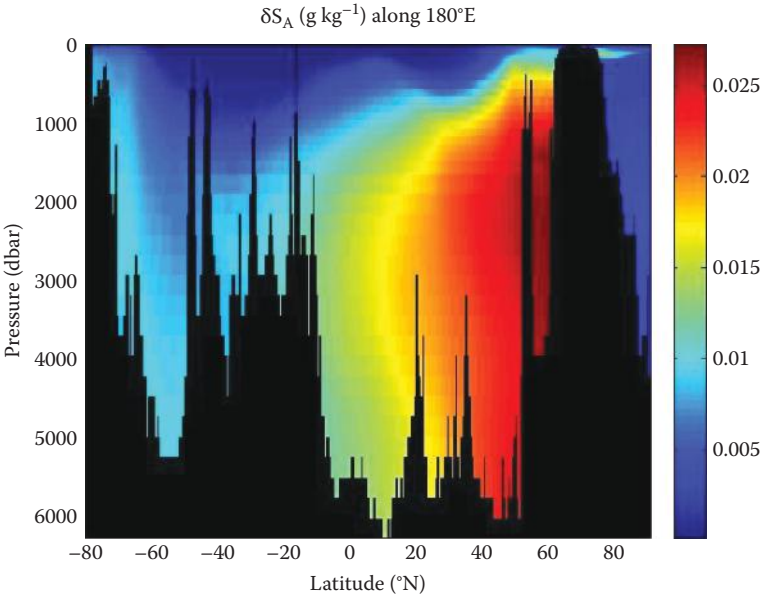

FIGURE 2.4
The concentrations of SiO_2 at 2000 m in Pacific Ocean waters.

The new thermodynamic equation of state requires an input of the absolute salinity. The use of the reference salinity is sufficient for all the properties except the density and enthalpy. Recent studies in the Arctic Ocean indicated that changes in dissolved organic carbon may also affect change in the density. Most of this material has a neutral charge affecting the density but not the conductivity.

2.3 Methods of Determination

The methods used to determine the major components of natural waters are given in detail elsewhere (Culkin, 1965; Kremling, 1976). Some of the popular methods that have been used are briefly discussed next.

2.3.1 Chloride

The chloride or chlorinity of seawater is determined by adding $AgNO_3$ to precipitate AgCl.

$$Ag^+ + \text{Seawater} \rightarrow AgCl(s) + AgBr(s) \tag{2.16}$$

Potassium chromate is added as an indicator. After the halides are removed, silver chromate is precipitated:

$$2Ag^+ + CrO_4^{2-} \rightarrow Ag_2CrO4_4 \text{ (red solid)} \tag{2.17}$$

Some workers have used other indicators, and modern workers use an automated potentiometric end point (using an Ag, AgCl electrode). Since the heat of precipitation of AgCl is quite high and exothermic (heat is given off), we have used a titration calorimeter to determine the end point (Millero, Schrager, and Hansen, 1974). Since the heat of solution of $AgNO_3$ is endothermic (heat is taken up), the end point is very sharp. The $AgNO_3$ is added by using a constant-flow burette, and the time required to reach the end point is recorded. The system can be calibrated using NaCl or standard seawater.

No matter what method is used to determine the end point, standard seawater of known chlorinity is used to standardize the $AgNO_3$ solution. Since the chlorinity is a conservative component of seawater, it is important to measure or determine its value when studying the other major components of the waters. The approximate value of Cl(‰) for seawater can be determined from conductivity or density measurements. The measurements of Cox, Culkin, and Riley (1967) yielded the equation

$$Cl(‰) = -0.050 + 15.66367R_{15} + 7.08943R_{15}^2 - 5.91110R_{15}^3 + 3.31363R_{15}^4 - 0.73240R_{15}^5 \tag{2.18}$$

for various ocean waters, where R_{15} is the conductivity ratio at 15°C of the sample relative to standard seawater. More reliable values for the chlorinity of ocean waters can be obtained from the density or the conductivity ratio of seawater as a function of the salinity determined using the practical salinity scale and the international equation of state for seawater.

2.3.2 Sulfate

The most widely used method to determine SO_4^{2-} in seawater is the addition of $BaCl_2$ and subsequent precipitation of $BaSO_4$, which is weighed. Since other salts coprecipitate (e.g., Ca^{2+}), errors can result from using this technique. Measurements relative to standard seawater of known concentration can be very precise. The end point of the titration of seawater with $BaCl_2$ can be determined using calorimetry (Millero, Schrager, and Hansen, 1974), potentiometry, or conductivity.

2.3.3 Bromine

Bromine is normally determined after being coprecipitated with Cl^- by the determination of the weight loss after the Br_2 is liberated. This requires large samples since the concentration of Br^- is quite low. The Br_2 is liberated by adding chromic acid or potassium permanganate. The liberated Br_2 can be determined colorimetrically or by titration.

2.3.4 Fluorine

Fluorine is analyzed in natural waters by using colorimetric methods or using a specific ion electrode. The details are given elsewhere (Kremling, 1976).

2.3.5 Bicarbonate and Carbonate

The concentrations of HCO_3^- and CO_3^{2-} are determined by measuring at least two parameters of the carbonate system (pH, the total alkalinity, TA; the total carbon dioxide, TCO_2; or the partial pressure of CO_2, pCO_2). In most routine work, pH and TA are used to characterize the carbonate system. More details of these measurements are discussed in Chapter 7.

2.3.6 Boric Acid and Borate

Boron exists mainly as boric acid in seawater. At a pH of 8, the borate ion is 25% of the total boron. The total boron is determined as boric acid by forming a complex with mannitol and glycol. It is then converted to a strong acid and titrated with a base. It is first necessary to destroy the organic boron compounds by oxidation with permanganate. Colorimetric techniques using a colored indicator such as the boric acid–curcumin complex are much quicker (Uppström, 1974). Recently, Lee and coworkers (2010) have improved on the earlier methods and determined more reliable concentrations for boric acid in seawater.

2.3.7 Magnesium

The classical method for determining Mg^{2+} is a gravimetric determination of the precipitate formed following the addition of ammonium phosphate (after the Ca^{2+} is removed). The magnesium ammonium phosphate is converted to magnesium pyrophosphate and weighed. In recent years, volumetric methods have been used. EDTA (ethylenediamine N,N,N,N′ tetraacetic acid) has been used to titrate Mg^{2+} after Ca^{2+} has been removed. The total equivalents of divalent ions can be determined by using an ion exchange resin or an EDTA titration. The Mg^{2+} is determined by difference after the subtraction of Ca^{2+} and Sr^{2+}. Problems in the determination of the end point were discussed by Carpenter and Manella (1973).

2.3.8 Calcium

The classical gravimetric method used to determine Ca^{2+} is precipitation as the oxalate. This can be used as a method to separate Ca^{2+} and Mg^{2+}. Calcium oxalate is weighed as is or ignited to $CaCO_3$ or CaO. As with all precipitation techniques, coprecipitation problems are encountered, and various steps have to be taken to obtain a pure precipitate. Most modern measurements of Ca^{2+} have been made using volumetric titrations. The complexing agent EGTA [ethylene glycol-bis (2-aminoethyl)-N,N,N′,N′ tetraacetic acid) is used. The end point is detected potentiometrically or colorimetrically using metallochromic indicators.

2.3.9 Potassium

Early measurements of potassium were made after removal of divalent ions. The total cations can be determined by ion exchange methods (titrating the released protons with base). The divalent ions are removed and determined by EDTA titration. Potassium can be determined by precipitation with chloroplatinate, K_2PtCl_{26}, which is sparingly soluble in 80% ethanol (the Na^+ salt is very soluble). Since potassium tetraphenylboron is not very soluble, it can be weighed after precipitation by adding sodium tetraphenylboron.

2.3.10 Sodium

Since the concentration of sodium is quite high, it cannot be accurately determined by direct methods. The classical direct determination is made by precipitation with zinc uranyl acetate, which is sparingly soluble. The most reliable method to determine Na^+ is by difference. This can be done on individual samples by determining the total cations (equal to the total equivalents of the anions) and subtracting the equivalent concentrations of K^+, Mg^{2+}, Ca^{2+}, and Sr^{2+}. Since seawater should have the same equivalent concentration of cations and anions, the preferred method is to determine the Na^+ after the other major components are determined (i.e., by difference).

2.4 Composition and Stoichiometry of Average Seawater

To examine the physical chemical properties of seawater, it is necessary to select a reasonably reliable composition for average seawater (salinity [S] = 35, pH = 8.1, and temperature [t] = 25°C). The major component measurements made by Cox, Culkin, Riley, and coworkers measured the major cations Na^+, K^+, Mg^{2+}, Ca^{2+}, and Sr^{2+} in seawater. These results are in reasonable agreement with the earlier results of Dittmar as recalculated by Lyman and Fleming (1940). With the exception of Ca^{2+}, all the studies demonstrated little or no depth dependence for the major cations. The value of gCa/Cl(‰) increased by 0.3 to 0.5% for deep waters because of the dissolution of $CaCO_3$(s). More is said in Chapter 7 about the dissolution of $CaCO_3$(s). In the major oceans, the values of g_i/Cl(‰) are reasonably constant. Small variations do occur in some areas because of unique features, such as gCa/Cl(‰) in the Red Sea. The values of g_i/Cl(‰) for average seawater are given in Table 2.3. As discussed further in the chapter, it was the estimated reference composition for seawater used when the physical properties were made (1970 to 1980). The values for Ca^{2+}, K^+, and Sr^{2+} were taken from the work of Culkin and Cox (1966) and Riley and Tongudai (1967);

TABLE 2.3

Composition of Reference Seawater (S_P = 35.000, pCO_2 = 337 µatm, and t = 25°C)

	g_i (g/kg)	AW	m_i (mol/kg-H_2O)	e_i (mol/kg-H_2O)	I_i (mol/kg-H_2O)
Na^+	10.78145	22.9898	0.4860573	0.4860573	0.4860573
Mg^{2+}	1.28372	24.3050	0.0547419	0.1094837	0.2189674
Ca^{2+}	0.41208	40.0780	0.0106566	0.0213133	0.0426266
K^+	0.3991	39.0983	0.0105796	0.0105796	0.0105796
Sr^{2+}	0.00795	87.6200	0.0000940	0.0001881	0.0003762
Cl^-	19.35271	35.4530	0.5657619	0.5657619	0.5657619
SO_4^{2-}	2.71235	96.0626	0.0292642	0.0585283	0.1170567
HCO_3^-	0.10481	61.0168	0.0017803	0.0017803	0.0017803
Br–	0.06728	79.9040	0.0008727	0.0008727	0.0008727
CO_3^{2-}	0.01434	60.0089	0.0002477	0.0004953	0.0009907
$B(OH)_4^-$	0.00795	78.8404	0.0001045	0.0001045	0.0001045
F^-	0.0013	18.9984	0.0000709	0.0000709	0.0000709
OH^-	0.00014	17.0073	0.0000085	0.0000085	0.0000085
$B(OH)_3$	0.01944	61.8330	0.0003259	0.0000000	
CO_2	0.00042	44.0095			
Σ =	35.16504		1.1605659	1.2552445	1.4452533
H_2O	964.83496		0.580283	0.627622	0.722627

Source: Millero et al. (2008). With permission.

the value for Mg^{2+} was taken from the work of Carpenter and Manella (1973); the values for SO_4^{2-} and Br^- were taken from the work of Morris and Riley (1966); the value for F^- was taken from that of Warner (1971); the value of Cl^- was determined from the chloride equivalent by subtracting the equivalent Br^-; and the value of Na^+ was determined by difference (i.e., by assuming the cation and anion equivalents were equal). The results for HCO_3^-, CO_3^{2-}, $B(OH)_3$, and $B(OH)_4^-$ were determined for seawater of pCO_2 = 370 µatm using B/Cl(‰) of 0.000232 (Uppström, 1974) and TA = 2296 µmol/kg (Millero et al., 1993). The dissociation constants of carbonic and boric acids were, respectively, taken from the work of Millero et al. (2006) and Millero (2002) and Dickson (1990) using the CO2sys Program (Pierrot et al., 2006).

It should be pointed out that this is the reference composition of seawater. The composition of seawater in the future will change due to the increasing concentration of CO_2 from the burning of fossil fuels. The concentration of CO_2 and HCO_3^- will increase, and the concentration of $B(OH)_4^-$ will decrease.

The composition of seawater in Table 2.3 can be used to develop equations that can estimate the values of molality, equivalents and ionals for the components of seawater as a function of practical salinity, as well as for seawater. The individual values of the molality and the like of the components (Ai) can be determined from equations for the values as a function of S_P:

$$m(ion) = m_i\,(S_P/35) \tag{2.19}$$

$$e(ion) = m_i\,(S_P/35) \tag{2.20}$$

$$I(ion) = m_i\,(S_P/35) \tag{2.21}$$

The total molality $\sum m_i/2$, equivalent $\sum e_i/2$, and ionic strength $\sum I_i/2$ for seawater as a function of S_P can be estimated from

$$m = \tfrac{1}{2}\,(\sum m_i\,(S_P/35) = 0.580283\,S_P/35) \tag{2.22}$$

$$e = \tfrac{1}{2}\,(\sum e_i\,(S_P/35) = 0.627622\,S_P/35) \tag{2.23}$$

$$I = \tfrac{1}{2}\,(\sum I_i\,(S_P/35) = 0.722627\,S_P/35) \tag{2.24}$$

The mean molecular M_T and equivalent weight E_T of seawater are given by

$$M_T = \tfrac{1}{2} \sum m_i\,AW_i = 62.793 \tag{2.25}$$

$$E_T = \tfrac{1}{2} \sum e_{i\,EW} = 58.046 \tag{2.26}$$

For the grams of water in 1 kg of seawater,

$$g_{H_2O} = 1000 - 1.00488\,S_P \tag{2.27}$$

These results can be used to aid in the preparation of 1 kg of artificial seawater. A recipe that can be used to make up artificial seawater is given in Table 2.4. It should be kept in

TABLE 2.4

Preparation of 1 kg of 35.00 of Artificial Seawater

Salt	Grams/Kilogram	Moles/Kilogram	Molecular Weight
Gravimetric Salts			
NaCl	24.8780	0.42568	58.4428
Na_2SO_4	4.1566	0.02926	142.0372
KCl	0.7237	0.00971	74.5550
$NaHCO_3$	0.1496	0.00178	84.0070
KBr	0.1039	0.00087	119.0060
$B(OH)_3$	0.0266	0.00043	61.8322
NaF	0.0030	0.00007	41.9882
	30.0413		
Volumetric Salts			
$MgCl_2$	5.2121	0.05474	95.211
$CaCl_2$	1.1828	0.01066	110.986
$SrCl_2$	0.0149	0.00009	158.526

Use 1 molar $MgCl_2$, $CaCl_2$, and $SrCl_2$ (standardize by $AgNO_3$ titration). 52.8 ml of 1 molar $MgCl_2$, 10.3 ml of 1 molar $CaCl_2$, and 0.1 ml of 1 molar $SrCl_2$ are needed. The densities of these solutions are 1.017 g/ml, 1.013 g/ml, and 1.131 g/ml, respectively, for $MgCl_2$, $CaCl_2$, and $SrCl_2$ solutions at 1 molar. The grams of water in each solution are given by

$$H_2O = g_{SOLN} - g_{SALT} = \text{ml} \times \text{density} - g_{SALT}$$

Addition of Water

g_{H_2O} to add = 1000 – g_{H_2O} from $MgCl_2$, $CaCl_2$, and $SrCl_2$

TABLE 2.5

Precision in Salinity Determined by Various Methods

1. Composition studies of major components	±0.01
2. Evaporation to dryness	±0.01
3. Chlorinity	±0.002
4. Density	±0.004
5. Conductivity	±0.001
6. Sound speeds	±0.03
7. Refractive index	±0.05

mind that the trace metal impurities in most reagent-grade salts are higher than in natural seawater. Thus, care must be taken when using artificial seawater solutions in biological studies.

2.5 Methods of Determining Salinity

As discussed, the salinity of seawater is normally determined by a conductance measurement using the practical salinity scale. Although this method yields very precise results, they are not always accurate since the conductance responds only to ionic components. In practice, any physical property (density, refractive index, sound speed, etc.) at a fixed temperature and pressure can be used to determine the salinity. Before we discuss these other methods, we examine the most popular method of measuring salinity by conductivity. In Table 2.5, the precision of the salinities determined using various methods is summarized. In routine measurements, it is possible to determine relative densities to $\pm 3 \times 10^{-6}$ g cm^{-3}, sound speeds to ±0.03 m s^{-1}, and refractive indexes to ±0.00001. These precisions are equivalent to errors in salinity of ±0.004, ±0.028, and ±0.053, respectively, for density, sound speeds, and refractive indices.

2.6 Causes of the Major Components Not Being Conservative

Although the major components of seawater are relatively constant, a number of factors can cause them to be nonconservative. This section examines some of the areas (estuaries, anoxic basins and sediments, hydrothermal vents, evaporated basins) where processes (such as precipitation, dissolution, evaporation, freezing, and oxidation) can change the composition of some major components of seawaters.

2.6.1 Estuaries

The concentration of salts in rivers is controlled by the nature of the rocks being weathered and the soil types, yielding groundwaters that differ in chemical composition. The total solids in most rivers are less than 200 mg kg^{-1} (ppm) or 0.2‰, but the ratios of SO_4^{2-}, HCO_3^-, K^+, Mg^{2+}, and Ca^{2+} to Cl^- are usually greater than in seawater. The relative composition of

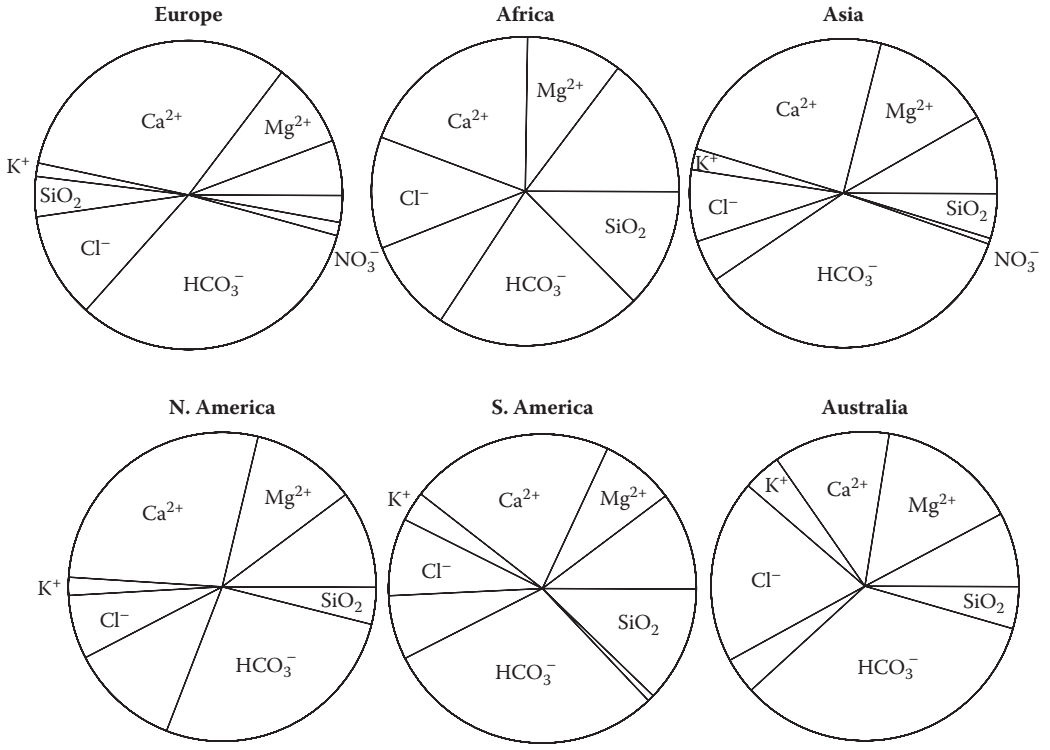

FIGURE 2.5
The major components of various rivers on the continents of the world.

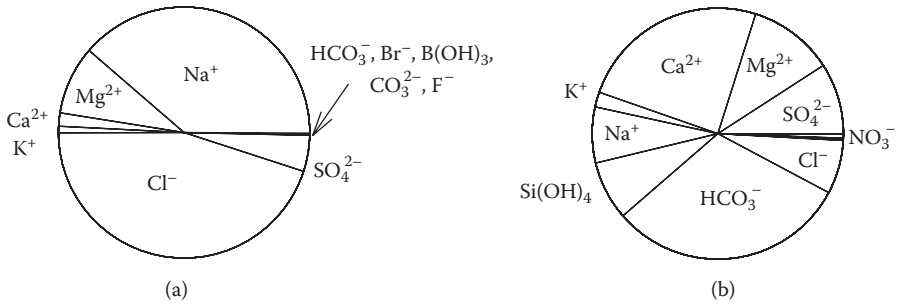

FIGURE 2.6
The equivalent fraction of the major constituents of the average world river and seawater.

rivers entering the oceans on various continents is shown in Figure 2.5. The composition of average world water is compared with normal seawater in Figure 2.6. Although the total dissolved solids varies from 70 to 200 ppm, the equivalent fractions of the major components of most rivers are similar. The major cations are Ca^{2+}, Mg^{2+}, and Na^+, and the major anions are HCO_3^-, SO_4^{2-}, and Cl^-. Most of the NaCl is recycled from sea salt aerosols. The SiO_2 is predominantly in the un-ionized form $Si(OH)_4$ at the pH of most rivers (7.3 to 8.0). The major constituents of world river water are Ca^{2+} and HCO_3^- (from weathering of $CaCO_3$).

FIGURE 2.7
Stations in the Baltic Sea.

I have analyzed (Millero, 1978) the formation of the Baltic Sea estuary (Figure 2.7) by mixing average Baltic river water with seawater. The Baltic is a stratified positive estuary with a large salinity and temperature gradient (Figure 2.8). The nutrients NO_3^- and PO_4^{3-} are quite high in the deep water because of the oxidation of plant material (Figure 2.9). The O_2 levels are quite low in the deep water because of this oxidation (Figure 2.10). As discussed, the dissolved constituents of an estuary are a linear function of Cl^-. The chemical data of Kremling (1969, 1970, 1972) for the major constituents are shown in Figure 2.11 and Figure 2.12, in which the grams of each component (g_i) per kilogram of seawater are plotted against the chlorinity. A summary of the intercepts (equal to g_R) is shown in Table 2.6. The total grams of salts (g_T) are given by

$$g_T = g_R + [(35.171 - g_R)/19.374]\ Cl(‰) \tag{2.28}$$

where g_R is the grams of river salts. Since the slopes are related to the river concentration, more reliable values of g_R can be obtained from

$$g_R = \frac{[g_E - g_{SW}]19.374}{19.374 - Cl(‰)} \tag{2.29}$$

and

$$g_{SW} = k_i \times Cl(‰) \tag{2.30}$$

where k_i is the average ratio of g_i/Cl for seawater (Table 2.1). The values of g_R determined from this equation have been determined from all the measurements of Kremling in 1967

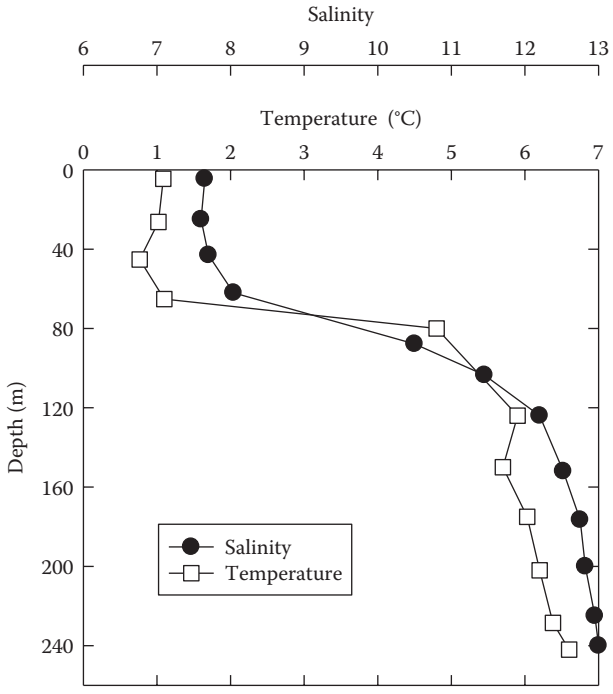

FIGURE 2.8
Salinity and temperature profiles for the Baltic Sea.

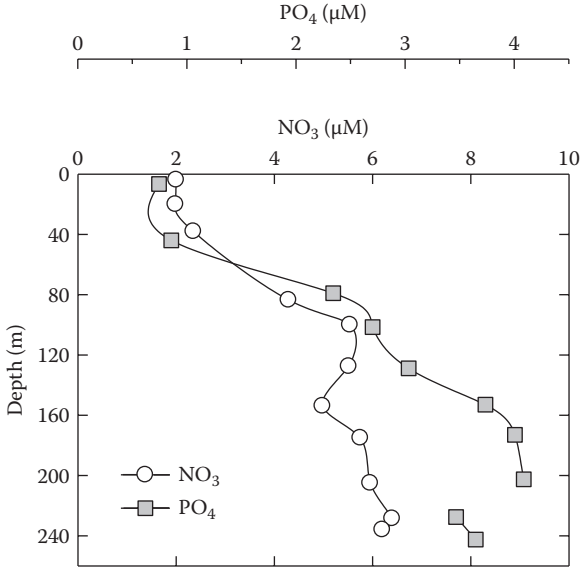

FIGURE 2.9
Phosphate and nitrate profiles for the Baltic Sea.

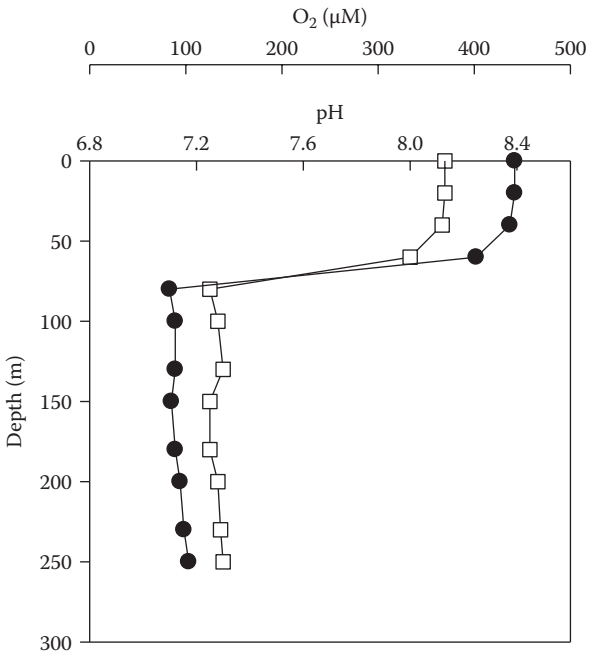

FIGURE 2.10
Oxygen and pH profiles for the Baltic Sea.

of $g_T = 0.121$ and can be compared to the earlier results of Lyman and Fleming of $g_T = 0.073$. This increase over the past 60 years is largely due to increases in Ca^{2+} and HCO_3^-. The SO_4^{2-} has decreased apparently because of the waters becoming more anoxic (see Figure 2.13). A comparison of Baltic river water and world river water is shown in Figure 2.14. Since the flow rate of the major rivers entering the Baltic has decreased (Figure 2.15), the increase in g_T can be attributed to less rainfall diluting the groundwater (which has a fixed concentration of Ca^{2+} and HCO_3^-). It is interesting to note that the flow rate is cyclic (with a cycle nearing that of the sunspot cycle of 11 years). This would lead to cycling of the input of solids into the estuary and cause a pulsing rate for the renewal of the deep waters (from the North Sea). One could postulate that the banding of FeS in the Baltic Sea sediments is caused by the pulsing flow rate of the rivers, which is caused, in turn, by sunspot activity. The examination of a deep basin in the Baltic (Figure 2.16) as a function of time shows a pulsing pattern (oxic to anoxic); however, the periods are quite short.

The practical salinity scale is frequently used to characterize the composition of estuarine waters. Since the composition of these waters is different from those used in setting up the scale (i.e., seawater diluted with pure water), it is appropriate to discuss its limitations. A typical estuarine solution can be formed by mixing world river with average seawater (Table 2.7). If the SiO_2 is left out of the river end member, the total grams of salts in 1 kg of solution are related to Cl by

$$g(E) = 0.092 + 1.80271\ Cl(‰) \tag{2.31}$$

Since salts are lost when seawater is evaporated, the true salinity ($S_T = g_T/1.0049$) is given by

$$S_T = 0.092 + 1.80183\ Cl(‰) \tag{2.32}$$

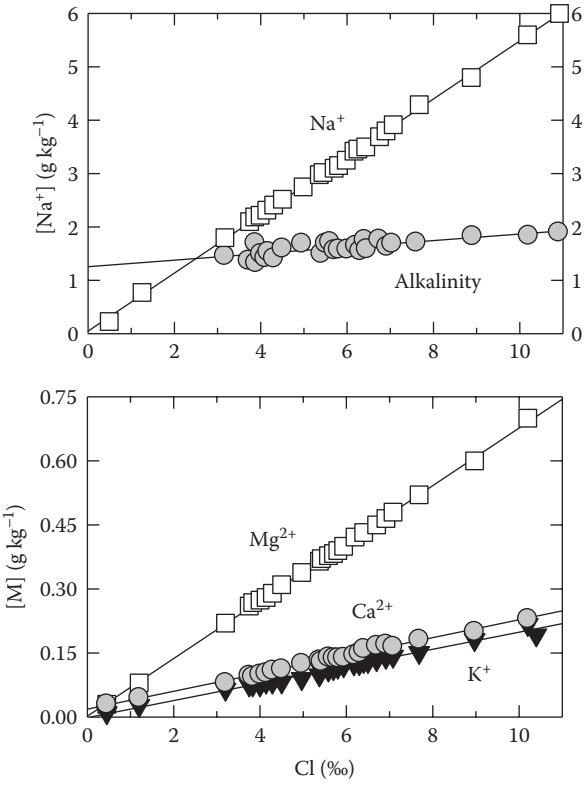

FIGURE 2.11
Concentrations of Na^+, Mg^{2+}, Ca^{2+}, K^+, and alkalinity (HCO_3^-) as a function of the chlorinity in the Baltic Sea.

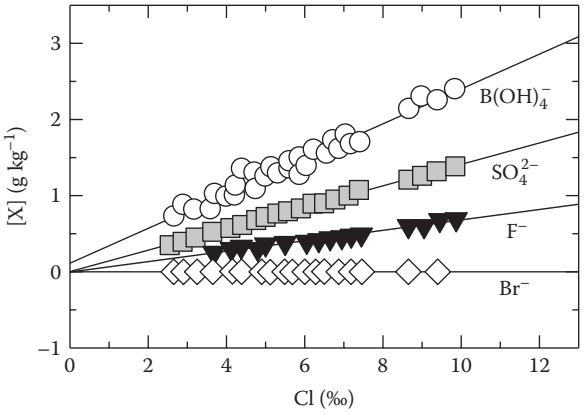

FIGURE 2.12
Concentrations of $B(OH)_4^-$, SO_4^{2-}, F^-, and Br^- as a function of chlorinity in the Baltic Sea.

TABLE 2.6

Composition of Baltic Surface Waters

Solute	1900 Data[a]	Best Estimate[b]
Na+	—	5.4 ± 3.8
Mg^{2+}	2.3	2.9 ± 0.5
Ca^{2+}	15.4	21.1 ± 0.6
K+	—	0 ± 0.5
Sr^{2+}	—	—
Cl^-	—	—
SO_4^{2-}	6.1	6.0 ± 1.0
HCO_3^-	49.3	84.6 ± 4.2
Br –	—	0.0 ± 0.8
$B(OH)_4^-$	—	—
F–	—	0.06 ± 0.1
$B(OH)_3$	—	0.8 ± 0.03
Totals	72.8	120.7 ± 11.5

[a] $g_T = 0.073 + 1.8110$ Cl(‰); Lyman and Fleming (1940) (1900 data).
[b] $g_T = 0.120 + 1.8092$ Cl(‰); Millero (1978) (1967 data).

The values of the practical conductivity salinity of the estuarine mixtures were found to be related by

$$S_{COND} = 0.044 + 1.803898 \text{ Cl}(‰) \tag{2.33}$$

while the values of salinity determined by density were given by

$$S_{DENS} = 0.092 + 1.80186 \text{ Cl}(‰) \tag{2.34}$$

The differences between S_A and S_P or S_ρ are shown in Figure 2.17. The values of salinity determined by density are in excellent agreement with the true salinity. These results indicate that density-derived salinities are more reliable for typical estuarine solutions than conductivity values. The lower values of S_{COND} are related to the differences in the equivalent conductance of the main components of seawater and world river water (see Table 2.8). The conductances of Na^+ and Cl^- are larger than Mg^{2+}, Ca^{2+}, and HCO_3^-; thus, at a given Cl(‰), the conductance of seawater diluted with pure water is greater than that of estuarine waters. Below Cl(‰) = 2.0, the conductivity of river water is 0.94 ± 0.02 lower than seawater diluted to the same Cl(‰). This can be compared to $\Lambda^\circ_{RW}/\Lambda^\circ_{SW} = 0.88$ calculated from infinite dilution conductivity data. Part of this difference is related to the limitation of the practical salinity scale to S = 2.000. The scale can be extended to lower salinities by using the equation

$$S = S_{PSS} - \frac{a_0}{1 + 1.5X + X^2} - \frac{b_0 f(t)}{1 + Y^{1/2} + Y + Y^{3/2}} \tag{2.35}$$

where S_{PSS} is the value determined from the practical salinity scale given previously, and the other parameters are given by $a_0 = 0.0080$, $b_0 = 0.0005$, $X = 400\ R_T$, $Y = 100\ R_T$, and $f(t) = (t - 15)/[1 - 0.0162(t - 25)]$. The addition of this term allows one to calculate reliable values

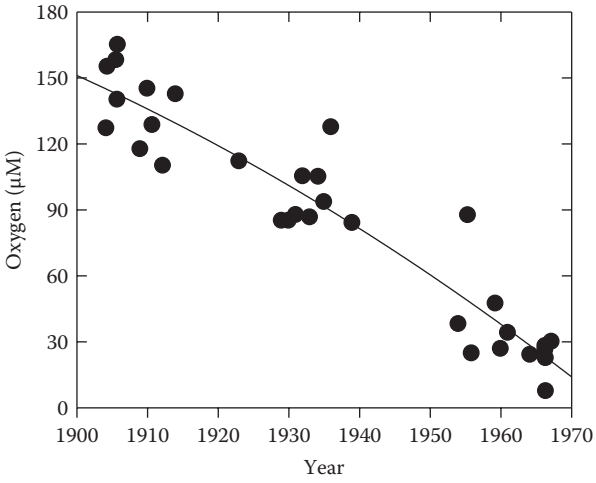

FIGURE 2.13
The concentration of oxygen as a function of time in a deep basin of the Baltic Sea.

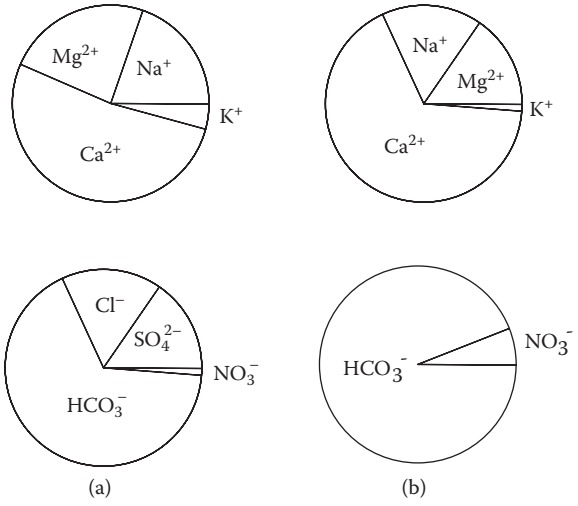

FIGURE 2.14
Comparison of the major sea salts in world and Baltic river waters.

of S_T for seawater diluted with pure water to dilute solutions. It also should prove useful in characterizing the salinity of rivers and dilute lakes.

These results indicate that it is possible to make reasonable estimates of the true salinity of an estuarine system if the composition of the river end member is known. For careful work, laboratory mixing experiments should be made, especially when the composition of the river end member is not known. As mentioned, one should calibrate the salinometer with seawater diluted with pure water to be sure it is working properly in dilute solutions. The maximum error is 35×10^{-6} g cm^{-3} in density. If the comparisons are made at the same S_T, the differences are within $\pm 3 \times 10^{-6}$ g cm^{-3}. Salinities derived from density will be reliable only when the river salts have an effect on density similar to that of sea salts. This is true for average river waters, but not for every river. The St. Lawrence River waters

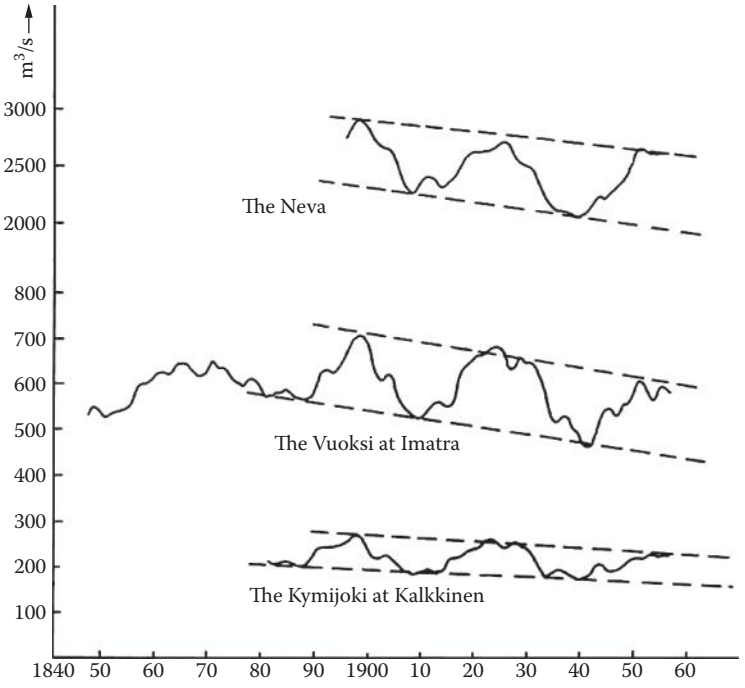

FIGURE 2.15
Mean values of the runoff of rivers into the Baltic Sea.

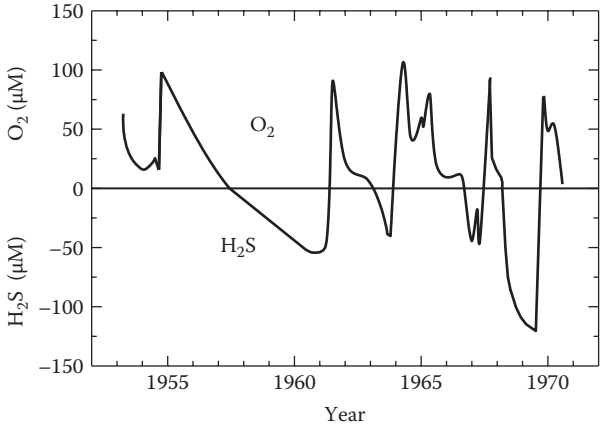

FIGURE 2.16
The concentrations of oxygen and hydrogen sulfide in a deep basin of the Baltic Sea.

have a density 14×10^{-6} g cm^{-3} larger than seawater diluted to the same Cl. These results indicate that, although dilute St. Lawrence River waters have conductivity similar to world river waters, the densities are different. Thus, for careful estuarine work, it is necessary to measure both density and conductivity as a function of chlorinity to fully characterize the system. If errors of ±0.04 in salinity and $\pm 50 \times 10^{-6}$ g cm^{-3} can be tolerated, the practical salinity scale and the international equation of state of seawater can be used for estuarine systems without a detailed knowledge of their ionic composition.

TABLE 2.7

Composition of 1 Liter of Average World River Water

Species	$10^6 g_i$	$10^3 n_i$	$10^3 e_i$	$10^3 I_i$
Na^+	6.5	0.283	0.283	0.283
Mg^{2+}	4.1	0.169	0.337	0.674
Ca^{2+}	15.0	0.374	0.749	1.496
K^+	2.3	0.059	0.059	0.059
Cl^-	7.8	0.220	0.220	0.220
SO_4^{2-}	11.2	0.117	0.233	0.466
HCO_3^-	58.4	0.950	0.950	0.950
CO_3^{2-}	—	0.002	0.004	0.008
NO_3^-	1.0	0.016	0.016	0.016
$Si(OH)_3O^-$	—	0.005	0.005	0.005
$1/2\Sigma =$		1.086	1.428	2.089
$Si(OH)_4$	21.5	0.213	0.213	—
	$g_T = 126.8$	$n_T = 1.299$	$e_T = 1.641$	$I_T = 2.089$

Note: To convert to molar units multiply by the density. To convert to molal units, divide by $X_{H_2O} = 0.96483$.

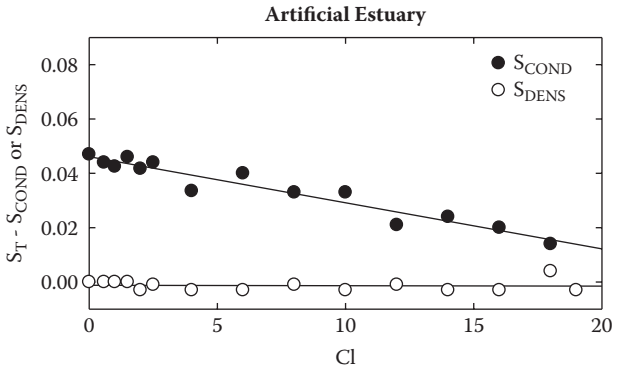

FIGURE 2.17
Comparison of the salinity determined from conductivity and density for estuarine waters.

2.6.2 Evaporation in Isolated Basins

The formations of evaporites in hot arid regions (Stassfurt deposits) were first studied by Van Hoff in 1912 (Borchert, 1965). During the slow evaporation of seawater, the precipitation of salts changes the composition of the solution. We have studied the changes in the composition of the major components of seawater in Mexican lagoons during evaporation to a salinity of close to 200 or Cl equal to 100. Our results are shown in Figure 2.18 and Figure 2.19. At a Cl of 40 (S = 72), there is a loss of Ca^{2+} and SO_4^{2-}, probably as $CaSO_4 \bullet 2H_2O$ (gypsum). The loss of HCO_3^- indicates that $CaCO_3$, as aragonite, may also be precipitated. The small decreases in Mg^{2+} and K^+ could be due to coprecipitation. Thermodynamic calculations indicate that the precipitation of $CaSO_4$ in the lagoon waters (Figure 2.20) occurs close to the predicted chlorinity. If seawater is evaporated further, other salts will precipitate (see Table 2.9).

TABLE 2.8

Calculation of the Infinite Dilution Equivalent Conductance of Various Waters at 25°C

		$E_i \Lambda^0_i$[a]		
Ion	Λ^0_i	**Seawater**	**River Water**	**St. Lawrence River**
Ca^{2+}	59.51	46.97	31.41	35.40
Mg^{2+}	53.50	9.32	12.71	13.15
Na+	50.10	38.71	9.67	7.24
K+	73.50	1.24	3.06	0.91
HCO_{3-}	44.50	0.14	29.79	25.19
SO_4^{2-}	89.02	7.46	13.14	13.89
Cl^-	76.35	68.77	11.83	18.61
NO_{3-}	71.46	0.20	0.81	—
	Λ^0 =	127.85[b]	112.2	114.41

[a] E_i is the equivalent function of species.
[b] $\Lambda^0 = \sum E_i \Lambda^0_i$.

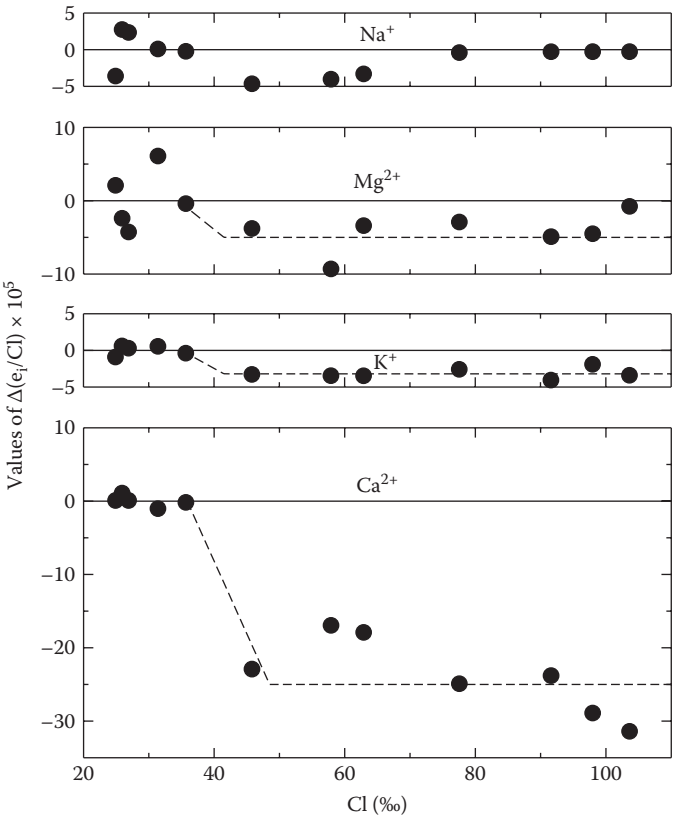

FIGURE 2.18
Values of the equivalents for cations divided by chlorinity for evaporating Mexican lagoon waters.

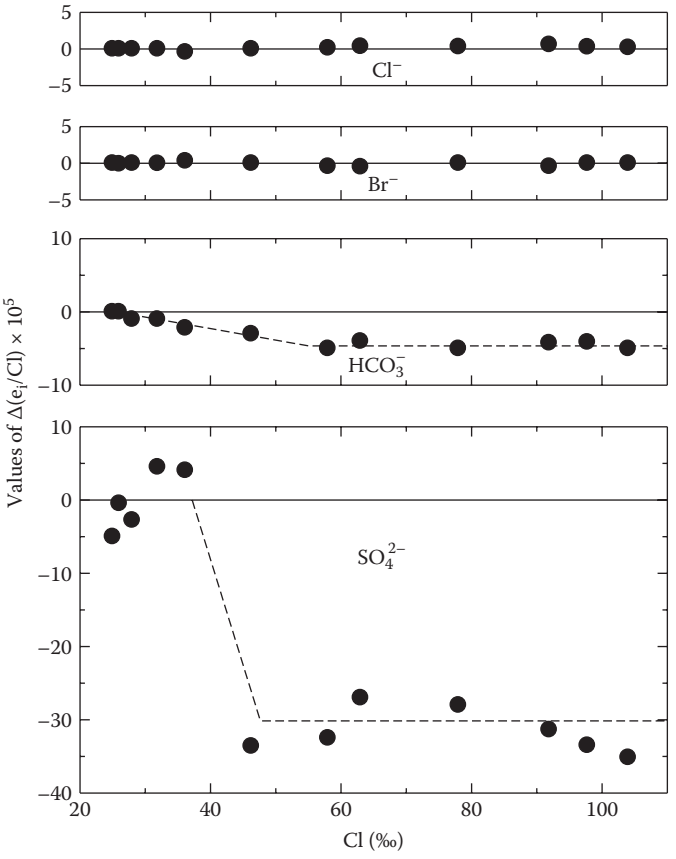

FIGURE 2.19
Values of the equivalents for anions divided by chlorinity for evaporating Mexican lagoon waters.

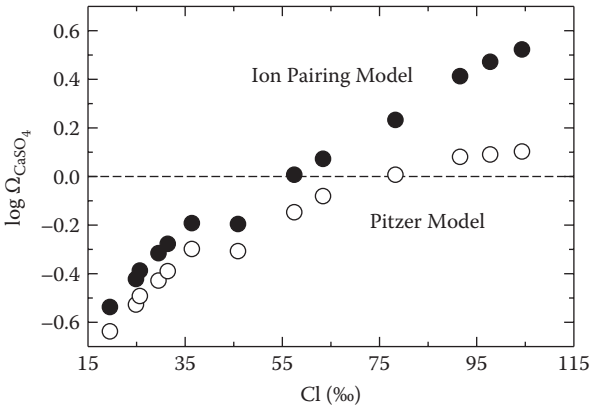

FIGURE 2.20
Values of the log of the saturation index (Ω = meas.$CaSO_4$/calc.$CaSO_4$) for evaporating Mexican lagoon waters.

TABLE 2.9

Sequence of Salts Formed from Evaporation of Seawater

Stage	Density	Wt% Liquid	Solid	% of Total Solid
	1.026	100		
I	1.140	50	$CaCO_3$ + $MgCO_3$	1
II	1.214	10	$CaSO_4$ (gypsum)	3
III	1.236	3.9	NaCl (halite)	70
IV	—	—	Na-Mg-K-SO_4 and KCl, $MgCl_2$	26

In laboratory experiments, Na, K, and $MgSO_4$ are formed in stage IV rather than K-Mg-Cl (the exact minerals formed depend on the temperature of evaporation). In nature, SO_4^{2-} is lost in brines, giving H_2S; thus, natural evaporate beds are almost devoid of sulfates. The most important solid phases in stage IV are KCl and $MgCl_2 \bullet 6H_2O$. Harvie and Weare (1980) used a thermodynamic model to examine the predicted phases precipitated during the evaporation of seawater. The results are given in Table 2.10.

2.6.3 Admixture with Brines

Fissures in the ocean floor in the Red Sea yield hot, highly saline water (45 to 58°C, S = 225 to 326‰) at 2000 m. The compositions of these waters are quite different from average seawater (see Figure 2.21). Confined brines can also be formed by the dissolution of evaporites at low temperatures. The Orca Basin, for example, in the Gulf of Mexico is formed by this method (Figure 2.22). These waters also have a composition different from average seawater (Figure 2.21). Mixtures formed with these brines will have values of g_i(Cl) governed by the two end numbers.

2.6.4 Precipitation and Dissolution

The dissolution of $CaCO_3$ in the form of aragonite and calcite in the deep oceans causes the Ca^{2+} concentration to increase by about 1% in the deep Pacific. Recent measurements from the North Pacific are shown in Figure 2.23. The normalized values of Ca^{2+} increase by as much as 1.3% in these waters. A deficiency of Ca^{2+} occurs when aragonite is precipitated on the Bahamas Banks and in the Red Sea (Wilson, 1975).

2.6.5 Submarine Volcanism

Molten magma has little effect on most of the major components of seawater. High F/Cl(‰) ratios, 8.0 to 9.0 × 10^{-5} (normal would be 6.7 × 10^{-5}), were found near the Mid-Atlantic Ridge, possibly from the injection of volcanic gases. Brewer (1975) suggested that the excess F may be present in colloidal form since the F ion electrode results have shown the same concentrations as surface samples (it could also be complexed with Ca or other trace metals). Recent studies in hydrothermal vents have shown changes in some of the major constituents (Si and Ca increase; Mg, K, B, and SO_4^{2-} decrease). More is said about these vent systems in Chapter 10.

TABLE 2.10

Predicted Sequence of Salts Precipitated from the Evaporation of Seawater

Segment	First Appearance	C.F.[a]	% H_2O Left	I[b]	aH_2O[c]	Faces
a	G + Sol.[d]	3.62	27.63	2.6	0.929	Pene-saline
b	A + Sol.	9.82	10.18	6.6	0.772	
c	A + H + Sol.	10.82	9.24	7.2	0.744	Saline
d	A + H + Gl + Sol.	13.15	7.60	7.5	0.738	
e		29.17	3.43	9.1	0.714	
f	A + H + Gl + Po + Sol.	38.50	2.60	10.1	0.697	Supersaline
g	A + H + Po + Sol.	44.76	2.23	10.7	0.685	
h	A + H + Po + Ep + Sol.	73.56	1.36	13.0	0.590	
	A + H + Po + Hx + Sol.	85.05	1.18	13.8	0.567	
	A + H + Po + Ki + Sol.	102.40	0.98	14.9	0.498	
i	A + H + Po + Ki + Car + Sol.	117.11	0.85	15.15	0.463	
	A + H + Ki + Car + Sol.	159.74	0.62	15.33	0.457	
	A + H + Ki + Car + Bi + Sol.	246	0.41	17.40	0.338	

Note: Mineral abbreviations: A, anhydrite, $CaSO_4$; Bi, bischofite, $MgCl_2{\cdot}H_2O$; Car, carnallite, $KMgCl_3{\cdot}6H_2O$; Ep, epsomite, $MgSO_4{\cdot}7H_2O$; G, gypsum, $CaSO_4{\cdot}2H_2O$; Gl, glauberite, $Na_2Ca(SO_4)_2$; H, halite, NaCl; Hx, hexahydrite, $MgSO_4{\cdot}6H_2O$; Ki, kieserite, $MgSO_4{\cdot}H_2O$; Po, polyhalite, $K_2MgCa_2(SO_4)_4{\cdot}2H_2O$.

[a] C.F. is the concentration factor (C.F. = 1.0 for seawater).

[b] I is the ionic strength.

[c] $a(H_2O)$ is the activity of water.

[d] Sol. is the solution.

2.6.6 Exchange between Atmosphere and Sea

Sea and atmospheric bubbles give off 10×10^9 tons of ions into the atmosphere each year. Most return directly or indirectly to the oceans. Considerable fractionation occurs. The bubbles gather dissolved species and particles to their surfaces that may take up certain ions selectively. White gap aerosols of ions and organics have a size of 0.1 to 20 μm and may cause nucleation of rain. Mainly Ca^{2+}, K^+, Mg^{2+}, and SO_4^{2-} are enriched relative to Na^+ in the atmosphere, whereas Cl^- and Br^- are impoverished. Many bubbles concentrate transition metals from strong complexing with organics. The ratio of Br^-/Cl^- is only slightly higher in air as both are neglected via bubble breaking (Duce, 1989). The gaseous form of Cl^- may be HCl, formed from salt and sulfur trioxide or NO_2. Photochemical oxidation of Br^- in the salt yields Br_2. The (I^-/Cl^-) ratio in the atmosphere is 777 times higher than in seawater as I_2 is formed by photochemical oxidation of I^-. The rate of I lost from the

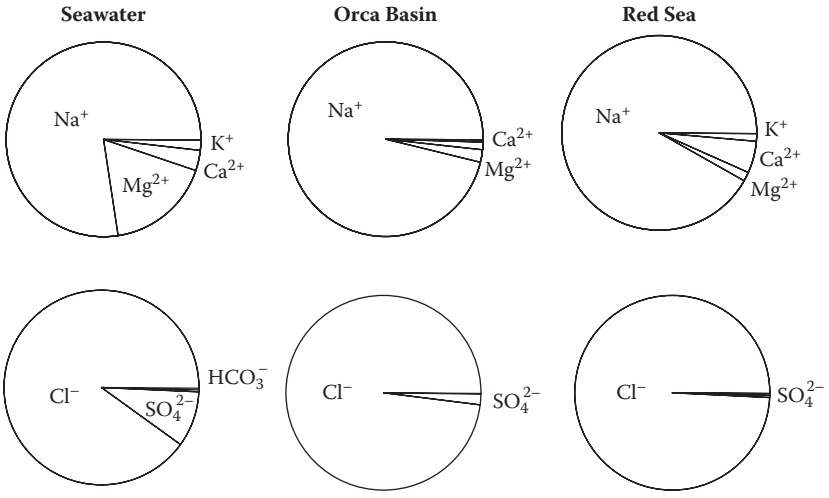

FIGURE 2.21
Comparison of the composition of various brines to average seawater.

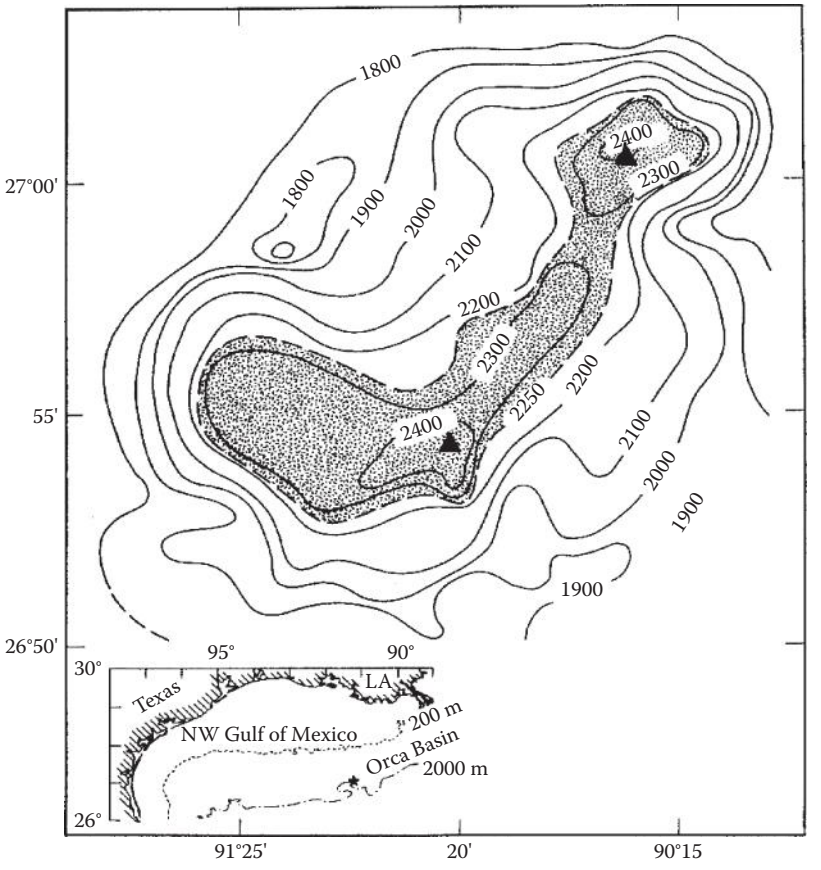

FIGURE 2.22
Location of the Orca Basin in the Gulf of Mexico.

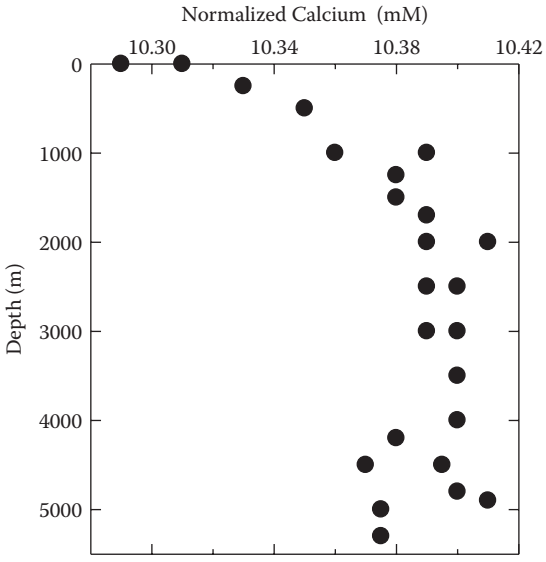

FIGURE 2.23
Depth profile of the normalized calcium in the North Pacific.

ocean has been estimated to be 4×10^{11} g yr^{-1}. High concentrations of B in rain probably result from distillation from the sea surface $B(OH)_3$, which has a high volatility.

2.6.7 Anoxic Basins

A number of anoxic basins exist (Black Sea, Cariaco Trench) in the world oceans (Richards, 1965). The SO_4^{2-}/Cl ratios in these basins are quite low because of bacteria using SO_4^{2-} as a source of O_2 giving off H_2S. The H_2S is lost by precipitation of FeS_2 and other sulfides (ZnS, CuS, etc.). Further discussion of these anoxic basins is found in Chapter 10.

2.6.8 Freezing

Sea ice has a higher (SO_4^{2-}/Cl) ratio than seawater (because of SO_4^{2-} incorporation into ice). Waters in the North Pacific in the minimum temperature layer (formed by melting ice) have been shown to be deficient in SO_4^{2-}. Differences may also occur in Ca/Cl because of precipitation of $CaCO_3$ in sea ice.

2.6.9 Interstitial Waters

Interstitial pore waters differ appreciably from seawater in some major components. The Cl^- is within ±1% of overlying water, with large variations from one locality to another. Changes in Ca^{2+} can result from the dissolution of $CaCO_3$ caused by the oxidation of plant material (giving CO_2), while changes in SO_4^{2-} can occur because of the production of H_2S by bacteria.

Changes in K^+ and other cations can occur by exchange with clay minerals. Mg may be depleted from uptake by chlorite or reaction with $CaCO_3$ to form dolomite. In contrast, K^+ is enriched because of the hydrolysis of feldspars. Sediment chemistry is discussed

further in this chapter. Changes in the composition of pore waters caused by temperature effects are important. Different ratios have been found for sediments when kept at *in situ* temperature. This is due to changes in the solution-solid equilibrium with temperature. If the samples are squeezed at *in situ* temperatures, the results are not affected.

2.7 Isotopic Variations

2.7.1 Hydrogen and Oxygen

Water is the principal constituent of seawater. In 1929, stable isotopes of oxygen were discovered, and in 1932 deuterium was discovered. Thus, it became apparent that naturally occurring water is a mixture of several species differing in molecular weight. There are three known isotopes of hydrogen (^{1}H, ^{2}H, or D [deuterium] and ^{3}H or T [tritium]) and six isotopes of oxygen (^{14}O, ^{15}O, ^{16}O, ^{17}O, ^{18}O, and ^{19}O). Tritium is radioactive with a half-life of 12.5 yr. The isotopes of ^{14}O, ^{15}O, and ^{19}O are also radioactive but are short lived and do not occur significantly in natural waters. The precise isotopic content of natural water depends on the origin of the sample; however, within the limits of variation, the abundance is (Table 2.11) 99.73% $^{1}H_2{}^{16}O$ (light water), 0.2% ^{18}O water, 0.04% ^{17}O water, and 0.032% $^{1}H^{2}H^{16}O$ water (HDO). It should be pointed out that the equilibrium

$$D_2O + H_2O = 2HDO \tag{2.36}$$

is always maintained. The hydrogen in water is 0.032/2 = 0.015% D. The presence of these isotopes can change some of the properties of water and thus must be considered major components of seawater.

Mass spectrophotometry is the best method of determining D and ^{18}O. Prior to D determination, the water sample is converted to hydrogen gas by reaction with hot zinc or uranium metal. In the determination of ^{18}O, the water sample is equilibrated with CO_2 gas, which is then analyzed by mass spectrophotometry.

Absolute isotopic abundances cannot yet be determined with sufficient accuracy to be of use in studies of their natural variations. In earlier work, D analyses were reported relative

TABLE 2.11

Composition of Water with Respect to the Different Forms of Water

Water Molecule	Portion in Total Water	Portion in Heavy Water	Comparable Concentration
$^{1}H_2{}^{16}O$	99.73	—	—
$^{1}H_2{}^{18}O$	0.20	73.5	Mg
$^{1}H_2{}^{17}O$	0.04	14.7	Ca
$^{1}H_2H^{16}O$	0.032	11.8	K
$^{1}H_2H^{18}O$	6×10^{-5}	0.022	N
$^{1}H_2H^{17}O$	1×10^{-5}	0.003	Al
$^{2}D_2{}^{16}O$	3×10^{-6}	0.001	P
$^{2}D_2{}^{18}O$	6×10^{-9}	2×10^{-6}	Hg
$^{2}D_2{}^{17}O$	1×10^{-9}	3×10^{-7}	Au

to local tap water. This was unsatisfactory since differences occur in the D content of tap waters. Some workers, in their $^{18}O/^{16}O$ work on natural waters, used the average of their isotopic data for a number of deep-water samples taken from the Atlantic, Pacific, and Indian Oceans as their standard. This, however, is not completely satisfactory. Harmon Craig pointed out the desirability of a standard reference for both D and ^{18}O analyses. He determined the D/H ratio for a set of ocean waters similar to the ones chosen by earlier workers for their ^{18}O data. He suggested that both D and ^{18}O data could be specified in terms of the National Bureau of Standards (NBS) isotopic reference samples No. 1 and No. 1-A. These are distilled water samples of large volumes, intended as a cross-check calibration to mass spectrophotometry labs. After consultation, Craig (1961) defined standard mean ocean water (SMOW) in terms of the NBS reference sample:

$$D/H(SMOW) = 1.050\ D/H(NBS)^{-1} \tag{2.37}$$

$$^{18}O/^{16}O(SMOW) = 1.008\ ^{18}O/^{16}O(NBS) \tag{2.38}$$

It was suggested that isotopic data for both isotopes be reported as parts per mille. Enrichment δ relative to defined SMOW is given by

$$\delta = [(R_{SAMPLE}/R_{SMOW}) - 1]1000 \tag{2.39}$$

where the values of R are isotopic ratios. SMOW is thus defined in terms of an actual water reference standard NBS-1 and provides a convenient and consistent zero reference level for reporting enrichment.

2.7.2 Deuterium

Ocean waters have widely different D/H ratios. Equatorial waters are richer in D than waters in high latitudes. D follows the same trend with depth as ^{18}O; that is, surface waters contain relatively more than deep waters. D/H varies from 6410 to 6536 for the Atlantic, Pacific, and Indian Oceans. In summary, high-latitude waters tend to contain less D than equatorial waters, and deep waters contain less D than surface waters.

2.7.3 Oxygen-18

The $^{18}O/^{16}O$ ratios of a number of freshwaters derived from snow, rain, lakes, and rivers as well as the oceans have been examined. The ^{18}O of freshwaters varies considerably; thus, ^{18}O in the oceans varies depending on how much freshwater is in the source. Melted snow can have values of ^{18}O 3.5 times greater than the waters from the Mississippi. For waters collected in the Alaska and California currents, the low salinity and high ^{18}O content are due to the melting of snow and ice.

Deep waters contain less ^{18}O than surface samples. The differences are greater than would be expected from evaporation. The deep water is diluted by sinking polar waters, with a consequential lowering of ^{18}O. Mediterranean waters (surface and deep) showed a much smaller difference because the high evaporation rate causes less fractionation of the isotopes, which in turn implies that freshwaters entering the ocean are less depleted in ^{18}O than in the other cases discussed. The deep waters of the Pacific have higher ^{18}O values

compared to deep Atlantic values since the waters are older and oxidation enriches the waters with ^{18}O.

The vapor pressure of HDO is lower than that of H_2O, which means that during evaporation, H_2O enters the vapor phase more readily than does HDO, with the result that D becomes preferentially concentrated in the residual water. This accounts for its higher concentrations in surface waters near the equator. In the precipitation process, the reverse is true. The residual phase vapor becomes depleted of HDO, which is preferentially precipitated. As the raindrop falls, further isotopic enrichment can take place because of evaporation, especially in dry climates.

Deuterium analyses of coexisting ice and arctic waters showed that the ice contained 2% more D than waters from which it was formed. In general, ^{18}O follows the same pattern as D; however, since the relative masses between ^{18}O and ^{16}O are smaller, the effects are also smaller. The $^{18}O/^{16}O$ ratio in snow is lower than in rain or seawater.

In general, the two isotopic ratios are quite variable in seawater. Both heavier isotopes are concentrated in surface water relative to deep water, but for different reasons. Evaporation causes the effect for D/H, while dilution by sinking polar waters produces a decrease of $^{18}O/^{16}O$ in deep water. Since organisms prefer ^{16}O, older waters have a larger $^{18}O/^{16}O$ ratio than younger waters.

2.7.4 Isotopes of Sulfur

Sulfur has four stable isotopes with atomic weights 32, 33, 34, and 36. The heaviest is the least abundantly occurring isotope. The $^{32}S/^{33}S$ ratio is 123.4 for seawater collected in the Pacific, Atlantic, and Arctic and North and Baltic Seas. This ratio is lower than that found in rainwater, suggesting that the SO_4^{2-} sulfur in precipitation is not derived from the salt spray. The most important agents in isotopic fractionation of S were SO_4^{2-}-reducing bacteria:

$$H^{34}S^- + {}^{32}SO_4^{2-} = H^{32}S^- + {}^{34}SO_4^{2-} \tag{2.40}$$

When SO_4^{2-} is reduced to HS^-, the equilibrium will produce H_2S that is deficient in the heavier S isotope. This will occur only in sediments or anaerobic water, and the effect will not alter the physical properties of seawater significantly. It is significant that SO_4^{2-} minerals occurring in marine evaporite deposits have the same $^{32}S/^{33}S$ ratio as seawater. The SO_4^{2-} minerals associated with precipitation in anaerobic conditions have a higher ratio (as high as 23.2 for some shales).

References and Further Reading

Aston, S.R., Estuarine chemistry, Chapter 41, *Chemical Oceanography*, Vol. 7, 2nd ed., Riley, J.P., and Chester, R., Eds., Academic Press, New York, 361–440 (1978).

Borchert, H., Principles of oceanic salt deposition and metamorphism, Chapter 19, *Chemical Oceanography*, Vol. 2, Riley, J.P., and Skirrow, G., Eds., Academic Press, New York, 205–276 (1965).

Brewer, P., Minor elements in sea water, Chapter 7, *Chemical Oceanography*, Vol. 1, 2nd ed., Riley, J.P., and Skirrow, G., Eds., Academic Press, New York, 416–496 (1975).

Carpenter, J.H., and Manella, M.E., Magnesium to chlorinity ratios in seawater, *J. Geophys. Res*., 78, 3621–3626 (1973).

Cox, R.A., The physical properties of seawater, Chapter 3, *Chemical Oceanography*, Vol. 1, Riley, J.P., and Skirrow, G., Eds., Academic Press, New York, 73–120 (1965).

Cox, R.A., Culkin, F., and Riley, J.P., The electrical conductivity/chlorinity relationship in natural seawater, *Deep-Sea Res*., 14, 203 (1967).

Craig, H., Standard for reporting concentrations of deuterium and oxygen-18 in natural waters, *Science*, 133, 1833 (1961).

Culkin, F., The major constituents, Chapter 4, *Chemical Oceanography*, Vol. 1, Riley, J.P., and Skirrow, G., Eds., Academic Press, New York, 121–161 (1965).

Culkin, F., and Cox, R.A., Sodium, potassium, magnesium, calcium and strontium in seawater, *Deep-Sea Res*., 13, 789 (1966).

Dickson, A.G., Thermodynamics of the dissociation of boric acid in synthetic seawater from 273.15 to 318.15 K, *Deep-Sea Res.*, 37, 755 (1990).

Dittmar, W. Report on the scientific results of the exploring voyage of HMS *Challenger*. *Physics and Chemistry* 1, 1–251. London (1884).

Duce, R.A., SEAREX: the Sea/Air Exchange program, in *Chemical Oceanography*, Vol. 10, Riley, J.P., Chester, R., and Duce, R.A., Eds., Academic Press, New York, 1–14 (1989).

Forchammer, G. On the composition of seawater in the different parts of the ocean. *Philosophical Transactions* 155, 203–262 (1865).

Grasshoff, K., Kremling, K., and Ehrhart, M., *Methods of Seawater Analysis*, Eds., 3rd ed., Wiley-VCH, Berlin (1999).

Harvie, C.E., and Weare, J.H., The prediction of mineral solubilities in natural waters: the Na-K-Mg-Ca-Cl-SO_4-H_2O system from zero to high concentration at 25°C, *Geochim. Cosmochim. Acta*, 44, 981 (1980).

Lee, K., Kim, T.-W., Byrne, R.H., Millero, F.J., Feely, R.A., and Liu, Y.-M., The universal ratio of boron to chlorinity for the North Pacific and North Atlantic oceans, *Geochim. Cosmochim. Acta*, 74, 1801–1811 (2010).

Lewis, E.L., Salinity: its definition and calculation, *J. Geophys. Res*., 83, 466 (1978).

Lyman, J., and Fleming, R.H., Composition of seawater, *J. Mar. Res*., 3, 134–146 (1940).

Kremling, K., Untersuchungen ber die chemische Zusammensetzung de Meerwasser aus Ostsee, I. Frühjahr, 1966, *Kieler Meeresf.,* 26, 81–104 (1969).

Kremling, K., Untersuchungen über die chemische Zusammensetzung de Meerwasser aus Ostsee, II. Frühjahr 1967, *Kieler Meeresf*., 26, 1–20 (1970).

Kremling, K., Untersuchungen über die chemische Zusammensetzung de Meerwasser aus Ostsee, III. Frühjahr 1969, *Kieler Meeresf.*, 37, 99–118 (1972).

Kremling, K., Determination of major constituents, Chapter 11, *Methods of Seawater Analysis*, 229–251, Kiel, Germany (1976).

Menache, M., Verification, par analyse isotopique de la validite de la methode de Cox, McCartney et Culkin tendant a l'obtention d'un etalon de masse volumique, *Deep-Sea Res*., 18, 449–456 (1971).

Millero, F.J., The physical chemistry of Baltic Sea waters, *Thalassia Jugoslavica*, 14, 1 (1978).

Millero, F.J., *Chemical Oceanography*, 3rd ed., Taylor & Francis, Boca Raton, FL (2006).

Millero, F.J, Graham, T., Huang, F., Bustos, H., and Pierrot, D., Dissociation constants for carbonic acid in seawater as a function of temperature and salinity, *Mar. Chem*., 100, 80–94 (2006).

Millero, F.J., Schrager, S.R., and Hansen, L.D., Thermometric titration analysis of seawater for chlorinity, sulfate, and alkalinity, *Limnol. Oceanogr*., 19, 711 (1974).

Millero, F.J., Zhang, J.Z., Fiol, S., Sotolongo, S., Roy, R.N., Lee, K., and Mane, S., The use of buffers to measure the pH of seawater, *Mar. Chem*., 44, 143 (1993).

Millero, F.J., Zhang, J.Z., Lee, K., and Campbell, D.M., Titration alkalinity of seawater, *Mar. Chem*., 44 153 (1993).

Mojica Prieto, F.J., and Millero, F.J., The values of $pK_1 + pK_2$ for the dissociation of carbonic acid in seawater, *Geochim. Cosmochim. Acta*, 66, 2529 (2002).

Morris, A.W., and Riley, J.P., The direct gravimetric determination of the salinity of sea water, *Deep-Sea Res*., 11, 899 (1964).

Morris, A.W., and Riley, J.P., The bromide/chlorinity and sulphate/chlorinity ratio in seawater, *Deep-Sea Res*., 13, 699 (1966).

Pierrot, D., Lewis, E., and Wallace, D.W.R., *MS Excel Program Developed for CO_2 System Calculations*, Rep. ORNL/CDIAC-105a, Carbon Dioxide Information Analysis Center, Oak Ridge National Laboratory, U.S. Department of Energy, Oak Ridge, TN (2006).

Richards, F.A., Dissolved gases other than carbon dioxide, in *Chemical Oceanography*, Vol. 1, Riley, J.P., and Skirrow, G., Eds., Academic Press, New York, 197–225 (1965).

Riley, J.P., Analytical chemistry of sea water, Chapter 21, *Chemical Oceanography*, Vol. 2, Riley, J.P., and Skirrow, G., Eds., Academic Press, New York, 295–424 (1965a).

Riley, J.P., Historical introduction, Chapter 1, *Chemical Oceanography*, Vol. 1, 1st ed., Riley, J.P., and Skirrow, G., Eds., Academic Press, New York, 1–41 (1965b).

Riley, J.P., Analytical chemistry of sea water, Chapter 19, *Chemical Oceanography*, Vol. 3, 2nd ed., Riley, J.P., and Skirrow, G., Eds., Academic Press, New York, 193–514 (1975).

Riley, J.P. and Chester, R., *Introduction to Marine Chemistry*, Academic Press, New York (1971).

Riley, J.P., and Tongudai, M., The major cation/chlorinity ratios in seawater of seawater, *Chem. Geol*., 2, 263 (1967).

Uppström, L.R., Boron/chlorinity ratio of deep-sea water from the Pacific Ocean, *Deep-Sea Res*., 21, 161 (1974).

Wallace, C., *Development of the Chlorinity–Salinity Concept,* Elsevier, New York (1974).

Warner, T.B., Normal fluoride content of seawater, *Deep-Sea Res*., 18, 1255 (1971).

Whitfield, M., Electroanalytical chemistry of sea water, Chapter 20, *Chemical Oceanography*, Vol. 4, 2nd ed., Riley, J.P., and Skirrow, G., Eds., Academic Press, New York, 1–154 (1975).

Wilson, T.R.S., Salinity and the major elements of sea water, Chapter 6, *Chemical Oceanography*, Vol. 1, 2nd ed., Riley, J.P., and Skirrow, G., Eds., Academic Press, New York, 365–413 (1975).

3

Minor Elements in Seawater

3.1 Classification of Elements

The elements found in seawater (see Figure 3.1) include most of those in the periodic table. Of these, only 14 elements (O, H, Cl, Na, Mg, S, Ca, K, Br, C, Sr, B, Si, and F) have concentrations greater than 1 ppm. Most of these elements (with the exception of Si) are generally unreactive elements (both chemically and biologically). Many of the remaining elements, called minor, are involved in inorganic and biological reactions in the marine environment. The biolimited elements N, P, and Si are discussed Chapter 8. The inert gases are also discussed separately in Chapter 6.

Bruland (1983) has tabulated the range and average concentration of a number of elements in seawater (salinity $S_P = 35$). His results are tabulated in Table 3.1. He conveniently divided the elements into three classes based on concentration (Figure 3.1):

1. Major elements: 0.05 to 750 m*M*
2. Minor elements: 0.05 to 50 μ*M*
3. Trace elements: 0.05 to 50 n*M*

Since many of these minor elements are metals, Goldberg (1965) divided them into three classes based on their electronic structure (see Table 3.2). This simple classification for metals is given in Table 3.2. Minor and trace elements in the ocean, because of their reactivity, have a wide range of concentrations (see Table 3.1 and Figure 3.2).

3.1.1 d^0 Cations

Ions of metallic elements with a rare gas configuration include the alkali metals (Li^+, Na^+, K^+, Rb^+, Cs^+, Fr^+); the alkaline earth metals (Be^{2+}, Mg^{2+}, Ca^{2+}, Sr^{2+}, Ba^{2+}, Ra^{2+}); and the lanthanide or rare earth series (La^{3+}, Ce^{3+}, Pr^{3+}, Nd^{3+}, Pm^{3+}, Sm^{3+}, Eu^{3+}, Gd^{3+}, Tb^{3+}, Dy^{3+}, Ho^{3+}, Er^{3+}, Tm^{3+}, Yb^{3+}, Lu^{3+}) plus the metals Al^{3+}, Sc^{3+}, Ti^{3+}, and Th^{4+}.

This group is characterized by the fact that its members form few complexes, mainly with F^- and ligands where oxygen is the donor atom (e.g., OH^-, SO_4^-, CO_3^{2-}, and PO_4^{3-}). There is little or no evidence that these metal ions form complexes with the heavier halides. In a given series, the stability of the complexes increases with increasing charge and, for cations of the same charge, with decreasing radius. This is shown in Table 3.3 for the formation of divalent metal complexes with F^- and OH^-. These results indicate that the strength of the complexes is related to electrostatic interactions (proportional to Z^2/r, where Z is the charge and r is the radius of an ion).

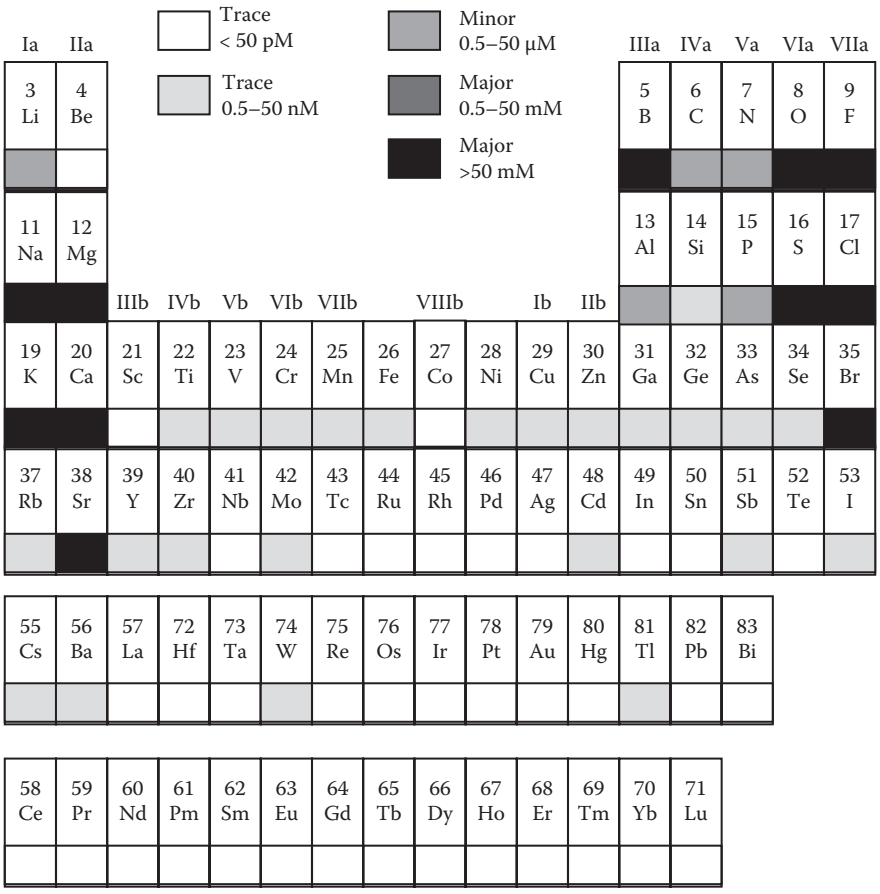

FIGURE 3.1
Classification of elements in ocean waters.

Here we discuss the various inorganic complexes of the d^0 metal ions that are the major components of seawater.

3.1.2 d^{10} Cations

Cations with an outer shell of 18 electrons include Ag^+, Zn^{2+}, Ga^{3+}, and Sc^{4+}. The univalent d^{10} metal ions behave in a different way from the d^0 metals. For these ions, the halide complexes are quite strong and increase in stability with increasing atomic weight or size of the ligand. This is shown as follows for the stability constants for the formation of silver and copper(I) halide complexes as a function of the radius of the halide ion:

Complex	CuX	AgX	Radius (Å)
MF	—	–0.3	1.36
MCl	2.7	3.0	1.81
MBr	3.2	4.3	1.95
MI	7.2	8.1	2.16

TABLE 3.1

Speciation, Concentration, and Distribution Types of Elements in Ocean Waters

Element	Probable Species	Range and Average Concentration	Type of Distribution
Li	Li^+	25 µ*M*	Conservative
Be	$BeOH^+$, $Be(OH)_2$	4–30 p*M*, 20 p*M*	Nutrient type
B	$B(OH)_3$, $B(OH)_4$	0.416 m*M*	Conservative
C	HCO_3^-, CO_3^{2-}	2.0–2.5 m*M*, 2.3 m*M*	Nutrient type
N	NO_3^-, (N_2)	0–45 µ*M*	Nutrient type
F	F^-, MgF^+, CaF^+	68 µ*M*	Conservative
Na	Na^+	0.468 *M*	Conservative
Mg	Mg^{2+}	53.2 m*M*	Conservative
Al	$Al(OH)_4^-$, $Al(OH)_3$	5–40 n*M*, 2 n*M*	Mid-depth minima
Si	$Si(OH)_4$	0–180 µ*M*	Nutrient type
P	HPO_4^{2-}, $MgHPO_4$	0–3.2 µ*M*	Nutrient type
S	SO_4^{2-}, $NaSO_4^-$, $MgSO_4$	28.2 m*M*	Conservative
Cl	Cl^-	0.546 M	Conservative
K	K^+	10.2 m*M*	Conservative
Ca	Ca^{2+}	10.3 m*M*	Conservative
Sc	$Sc(OH)_3$	8–20 p*M*, 15 p*M*	Surface depletion
Ti	$Ti(OH)_4$	Few p*M*	?
V	HVO_4^{2-}, $H_2VO_4^-$	20–35 n*M*	Surface depletion
Cr	$Cr\ O_4^{2-}$	2–5 n*M*, 4 n*M*	Nutrient type
Mn	Mn^{2+}	0.2–3 n*M*, 0.5 n*M*	Depletion at depth
Fe	$Fe(OH)_3$	0.1–2.5 n*M*, 1 n*M*	Surface and depth depletion
Co	Co^{2+}, $CoCO_3$	0.01–0.1 n*M*, 0.02 n*M*	Surface and depth depletion
Ni	$NiCO_3$	2–12 n*M*, 8 n*M*	Nutrient type
Cu	$CuCO_3$	0.5–6 n*M*, 4 n*M*	Nutrient type, scavenging
Zn	Zn^{2+}, $ZnOH^+$	0.05–9 n*M*, 6 n*M*	Nutrient type
Ga	$Ga(OH)_4^-$	5–30 p*M*	?
As	$HAsO_4^{2-}$	15–25 n*M*, 23 n*M*	Nutrient type
Se	SeO_4^{2-}, SeO_3^{2-}	0.5–2.3 n*M*, 1.7 n*M*	Nutrient type
Br	Br^-	0.84 n*M*	Conservative
Rb	Rb+	1.4 µ*M*	Conservative
Sr	Sr^{2+}	90 µ*M*	Conservative
Y	YCO_3^+	0.15 n*M*	Nutrient type
Zr	$Zr(OH)_4$	0.3 n*M*	?
Nb	$NbCO_3^+$	50 p*M*	Nutrient type (?)
Mo	MoO_4^{2-}	0.11 µ*M*	Conservative
Tc	TcO_4^-	No stable isotope	?
Ru	?	<0.05 p*M*	?
Rh	?	?	?
Pd	$PdCl_4$	0.2 p*M*	?
Ag	$AgCl_2^-$	0.5–35 p*M*, 25 p*M*	Nutrient type
Cd	$CdCl_2^-$	0.001–1.1 n*M*, 0.7 n*M*	Nutrient type
In	$In(OH)_3$	1 p*M*	?
Sn	$Sn(OH)_4$	1–12 p*M*, 4 p*M*	Surface input

continued

TABLE 3.1 (continued)

Speciation, Concentration, and Distribution Types of Elements in Ocean Waters

Element	Probable Species	Range and Average Concentration	Type of Distribution
Sb	$Sb(OH)_6^-$	1.2 n*M*	?
Te	TeO_3^{2-}, $HTeO_3^-$	?	?
I	IO_3^-	0.2–0.5 μ*M*, 0.4 μ*M*	Nutrient type
Cs	Cs^+	2.2 n*M*	Conservative
Ba	Ba^{2+}	32–150 n*M*, 100 n*M*	Nutrient type
La	$LaCO_3^+$	13–37 p*M*, 30 p*M*	Surface depletion
Ce	$CeCO_3^+$	16–26 p*M*, 20 p*M*	Surface depletion
Pr	$PrCO_3^+$	4 p*M*	Surface depletion
Nd	$NdCO_3^+$	12–25 p*M*, 10 p*M*	Surface depletion
Sm	$SmCO_3^+$	3–5 p*M*, 4 p*M*	Surface depletion
Eu	$EuCO_3^+$	0.6–1 p*M*, 0.9 p*M*	Surface depletion
Gd	$GdCO_3^+$	3–7 p*M*, 6 p*M*	Surface depletion
Tb	$TbCO_3^+$	0.9 p*M*	Surface depletion
Dy	$DyCO_3^+$	5–6 p*M*, 6 p*M*	Surface depletion
Ho	$HoCO_3^+$	1.9 p*M*	Surface depletion
Er	$ErCO_3^+$	4–5 p*M*, 5 p*M*	Surface depletion
Tm	$TmCO_3^+$	0.8 p*M*	Surface depletion
Yb	$YbCO_3^+$	3–5 p*M*, 5 p*M*	Surface depletion
Lu	$LuCO_3^+$	0.9 p*M*	Surface depletion
Hf	$Hf(OH)_4$	<40 p*M*	?
Ta	$Ta(OH)_5$	<14 p*M*	?
W	WO_4^{2-}	0.5 n*M*	Conservative
Re	ReO_4^-	14–30 p*M*, 20 p*M*	Conservative
Os	?	?	?
Ir	?	0.01 p*M*	?
Pt	$PtCl_4^{2-}$	0.5 p*M*	?
Au	$AuCl_2^-$	0.1–0.2 p*M*	?
Hg	$HgCl_4^{2-}$	2–10 p*M*, 5 p*M*	?
Tl	Tl^+, TCl	60 p*M*	Conservative
Pb	$PbCO_3$	5–175 p*M*, 10 p*M*	Surface input, depletion at depth
Bi	BiO^+, $Bi(OH)_2^+$	<0.015–0.24 p*M*	Depletion at depth

This order is due to the increase in polarizability of the d^{10} electrons in the metals and the large halide ligands. The complexes thus have more covalent character. Since the concentration of Cl^- in seawater is much larger than that of the other halides, the Cl^- complexes will normally dominate (the values of K_{MX} for the heavier halides are not large enough to compensate for the low concentration). It is possible, however, for OH^- ions to compete successfully with Cl^-. For Cl^- complexes to predominate, the value of $\log K_{MCl} - \log K_{MOH}$ must be greater than about –5.4. The values of $\log K_{MCl}$ and $\log K_{MOH}$ for various metal ions are shown in Table 3.4. From this table, it is evident that the strength of the Cl^- complexes is greater than for the OH^- complexes for Ag^+, Cd^{2+}, Hg^{2+}, and Zn^{2+} but not for Cu^{2+} and Pb^{2+}. The SO_4^{2-} ion cannot compete with Cl^- and OH^- ions for the formation of complexes with the d^{10} cations. The addition of higher concentrations of Cl^- (e.g., brines) can contribute to

TABLE 3.2

Electronic Configuration of Atoms

			K	L		M			N			
Period	**Z**	**Element**	**s**	**s**	**p**	**s**	**p**	**d**	**s**	**p**	**d**	**f**
1	1	H	1									
	2	He	2									
2	3	Li	2	1								
	4	Be	2	2								
	5	B	2	2	1							
	6	C	2	2	2							
	7	N	2	2	3							
	8	O	2	2	4							
	9	F	2	2	5							
	10	Ne	2	2	6							
3	11	Na	2	2	6	1						
	12	Mg	2	2	6	2						
	13	Al	2	2	6	2	1					
	14	Si	2	2	6	2	2					
	15	P	2	2	6	2	3					
	16	S	2	2	6	2	4					
	17	Cl	2	2	6	2	5					
	18	Ar	2	2	6	2	6					
4	19	K	2	2	6	2	6		1			
	20	Ca	2	2	6	2	6		2			
	21	Sc	2	2	6	2	6	1	2			
	22	Ti	2	2	6	2	6	2	2			
	23	V	2	2	6	2	6	3	2			
	24	Cr	2	2	6	2	6	5	1			
	25	Mn	2	2	6	2	6	5	2			
	26	Fe	2	2	6	2	6	6	2			
	27	Co	2	2	6	2	6	7	2			
	28	Ni	2	2	6	2	6	8	2			
	29	Cu	2	2	6	2	6	10	1			
	30	Zn	2	2	6	2	6	10	2			
	31	Ga	2	2	6	2	6	10	2	1		
	32	Ge	2	2	6	2	6	10	2	2		
	33	As	2	2	6	2	6	10	2	3		
	34	Se	2	2	6	2	6	10	2	4		
	35	Br	2	2	6	2	6	10	2	5		
	36	Kr	2	2	6	2	6	10	2	6		

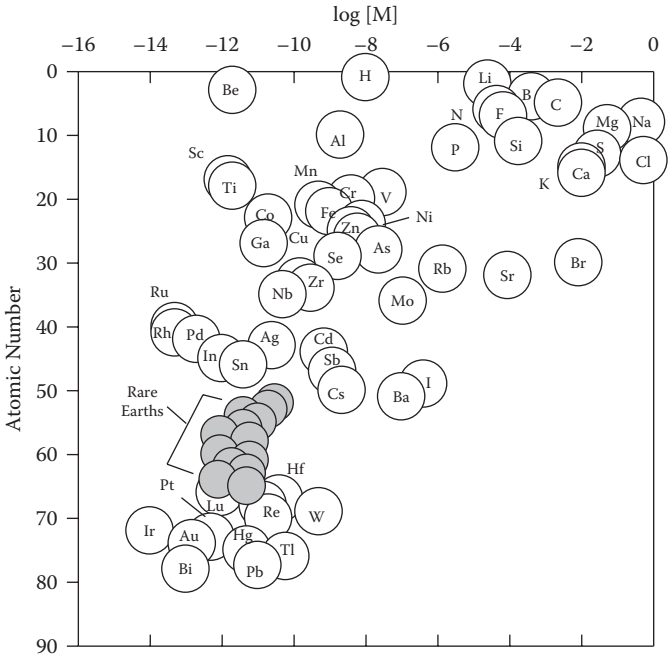

FIGURE 3.2
The range of concentrations of elements in seawater.

TABLE 3.3

Stability Constants for the Formation of Fluoride and Hydroxide Complexes

Ion	Log K_{MF}	Log K_{MOH}	Radius
Be^{2+}	4.29	10.28	0.31 Å
Mg^{2+}	1.82	2.3	0.65
Ca^{2+}	1.04	1.4	0.99
Sr^{2+}	—	0.9	1.13
Ba^{2+}	0.45	0.8	1.35

TABLE 3.4

Stability Constants for the Formation of Chloride and Hydroxide Complexes

Ion	Log K_{MCl}	Log K_{MOH}	Log K_{MCl} – LogK_{MOH}
Ag^{+}	3.1	2.3	0.8
Cd^{2+}	2.0	5.5	–3.5
Hg^{2+}	7.3	11.5	–4.2
Zn^{2+}	–0.5	4.4	–4.9
Cu^{2+}	0.4	6.3	–5.9
Pb^{2+}	1.5	7.8	–6.3

the formation of stronger Cl^- complexes for many metals. For example, mercury can form higher-order complexes with chloride.

$$Hg^{2+} + Cl^- \rightarrow HgCl^+ \quad (3.1)$$

$$HgCl^+ + Cl^- \rightarrow HgCl_2^0 \quad (3.2)$$

$$HgCl_2^0 + Cl^- \rightarrow HgCl_3^- \quad (3.3)$$

$$HgCl_{3-} + Cl^- \rightarrow HgCl_4^{2-} \quad (3.4)$$

$$HgCl_4^{2-} + Cl^- \rightarrow HgCl_5^{3-} \quad (3.5)$$

To evaluate the complete speciation or form of these heavy metals in seawater, it is necessary to consider the competition of all the ligands (Cl^-, Br^-, OH^-, HCO_3^-, CO_3^{2-}, etc.) for a given metal and the major divalent cations in seawater (Mg^{2+}, Ca^{2+}, and Sr^{2+}) for a given anion. The speciation of the divalent heavy metals (Cd^{2+}, Hg^{2+}, Zn^{2+}, Cu^{2+}, and Pb^{2+}) in seawater and river waters is discussed further in the chapter.

3.1.3 Transition Metals between d^0 and d^{10}

The transition metal cations, in which the number of d electrons is greater than zero and less than 10, represent this group. These include Mn^{2+}, Fe^{2+}, Co^{2+}, Ni^{2+}, Cu^{2+}, and Zn^{2+} ions. These metals have been extensively studied and form strong complexes with organic molecules (ligands). From such work has evolved the so-called Irving-Williams order, which states that for almost every ligand the stability of its complexes increases in the order

$$Mn^{2+} < Fe^{2+} < Co^{2+} < Ni^{2+} < Cu^{2+} > Zn^{2+}$$

An example of this order is shown in Table 3.5 for the formation of complexes with the organic ligands EDTA (ethylenediamine N,N,N′,N′ tetraacetic acid), ethylenediamine, and nitrilotriacetic acid (NTA). The cause of this order is related to the stability of the electronic structure of the various metals with a given ligand. Copper normally forms the strongest complexes with organic ligands. This is related to the unique ability of the eight d electrons in copper to form a hybrid configuration.

TABLE 3.5

Stability Constants for the Formation of Organic Ligands with Metals

	log K		
Ion	**EDTA**	**Ethylenediamine**	**Nitrilotriacetic Acid**
Mn^{2+}	14	2.7	7.4
Fe^{2+}	14	4.3	8.3
Co^{2+}	16	5.9	10.5
Ni^{2+}	18	7.9	11.4
Cu^{2+}	19	10.5	12.8
Zn^{2+}	16	6.0	10.5

3.2 Residence Times

An element can have a low concentration in seawater for two reasons:

1. It may be very reactive and thus be rapidly removed to the sediments.
2. It may occur in very low concentrations in its source from crystalline rocks or gaseous emanations from the interior of the earth.

For example, Al^{3+}, although a minor element in seawater, is one of the most predominant constituents of igneous rocks; its high reactivity in the marine environment reduces its concentration. The element Cs^{+}, on the other hand, has a low concentration in seawater and in crystalline rocks. Insight into the comparative behavior of elements can thus be gained by considering the relative reactivity of the elements based on the average time they spend in seawater before removal to the sediments or the degree of undersaturation of the element in seawater. These areas are discussed in the following sections.

Barth (1952) was the first to introduce the concept of the ocean as a simple reservoir for the elements that are introduced into it during the major sediment cycle. He assumed a steady-state system in which the amount of an element entering per unit time is equal to or compensated by the settling out of an equivalent amount. The residence time τ can then be defined as the average time that a substance remains in seawater before removal by some precipitation or adsorption process and is given by

$$\tau = \text{Total mass of the element in seawater/mass supplied per year}$$

It is further assumed that there is complete mixing of the element in a time that is short compared to the residence time. If one uses a steady rate model for the river input Q and sediment removal R of an element A, we have

$$Q \rightarrow A \rightarrow R$$

The change in A with time t gives $dA/dt = Q - R = 0$. If the removal is proportional to the concentration (first-order removal), we have $R = k[A]$, and the residence time is given by

$$\tau = 1/k = [A]/R = [A]/Q \tag{3.6}$$

Elements are introduced into the ocean by three methods:

1. Fallout of substances from the atmosphere
2. Influx of river water
3. Influx from the interior of the earth

Barth (1952) used estimates of the river input Q of various elements to estimate the residence time of elements. Since some elements come into the oceans from rivers in a solid phase (Si in clay minerals), care must be taken when estimating the river input. Care must also be taken to consider the recycling of elements from the sea to the land and back to the sea. The Cl^{-} ion, for example, coming into the oceans from rivers is largely recycled

TABLE 3.6

Residence Times of Elements in Seawater

	Residence Time (million of years)	
Element	**River Input**	**Sedimentation**
Na	210	260
Mg	22	45
Ca	1	8
K	10	11
Sr	10	19
Si	0.935	0.01
Li	12	19
Rb	6.1	0.27
Ba	0.05	0.084
Al	0.0031	0.0001
Mo	2.15	0.5
Cu	0.043	0.05
Ni	0.015	0.018
Ag	0.25	2.1
Pb	0.00056	0.002

sea salt (brines) that is transported to the land from the sea. As discussed in Chapter 10, the input of elements from hydrothermal vents can change the residence times determined from inputs only from rivers. Estimates of the residence times from river inputs are given in Table 3.6 and shown plotted versus atomic number in Figure 3.3. Also given in Table 3.6 are the residence times determined from the sedimentation rates of the elements R.

The agreement between the two methods of calculating residence times is quite reasonable considering the simplicity of the model for the oceans. The values span six orders of magnitude: Na with 2.6×10^8 yr to Al of 100 yr. One further condition must be satisfied. Both A and Q should not change during a period on the order of three to four times τ. Even for Na, this assumption appears to be valid since 10^9 years for the age of the oceans is in agreement with present-day geological concepts.

The elements with long residence times are characterized by the lack of reactivity of their aqueous ions in the oceans. The decrease in residence times of the alkali metals in going from Na^+ to Cs^+ reflects variations in their ocean reactivities. The primary reactions regulating the concentrations of the alkaline metals may involve ion-exchange equilibria with clay minerals on the seafloor. For the cations, the retention on clay surfaces increases with increasing ionic radius (i.e., decreasing hydrated radius). Thus, the decrease in residence times with increasing atomic numbers is in accord with the known behavior of the alkali metals. Certain elements (Be^{2+}, Al^{2+}, Ti^{3+}, Cr^{3+}, Fe^{2+}, Nb^{3+}, and Th^{4+}) have residence times less than 1000 yr, which is on the order of the mixing times for ocean waters. These elements enter the oceans as particulate particles from the continents or volcanic activity in the form of clay mineral, feldspars, and so on; thus, they rapidly settle to the sediments. Some of these elements are also reactive with substances such as ferromanganese minerals and zeolites. Thus, their entry as solids and their high chemical reactivity can account for their low residence times. The absolute values of these residence times are somewhat tenuous because of the assumption that there is complete mixing of such elements in the oceans.

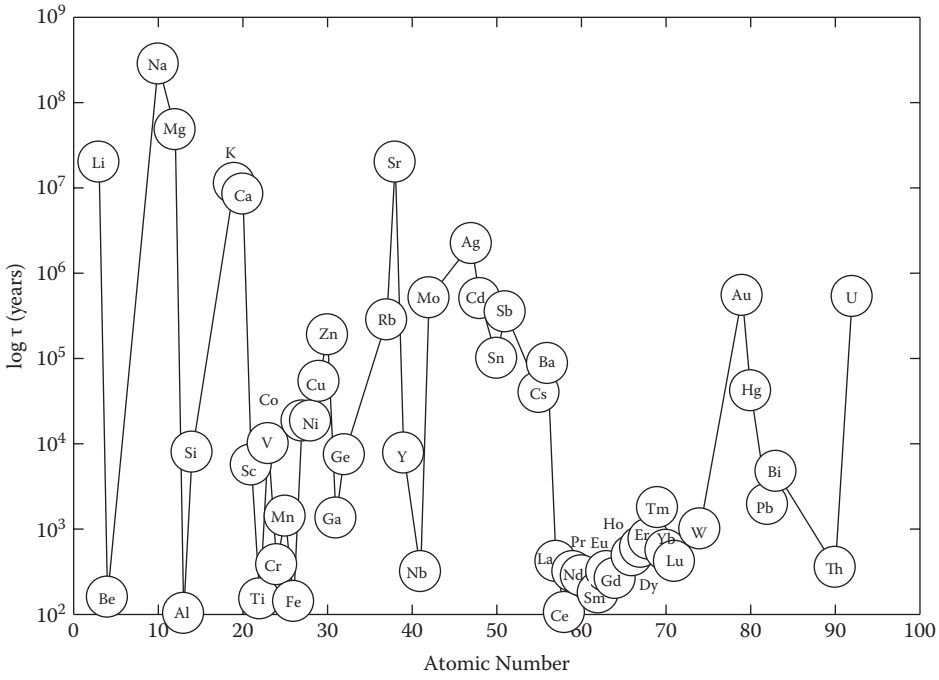

FIGURE 3.3
The residence time of elements in seawater plotted versus atomic number.

Nevertheless, certain deductions can be made with regard to their geochemistry. Ocean to ocean and temporal variations of these elements are to be expected. For example, the short residence times of Th^{4+} in the oceans allows for various water masses to maintain different concentrations. Certain minor elements have intermediate values of residence times: Mn (7000 yr), Zn (180,000 yr), Co (18,000 yr), and Cu (65,000 yr). The reactivities of some of these elements are clearly connected with the formation of plant material (that is, active and nonactive uptake).

Whitfield and Turner (1987) have developed a semiempirical correlation of the residence times for elements:

$$\log \tau = 2.6 \log[C_{SW}/C_{RW}] + a\,\Delta H_h + b \tag{3.7}$$

where C_{SW} and C_{RW} are the concentration of the element in seawater (SW) and river water (RW), respectively; ΔH_h is the heat of hydration of the element; and a = 0.00452 and b = –0.6 are adjustable parameters. The reliability of this equation is shown in Figure 3.4, which compares the observed and calculated residence times for a number of elements.

Many workers have examined the relative reactivity of elements in seawater based on the degree of saturation. If the solubility of a given element controls its concentration in the ocean, one would expect the more soluble elements to have the longest residence times. Some of the metals that have been considered with this in mind (Goldberg, 1965) are given in Table 3.7. The most insoluble compound for each element is given in this table along with the ratio of the saturated concentration to the measured concentration R. The value

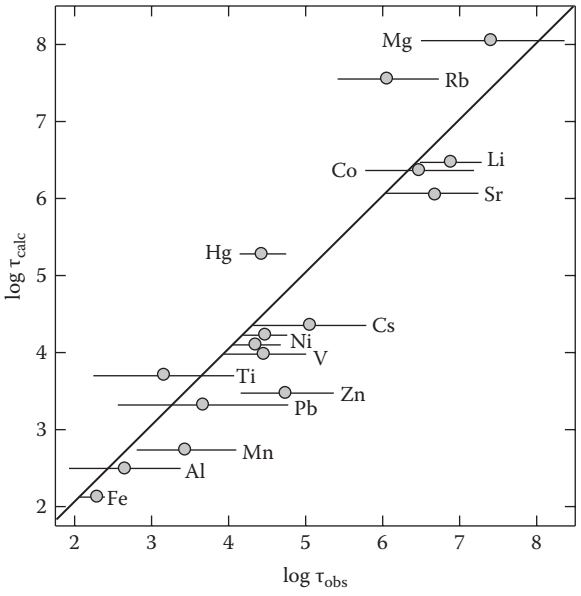

FIGURE 3.4
Calculated and observed residence times.

TABLE 3.7

Comparison of Ratio of Saturated Concentration to Measured Values and Residence Times

Metal	Insoluble Compound	R[a]	Years
Pb^{2+}	$PbCO_3$	10,000–20,000	2,000
Ni^{2+}	$Ni(OH)_2$	10,000–225,000	18,000
Co^{2+}	$CoCO_3$	50,000–400,000	18,000
Cu^{2+}	$CuCO_3$	133–266	50,000
Ba^{2+}	$BaSO_4$	3.7	84,000
Zn^{2+}	$ZnCO_3$	120–250	180,000
Cd^{2+}	CdOHCl	40,000–10,000,000	500,000
Ca^{2+}	$CaCO_3$	0.25–1.2	8,000,000
Sr^{2+}	$SrCO_3$	2.75	190,000,000
Mg^{2+}	$MgCO_3$	27	450,000,000

[a] Measure of degree of undersaturation. R, saturation concentration/measured concentration.

of R is used as a measure of the undersaturation of a given element. One would expect the elements with small values of R to have the longest residence times. Although this is generally true, many reactive elements have a short residence time and concentration well below the saturation limits. These results mean that factors other than solubility control the reactivity of most elements in the oceans.

3.3 Distribution of Trace Elements in the Oceans

In recent years, there has been a rapid increase in our knowledge of the distribution of minor trace elements (mostly metals) in the oceans. This recent revolution is related to major advances in instrumentation and the elimination or control of contamination during sampling, storage, and analysis. Bruland (1983) has reviewed these developments. Preconcentration techniques such as chelation on resins and coprecipitation have been used to separate an element from the major components of seawater, and measurements of trace elements at levels of nanomoles and picomoles per kilogram have been achieved. The distributions of the elements were found to be consistent with known biological and physical behavior. Ultraclean room techniques pioneered by Patterson and coworkers (Schaule and Patterson, 1983) in studies of lead and the use of specially designed hydrowires (Kevlar) and sample bottles (Teflon coated) provided reliable data for trace metals such as Mn, Cu, Cd, Ni, Ba, and Fe. Surface values for Pb, Hg, Cu, Ni, and Zn were obtained using rafts and by collecting the samples by hand. More recently, Biller and Bruland (2012), as part of the GEOTRACES program, have determined profiles of Mn, Pb, Fe, Co, Zn, Cu, Ni, and Cd in the North Atlantic and Pacific Oceans. These new results are a prelude to the expected results for these metals throughout the world oceans. The types of profiles found for various elements can be divided into a number of general categories. Some for the various types of profiles are as follows:

1. **Conservative profile:** A constant ratio of the concentration of the element to chlorinity or salinity is found for some elements because of their low reactivity. The major components of seawater and trace metals such as Li^+, Rb^+, and Cs^+ and anions such as molybdenum (MoO_4^{2-}) and tungsten (WO_4^{2-}) exhibit this type of behavior (see Figure 3.5).
2. **Nutrient type profile:** A depletion of an element in surface waters and enrichment at depth is a nutrient type profile. The element is removed from the surface waters by uptake by plankton or adsorption to biologically produced particulate matter. It is regenerated in deep waters when the biologically produced particulate matter is oxidized by bacteria. Three types of nutrient type profiles are found:
   a. The shallow water regeneration that leads to a maximum near 1 km, similar to the nutrients PO_4^{3-} and NO_3^-. The metal Cd^{2+} provides a good example of this type of nutrient behavior (see Figure 3.6). This behavior indicates that the element is associated with the soft parts of living and dead biological material. De Baar and coworkers (De Baar et al., 1994; Löscher et al., 1997) have shown that many metals show a near-linear correlation with nitrate and phosphate (Figure 3.7). Boyle (1992) has shown that this relationship can be used to estimate the phosphate in ocean water from the coprecipitated Cd in shells. By dating the shells, he has been able to estimate the past phosphate in North Atlantic deep waters as a function of time.
   b. The deep regeneration cycle leading to a deep maximum is observed for metals of this type, similar to the distribution of silica and total alkalinity. Examples of this type include the elements Zn^{2+}, Ge^{3+}, Ba^{2+}, and Ni^{2+} (see Figure 3.8 through Figure 3.11).

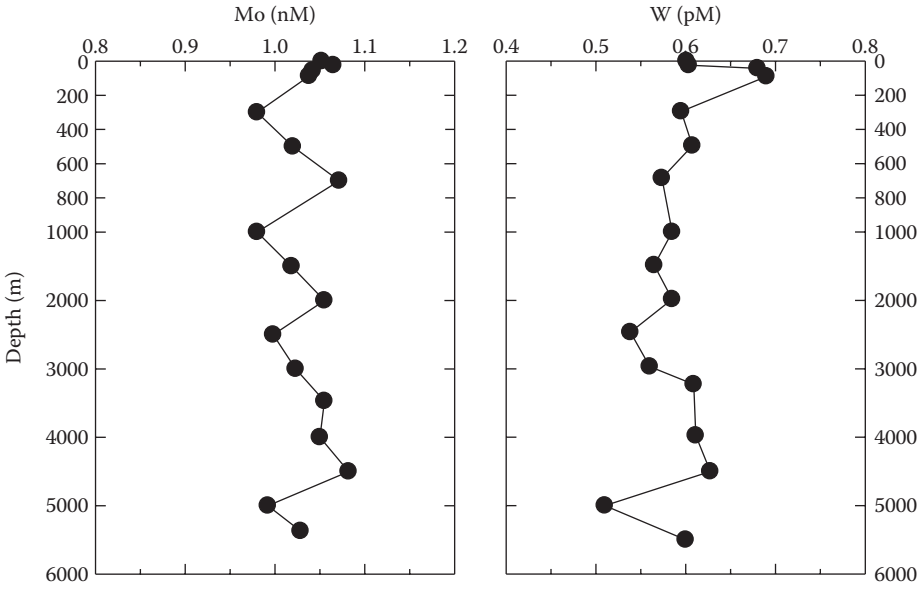

FIGURE 3.5
Profiles of molybdenum (Mo) and tungsten (W) in the Pacific Ocean.

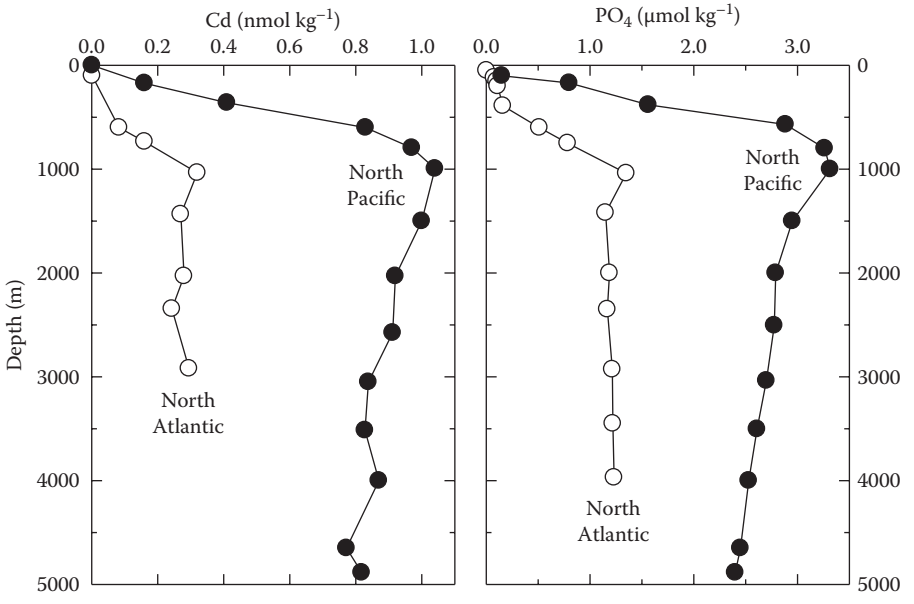

FIGURE 3.6
Profiles of cadmium (Cd) and phosphate (PO_4) in the Atlantic and Pacific Oceans.

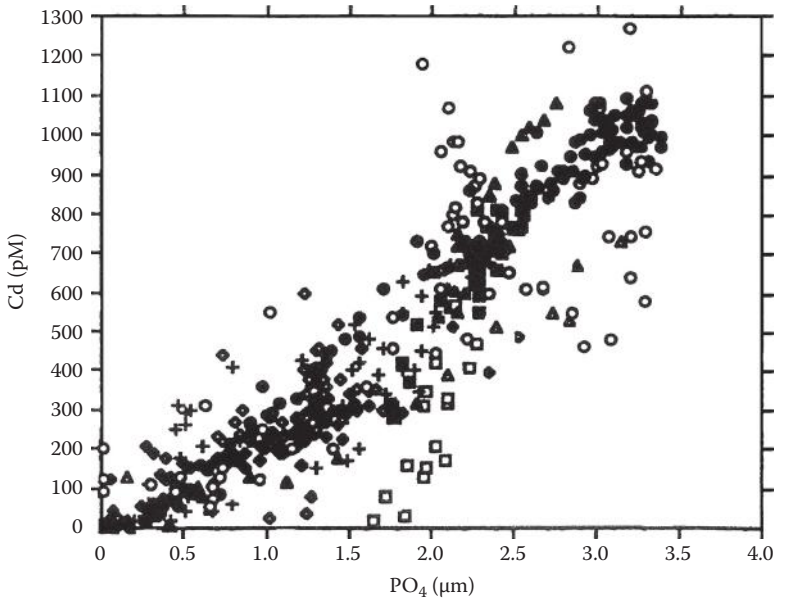

FIGURE 3.7
Plot of cadmium as a function of phosphate.

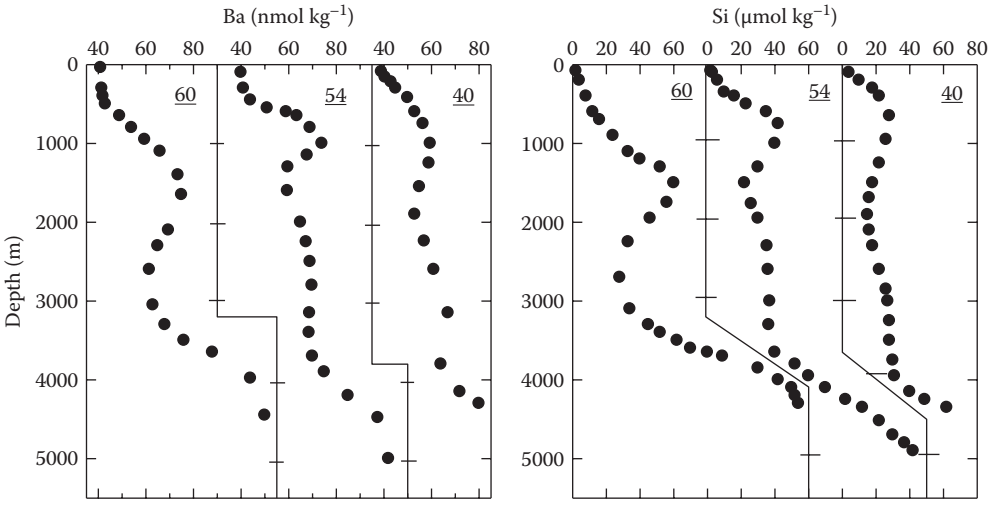

FIGURE 3.8
Comparison of barium (Ba) and silica (Si) profiles in the South Atlantic.

c. The combination of shallow and deep generation is inferred from the nutrient type profiles of Ni and Se (see Figure 3.11 and Figure 3.12). Recent results for Ag also show this mixed type of behavior (Figure 3.13). These metals appear to be affected by phytoplankton and diatoms or calcifiers.

The recent profiles for Ni, Zn, and Cd in the North Atlantic and Pacific Oceans by Biller and Bruland (2012) are similar to the earlier results. Their new results for

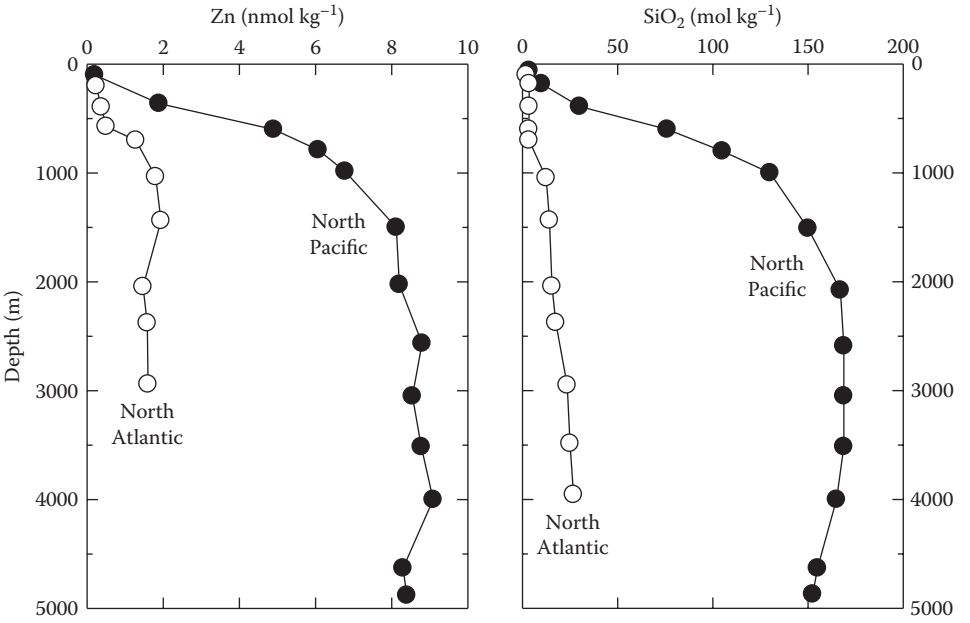

FIGURE 3.9
Profiles of zinc (Zn) and silicate (SiO_2) in the Atlantic and Pacific Oceans.

Mn, Fe, and Co (Figures 3.14, 3.15, and 3.16, respectively) are more complicated than the other transition metals. The Mn is higher in surface waters but appears to go through a maximum in the Pacific. The profiles of Fe and Co are low in surface waters and go through a maximum in intermediate waters. The increase of Mn and Fe near the O_2 minimum may be related to the formation of reduced forms of these metals. The recent results of Biller and Bruland (2012) for copper are shown in Figure 3.17. The surface values of Cu in the Atlantic and Pacific are similar and increase slowly in deeper waters. Cu does not appear to be directly related to the soft or hard parts of plants. Over the next 10 years, some of these causes will be elucidated as the GEOTRACES measurements continue.

3. **Surface enrichment and depletion at depth:** Elements of this type have a surface input from the atmosphere, rivers, and land and are rapidly removed from seawater. The residence times of these elements are very short. The metal Pb is a good example of an element entering the oceans via the atmosphere. The results off the coast of Bermuda as a function of time are shown in Figure 3.18. The high surface input of lead is largely the result of its past use as an antiknock agent in gasoline. Over time, it is removed by precipitation or adsorption to particles (Wu and Boyle, 1997). The exact mechanism for the scavenging of lead is not well defined at present. It is interesting to note that the recent measurements of Pb in the Atlantic and Pacific Oceans by Biller and Bruland (2012) are different from the earlier measurements (see Figure 3.19). The surface values of Pb are higher in the Pacific Ocean than in the past. This may be due to the higher concentrations of Pb in dust in Asia from the use of coal to produce electricity. The deep Atlantic and Pacific values of Pb are lower due to the loss as the waters move from the Atlantic to the Pacific Ocean as found in earlier studies.

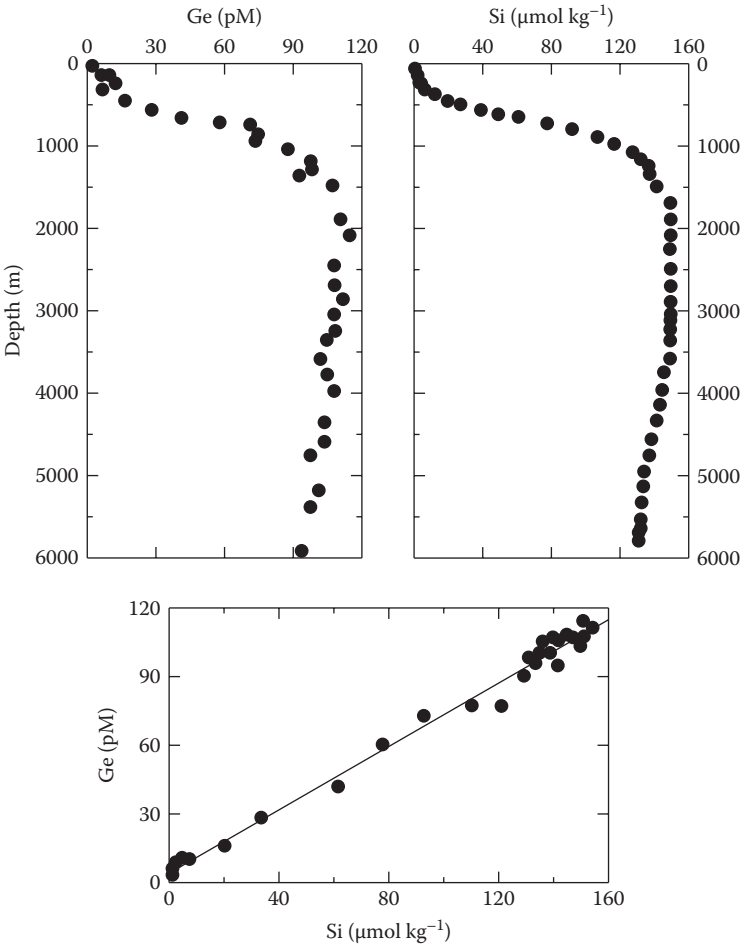

FIGURE 3.10
Comparison of the profiles of germanium (Ge) and silica (Si) in Pacific waters.

The metal Mn^{2+} is a good example of an element that enters surface waters via rivers or release from shelf sediments off California (see Figure 3.20). Elements that can occupy different oxidation states can also exhibit this type of profile. The reduction of metal in surface waters can be caused by biological and photochemical processes. The subsequent oxidation can lead to an oxidized form that is insoluble in seawater. The elements Cr^{3+}, As^{3+}, and I^- fall into this classification.

4. **Middepth minima:** A middepth minimum can result from a surface input and regeneration at or near the bottom or scavenging throughout the water column. The metals Cu^{2+}, Sn^{4-}, and Al^{3+} show this type of profile. Profiles for the distribution of Al in the Atlantic and Pacific are shown in Figure 3.21. The input into the surface oceans comes from the fallout of atmospheric dust that originates on the continents. The input of dust from Africa (Sahara Desert) into the Atlantic is much higher than the values from China (Gobi Desert) to the Pacific. The Al is quickly scavenged from surface water by adsorption on plant material or the uptake of plants. The particles settle into the deep oceans and are deposited in the sediment.

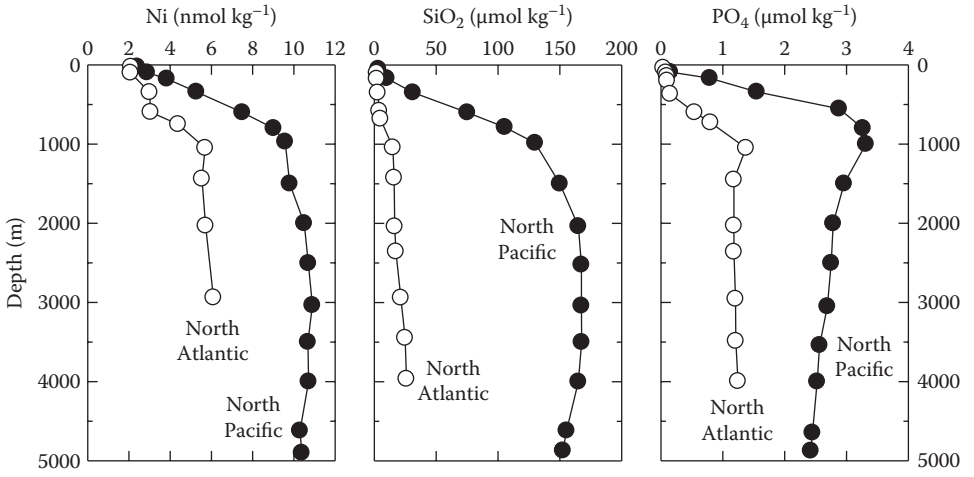

FIGURE 3.11
Comparison of the profiles of nickel (Ni) to silicate (SiO_2) and phosphate (PO_4) in the Atlantic and Pacific Oceans.

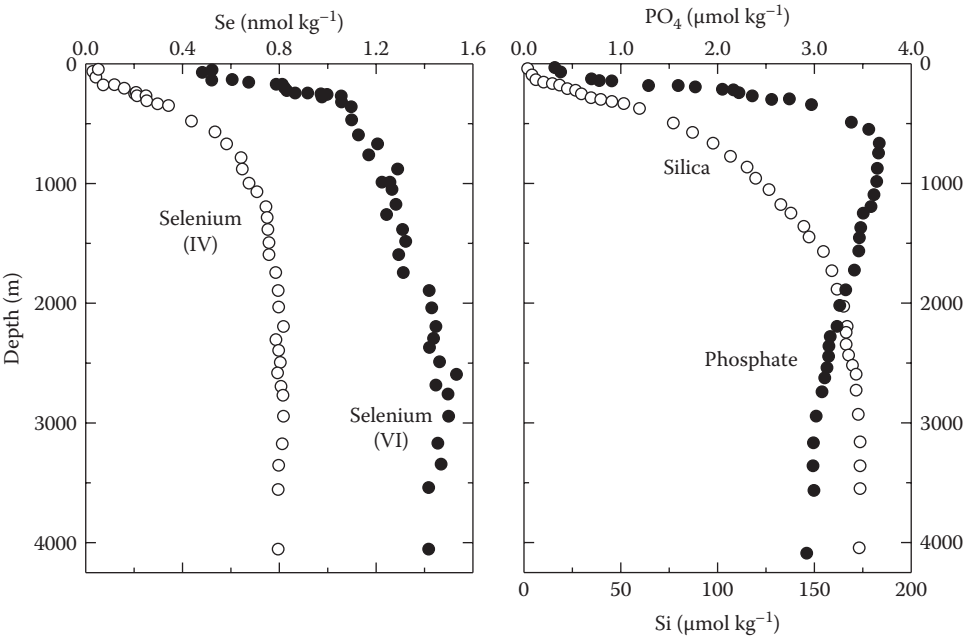

FIGURE 3.12
Comparison of the profiles of selenium (Se) to silica (Si) and phosphate (PO_4) in the Pacific Ocean.

The resuspension and flux of Al from the sediments leads to an increase in the concentration in bottom waters.

5. **Middepth maxima:** A profile of this type can result from a hydrothermal input from the midocean ridge system. The elements Mn^{2+} and ^3He are good examples of this type of profile (see Figure 3.22 and Figure 3.23). The fluxes of these elements from hydrothermal plumes (Chapter 10) have been used to trace them in deep ocean waters.

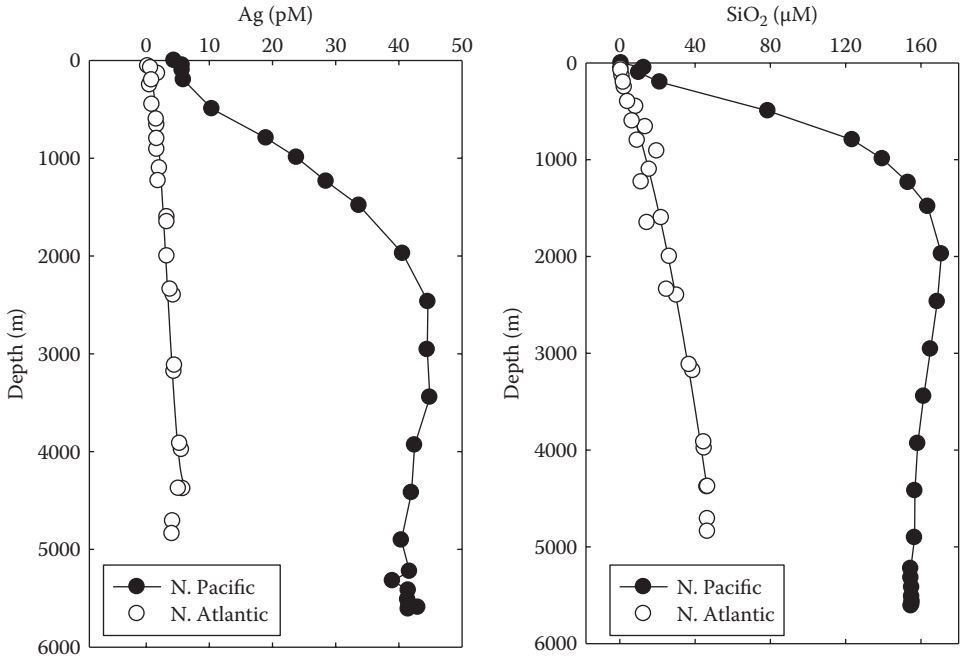

FIGURE 3.13
Comparison of the profiles of silver (Ag) to silicate (SiO_2) in the Atlantic and Pacific Oceans.

6. **Middepth maxima or minima in the suboxic layer** (~1 km): A large suboxic layer exists in some regions of the Pacific and Indian Oceans. Reduction and oxidation processes in the water column or adjacent slope sediments can yield maxima of the reduced forms (Fe^{2+}, Mn^{2+}, and Co^{2+}, Figures 3.14, 3.15, and 3.16, respectively). Minima may occur due to insoluble or scavenged metals by solid phases (Cr^{3+}).
7. **Maxima and minima in anoxic waters:** In areas of restricted circulation such as the Black Sea, the Cariaco Trench, and fjords, the water can become anoxic (devoid of O_2) with the production of H_2S. Near the interface between the two waters, redox processes can occur that cause maxima and minima from solubility changes of the various species. Fe^{2+} and Mn^{2+}, for example, have maxima because of the increased solubility of the reduced forms (see Figure 3.24 and Figure 3.25). These maxima are due to oxidation and reduction of iron and manganese near the oxic–anoxic interface. More is said about anoxic waters in Chapter 10.

Many of the metals studied have higher concentrations in the Pacific than in the Atlantic (see Table 3.8). Exceptions are Pb^{2+} and Al^{3+}. The higher values in the deep Pacific are attributed to the older water accumulating more metals from surface waters. For Pb^{2+} and Al^{3+}, the higher surface input in the Atlantic leads to higher values in the deep Atlantic waters. Since these metals are quickly scavenged from seawater, they do not accumulate in the deep waters of the Pacific. The higher concentration of most metals on shelves (Table 3.9) indicates a land source (rivers or sediments), while the higher concentration (Table 3.10) in the Atlantic central gyre indicates an atmospheric input (from African dust).

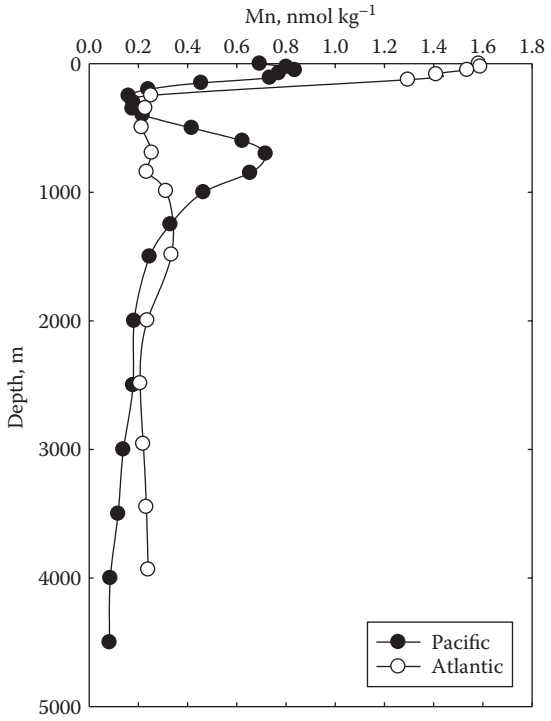

FIGURE 3.14
Profiles of Mn in the Atlantic and Pacific Oceans.

3.4 Biological Interactions

The interactions of trace elements with marine organisms have been studied by many workers. Bowen (1966) has summarized these interactions, which are outlined next, in terms of concentration factors (concentration in the organism relative to a given volume of seawater).

1. Cl^- is rejected by organisms.
2. Na^+, Mg^{2+}, Br^-, F^-, and SO_4^{2-} have concentrations in organisms similar to seawater (concentration factors of 1.0).
3. Most of the other elements, with the exception of the noble gases, are strongly concentrated in living tissue.
4. The order of affinity of organisms for cations is

   $$4+ > 3+ > 2+ \text{ transition} > 2+ \text{ group IIA} > 1+ \text{ group I metals.}$$

   For plankton, the order is

   $$Fe^{3+} > Al^{3+} > Ti^{3+} > Cr^{3+} > Ga^{3+} > Zn^{2+} > Pb^{2+} > Cu^{2+} > Mn^{2+} > Co^{2+} > Cd^{2+}$$

   This order does not agree with the Irving-Williams order. The formation of complexes with surface ligands does not control the uptake by plankton.

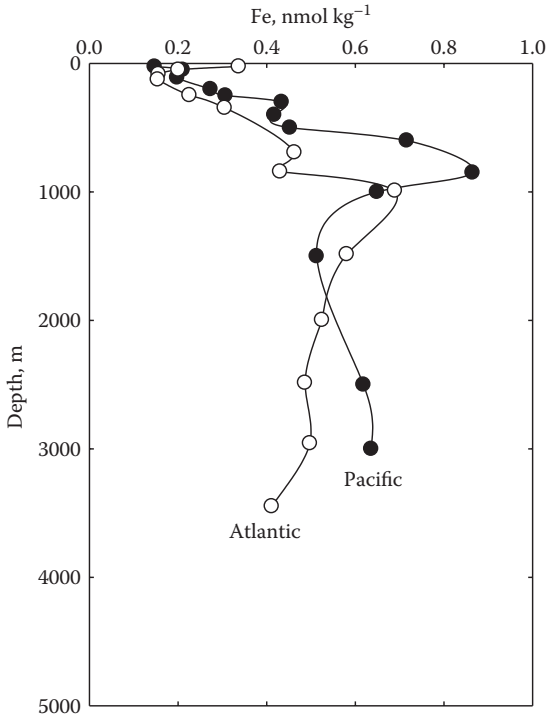

FIGURE 3.15
Profiles of Fe in the Atlantic and Pacific Oceans.

5. Heavy group elements of a particular class are taken up more strongly than lighter elements.
6. The affinity of organisms for anions increases with increasing ionic charge and in a given group with increasing weight of the central atom:

$$F^- < Cl^- < Br^- < I^-$$

$$SO_4^{2-} < MoO_4^{2-} < WO_4^{2-}$$

7. The lower organisms concentrate elements more strongly than higher organisms.
8. Heavy metals are frequently concentrated in the digestive or renal organs.

The biosphere can affect minor elements by the following:

1. The regulation of dissolved and particulate organic material as a function of time and space. This material can interact with minor elements and change their reactivity.
2. The concentration of elements in living and nonliving organic material. The active and inactive uptake can redistribute elements from surface to deep waters. The concentration of organics on nonliving particles may also increase the adsorption on these particles.

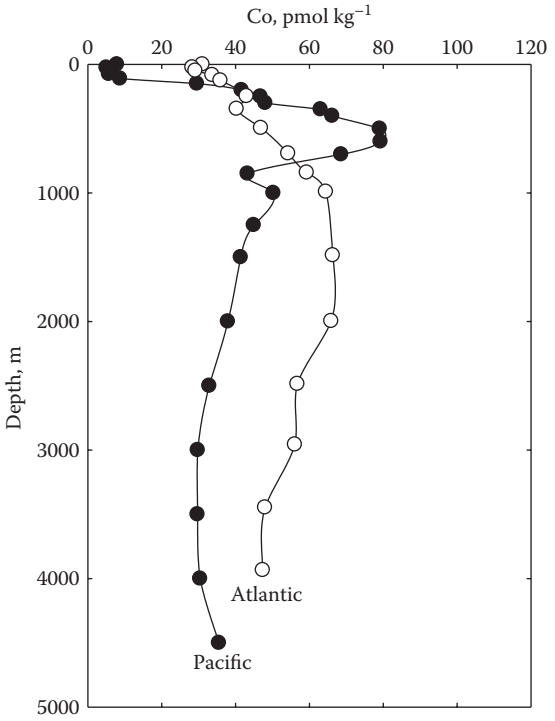

FIGURE 3.16
Profiles of Co in the Atlantic and Pacific Oceans.

These effects can account for the movement of elements from surface waters to the sediments. This movement can be caused by

1. Active uptake by organisms (Fe^{2+}, Zn^{2+}, Mn^{2+})
2. Passive uptake by organisms (heavy metals)
3. Adsorption on particulate matter (Pb^{2+}, Cu^{2+})
4. Remobilization from sediments by oxidation (Mn^{2+})
5. Precipitation (Fe^{3+})

The active uptake of metals may be due to their use in enzyme systems (V, Cr, Mn, Fe, Co, Ni, Cu, Zn, and Mo). Passive uptake may be due to the adsorption on organic particles caused by interactions with surface groups (carboxylic, phenolic).

It is well known that a number of metals are concentrated in biological materials. This has led to the suggestion that their source in the deep ocean comes from the death of marine organisms with subsequent remineralization during oxidation. An alternate explanation may be that metals may be carried to the deep ocean by adsorption on organic matter, both living and dead. We have found, for example, that Cu^{2+} is adsorbed on bacteria that are living or dead (see Figure 3.26). The absorption is quite fast (Figure 3.27), and the Cu^{2+} can be desorbed by acidifying the solutions. The adsorption increases with increasing pH, which indicates that surface –OH and –COOH groups may be involved in the process. Fisher (1986) has shown that adsorption of a number of metals to living and dead phytoplankton

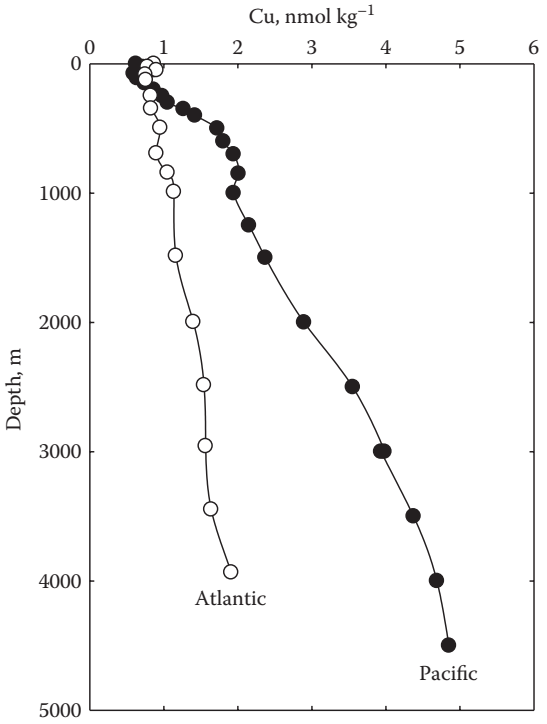

FIGURE 3.17
Profiles of Cu in the Atlantic and Pacific Oceans.

was similar and proportional to the hydrolysis constants of the metals (see Figure 3.28) and to the residence times (Figure 3.29). These results suggest that the scavenging of metals in the oceans may be the result of ionic interactions with surface groups on living and dead organic matter in the oceans. Fisher also showed (see Figure 3.30) that the toxicity of metals to plankton was related to hydrolysis constants.

The above discussion is not meant to rule out nonbiological transport since it is well known that many metals can be coprecipitated by SiO_2 and $CaCO_3$ or adsorbed on minerals in ocean waters. In an oxidizing environment, for example, many metals (Fe^{2+}, Cu^{2+}, Ni^{2+}, Co^{2+}, etc.) are concentrated on Mn nodules. In a reducing environment, a number of metals are coprecipitated or adsorbed by pyrite (FeS_2). The oxidation of Fe^{2+} and Mn^{2+} results in the formation of solids that can adsorb many metals. In summary, each metal may be influenced by biological or nonbiological processes. Future studies are needed to elucidate that these processes actually are responsible for the distribution of many of the elements present in the oceans.

Although most minor elements that enter the oceans eventually are removed to the sediments, many are recycled. The removal process is related to the interactions of elements with particles (Whitfield and Turner, 1987). The production, sinking, and decomposition of particulate matter are thus important in controlling the recycling of metals. Phytoplankton are the primary producers of particles in the surface oceans. These plants are grazed on by zooplankton and are packaged into fecal pellets. They have sinking rates of a few meters to thousands of meters per day. The oxidation and dissolution of these particles can recycle some of the elements. Recent work has shown that large particles are responsible for the

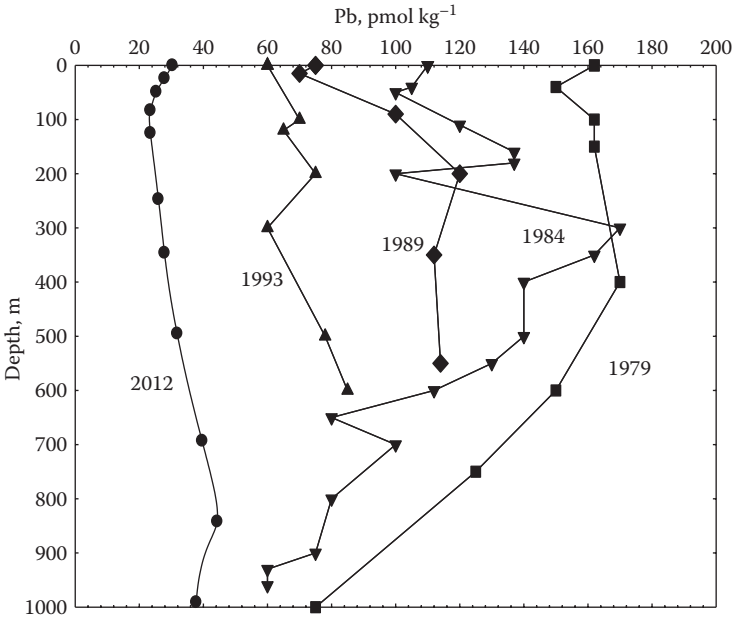

FIGURE 3.18
Profiles of lead (Pb) in the Atlantic Ocean waters off Bermuda as a function of time. (Adapted from Wu, J.F., and Boyle, E.A., *Geochim. Cosmochim. Acta*, 61, 3283, 1997, and Biller, D.V., and Bruland, K.W., *Mar. Chem.*, 130, 12–20, 2012.)

bulk transport of materials to the deep sea. These particles have been studied by catching them in sediment traps or by using large-volume pumping systems. This cycling of C, N, P, and S as well as trace metals was studied in a large multi-institutional study called the Joint Global Ocean Flux Study (JGOFS). Surface trace metals have been recently studied as part of the Climate Variability and Predictability (CLIVAR) study. The recent results for Fe and Al (Landing, Personal Communication) in the Atlantic off the coast of Africa are shown in Figure 3.31. The Al is high in the surface waters from the input of African dust and removed in deeper waters. The Fe is taken out of the surface water apparently by plankton and put back into the deeper waters by the breakdown of the plankton by bacteria or zooplankton.

GEOTRACERS will measure a number of trace metals along a number of cruise tracks from the surface to deep waters. This program will yield a large amount of information on the biogeochemistry of the world oceans.

3.5 Geochemical Balance of Elements

There is a continual interaction between the oceans and the land. The water from the oceans evaporates, comes down as rain, and attacks the rocks and soil. The rivers of the world carry the weathered products (dissolved and suspended) to the oceans. Sediments are formed on continental shelves, and fine particles are carried throughout the oceans. A number of geochemists have been concerned with geochemical processes with an interest in the evolution of seawater, sedimentary cycling, and the controls of the composition of

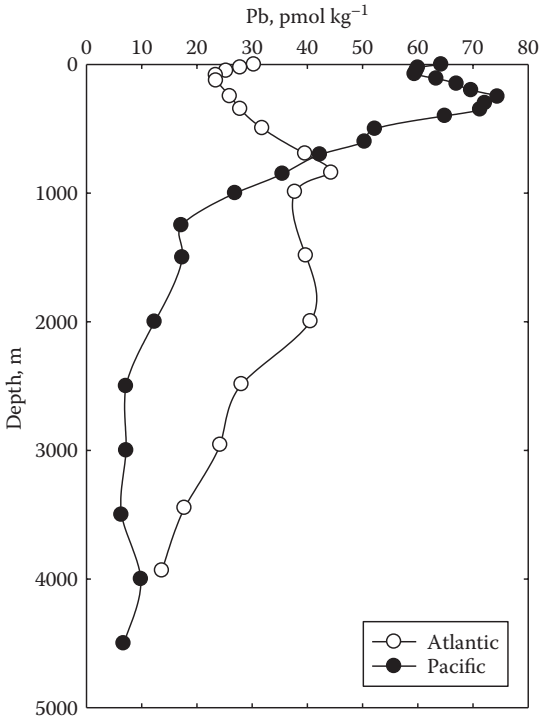

FIGURE 3.19
Recent profiles of Pb in the Atlantic and Pacific Oceans.

the oceans. By comparing the present composition of dissolved ions in the oceans (moles per square centimeter of the surface of the earth) with the amount delivered, attempts have been made to prepare a geochemical balance. Sillén (1967) tabulated the amounts of some of the major components of seawater delivered by rivers over the past 100 million years. These estimates are compared to the amounts in the present oceans in Table 3.11. Most of the elements show an excess amount added over this period of time. The Na^+ and Cl^- delivered to the oceans is mostly sea spray that is washed back to the oceans. The other ions, however, are the result of weathering of rocks and soils. In addition to the dissolved materials, 300 to 600 kg cm^{-3} of solid material have been delivered to the oceans in the past 100 million years. These solids are mostly clay minerals that can participate in ion-exchange reactions with the components of seawater and go through phase transformations.

Some geochemists have attempted to develop a geochemical balance between the material added to the rivers and the amount delivered to the sediments. These attempts were started in 1993 by Goldsmith. He considered that the reaction

$$\text{Igneous rocks} + \text{Volatiles} \rightarrow \text{Seawater} + \text{Sediments} + \text{Air} \tag{3.8}$$

controls the composition of rocks and seawater and attempted to balance the reaction. He concluded that 600 g of rock would lead to 600 g of sediments. More recent attempts have been made by Garrels and Mackenzie (1971). The steady-state model for the circulation of elements in the sedimentary cycle is shown in Figure 3.32. The fluxes are in units of 10^{14} g yr^{-1}. Unlike the earlier model of Goldsmith, recent work has the weathering reaction going

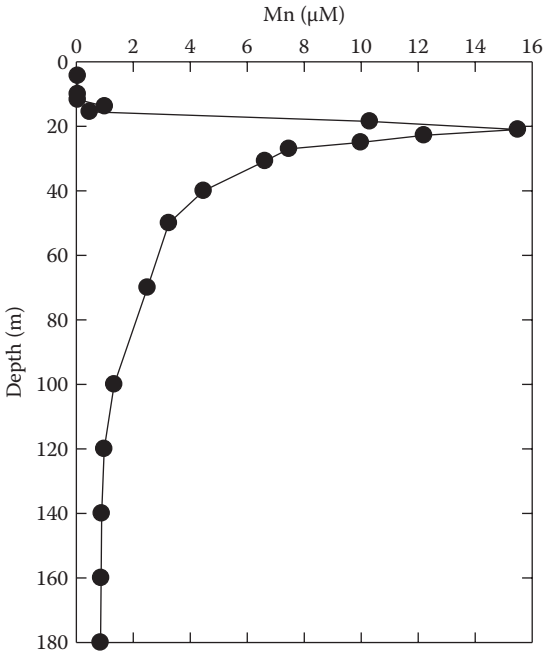

FIGURE 3.20
Profile of manganese (Mn) in the North Pacific off the coast of California.

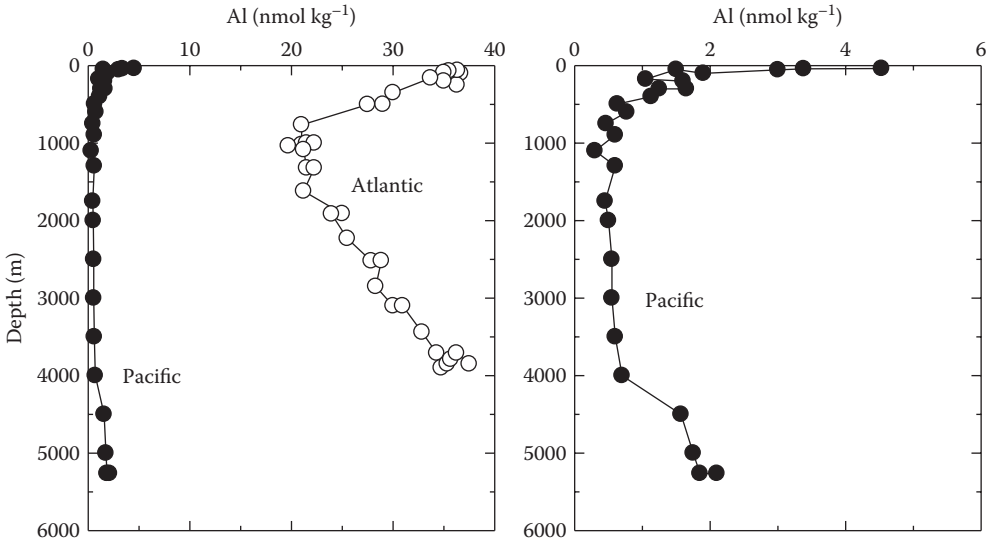

FIGURE 3.21
Profiles of aluminum (Al) in Atlantic and Pacific Ocean waters.

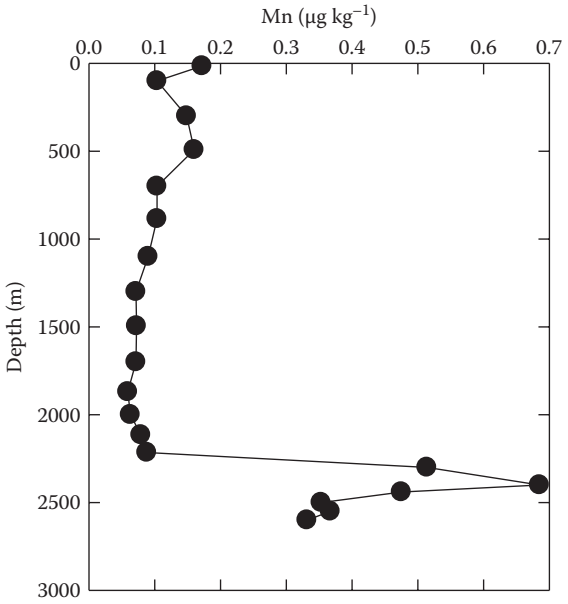

FIGURE 3.22
Profile of manganese (Mn) in the Pacific Ocean showing hydrothermal input from Mid-Pacific Ridge.

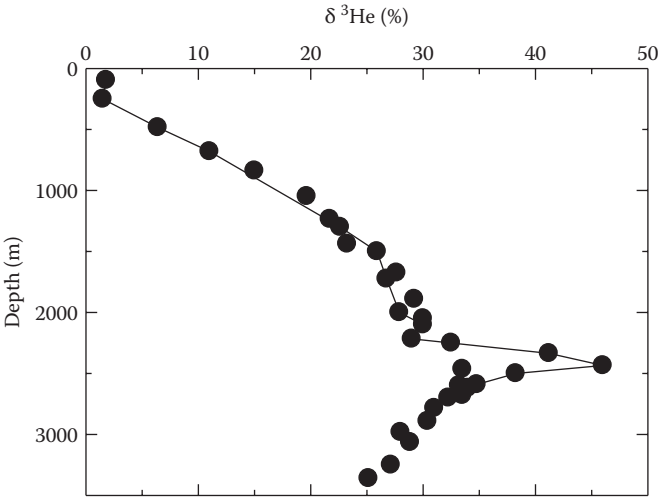

FIGURE 3.23
Profile of helium (He) in the Pacific Ocean showing hydrothermal input from Mid-Pacific Ridge.

both ways; that is, reverse weathering or igneous rocks are formed during seafloor spreading. The earlier models gave a reasonable balance between the rocks and the sediments for most elements (see Table 3.12). For the elements B, S, Cl, As, Se, Br, and I, an excess was found, presumably of a volcanic origin. With the recent discovery of the flux of materials coming from hydrothermal vents, these values will need some modification for some elements.

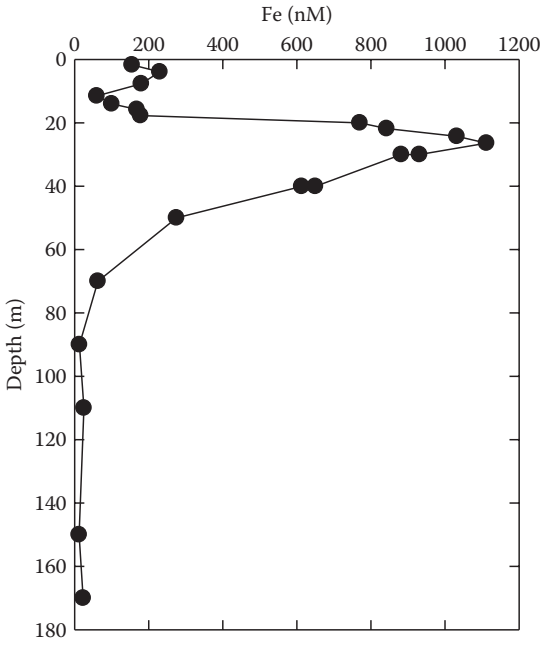

FIGURE 3.24
Profile of iron(II) (Fe) in the Framvaren Fjord, Norway.

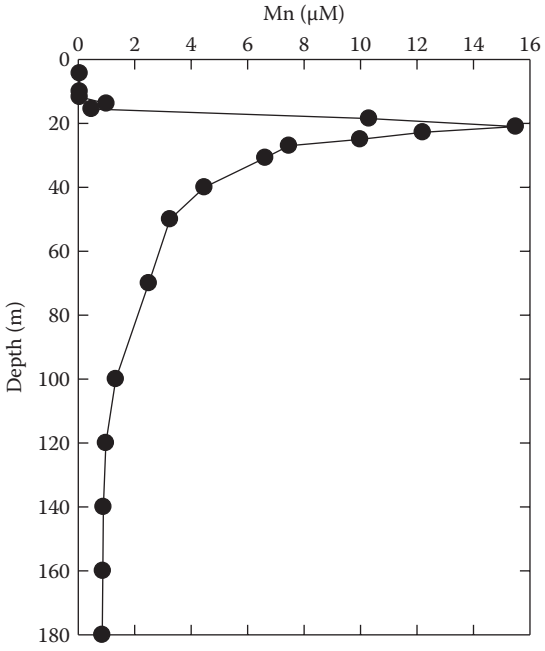

FIGURE 3.25
Profile of manganese(II) (Mn) in the Framvaren Fjord, Norway.

TABLE 3.8

Metals in Atlantic and Pacific Deep Waters (n*M*)

Metal	Atlantic	Pacific	P/A
Cd	0.29	0.94	3.2
Zn	1.5	8.2	5.5
Ni	5.7	10.4	1.8
Cu	1.7	2.7	1.6
Mn	0.6	—	—

TABLE 3.9

Metals on Shelf versus Open Sea Surface Waters

Metal	Shelf	Open
Mn	21 n*M*	2.4 n*M*
Ni	5.9 n*M*	2.3 n*M*
Cu	4.0 n*M*	1.2 n*M*
Zn	2.4 n*M*	0.06 n*M*
Cd	200 p*M*	2 p*M*

TABLE 3.10

Metals in Central Gyres

Metal	Atlantic	Pacific
Mn	2.4 n*M*	1.0 n*M*
Cu	1.2 n*M*	0.5 n*M*
Ni	2.1 n*M*	2.4 n*M*
Zn	0.06 n*M*	0.06 n*M*
Cd	2 p*M*	2 p*M*

Sillén (1967) suggested some imaginary experiments to represent the real ocean system. He visualized the formation of the oceans as the result of mixing water with a number of minerals. This mixing, performed perhaps by a well-known bartender, took place over a period of time to ensure equilibrium. The first model he considered is given in Figure 3.33. The ion exchange reaction

$$1.5\ Al_2Si_2O_5(OH)_4(s) + K^+ \rightarrow KAl_3Si_3O_{10}(OH)_2(s) + 1.5\ H_2O + H^+ \quad (3.9)$$

Kaolinite **K-mica**

can control the ratio of H^+ and pH of the oceans.

Applying equilibrium conditions for this reaction (at constant Cl^- and temperature) gives

$$K = [H^+]/[K^+] \quad (3.10)$$

$$[K^+] + [H^+] = [Cl^-] + Kw/[H^+] \quad (3.11)$$

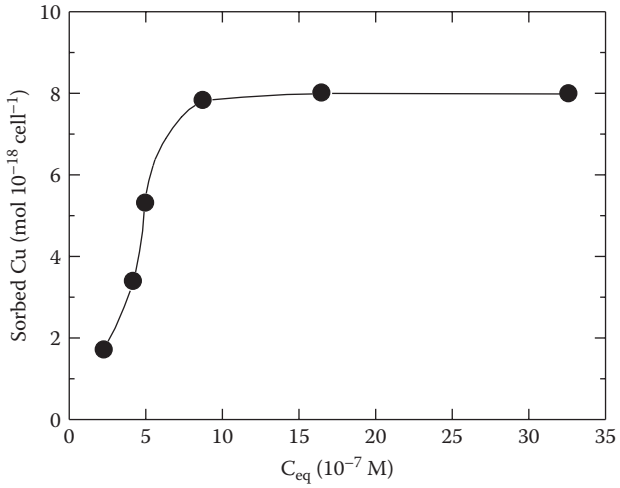

FIGURE 3.26
The adsorption of Cu(II) to the surface of bacteria as a function of Cu.

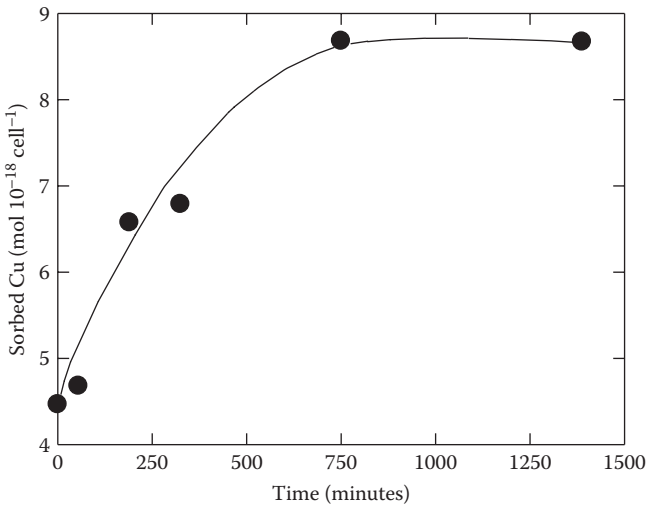

FIGURE 3.27
The adsorption of Cu(II) to the surface of bacteria as a function of time.

The ratio of $[H^+]/[K^+]$ is fixed; thus, the addition of HCl or KOH will return it to its original value as long as $[Cl^-]$ and temperature are constant. The system is thus a pH stat rather than a buffer as long as Cl^- and temperature are constant and no phases completely disappear. This simple result suggests that the pH and the major ionic concentrations of seawater are controlled by clay exchange reactions. When Sillén made this suggestion, most oceanographers were shocked, as they thought that the pH of the oceans was controlled by the carbonate system and the clays acted only as the walls of the container. Experimental studies yield $K = 10^{-6}$ to $10^{-6.5}$ (25°C) for the reaction, while the ratio is $10^{-6.2}$ in seawater. For

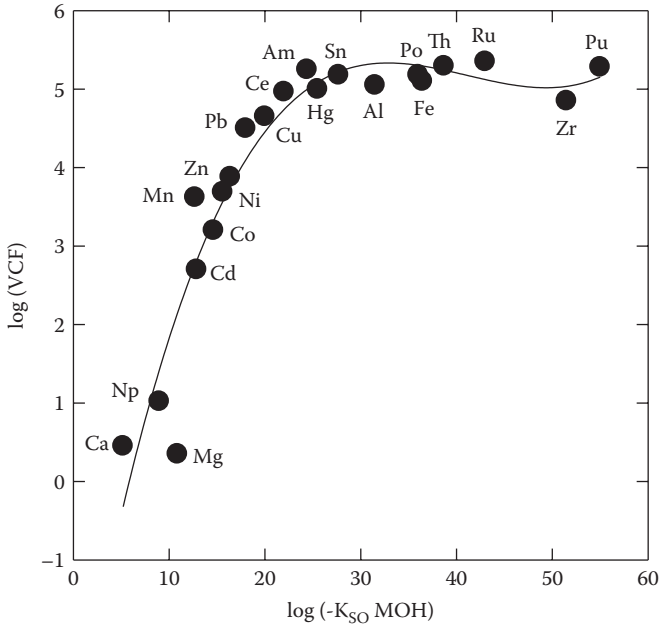

FIGURE 3.28
Values of the volume concentration factor (VCF) for metals to phytoplankton plotted versus the solubility of metal hydroxide. (From Fisher, N.S., *Limnol. Oceanogr.*, 3, 443, 1986. With permission.)

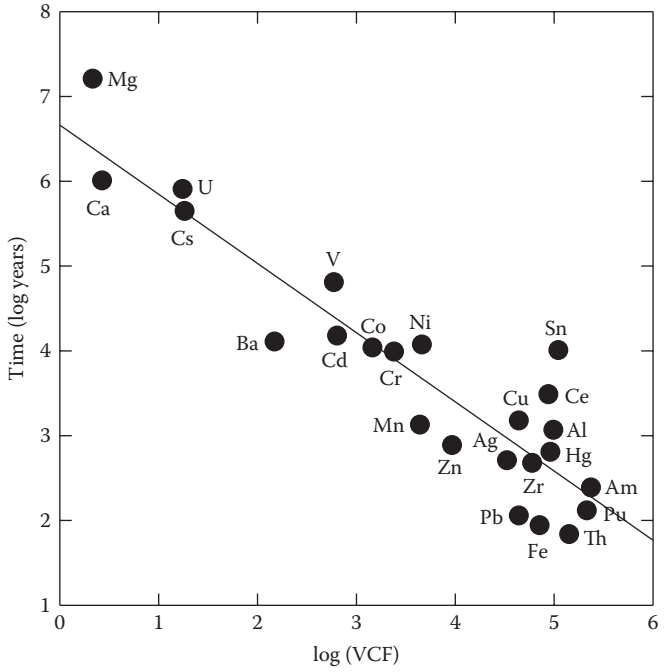

FIGURE 3.29
The residence time for metals plotted versus the volume concentration factor (VCF). (From Fisher, N.S., *Limnol. Oceanogr.*, 3, 443, 1986. With permission.)

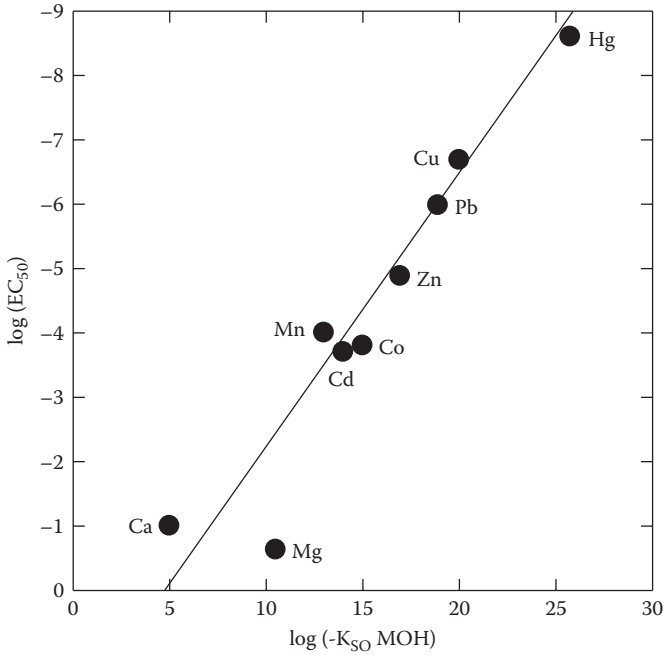

FIGURE 3.30
The effective concentration of metal that reduces phytoplankton growth rate by 50% (EC_{50}) plotted versus the solubility of metal hydroxide. (From Fisher, N.S., *Limnol. Oceanogr.*, 3, 443, 1986. With permission.)

the equilibrium between kaolinite and montmorillonite in a five-component system with Na^+, we have

$$1.5\ Al_2Si_2O_5(OH)_4(s) + Na^+ \rightarrow NaAl_3Si_3O_{10}(OH)_2\ (s) + 1.5\ H_2O + H^+ \qquad (3.12)$$

Kaolinite **Montmorillonite**

The ratio of H^+/Na^+ is also near the ratio in seawater. Since fresh clays are transformed in a day or two, forming new phases in a couple of years, most workers have found the silicate theory to be reasonable. Recent workers have also demonstrated that SiO_2 dissolves more rapidly in seawater than was once thought. Sillén also considered a more complicated nine-component system:

1. Seawater
2. SiO_2 (quartz)
3. $CaCO_3$ (calcite)
4. Kaolinite
5. Illite
6. Chlorite
7. Montmorillonite
8. Phillipsite
9. Atmosphere

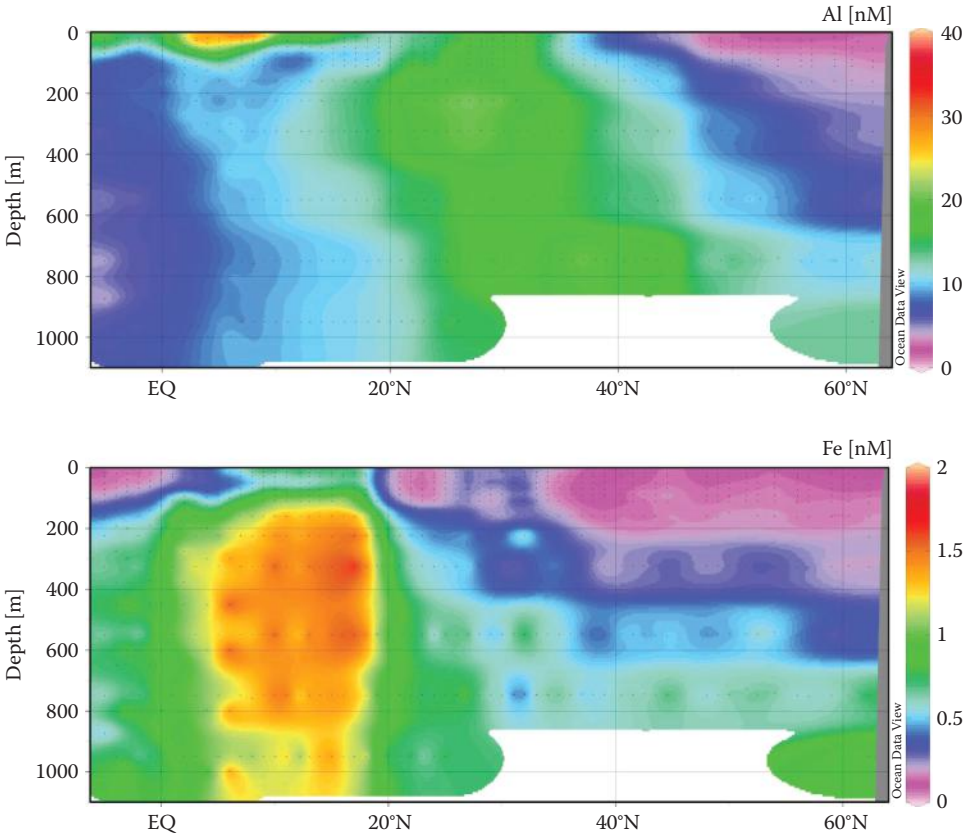

FIGURE 3.31
Section of Fe and Al off the coast of Africa in the Atlantic Ocean.

TABLE 3.11

Present Concentration (mol cm^{-2} of surface) of Major Components of Seawater Compared with the Amount Added by Rivers over Past 100 Million Years

	Na	Mg	Ca	K	Cl	SO_4	CO_3	NO_3
Present	129	15	2.8	2.7	150	8	0.3	0.01
Added by rivers	196	122	268	42	157	84	342	11
Excess added	67	107	265	39	7	76	342	11

Mg was found to be a problem, as well as SiO_2. More recent results on hydrothermal vents can explain these differences (Chapter 10). Mg is lost from the oceans, and Si is added by the reactions that take place in hydrothermal vent systems.

Turner et al. (1981) have shown a correlation between the residence time of an element in the oceans and the partitioning of that element between rocks and seawater. They defined the ocean–rock partition coefficient K_Y by

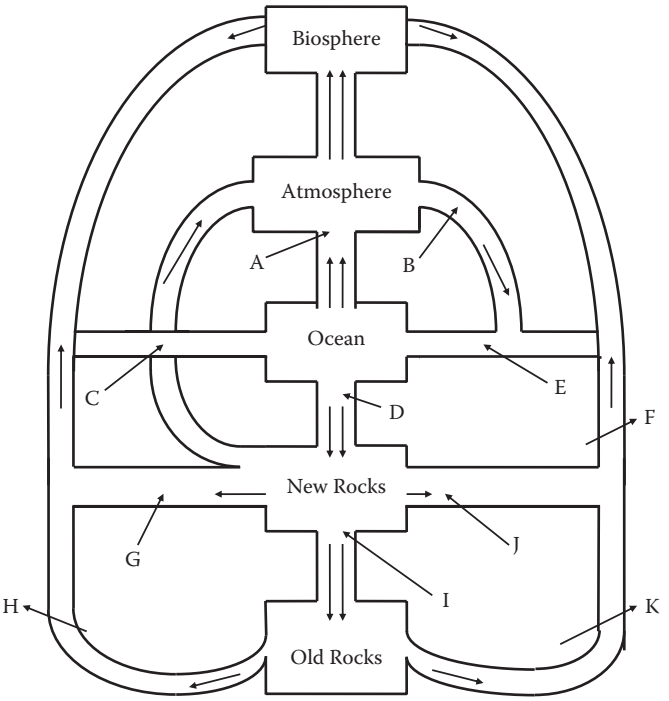

A. Ocean to Atmosphere
B. Atmosphere to Streams
C. Total Suspended Load of Streams
D. Total Sediment Flux
E. Dissolved Load of Streams
F. Total Flux Dissolved from Rocks
G. Suspended Load from New Rocks
H. Suspended Load from Old Rocks
I. Flux from New Rocks to Old Rocks
J. Dissolved Load from New Rocks
K. Dissolved Load from Old Rocks

New Rocks
4800×10^{20} g of elements (150×10^{6}y)

Biosphere
0.01×10^{20} gC Living
0.04×10^{20} gC Dead

Old Rocks
8450×10^{20} g of elements (663 × 106 y)

Atmosphere
0.065×10^{20} g C as CO_2

Ocean
500×10^{20} g of elements

FIGURE 3.32
The cycle of elements on the earth.

$$K_Y = Y_C/Y_A \tag{3.13}$$

where Y_A is the rate of transport of material from crustal rock, and Y_C is the rate of transport from the oceanic reservoir. The value of Y_A has been corrected for recycled sea spray. The logarithm of the mean residence time was found to be a linear fraction of the log of the partition coefficient:

$$\log \tau = 0.53 \log K_Y + 6.15 \tag{3.14}$$

TABLE 3.12

Concentration of Various Components of the Geochemical Cycle of the Oceans

Component	Rock	Volatile	Air	SW	Sediments
H_2O	—	54.90	—	54.90	—
Cl(HCl)	—	0.94	—	0.55	0.40
Na($NaO_{.5}$, NaOH)	1.47	—	—	0.47	1.00
Ca(CaO, $Ca(OH)_2$)	1.09	—	—	0.01	1.08
Mg(MgO, $Mg(OH)_2$)	0.87	—	—	0.05	0.82
K($KO_{.5}$, KOH)	0.79	—	—	0.01	0.78
Si(SiO_2)	12.25	—	—	—	12.25
Al($AlO_{1.5}$, $Al(OH)_3$)	3.55	—	—	—	3.55
C(CO_2)	0.03	1.05	—	0.002	1.08
C(s)	—	1.01	—	—	1.01
O_2	—	0.022	0.022	—	—
Fe(FeO, $Fe(OH)_2$)	0.52	—	—	—	0.53
($FeO_{1.5}$, FeOH)	0.38	—	—	—	0.38
Ti(TiO_2)	0.12	—	—	—	0.12
S	0.02	0.06	—	0.03	0.05
F(HF)	0.05	—	—	—	0.05
P($PO_{2.5}$,H_3PO_4)	0.04	—	—	—	0.04
Mn($MnO_{1\text{ to }2}$)	0.05	—	—	—	0.05
N_2	—	0.082	0.082	—	—

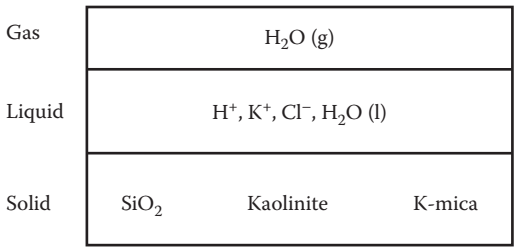

FIGURE 3.33
Sillén ion exchange model.

(see Figure 3.34). The value of τ_R = 1000 revolutions per million years is the stirring revolution of the ocean, which is assumed to be 2000 million years old and in a steady state.

Turner et al. (1981) also showed that the values of the partition coefficients K_Y were related to the electronegativity of the elements Q_{YO} by

$$\log K_Y = -1.55\, Q_{YO} + 3.69 \tag{3.15}$$

where the electronegativity is given in electron volts (eV).

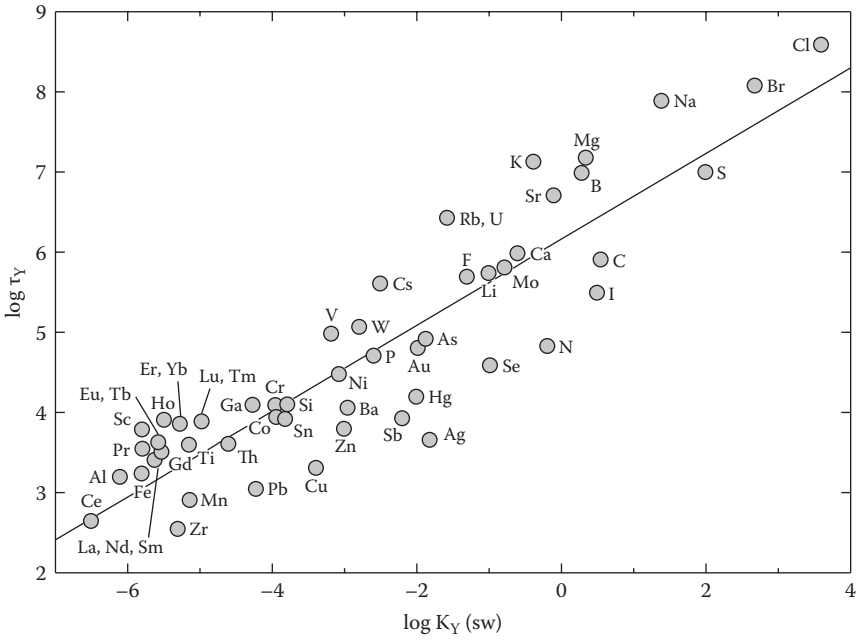

FIGURE 3.34
The log of the mean residence time τ versus the log of the partition.

$$Q_{YO} = (X_Y - Y_O)^2 \tag{3.16}$$

where the value of Q_{YO} is a measure of the electrostatic contribution to the Y-O bond energy or a measure of the attraction of an element (Y) for the oxide-based mineral. The values for X are values of the electronegativity of various elements.

Meybeck (1987) has examined chemical weathering by considering the ions formed from various rock types. The abundance of the major rock types is given in Table 3.13. His estimates for the origins of the major components of the rock types released to the rivers are given in Table 3.14. Ca and Mg come mostly from shale and carbonate rocks, Na and Cl from rock salt, SO_4 from shale and gypsum, HCO_3 from shale and carbonate, and K from sandstone and carbonate rocks. The sources of the dissolved river salts carried to the oceans by the weathering of the various rock types are given in Table 3.15. These results point out the importance of the weathering process in controlling the input of the major components to the oceans.

TABLE 3.13

Outcrop Abundance of Major Rock Types on Land (percentage by area)

Plutonic rocks	11%	Granite	10.40%
		Gabbro and peridotite	0.60%
Metamorphic rocks	15%	Gneiss	10.40%
		Mica schist	1.50%
		Quartzite	0.80%
		Marble	0.40%
		Amphibolite	1.90%
Volcanic rocks	7.9%	Basalt	4.15%
		Andesite	3.00%
		Rhyolite	0.75%
Sandstones	15.8%	Quartz sandstone	12.60%
		Arkose	0.80%
		Graywacke	2.40%
Shales	33.1%		
Carbonate sedimentary rocks	15.9%	Detrital carbonate rock	5.90%
		Dolomite	3.65%
		Limestone	6.35%
Evaporites	1.3%	Gypsum	0.75%
		Halite	0.55%

TABLE 3.14

Origins of Weathering Products by Rock Types (percentage of total amount released)

	SiO_2	Ca^{2+}	Mg^{2+}	Na^+	K^+	Cl^-	SO_4^{2-}	HCO_{3-}	Σ+
Granite	10.9	0.60	1.2	5.9	4.9		2.0	1.6	1.6
Gabbro	0.75	0.0	1.1	0	0		0.3	0.3	0.3
Gneiss and micaschists	11.7	1.10	2.8	6.6	8.2		4.6	2.0	2.4
Miscellaneous metamorphic	1.5	4.7	3.2	0.3	1.6		1.7	4.7	3.7
Volcanic rocks	11.1	1.8	4.9	5.4	6.6		0.5	4.2	3.1
Sandstone	16.6	2.1	3.8	5.2	19.6		9.6	2.3	3.2
Shale	35.1	19.9	30.7	22.6	41.0	7.4	30.3	22.5	23.1
Carbonate rocks	11.3	60.4	39.3	3.5	13.1		8.6	59.5	46.7
Gypsum	0.5	7.2	7.2	4.9	1.6	10.0	32.7	1.7	6.8
Rock salt	0.4	2.2	5.8	45.6	3.3	82.6	9.6	1.2	9.1
TOTAL%	100	100	100	100	100	100	100	100	100
10^{12} g/yr	320	504	118	132	24	120	280	1950	

Note: Σ+ = sum of cations (milliequivalent/liter).

TABLE 3.15

Sources of River Dissolved Load Carried to the Oceans (in percentage of total amount released by weathering)

							SO_4^{2-}			
Model	**SiO_2**	**Ca^{2+}**	**Mg^{2+}**	**Na^+**	**K^+**	**Cl^-**	**Pyr.[a]**	**SO_4[b]**	**HCO^{3-}**	**Σ+**
Atmosphere									67	
Silicates	92.5	26	48	46	95	0	40	18		35
Carbonates	0	67	42	0	0	0	0	0	33	51
Evaporites	0	7	10	54	5	100	0	42		14
Amorphous silica	7.5									

Note: Σ+, sum of cations.

[a] SO_4^{2-} resulting from pyrite and organic sulfur oxidation.

[b] SO_4^{2-} resulting from sulfate mineral dissolution.

References and Further Reading

Barth, T.W., *Theoretical Petrology*, Wiley, New York (1952).

Biller, D.V., and Bruland, K.W., Analysis of Mn, Fe, Co, Ni, Su, Zn, Cd and Pb in seawater using the Nobias-chelate PA1 resin and magnetic sector inductively coupled plasma mass spectrometer (ICP_MS), *Mar. Chem.*, 130, 12-20 (2012).

Bowen, H.H.M., *Trace Elements in Biochemistry*, Academic Press, London (1966).

Boyle, E.A., Cadmium and δ13C paleochemical ocean distributes during stage 2 glacial maximum, *Annu. Rev. Earth Planet Sci.*, 20, 245 (1992).

Brewer, P., Minor elements in sea water, Chapter 7, *Chemical Oceanography*, Vol. 1, 2nd ed., Riley, J.P., and Skirrow, G., Eds., Academic Press, New York, 416–496 (1975).

Bruland, K.W., Trace elements in sea–water, Chapter 45, *Chemical Oceanography*, Vol. 8, 2nd ed., Riley, J.P., and Chester, R., Eds., Academic Press, New York, 157–220 (1983).

De Baar, H.J.W., Saager, P.M., Nolting, R.F., and Van der Meer, J., Cadmium versus phosphate in the world ocean, *Mar. Chem.*, 46, 261 (1994).

Fisher, N.S., On the reactivity of metals for marine phytoplankton, *Limnol. Oceanogr.*, 31, 443 (1986).

Garrels, R.M., and Christ, C.L., *Solutions, Mineral and Equilibria*, Harper and Row, New York (1965).

Garrels, R.M., and Mackenzie, F.T., *Evolution of Sedimentary Rocks*. W. W. Norton & Co., New York, 539 (1971).

Goldberg, E., Minor elements in sea water, Chapter 5, *Chemical Oceanography*, Vol. 1, Riley, J.P., and Skirrow, G., Eds., Academic Press, New York, 163–196 (1965).

Goldsmith, V.M., *Fortsch. Mineral. Krist. Petrogr.*, 17, 112 (1967).

Horne, R., *Marine Chemistry*, Wiley-Interscience, New York, 568 (1969).

Löscher, B.M., van der Meer, J., de Baar, H.J.W., Saager, P.M., and de Jong, J.T.M., The global Cd/phosphate relationship in deep ocean waters and the need for accuracy, *Mar. Chem.*, 59, 87 (1997).

Mackenzie, F.T., Sedimentary cycling and the evolution of sea water, Chapter 5, *Chemical Oceanography*, Vol. 1, 2nd ed., Riley, J.P., and Skirrow, G., Eds., Academic Press, New York, 309–364 (1975).

Meybeck, M., Global chemical weathering of surficial rocks estimate from river dissolved loads, *Am. J. Sci.*, 287, 401 (1987).

Nicholls, G.D., The geochemical history of the oceans, Chapter 20, *Chemical Oceanography*, Vol. 2, Riley, J.P., and Skirrow, G., Eds., Academic Press, New York, 277–294 (1965).

Schaule, B.K., and Patterson, C.C., Perturbations of the natural lead depth profile in the Sargasso Sea by industrial lead, in *Trace Metals in Sea Water*, NATO Conf. Series, Wong, C.S., et al., Eds., 487–503 (1983).

Sillén, L.G., How have sea water and air got their present compositions? *Chem. Brit.*, 3, 291–297 (1967).

Turner, D.R., Whitfield, M., and Dickson, A.G., The equilibrium speciation of dissolved components in freshwater and seawater at 25°C and 1 atm pressure, *Geochim. Cosmochim. Acta*, 45, 855 (1981).

Whitfield, M., and Turner, D.R., The role of particles in regulating the composition of seawater, Chapter 17, *Aquatic Surface Chemistry*, Stumm, W., Ed., Wiley-Interscience, New York (1987).

Wong, C.S., et al., Eds., *Trace Metals in Sea Water*, Plenum Press, New York (1983).

Wu, J.F., and Boyle, E.A., Lead in western North Atlantic Ocean: complete response to leaded phase out, *Geochim. Cosmochim. Acta*, 61, 3283 (1997).

4

Ionic Interactions

4.1 Introduction

There has been an increasing concern for the geochemical fate of trace metals in the marine environment. Many baseline studies have been made to determine the total concentration of these metals in the solution phase, the gas phase, and the solid phase (i.e., on and in living and nonliving material). Although these studies have been useful in indicating the fate of trace metals in the marine environment, little progress has been made in determining the mechanisms involved (physical, chemical, and biological) in the transfer of metals between phases. Part of the reason for this lack of understanding of trace metals in the marine environment comes from the difficulties in detecting experimentally the true activity (both thermodynamic and biochemical) of the trace metals; because of their low concentrations, conventional electrode methods of determining thermodynamic activity are difficult to apply. Although it is possible to detect the activity of some metals, we are at present forced to use models to estimate the thermodynamic activity of most trace metals to make comparisons with biological studies.

The importance of knowing the true biological activity (rather than total concentration) of metal ions in seawater has been suggested by a number of workers. For example, we have found that the growth depression by copper of the bacterium *Vibrio alginolyticus* was affected by complex formation. This variation in copper toxicity is due to the presence of differing concentrations of free copper because of the formation of complexes with ligands such as fulvic acids.

Synthetic ligands (like NTA [nitriloacetic acid]) and natural organic ligands can have similar effects in the marine environment. Three possible consequences may follow the addition of such a ligand: (a) Metals may become solubilized and transported from regions of high concentration to uncontaminated regions; (b) because of overcomplexation, necessary metals may not be available for the growth of marine organisms; (c) reducing the natural metal toxicity may cause increased numbers of pathogenic organisms to occur.

The important role that free or complexed metal ions plays in productivity has also been pointed out by a number of workers. For example, Barber and Ryther (1969) reported that phytoplankton blooms in newly upwelled waters off the Peru coast are conditioned by the organics in seawater. They suggested that the organic compounds are necessary to make the trace metals available for growth. However, Steeman-Nielson and Wium-Anderson (1970) suggested that the organic conditioning is due to the reduction in copper toxicity (caused by complexation). Although it is not currently possible to state with certainty which of the suggested roles of organic ligands (or both) is true, we can state that it is the form of the metal (not the total amount) that is important in determining its biological and geochemical activity. The determination of the form of a given element is called *speciation*.

We shall now discuss the ionic interactions that can affect the state or structure of metal ions in seawater. Whether the thermodynamic activities can be directly related to biological activities remains to be seen. It must also be kept in mind that the most probable thermodynamic state may not be the state found in the marine environment because of the slow kinetics of the formation and degradation of metal complexes and various redox pairs.

To understand ionic interactions in aqueous electrolyte solutions, various chemical models have been developed. The development of a chemical model for natural waters has been strongly influenced by the coupling of physical chemical solution theory and marine chemical, analytical, and experimental data. The major trends of the development of a chemical model for seawater have resulted from the application of methods developed on the physical chemistry of electrolyte solutions. In the past, it has taken a long time for the physical chemical trends to influence marine chemistry. For example, it took 40 years before the Arrhenius theory was accepted in oceanography and 30 years before the quantitative aspects of the Debye–Hückel (1923) and Bjerrum (1926) theories were applied to seawater by Garrels and Thompson (1962). Although Wirth (1940) introduced the oceanographic community to the theoretically derived concentration behavior for densities in 1940, it has only been recently used to represent the equation of state of seawater.

In recent years, this trend has changed; it is hoped marine chemistry will accept and apply these new theories and models to geochemical and biochemical problems. The application of chemical models to examine ionic interactions in natural waters has been confined to two major areas: (a) those that are concerned with the bulk thermodynamic and transport properties of marine waters and (b) those that are concerned with the effect of marine waters on the activity of dissolved solutes. This is discussed in more detail elsewhere in this chapter. To understand the state and structure of an ion in seawater, one must take a number of steps. We examine the state of an ion in seawater by considering two processes: (a) the ion–water interactions that occur when an ion is transferred from the ideal gas state to an infinitely large reservoir of water (i.e., where ions cannot interact with one another),

$$M^+ \text{ (ideal gas)} \rightarrow M^+ \text{ (infinite dilute solution)} \tag{4.1}$$

and (b) the ion–ion interactions that occur when an ion is transferred from infinite dilution to seawater (where interactions of all of the ions in the mixture affect the state (i.e., plus–plus, plus–minus, and minus–minus interactions):

$$M^+ \text{ (infinite dilute solution)} \rightarrow M^+ \text{ (seawater)} \tag{4.2}$$

Before these two processes are discussed, we examine the unique properties of water as a solvent system.

4.2 Water, the Unique Solvent

Although water makes up 96.5% of ocean waters and accounts for many of the unique physical and chemical properties of seawater, its importance has been neglected by many oceanographers. Horne (1972) attempted to stress the importance of understanding the

nature of water and its interactions in natural waters. As chemical oceanography becomes a less-descriptive science and moves to one that attempts to probe the chemical processes occurring in the oceans, this approach will become more popular. One must keep in mind that the ultimate aim of a marine chemist is to obtain a molecular-level understanding of the chemical processes that occur in the marine environment. To do this, one eventually must understand the role water plays in these molecular interactions. With this in mind, we discuss some of the unique properties of water and its structure in this section.

The unique position of water compared to other similar compounds in nature can be of great importance in various meteorological, oceanographic, geochemical, and biochemical processes. This uniqueness can be demonstrated by comparing its physical and chemical properties to other liquids. Let us first examine the boiling point of water (the temperature at which the vapor pressure is equal to the atmospheric pressure) compared to other liquids of similar structure (Figure 4.1). It is obvious from this figure that water appears to have a much higher boiling point than expected. It should be kept in mind that the boiling point T_b of a given series usually increases with increasing molecular weight. This higher boiling point indicates that it takes more energy than expected to get the water molecule into the gas state. The melting point T_m for water is also higher than expected. This indicates that it takes more energy to melt ice than expected.

It is also possible to show the uniqueness of water by comparing its other physical and chemical properties with other liquids. This is done in Table 4.1. The high dielectric constant of water (80) is the result of the high dipole moment. This also results in a high dissociation ($K = 1 \times 10^{-14}$) of $H_2O \rightarrow H^+ + OH^-$. The great dissolving properties of H_2O are

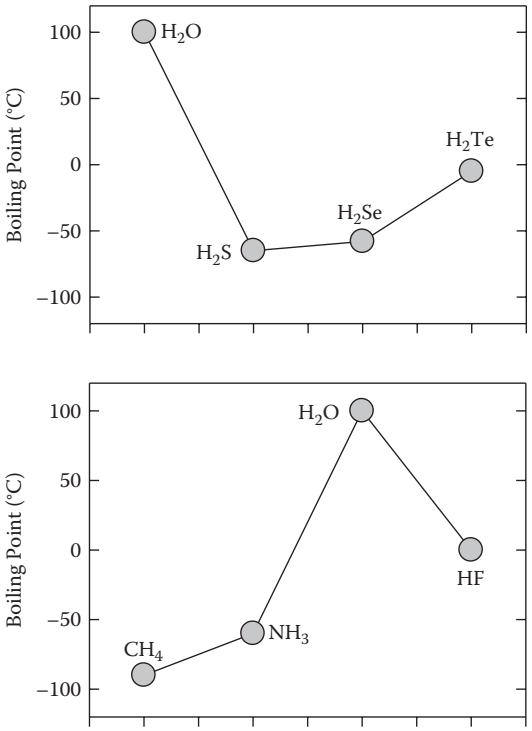

FIGURE 4.1
Boiling points of compounds similar to water.

TABLE 4.1

Comparison of Physical Properties of H_2O, MeOH, and n-Heptane

Property	H_2O	MeOH	n-Heptane
MW	18	32	100
Dipole moment (Debye's)	1.84	1.70	>0.2
Dielectric constant	80	24	1.97
Density (gm cm^{-3})	1.0	0.79	0.73
Boiling point (°C)	100	65	98.4
Melting point (°C)	0	–98	–97
Specific heat (cal g^{-1} deg^{-1})	1.0	0.56	0.5
ΔH_{vap} (cal g^{-1})	540	263	76
ΔH_{fus} (cal g^{-1})	79	22	34
Surface tension (dynes cm^{-1})	73	23	25
Viscosity at 20°C (poise)	0.01	0.006	0.005
Compressibility at 25°C (atm^{-1})	4.57×10^{-11}	12.2×10^{-11}	14×10^{-11}

also due to its high dielectric constant. Only a few inorganic components have higher dielectric constants: D (NH_3) = 23, D (HF) = 85, D (HCN) = 95, D (SO_2) = 140. The hydrating properties of water are well known; however, the causes are not clearly known.

The unique bond angle and ability to form hydrogen bonds results in long-range order in water (and ice) that is unique compared to most other liquids. Each water molecule has the opportunity to combine with up to four other water molecules through hydrogen bonds (see Figure 4.2). All of these unique properties of water can be traced to the structure of the individual water molecules and how they interact with one another. One might expect the atoms in water to be at a bond angle of 180°, but they actually form a bond angle of 105°. As a result of the intermolecular forces in the water molecule not being completely balanced (105° bond angle), the water molecule has an electric dipole. The separation of the negative charge on the unpaired electrons and the positive charge on the protons results in a dipole moment of 1.84D (D = Debye; 1 D is equivalent to the separation of two point charges of opposite sign at a distance of 1 Å, 10^{-8} cm). This is shown in Figure 4.3. Since there are actually two points of negative and two points of positive charge separation on a water molecule, one has a quadrupole moment. This is shown in Figure 4.4. This quadrupole moment results from dipole–dipole interactions, which are the electrical analogy to moments of inertia.

The dipole–dipole interaction of two water molecules causes hydrogen bonding in water. A given water molecule has the ability to form four hydrogen bonds (see Figure 4.5). The energies involved in hydrogen bonding are in general much larger than most dipole–dipole interactions; thus, they should be classified separately. The ΔH for the formation of a hydrogen bond is small (~1 to 10 kcal mol^{-1}) compared to most compounds that form chemical bonds of 100 kcal mol^{-1}. The hydrogen bond is not completely electrostatic in nature. It has some covalent character because of the sharing of the unpaired electrons on the oxygen of one water molecule with protons of another. This hydrogen bonding in water causes many of its physical and chemical properties to be different. The effects of temperature and pressure on many of the properties of water are unique compared to other liquids. The effects of temperature (Figure 4.6) on the specific volume, sound speed, compressibility, and specific heat all show a maximum or minimum at a given

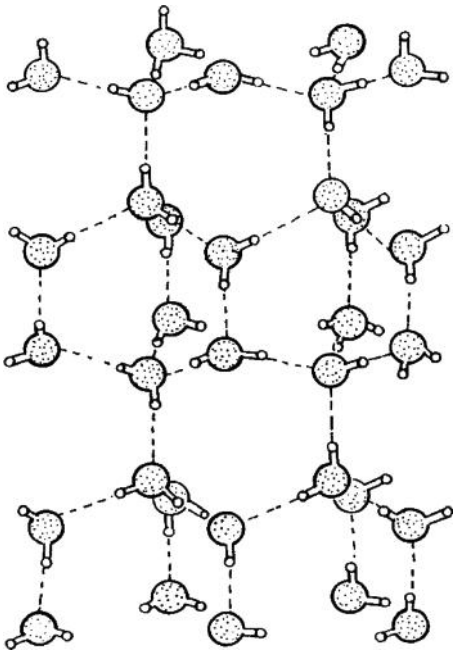

FIGURE 4.2
The structure of ice I.

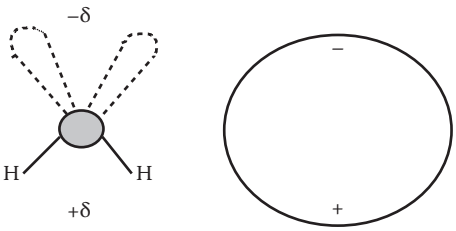

FIGURE 4.3
The water dipole.

temperature. Although the inflections do not occur at the same temperature, they appear to be due to changes in the structure of the liquid. For example, the specific volumes indicate that from 0 to 4°C some ice-like structure may be broken down, and at temperatures above 4°C, the volume increases with increasing temperature, like other fluids. The effect of pressure on the viscosity of water (Figure 4.7) also appears to be unique at temperatures below 30°C. One would expect that the application of pressure to a fluid would increase with an increase in pressure. Water below 30°C shows a decrease as the pressure is first applied. This may be due to the pressure initially breaking down some open structure of water at the lower temperatures. These so-called anomalies of water can have an effect on the properties of natural waters (Table 4.2). For example, the high heat capacity of water prevents extreme ranges in the temperature in coastal regions.

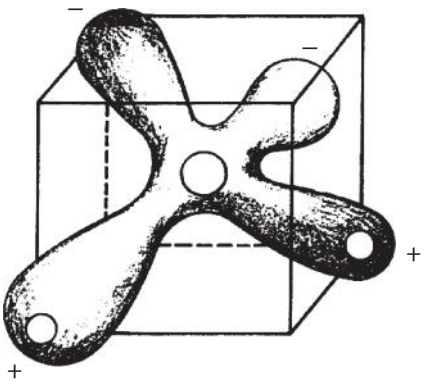

FIGURE 4.4
The three-dimensional structure of the water molecule.

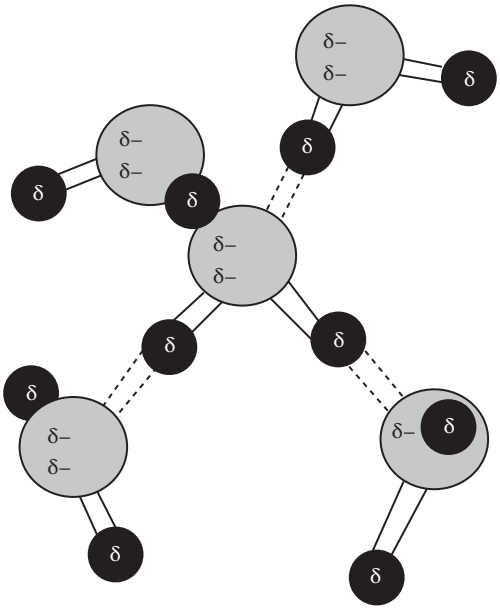

FIGURE 4.5
The hydrogen-bonded structure of water molecules.

4.3 Review of the Structure of Water

The theories of water structure are now briefly reviewed. Several reviews and monographs have appeared summarizing the status of research on the structure of water. An excellent survey was given in the books edited by Franks (1972). We can divide the water structure models into two major categories: the uniformist, or average, models and the mixture models. Both models recognize that water is a very structured liquid; the major difference between the two models is that in the mixture models the simultaneous existence of at least two different states of water is thought to be present.

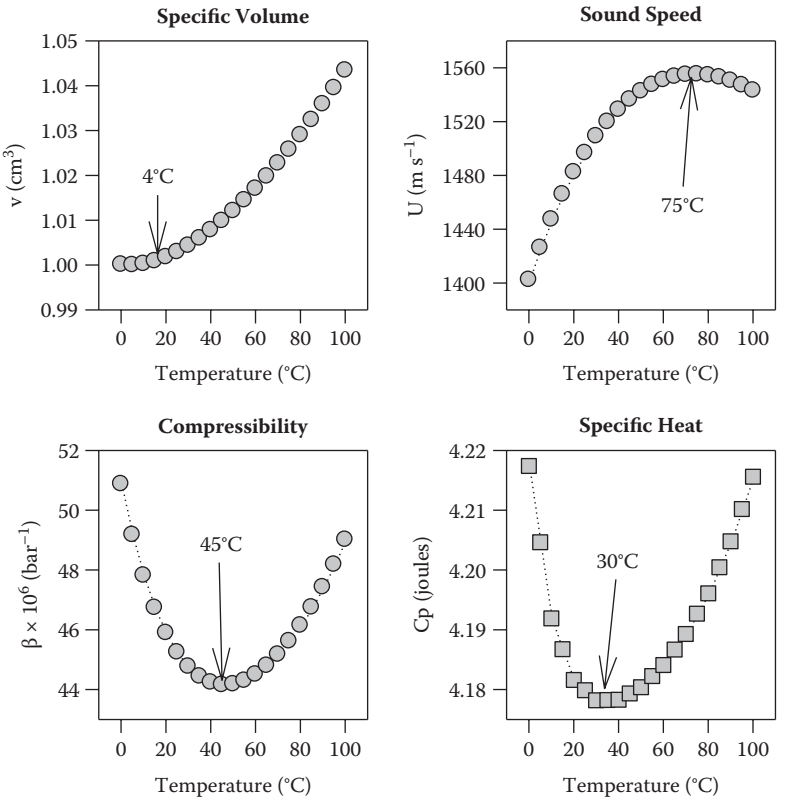

FIGURE 4.6
The effects of temperature on the specific volume (1/density), sound speed, compressibility, and heat capacity for water.

4.3.1 Uniformist (Average) Models

Bernal and Fowler (1933), Pople (1951), Wall and Horning (1965), and Falk and Kell (1966) were proponents of the uniformist model. The basic element of the uniformist view is that no local domains exist in water with a different structure from that of any other arbitrarily chosen element of water. In the process of averaging, the individual water molecule behaves at any time much like any other water molecule is behaving. Bernal and Fowler's (1933) original model has been used and has worked well in many applications. Pople's (1951) treatment gave a far greater qualitative insight into the structure of water. Pople explained the maximum density of liquid water as resulting from two opposing effects—increase in volume caused by expansion of the lattice structure and a bending of the H bonds. Thus, this model treats liquid water as an "ice-like" lattice with differences caused by the bending of bonds, not the breaking of bonds.

4.3.2 Mixture Models

The mixture models have received more notice over the years. We can divide the mixture models into the following categories:

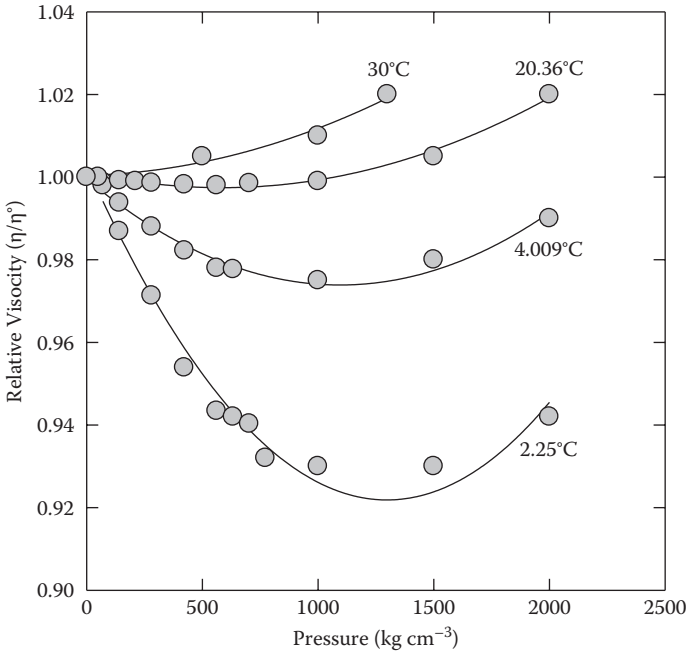

FIGURE 4.7
The effect of pressure on the viscosity of water at various temperatures.

1. **Broken-down ice lattice models:** ice-like units in equilibrium with monomers
2. **Cluster models:** H-bonded clusters in equilibrium with monomers
3. **Clathrate models:** clathrate-like cages in equilibrium with monomers
4. **Significant structure model** or **Eucken's polymer model:** bulky species that are not necessarily a monomer

In each case, at least two different species of water exist—a bulky species representing some type of structured units and a dense species such as a monomer. A sketch of a popular mixture model called the flickering cluster model is shown in Figure 4.8. Water monomers are thought to be in a dynamic equilibrium with large clusters of hydrogen-bonded waters.

4.3.2.1 Ice-Like Models

Rowland (1880) was the first to suggest equilibrium between ice I and monomer. Samoilov (1965) proposed a model in which the monomeric H_2O molecules are "tucked away" in the interstitial spaces of an ice-like lattice (Figure 4.9). Since ice has 13 known crystal phases (Ball, 1999) and a number of amorphous forms (Guthrie et al., 2003), some workers have assumed that the structured form is ice-like. Tammann (1895), for example, suggested that there should be as many types of structures in liquid water as there are types of ice (e.g., ice I, II, etc.; Figure 4.10). The very careful x-ray diffraction study of Danford and Levy (1962) was found to be in good agreement with a broken-down ice structure model. They suggested that the monomeric water molecules occupy positions in the interstices of the ice. (This is similar to the Samoilov model.) Although the model has been used to successfully

TABLE 4.2

Summary of Anomalous Properties of H_2O

Property	Results
1. High heat capacity	Prevents extreme ranges of temperature
	Heat transfer by water movement is large
	Maintains uniform body temperatures
2. High heat of fusion	Thermostatic effect of freezing and melting
3. High heat of evaporation	Important in transfer from heat to water to atmosphere
4. Thermal expansion	Fresh H_2O and dilute seawater have maximum density above T_m (the melting point)
	Controls the temperature density distribution and vertical circulation in lakes
5. High surface tension	Important in cell physiology
	Controls certain surface behavior and drop formation
6. High dielectric constant	Important in causing salts to ionize and become electrolytes (dissolving power)
7. Little electrolyte dissociation	H^+ and OH^- behavior very important in many geological and biological processes
8. High transparency	Adsorbs radiant energy in the infrared and ultraviolet; little is visible; important to physical and biological process
9. High conduction of heat	Important only on small scale as in living cells; eddy conductance is greater
10. Cp and β changes with temperature are different from other fluids	Unique behavior of thermoproperties of solutes in solution
11. High viscosity	Important to physical behavior (waves, etc.) and cell movement
12. Density of solid ice is less than density of liquid at melting point	Important for many geochemical, atmospheric, and biological processes

reproduce the x-ray data, many adjustable parameters were used; thus, there has been criticism of this model. Davis and Litovitz (1965) suggested a model involving puckered hexagonal rings similar to the ice rings formed in the basal plane of ice. Density variations are accounted for by assuming two rings exist: an open-packed, ice-like ring and a closed-packed ring structure.

4.3.2.2 Cluster Theories

Stewart (1931) was the first to suggest the existence of clusters based on his x-ray work. The clusters contained 10,000 water molecules. Nemethy and Scheraga (1962) built on the Frank and Wen (1957) concept of flickering clusters using statistical thermodynamics. They have used this model to calculate the thermodynamic properties of H_2O. The authors considered unbonded water molecules and water molecules with 1, 2, 3, and 4 H bonds per molecule. The average cluster varies from 91 to 25 molecules from 0 to 70°C. At 25°C, the cluster size is about 50 molecules. Monomeric molecules range from fractions of 0.24 to 0.29 from 0 to 70°C (i.e., 24% of the bonds are broken at 0°C on melting). Others have made similar calculations by assigning energy bands instead of levels for different states of the H bonding. Only three species are considered: free H_2O, one OH group bonded, and two OH groups bonded molecules. They have been able to calculate the thermodynamic properties with great accuracy using these models and formulated models using clusters of H_2O molecules of 100 to 700 molecules.

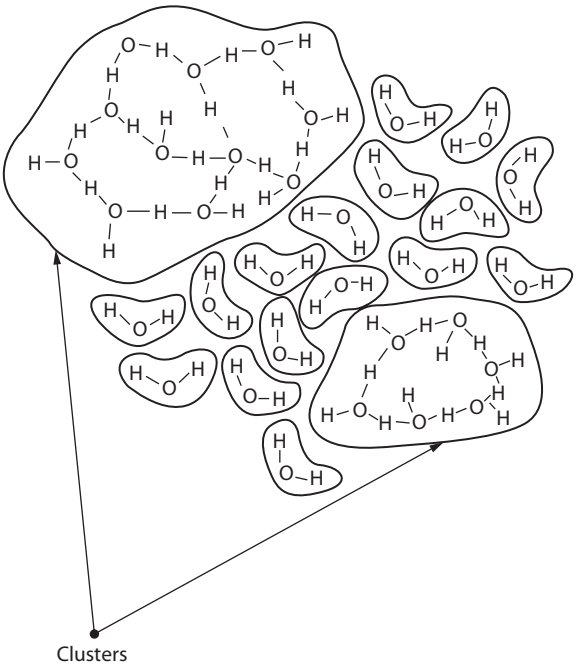

FIGURE 4.8
The Frank and Wen flickering cluster model for the structure of water.

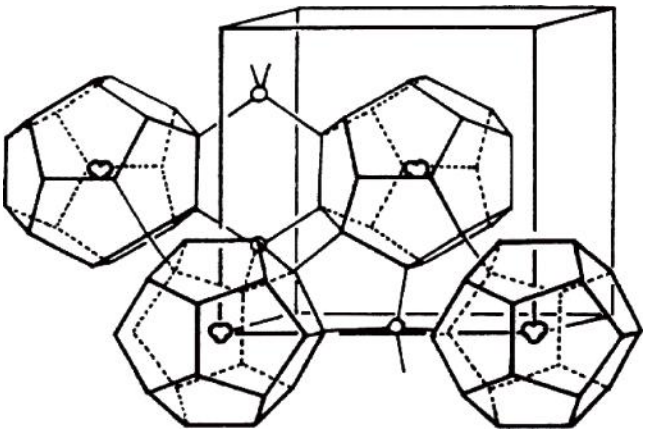

FIGURE 4.9
The Pauling self-clathrate model for the structure of water.

4.3.2.3 Clathrate Cage Models

Pauling (1960) originally postulated the clathrate cage model. He noted the existence of clathrate hydrates of many inert gases and suggested that water is its own clathrate hydrate. Frank and Quist (1961) developed this model and successfully calculated thermodynamic properties of water in good agreement with experimental values. In the clathrate model, discrete sites exist in the host lattice (for other H_2O molecules or solute molecules).

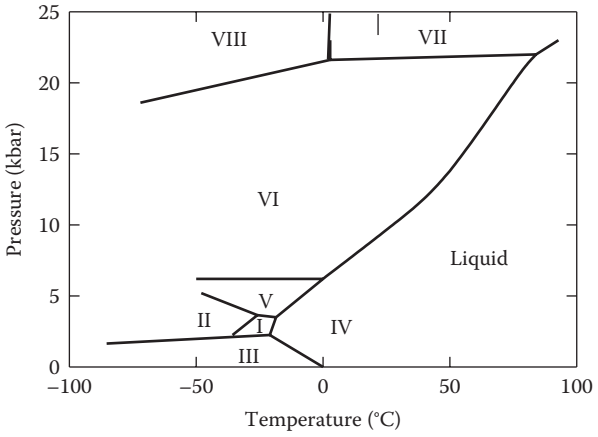

FIGURE 4.10
Phase diagram for the various forms of ice.

4.3.2.4 Significant Structure Theory and Eucken's Polymer Model

The bulky species is ice-like (not necessarily like ice I). The dense species is not necessarily a monomer but may be another ice-like species of higher density. Eyring, Ree, and Hirai (1958) used significant structure theory—a specific element exists with fluidized vacancies in addition to the individual monomers. Others have extended this treatment by recognizing that the amount of free monomeric water is small. Thus, the significant structures are cage-like clusters with 16 molecules (density of ice I) within equilibrium in an ice III–like structure. Fluidized vacancies are produced during melting (contraction occurs from the packing of single H_2O molecules into voids of ice I–like clusters). This model has been used to successfully predict the minimum at 4°C in density, the vapor pressure, and the specific heat (combined with Eyring's rate theory, this model has been used to calculate the pressure dependence of relative viscosity of H_2O).

Eucken (1949) treated water as a mixture of distinctly associated species of dimers, tetramers, and octamers. Although this method is probably not correct, Wicke (1966) has suggested that dimers may exist near the critical point. Eucken's theory is interesting in that it is able to estimate thermodynamic properties that agree with the experimental results; however, the model is not correct. It is thus important to note that the fact that a model is able to calculate accurate properties of water does not prove the model is correct. A more critical test of a water theory is its ability to predict correctly, even if only quantitatively, a large variety of widely different properties of water. One of the major difficulties of the mixture models that assume the dense species is monomeric water is in explaining how mere van der Waals forces can provide enough attraction for the single water molecule to avoid escaping into the vapor state. The water molecules in a clathrate cage must also possess some unique properties. It is difficult to see how H_2O molecules with their large dipole moment can exist in a clathrate cage with strong interactions. Experimental studies have not proved that H_2O molecules reside in clathrate cages.

It is important to understand that when we think of the structure of a liquid, it is necessary to consider the timescale used to measure that structure. Depending on the experimental techniques used (see Figure 4.11), one will take a picture that is related to the shutter speed of the camera. Thermodynamic measurements see an average structure.

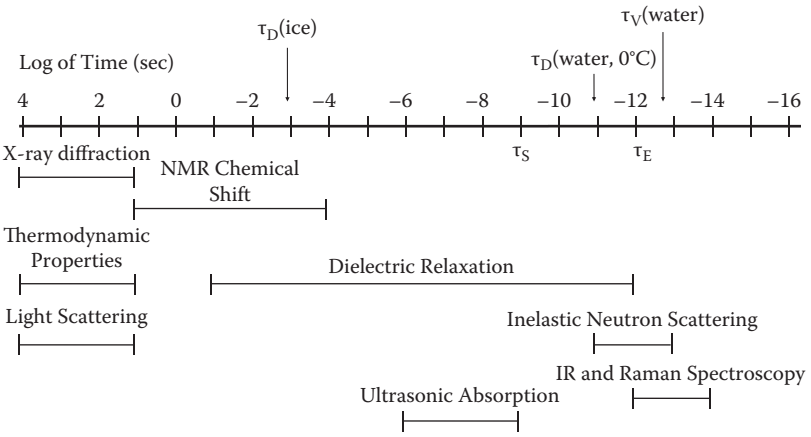

FIGURE 4.11
Comparison of the times of water movements to the times required to make various measurements.

The time molecules move (i.e., the time for molecular displacements) is 10^{-5} s in ice and 10^{-11} s in the liquid. Recent studies have been made by using techniques that can examine the structure of liquids at very fast rates. These studies are briefly reviewed next.

The structure of water just outlined and discussed more recently (Ohmine and Tanaka, 1993) has received some major interest. The debate on the unique structure of water continues (Soper, 2000; Pratt, 2002). These new studies have used ultrafast probes to study the structure of water. Ruan et al. (2004) studied thin ice films using laser pulses and measured the structural change by electron diffraction. Their results show a transient structure of water on hydrophobic surfaces. The water molecules at the surface appear to be more gas-like than in a three-dimensional network. The work of Wernet et al. (2004) indicates that water molecules have only two hydrogen bonds (one a donor and the other an acceptor hydrogen bond). These results do not agree with the earlier accepted view that each water molecule is involved in three or four hydrogen bonds. They believed that water molecules in the liquid resemble water on the surface of ice, and that 80% of the water molecules have only two strong hydrogen bonds on the subfemtosecond (10^{-15}-s) timescale. These stronger hydrogen bonds are surrounded by a cluster of weak hydrogen bonds. The static picture based on x-ray absorption and neutron diffraction integrates the structure of time, giving an average picture of the three-dimensional structure in the liquid.

These snapshot pictures of liquid water are not consistent with the structure that comes from some earlier molecular dynamics simulations. More recent molecular dynamics studies by Kuo and Mundy (2004) of the liquid–vapor interface were able to reproduce and quantify the structure of water on interfaces. Their work supports some measurements (Du et al., 1993; Raymond et al., 2003) that provide proof that water at interfaces has dangling OH bonds, which they called "acceptor-only" hydrogen bonds. These acceptor-only waters are 19% while the "single-donor" waters are 66% of the waters at the interface.

These studies have changed our ideas of the structure at interfaces. For example, the hydration of halides (F, Cl, Br, I) is partitioned at the interface. The order of the ions from the interface is I, Br, Cl, F. The most hydrated species is in the bulk water, while I is close to the interface. This may be important for the behavior of halides at the interface of aerosols.

4.4 Ion–Water Interactions

To understand the behavior of ions in seawater, it is important to be able to understand the interactions of ions with water molecules. To study these ion–water interactions, one must study the thermodynamic and transport properties of electrolytes at infinite dilution. In practice, it is not possible to make direct measurements at infinite dilution; thus, the infinite dilution thermodynamic properties are extrapolated from experimental results at finite low concentrations (with the aid of the Debye–Hückel equations for long-range ion–ion interactions). Since one normally studies the ion–water interactions in solution where no ion–ion interactions occur, it is necessary to select an initial state devoid of ion–ion interactions. The initial state normally selected is that of ions in a vacuum at an infinitely low pressure (i.e., the ideal gas). One considers then the changes in properties such as free energy ΔG_h^o, enthalpy ΔH_h^o, and entropy ΔS_h^o for the process denoted by Equation 4.1 (called, respectively, the hydration free energies, enthalpies, and entropies). The methods used to calculate these thermodynamic hydration functions are discussed elsewhere (Robinson and Stokes, 1959). The methods used to calculate the ΔH_h^o are shown in Figure 4.12. The thermodynamic cycles (Born–Haber) shown in this figure demonstrate that the energy involved in holding a crystal together (the crystal lattice energy) is related to the heats involved in the ionization, sublimation, dissociation, and formation of the compound. All can be determined experimentally, as can the heat of solution of a given crystal.

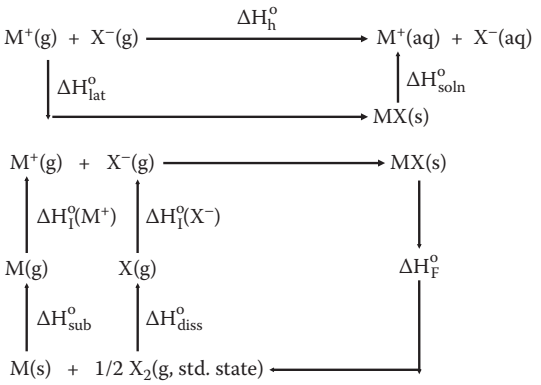

$$\Delta H_h^o = \Delta H_{Lat}^o + \Delta H_{soln}^o$$
$$= -\Delta H_F^o + \Delta H_{diss}^o + \Delta H_{sub}^o + \Delta H_I^o(M^+) + \Delta H_I^o(X^-) + \Delta H_{soln}^o$$

ΔH_h^o = Heat of hydration
ΔH_I^o = Heat of gas phase ionization
ΔH_{sub}^o = Heat of sublimation
ΔH_{diss}^o = Heat of dissociation
ΔH_F^o = Heat of formation
ΔH_{lat}^o = Heat of crystal lattice formation
ΔH_{soln}^o = Heat of solution

FIGURE 4.12
The methods used to calculate the enthalpies of hydration for an electrolyte.

Since we are interested in the transfer of ions (M^+) rather than electrolytes (MX), it is necessary to make some nonthermodynamic assumptions concerning the differences between the properties of cations and anions. The details of such methods are discussed elsewhere (Millero, 1977). Once the selection is made for the absolute thermodynamic quantity of one ion (usually the proton), the values for the other ions can be easily determined by the additivity principle:

$$\Delta H_h^o(MX) = \Delta H_h^o(M^+) + \Delta H_h^o(X^-) \tag{4.3}$$

Values of ΔG_h^o, ΔH_h^o, and ΔS_h^o for some metal ions are given in Table 4.3. To truly understand ion–water interactions, one must know something about the structure of water. Since the structure of water is very complex, one must use simple models for the interaction between ions and water molecules. These models serve as mental pictures and reproduce approximately what occurs in the real system. The better they are able to predict the

TABLE 4.3

Thermodynamics of Hydration of Ions at 25°C

Ion	r (Å)	$-\Delta G_h^0$ (kcal mol^{-1})	$-\Delta H_h^0$ (kcal mol^{-1})	$-\Delta S_h^0$ (kcal mol^{-1}deg^{-1})
H^+	—	260.5	269.8	31.3
Li^+	0.60	122.1	132.1	33.7
Na^+	0.95	98.2	106.0	26.2
Ag^+	1.26	114.5	122.7	27.6
K^+	1.33	80.6	85.8	17.7
Tl^+	1.40	82.0	87.0	16.7
Rb^+	1.48	75.5	79.8	14.8
NH_{4+}	1.60	—	84.8	—
Cs^+	1.69	67.8	72.0	14.1
Cu^+	0.96	136.2	151.1	50.0
Be^{2+}	0.31	—	594.6	—
Mg^{2+}	0.65	455.5	477.6	74.3
Ni^{2+}	0.72	494.2	518.8	82.4
Co^{2+}	0.74	479.5	503.3	80.0
Zn^{2+}	0.74	484.6	506.8	74.5
Fe^{2+}	0.76	456.4	480.2	79.8
Mn^{2+}	0.80	437.8	459.2	72.1
Cu^{2+}	0.96	498.7	519.7	73.9
Cd^{2+}	0.97	430.5	449.8	65.2
Ca^{2+}	0.99	380.8	398.8	60.8
Hg^{2+}	1.10	436.3	—	—
Sr^{2+}	1.13	345.9	363.5	59.2
Pb^{2+}	1.20	357.8	371.9	47.4
Ba^{2+}	1.35	315.1	329.5	48.5
Al^{3+}	0.50	1103.3	1141.0	126.6
Fe^{3+}	0.64	1035.5	1073.4	127.5
Cr^{3+}	0.69	—	1079.4	—
Y^{3+}	0.93	859.5	891.5	107.6
Sc^{3+}	0.81	929.3	962.7	112.5
La^{3+}	1.15	—	811.9	—

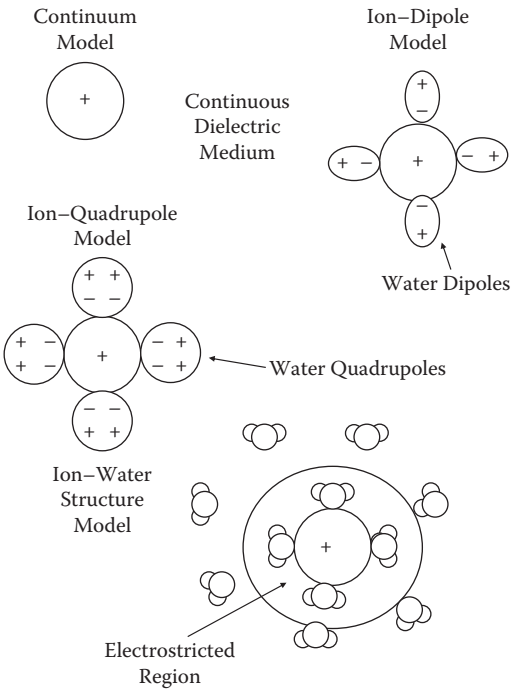

FIGURE 4.13
Models used to explain ion–water interactions.

experimental properties of the real system, the better they serve as aids to understanding the real system. Before we discuss these models (see Figure 4.13), we first examine what happens when a salt is added to water.

The addition of salt to water complicates the structure and properties of water to a large degree. We start by considering the effect of adding sufficient NaCl to water to make synthetic seawater of 3.5% NaCl by weight. The addition of 35 g of NaCl to 965 g of H_2O gives the following molality:

$$m = (35/965)(1000/58.48) = 0.62 \tag{4.4}$$

What happens when the solution is formed?

$$NaCl\ (c) \rightarrow Na^+(aq) + Cl^-(aq) \tag{4.5}$$

1. About 0.6 kcal of heat is absorbed (an endothermic reaction). This absorption of heat indicates that the solution process involves the making and breaking of chemical bonds. Since the heat involved in forming the NaCl(s) from the gaseous ions ($M^+ + X^-$) is quite large,

$$Na^+(g) + Cl^-(g) \rightarrow NaCl\ (crystal) \tag{4.6}$$

$$\Delta H^o = 181\ kcal\ mol^{-1}$$

The heat involved in hydrating the ions Na^+ and Cl^- is also quite large:

$$Na^+(g) + Cl^-(g) \rightarrow Na^+(aq) + Cl^-(aq) \tag{4.7}$$

This can be clearly demonstrated by examining the Born–Haber cycle for the hydration of NaCl (ΔH_h is the heat of hydration of the ions). This heat of hydration for the salt (MX) is given by

$$M^+(g) + X^-(g) \rightarrow M^+(aq) + X^-(aq) \tag{4.8}$$

It is related to the heats of the reactions of the formation of MX in the solid state:

$$M^+(g) + X^-(g) \rightarrow MX(s) \tag{4.9}$$

which is called the lattice heat and the heat of solution of the salt.

$$MX(g) \rightarrow M^+(aq) + X^-(aq) \tag{4.10}$$

$$\Delta H_h = \Delta H_{LATTICE} + \Delta H_{SOLN} \tag{4.11}$$

For NaCl,

$$\Delta H_h = 181 + 0.6 = 182 \text{ kcal mol}^{-1} \tag{4.12}$$

The fact that ΔH_h is the same order of magnitude as $\Delta H_{LATTICE}$ indicates that the energies involved in solvating the ions are the same order of magnitude as those forming ionic bonds in a crystal.

2. The solution formed after the addition of NaCl no longer freezes at 0°C, but does at approximately 2.3°C. The freezing point depression is given approximately by

$$\Delta T_f = 1.86\nu m \tag{4.13}$$

where ν is the number of ions formed when the salt completely dissociates. This equation gives $\Delta T_f = 2.3$°C, $T_f = -2.3$°C. This indicates that the interaction of Na^+ and Cl^- with water breaks down the structure of water.

3. The solution also boils at a higher temperature. The boiling point elevation is given by

$$\Delta T_h = 0.52\nu m \tag{4.14}$$

This equation gives $\Delta T_h = 0.63$ or $T_b = 100.63$°C. This indicates that the hydration interactions tend to keep the water molecules in the liquid state.

4. The vapor pressure of the NaCl solution is lower than for pure water. The ratio of the vapor pressure over the solution $P/P_{H2O} = 0.98$. The 2% depression in vapor pressure also indicates that the hydration "ties up" the water molecules, making it harder for them to go into the gaseous state.

5. The electrical conductance of the solution is increased by 10,000 (10^{-6} ohm^{-1} cm^{-1} to 4.68×10^{-2} Ω^{-1} cm^{-1}). This indicates that the ions are able to carry a charge through solution.
6. The temperature of the maximum density is lowered by 8°C to –4°C. This (like seawater) is below the freezing point. These results indicate that the hydration process breaks down the water structure.
7. The osmotic pressure (~26 atm) is created. This pressure is related to the vapor pressure, freezing point, and boiling point effects (it is a colligative property). It can be determined from

$$\pi = -(RT/V_{H_2O})\ln a_{H_2O} \tag{4.15}$$

where a_{H_2O} is the activity of water in the solution (P/P_{H_2O}), and V_{H_2O} is the molar volume of water in the solution (V_{H_2O} = MW/ρ). This osmotic pressure can act as a driving force for the diffusion of water through membranes. The H_2O molecules interact very strongly with ions. Many electrolytes hold onto their water molecules with such tenacity that the solids crystallize with a definite number of water molecules.

An understanding of ion–water interactions and ion–ion interactions is thus a prerequisite for making any progress in understanding the chemistry of seawater. One might ask the question, how many H_2O molecules are hydrated to the Na^+ or Cl^- ions? Estimates range from 2 to 70 depending on how the measurements were made. This large variety of numbers is due to the hydration volume around an ion not having a definite boundary. Thus, some methods count the H_2O molecules that are not firmly bound by the ion. Another question one might ask is, how many of the hydrated water molecules move when the ion moves? To answer this question, we must know the exact time that an H_2O molecule remains on an ion. This is normally not long, and it is probably not realistic to try to distinguish between the stationary and the kinetic hydration atmosphere of an ion.

For most of the ions of importance in seawater chemistry, the major factor determining the extent or strength of hydration is the charge density (the Z/r ratio). A higher charge density of an ion will lead to greater hydration.

4.4.1 Electrostriction

Another unexpected phenomenon on the formation of an NaCl solution is electrostriction. For example, the density of solid NaCl is 2.165 g cm^{-1}. The volume of 35 g of NaCl would thus occupy 16.2 cm^3 mol^{-1} of space. The density of water at 25°C is 0.997 g cm^{-1}; thus, the volume of 965 g of water is 967.9 cm^3. If the volumes are conservative, on mixing the solution would have a volume of 16.2 + 967.9 cm^3 = 984.1 cm^3. Since the density of the solution is 1.0232 g cm^{-3}, the actual volume is 977.3 cm^3. Thus, the volume of the solution is decreased by 984.1 – 977.3 = 6.8 cm^3. This decrease in volume is called electrostriction and is caused by ion–water interactions. The ion draws the water molecules inward, compressing the solvent. The water molecules near an ion have a higher density than the bulk water. This effect is important for two reasons: (a) This hydration changes the mobility of ions, and (b) the effect of pressure on ionic equilibria forces reactions to the smallest volume. Since ions in solution have a smaller effective volume, pressure will force solids to have a higher solubility.

The continuum model (Figure 4.13) is an example of a crude model that can serve as an approximation for the real system. Drude and Nernst (1884) first used this model to explain the decrease in volume that occurs when an electrolyte is dissolved in water. Born (1920) popularized the model, and his name is normally attached to its use. In the model, an ion is pictured as a solid sphere of radius r bearing a charge Ze (where Z is the valence and e is the electrostatic charge), and the solvent is a structureless continuous dielectric medium. Using electrostatics, the ΔG_h^o (in units of kcal mol^{-1}) is given by (at 25°C)

$$\Delta G_h^o = -(Ne^2Z^2/2r)(1 - 1/D) = -163.89\ Z^2/r \tag{4.16}$$

where N is Avogadro's number, r is the radius in angstrom units (1 Å = 1 × 10^{-8} cm), and D is the dielectric constant of water (78.36 at 25°C). By appropriate differentiation of Equation 4.16 with respect to temperature T, it is possible to determine the other thermodynamic hydration functions ΔS_h^o (in units of calories degree^{-1} mol^{-1}) and ΔH_h^o (in units of kilocalories mol^{-1}):

$$\Delta S_h^o = (Ne^2Z^2/2r)(\partial \ln D/\partial T)_P = -9.649\ Z^2/r \tag{4.17}$$

$$\Delta H_h^o = (-Ne^2Z^2/2r)[1 - 1/D - (T/D)(\partial \ln D/\partial T)_P] = -166.78\ Z^2/r \tag{4.18}$$

A comparison of the experimental values of ΔG_h^o, ΔH_h^o, and ΔS_h^o plotted versus Z^2/r is shown in Figure 4.14 through Figure 4.16. It is apparent from these figures that the Born model offers a reasonable first approximation to the magnitude, radius, and charge dependence of ΔG_h^o, ΔH_h^o, and ΔS_h^o. A close examination of the data shows a number of significant deviations. For example, values of ΔH_h^o for the transition metals (Ca^{2+} to Zn^{2+}) given in Figure 4.17 do not increase in magnitude with increasing atomic number (decreasing radius). This is due to the three-dimensional orbitals not being spherically symmetrical (i.e., the hydrated water molecules do not have the same energy).

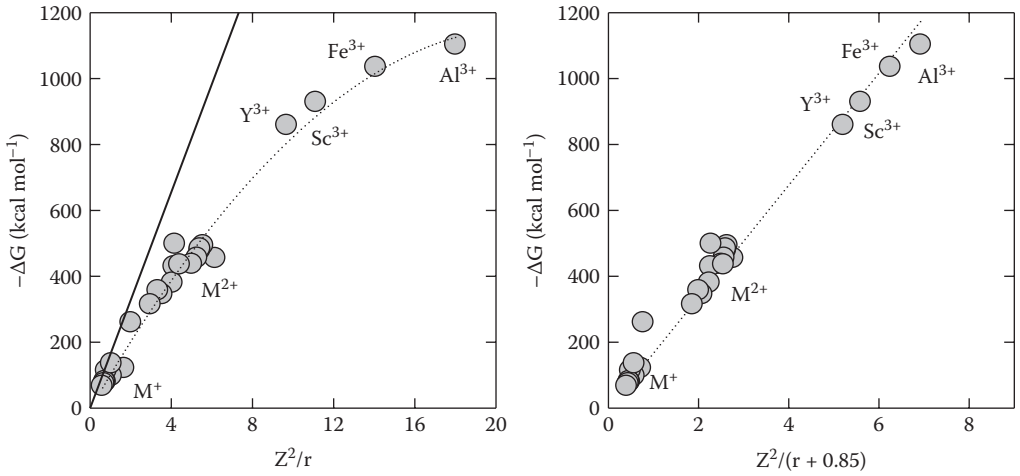

FIGURE 4.14
Values of the free energy of hydration for metals versus the charge (Z) squared divided by the crystal radii (r and r + 0.95 Å).

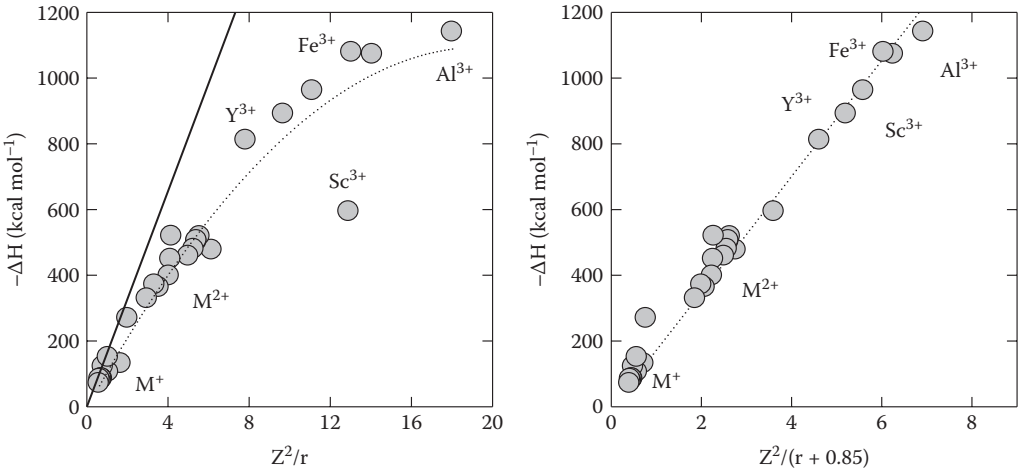

FIGURE 4.15
Values of the enthalpy of hydration for metals versus the charge (Z) squared divided by the crystal radii (r and r + 0.95 Å).

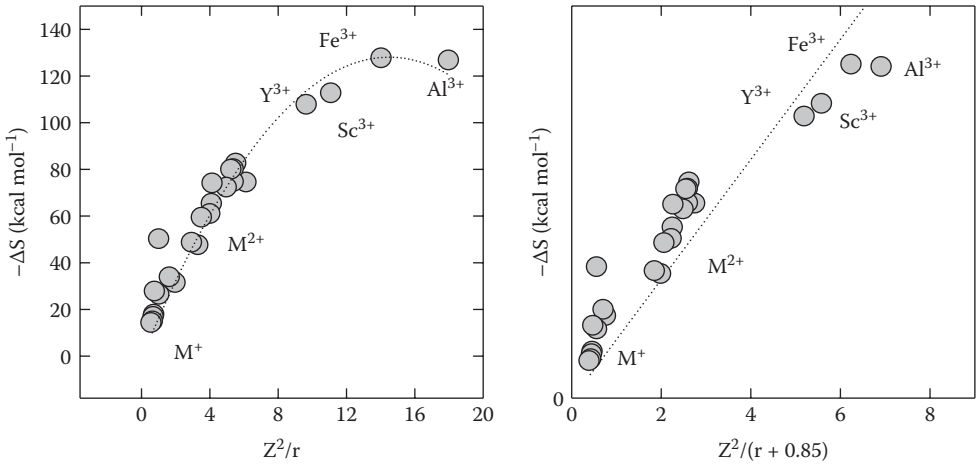

FIGURE 4.16
Values of the entropy of hydration for metals versus the charge (Z) squared divided by the crystal radii (r and r + 0.95 Å).

By further differentiation of Equation 4.16 through Equation 4.18, it is possible to obtain information about the size and structure of the hydration sphere. From the pressure dependence of ΔG_h^o, one obtains the volume change (electrostriction):

$$V^o(\text{elect}) = (-NZ^2e^2/2Dr)(\partial \ln D/\partial P)_T = -4.175\ Z^2/r \tag{4.19}$$

Further differentiation of Equation 4.19 with respect to T and P gives the electrostriction partial molal expansibility ($E^o = \partial V^o/\partial T$) and compressibility ($K^o = -\partial V^o/\partial P$).

$$E^o(\text{elect}) = (-NZ^2e^2/2Dr)[(\partial \ln D/\partial P) - (\partial \ln D/\partial T) \times (\partial \ln D/\partial P)_T] = -2.74 \times 10^{-2} Z^2/r \tag{4.20}$$

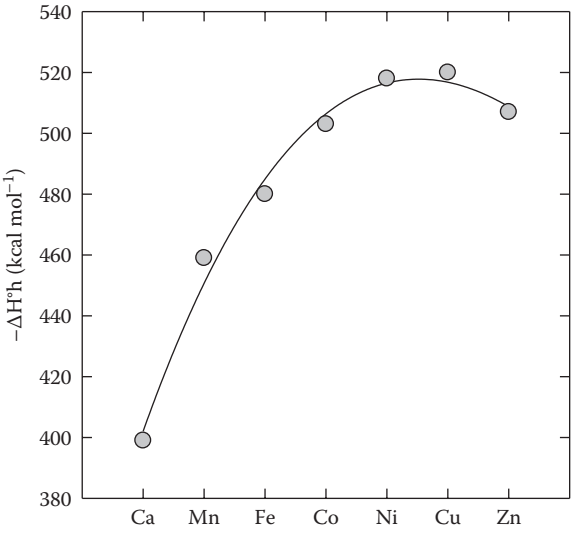

FIGURE 4.17
Values of the enthalpy of hydration for the transition metals.

$$K^{o}(\text{elect}) = (NZ^2e^2/2Dr)\left[(\partial \ln D/\partial P^2)T - (\partial \ln D/\partial P)_T^2\right] = -8.31\times10^{-4}Z^2/r \qquad (4.21)$$

Similar differentiation of the solution component of Equation 4.16 with respect to temperature yields the electrostatic partial molal entropy ($-\partial G^o/\partial T = S^o$) and heat capacity $-\partial(S^o/\partial T)/\partial T = \partial H^o/\partial T = C^o_P$.

$$S^{o}(\text{elect}) = (NZ^2e^2/2Dr)(\partial \ln D/\partial T)_P = -9/65Z^2/r \qquad (4.22)$$

$$C^{o}_{P}(\text{elect}) = (NZ^2eT^2/2Dr)\left[(\partial^2 \ln D/\partial T^2)_P - (\partial \ln D/\partial T)_P^2\right] = -12.96\ Z^2/r \qquad (4.23)$$

The partial molal properties of ions in solution contain a minimum of two terms, an intrinsic contribution and an electrical contribution. For example, for the partial molal volume of an ion, we have

$$V^{o}(\text{ion}) = V^{o}(\text{int}) + V^{o}(\text{elect}) \qquad (4.24)$$

where the intrinsic partial molal volume V^o(int) is equal to the size of the ion, V^o(cryst) = $(4\pi N/3)r^3 = 2.52\ r^3$ (when r is expressed in Å units) plus the packing effects, and the electrostriction partial molal volume V^o(elect) is the decrease in volume caused by ion–water interactions. Thus, to plot the various partial molal properties versus Z^2/r, one must estimate the intrinsic term. For V(int), one can use the semiempirical values from

$$V^{o}(\text{int}) = 4.48\ r^3 \qquad (4.25)$$

while for S^o(int), one can use

$$S^{o}(\text{int}) = 3/2\ \ln[AW] \qquad (4.26)$$

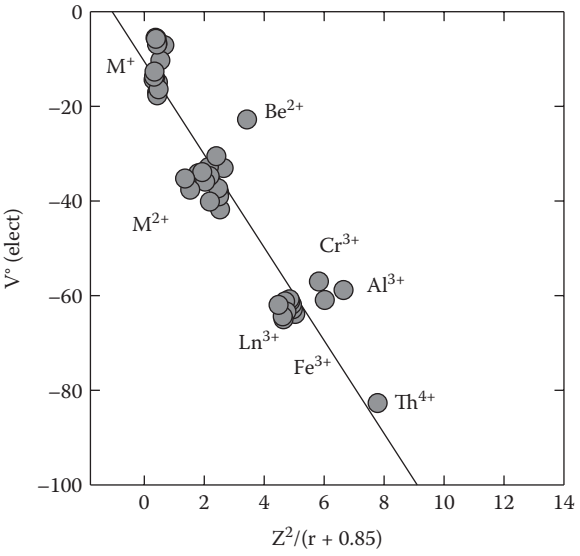

FIGURE 4.18
Values of the molar volume of electrostriction for metals versus the charge (Z) squared divided by the crystal radii (r).

where AW is the atomic weight. Plots of V^o(elect) and S^o(elect), calculated by using Equations 4.24 and Equation 4.25, respectively, versus Z^2/r are shown in Figure 4.18 and Figure 4.19. Although the general features of these figures agree with the Born model, a look at the fine structure shows some discrepancies. For example, the V^o(elect) of many divalent and trivalent ions appear to be nearly independent of r, and the charge dependence of V^o(elect) does not appear to be directly related to Z^2.

A number of workers have attempted to extend the Born model to account for these discrepancies by adjusting the size of the radii (e.g., Latimer, Pitzer, and Slansky, 1939, have added 0.85 Å to cations and 0.1 Å to anions to obtain linear plots) and adjusting the dielectric constant of the solvent as one approaches an ion (e.g., Laidler and Pegis, 1957, have suggested the effective dielectric constant is about 2 near an ion). These methods, however, do not consider the structure of the water molecule. In recent years, workers have used structural hydration models to examine ion–water interactions (see Figure 4.13). The structural models consider the ion–dipole interactions, ion–quadrupole interactions, and effects related to the structure of water.

Although a full discussion of these models is beyond the scope of this chapter, they can be summarized as follows: By considering the interaction of an ion with a water dipole, one can account for the molecular structure of the water molecule. By considering the interaction of an ion with a water quadrupole, one considers the difference in the thermodynamic properties of cations and anions of the same size. The water structure effects lead to a region between the oriented dipoles in the electrostricted region and bulk water—the water molecules are partially oriented by the ion and affected by the bulk water structure. Many workers have divided ions into two classes: (a) structure makers, which have a net effect of making more structure around the ion, and (b) structure breakers, which have a net effect of breaking down the structure of water. In general, the use of these terms is ambiguous, as we know little about the structure being made or broken. By confining our

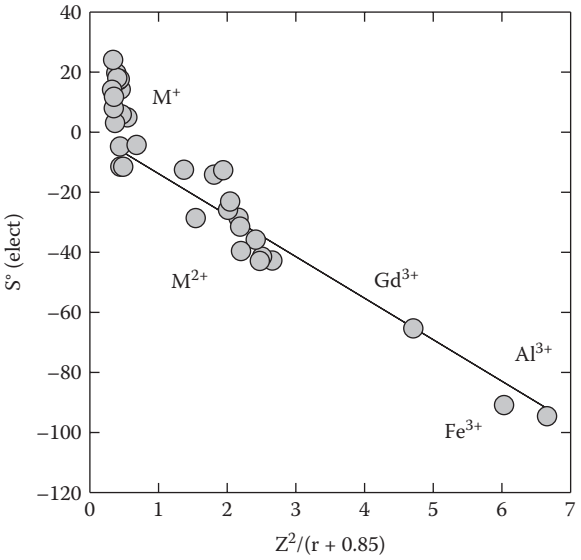

FIGURE 4.19
Values of the molar entropy of electrostriction for metals versus the charge (Z) squared divided by the crystal radii (r + 0.95 Å).

arguments to hydration effects [V^o(elect)], it is possible to discuss ion–water interactions using Equation 4.24 or its equivalent for other thermodynamic properties.

If we use a hydration model for ion–water interactions, the V^o(elect) can be related to the number of water molecules affected by the ion (i.e., the hydration number h),

$$V^o(\text{elect}) = V^o(\text{ion}) - V^o(\text{int}) = h\,(V^o_E - V^o_B) \tag{4.27}$$

where V^o_E is the molal volume of water in the electrostricted region, and V^o_B is the molal volume of water in the bulk phase (18.0 $cm^3\ mol^{-1}$). Due to the difficulties of determining V^o(int), it is not possible to unambiguously solve this equation. By differentiating Equation 4.24 with respect to pressure, we get the partial molal compressibility:

$$K^o(\text{ion}) = K^o(\text{int}) + K^o(\text{elect}) \tag{4.28}$$

If we assume K^o(int) = 0, we can combine this equation with the differential of Equation 4.27 (assuming h and V^o_E are not functions of pressure) and get

$$K^o(\text{ion}) - K^o(\text{elect}) = -\partial V^o(\text{elect})/\partial P = h(\partial V^o_B/\partial P) = -hV^o_B\,\beta^o_B \tag{4.29}$$

where $\beta^o_B = -(1/V^o_B)(\partial V^o_B/\partial P)$ is the compressibility of bulk water (45.25×10^{-6} bar^{-1} at 25°C). By rearrangement of Equation 4.28, we get for the hydration number

$$h = -K^o(\text{ion})/V^o_B\,\beta^o_B \tag{4.30}$$

Hydration numbers for some cations and anions calculated from Equation 4.30 are given in Table 4.4. By examining V^o(elect) and K^o(ion) = K^o(elect) for various ions, it is possible to calculate ($V^o_E - V^o_B$). Combining equations, we have

$$V^o(\text{elect}) = -[(V^o_E - V^o_B)/V^o_B\,\beta^o_B]\,K^o(\text{elect}) = -k\,K^o(\text{elect}) \tag{4.31}$$

TABLE 4.4

Hydration Numbers of Solutes at 25°C Determined from Compressibility Data

Cations	h	Anions	h	Ion Pairs	h
Li+	2.8	F–	5.6	$MgSO_4^0$	15.3
Na+	3.7	Cl–	2.0	$MnSO_4^0$	14.2
K+	2.9	Br–	1.2	$LaSO_{4+}$	17.3
Rb+	2.9	I–	0.1	$LaFeCN_6^0$	18.3
Cs+	2.5	OH–	6.4		
Ag+	3.4	SO_4^{2-}	8.6		
NH_{4+}	0.4	CO_3^{2-}	12.8		
Mg^{2+}	7.8				
Zn^{2+}	5.9				
Cu^{2+}	7.6				
Cd^{2+}	8.5				
Ca^{2+}	6.5				
Ba^{2+}	9.2				
La^{3+}	14.7				

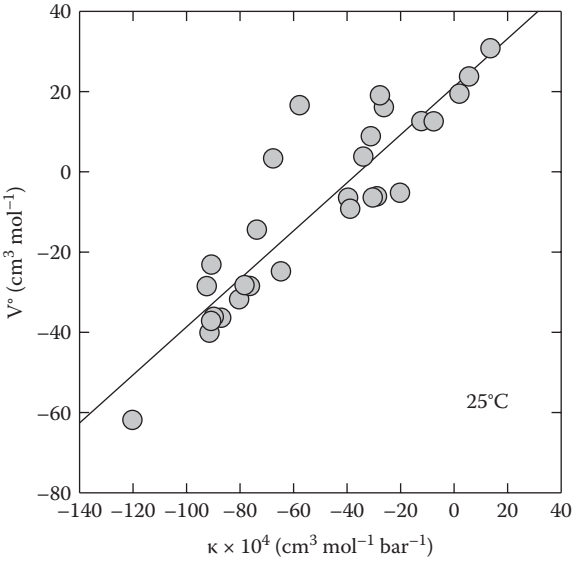

FIGURE 4.20
Correlation of the molar volumes and compressibilities of electrostriction for metals.

A plot of V^o(elect) versus K^o(ion) is shown in Figure 4.20. From Figure 4.20, we obtain k = 4800 bars, which can be compared to

$$k = -(\partial \ln D/\partial P)/[(\partial \ln D/\partial P) - (\partial \ln D/\partial P)^2] = 5000 \text{ bars} \quad (4.32)$$

from the Born model. Using the value of k = 4800 bars, we obtain $(V^o_E - V^o_B) = -3.9$ cm^3 mol^{-1}. Combining this value with $V^o_B = 18.0$ cm^3 mol^{-1}, we find $V^o_E = 14.1$ cm^3 mol^{-1}, which

is a lot larger than the crystal molal volume of water $V^o(cryst) = 2.52 \times (1.38)^3 = 6.6\ cm^3\ mol^{-1}$ or the value corrected for packing effects $V^o(int) = 4.48 \times (1.38)^3 = 11.8\ cm^3\ mol^{-1}$. Thus, the water molecules in the electrostricted region are not as tightly packed as one might expect. Part of this difference may, however, be caused by the water molecules in the so-called broken-down region. The solution properties of the other partial molal properties can also be treated by using the hydration model.

4.4.2 Proton Structure in Aqueous Solutions

The structure of the proton in the gas phase and in solution has been characterized by the formula $H^+(H_2O)_n$. Most of the earlier studies have been related to small clusters with $n > 10$. Eigen (1964) suggested that $n = 1$, H_3O^+, while Zundel (1974) suggested that $n = 2$, $H_2O \cdots H^+ \cdots OH_2$. The most stable structure for small clusters is thought to consist of about six water molecules in a two-dimensional structure (Figure 4.21). These differ from the three-dimensional structure in aqueous solutions of six water molecules. Studies of the structure of clusters of water have been made in the gas phase using infrared (IR) spectroscopy of the OH stretching. Earlier measurements by Searcy and Fenn (1974) found that water clusters with $n = 21$ dominated the IR spectra, forming a "magic number." This cluster of $n = 21$ is similar to the dodecahedron structure of methane hydrate (Figure 4.22) (Zwier, 2004). They found that at small sizes two-dimensional structures exist ($10 < n < 21$) with two nanometer cages of $n > 21$. The magic number of clusters is $n = 21$ as found in earlier studies. Dangling OH groups arise from water molecules at similar binding sites. Two studies have been made on the structure of water where $n > 10$ (Miyazaki et al., 2004; Shin et al., 2004). At present, it is not certain if the $n = 21$ clusters contain the H_3O^+ species inside the clathrate cage as with methane hydrate or if they are on the surface of the cage (Figure 4.23) (Zwier, 2004).

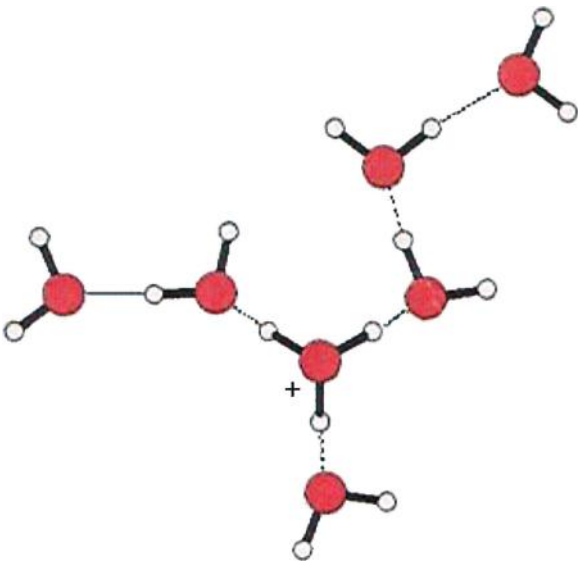

FIGURE 4.21
The suggested structure of a hydrated proton (H_3O^+) with six water molecules. (Data from Zwier, T.S., *Science* 304, 1119, 2004. With permission.)

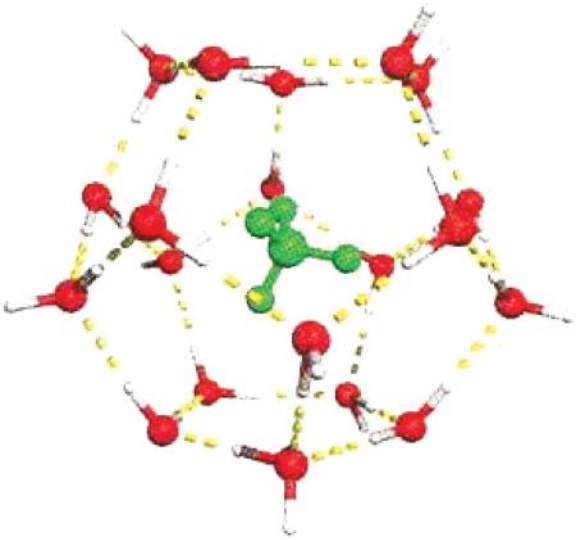

FIGURE 4.22
The dodecahedra structure of a methane hydrate cluster with 21 water molecules. (Data from Zwier, T.S., *Science* 304, 1119, 2004. With permission.)

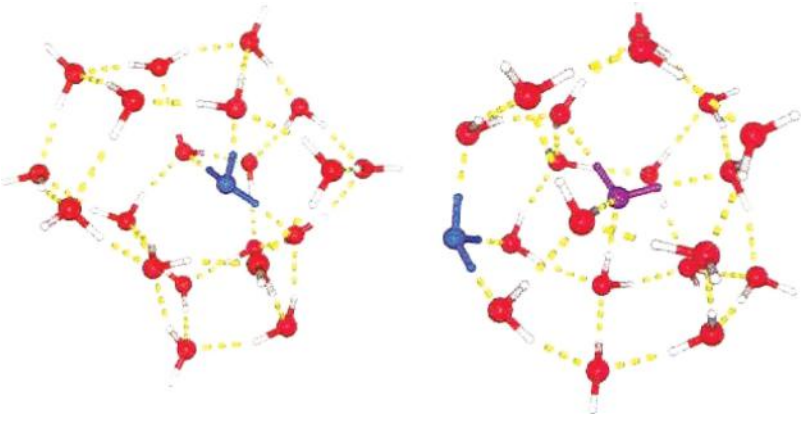

FIGURE 4.23
Possible structures of the hydrated proton on the surface or interior of a cluster of 21 water molecules. (Data from Zwier, T.S., *Science* 304, 1119, 2004. With permission.)

4.5 Ion–Ion Interactions

Now that we have a reasonable understanding of the structure of an ion in solution at infinite dilution, we can consider what happens as the concentration is increased. To obtain an understanding of these ion–ion interactions experimentally, the activity coefficient as well as its pressure ($V - V^o$) and temperature ($H - H^o$) dependence are studied. By studying the thermodynamic properties of two-ion systems (M^+, X^-), one can obtain an understanding of plus–minus interactions, and by studying three-ion systems (M^+, N^+, X^- or M^+, X^-, Y^-), one

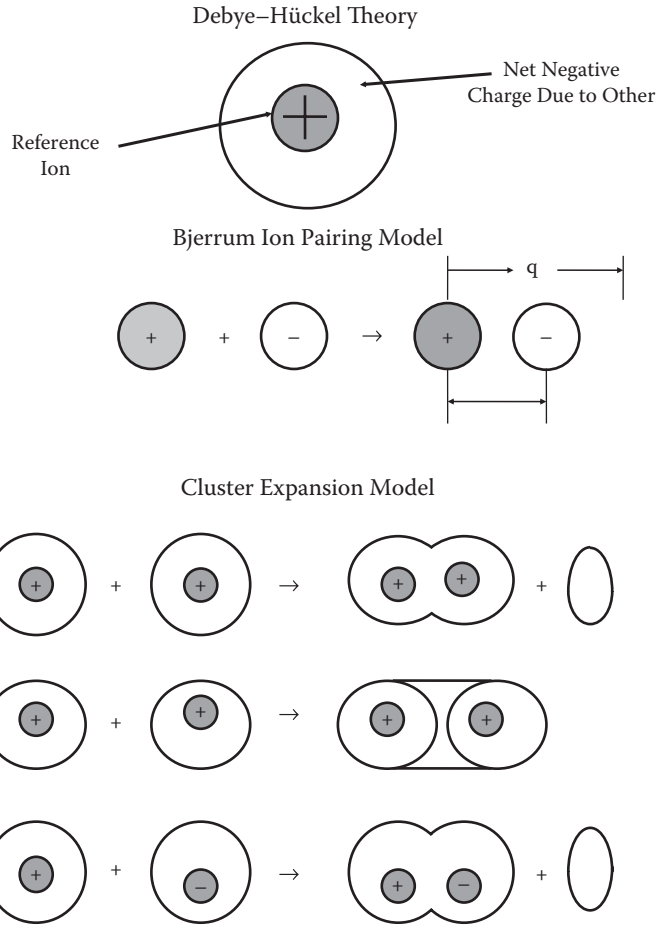

FIGURE 4.24
Models used to explain ion–ion interactions.

can study plus–plus and minus–minus interactions. As in the case of ion–water interactions, it is useful to use models (see Figure 4.24) to examine these interactions. A thorough discussion of the models used to treat ion–ion interactions is given elsewhere. Some of the models include the continuum models (the Debye–Hückel theory and Bjerrum ion-pairing theory). These models assume that the nonideal behavior of an electrolyte is due entirely to electrical effects. The structural models attempt to account for hydration effects as well as specific interactions. The more recent cluster theories of Friedman (1960) make no attempt to separate the electrical and nonelectrical interactions (except in the limit). They also consider the importance of all the possible interactions in solution (plus–plus, plus–minus, and minus–minus).

The starting point for all discussions of ion–ion interactions is the Debye–Hückel theory. The theory predicts that the mean activity coefficient $\gamma_{\pm}$ of an electrolyte is given by

$$\ln \gamma_{\pm} = -S_f I^{1/2}/(1 + A_f a I^{1/2}) \tag{4.33}$$

where S_f and A_f are constants related to absolute temperature T, and the dielectric constant D of water (for a 1-1 electrolyte, $S_f = 0.5116$ and $A_f = 0.3292$ at 25°C), $I = 1/2\ \Sigma\nu_i\ Z_i^2\ m_i$ is the molal ionic strength (ν_i is the number, Z_i is the charge, and m_i is the molality of ionic species[i]), and (a) is the ion size parameter in angstrom units. This equation serves as a limit in dilute solutions; however, it fails at the high ionic strength of seawater because of (a) defects in some of the basic assumptions (e.g., treating ions as point charges in a continuous dielectric medium) and (b) deviations that occur because of noncoulombic effects such as hydration (the Debye–Hückel theory considers only electrical effects).

The classical method of examining the deviations from the Debye–Hückel theory in concentrated solutions is to use various extended forms involving one or more arbitrary constants. The difference between this form and the experimental data is attributed to noncoulombic effects. For example, Guggenheim (1935) used the equation

$$-\log \gamma_{\pm} = 0.551\ Z_M Z_X\ I^{1/2}/(1 + I^{1/2}) + 2\nu\ B_{MX} m \tag{4.34}$$

where $\nu = 2\nu_M\ \nu_X/(\nu_M + \nu_X)$, I is the molal ionic strength, and m is the molality. By differentiating Equation 4.34 with respect to temperature and pressure, it is possible to examine the specific interaction model as a function of temperature and pressure.

The most popular method of treating the deviations from the Debye–Hückel theory in concentrated solutions is the ion-pairing method of Bjerrum. This method assumes that short-range interactions can be represented by the formation of ion pairs:

$$M^+ + A^- \rightarrow MA^o \tag{4.35}$$

A characteristic association constant is assigned to this formation:

$$K_A = a_{MA}/a_M a_A = ([MA]/[M+][A-])(\gamma_{MA}/\gamma_{M\gamma A}) \tag{4.36}$$

where a_i, [i], and γ_i are, respectively, the activity, molal concentration, and activity coefficient of species i. There are four classes of ion pairs (Figure 4.25):

1. **Complexes:** when the ions are held in contact by covalent bonds
2. **Contact ion pairs:** when the ions are in contact and linked electrostatically (with no covalent bonding)
3. **Solvent-shared ion pairs:** pairs of ions linked electrostatically, separated by a single water molecule
4. **Solvent-separated ion pairs:** pairs of ions linked electrostatically but separated by more than one water molecule

Bjerrum defined the distance between oppositely charged ions that can be classified as being associated by $q = Z + Z - e^2/2DkT$, where Z_i is the charge on the ion i, e is the electrostatic charge, D is the dielectric constant, k is the Boltzmann constant, and T is the absolute temperature. In this treatment, two ions of opposite charge are considered to form an ion pair when they are between å, the ion size parameter, and q. This can include ion pairs of classes 2, 3, and 4. The Bjerrum (1926) theory predicts greater ion pair formation the higher the valencies and the smaller the dielectric constant of the solvent are, which is in agreement with experimental results.

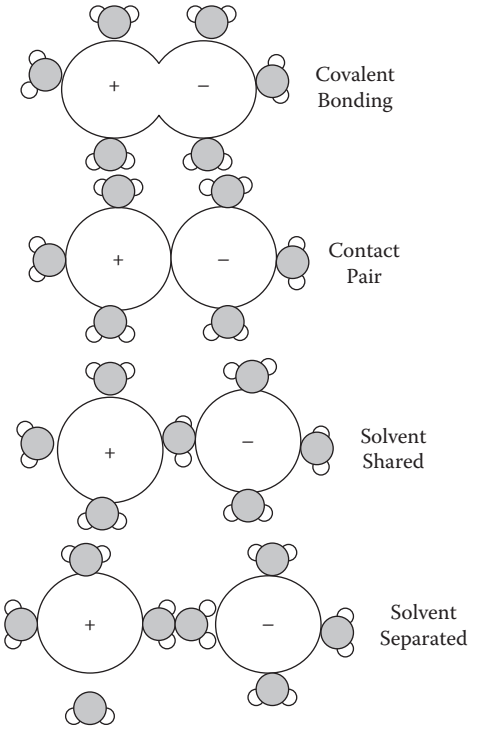

FIGURE 4.25
Types of ion pairs.

Many workers have criticized the Bjerrum theory because of the arbitrary cutoff distance. It has now been superseded by other theories. For example, the model of Fuoss (1958) considers only anions on the surface of a cation in volume, V = 2.52 a^3, to be ion pairs. Fuoss obtained

$$K_A = (4\pi Na^3/3000)\exp(Z + Z - e^2/DakT) \tag{4.37}$$

where the first term is the excluded volume around the cation. Others have further expanded these methods and discussed the shortcomings of the model. Studies of electrolyte solutions have been made by using the cluster expansion method of Friedman (1960). This method in simple terms considers all the interactions in a solution and makes no attempt to separate coulombic and noncoulombic terms. For example, for the major sea salts (NaCl + $MgSO_4$) there are a number of possible interactions to consider:

Interactions	Possible Types
Plus–plus	Na–Na, Mg–Mg, Na–Mg
Minus–minus	Cl–Cl, SO_4–SO_4, Cl–SO_4
Plus–minus	Na–Cl, $MgSO_4$, Mg–Cl, $NaSO_4$

These interactions can be represented by the cross-square diagram shown in Figure 4.26. By studying the mixtures along the side of this diagram, one can obtain information about plus–plus and minus–minus interactions; by studying individual salts and the sum

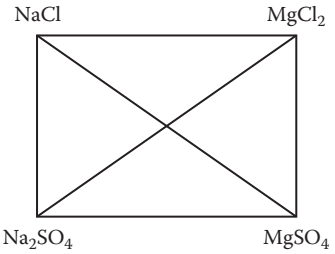

FIGURE 4.26
The cross-square diagram for the major sea salts.

around the sides ($MgSO_4 = MgCl_2 + Na_2SO_4 - 2NaCl$), one can study plus–minus interactions. The cross terms represent the mixtures (or simple seawater). Since the plus–plus and minus–minus terms are small, the total activity coefficients can be estimated from

$$\log \gamma_{\pm}^{T}(MX) = \log \gamma_{\pm}^{o}(MX) + \text{Plus–plus terms} + \text{Minus–minus terms} \tag{4.38}$$

where $\log \gamma_{\pm}^{o}(MX)$ is the value for MX in itself at the ionic strength of the mixture, and the other terms are related to interactions caused by mixing. For example, for NaCl in seawater we have

$$\text{Plus–plus} = (Na–Mg) + (Na–K) + (Na–Ca) + \cdots \tag{4.39}$$

$$\text{Minus–minus} = (Cl–SO_4) + (Cl–HCO_3) + (Cl–Br) + \cdots \tag{4.40}$$

where the terms in parentheses are weighted according to the composition of the mixture. This is discussed further elsewhere in this chapter.

Before we examine the use of the methods described in the previous section to determine the activity of a metal ion in seawater,

$$a_M = [M]_T \gamma_T (M) \tag{4.41}$$

Some of the factors that control the state of an ion in seawater are

1. The Eh
2. The pH
3. The inorganic ligands
4. The organic ligands

The Eh of seawater may control the oxidation state of a metal ion. For a metal ion that can exist in two oxidation states, we have

$$Ox + ne^- = Red \tag{4.42}$$

where Ox is the oxidized form, Red is the reduced form, and n is the number of electrons (e^-) transferred. The equilibrium constant is given by

$$\log K = \log a_{Red} - \log a_{Ox} + n\,pE \tag{4.43}$$

where a_i is the activity of i, and pE = –log a_{Ox}, the log of the activity of an electron. Rearranging this equation, we have

$$pE = pE^0 + (1/n)\log a_{Ox}/a_{Red} \tag{4.44}$$

where $pE^0 = (1/n)$ log K. Since pE = Eh/(2.303RT/F), we have the more familiar form

$$Eh = Eh^0 + (2.303RT/nF) \log a_{Ox}/a_{Red} \tag{4.45}$$

where $Eh^0 = (2.303RT/nF)$ log K = (0.0591/n) log K at 25°C.

The upper theoretical limit of the pE or Eh of oxygenated water is controlled by the reaction

$$1/2\ O_2(g) + 2H+ + 2e^- = H_2O(aq) \tag{4.46}$$

Using log K = 41.6, log aH_2O = –0.01, and pH = 8.1 at 25°C, the pE is given by

$$pE = (\log P + 50.7)/4 \tag{4.47}$$

at log P = –0.69, pE = 12.5, or Eh = 0.73 V. The experimentally measured values (about 0.5 to 0.6 V) for the Eh of open surface seawater are lower than this theoretical value. By using the reaction

$$O_2 + 2H^+ + 2e^- = H_2O_2 \tag{4.48}$$

one obtains a lower theoretical pE = 6.3 or Eh = 0.4 V (taking $[H_2O_2] = 10^{-7}$ M), which is closer to the experimentally determined values.

For anoxic conditions, the negative pE or Eh is thought to be controlled by the reactions

$$SO_4^{2-} + 9H^+ + 8e^- = HS^- + 4H_2O \tag{4.49}$$

$$SO_4^{2-} + 8H^+ + 6e^- = S^o(s) + 4H_2O \tag{4.50}$$

Using log K = 34.0 and 36.6, respectively, for Reactions 4.49 and 4.50, the pE is given by

$$pE = [-\log(HS^-) - 41.4]/8 \tag{4.51}$$

$$pE = [-\log(SO_4^{2-}) - 41.4]/8 \tag{4.52}$$

at $(HS^-) = 10^{-3}$ to 10^{-6}, pE = –4.8 to –4.4 or Eh = –0.28 to –0.26 V.

The pH and Eh environments that one encounters in marine waters are shown in Figure 4.27. The upper and lower limits are determined by the properties of water. The cross-textured and dotted bands represent the stability band for oxygen (4 to 260 *M*) and sulfide (10^{-3} to 10^{-6} *M*) concentrations as given by Reactions 4.49 and 4.50. Most ocean waters have pH values between 7.6 and 8.3 and Eh values greater than 0.2 V. A sample calculation of the oxidation state of a metal in seawater is made for the iron system examined by Kester, Byrne, and Liang (1975). The two oxidation states of iron are related by

$$Fe^{3+} + e^- = Fe^{2+} \tag{4.53}$$

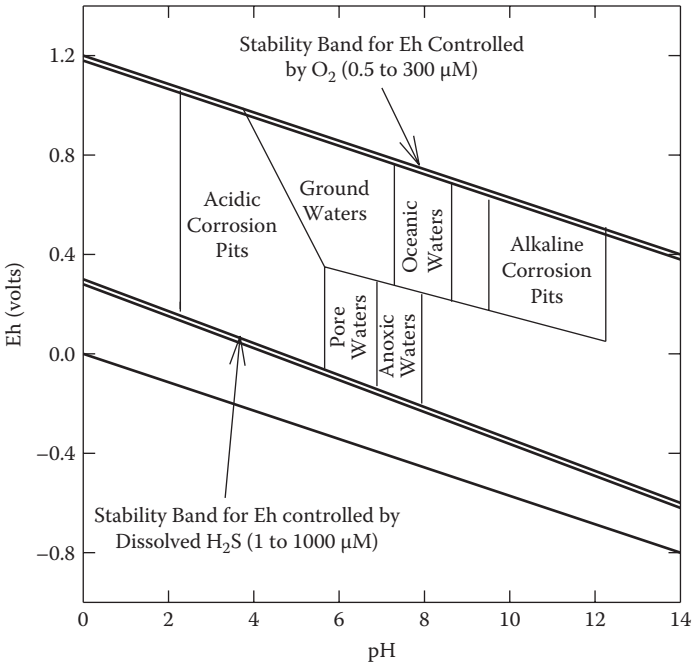

FIGURE 4.27
Values of the electrical potential Eh for natural waters of various pH.

Using Equation 4.45, the oxidation state can be determined from

$$Eh = Eh^0 + (2.3RT/nF)\log[a_{Fe}(III)/a_{Fe}(II)] \tag{4.54}$$

Using $Eh^0 = 0.771$ V at 25°C, we obtain $a_{Fe}(III)/a_{Fe}(II) = 2.43 \times 10^{-18}$ when Eh = −0.27 V. It should be pointed out that these ratios are at infinite dilution and do not include the effects of complex formation (which usually stabilizes a system against reduction). To determine the concentration ratios at higher ionic strengths, one must estimate the stoichiometric activity coefficients of the ions:

$$[Fe^{3+}]_T/[Fe^2]_T = [a_{Fe}(III)/a_{Fe}(II)]\gamma_T(Fe^{2+})/\gamma_T(Fe^{3+}) \tag{4.55}$$

Kester et al. (1975) have also examined the ion pairing of Fe^{3+} and Fe^{2+} in seawater, which can be used to estimate the activity coefficient ratio. Although redox calculations are quite simple, some of the problems inherent in these calculations are as follows:

1. Equilibrium is not reached (i.e., the process is kinetically controlled).
2. Biological activity may change the oxidation state.
3. Photochemical processes may control the state.
4. Other important species may be neglected (e.g., organic complexes).
5. Unreliable analytical and thermodynamic data are available for the actual system.

The pH can affect the metals directly by hydrolysis equilibrium:

$$M^{2+} + H_2O = M(OH)^{+} + H^{+} \tag{4.56}$$

and by affecting the form of the ligands:

$$HCO_3^{-} = H^{+} + CO_3^{2-} \tag{4.57}$$

The effect of pH on the state of iron in marine waters has been examined by Kester, Byrne, and Liang (1975). These results are shown in Figure 4.28. The major form of iron at the pH and Eh of seawater is $Fe(OH)_3$. Since the OH^- concentration is a function of pH, the relative forms of Fe^{3+} are quite pH dependent. Near the pH limits of 7 and 10, there is a transition between $Fe(OH)_2^{+} \rightarrow Fe(OH)_3$ and $Fe(OH)_3 \rightarrow Fe(OH)_4^{-}$. These results suggest that iron can alternate between cationic and anionic species, which would strongly influence the ion-exchange characteristics of colloidal iron as well as its transport properties. More recently, we have developed a speciation model for Fe(II) and Fe(III). The speciation of Fe(III) as a function of pH determined from the model in seawater is shown in Figure 4.29. As shown by earlier workers, the hydrolysis of Fe(III) dominates except at low pH.

The inorganic ligands affecting metals include the major anionic components of seawater (Cl^-, SO_4^{2-}, HCO_3^{2-}, Br^-, $B(OH)_4^-$, and F^-) and some of the minor anionic components (OH^-, $H_2PO_4^-$, and NO_3^-, to mention a few). It is difficult to classify the types of organic ligands one must consider since little is known about the composition of the organics in seawater. EDTA (ethylenediamine N,N,N,N′ tetraacetic acid) is frequently used as a model; however, the more important organic ligands may be made up of humic and fulvic acids

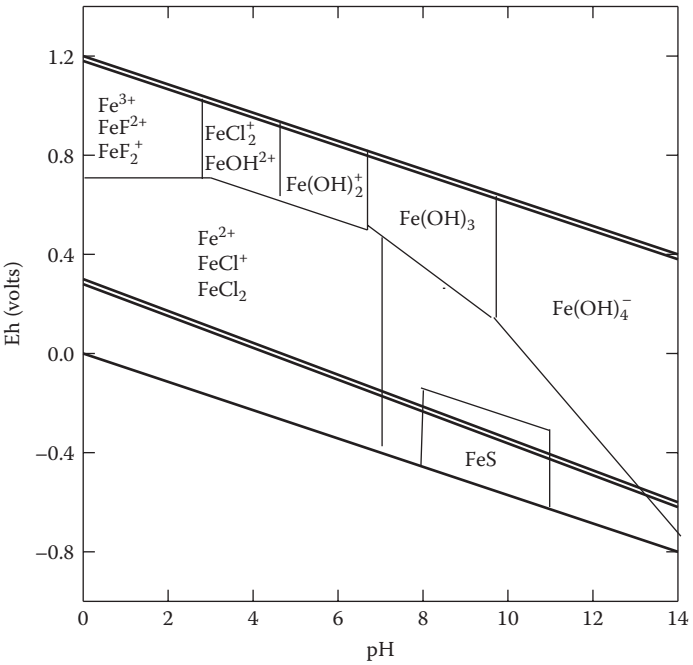

FIGURE 4.28
The various forms of iron in seawater as function of Eh and pH.

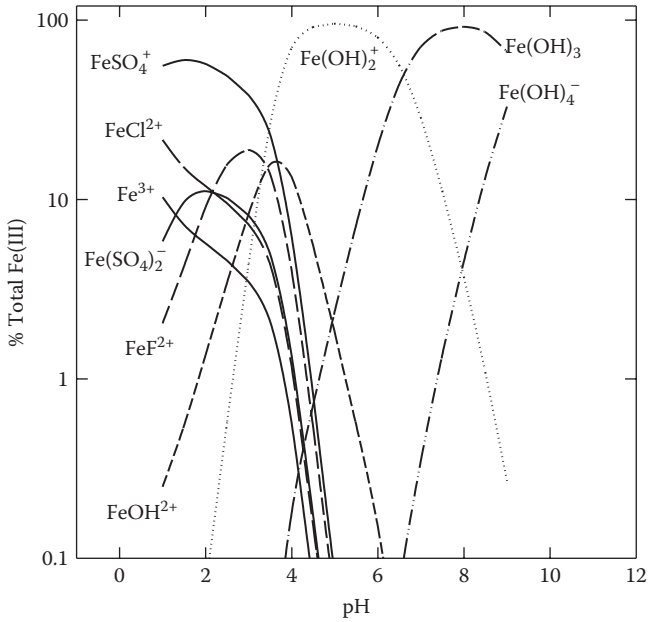

FIGURE 4.29
The speciation of Fe(III) as a function of pH in seawater at 25°C.

and their derivatives. For the present, it is not possible to consider these organic ligands, although we realize they may be of great importance. It should be pointed out that all the model calculations made by using various organic ligands indicate that organic ligands have little effect on the speciation of most trace metals (i.e., compared to the major inorganic ligands).

We now examine the use of the ion-pairing model and the specific interaction model to estimate the total activity coefficient of the major ions of seawater. Owing to the large amount of thermodynamic data available for the major sea salts, it is possible to apply both methods. As we will see, for the minor or trace metals, we can use at present only the ion-pairing methods.

4.5.1 Ion-Pairing Model

The speciation forms in which various metals can exist are shown in Figure 4.30. Most models confine the speciation to the dissolved species. To examine the colloidal forms of metals, one must use filters of various sizes or use such techniques as dialysis to separate the various forms. Some of the methods used to determine individual species include

1. Physical separation based on size
2. Equilibrium distributions using adsorption, ion exchange, redox equilibria, and so on
3. Potentiometric methods using ion-selective electrodes
4. Electrode kinetics such as polarography
5. Detection of structure using optical methods
6. Bioassay techniques by which metals may act as a catalyst or inhibitor

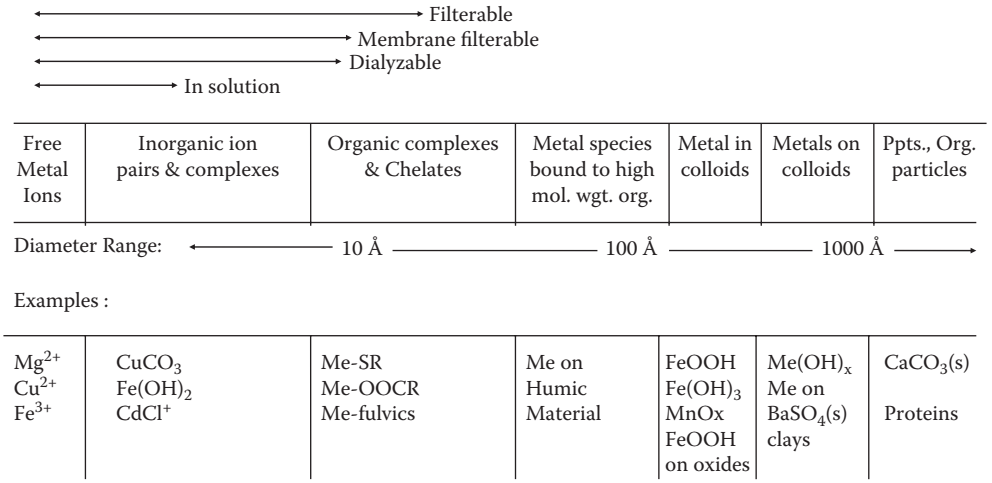

FIGURE 4.30
The various forms of elements in natural waters. Ppts. = parts per thousand.

TABLE 4.5

Division of Solutes into Hard and Soft Acids

Hard Acids	Borderline	Soft Acids
All A-metal cations plus Cr^{3+}, Mn^{3+}, Fe^{3+}, Co^{3+}, Bi^{3+}, UO^{2+}, VO^{2+}	All bivalent transition metal cations plus Zn^{2+}, Pb^{2+}, Bi^{3+}	All B-metal cations minus Zn^{2+}, Pb^{2+}
Also species like BF_3, BCl_3, SO_3, RSO_{2+}, RPO_{2+}, CO_2, RCO+, R_3C+	SO_2, NO+, $B(CH_3)_3$	All metal atoms, bulk metals, I_2, Br_2, ICN, I+, Br+
Class A metals: Cations are all those with an electronic configuration of noble gases (H+, Li+, Na+, K+, Rb+, Cs+, Be^{2+}, Mg^{2+}, Ca^{2+}, Sr^{2+}, Ba^{2+}, $Al^{3+,}$ Sc^{3+}, La^{3+}, Si^{4+}, Ti^{4+}, Zr^{4+}, Th^{4+})		
Transition metals: Cations with 1–9 outer-shell electrons (V^{2+}, Cr^{2+}, Mn^{2+}, Fe^{2+}, Co^{2+}, Ni^{2+}, Cu^{2+}, Ti^{3+}, V^{3+}, Cr^{3+}, Mn^{3+}, Fe^{3+}, Co^{3+})		
Class B metals: Cations with electron numbers 10 or 12 (Cu+, Ag+, Au+, Tl+, Ga+, Zn^{2+}, Cd^{2+}, Hg^{2+}, Pb^{2+}, Sn^{2+}, Tl^{3+}, Au^{3+}, In^{3+}, Bi^{3+})		

The classification of metals made by Goldberg (1965) can be expanded using the Pearson division of solutes into hard and soft acids (see Table 4.5).

When using the ion-pairing model, the activity of the free ion i is given by

$$a_i = [i]_F \gamma_F(i) \tag{4.58}$$

where $[i]_F$ is the molal concentration, and $\gamma_F(i)$ is the activity coefficient of the free or uncomplexed ion. This value of γ_F is assumed to be only a function of the ionic strength and independent of the relative composition. Since the activity coefficient of the ion is also related to the total concentration and activity coefficient by

$$a_i = [i]_T \gamma_T(i) \tag{4.59}$$

the total or stoichiometric activity coefficient is given by

$$\gamma_T(i) = ([i]_F/[i]_T)\ \gamma_F(i) \tag{4.60}$$

This total activity coefficient is the one desired to obtain activities from total concentrations (i.e., using Equation 4.60). The term $\alpha_F = [i]_F/[i]_T$ is the fraction of free ions in a solution of fixed composition and ionic strength. If a series of one-to-one complexes is formed,

$$M_i + X_i \rightarrow M_iX_i \tag{4.61}$$

the ion-pairing constant for the formation of $M_iX_i^o$ is given by

$$K^*_{MX} = [M_iX^0]/[M^+_i][X_i] \tag{4.62}$$

$$K_{MX}^* = K_{MX}[\gamma_F(M)\ \gamma_F(X)/\gamma_F[M_iX_0] \tag{4.63}$$

where K_{MX} is the thermodynamic constant in pure water, K_{MX}^* is the stoichiometric constant, and $\gamma_F(i)$ is the activity coefficient of species i. The total concentration of M_i and X_i is given by

$$[M_i]_T = [M_i]_F + \Sigma\ [M_iX_i^0] \tag{4.64}$$

$$[X_i]_T = [X_i]_F + \Sigma\ [M_iX_i^0] \tag{4.65}$$

where $\Sigma\ [M_iX_i^o]$ is the sum of all the various ion pairs in the solution. By combining these equations with Equation 4.62, we have

$$\alpha_M = [M]_F/[M]_T = (1 + \Sigma\ K_{MX}^*[X_i]_F)^{-1} \tag{4.66}$$

$$\alpha_X = [X]_F/[X]_T = (1 + \Sigma\ K_{MX}^*[M_i]_F)^{-1} \tag{4.67}$$

These equations can be solved by a series of iterations if K_{MX}^* is known. Several computer programs are available to aid in these iterations. The results, however, are dependent on the quality of the values of K_{MX}^*, which are functions of ionic strength and, to a degree, the composition of the solutions. The fraction of a given ion pair can be obtained from

$$[MX_i]/[M]_T = K_{MX}^*[X_i]_F\ \alpha_M \tag{4.68}$$

$$[M_iX]/[X]_T = K_{MX}^*[M_i]_F\ \alpha_X \tag{4.69}$$

It should be pointed out that the form of the given complex does not affect the thermodynamic activity of M or X.

$$\gamma_T(M) = \alpha_M\ \gamma_F(M) \tag{4.70}$$

$$\gamma_T(X) = \alpha_X\ \gamma_F(X) \tag{4.71}$$

For the major ionic components of seawater, Millero and Schreiber (1982) have given the ionic strength function for K_{MX}^* and $\gamma_F(i)$ for a number of ions. These equations can be used to calculate the speciation and activity coefficients of the major components of natural waters using a personal computer.

TABLE 4.6

Ion-Pairing Constants for the Major Ion Pairs in Seawater at S = 35 and t = 25°C

Ion	K^*_{HX}	K^*_{NaX}	K^*_{KX}	K^*_{MgX}	K^*_{CaX}	K^*_{SrX}
Cl^-	—	—	—	—	—	—
SO_4^{2-}	31.35	2.15	1.66	10.41	11.04	7.13
HCO_3^-	—	0.28_4	—	2.18	2.20	2.14
Br^-	—	—	—	—	—	—
CO_3^{2-}	—	2.38	—	77.06	138.84	135.0
$B(OH)_4^-$	—	0.70	—	8.07	13.28	4.65
F^-	880.4	0.10	—	19.6	4.56	2.35
OH^-	—	0.37	—	48.88	5.52	1.79

TABLE 4.7

Calculations of the Fraction of Free Cations and Anions after Various Iterations

	Iteration			
Ion	**1st**	**2nd**	**3rd**	**4th**
H^+	1.0000	0.7342	0.7268	0.7266
Na^+	1.0000	0.9771	0.9763	0.9763
K^+	1.0000	0.9826	0.9820	0.9820
Mg^{2+}	1.0000	0.8952	0.8918	0.8917
Ca^{2+}	1.0000	0.8888	0.8851	0.8850
Sr^{2+}	1.0000	0.9235	0.9209	0.9208
OH^-	0.2555	0.2760	0.2767	0.2767
HCO_3^-	0.7806	0.7919	0.7923	0.7923
F^-	0.4608	0.4875	0.4884	0.4884
$B(OH)_4^-$	0.5199	0.5395	0.5401	0.5402
SO_4^{2-}	0.3635	0.3768	0.3773	0.3773
CO_3^{2-}	0.1271	0.1382	0.1386	0.1387

The fraction of the free cations and anions can be determined for Equations 4.66 and 4.67. The desired ion-pairing constants for K_{MX}^* are given in Table 4.6.

To start the iteration, one can assume that $\alpha_M = 1.0$ and calculate the values of α_X. These values of α_X are used to make an estimate of $[X]_F = \alpha_X [X]_T$, and the values of α_M are estimated. The new α_M is used to determine $[M]_F = \alpha_M [M]_T$, and the process is repeated until a self-consistent set of α_i is found. A sample of the values obtained by various iterations is given in Table 4.7. It is clear from this table that after three iterations, a self-consistent set of α_is is obtained. These values can be used to determine the total activity coefficients of the various ions (Table 4.8). It is also possible to determine the fraction of the various forms of each metal and anion shown in Figure 4.31 and Figure 4.32.

The validity of these total activity coefficients can be demonstrated by calculating the dissociation constant for boric acid in seawater. The K^*_{HB} is given by

$$K_{HB}^* = K_{HB}\, \gamma_{HB}/\gamma_{HB} = 10^{-9.24} \times 1.09/(0.688 \times 0.351) = 10^{-8.54} \tag{4.72}$$

TABLE 4.8

Values for $[i]_T$, $[i]_F$, α_i, $\gamma_F(i)$, and $\gamma_T(i)$ for the Major Ionic Components of Seawater at S = 35 and t = 25°C

Ion	$[i]_T$	α_i	$[i]_F$	$\gamma_F(i)$	$\gamma_T(i)$
H+	—	0.7266	—	0.947	0.688
Na+	0.48610	0.9763	0.47458	0.707	0.690
K+	0.01058	0.9820	0.01037	0.628	0.616
Mg^{2+}	0.05474	0.8917	0.04878	0.286	0.255
Ca^{2+}	0.01066	0.8850	0.00943	0.258	0.228
Sr^{2+}	0.00009	0.9208	0.00008	0.251	0.231
Cl–	0.56577	1.0000	0.56577	0.628	0.628
OH^-	—	0.2769	—	0.853	0.236
F^-	0.00007	0.4883	0.00003	0.681	0.333
Br^-	0.00087	1.0000	0.00087	0.646	0.646
HCO_{3-}	0.00193	0.7924	0.00153	0.677	0.536
$B(OH)_{4-}$	0.00009	0.5403	0.00005	0.650	0.351
SO_4^{2-}	0.02927	0.3771	0.01097	0.224	0.085
CO_3^{2-}	0.00020	0.1386	0.00003	0.207	0.029
H_2PO_{4-}	—	0.7860	—	0.502	0.395
HPO_4^{2-}	—	0.2968	—	0.167	0.050
PO_4^{3-}	—	0.00147	—	0.0284	0.000042

This calculated value can be compared to the measured value of $10^{-8.60}$ measured by Hansson (1973). The results of similar calculations for other acids are shown in Table 4.9. The calculated values are in good agreement with the measured values and demonstrate the reliability of the model.

The speciation of minor components of seawater can be made using the concentrations of free cations and anions given in Table 4.8. These calculations can be made without making any iterations since minor components do not affect the speciation of the major components. A sample calculation for the PO_4^{3-} ion is

$$\alpha_{PO_4} = (1 + K^*_{NaPO_4}[Na]_F + K^*_{MgPO_4}[Mg]_F + K^*_{CAPO_4}[Ca]_F)^{-1} \tag{4.73}$$
$$= 0.0016$$

Since the value of $\gamma_F = 0.0252$ for PO_4^{3-}, the value of $\gamma_T = 4 \times 10^{-5}$.

For the calculation of the fraction of free trace metals in seawater, one needs reliable values of K^*_{MX} for the metal with the major anions at an ionic strength of 0.7. Reliable values of K^*_{MX} are not normally available. Whitfield and coworkers (Turner, Whitfield, and Dickson, 1981) have made these calculations using the best available data. Their results are given in Table 4.10. Since reliable values of K^*_{BMX} are available for Cu^{2+} (Table 4.11), it is possible to demonstrate how the method is used. The function of free Cu^{2+} is given by

$$\alpha_{Cu} = (1 + K^*_{CuSO_4}[SO_4]_F + K^*_{CuHCO_3}[HCO_3]_F + K^*_{CuCO_3}[CO_3]_F + K^*_{CuCO_2}[CO_3]_F^2 + K^*_{Cu(OH)}[OH]_F + K^*_{Cu(OH)_2}[OH]_F^2)^{-1} \tag{4.74}$$

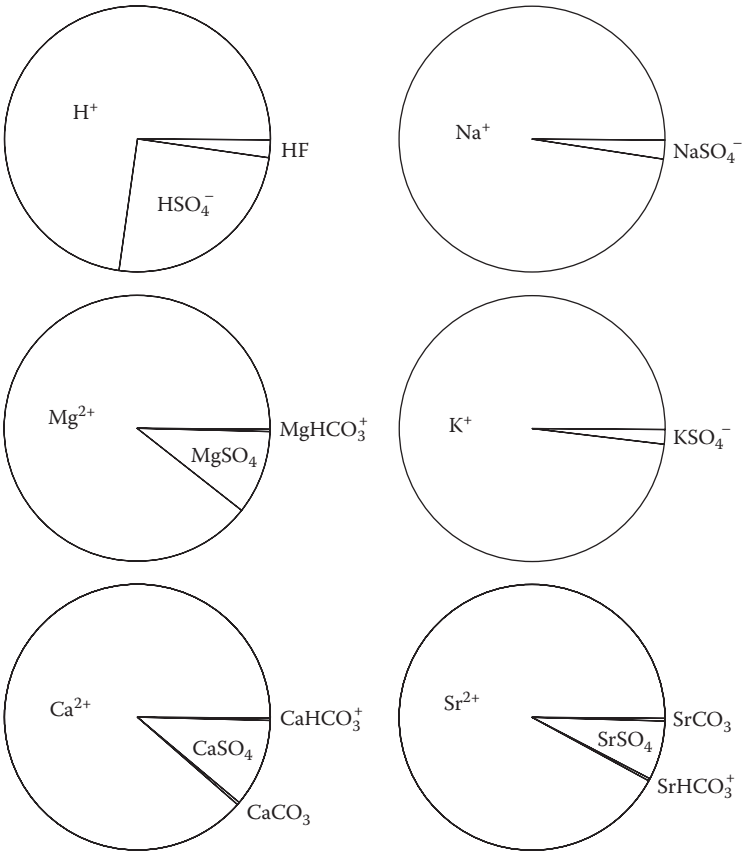

FIGURE 4.31
The speciation of cations in seawater.

The various forms of Cu^{2+} calculated from Equation 4.74 are given in Table 4.12 and shown in Figure 4.33. At a pH of 8.1 and 25°C, the dominant forms are $CuCO_3^o$ (74%) and $Cu(CO_3)_2^{2-}$ (14%). The speciation of divalent and trivalent metals over a wide range of concentrations can be made using the equations of Millero and coworkers (Millero and Hawke, 1992; Millero, 1992, 2001). Calculations as a function of temperature can be made using the equation of Byrne, Kump, and Cantrell (1988).

4.5.2 Specific Interaction Model

Although the ion-pairing model yields reliable estimates of activity coefficients in dilute solutions (below 1 m), it is not as reliable at higher ionic strengths. This is largely because it does not consider the interactions of ions of the same sign (plus–plus and minus–minus interactions). Ionic solution theory suggests that activity coefficients in electrolyte mixtures should be of the form

$$\ln\gamma = DH + \Sigma B_{ij}\, m_j + \Sigma C_{ijk}\, m_j m_k \tag{4.75}$$

where DH is a Debye–Hückel term, B_{ij} is a term related to binary interactions of all the components (plus–minus, plus–plus, and minus–minus), and C_{ijk} is related to ternary

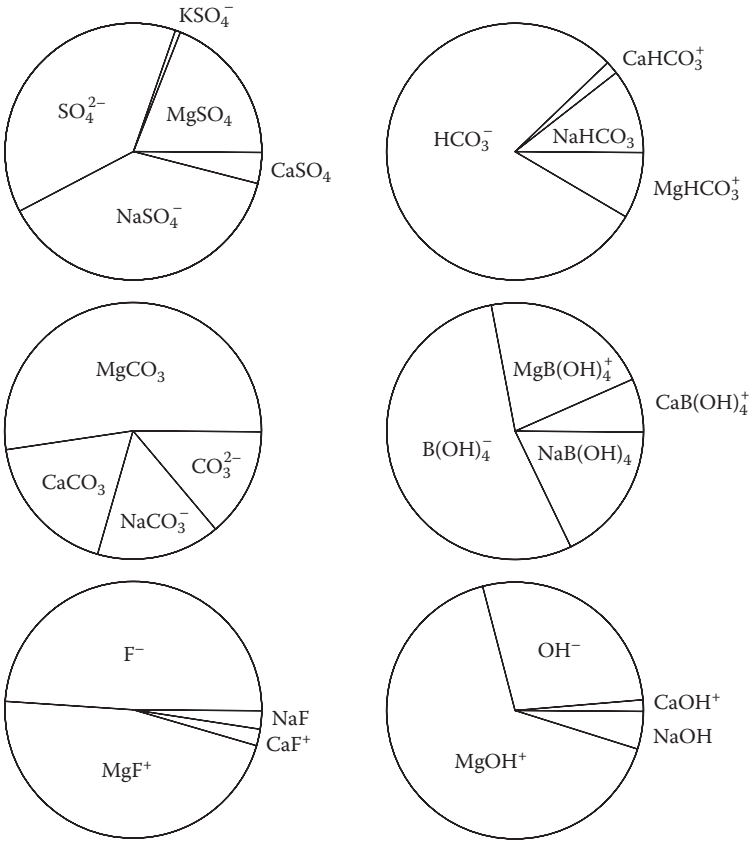

FIGURE 4.32
The speciation of anions in seawater.

TABLE 4.9

Comparison of the Measured and Calculated pK^*_{HA} for Acids in Seawater at 25°C

	pK^*_{HA}		
Acid	**Calculated**	**Measured**	**ΔpK**
H_2O	13.21	13.18	0.03
$B(OH)_3$	8.59	8.60	–0.01
H_2CO_3	5.86	5.84	0.02
HCO_{3-}	8.96	8.93	0.03
NH_{4+}	9.345	9.351	–0.006
H_3PO_4	1.55	1.57	–0.02
H_2PO_{4-}	6.14	5.94	0.20
HPO_4^{2-}	9.11	8.93	0.18

TABLE 4.10

The Fraction of Free Metals and the Dominant Forms in Fresh and Seawater

Cation	Free	OH	F	Cl	SO_4	CO_3	Log α
Freshwater at pH = 6							
Ag^{+}	72	[a]	[a]	28	[a]	[a]	0.15
Al^{3+}	[a]	90	10	—	—	[a]	3.14
Au+	[a]	—	—	100	—	—	6.08
Au^{3+}	[a]	100	—	[a]	—	—	21.98
Ba^{2+}	99	[a]	[a]	[a]	1	[a]	0.01
Be^{2+}	15	57	28	[a]	[a]	[a]	0.82
Bi^{3+}	[a]	100	[a]	[a]	[a]	—	9.08
Cd^{2+}	96	[a]	[a]	2	2	[a]	0.02
Ce^{3+}	72	[a]	3	[a]	22	3	0.14
Co^{2+}	98	[a]	[a]	[a]	2	[a]	0.01
Cr^{3+}	[a]	98	[a]	[a]	1	—	2.41
Ca^{2+}	100	—	0	[a]	—	—	0.00
Cu+	95	0	0	5	0	0	0.02
Cu^{2+}	93	1	[a]	[a]	2	4	0.03
Dy^{3+}	65	1	6	[a]	21	7	0.19
Er^{3+}	63	1	7	[a]	19	10	0.20
Eu^{3+}	71	1	3	[a]	21	4	0.15
Fe^{2+}	99	[a]	[a]	[a]	1	[a]	0.01
Fe^{3+}	[a]	100	[a]	[a]	[a]	[a]	6.41
Ga^{3+}	[a]	100	[a]	[a]	—	[a]	7.80
Gd^{3+}	63	1	5	[a]	22	9	0.20
Hf^{4+}	[a]	100	[a]	[a]	[a]	[a]	13.28
Hg^{2+}	[a]	8	[a]	92	[a]	[a]	6.88
Ho^{3+}	65	1	7	[a]	19	8	0.19
In^{3+}	[a]	100	[a]	[a]	[a]	[a]	5.53
La^{3+}	73	[a]	1	[a]	25	1	0.14
Li^{3+}	100	[a]	—	0	[a]	0	0.00
Lu^{3+}	59	1	8	[a]	15	17	0.23
Mn^{2+}	98	[a]	[a]	[a]	2	[a]	0.01
Nd^{3+}	70	1	3	[a]	24	3	0.15
Ni^{2+}	98	[a]	[a]	[a]	2	[a]	0.01
Pb^{2+}	86	2	[a]	1	4	7	0.06
Pr^{3+}	72	1	2	[a]	23	2	0.14
Rb^{+}	100	—	—	[a]	—	—	0.00
Sc^{3+}	[a]	43	41	[a]	[a]	15	2.80
Sm^{3+}	68	1	3	[a]	25	4	0.17
Sn^{4+}	[a]	100	—	—	—	—	24.35
Tb^{3+}	67	1	6	[a]	22	4	0.18
Th^{4+}	[a]	100	[a]	[a]	[a]	[a]	7.94
TiO^{2+b}	[a]	100	—	—	[a]	—	7.17
Tl^{+}	100	[a]	[a]	[a]	[a]	—	0.00
Tl^{3+}	[a]	100	—	[a]	[a]	—	14.62
Tm^{3+}	66	1	8	[a]	20	6	0.18

TABLE 4.10 (continued)

The Fraction of Free Metals and the Dominant Forms in Fresh and Seawater

Cation	Free	OH	F	Cl	SO_4	CO_3	Log α
U^{4+}	[a]	100	[a]	[a]	[a]	—	14.02
UO_2^{2+}[b]	12	18	8	[a]	1	60	0.91
Y^{3+}	63	1	17	[a]	14	4	0.20
Yb^{3+}	58	1	7	[a]	17	17	0.24
Zn^{2+}	98	[a]	[a]	[a]	2	[a]	0.01
Zr^{4+}	[a]	100	[a]	[a]	[a]	—	14.33
Seawater at pH = 8.2							
Ag^{+}	[a]	[a]	[a]	100	[a]	[a]	5.26
Al^{3+}	[a]	100	[a]	—	—	[a]	9.22
Au^{+}	[a]	—	—	100	—	—	12.86
Au^{3+}	[a]	100	[a]	9	5	[a]	27.30
Ba^{2+}	86	[a]	[a]	9	5	[a]	0.07
Be^{2+}	[a]	99	2	[a]	[a]	[a]	2.74
Bi^{3+}	[a]	100	[a]	[a]	[a]	—	14.79
Cd^{2+}	3	[a]	[a]	97	[a]	[a]	1.57
Ce^{3+}	21	5	1	12	10	51	0.68
Co^{2+}	58	1	[a]	30	5	6	0.24
Cr^{3+}	[a]	100	[a]	[a]	[a]	—	5.82
Ca^{2+}	93	—	—	7	—	—	0.03
Cu+	[a]	—	—	100	—	—	5.18
Cu^{2+}	9	8	[a]	3	1	79	1.03
Dy^{3+}	11	8	1	5	6	68	0.94
Er^{3+}	8	12	1	4	4	70	1.08
Eu^{3+}	18	13	1	10	9	50	0.74
Fe^{2+}	69	2	[a]	20	4	5	0.16
Fe^{3+}	[a]	100	[a]	[a]	[a]	[a]	11.98
Ga^{3+}	[a]	100	[a]	[a]	—	[a]	15.35
Gd^{3+}	9	5	1	4	6	74	1.02
Hf^{4+}	[a]	100	[a]	[a]	[a]	—	22.77
Hg^{2+}	[a]	[a]	[a]	100	[a]	[a]	14.24
Ho^{3+}	10	8	1	5	5	70	0.99
In^{3+}	[a]	100	[a]	[a]	[a]	[a]	11.48
La^{3+}	38	5	1	18	16	22	0.42
Li^{3+}	99	[a]	—	—	1	—	0.00
Lu^{3+}	5	21	1	1	1	71	1.32
Mn^{2+}	58	[a]	[a]	37	4	1	0.23
Nd^{3+}	22	8	1	19	12	45	0.66
Ni^{2+}	47	1	[a]	34	4	14	0.33
Pb^{2+}	3	9	[a]	47	1	41	1.51
Pr^{3+}	25	8	1	12	13	41	0.61
Rb+	95	—	—	5	—	—	0.02
Sc^{3+}	[a]	100	[a]	[a]	[a]	[a]	7.41
Sm^{3+}	18	10	1	8	11	52	0.75

continued

TABLE 4.10 (continued)

The Fraction of Free Metals and the Dominant Forms in Fresh and Seawater

Cation	Free	OH	F	Cl	SO_4	CO_3	Log α
Sn^{4+}	[a]	100	—	—	—	—	32.05
Tb^{3+}	16	11	1	8	9	55	0.80
Th^{4+}	[a]	100	[a]	[a]	[a]	[a]	0.80
TiO^{2+}[b]	[a]	100	—	—	[a]	—	11.14
$Tl+$	53	[a]	[a]	45	2	—	0.28
Tl^{3+}	[a]	100	—	[a]	[a]	—	20.49
Tm^{3+}	11	21	1	5	6	55	0.94
U^{4+}	[a]	100	[a]	[a]	[a]	—	23.65
UO_2^{2+}[b]	[a]	[a]	[a]	[a]	[a]	100	6.83
Y^{3+}	15	14	3	7	6	54	0.81
Yb^{3+}	5	9	1	2	3	81	1.30
Zn^{2+}	46	12	[a]	35	4	3	0.34
Zr^{4+}	[a]	100	[a]	[a]	[a]	—	23.96
Freshwater at pH = 9							
$Ag+$	65	[a]	[a]	25	[a]	9	0.18
Al^{3+}	[a]	100	[a]	—	—	[a]	12.95
$Au+$	[a]	—	—	100	—	—	6.07
Au^{3+}[b]	[a]	100	—	[a]	—	—	30.93
Ba^{2+}	96	[a]	[a]	[a]	1	3	0.02
Be^{2+}	[a]	100	[a]	[a]	[a]	[a]	4.47
Bi^{3+}	[a]	100	[a]	[a]	[a]	—	18.01
Cd^{2+}	47	4	[a]	1	1	47	0.33
Ce^{3+}	[a]	5	[a]	[a]	[a]	95	2.37
Co^{2+}	20	7	[a]	[a]	[a]	73	0.70
Cr^{3+}	[a]	100	[a]	[a]	[a]	—	9.08
Ca^{2+}	100	—	—	[a]	—	—	0.00
$Cu+$	95	—	—	5	—	—	0.02
Cu^{2+}	[a]	3	[a]	[a]	[a]	96	2.62
Dy^{3+}	[a]	46	[a]	[a]	[a]	54	3.01
Er^{3+}	[a]	78	[a]	[a]	[a]	22	3.54
Eu^{3+}	[a]	18	[a]	[a]	[a]	82	2.48
Fe^{2+}	27	8	[a]	[a]	[a]	65	0.57
Fe^{3+}	[a]	100	[a]	[a]	[a]	[a]	14.99
Ga^{3+}	[a]	100	[a]	[a]	—	[a]	19.31
Gd^{3+}	[a]	14	[a]	[a]	[a]	86	2.92
Hf^{4+}	[a]	100	[a]	[a]	[a]	—	27.61
Hg^{2+}	[a]	100	[a]	[a]	[a]	[a]	11.79
Ho^{3+}	[a]	48	[a]	[a]	[a]	52	3.08
In^{3+}	[a]	100	[a]	[a]	[a]	[a]	14.57
La^{3+}	2	10	[a]	[a]	[a]	88	1.78
$Li+$	100	[a]	—	—	[a]	—	0.00
Lu^{3+}	[a]	92	[a]	[a]	[a]	8	4.21
Mn^{2+}	62	1	[a]	[a]	1	35	0.20
Nd^{3+}	[a]	9	[a]	[a]	[a]	90	2.33

TABLE 4.10 (continued)

The Fraction of Free Metals and the Dominant Forms in Fresh and Seawater

Cation	Free	OH	F	Cl	SO_4	CO_3	Log α
Ni^{2+}	9	2	[a]	[a]	[a]	90	1.07
Pb^{2+}	[a]	5	[a]	[a]	[a]	95	2.73
Pr^{3+}	1	9	[a]	[a]	[a]	90	2.23
Rb+	100	—	—	[a]	—	—	0.00
Sc^{3+}	[a]	100	[a]	[a]	[a]	[a]	10.82
Sm^{3+}	[a]	14	[a]	[a]	[a]	86	2.49
Sn^{4+}	[a]	100	—	—	—	—	36.27
Tb^{3+}	[a]	32	[a]	[a]	[a]	68	2.67
Th^{4+}	[a]	100	[a]	[a]	[a]	[a]	19.86
TiO^{2+}[b]	[a]	100	—	—	[a]	—	13.15
Tl+	100	[a]	[a]	[a]	[a]	—	0.00
Tl^{3+}	[a]	100	—	[a]	[a]	—	23.57
Tm^{3+}	[a]	86	8	[a]	[a]	14	3.51
U^{4+}	[a]	100	[a]	[a]	[a]	—	28.77
UO_2^{2+}	[a]	[a]	[a]	[a]	[a]	100	8.61
Y^{3+}	[a]	14	[a]	[a]	[a]	85	2.57
Yb^{3+}	[a]	62	[a]	[a]	[a]	38	3.59
Zn^{2+}	6	78	[a]	[a]	[a]	16	1.20
Zr^{4+}	[a]	100	[a]	[a]	[a]	—	28.81

Note: —, Ligand not considered.

[a] Calculated abundance less than 1%.

[b] Classified as fully hydrolyzed oxidation states.

TABLE 4.11

Stability Constants of Cu^{2+} Complexes in Seawater at 25°C

Complex	$\log K^*_{MX}$
$CuOH^+$	–8.14
$Cu(OH)_2$	–16.73
$CuSO_4$	1.37
$CuCO_3$	5.67
$Cu(CO_3)_2$	9.34
$CuHCO_3$	1.06

interactions of all the components (plus–minus–plus, plus–minus–minus, and minus–plus–plus). Pitzer has given some general equations that can be used to estimate the activity coefficient of ions that account for all the ionic interactions that occur in a mixed-electrolyte solution. In their simplest form, they are

$$\ln\gamma_M = Z_M^2 f\gamma + 2\Sigma_a m_a(B_{Ma} + EC_{Ma}) + Z_M{}^{2\Sigma}{}_{c\Sigma a}\, m_c m_a B_{ca} + Z_{M\Sigma c\Sigma a} m_c m_a C_{ca} \qquad (4.76)$$

$$\ln\gamma_X = Z_X^2 f\gamma + 2\Sigma_c m_c(B_{cX} + EC_{cX}) + Z_X{}^{2\Sigma}{}_{c\Sigma a}\, m_c m_a B_{ca} + Z_{X\Sigma c\Sigma a}\, m_c m_a C_{ca} \qquad (4.77)$$

TABLE 4.12

Speciation of Cu^{2+} in Seawater (pH = 8.1, S = 35, and t = 25°C

Species	Fraction	%
Cu^{2+}	0.0390	3.9
CuOH+	0.0486	4.9
$Cu(OH)_2$	0.0220	2.2
$CuSO_4$	0.0101	1.0
$CuCO_3$	0.7379	73.8
$Cu(CO_3)_2^{2-}$	0.1417	14.2
$CuHCO_{3+}$	0.0006	0.1

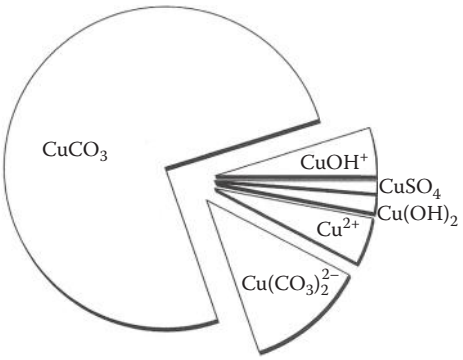

FIGURE 4.33
The various forms of Cu^{2+} in seawater.

where Z_i is the charge on the ion; a and c are anions and cations of the media, respectively; m_i is the molalities, $E = 1/2\Sigma\, m_i Z_i$ is the equivalent molality, and $f\gamma$ is a Debye–Hückel term:

$$f_\gamma = -0.392[I^{1/2}/(1 + 1.2I^{1/2}) + (2/1.2)\,(1 + 1.2I^{1/2})] \tag{4.78}$$

and the interaction terms B_{MX}, B_{MX}^1, and C_{MX} are given for 1-1 electrolytes by

$$B_{MX} = \beta^0_{MX} + (\beta^{1/2}_{MX}\ I)[1 - (1 + 2I^{1/2})\exp(-2I^{1/2}) \tag{4.79}$$

$$B_{MX} = (\beta^{1/2}_{MX}\ I^2)\ [-1 + (1 + 2I^{1/2} + {}^2I)\exp(-2I^{1/2})] \tag{4.80}$$

$$C_{MX} = C^\phi/(2|Z_M Z_X|^{1/2}) \tag{4.81}$$

Values of β^0, β^1, and C^ϕ for various electrolytes are tabulated elsewhere (Pitzer, 1991).

Although the equations may appear to be quite complicated, they are easy to use if the calculations are made on a personal computer. These equations account for all the binary interactions. To account for triplet interactions, it is necessary to consider two more terms:

$$\ln \gamma_M = \text{Equation 4.86} + \Sigma_c m_c(2\theta m_c + \Sigma_a m_a \Psi m_{ca}) + \Sigma\Sigma m_a m_{a'} \Psi_{aa} M \tag{4.82}$$

$$\ln \gamma_X = \text{Equation 4.87} + \Sigma_a m_a(2\theta_{Xa} + \Sigma_c m_c \Psi_{cc} X) + \Sigma\Sigma m_{cc}\, \Psi_{cc}\, X \tag{4.83}$$

The values of θ_{ij} are related to the interaction of like-charged ions (e.g., $Na^+ - K^+$), and the values of Ψ_{ijk} are related to the triplet interactions (e.g., $Na^+ - K^+ - Cl^-$). If the values of B_{MX}, B'_{MX}, and C_{MX} are calculated at a given ionic strength (as well as $f\gamma$ and E), the calculation of γ is straightforward. This can be demonstrated by giving the equations for M and X in a simple seawater media made up of Na^+, Mg^{2+}, Cl^-, and SO_4^{2-}. The equations are

$$\begin{aligned}\ln\gamma_M = {} & Z_M^2 f^\gamma + 2m_{Cl}(B_{MCl} + EC_{MCl}) + 2m_{SO_4}(B_{MSO_4} + EC_{MSO_4}) \\ & + m_{Na}m_{Cl}(Z_M^2 B^1_{NaCl} + Z_m C_{NaCl}) + m_{Mg}m_{Cl}(Z_M^2 B^1_{MgCl_2} + Z_m C_{MgCl_2}) \\ & + m_{Na}m_{SO_4}(Z_M^2 B^1_{NaSO_4} + Z_M C_{Na_2SO_4}) + m_{Mg}m_{SO_4}(Z_M^2 B^1_{MgSO_4} + Z_m C_{MgSO_4})\end{aligned} \tag{4.84}$$

$$\begin{aligned}\ln\gamma_X = {} & Z_X^2 f^\gamma + 2m_{Na}(B_{NaX} + EC_{NaX}) + 2m_{Mg}(B_{MgX} + EC_{MgX}) \\ & + m_{Na}m_{Cl}(Z_M^2 B^1_{NaCl} + Z_X C_{NaCl}) + m_{Mg}m_{Cl}(Z_X^2 B^1_{MgCl_2} + Z_X C_{MgCl_2}) \\ & + m_{Na}m_{SO_4}(Z_X^2 B^1_{NaSO_4} + Z_X C_{NaSO_4}) + Z_X C_{NaSO_4} + m_{Mg}m_{SO_4}(Z_X^2 B_{MgSO_4} + Z_X C_{MgSO_4})\end{aligned} \tag{4.85}$$

It first should be noticed that the double sum terms, $m_{Na}m_{Cl}$, and so on, are the same in both equations and are only functions of the media. It is thus possible to calculate and sum all the B^1 and C terms into

$$Z_M{}^2\, \Sigma\Sigma + Z_M \Sigma \tag{4.86}$$

where

$$\Sigma\Sigma = B'_{NaCl} + B'_{MgCl_2} + B'_{NaSO_4} + B'_{MgSo_4} \tag{4.87}$$

$$\Sigma = C_{NaCl} + C_{MgCl_2} + C_{NaSO_4} + C_{MgSo_4} \tag{4.88}$$

For seawater, $\Sigma = 0.03503$ and $\Sigma\Sigma = 0.00027$, which can be compared to $\Sigma = 0.03234$ and $\Sigma\Sigma = 0.00033$ in NaCl and $\Sigma = 0.03543$ and $\Sigma\Sigma = 0.00026$ in NaCl + $MgSO_4$. Since the values of Σ and $\Sigma\Sigma$ do not vary much, they are not strong functions of the media composition. If the Pitzer B_{MX} and C_{MX} are known for Na^+ and Cl^- salts, it is possible to make a reliable estimate of γ_T for many ions for seawater media. If the appropriate terms are available for Mg^+ and SO_4^{2-} salts, the estimates are more reliable. Estimates for some simple ions are given in Table 4.13.

To make reliable estimates for some of the anions, it is necessary to consider the strong interactions that occur between Mg^{2+} and Ca^{2+}. For H^+, it is also necessary to consider the strong interactions with SO_4^{2-}. The values for H^+, F^-, OH^-, HCO_3^-, $B(OH)_4^-$, and CO_3^{2-} in seawater in Table 4.13 have been corrected for these effects. At present, reliable Pitzer parameters and the necessary ion-pairing constants are available for all the major components of seawater at 25°C. More recent work has extended the parameters to 25°C for Na^+, Mg^{2+}, Ca^{2+}, Cl^-, and SO_4^{2-}. Future work will include reliable data for more ions over a wide range of temperatures.

TABLE 4.13

Estimated Activity Coefficients of Ions in Various Media

Ion	NaCl	NaCl + $MgSO_4$	Seawater
H+	0.779	0.739	0.546
Na+	0.664	0.668	0.667
K+	0.619	0.629	0.628
NH_{4+}	0.616	0.625	0.624
Mg^{2+}	0.283	0.240	0.240
Ca^{2+}	0.259	0.215	0.215
Sr^{2+}	0.254	0.212	0.212
Ba^{2+}	0.224	0.192	—
Mn^{2+}	0.252	0.217	—
Fe^{2+}	0.255	0.218	—
Co^{2+}	0.257	0.220	—
Ni^{2+}	0.266	0.225	—
Cu^{2+}	0.223	0.193	—
Zn^{2+}	0.235	0.206	—
F–	0.595	0.620	0.299
Cl–	0.664	0.668	0.667
Br–	0.688	0.694	0.692
OH–	0.670	0.672	0.216
HCO_{3-}	0.552	0.597	0.556
$B(OH)_{4-}$	0.513	0.559	0.418
CO_3^{2-}	0.164	0.134	0.039
SO_4^{2-}	0.131	0.115	0.113

The correction for ion pairs is simple to make. For example, for H^+ the desired γ_T is given by

$$\gamma_T = \gamma_F(1+\beta_{HSO_4}[SO_4])^{-1} \tag{4.89}$$

where γ_F is the value for all the anions except SO_4^{2-}. Using $\beta_{HSO4} = 12.0$, one obtains

$$\gamma_T = 0.739(1+12.0\times0.02947) = 0.546 \tag{4.90}$$

The reliability of the Pitzer-generated activity coefficients can be demonstrated by calculating the K_2^* for carbonic acid in seawater. The value is given by

$$K_2^* K_2\gamma_{HCO_3}/\gamma_H\gamma_{CO_3} = 10^{-10.33}\times0.556/0.546\times0.039 = 10^{-8.91} \tag{4.91}$$

This calculated value can be compared to the measured value of $pK_2^* = 8.93$.

The major advantage of the Pitzer (1991) equations is that they can be used over a wide range of compositions and ionic strengths without iterations. The equations can be used to estimate the free activity coefficients of minor cations and anions needed to use the ion-pairing model that must be considered for strong interactions (such as metal–OH– interactions). Attempts have been made (Millero, 1992) to combine the Pitzer specific interaction and ion-pairing model to determine the speciation and activity coefficients of metals in

natural waters. The stability constants and the activity coefficients of free ions are determined using the Pitzer equations. The strong interactions of metals with anions such as OH^-, CO_3^{2-}, and so on are accounted for by the ion-pairing model.

Honig and Nicholls (1995) have shown that there has been a major revival in the use of electrostatics for studying the interactions of charged ions and polar molecules in aqueous solutions. This has been accomplished by the development of numerical and computational methods that can be used to quickly solve the Poisson–Boltzmann equation, which describes the electrostatic interactions of charged molecules in a continuous dielectric medium (similar to the Born and Debye–Hückel models). These methods have been used to examine the electrostatic interactions of complex molecules (proteins) with different charge distributions. The graphic representation of the results can be used to examine the surface charge of proteins and nucleic acids involved in binding metals and polar solutes. These methods may prove useful in examining the interactions of metals with model colloids and organic ligands in natural waters.

4.6 Physical Properties of Seawater

Knowledge of ionic interactions in seawater can also affect the physical properties of ocean waters. Since the composition of natural waters can be quite different (see Figure 4.34 and Figure 4.35), it would be useful to have models that can be used to describe how the ionic components affect the physical properties of seawater. In recent years, a great deal of

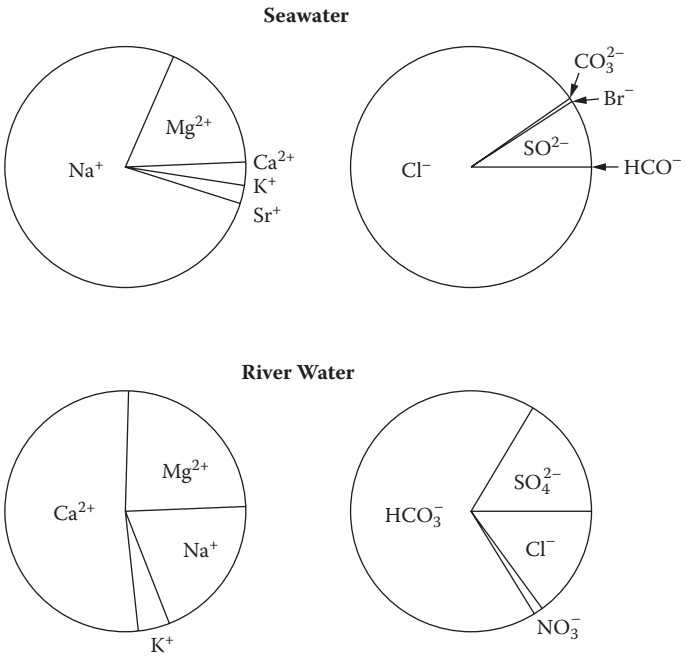

FIGURE 4.34
Comparison of the composition of the major components in seawater and river water .

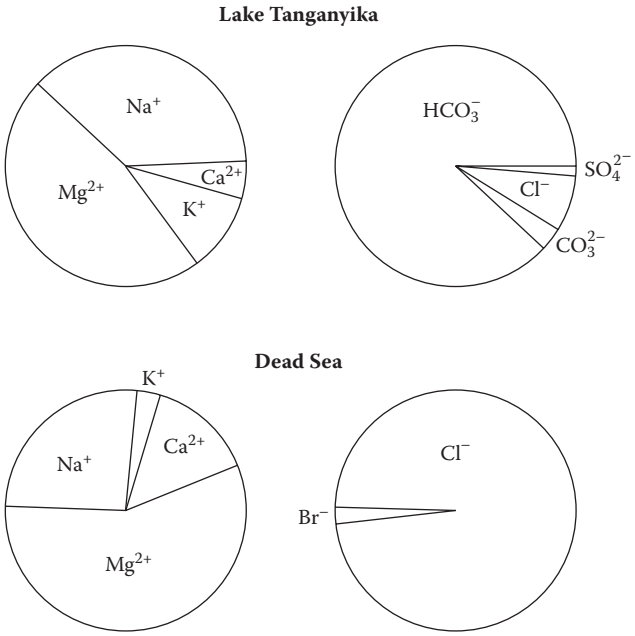

FIGURE 4.35
Comparison of the composition of Lake Tanganyika and Dead Sea waters.

progress has been made in interpreting and modeling the physical–chemical properties of mixed electrolyte solutions. These models have been used to estimate the properties of seawater using known properties for sea salts. This is done by using the apparent molal properties ϕ of the solution. The apparent molal property is related to the change that occurs when a salt is added to water. The apparent molal property is defined by

$$\phi = \Delta\rho/n = (P - P^0)/n \tag{4.92}$$

where n is the number of moles of salt added, P is the property of the solution, and P^o is the property of water. The major reason the apparent molal property is useful is the fact that it is nearly additive for a mixture. The additivity, called Young's rule, is given by

$$\phi = \Sigma N_i \phi_i \tag{4.93}$$

where $N_i = n_i/nT$ is the mole fraction of electrolyte i in the mixture, and ϕ_i is the molal property of i at the ionic strength of the mixture. In terms of the ionic components of a mixed electrolyte solution, the equation becomes

$$\phi = \Sigma_M \Sigma_X E_M E_X \phi(MX) \tag{4.94}$$

where E_M and E_X are the equivalent fractions of cations M and anions X, and $\phi(MX)$ is the apparent property of electrolyte MX at the ionic strength of the mixture. For the major components of seawater, this sum can be made three ways:

1. $\phi(SW) = E_{Na}E_{Cl}\phi(NaCl) + E_{Mg}E_{SO_4}\phi(MgSO_4)$
2. $\phi(SW) = E_{Na}E_{SO_4}\phi(Na_2SO_4) + E_{Mg}E_{Cl}\phi(MgCl_2)$
3. $\phi(SW) = E_{Na}E_{Cl}\phi(NaCl) + E_{Na}E_{SO_4}\phi(MgSO_4) + E_{Mg}E_{Cl}\phi(MgCl_2) + E_{Mg}E_{SO_4}\phi(MgSO_4)$.

Experimentally, it is found that the third summation works best because it considers the weighted sum of all the possible cation–anion interactions. These plus–minus interactions represent the major ionic interactions that occur in the mixture. Once the ϕ for the mixture is estimated, a given physical property can be determined from

$$P = P^o + \phi\, e_T \tag{4.95}$$

where e_T is the total equivalent of the ionic components of the mixture. Comparisons of the measured and calculated densities of seawater using this simple additivity method are shown in Table 4.14. The calculated values are in good agreement with the measured values. At higher ionic strengths (e.g., brines), the estimates are not as reliable.

These larger errors at higher ionic strengths are related to excess mixing parameters. These excess mixing properties can be studied by mixing two electrolyte solutions at a constant ionic strength. For the mixing of the major sea salts, there are six possible mixtures that can be given in Figure 4.36. The salts around the sides of this diagram have either a common cation or anion during mixing. A number of studies by Young (1951) have shown that the excess mixing properties ΔP_{EX} follow some simple rules:

TABLE 4.14

Differences in the Measured and Calculated Densities (g cm^{-3}) of Seawater at 25°C

I	S	$\Delta\rho$, 10^6
0.11	5	–4
0.21	10	–7
0.31	15	–7
0.41	20	–5
0.51	25	1
0.61	30	11
0.72	35	24

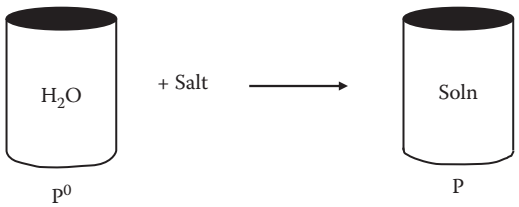

FIGURE 4.36
Formation of a solution from the addition of a salt to water.

1. The values of ΔP_{EX} in dilute solutions are not very large and can be assumed to be zero. This leads to the additivity of ϕ, or Young's (1951) first rule.
2. The values of ΔP_{EX} for mixtures with a common anion or cation are not strongly affected by the common ion. For example, the ΔP_{EX} for mixing NaCl and KCl is nearly the same as that for mixing NaBr and KBr.

$$\Delta P_{EX}(\text{NaCl-KCl}) = \Delta P_{EX}(\text{NaBr-KBr}) \tag{4.96}$$

   Since this mixing process is largely related to cation–cation and anion–anion interactions, as a first approximation, plus–plus and minus–minus interactions are independent of the other ions in the solutions.
3. The third rule is called the cross-square rule and is given by

$$\Sigma = \Sigma X \tag{4.97}$$

   which states the sum of the excess mixing properties around the sides of the diagram given is equal to the sum of the excess properties of the cross mixtures. For the major sea salts, this gives

$$\begin{aligned}&\Delta P_{EX}(\text{NaCl} + \text{Na}_2\text{SO}_4) + \Delta P_{EX}(\text{MgCl}_2 + \text{MgSO}_4) + \Delta P_{EX}(\text{NaCl} + \text{MgCl}_2)\\ &+ \Delta P_{EX}(\text{MgSO}_4 + \text{Na}_2\text{SO}_4) = \Delta P_{EX}(\text{NaCl} + \text{MgSO}_4) + \Delta P_{EX}(\text{Na}_2\text{SO}_4 + \text{MgCl}_2)\end{aligned} \tag{4.98}$$

This simplifies the estimation of the ΔP_{EX} for a complicated mixture like seawater. The addition to Young's simple rule gives

$$\phi = \Sigma_M \Sigma_X E_M E_X \varphi(MX) + \Delta P_M/e_T \tag{4.99}$$

where $\Delta P_M/e_T$ is given by

$$\begin{aligned}\Delta P_M/e_T = (e_T/4)[&\Sigma E_X E_N E_X (Z_M + Z_X)(Z_N + Z_X)\,\Delta P(M, N)^X\\ &+ E_X E_N E_M (Z_M + Z_X)(Z_M + Z_Y)\,\Delta P(X, Y)^M]\end{aligned} \tag{4.100}$$

where Z_i is the absolute charge on ion i, $\Delta P(M,N)^X$ is the excess mixing properties for MX + NX, and $\Delta P(X,Y)$ is the excess mixing properties for NX + NY. This equation attempts to account for cation–cation and anion–anion interactions in the mixture by neglecting triplicate interaction (Young's third rule). Since the values of ΔP_{EX} are symmetrical around the ionic strength fraction (see Figure 4.37), the values of ΔP needed to estimate ΔP_M for the mixture can be the value near y = 0.5.

For a seawater solution, the value of $\Delta P_M/e_T$ is given by

$$\begin{aligned}\Delta P_M/e_T = (e_T/4)[&E_{Na}E_{Mg}E_{Cl}(Z_{Na}+Z_{Cl})(Z_{Mg}+Z_{Cl})\Delta P(\text{NaCl}+\text{MgCl})\\ &+E_{Na}E_{Mg}E_{SO_4}(Z_{Na}+Z_{SO_4})(Z_{Mg}+Z_{SO_4})\Delta P(\text{Na}_2\text{SO}_4+\text{MgSO}_4)\\ &+E_{Cl}E_{SO_4}E_{Na}(Z_{Na}+Z_{Cl})(Z_{Na}+Z_{SO_4})\Delta P(\text{NaCl}+\text{Na}_2\text{SO}_4)\\ &+(Z_{Mg}+Z_{Cl})(Z_{Mg}+Z_{SO_4})\Delta P(\text{MgCl}_2+\text{MgSO}_4)]\end{aligned} \tag{4.101}$$

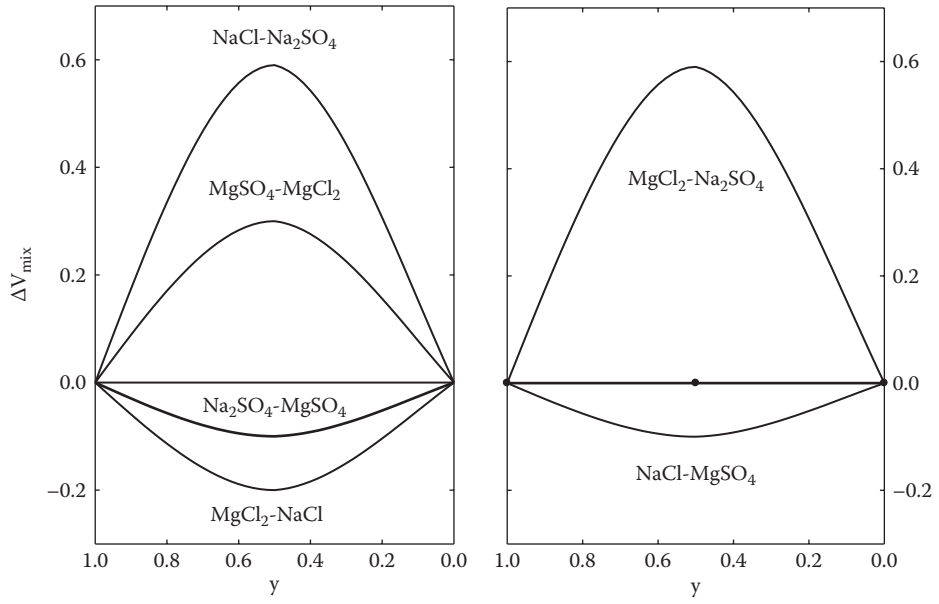

FIGURE 4.37
Values for the volume of mixing the major sea salts versus the ionic strength fraction Y_3.

TABLE 4.15

Comparison of the Measured and Calculated Densities (g cm^{-3}) of Red Sea Brines Diluted with Water at 25°C

I	Measured $(\rho - \rho_0)10^3$	$\Delta\rho$, 10^6
0.470	18.360	–18
1.218	46.136	81
1.752	64.986	134
2.614	93.984	199
3.561	123.974	211
4.234	144.207	235
5.333	175.610	297
6.124	197.281	444

The importance of using these mixing terms to estimate the physical properties of a mixture is demonstrated in Table 4.15. The estimated densities are in better agreement with the measured values when the excess mixing terms are considered (ΔV_{EX} in this case, the volume of mixing the major sea salts).

For most physical properties in dilute solutions, the estimates can be made without the ΔP_{EX} term. The apparent molal property, like the volume, can be considered to be made up of two major components: an ion–water interaction term and an ion–ion interaction term. The physical property of seawater is given by

$$P = P^o + \Sigma \text{ ion-water} + \Sigma \text{ ion-ion} \tag{4.102}$$

where the term Σ ion-water is the weighted sum of the ion–water interactions of the major ions of the solution, and Σ ion-ion is the weighted sum of the ion–ion interactions of the major ions of the solution. The first term is completely additive and is related to ion–water interactions in pure water. The second term is related to all the possible ion–ion interactions in the solutions. These interactions can be estimated using the Pitzer approach and are related to

$$\Sigma \text{ ion-ion} = \text{DH} + \Sigma \text{ Binary} + \Sigma \text{ Ternary} \tag{4.103}$$

where the binary interactions are related to β^0, β^1, and θ, and the ternary interactions are related to Cϕ and Ψ. Thus, the use of Young's rule is embodied in the formulation of the Pitzer equations. The β^0, β^1, and C^ϕ terms are for all the binary components (NaCl, Na_2SO_4, $MgCl_2$, etc.), and the θ and Ψ terms are for all the ternary mixtures (NaCl + Na_2SO_4, NaCl + $MgCl_2$, etc.). This general approach, although somewhat complicated, can account for all the possible interactions in a stepwise manner.

References and Further Reading

Ball, P., *H_2O: A Bibliography of Water*, Weidenfeld and Nicolson, London (1999).

Barber, R.T., and Ryther, J.H., Organic chelators: factors affecting primary production in the Cromwell Current upwelling, *J. Exp. Mar. Biol. Ecol*., 3, 191 (1969).

Bernal, J.D., and Fowler, R.H., A theory of water and ionic solution, with particular reference to hydrogen and hydroxyl ions, *J. Chem. Phys.*, 1, 515 (1933).

Bjerrum, N., Ion association. I. Influence of ionic association on the activity of ion at moderate degree of association, *Kgl. Danske Videnskab Selskab. Mat. Fys. Medd*., 7, 1 (1926).

Born, M., Volumes and heats of hydration of ions, *Z. Physik.*, 1, 45 (1920).

Byrne, R.H., Kump, L.R., and Cantrell, K.J., The influence of temperature and pH on trace metal speciation in seawater, *Mar. Chem*., 25, 163 (1988).

Danford, M.D., and Levy, H.A., The structure of water at room temperature, *J. Am. Chem. Soc*., 84, 3965 (1962).

Davis, C., and Litovitz, T., Two-state theory of the structure of water, *J. Chem. Phys*., 42, 2563 (1965).

Debye, P., and Hückel, E., Zür Theorie der Electrolyte. I. Gefrierpunkterniedindung und verwandte Erscheinungen, *Phys. Z.*, 24, 185 (1923).

Drude, P., and Nernst, W., Electrostriction of free ions., *Z. Phys. Chem. (Frankfort*), 15, 9 (1884).

Du, Q., Superfine, R., Freysz, E., and Shen, Y.R., Vibrational spectroscopy of water at the vapor/water interface, *Phys. Rev. Lett.*, 70, 2313 (1993).

Eigen, M., Proton transfer, acid-base catalysis and enzymatic hydrolysis, I. Elementary processes, *Angew. Chem. Int. Ed*., 3, 1 (1964).

Eucken, A., *Z. Elektrochem*, 53, 102 (1949).

Eyring, H., Ree, T., and Hirai, N., Significant structures in the liquid state, *Proc. Natl. Acad. Sci.*, 44, 683 (1958).

Falk, M., and Kell, G.S., Thermal properties of water: discontinuities questioned, *Scienc*e, 155, 1013 (1966).

Frank, H.S., and Quist, A.S., Pauling's model and the thermodynamic properties of water, *J. Chem. Phys*., 34, 604 (1961).

Frank, H.S., and Wen, W.Y., Structural aspects of ion–solvent interactions in aqueous solutions, *Discussions Faraday S*oc., 24, 133 (1957).

Franks, F., *Water: A Comprehensive Treatise*, *the Physics and Physical Chemistry of Water*, Plenum Press, New York, 596 (1972).
Friedman, H.L., Mayer's ionic solution theory applied to electrolyte mixtures, *J. Chem. Phys*., 32, 1134 (1960).
Fuoss, R.M., Ionic association III. The equilibrium between ion pairs and free ions, *J. Am. Chem. Soc*., 80, 5059 (1958).
Garrels, R.R., and Thompson, M.E., A chemical model for seawater at 25°C and one atmosphere total pressure, *Am. J. Sci*., 260, 57 (1962).
Goldberg, E., Minor elements in sea water, Chapter 5, *Chemical Oceanography*, Vol. 1, Riley, J.P., and Skirrow, G., Eds., Academic Press, New York, 163–196 (1965).
Guggenheim, E.A., Thermodynamic properties of aqueous solutions of strong electrolytes, *Philos. Mag.,* 19, 588 (1935).
Guthrie, M., Urquidi, J., Tuld, S.A., Benmore, S.J., Klug, D.D., and Neuefeind, J., Direct structural measurements of relaxation processes during transformations in amorphous ice, *Phys. Rev. B*, 68, 184110 (2003).
Hansson I., A new set of acidity constants for carbonic acid and boric acid in seawater, *Deep-Sea Res.,* 20, 461 (1973).
Honig, A., and Nicholls, A., Classical electrostatics in biology and chemistry, *Science,* 268, 1144 (1995).
Horne, R.A., *Water and Aqueous Solutions*, John Wiley and Sons, NY, 837 pp. (1972).
Kester, D.R., Byrne, R.H., and Liang, Y.J., Redox reactions and solution complexes of iron in marine systems, *ACS Symp.,* 18, 56–79 (1975).
Kramer, C.J.M., and Duinker, J.C., *Complexation of Trace Metals in Natural Waters*, Martinus Nijhoff/W. Junk, The Hague (1984).
Kuo, L.-F., and Mundy, C.J., An *ab initio* molecular dynamics study of the aqueous liquid–vapor interface, *Science*, 303, 658 (2004).
Laidler, K.J., and Pegis, C., The influence of dielectric saturation on the thermodynamic properties of aqueous ions, *Proc. Roy. Soc., London*, A241, 80 (1957).
Latimer, W.M., Pitzer, K.S., and Slansky, C.M., The free energy of hydration of gaseous ions, and absolute potential of the normal calomel electrode, *J. Chem. Phys*. 7, 108 (1939).
Millero, F.J., Thermodynamic models for the state of metal ions in seawater, Chapter 17, *The Sea, Ideas and Observations*, Vol. 6, Goldberg, E.D., Ed., Wiley, New York, 653–693 (1977).
Millero, F.J., Effects of pressure and temperature on activity coefficients, Chapter 2, *Activity Coefficients in Electrolyte Solutions*, Vol. 2, Pytkowicz, R.M., Ed., CRC Press, Boca Raton, FL, 63–151 (1979).
Millero, F.J., The stability constants for the formation of rare earth inorganic complexes as a function of ionic strength, *Geochim. Cosmochim. Acta*, 56, 3123 (1992).
Millero, F.J., Influence of pressure on chemical processes in the sea, Chapter 43, *Chemical Oceanography*, Vol. 8, 2nd ed., Riley, J.P., and Chester, R., Eds., Academic Press, New York, 1–88 (1983).
Millero, F.J., The activity of metal ions at high ionic strengths, in *Complexation of Trace Metals in Natural Waters*, Kramer, C.J.M., and Duinker, J.C., Eds., Martinus Nijhoff/W. Junk, The Hague, 187–200 (1984).
Millero, F.J., *The Physical Chemistry of Natural Waters*, Wiley-Interscience, New York (2001).
Millero, F.J., and Hawke, D.H., Ionic interactions of divalent metals in natural waters, *Mar. Chem*., 40, 19 (1992).
Millero, F.J., and Schreiber, D.R., Use of the ion pairing model to estimate activity coefficients of the ionic components of natural waters, *Am. J. Sci*., 282, 1508 (1982).
Millero, F.J., Yao W., and Aicher, J., The speciation of Fe(II) and Fe(III) in seawater, *Mar. Chem.*, 50, 21 (1995).
Millero, F.J., Seawater as a multicomponent, in *The Sea, Ideas and Observation*s, Vol. 5, Goldberg, E.D., Ed., Wiley-Interscience, New York, 3–80 (1974).
Miyazaki, M., Fujii, A., Ebata, T., and Mikami, N., Infrared spectroscopic evidence for protonated water clusters forming nanoscale cages, *Science,* 303, 1134 (2004).
Morel, F.M.M., *Principles of Aquatic Chemistry*, Wiley, New York (1983).

Nemethy, G., and Scheraga, H.A., Structure of water and hydrophobic bonding in proteins. I. A model for the thermodynamic properties of liquid water, *J. Chem. Phys*., 36, 3382 (1962).
Ohmine, L., and Tanaka, H., Fluctuations, relaxations and hydration in liquid water: hydrogen-bond rearrangement dynamics, *Chem. Rev*., 93, 2545 (1993).
Pauling, L., *The Nature of the Chemical Bond*, 3rd ed., Cornell Press, Ithaca, NY, Chapter 5 (1960).
Pitzer, K.S., *Activity Coefficients in Electrolyte Solutions*, 2nd ed., CRC Press, Boca Raton, FL (1991).
Pople, J.A., Molecular association in liquids. II. A theory of the structure of water, *Proc. Roy. Soc. London*, **A**205, 163 (1951).
Pratt, L.R., Ed., Thematic issue: water, *Chem. Rev*., 102 (2002).
Raymond, G.L. et al., Hydrogen-bonding interactions at the vapor/water interface investigated by vibrational sum-frequency spectroscopy of HOD/H_2O/D_2O mixtures and molecular dynamics, *J. Phys. Chem*., 107, 546 (2003).
Robinson, R.A., and Stokes, R.H., *Electrolyte Solutions*, 2nd ed., Butterworths, London, 455 (1959).
Rowland, H.A., On the mechanical equivalent of heat with subsidiary researches on the variation of the mercurial from the air thermometer and on the variation of the specific heat of water, *Proc. Am. Acad. Arts Sci.*, 15, 75 (1880).
Rowlinson, J.S., The second virial coefficients of polar gases,*Trans Faraday Soc*., 45, 974 (1949).
Ruan, C.-Y, Lobastov, V.A., Vigliotti, F., Chen, S., and Zewail, A.H., Ultrafast electron crystallography of interfacial water, *Science*, 304, 80 (2004).
Samoilov, O.Y., *Structure of Aqueous Electrolyte Solutions*, Ives, D.J., Trans., Consultants Bureau, New York (1965).
Searcy, J.Q., and Fenn, J.B., Clustering of water on hydrated protons in a supersonic free jet expansion, *J. Chem. Phys*., 61, 5282 (1974).
Shin, J.W., Hammer, N.I., Diken, E.B., Johnson, M.A., Walters, R.S., Jaeger, T.D., Duncan, M.A., Christie, R.A., and Jordan, K.D., Infrared signature of structures associated with the $H^+(H_2O)n$ (N = 6 to 27) clusters, *Science*, 304, 1137 (2004).
Soper, A.K., Ed., The structure of the first coordination shell in liquid water, *Chem. Phys*., 258 (2000).
Steeman-Nielson, E., and Wium-Anderson, S., Copper ions as poison in the sea and fresh water, *Mar. Biol*., 6, 93 (1970).
Stewart, G.W., X-ray diffraction water. The nature of molecular association, *Phys. Rev.*, 37, 9 (1931).
Stumm, W., and Brauner P.A., Chemical speciation, Chapter 3, *Chemical Oceanography*, Vol. 1, 2nd ed., Riley, J.P., and Skirrow, G., Eds., Academic Press, New York, 173–239 (1975).
Stumm, W., and Morgan, J.J., *Aquatic Chemistry*, Wiley, New York (1970).
Tammann, G.H., Uber die Beziehungen zwischen den inneren Kraften und Eigenschaften der Lösungen, *Z. Physik. Chem.,* 17, 620–636 (1895).
Turner, D.R., Whitfield, M., and Dickson, A.G., The equilibrium speciation of dissolved components in freshwater and seawater at 25°C and 1 atm pressure, *Geochim. Cosmochim. Acta*, 45, 855 (1981).
van den Berg, C.M.G., Electroanalytical chemistry of sea-water, Chapter 51, *Chemical Oceanography*, Vol. 9, 2nd ed., Riley, J.P., Ed., Academic Press, New York, 198–246 (1989).
Wall, T.T., and Horning, D.F., Raman intensities of HDO and structure in liquid water, *J. Chem. Ph*ys., 43, 2079 (1965).
Wernet, P., Nordlund, D., Bergmann, U., et al., The structure of the first coordination shell in liquid water, *Science,* 304, 995 (2004).
Whitfield, M., Sea water as an electrolyte solution, Chapter 2, *Chemical Oceanography*, Vol. 1, 2nd ed., Riley, J.P., and Skirrow, G., Eds., Academic Press, New York, 44–171 (1975).
Wicke, E., Structure formation and molecular mobility in water and in aqueous solutions, *Angew. Chem*., 5, 106–122 (1966).
Wirth, H.E., The problem of the density of seawater, *J. Mar. Res*., 3, 230 (1940)
Young, T.F., Recent developments in the study of interactions between molecules and ions, and of equilibrium in solutions, *Rec. Chem. Progr.,* 12, 81 (1951).
Zundel, G., *Z. Phys. Chem.* 58, 225 (1974).
Zwier, T.S., Enhanced: the structure of protonated water clusters, *Science,* 304, 1119 (2004).

5

Atmospheric Chemistry

5.1 Introduction

In recent years, there has been an increasing interest in atmospheric chemistry. Since the oceans are in intimate contact with the atmosphere and may act as a source or sink for atmospheric gases, it is appropriate to briefly examine this area of science. The early interest in the atmosphere was related to the formation of photochemical smog in various cities. Smog is formed by complicated interactions of unburned hydrocarbons from automobiles and power plants and nitrogen oxides. The sun provides the necessary energy to furnish reactive species. More recently, interest in atmospheric chemistry has focused on the formation of acid rain (HNO_3 and H_2SO_4) from the oxidation of NO_X and SO_2 gases that result from the oxidation of fossil fuels. The decrease in the ozone layer resulting from the use of chlorofluorohydrocarbons (CFCs) has also prompted new interest in atmospheric chemistry. Interest has also been focused on the increasing concentration of gases that can absorb infrared (IR) energy. These gases (CO_2, CH_4, etc.) contribute to the warming of the atmosphere or the so-called greenhouse effect.

Since many of the chemical reactions of interest occur near the surface of the earth, it is important to briefly examine the various layers of the atmosphere. The atmosphere can be divided into four layers (see Figure 5.1): the troposphere (0 to 10 km), the stratosphere (10 to 50 km), the mesosphere (50 to 100 km), and the thermosphere (100 to 1000 km). These layers are marked by changes in the temperature of the atmosphere. From the surface to 10 km, the temperature decreases to a minimum at the tropopause. In the stratosphere, the temperature increases to a maximum at the stratopause. In the mesosphere, the temperature decreases to a minimum at the mesopause. In the thermosphere, the temperature increases again as the atmosphere diminishes. The changes in the temperature of the atmosphere are related to the concentration of gases and the chemical reactions that occur at various levels of the ocean. The height above the surface of the earth is similar to the depth of water in the oceans. Since both fluids are compressible, changes in the height or depth can change the temperature. The effect is easier to characterize in the atmosphere since the gases behave in a near-ideal manner and can be approximated using the ideal gas equation. The change in pressure with height z is related to the density ρ and acceleration of gravity g ($dp/dz = -\rho z$).

For an ideal gas, the change in the adiabatic temperature with height can be determined ($dT/Dz = -Mg/Cp$, where M is the molecular weight and Cp is the heat capacity). This equation gives a change in the temperature of –9.8°/km. The decrease in the temperature of the atmosphere from the surface to the tropopause is due to this adiabatic cooling. The increase in the temperature between the stratosphere and the mesosphere, which goes through a maximum at the stratopause, is the result of the adsorption of energy by ozone

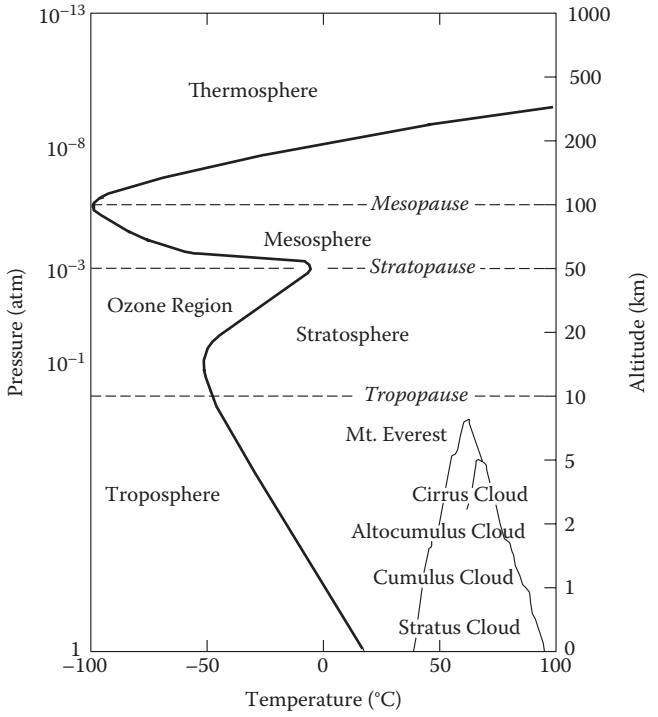

FIGURE 5.1
Changes in the temperature mark four layers of the atmosphere.

molecules (O_3). As the atmospheric gases decrease above the mesopause, the temperature increases into outer space.

Chemical reactions between the major constituents of the atmosphere occur at slow rates. The formation of active species occurs because of the influence of light and causes a number of rapid reaction chains. The chemistry of the lower atmosphere is often referred to as tropospheric photochemistry since it is driven by the absorption of photons.

The flux of solar photons as a function of wavelength is shown in Figure 5.2. Most of the radiation below 290 nm does not reach the troposphere. Photons with wavelengths shorter than 240 nm are absorbed by O_2 and N_2 molecules in the thermosphere. This results in the formation of ozone, O_3:

$$O_2 + h\upsilon \rightarrow 2\,O\cdot \tag{5.1}$$

$$O_2 + O + M \rightarrow O_3 + M \tag{5.2}$$

where M represents another molecule of oxygen or nitrogen that is unchanged in the reaction. The concentration of O_3 formed in this manner peaks in the lower stratosphere (see Figure 5.3). The ultraviolet (UV) radiation can also stimulate dissociation of O_3:

$$O_3 + h\upsilon \rightarrow O_2 + O(^1D) \tag{5.3}$$

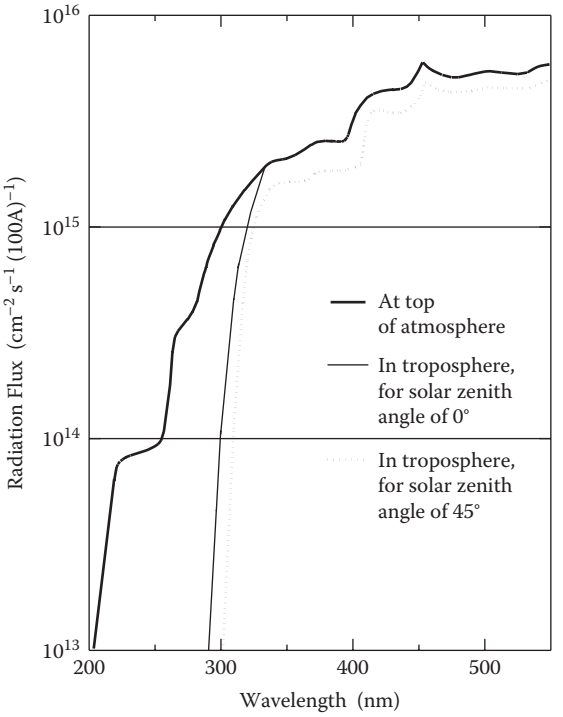

FIGURE 5.2
The solar radiation that reaches various layers in the troposphere. Most solar radiation below 290 nm does not reach the troposphere.

This reaction is responsible for the absorption of light between 240 to 300 nm. The electronically excited oxygen O(^{1}D) formed in the dissociation of O_3 is responsible for the formation of odd nitrogen radicals and odd hydrogen radicals:

$$N_2O + O(^1D) \rightarrow 2\ NO\cdot \tag{5.4}$$

$$H_2O + O(^1D) \rightarrow 2\ OH\cdot \tag{5.5}$$

More will be said about these reactions. The O_3 that is broken apart by photons forms oxygen atoms that quickly re-form O_3 by reactions with O_2. This leads to a steady-state buildup of O_3. The O_3 dies off when it collides with an O atom, forming two oxygen molecules:

$$O_3 + O \rightarrow 2\ O_2 \tag{5.6}$$

Other reactions that destroy O_3 in the stratosphere (such as reactions with atomic Cl) will be discussed further. The maximum in the concentration of ozone in the stratosphere can be attributed in the upper portion to the exponential decrease in O_2 and in the lower portion to the fall-off in the intensity of UV light as the solar light penetrates into the increasingly dense atmosphere.

Since the light reaching the troposphere has wavelengths above 300 nm, there is not enough energy available to break O–O bonds with strength of 120 kcal mol^{-1}. This means that O_2

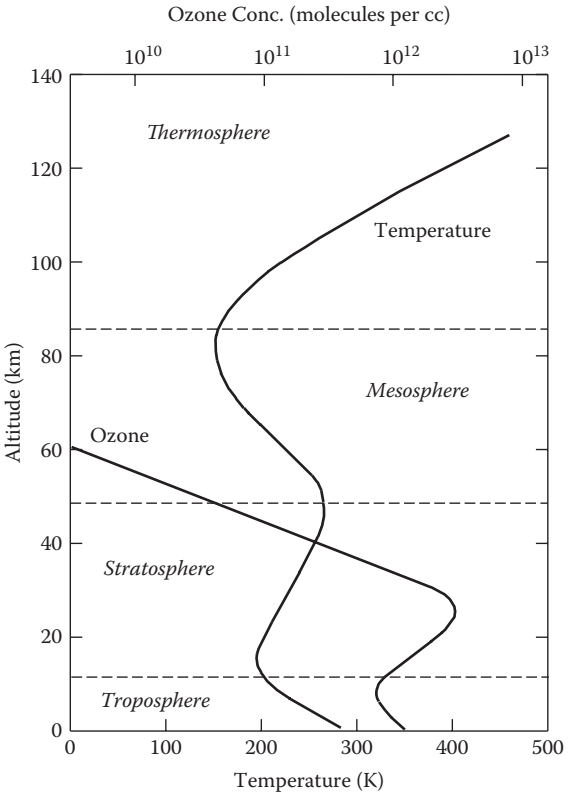

FIGURE 5.3
The concentration of ozone in various layers of the atmosphere.

cannot oxidize reduced gases in the troposphere. At one time, it was thought that O_3 and H_2O_2 were oxidizers in the troposphere. Now, the OH· radical is thought to be the oxidizer.

The production of OH· radicals is initiated by the photolysis of O_3. Ozone is present in the troposphere at concentrations from 10 to 100 ppb and has bond energy of 26 kcal mol^{-1}. Solar photons with wavelengths between 315 and 1200 nm can dissociate O_3 and produce an oxygen atom in its ground electronic state:

$$O_3 + h\upsilon\ (1200 > \lambda > 315\ nm) \rightarrow O_2 + O(^3P) \tag{5.7}$$

The $O(^3P)$ atom rapidly re-forms ozone by reaction with O_2 in a three-body reaction:

$$O(^3P) + O_2 + M \rightarrow O_3 + M \tag{5.8}$$

where M is N_2 or O_2. This sequence results in no net chemical effect. When ozone reacts with wavelengths shorter than 315 nm, an electronically excited oxygen atom is produced:

$$O_3 + h\upsilon\ (\lambda < 315\ nm) \rightarrow O(^1D) + O_2 \tag{5.9}$$

The $O(^1D)$-to-$O(^3P)$ transition is forbidden and results in a relatively long lifetime for $O(^1D)$ of 100 s. The $O(^1D)$ most often collides with N_2 or O_2 (M):

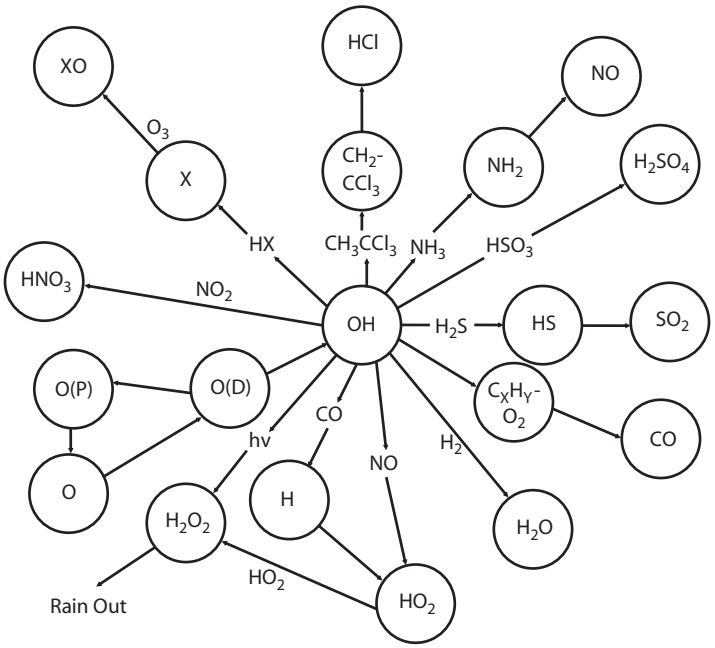

FIGURE 5.4
The photochemical control of OH· radicals on trace gases.

$$O(^1D) + M \rightarrow O(^3P) + M \tag{5.10}$$

This ultimately reacts with O_2 to form O_3, which also results in no net chemical change. Occasionally, $O(^1D)$ collides with water to generate two hydroxyl radicals:

$$O(^1D) + H_2O \rightarrow 2\ OH\cdot \tag{5.11}$$

This reaction sequence is the primary source of hydroxyl radicals in the troposphere. The OH· radical formed in this manner is thought to control the concentration of many trace gases (see Figure 5.4).

The removal of OH· from the atmosphere results from the reactions

$$CO + OH\cdot \rightarrow CO_2 + H\cdot \tag{5.12}$$

$$CH_4 + OH\cdot \rightarrow CH_3 + H_2O \tag{5.13}$$

Both the H· and the ·CH_3 radicals combine rapidly with O_2 to form hydroperoxyl (HO_2) and methyperoxyl (CH_3O_2) radicals. The hydroperoxyl radical, however, can regenerate OH· radicals:

$$HO_2 + NO \rightarrow NO_2 + OH\cdot \tag{5.14}$$

$$HO_2 + O_3 \rightarrow 2O_2 + OH\cdot \tag{5.15}$$

It can also lead to the chain termination:

$$HO_2 + OH\cdot \rightarrow H_2O + O_2 \tag{5.16}$$

$$HO_2 + HO_2 \rightarrow H_2O_2 + O_2 \tag{5.17}$$

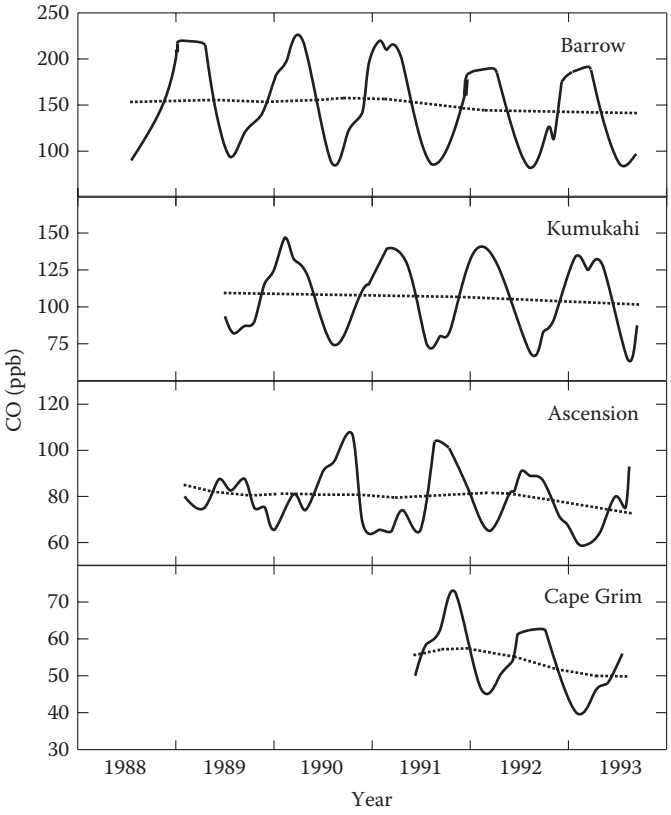

FIGURE 5.5
The changes in the concentration of CO in the atmosphere at different locations as a function of time.

The hydrogen peroxide (H_2O_2) is removed in rain. The chemistry of the methyperoxyl radical (CH_3O_2) is quite complicated, and not all of its reactions are known at present. Mathematical models have been used to simulate these reactions, and the average OH· concentration is about 2 to 20 × 10^5 radicals per cubic centimeter, with the highest levels in the tropics. Model calculations predict that about 20% more OH· radicals should be found in the Southern Hemisphere. This is caused by the higher CO concentrations in the Northern Hemisphere. Direct measurements of OH· radicals in the atmosphere are difficult to make because of their low concentration and high reactivity. The largest loss of the OH· radical in the troposphere is the oxidation of CO, which is controlled by the concentration of CO. The distributions of CO shown in Figure 5.5 have been measured as a function of time in a number of locations (Novelli et al., 1994). The levels range from 45 to 250 ppb, decreasing from the north to the south. The levels are highest in the late winter and early spring and decrease in the summer.

Over recent years, the CO appears to have decreased in the northern latitudes by 7.3 ppb yr^{-1} and in the southern latitudes by 4.2 ppb yr^{-1}. This recent decrease is opposite to the 1 to 2% increase that has occurred in the Northern Hemisphere over the past 30 years. The input of CO into the atmosphere is dominated by fossil fuel combustion, industrial

emissions, biomass burning, and oxidation of CH_4 and nonmethane hydrocarbons. The reaction with OH· accounts for 90 to 95% of the sinks. This decrease cannot be fully explained as the result of more efficient use of fossil fuels. It may be related to higher levels of OH· radicals in the atmosphere or possibly caused by the decrease of O_3 in the stratosphere from the eruption of Mount Pinatubo in June 1991. The decrease in O_3 may result in an increase in the UV radiation reaching the troposphere and increased production of OH· radicals from the photolysis of O_3. A number of other factors can influence the sources and sinks of CO. Further measurements are needed to confirm the downward trend. It is interesting to note that the decreases of CO_2, methane, and nitrous oxide also showed a slowdown in their increase beginning in 1991, while the input of oxygen showed an increase. Although these results may be caused by independent effects, they point out how small changes in the conditions in the atmosphere can lead to dramatic changes in the concentrations of gases.

5.1.1 Composition of the Atmosphere

The atmosphere is composed of major gases (N_2, O_2, Ar, H_2O, and CO_2 at mole fractions); minor gases (Ne, He, CH_4, and CO at parts per million); and a number of trace gases (O_3, NO, N_2O, and SO_2 at parts per billion; CCl_2F_2, CF_4, and NH_3 at parts per trillion); and radicals such as OH· as atoms or molecules per cubic centimeter. In addition to gases, the atmosphere also has condensed phases (clouds, aerosols) that contain numerous compounds (H_2SO_4, HNO_3, etc.). The mole fractions of the major conservative gases of the atmosphere are given in Table 5.1. The errors (±) of the mole fractions reflect the constancy and precision of the composition. The compositions of some minor gases in the atmosphere are given in Table 5.2. These gases originate from biological, industrial, and photochemical processes. The concentration of the minor gases varies according to variations in their industrial and biological sources.

The distributions of gases in the atmosphere are a function of their molecular weight and reactivity (Figure 5.6). High molecular weight gases (Xe, Kr) are concentrated near

TABLE 5.1

Abundance of the Major Conservative Atmospheric Gases

Gas	Mole Fraction in Dry Air (X_i)
N_2	0.78084 ± 0.00004
O_2	0.20946 ± 0.00002
Ar	$(9.34 \pm 0.01) \times 10^{-3}$
CO_2	$(3.5 \pm 0.1) \times 10^{-4}$
Ne	$(1.818 \pm 0.004) \times 10^{-5}$
He	$(5.24 \pm 0.004) \times 10^{-6}$
Kr	$(1.14 \pm 0.01) \times 10^{-6}$
Xe	$(8.7 \pm 0.1) \times 10^{-8}$

Source: Data from Kester, D.R. Dissolved gases other than CO_2, in *Chemical Oceanography*, 1975.

TABLE 5.2

The Composition of Minor Gases in the Atmosphere

Species	X_i Actual	Reliability	Source	Sink
CH_4	1.7×10^{-6}	High	Biog.	Photochem.
CO	$0.5 – 2 \times 10^{-7}$	Fair	Photo., anthr.	Photochem.
O_3	5×10^{-8} (clean) 4×10^{-7} (polluted) 10^{-7} to 6×10^{-6} (stratosphere)	Fair	Photo.	Photochem.
$NO + NO_2$	$10^{-8} – 10^{-12}$	Low	Lightning, anthr., photo.	Photochem.
HNO_3	$10^{-9} – 10^{-11}$	Low	Photo.	Rainout
NH_3	$10^{-9} – 10^{-10}$	Low	Biog.	Photo., rainout
N_2O	3×10^{-7}	High	Biog.	Photo.
H_2	5×10^{-7}	High	Biog., photo.	Photo.
OH	$10^{-15} – 10^{-12}$	Very low	Photo.	Photo.
HO_2	$10^{-11} – 10^{-13}$	Very low	Photo.	Photo.
H_2O_2	$10^{-10} – 10^{-18}$	Very low	Photo.	Rainout
H_2CO	$10^{-10} – 10^{-9}$	Low	Photo.	Photo.
SO_2	$10^{-11} – 10^{-10}$	Fair	Anthr., photo.	Photo., volcanic
CS_2	$10^{-11} – 10^{-10}$	Low	Anthr., biol.	Photo.
OCS	5×10^{-10}	Fair	Anthr., biol., photo.	Photo.
CH_3CCl_3	$0.7–2 \times 10^{-10}$	Fair	Anthr.	Photo.

the earth, while lighter gases (H_2, He) extend to the outer atmosphere. The distribution of gases in the atmosphere is related to their lifetimes. The atmospheric lifetimes vary from seconds to hundreds of years (see Figure 5.7). These lifetimes can be compared to interhemispheric mixing times of years to intrahemispheric mixing times of months. Water has the shortest lifetime in the atmosphere (6 to 15 days, from the equator to the polar regions). Gases such as methane and carbon monoxide that have continental sources have different distributions between the hemispheres because of their different lifetimes (see Figure 5.8). The long lifetime of methane (7 years) results in a nearly uniform distribution between hemispheres. The more reactive carbon monoxide (65 days) is concentrated near its sources in the north. The slow movement of gases between hemispheres is caused by the intertropical convergence zone (ITCZ). The ITCZ is caused by air rising near the equator. This prevents mixing across the two hemispheres and results in interhemispheric mixing times of 1 to 2 yr. The fast intrahemispheric mixing can be demonstrated by following the movement of dust and particles from the El Chichon volcanic eruption in 1982 (see Figure 5.9). The eruption occurred April 4 and moved completely around the Northern Hemisphere by April 25.

The concentrations of trace gases in the atmosphere are controlled by a complex combination of processes. Factors that affect the temporal and spatial variability of gases are the source (strength and variability) and sinks (mechanisms and variability) and lifetime. The variability close to the sources (polluted air) is dominated by the variations in the source (automobile traffic), while the variability in remote areas (over the oceans) is controlled by the sinks or lifetimes. The variability of the concentrations of trace gases is inversely related to the residence time. The concentrations of trace gases in the atmosphere are higher than would be expected based on thermodynamic calculations. The principal sources of these gases are

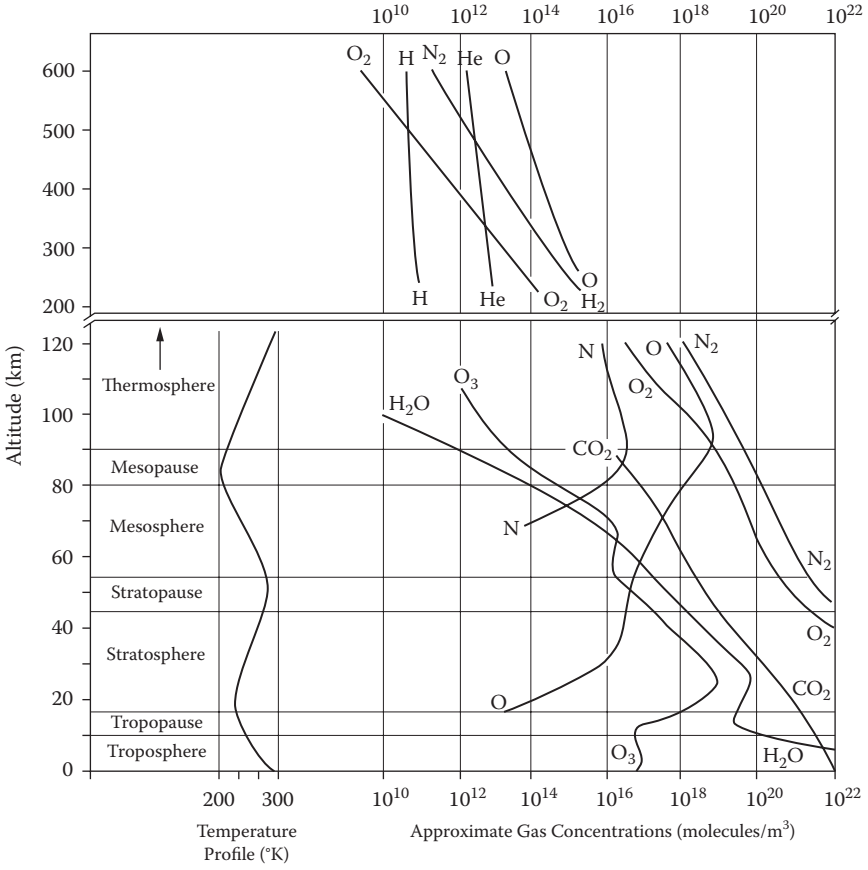

FIGURE 5.6
The approximate concentration of gases in the atmosphere as a function of altitude.

1. Biogenic (CH_4, NH_3, N_2O, H_2, CS_2, OCS)
2. Photochemical (CO, O_3, NO_2, HNO_3, H_2, OH, HO_2, H_2O_2, H_2CO)
3. Lightning (NO, NO_2)
4. Volcanic (SO_2)

The sinks of these gases are largely photochemical, with the exception of H_2O_2, HNO_3, and H_2SO_4, which are lost because of rainout.

All three phases of water exist in the atmosphere. The partial pressure of water under ordinary conditions is quite small (30 to 40 mbar, which corresponds to 25 gm^3). In typical clouds, little of this is in the condensed phase (stratus clouds have 0.3 to 1 gm^3).

These clouds are important since they deliver water from the atmosphere to the earth's surface, and they scavenge a number of materials from the air and deliver them to the surface. The formation of clouds is due to particles that act as cloud condensation nuclei (CCN). These particles must be small enough to have small settling velocities. They are soluble in water. In the past, it was thought that NaCl from sea spray was the main CCN. More recent studies indicate that sulfate particles (H_2SO_4 and $[NH_4]_2SO_4$) dominate. Following the growth of droplets by condensation, further growth occurs by collisions. Large water

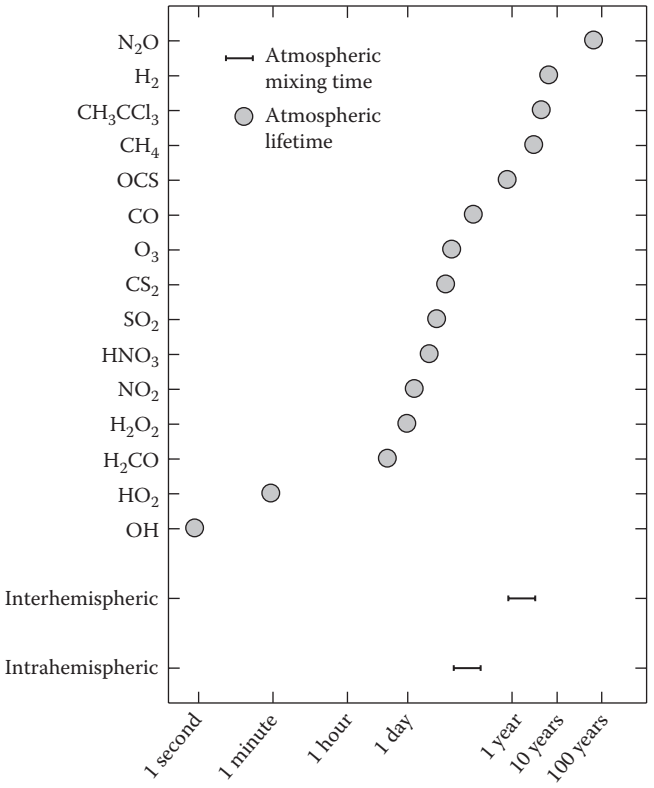

FIGURE 5.7
The atmospheric lifetimes of trace gases in the troposphere vary from 1 second to 100 years.

particles and heavy precipitation occur when ice is present (typically at temperatures of –5 to –20°C). Ice particles grow during collisions, and falling can result in the formation of hail (if frozen) or rain (if it melts). The compounds dissolved in CCN can be made up of dissolved gases (SO_2, NH_3, HCHO, H_2O_2, HNO_3) and salts ($[NH_4]_2SO_4$, NaCl, etc.). More will be said about sulfur compounds.

5.2 Nitrogen Gases

The reactive nitrogen species in the lower atmosphere (Table 5.3) are NO, NO_2, and HNO_3. These species are coupled by a series of reactions that cycle the various species. The reactions of these species are shown in Figure 5.10. The reaction of nitric oxide with hydroperoxyl radicals is of special interest:

$$NO + HO_2 \rightarrow NO_2 + OH\cdot \tag{5.18}$$

This reaction regenerates OH· from HO_2. It also leads to the generation of ozone by the following:

$$NO_2 + h\upsilon \rightarrow NO + O\cdot \tag{5.19}$$

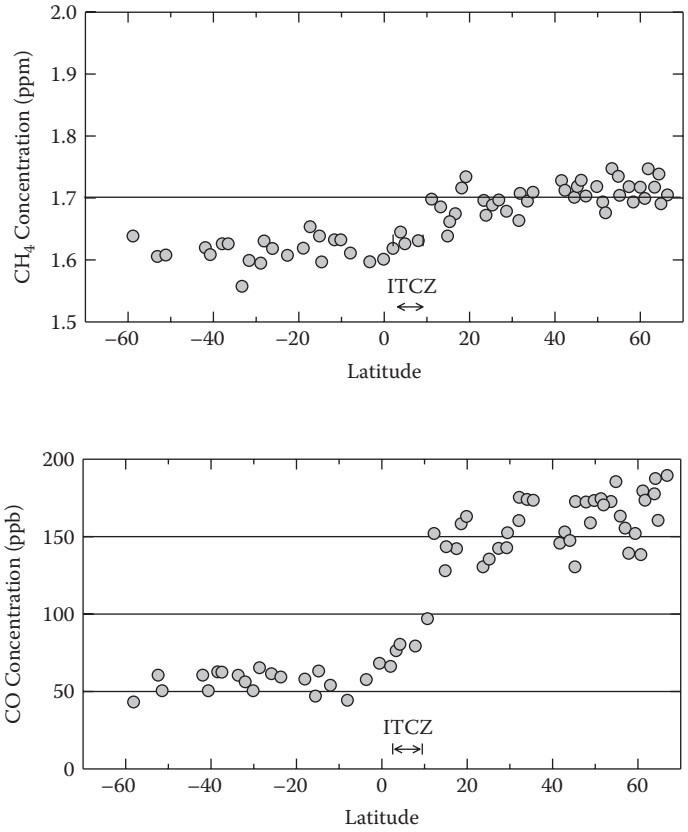

FIGURE 5.8
The distribution of methane (top) and carbon monoxide (bottom) between the hemispheres.

$$O\cdot + O_2 + M \rightarrow O_3 + M \tag{5.20}$$

where M = N_2 or O_2. The burning of fossil fuels (e.g., in automobiles) produces large amounts of CO and NO. The CO comes from incomplete combustion of hydrocarbons, and the NO is formed from N_2 and O_2 at high temperatures. As a result of the use of catalytic converters on cars and trucks, the output of these gases will be lessened (Jacoby, 2012). Although CO causes the OH· levels to decrease, NO can enhance the OH· levels, especially in remote areas. The nitrogen oxides are rapidly removed from the atmosphere as HNO_3, which is soluble in rainwater. It also can be attached to aerosols and particles and removed as dry deposition. The HNO_3 in rainwater is one of the components of acid rain. Although the importance of HNO_3 as a component of acid rain has been known to affect the pH of rain, recent work (see Figure 5.11) indicates that atmospheric sources of nitrate may also contribute to the eutrophication of the Chesapeake Bay.

The N_2O in the atmosphere can also reduce the stratospheric ozone (see Figure 5.12). Bacterially produced N_2O can break down at high altitudes by the absorption of light:

$$N_2O + h\upsilon \rightarrow N + NO \tag{5.21}$$

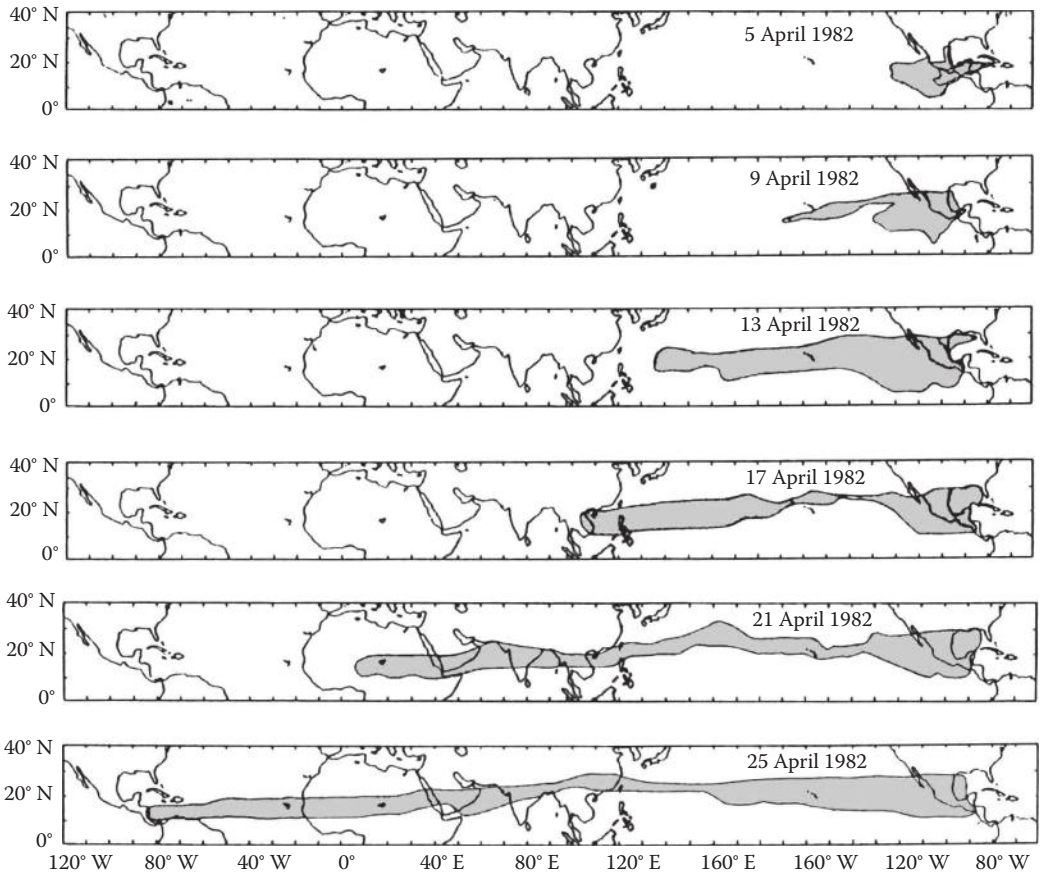

FIGURE 5.9
The movement of dust and particles in the Northern Hemisphere after the El Chichon volcano eruption.

TABLE 5.3

Concentration of Atmospheric Nitrogen Compounds

Species	Concentration	Source	Sink
N_2	78.9084%	Primitive volatile	Biological, lightning
NH_3	0–10 ppbv	Biological	Precipitation
RNH_2	—	Biological	Precipitation
N_2O	0.1–0.4 ppmv	Biological	Photolysis in stratosphere
NO	0–0.5 ppmv	Oxidation	HNO_3
NO_2	—	NO oxidation	HNO_3
HNO_2	—	OH + NO	Precipitation
HNO_3	—	OH + NO	Precipitation

Source: Data from Carlson, R.J., The atmosphere, in *Global Biogeochemical Cycles*, Butcher, S.S., Charleson, R.J., Orians, G.H., and Wolfe, G.V., Eds., Academic Press, New York, 1992.

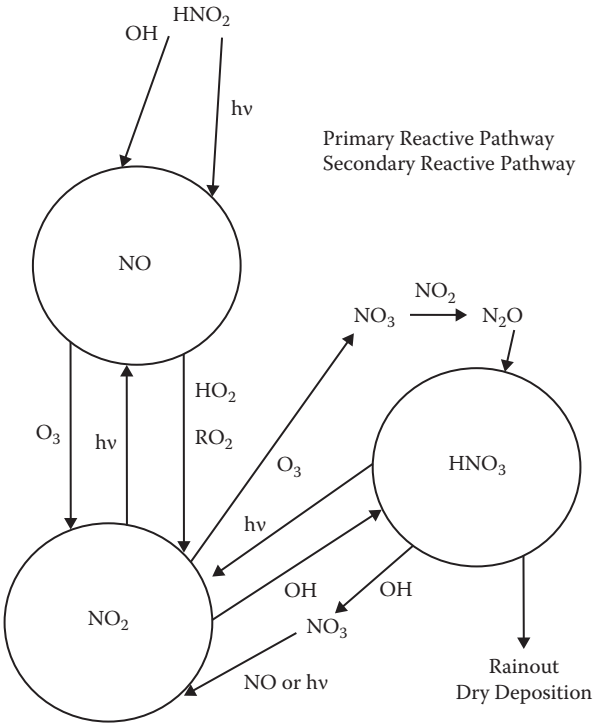

FIGURE 5.10
The major reactive nitrogen species in the troposphere.

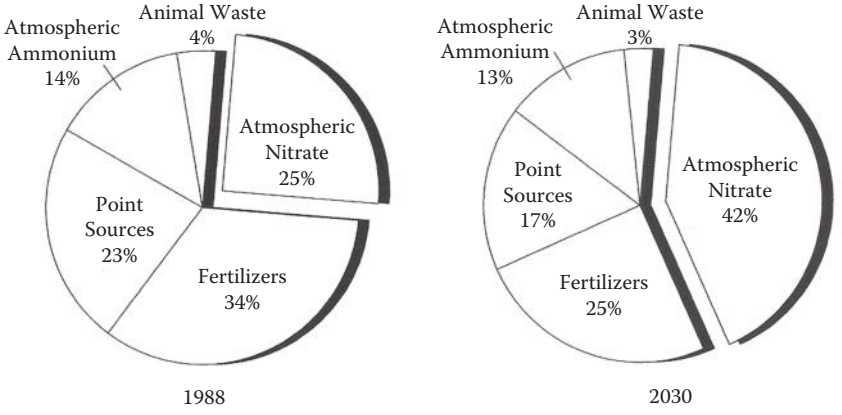

FIGURE 5.11
The atmospheric sources of nitrate to the Chesapeake Bay showing likely increase by the year 2030.

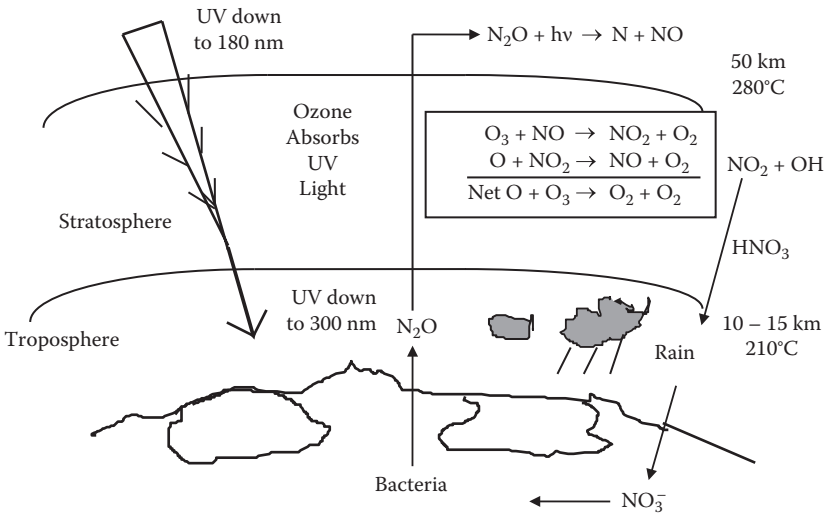

FIGURE 5.12
The effect of nitrogen oxides on the concentration of stratospheric ozone.

The NO formed can react with O_3 in a chain reaction:

$$O_3 + NO \rightarrow NO_2 + 2O\cdot \tag{5.22}$$

$$O\cdot + NO_2 \rightarrow NO + O_2 \tag{5.23}$$

The net reaction is

$$O\cdot + O_3 \rightarrow 2O_2 \tag{5.24}$$

The concern that sulfur species cause acid rain has led to an interest in the sulfur cycle. Biogenic processes emit a number of sulfur species (H_2S, CH_3SCH_3, OCS). These reduced species are oxidized to SO_2 by OH· radicals. SO_2 can also be directly injected into the atmosphere as a by-product of the oxidation of fossil fuels. The lifetime of SO_2 is between a few days to a month. The removal of SO_2 occurs by rainout and wet and dry deposition (see Figure 5.13) after the oxidation of SO_2 to H_2SO_4. The H_2SO_4 is incorporated into cloud droplets and aerosols. The oxidation can occur in the gas phase, the solution phase, or on particles (see Figure 5.14).

The term *acid rain* was first used by Angus Smith to describe the effect industrial emissions had on the precipitation in Great Britain. The pH of water in equilibrium with atmospheric CO_2 has a value of 5.6. In uncontaminated areas, the pH is closer to 5.0 because of natural levels of acids. In most urban areas, the pH is normally lower than 5.0. In Europe and North America, 90% of the sulfur comes from the burning of fossil fuels (Table 5.4). The lower pH of the rain (pH = 4.6 to 4.7) is normally attributed to the concentrations of HNO_3 and H_2SO_4 formed by the oxidation of NO_X and SO_2. Organic acids may also be important components of acidic rain, especially in remote areas. Many areas are sensitive to acid rain. These include many northern lakes that have low alkalinity (<50 μ*M*) and vast forest areas.

The effects of acid rain have led to lower alkalinity to Mg^{2+} and Ca^{2+} ratios. Fish can tolerate values of pH as low as 5.5. Juvenile fish and many organisms can be affected at

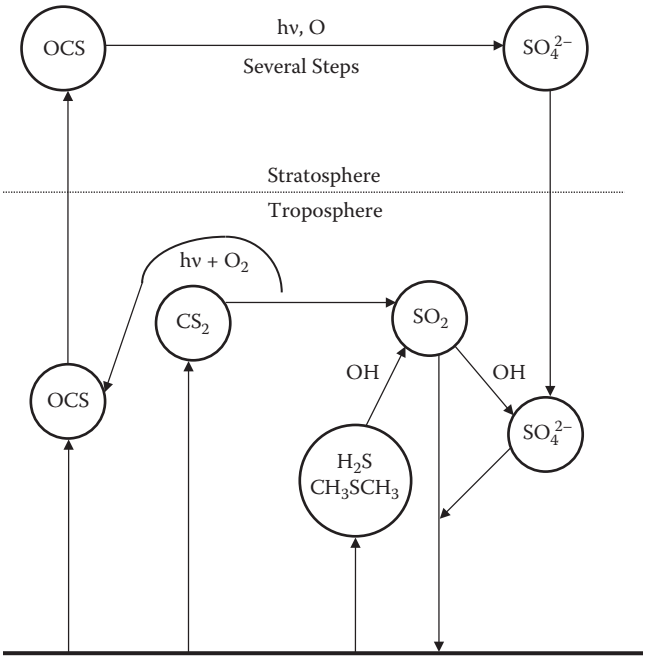

FIGURE 5.13
The sulfur cycle in the atmosphere.

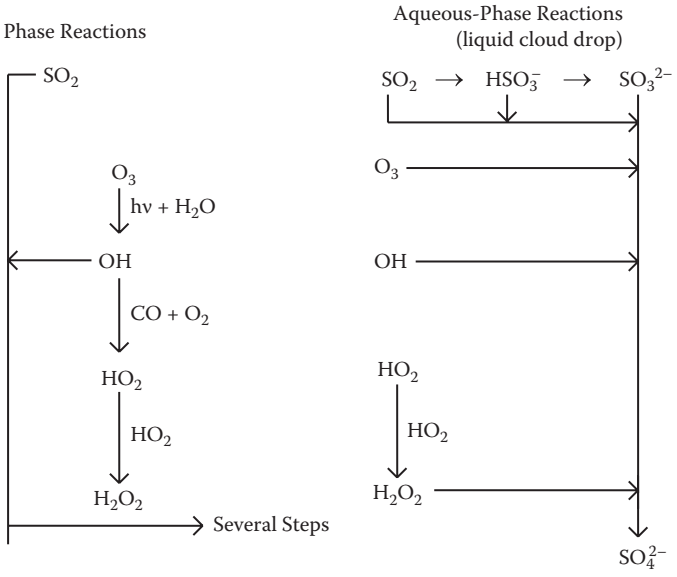

FIGURE 5.14
The gas and liquid phase reactions of sulfur in the atmosphere.

TABLE 5.4

Composition of Marine Rainwater from the Mediterranean and North Atlantic

Ion	North Atlantic	Mediterranean
pH	4.3–5.8	4.03–6.88
H^+	1.7–50.1 μ*M*	0.1–93.3 μ*M*
NH_4^+	—	4–40
Na^+	1.7–64.6	17–1620
Mg^{2+}	1–653	3–211
K^+	1–130	1–42
Ca^{2+}	2–119	2–112
NO_3^-	1–38	4–97
Cl^-	8–6900	20–2260
SO_4^{2-}	2–341	9–115
HCO_3^-	4.1	9–152

Source: Data from Losno, R. et al., *Atm. Environ.*, 25A, 763, 1991.

values of pH above 5.5. This can cause starvation of predatory fish. Acidic streams have frequently had fish kills caused by pulses of acidic waters during the spring snow melt. The lower pH of lakes and streams can also cause aluminum to be released from the sediments. Ionic aluminum, Al^{3+}, appears to be toxic, while the hydrolyzed forms are nontoxic ($Al[OH]_{2+}$, $Al[OH]^{2+}$, etc.). Recent studies have shown that exchange reactions of H^+ with sediments may lessen the effect of acid rain on a lake. The recovery of a lake may be fast if the basic components of the soil are not lost. It is unlikely, however, that the original pH will be reached for years, and widespread stocking will be necessary to bring back game fish and the resultant food chains.

5.3 Greenhouse Gases

The likelihood that CO_2 increases will cause global climate changes is now well accepted. Less is known, however, of the effects of other trace gases on the climate. Gases such as CH_4, O_3, N_2O, and CFCs such as CCl_3F (CFC-11) and CCl_2F_2 (CFC-12) can contribute to the increasing temperature of the troposphere. Solar radiation is absorbed by the atmosphere, providing energy for many processes. The UV energy coming to the top of the atmosphere is shown in Figure 5.15. The IR energy back-irradiated to the atmosphere is a function of the temperature of the earth (285 K or 12°C). The amount of solar energy that affects the earth is shown in Figure 5.16. For the global climate to be balanced, the absorbed radiation must be equal to the outgoing radiation. The trapping of some of the thermal radiation by particles and molecules increases the surface temperature by 10 to 15°C compared to what it would be without these molecules. This process of absorption of (IR) energy radiated from the earth is called the *greenhouse effect*.

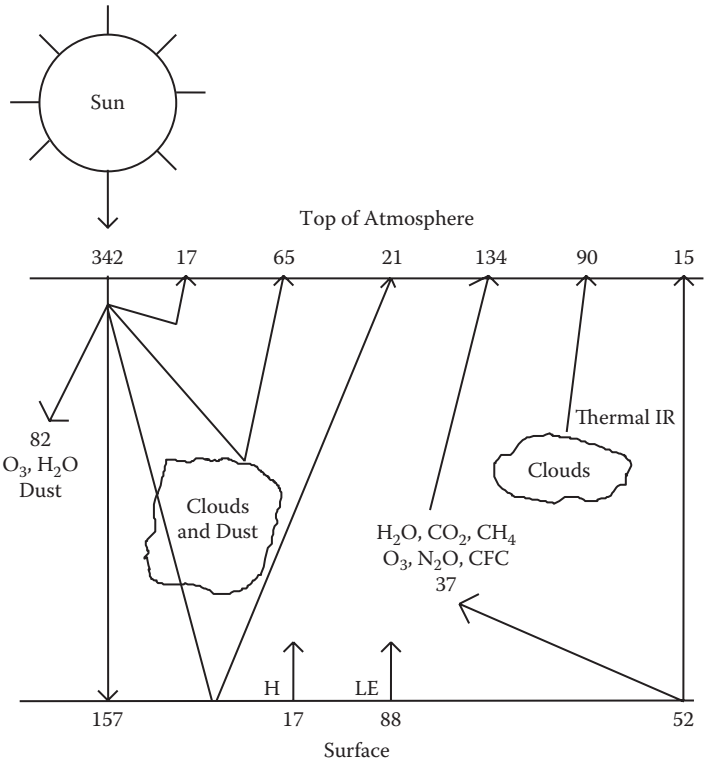

FIGURE 5.15
The amount of energy (W m^{-2}) that affects the earth.

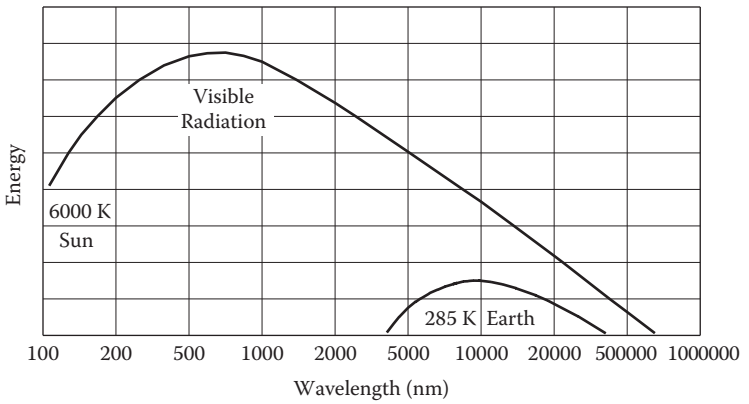

FIGURE 5.16
The visible radiation reaching the earth and the infrared radiation emitted by the earth.

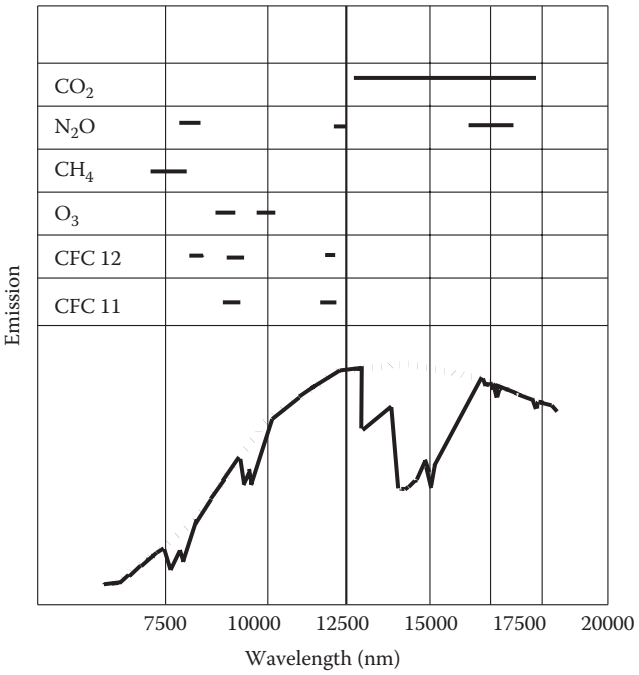

FIGURE 5.17
The adsorption of infrared radiation by greenhouse gases in the atmosphere.

The effect of the various gases in the atmosphere in adsorbing the IR energy is shown in Figure 5.17. Clouds and water vapor are dominant contributors to this process. Other atmospheric gases, although present in small amounts, can also contribute to this trapping of thermal radiation. Gases that absorb strongly in the IR region where water vapor and CO_2 do not strongly absorb can have the biggest effects. The so-called window that exists between 7,500 nm and 12,000 nm is of particular importance because water vapor and CO_2 do not absorb in this region, and the earth's emission is at a maximum at 10,000 nm. Without these active constituents, the earth would lose thermal radiation as a black body (~387 W m^{-2}). The actual radiative flux at the top of the atmosphere is 239 W m^{-2}, so about 148 W m^{-2} (38%) is trapped. Changes in the trapping of 1 W m^{-2} (0.3%) can change the balance sufficiently to change the climate. The current trapping by trace constituents of the atmosphere is given in Table 5.5. The preindustrial estimates of the trace gas concentrations and the change in thermal trapping are given in Table 5.6. Since the concentrations of all the greenhouse gases are increasing, these changes will become larger in future years.

One would expect from comparing the two tables that there has been approximately a 200% increase in the ΔQ caused by industrial processes. It is difficult, however, to translate the increases in ΔQ to an increase in the global temperature. Although some measurements (see Figure 5.18) indicate that the temperature has increased, it is hard to attach a reliable estimate of changes in ΔQ with changes in ΔT. The increase of CO_2 over the past 260 years has been well documented (Figure 5.19). This increase in the CO_2 is caused by the increased use of fossil fuels (coal, petroleum, and natural gas; Figure 5.20). The contributions of the emissions of fossil fuel CO_2 by the United States is compared to other countries

TABLE 5.5

Trapping of IR Radiation by Trace Gases (ΔQ, W m^{-2})

Gas	Present Level	Present ΔQ	Lifetime
CO_2	345 ppm	2.0	10–15 yr
CH_4	1.7 ppm	1.7	7–10
O_3	10 –100 ppb	1.3	0.5
N_2O	340 ppb	1.3	100
CFC-11[a]	0.22 ppb	0.06	75
CFC-12[b]	0.38 ppb	0.12	100
		6.5	

[a] CCl_3F.
[b] CCl_2F_2.

TABLE 5.6

Preindustrial Trapping of IR Radiation of Trace Gases

Gas	Past Level	Past ΔQ
CO_2	275 ppm	1.3
CH_4	0.7 ppm	0.6
O_3	0–25% less	0–0.2
N_2O	285 ppb	0.05
CFC-11	0	0
CFC-12	0	0
		2.2

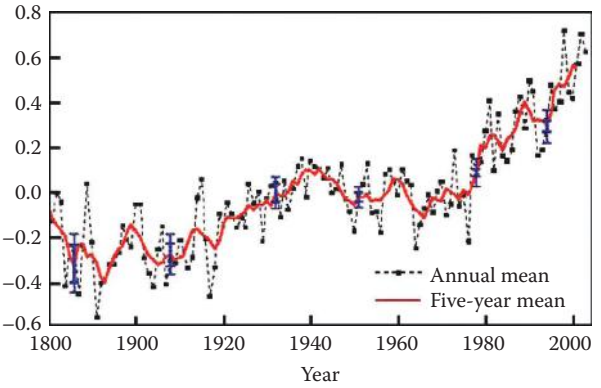

FIGURE 5.18
The temperature anomaly over the last 200 years.

in Figure 5.21. The present contributions of Asia are equivalent to the United States and will be greater than the United States in the future. Although the United States has 5% of the world's population, we produce 20% of the fossil fuel CO_2. This is shown more clearly in Figure 5.22, where the per capita fossil fuel emissions are shown for various countries. The United States produces 30% more per capita than the nearest country (Australia).

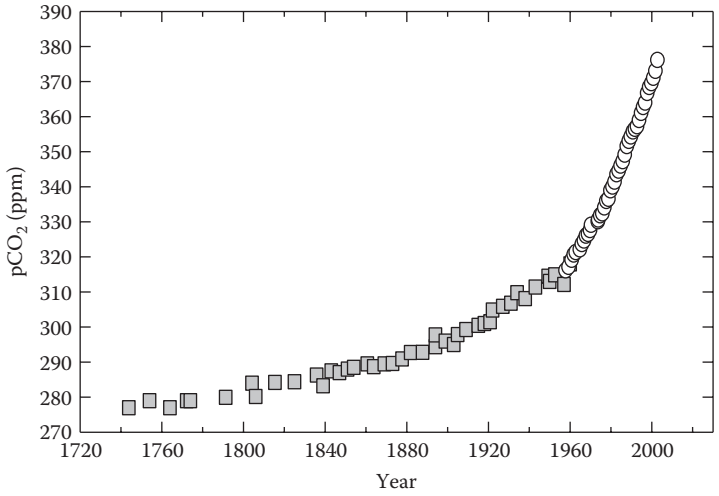

FIGURE 5.19
The increase of the partial pressure of carbon dioxide in the atmosphere over the last three centuries.

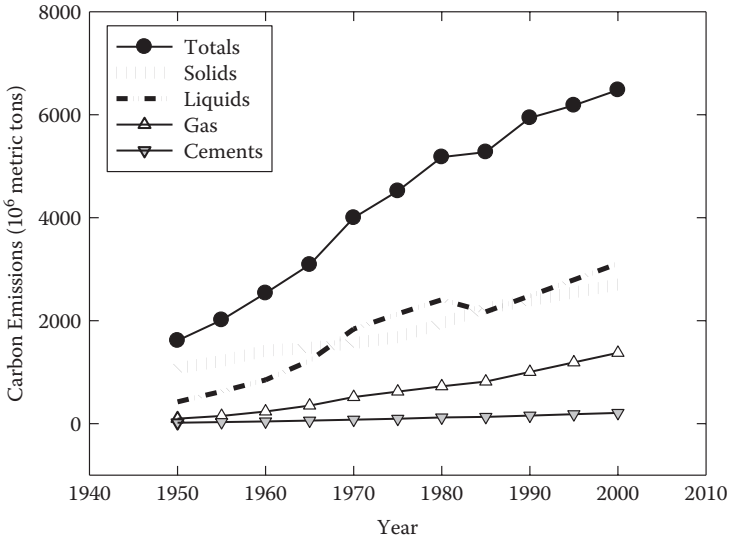

FIGURE 5.20
The CO_2 emissions into the atmosphere from fossil fuel consumption (liquids and gases) and cement.

The measurements of the pCO_2 in the atmosphere by Keeling and Whorf (2004) starting in 1958 at the Mauna Loa Observatory in Hawaii demonstrated that CO_2 is increasing (Figure 5.23). The annual cycling of pCO_2 in the atmosphere shown after the removal of the increases (Figure 5.24) is caused by variations in the photosynthesis and respiration of land plants. The maximum occurs in April and May, and the minimum occurs in September and October. In recent years, the values of pCO_2 have been measured at other locations (Figure 5.25). The increases were the same (1.5 ppm/year) as at Mauna Loa, but the yearly variations were larger in Alaska and smaller in the South Pole. The

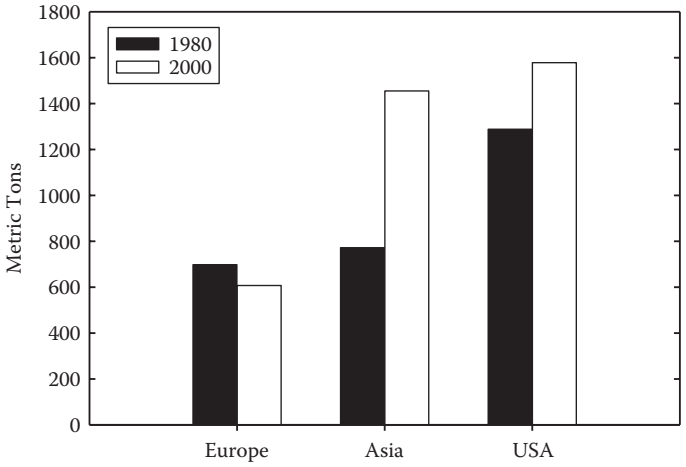

FIGURE 5.21
The emissions of fossil fuel CO_2 by various regions.

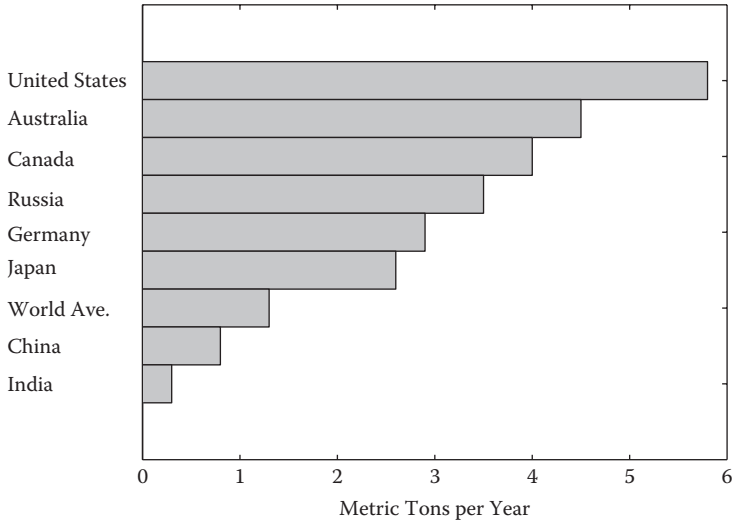

FIGURE 5.22
The per capita emissions of fossil fuel CO_2 by various countries. World Ave. = world average.

concentration of CO_2 in the atmosphere in the past has been determined by measuring the concentration of CO_2 in the air trapped in ice cores (Figure 5.19, squares). The extension of the pCO_2 record back 10,000 years shows that the level of CO_2 in the atmosphere has increased and decreased through time. The levels are lower during glacial times and higher during nonglacial times. These increases and decreases in CO_2 have followed the global temperatures (Figure 5.26). We do not know if the fluctuations in CO_2 caused the changes in the temperature or vice versa.

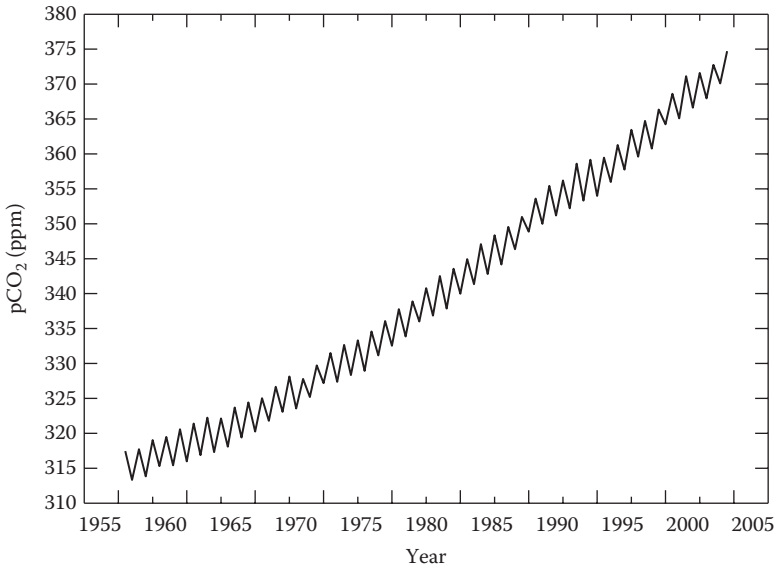

FIGURE 5.23
The increase of carbon dioxide at Hawaii showing the annual cycling over the last 42 years. (Data from Keeling, C.D., and Whorf, T.P., in *Trends: A Compendium of Data on Global Change*, Carbon Dioxide Information Analysis Center, Oak Ridge, TN, 2004.)

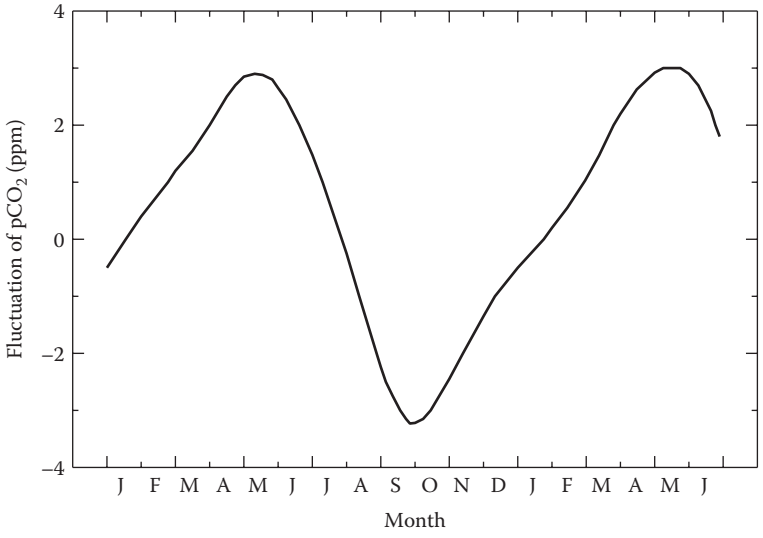

FIGURE 5.24
The mean annual cycling of carbon dioxide in the atmosphere.

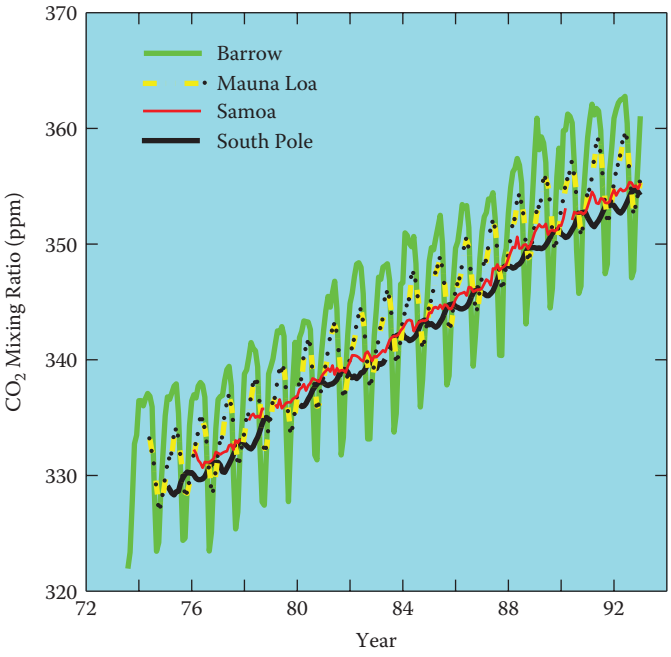

FIGURE 5.25
The difference in the annual cycling of carbon dioxide in the atmosphere at various locations.

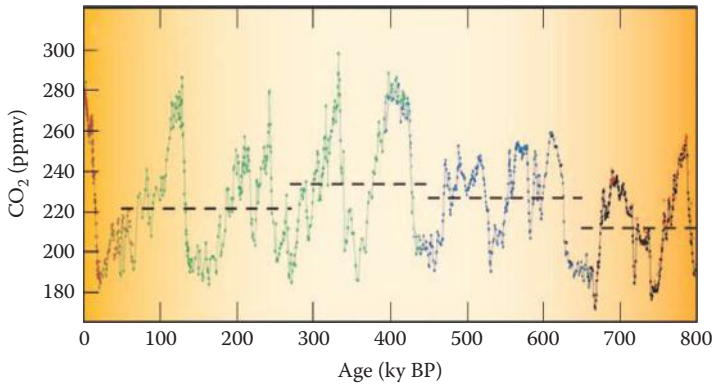

FIGURE 5.26
The variations of carbon dioxide and temperature as recorded in the Vostok ice core during the last climate cycle.

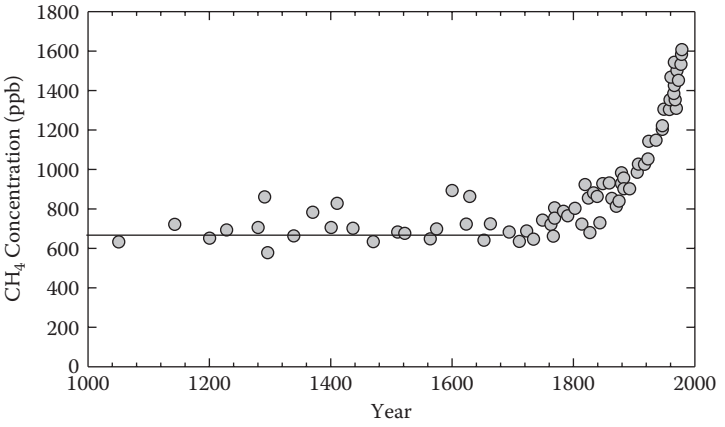

FIGURE 5.27
The increase in the atmospheric methane concentrations.

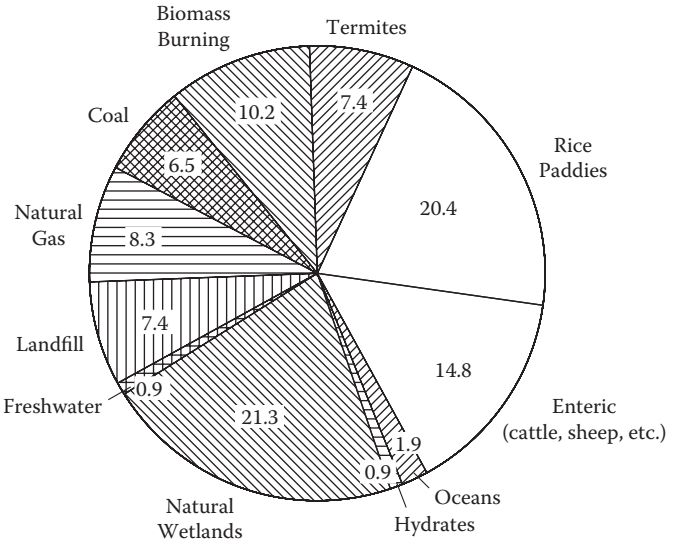

FIGURE 5.28
The sources and relative inputs of methane (wt. %) into the atmosphere.

Recent work has also demonstrated that CH_4 has increased dramatically as well (see Figure 5.27). The sources of methane to the atmosphere (550 Tg yr^{-1}) are shown in Figure 5.28. The largest sources are from wetlands (21%) and rice paddies (20%). Other sources include cattle (15%), biomass burning (10%), natural gas (8%), termites (7.4%), landfills (7.4%), coal (6.5%), and the oceans (2%). The increase in methane is not well understood. The inputs into the atmosphere in the Southern Hemisphere (from the oceans) appear to have an annual cycle, while the inputs into the Northern Hemisphere (from industry) have a more complicated cycle.

Various workers have attempted to estimate the long-term effects of the addition of greenhouse gases to the atmosphere. The projected increases of the gases in 2050 are given in Table 5.7. A number of workers have attempted to estimate the effect the projected

TABLE 5.7

Trapping of IR Radiation by Trace Gases in 2050

Gas	2050 Levels	ΔQ
CO_2	440–600 ppm	0.9–3.2
CH_4	2.1–4.0 ppm	0.2–0.9
O_3	15–50% more	0.2–0.6
N_2O	350–450 ppb	0.1–0.3
CFC-11	0.7–3.0 ppb	0.23–0.7
CFC-12	2.0–4.8 ppb	0.6–1.4
		2.2–7.2

TABLE 5.8

Estimated Increase in Temperature Caused by Increases in the Concentration of Trace Gases

Gas	Assumed Increase	Temperature Change (°C)
CO_2	2	2.6
H_2O	2	0.65
O_3	0.75	0.4
N_2O	2	0.65
NH_3	2	0.12
HNO_3	2	0.08
CH_4	2	0.26
SO_2	2	0.02
CFCs	20	0.65
		4.63

increase of trace gases will have on the temperature in the next century. The models used to make these estimates are quite complicated and may not be reliable; however, at present this is the best one can do. The increases in temperature estimated by assuming various increases in trace gases are given in Table 5.8. Although CO_2 makes up to 75% of the increase, other gases are important and will become more important in the future (see Figure 5.29). Recently, it has become apparent that volcanic eruptions can produce gases and particles that can influence global temperature (see Figure 5.30). The decrease in global temperature may be the result of the formation of more clouds (from the SO_2) or reflection (from the particles).

5.4 Effects of Global Change

At the present time, most scientists agree that

Certain gases are transparent to incoming solar UV but adsorb IR.

Atmospheric concentrations of greenhouse gases are increasing.

As the gases increase, so will the average global temperature.

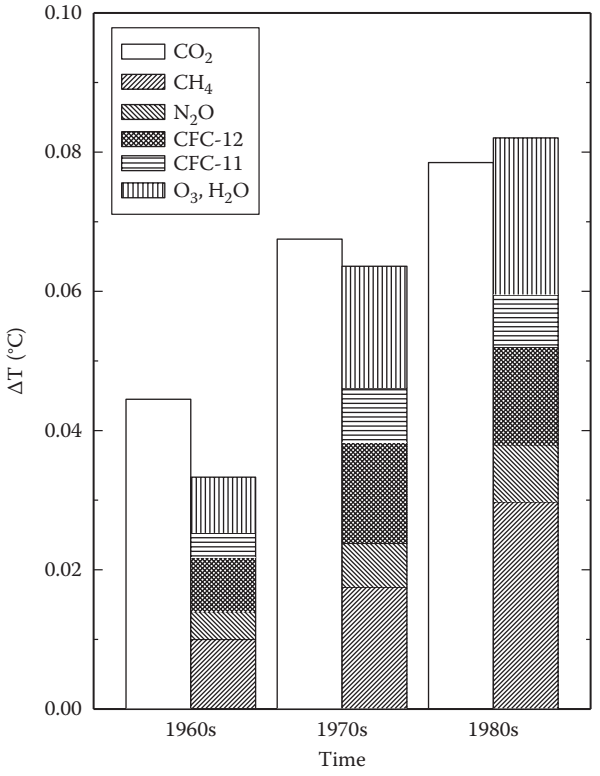

FIGURE 5.29
The relative effects of various trace gases on greenhouse warming.

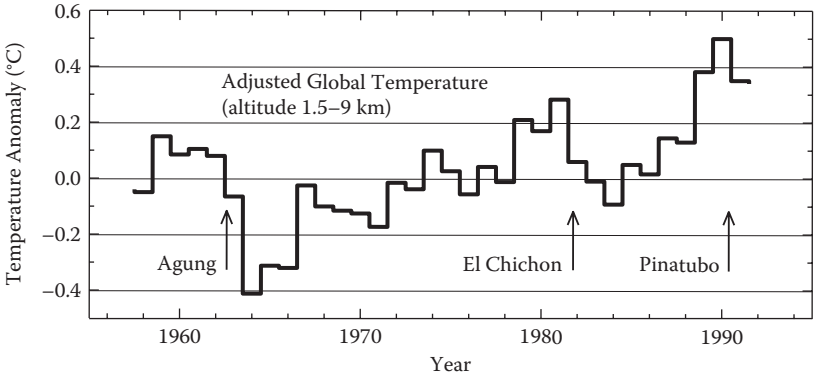

FIGURE 5.30
The effect of volcanic eruptions on the average global temperature.

Some questions with answers that are not known at the present time with certainty are

What is the timing and severity of the warming?
What are the regional distributions of the impacts?
What are the magnitudes of the feedback processes?

It is useful to briefly review the state of our understanding of these issues. As discussed, the increase of CO_2 in the atmosphere is largely related to the burning of fossil fuels. The increase of greenhouse gases in the atmosphere and the resultant increase in the temperature of the earth can cause some global changes. Some of those include

Sea-level rise: The increase in the temperature can cause an increase in the volume of seawater and a subsequent increase of sea level. The increased temperature can also melt ice on land, which would increase the sea level. For example, if the ice on Antarctica melts, the sea level may rise by 70 m.

Extreme weather events: These can result from the higher temperature of the surface waters in the oceans. Hurricanes, for example, can become more frequent and stronger in warmer waters. Some have speculated that if the temperatures of North Atlantic surface waters become too warm, they will not be able to sink to form North Atlantic deep water. This could have large-scale climate effects on the earth.

Spread of tropical diseases: The warmer waters in tropical regions may result in an increase in tropical diseases such as malaria and typhoid fever.

Species extinctions: The increase in the temperature of ocean waters may cause coral bleaching of reefs.

There is some evidence that the ice cover in the Arctic Ocean is thinning because of global warming. These results come from submarine measurements from 1957 to 1997. The ice has decreased by as much as 3 m over the past 40 years. Some predict that the ice will completely disappear in the Arctic in the summer in 50 years. There is also some evidence that surface ocean waters have increased over the past 20 years. For example, the heat content of the waters has increased over the past 50 years. This means that part of the increase in the temperature of the atmosphere has been used to heat up the surface waters of the oceans. Although current measurements indicate that the sea level is rising, we cannot accurately predict what it will be in the future. We can, however, estimate the level based on the possible increases in the temperature. If the temperature increases by 3°C over the next 50 years, the sea level could rise by 80 cm, or 32 inches. Recently, some have predicted that if the ice on Antarctica melts, the ocean will rise by as much as 70 m (~200 ft). This increase in sea level can cause an inundation of water in some coastal areas and result in more serious coastal flooding from hurricanes and typhoons. Some Web sites for more information on global warming are www.ipcc.ch, www.ucsusa.org, and www.iclei.org.

5.4.1 Effects of Global Warming on the Oceans

The increase in CO_2 in the atmosphere causes a number of stresses on the surface waters of the oceans. Gruber (2011) has recently discussed the following stresses:

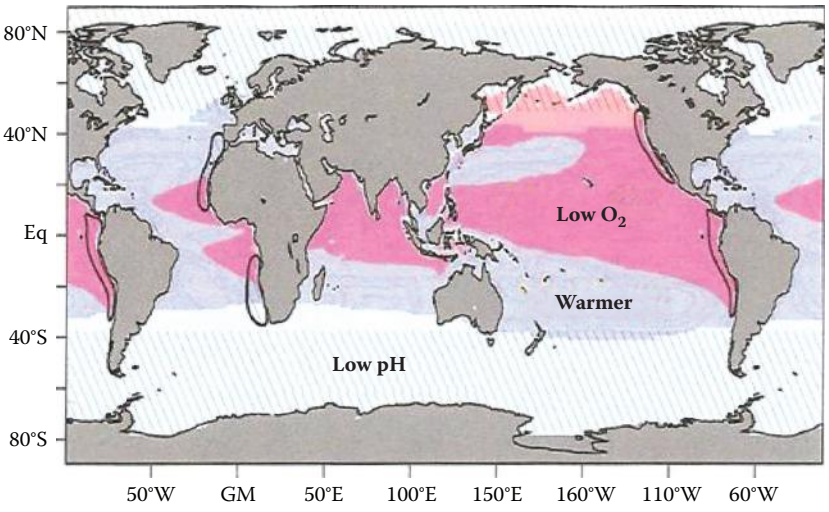

FIGURE 5.31
The warming of the surface waters leads to ocean stratification, which affects the physical, chemical, and biological processes in the surface waters.

1. Warming of surface waters
2. Deoxygenation of surface waters
3. Ocean acidification of surface waters

The areas affected are shown in Figure 5.31 (Gruber, 2011). The warming of the surface waters results in stratification. The stratification results in lower O_2 levels in the surface waters. These changes can result in stress on biological processes and organisms. The increasing CO_2 can dissolve in seawater and lower the pH. These last effects are discussed in more detail in Chapters 6 and 7.

5.5 Loss of Ozone

It has been known for some time that gases produced by humans can contribute to the loss of ozone in the stratosphere. The effect of naturally produced N_2O was discussed previously (see Figure 5.12). Chlorine can also reduce O_3 by the following reactions (see Figure 5.32):

$$O_3 + Cl\cdot \rightarrow ClO + O_2 \tag{5.25}$$

$$O\cdot + ClO \rightarrow Cl\cdot + O_2 \tag{5.26}$$

The net reaction is

$$O\cdot + O_3 \rightarrow 2O_2 \tag{5.27}$$

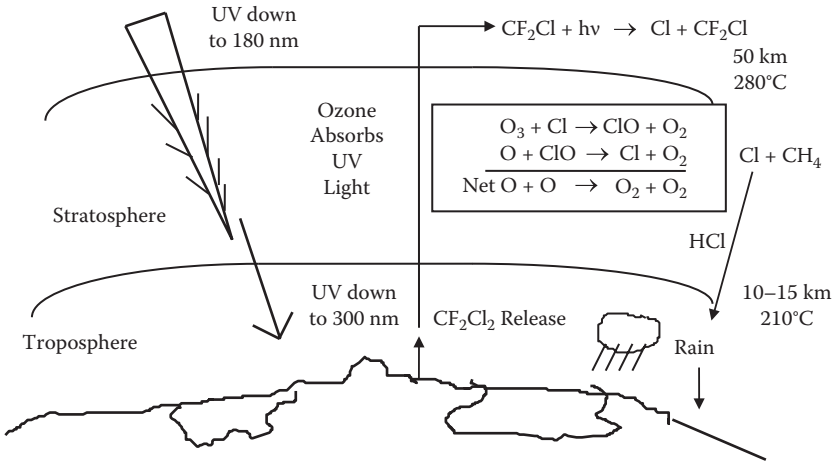

FIGURE 5.32
The effect of chlorine on the concentration of ozone in the stratosphere.

Free atomic chlorine is produced by the photodissociation of CFCs (CFC-11 and CFC-12):

$$CCl_2F_2 + h\upsilon \rightarrow CClF_2 + Cl\cdot \tag{5.28}$$

$$CCl_3F + h\upsilon \rightarrow CCl_2F + Cl\cdot \tag{5.29}$$

These CFCs reach the high altitudes where light of sufficient energy can cause dissociation because of their long lifetimes (CFC-11, $\tau = 75$ yr; CFC-12, $\tau = 110$ yr). As mentioned, NO· and OH· radicals can also reduce ozone:

$$NO\cdot + O_3 \rightarrow NO_2 + O_2 \tag{5.30}$$

$$NO_2 + O\cdot \rightarrow NO\cdot + O_2 \tag{5.31}$$

$$OH\cdot + O_3 \rightarrow HO_2 + O_2 \tag{5.32}$$

$$HO_2 + O\cdot \rightarrow OH\cdot + O_2 \tag{5.33}$$

The net effect of both reaction paths is the destruction of two ozone molecules (the primary reaction with O_3 and the destruction of O· that would have formed O_3).

The reactive species are removed by reactions that produce stable species or water-soluble species that are rained out:

$$Cl\cdot + CH_4 \rightarrow HCl + \cdot CH_3 \tag{5.34}$$

$$Cl\cdot + HO_2 \rightarrow HCl + O_2 \tag{5.35}$$

$$NO_2 + OH\cdot \rightarrow HNO_3 \tag{5.36}$$

$$OH\cdot + HO_2 \rightarrow H_2O + O_2 \tag{5.37}$$

Photodissociation or other free radical reactions can reverse these reactions:

$$OH\cdot + HCl \rightarrow H_2O + Cl\cdot \quad (5.38)$$

$$HNO_3 + h\upsilon \rightarrow OH\cdot + NO_2 \quad (5.39)$$

$$HO_2 + NO\cdot \rightarrow OH\cdot + NO_2 \quad (5.40)$$

$$OH\cdot + CO \rightarrow CO_2 + H\cdot \quad (5.41)$$

With increasing CFC production (see Figure 5.33), one would expect that the formation of Cl by photodissociation would be more important in removing O_3 in future years. Even though the aerosol usage of CFCs has decreased, nonaerosol usage has increased. The increase of CFCs, methylchloroform, carbon tetrachloride, and nitrous oxides since 1978 has been documented by direct measurements (see Figure 5.34). The decrease in O_3 levels will increase the amount of UV radiation that reaches the earth. This is shown in Figure 5.35. This plot includes all the wavelengths weighted according to how damaging they are to biological systems (300 to 345 nm). A 100% decrease of O_3 will increase the damaging UV flux by about 18%.

Recent attention to the destruction of O_3 has concentrated in the Antarctic region over the years from 1960 to 1992 (see Figure 5.36) in the springtime. This has caused the so-called ozone hole over the South Pole (Figure 5.37). This springtime loss of ozone extends well north of Antarctica (see Figure 5.38). It should be pointed out that one Dobson unit equals a concentration of O_3 of one molecule in every 10^9 total molecules. Work showed that the size of the ozone hole increased considerably over the years 1980 to 2004 (see Figure 5.39). Since the global concentrations of O_3 show large variations (see Figure 5.40), it is difficult to distinguish trends over time.

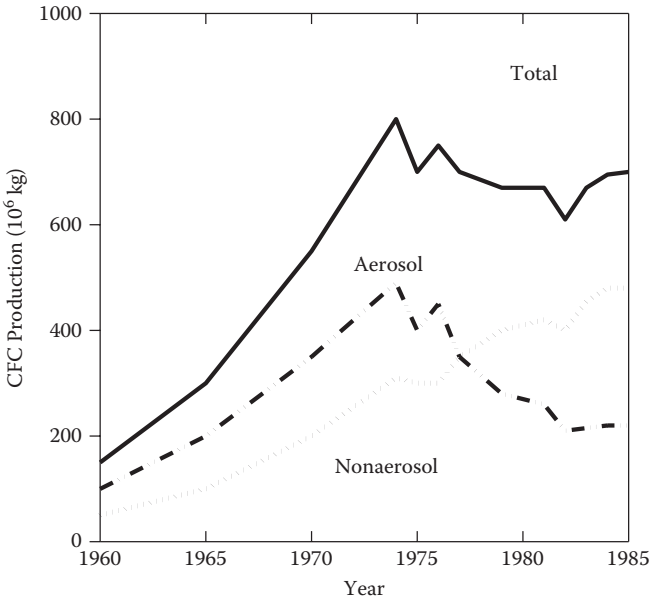

FIGURE 5.33
The production of chlorofluorocarbons (CFCs) from 1960 to 1985.

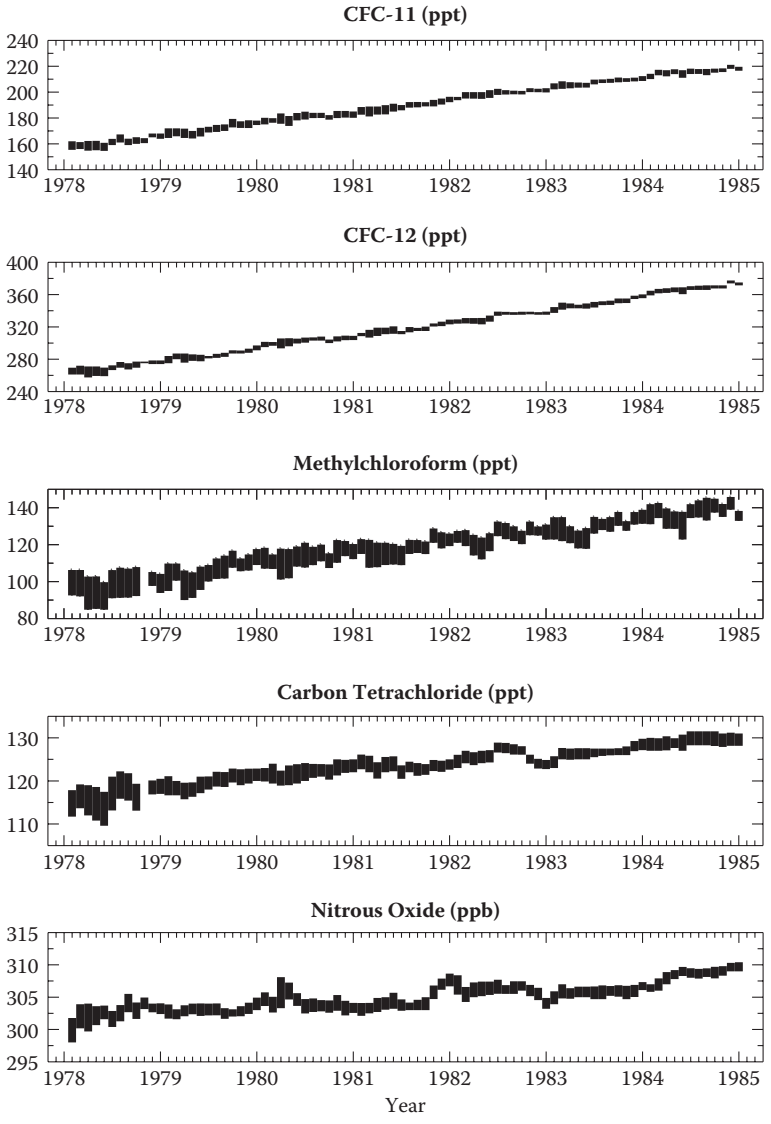

FIGURE 5.34
The increase in the concentration of chlorinated compounds and nitrogen oxide in the atmosphere.

The loss of ozone in Antarctica in the springtime has been attributed to the formation of ClO (see Figure 5.41). The large effects in the springtime have been attributed to a dynamic uplifting of the lower stratosphere as well as catalytic cycles involving Cl. One potential cycle is

$$ClO + ClO \rightarrow Cl_2O_2 \tag{5.42}$$

$$Cl_2O_2 + M \rightarrow Cl_2 + O_2 + M \tag{5.43}$$

$$Cl_2 + h\upsilon \rightarrow 2Cl\cdot \tag{5.44}$$

$$2Cl\cdot + 2O_3 \rightarrow 2ClO + 2O_2 \tag{5.45}$$

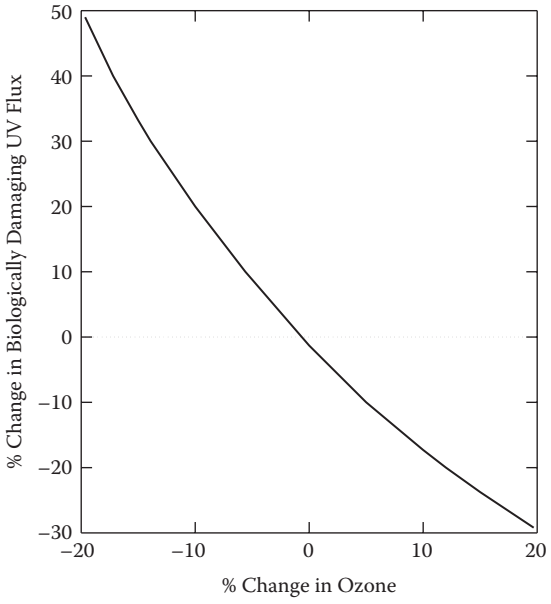

FIGURE 5.35
The changes in the biologically damaging ultraviolet (UV) flux as a function of changes in the ozone levels.

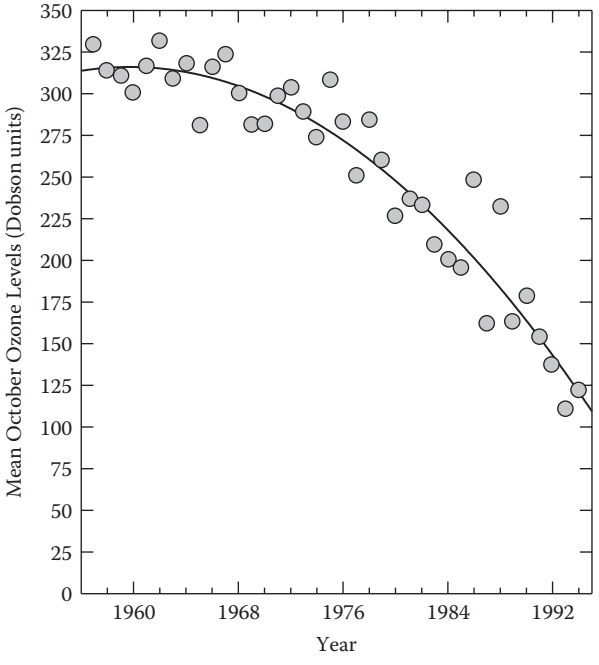

FIGURE 5.36
The decline of springtime ozone over the Antarctic from 1956 to 1988.

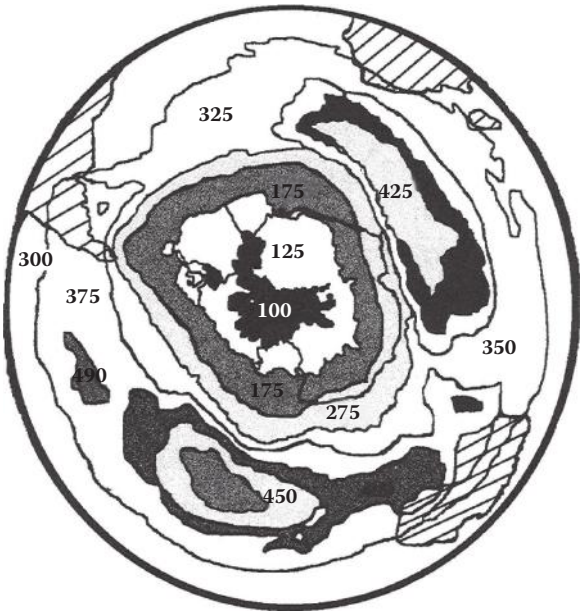

FIGURE 5.37
The ozone hole in the Antarctic region.

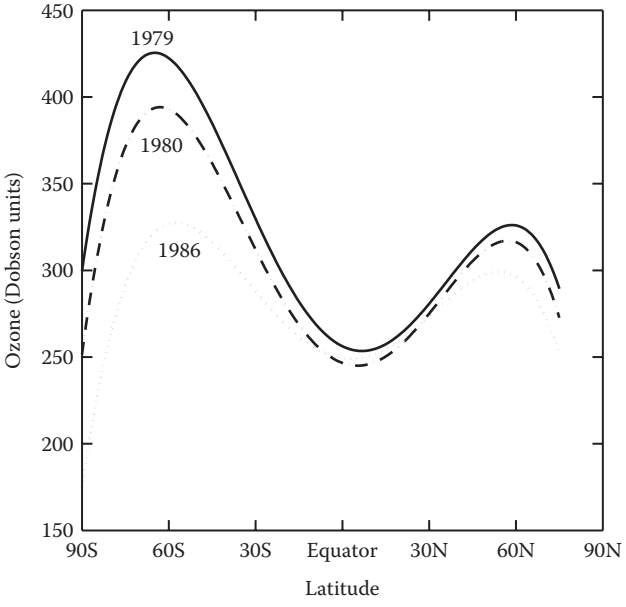

FIGURE 5.38
The levels of ozone as a function of latitude.

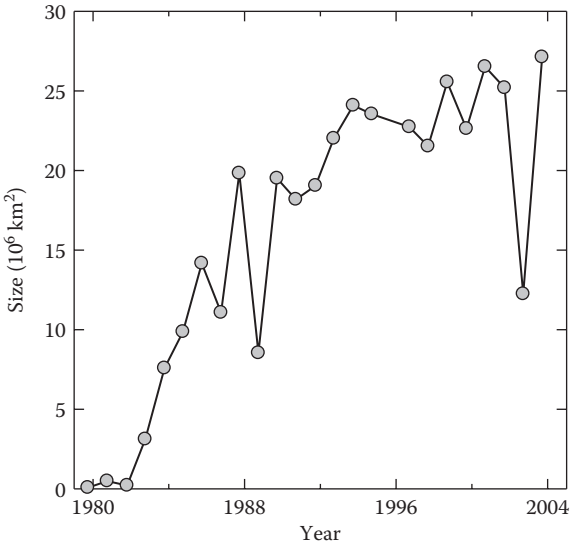

FIGURE 5.39
The increase in the size of the ozone hole in the Antarctic.

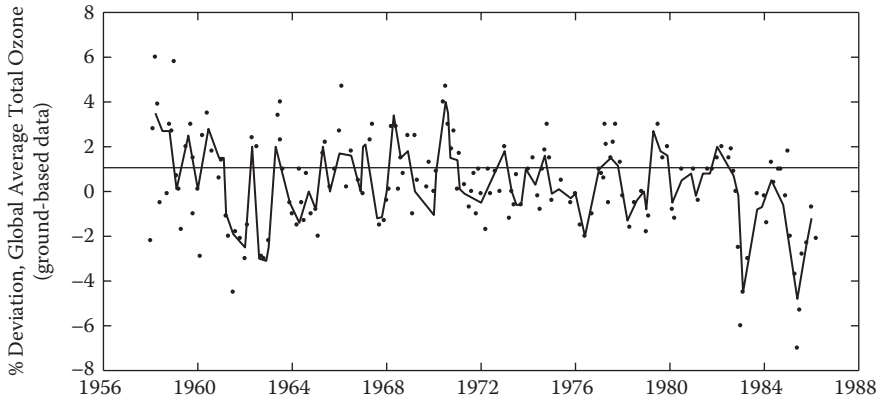

FIGURE 5.40
The fluctuations of the global average total ozone as a function of time.

The net reaction is

$$2O_3 \rightarrow 3O_2 \tag{5.46}$$

The reaction of Cl or ClO with CH_4 and NO_2 can produce inert compounds:

$$Cl\cdot + CH_4 \rightarrow HCl + CH_3 \tag{5.47}$$

$$ClO + NO_2 \rightarrow ClONO_2 \tag{5.48}$$

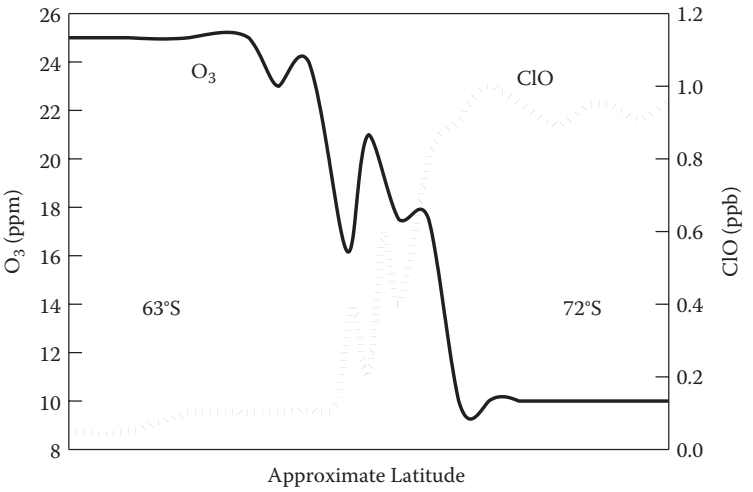

FIGURE 5.41
The relationship between O_3 and ClO in the Antarctic.

Low levels of NO_2 are needed to prevent the formation of $ClONO_2$. Reactions on ice have been proposed to explain how the inert compound becomes active:

$$ClONO_2 + HCl \rightarrow Cl_2 + HNO_3 \tag{5.49}$$

$$ClONO_2 + H_2O \rightarrow HOCl + HNO_3 \tag{5.50}$$

The unique meteorology of Antarctica results in a circulation of air in the stratosphere that is different from the Northern Hemisphere. A stream of air called the polar vortex tends to circle the South Pole in the winter. Air trapped in the vortex becomes very cold (–90°C) and forms clouds even in very dry conditions. These clouds provide ice crystals that have been shown by laboratory studies to cause molecules of HCl and $ClONO_2$ to react. The Cl_2 gas formed is released to the gas phase, whereas HNO_3 remains in the ice. The Cl_2 reacts with light to produce 2Cl·, which further reacts with O_3 to produce more ClO. The total reaction sequence is

$$ClONO_2 + HCl \rightarrow Cl_2 + HNO_3 \tag{5.51}$$

$$Cl_2 + h\upsilon \rightarrow 2Cl\cdot \tag{5.52}$$

$$2Cl\cdot + 2O_3 \rightarrow 2ClO + 2O_2 \tag{5.53}$$

$$ClO + NO_2 \rightarrow ClONO_2 \tag{5.54}$$

The net reaction is

$$HCl + 2O_3 + NO_2 \rightarrow HNO_3 + 2O_2 + ClO \tag{5.55}$$

The HCl gets rid of NO_2 and forms ClO, which further removes O_3. Although these reactions explain the formation of the ozone hole formed in Antarctica, further work is needed

to predict the loss of O_3 in the global atmosphere. As humans continue to add gases that upset the natural balance to the atmosphere, there will continue to be changes in the climate that affect life on the earth.

Work has also indicated that iodine may be important along with chlorine and bromine in the destruction of ozone. The loss of ozone in temperate regions above 20 km have puzzled scientists for years. Chlorine and bromine are important at higher altitudes, but they cannot account for the loss in the lower stratosphere. The reaction sequence for iodine is postulated to be (Solomon and Ravishankara, 1994):

$$HO_2 + IO \rightarrow HOI + O_2 \tag{5.56}$$

$$HOI + h\upsilon \rightarrow OH + I \tag{5.57}$$

$$I + O_3 \rightarrow IO + O_2 \tag{5.58}$$

$$OH + O_3 \rightarrow HO_2 + O_2 \tag{5.59}$$

The possible effect of iodine on the depletion of ozone is complicated by the fact that trifluoromethyl iodide (CF_3I) has been proposed as a possible replacement for ozone-depleting halons used to fight fires. It was thought that this compound would not pose a problem for the depletion of the ozone layer because the carbon iodine bonds are readily photolysed by sunlight and never reach the stratosphere. Naturally formed methyl iodine produced by marine life is thought to be much higher than the present industrial emissions. As scientists rush to make further measurements of iodine, the jury will remain out.

Finally, although the Montreal Accord stopped the use of CFCs, the levels of chlorine in the stratosphere will decrease at a slow rate (see Figure 5.42). Thus, the decrease in the ozone levels will continue for some time.

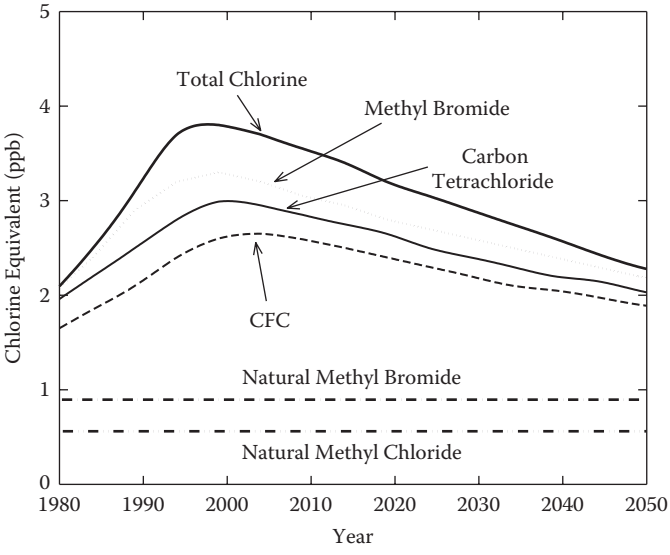

FIGURE 5.42
The levels of chlorine in the stratosphere as a result of the Montreal Protocol.

5.6 The Global Sulfur Cycle

In recent years there has been interest in the global sulfur cycle (Saltzman and Cooper, 1989). This interest is related to the production of reduced sulfur compounds from the burning of sulfur fuels (SO_2) and the production of reduced sulfur compounds from plants (dimethylsulfide [DMS]). These compounds can be oxidized to H_2SO_4, which can serve as CCN and affect the climate. The estimates of the natural sulfur emissions (Tmol S yr^{-1}) are given in Table 5.9. The levels of 1.2 to 2.8 Tmol yr^{-1} can be compared to the value of 2.5 ± 0.3 Tmol yr^{-1} for man-made sulfur emissions (T = tera = 10^{12}). From this comparison, it is apparent that the natural levels, although not well known, are the same order of magnitude as the man-made levels. This has led to an increased interest in the natural biogeochemistry of sulfur and the cycling of sulfur across the air–sea interface. The uncertainties in the natural sulfur cycle are due to

1. Difficulty in measuring H_2S at low levels in unpolluted areas
2. Problems in measuring fluxes from forest and brush ecosystems
3. Poor geographical coverage of existing data

The most important sources are from the burning of fossil fuels and the oceans.

The reduction of sulfate to volatile sulfur compounds is due to biological processes. The major volatile coming from the oceans is DMS. The DMS is produced from dimethlysulfonium propionate (DMSP) produced in marine algae from the protein methionine.

$$\underset{\text{(DMSP)}}{(CH_3)_2\text{-}CH_2CH_2COO^-} \rightarrow \underset{\text{(DMS)}}{CH_3SCH_3} + \underset{\text{(acrylic acid)}}{CH_2 = CHCOOH} \tag{5.60}$$

DMSP is thought to be osmostatic or osmoregulatory in marine algae. It is present at high levels in dinoflagellates, coccolithophores, and cyanobacteria. Since the surface waters are supersaturated with DMS, it is released to the atmosphere, especially during phytoplankton blooms. The contribution of DMS from land and ocean plants is nearly equal to the industrial input of reduced sulfur (SO_2). DMS has a lifetime of 8 to 49 h. It can be oxidized by OH radicals in the day and nitrate radicals at night. The major products from the oxidation of DMS are SO_2 and methanesulfonic acid (CH_3SO_3H [MSA]). The SO_2 can be quickly

TABLE 5.9

Concentration of Atmospheric Sulfur Compounds

Species	Concentration	Sources	Sinks
SO_2	0–0.5 ppmv (urban)	Fossil fuels (oxid)	Oxidation to SO_4
	20–200 pptv (remote)	Biological (DMS)	Oxidation to SO_2
H_2S	0–40 pptv	Biological	Oxidation to SO_2
CH_3SH	>ppbv	Paper pulping	Oxidation to SO_2
CH_3CH_2SH	>ppbv	Paper pulping	Oxidation to SO_2
OCS	500 pptv		Destruction in stratosphere
CH_3SCH_3	20–200 pptv	Oceanic plankton	Oxidation to SO_2
CH_3SSCH_3	Small		Oxidation to SO_2
CS_2	10–20 pptv		Destruction in stratosphere

TABLE 5.10

Compounds in Aerosol Particles in the Atmosphere

Species	Formula
Sulfuric acid	H_2SO_4
Sulfurous acid	H_2SO_3
Sulfonic acid	$R\text{-}SO_3H$
Nitric acid	HNO_3
Ammonium sulfate	$(NH_4)_2SO_4$
Ammonium bisulfate	NH_4HSO_4
Ammonium nitrate	NH_4NO_3
Magnesium sulfate	$MgSO_4$
Calcium	$CaSO_4$
Sodium sulfate	Na_2SO_4

Source: Data from Carlson, R.J., The atmosphere, in *Global Biogeochemical Cycles*, Butcher, S.S., Charleson, R.J., Orians, G.H., and Wolfe, G.V., Eds., Academic Press, New York, 1992.

oxidized to SO_4^{2-}, while MSA is fairly stable and slowly oxidized to SO_2. Other products of the oxidation include dimethyl sulfoxide (DMSO) and dimethyl sulfone ($DMSO_2$). MSA is a strong acid, and its atmospheric chemistry is dominated by aqueous processes. It is thus very rapidly incorporated into aerosols by nucleation and coagulation. The sulfur compounds present in aerosol in the atmosphere are listed in Table 5.10. The Mg, Ca, and Na sulfates come largely from marine sources.

Due to its stability, MSA has been used as a tracer for biogenic sulfur (DMS) emissions in ice cores (Saltzman, Whug, and Mayewski, 1997). The amount of non-sea-salt sulfate (NSS) in marine aerosols can be calculated by assuming that the salt-derived sulfate is related to sodium by its seawater value:

$$NSS - SO_4 = [SO_4^{2-}]_T - X[Na^+] \tag{5.61}$$

where X = 0.2517, and $[Na^+]$ is the concentration of sodium in the aerosol. The NSS can be produced by the burning of fossil fuels, volcanoes, biomass burning, and the oxidation of DMS. The ratio of MSA/NSS-SO_4 can be used to discriminate between the biogenic and nonbiogenic contributions to the marine sulfur budget.

The distribution of DMS exhibits a pattern that is similar to primary production. The greater the biological activity, the higher the production of DMS. It is high near the marine boundary layer and decreases with height in the atmosphere. The distribution of MSA in aerosols from the photochemical oxidation of DMS is similar. The NSS-SO_4 is low at the marine boundary layer and increases with height, showing a correlation with SO_2 (see Figure 5.43). The long-range transport of SO_2 can result in elevated levels of SO_2 and NSS-SO_4 in the high troposphere.

The aerosols of MSA and SO_4 can act as CCN and influence the albedo (reflectance) of the upper atmosphere and the earth's climate (Figure 5.44). Some have speculated that this can lead to a so-called feedback effect. The growth of plants in the surface of the oceans can result in the formation of clouds and a resulting cooling of the earth that counteracts the effects of the greenhouse gases.

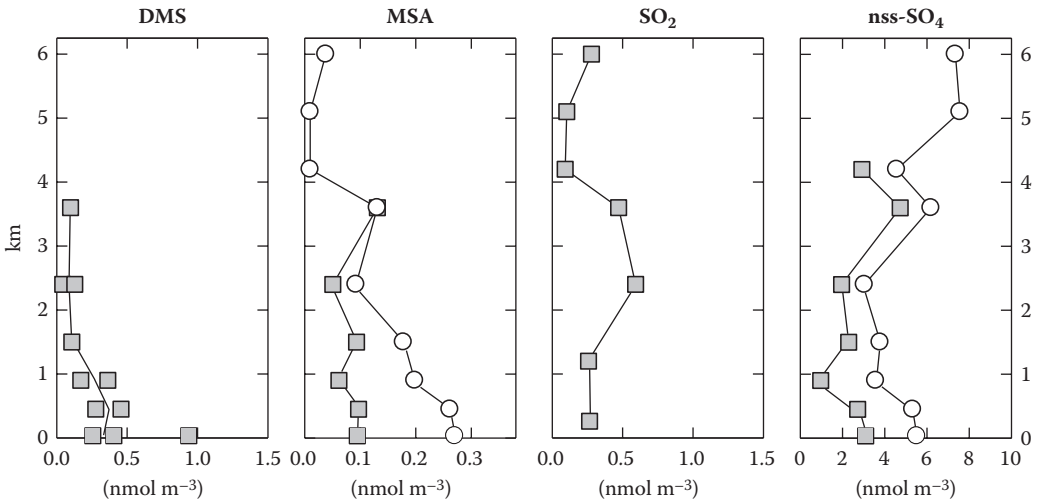

FIGURE 5.43
The vertical distribution of dimethylsulfide (DMS), methanesulfonate aerosol (MSA), sulfur dioxide (SO_2), and non-sea-salt sulfate (nss-SO_4) in the atmosphere over the northeastern Pacific.

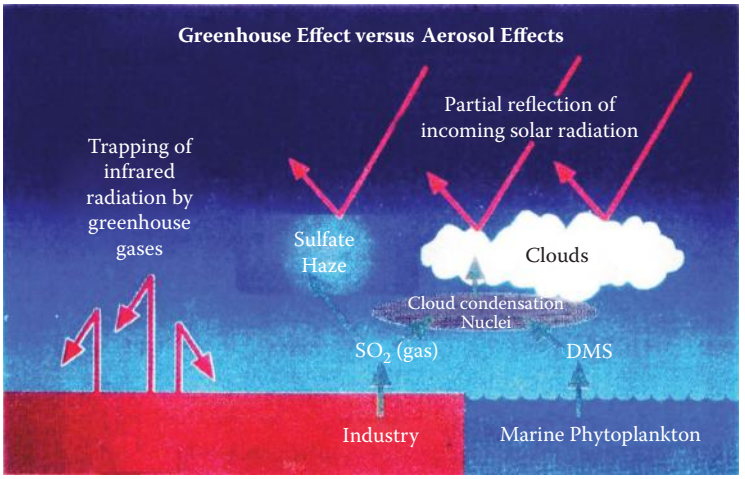

FIGURE 5.44
The effect of aerosols and greenhouse gases on the balance of incoming and outgoing radiation.

5.7 Atmospheric Aerosols

In recent years, a number of studies have shown that aerosols from the continents can have an effect on climate (Evan et al., 2011; Booth et al., 2012) and the input of chemicals (Fe) to the oceans (Prospero et al., 2002; Le Roux et al., 2011; Sholkovitz et al., 2012; Trapp, Millero, and Prospero, 2010). The input of aerosols to the Atlantic come from the Sahara desert and those into the Pacific come from the Gobi desert (Figure 5.45). The average dust input to the Atlantic Ocean is shown in Figure 5.46.

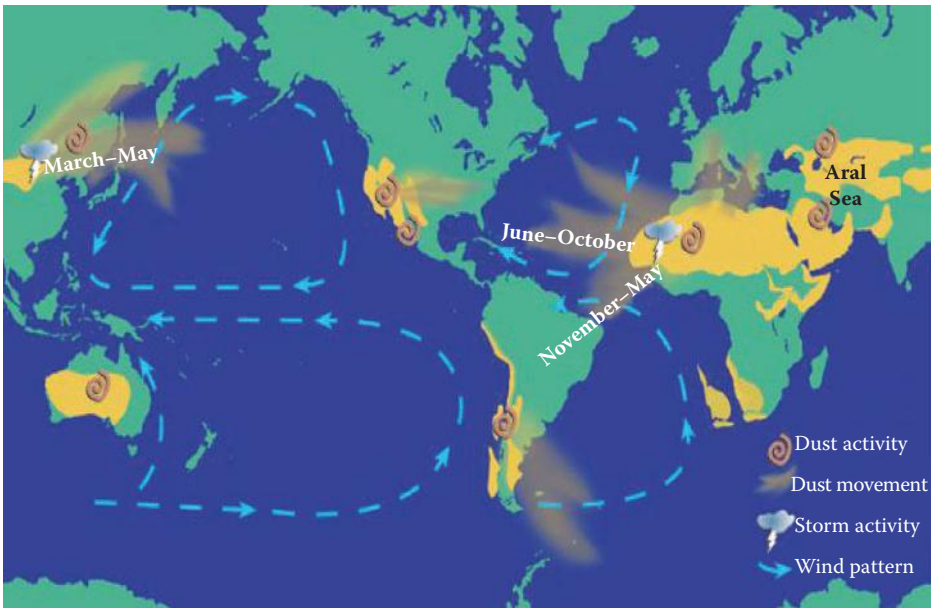

FIGURE 5.45
The input of aerosols to the world oceans.

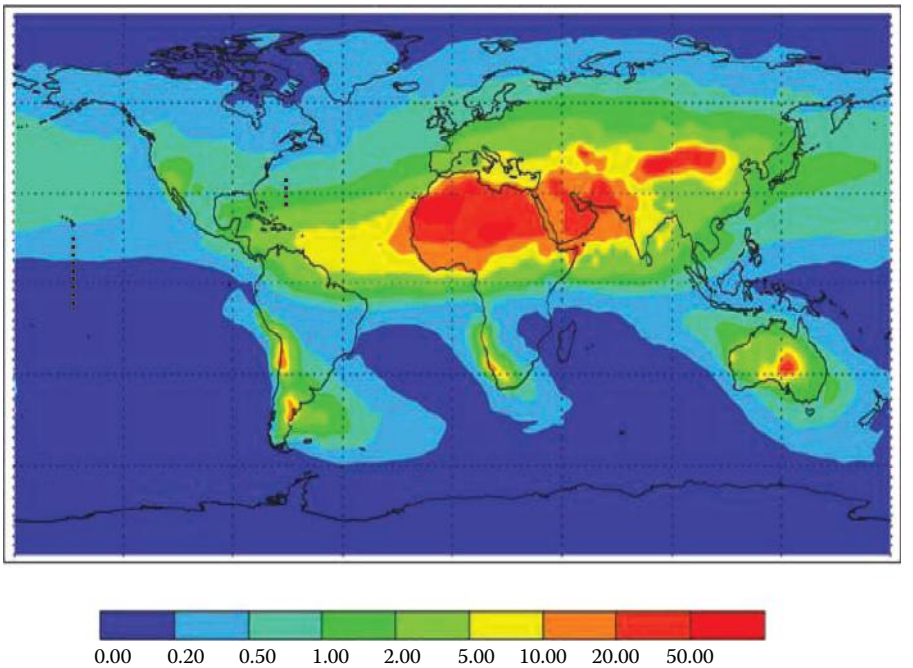

FIGURE 5.46
The average dust deposition (g/m^2/year) of aerosols to the Atlantic Ocean.

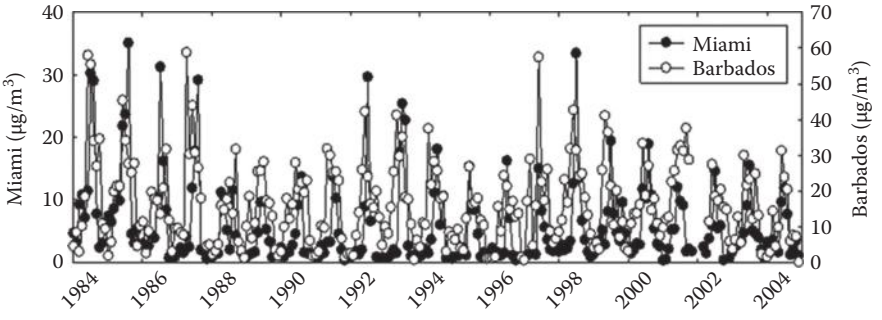

FIGURE 5.47
The monthly mean dust concentrations at Miami and Barbados from 1984 to 2004. (From Trapp, J.M., Millero, F.J., and Prospero, J.M., *Geochem. Geophys. Geosyst.*, 11, 2000. With permission.)

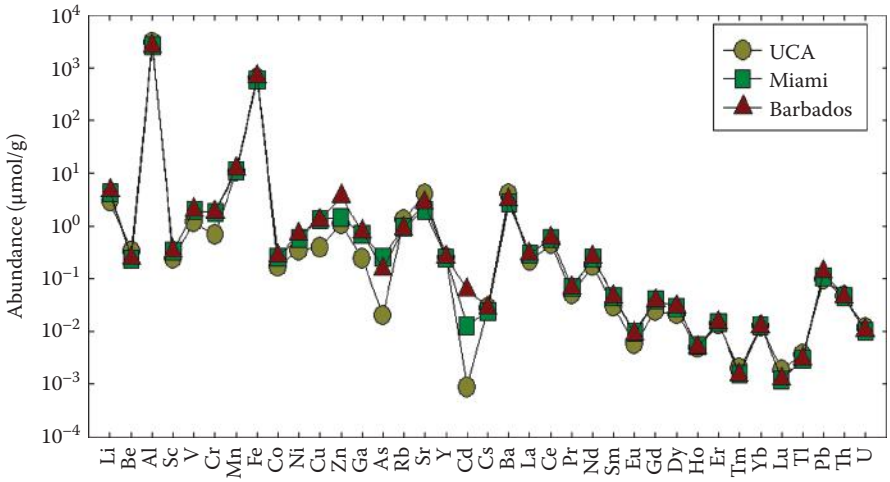

FIGURE 5.48
The chemical compositions of aerosols at Miami and Barbados compared to upper crustal abundances (UCAs). (From Trapp, J.M., Millero, F.J., and Prospero, J.M., *Geochem. Geophys. Geosyst.*, 11, 2000. With permission.)

Prospero (1999) has been monitoring the dust from Africa from stations in Barbados and Miami for a number of years. The monthly inputs of dust at these stations from 1984 to 2004 are shown in Figure 5.47. The largest concentrations occur in the summer months.

The chemical concentrations of the elements in dust are shown in Figure 5.48 (Trapp, Millero, and Prospero, 2010). The concentrations are similar at Miami and Barbados and to the concentrations in upper crustal abundances (UCAs). The concentrations of Al and Fe are the highest since they make up the major components of minerals. The concentrations of total Fe are linearly related to the concentration of Mn in the dust (Figure 5.49). This is similar to the ratio of Fe to Mn in minerals. The fractional concentrations of Fe throughout the year correlate with the concentration of total dust (Trapp, Millero, and Prospero, 2010) (see Figure 5.50). Sholkovitz et al. (2012) have recently synthesized the global aerosol data. The fractional amounts of Fe (%) in dust were found to vary with the total dust in a hyperbolic way (Figure 5.51) (Trapp et al., 2010; Sholkovitz et al., 2012). They find that global-scale data are all adequately described by a simple two-component mixing model. The Fe(%) is

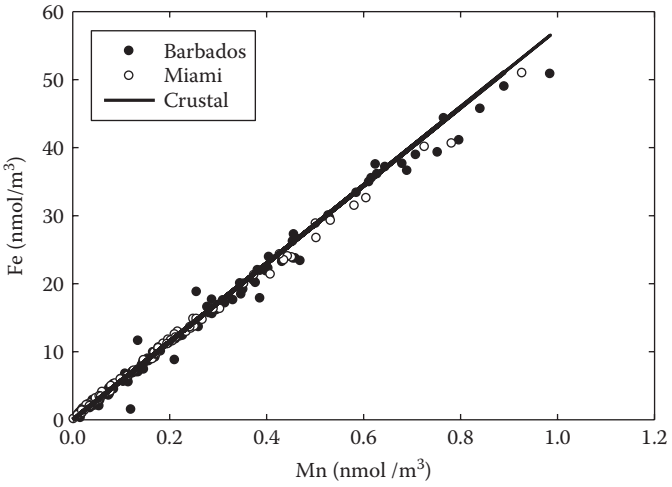

FIGURE 5.49
The correlation of Fe and Mn in aerosols collected in Barbados and Miami.

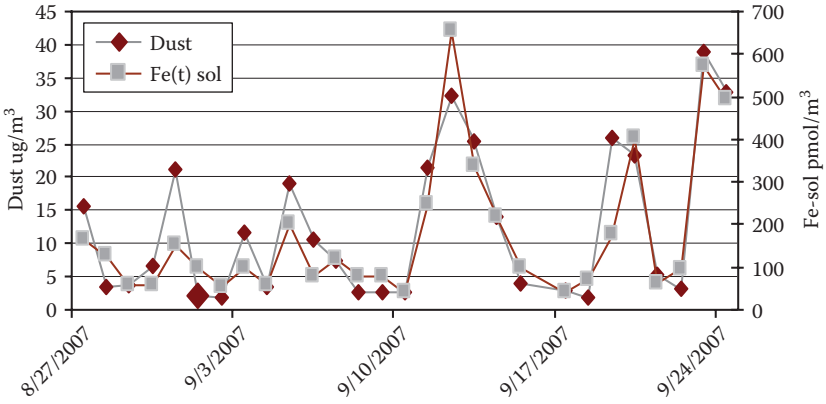

FIGURE 5.50
The input of dust and iron monthly in 2007.

due to the conservative mixing of combustion aerosols [from burning, low total Fe and high Fe(%); and mineral dust, high total Fe and low Fe(%)]. This implies that aerosols from combustible fuels are the major source of soluble Fe to the oceans.

Organic aerosols usually form over land, have different sources, and undergo chemical processing in the atmosphere (Figure 5.51). This leads to aerosol hazes that are frequently seen in cities. The photochemical processes that occur lead to smog. It is interesting to note that most new cars now have catalytic mufflers that can remove NO and CO produced in automobile engines (Jacoby, 2012). This brings me back to my first job many years ago working on catalytic mufflers for an oil company. The NO was formed at high temperatures in the engine (cruising at high speeds), and the CO was formed during idling or accelerating.

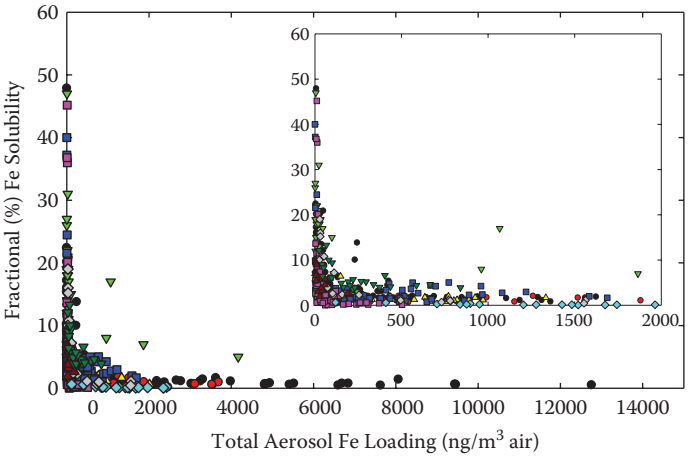

FIGURE 5.51
The fractional Fe solubility versus total Fe loading. (Adapted from the data of Sholkovitz et al., *Geochim. Cosmochim. Acta*, 89, 173–189, 2012.)

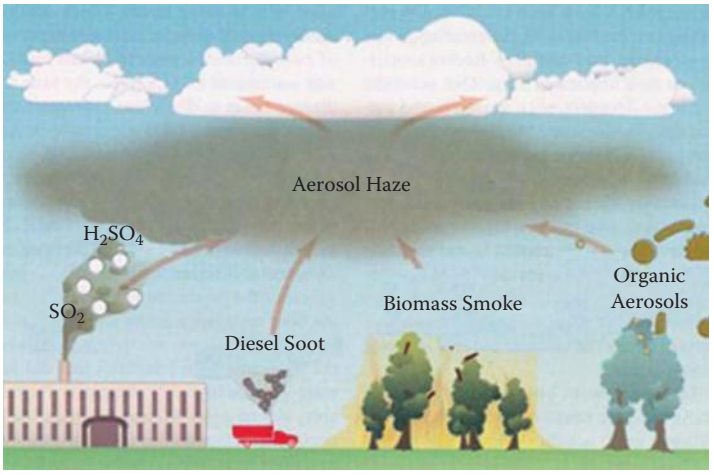

FIGURE 5.52
Sources of aerosol haze.

References and Further Reading

Berg, W.W., Jr., and Winchester, J.W., Aerosol chemistry of the marine atmosphere, Chapter 38, *Chemical Oceanography*, Vol. 7, 2nd ed., Riley, J.P., and Chester, R., Eds., Academic Press, New York, 173–231 (1978).

Booth, B.B.B., Dunstone, N.J., Halloran, P.R., Andrews, T., and Bellouin, N., Aerosols implicated as a prime driver of twentieth-century North Atlantic climate variability, *Nature*, 484, 228–232 (2012).

Carlson, R.J., The atmosphere, in *Global Biogeochemical Cycles*, Butcher, S.S., Charleson, R.J., Orians, G.H., and Wolfe, G.V., Eds., Academic Press, New York (1992).

Chameides, W.L., and Davis, D.D., Chemistry in the troposphere, *Chem. Eng. News,* Oct. 4, 36–52 (1982).
Evan, A.T., Kossin, J.P., Chul, E.C., and Ramanathan, V., Arabian Sea tropical cyclones intensified by emissions of black carbon and other aerosols, *Nature*, 479, 94–97 (2011).
Gruber, N., Warming up, turning sour, losing breath: ocean biogeochemistry under global change, *Phil. Trans. R. Soc*., A369, 1980–1996 (2011).
Jacoby, M., Ever-cleaner auto exhaust, *Chem. Eng. News*, May 21, 10–16 (2012).
Johnson, R.W., and Gordon, G.E., *The Chemistry of Acid Rain*, ACS Symp. 349, ACS, Washington, DC (1987).
Keeling, C.D., and Whorf, T.P., Atmospheric Carbon Dioxide (CO_2) Records from Sites in the SIO Air Sampling Network (1957-2002), in CDIAC in *Trends: A Compendium of Data on Global Change,* Carbon Dioxide Information Analysis Center, Oak Ridge, TN (2004).
Le Roux, V., Dasgupta, R., and Lee, C.-T. A. Mineralogical heterogeneities in the Earth's mantle: constraints from Mn, Co, Ni and Zn partitioning during partial melting. *Earth and Planetary Science Letters*, 307, 395–408 (2011).
Losno, R., Bergametti, G.,Carlier, P., and Mouvier, G., Major ions in marine rainwater with attention to sources of alkaline and acidic species. *Atm. Environ.*, 25A, 3/4, 763–770 (1991).
Muhs, D.R., Budahn, J.R., Skipp, G., Prospero, J.M., and Herwitz, S.R., Soil genesis on the island of Bermuda in the Quaternary: the importance of African dust transport and deposition, *J. Geophys. Res.–Earth Surface,* doi:10.1029/2012JF002366 (2012).
Novelli, P., Masarie, K., Tans, P., and Lang, P., Recent changes in atmospheric carbon monoxide, *Science*, 263, 1587 (1994).
Prospero, J.M., Long-term measurements of the transport of African mineral dust to the southeastern United States: implications for regional air quality, *J. Geophys. Res*., 104, 15,917–15,927 (1999).
Prospero, J.M., Ginoux, P., Torres, O., Nicholson, S.E., and Gill, T.E., Environmental characterization of global sources of atmospheric soil dust identified with the Nimbus 7 total ozone mapping spectrometer (TOMS) absorbing aerosol product, *Rev. Geophys.*, 40, 1002 (2002).
Saltzman, E.S., and Cooper, W.J., *Biogenic Sulfur in the Environment,* ACS Symp. Series, 393, ACS, Washington, DC (1989).
Saltzman, E.S., Whug, P.Y., and Mayewski, P.A., Methanesulfonate in the Greenland ice sheet Project 2 ice core, *J. Geophys. Res.*, 102, 26649 (1997).
Seinfeld, J.H., *Atmospheric Chemistry and Physics of Air Pollution*, Wiley, New York (1986).
Sholkovitz et al., Fractional solubility of aerosol iron: synthesis of a global-scale data set, *Geochim. Cosmochim. Acta*, 89, 173–189 (2012).
Solomon, S., and Ravishankara, A.R., Ozone depletion and global warming potential of CF_3I, *J. Geophys. Res*., 99, 20929 (1994).
Trapp, J.M., Millero, F.J., and Prospero, J.M., Trends in the solubility of iron in dust-dominated aerosols in the equatorial Atlantic trade winds: importance of iron speciation and sources, *Geochem. Geophys. Geosyst*., 11, Q01034 (2000).
Trapp, J.M., Millero, F.J., and Prospero, J.M., Temporal variability of the elemental composition of African dust measured in trade wind aerosols at Barbados and Miami, *Mar. Chem*., 120, 71–82 (2010).

6

Dissolved Gases Other than CO_2

6.1 Introduction

Many workers have examined the concentration of dissolved gases in marine waters like seawater. Most of the earlier work has been reviewed by Richards (1965) and by Kester (1975). The most widely studied gas (excluding CO_2) is oxygen. Attempts have been made to separate the physical and biological processes that control the distribution of O_2. Studies have also been conducted on the unreactive or conservative gases (N_2 and Ar) and the noble gases (He, Ne, Kr, and Xe). The regular distribution of the conservative gases has been used to study the exchange processes across the air–sea interfaces. The irregular distribution of He and Rn have been used to study exchange processes across the sediment–water interface.

CO_2 is considered in the next chapter on the carbon dioxide or carbonate system. It is separated from other gases because it is involved in the pH buffer system of marine waters. Since the source of most gases is the atmosphere, we first consider the composition of the atmosphere and the subsequent transfer across the air–sea interface.

6.2 Composition of the Atmosphere

The atmosphere is made up of the major gases (N_2, O_2, and Ar) and the minor unreactive gases (Ne, He, Kr, and Xe). Water vapor is the most varied component of the atmosphere. Unstable minor gases (CO, NO_2, and CH_4) are produced by biological processes and human activities. These gases will vary from place to place because of the different sources and sinks.

Dalton's law of partial pressures can be used to represent the composition of the atmosphere. This law simply states that the total pressure P_T of a mixture of gases in a fixed volume V is equal to the sum of the partial pressures of the components of the mixture. For the atmosphere, this gives

$$P_T = \sum P_i = P_{N_2} + P_{O_2} + P_{Ar} + P_{H_2O} \tag{6.1}$$

where the values of P_i are the partial pressures of the major gaseous components i. If the gases are assumed to obey the ideal gas law, the partial pressure of each gas is given by

$$P_i = n_i RT/V \tag{6.2}$$

where n_i is the number of moles of gas i (the number of molecules is equal to n_iN, where Avogadro's number $N = 6.024 \times 10^{23}$ molecules per mol), $R = 0.082057$ (dm^3 atm mol^{-1} K^{-1}), and T is the absolute temperature ($T = t°C + 273.15$).

The composition of the gases in dry air, expressed as the mole fraction, is

$$X_i = n_i/n_T = P_i/P_T \tag{6.3}$$

where $n_T = \sum n_i$. The mole fractions of the major gases in the atmosphere were given in Table 5.1. The values of X_i are equal to the partial pressures P_i for ideal gases when the total pressure $P_T = 1$ atm. The nonideal behavior of a gas can be estimated from the Van der Waals equation of state:

$$(P_i + n_i^2\,\mathbf{a}/V2)(V - n_i\mathbf{b}) = n_iRT \tag{6.4}$$

where **a** is related to intermolecular attraction, and **b** is related to the finite volume and compressibility of the gases. The coefficients **a** and **b** for Equation 6.4 are given in Table 6.1 (Kester, 1975). The molar volumes of the gases at 0°C and 1 atm (standard temperature and pressure, STP) calculated from Equation 6.4 are also given in Table 6.1. The values deviated from ideal gas behavior (22.414 dm^3 mol^{-1}) by +0.1% for He to –0.67% for Kr. For accurate calculations, Equation 6.4 should be used; more exact equations of state for these gases are available, but near STP, Equation 6.4 is adequate to ±0.05%.

Although the mole fractions of the major gases in the atmosphere do not vary geographically or with altitude (to 95 km), the fraction of water vapor does vary significantly. These variations are accounted for by making corrections for the humidity (%) of the air at a given temperature. The partial pressure of water vapor is given by

$$P_{H_2O} = (h/100)P_0 \tag{6.5}$$

when P_0 is the vapor pressure of water (kPa) at a given temperature.

$$\ln P_0 = -0.493048 + 0.07263769\,t - 0.000294549\,t^2 + 9.79832\,10^{-7}\,t^3 - 1.86536\,10^{-9}\,t^4 \tag{6.6}$$

TABLE 6.1

van der Waals Coefficients for Atmospheric Gases

Gas	van der Waals Coefficients a	van der Waals Coefficients b	Molar Volume at STP (dm^3 mol^{-1})
N_2	1.390	0.03913	22.391
O_2	1.360	0.03183	22.385
Ar	1.345	0.03219	22.386
CO_2	3.592	0.04267	22.296
Ne	0.2107	0.01709	22.421
He	0.03412	0.02370	22.436
Kr	2.318	0.03978	22.350
Xe	4.194	0.05105	22.277

Source: Data from Kester, D.R., Dissolved gases other than CO_2, in *Chemical Oceanography*, Vol. 1, 2nd ed., J.P. Riley and G. Skirrow, Eds., Academic Press, New York, 498–556, 1975.

TABLE 6.2

Isotopic Abundance of Atmospheric Gases

Element	Mass Number	Mole%	Element	Mass Number	Mole%
H (in H_2O)	1	99.98	Kr	78	0.354
H (in H_2O)	2	0.02	Kr	80	2.27
He	3	1.1×10^{-4}	Kr	82	11.56
He	4	100.0	Kr	83	11.55
C (in CO_2)	12	98.9	Kr	84	56.90
C (in CO_2)	13	1.1	Kr	86	17.37
C (in CO_2)	14	9.5×10^{-13}			
N	14	99.62	Xe	124	0.096
N	15	0.38	Xe	126	0.090
O	16	99.757	Xe	128	1.919
O	17	0.039	Xe	129	26.44
O	18	0.204	Xe	130	4.08
Ne	20	90.92	Xe	131	21.18
Ne	21	0.257	Xe	132	26.89
Ne	22	8.82	Xe	134	10.44
Ar	36	0.337	Xe	136	8.87
Ar	38	0.063			
Ar	40	99.600			

Source: Data from Kester, D.R., Dissolved gases other than CO_2, in *Chemical Oceanography*, Vol. 1, 2nd ed., J.P. Riley and G. Skirrow, Eds., Academic Press, New York, 498–556, 1975.

At temperature t = 25°C and humidity (h) = 100%, the vapor pressure of water is 3.169 kPa or 0.03169 bar. Thus, the water will contribute 3% to the total pressure (similar to Ar). The partial pressure of the other gases can be converted to dry air using

$$P_i = [P_T - (h/100)P_{H_2O}]X_i \tag{6.7}$$

The stable isotopic composition of atmospheric gases is summarized in Table 6.2 (Kester, 1975). The values of the mole percentage were calculated using 5×10^{21} g or 1.71×10^{20} moles for the total atmosphere.

6.3 Dissolution of Gases in Seawater

The concentration of a gas in solution is related to the partial pressure by Henry's law:

$$P_i = k_i[i] \tag{6.8}$$

where [i] is the concentration of the dissolved gas (expressed in mol kg^{-1} of solution), and k_i is the Henry's law constant. The parameter k_i will depend on the particular gas, the salinity or ionic strength of the solution, the temperature, and total pressure. Equilibrium is obtained when the partial pressure of the gas in solution is equal to the value in the gas phase:

$$P_i(\text{soln}) = P_i(\text{gas}) \tag{6.9}$$

The concentration of a gas at equilibrium is given by

$$[i] = P_i(gas)/k_i \tag{6.10}$$

The concentration of a gas in solution can be expressed by a variety of scales. Most physical chemists express the concentration as molality (mol $[kgH_2O]^{-1}$) or mole fraction. These scales are useful since the magnitude is not affected by the composition of the gas phase and is independent of temperature. Much of the earlier solubility of gases in seawater was expressed in terms of the Bunsen coefficient, which is the value of [i] expressed in cubic centimeters of a gas at STP per cubic centimeters of solution at the temperature in question when the $P_i = 1.0$ atm. Since the volume of each gas is different at STP, this has led to confusion. For practical reasons, the most convenient scale to use is moles per kilogram of seawater when P_i is the partial pressure and the total pressure is 1 standard atmosphere (1.013 bar). The correction for P_i for different total pressures (in atm) and percentage humidity (h) from standard values is given by

$$P_{i'} = P_i\,(P_T - P_S\,h/100)/(1 - P_S) \tag{6.11}$$

where $P_{i'}$ is the corrected partial pressure of the gas, and P_S is the vapor pressure of water in seawater at a given temperature and salinity (S). It can be calculated from

$$P_S = P_0 + A\,S + B\,S^{3/2} + C\,S^2 \tag{6.12}$$

where P_0 is the vapor pressure of water at S = 0 (Equation 6.6):

$$A = -3.7433 \times 10^{-3} + 1.6537 \times 10^{-4}\,t - 1.9667 \times 10^{-6}\,t^2 - 2.435 \times 10^{-7}\,t^3 \tag{6.13}$$

$$B = 5.2556 \times 10^{-4} - 7.72660 \times 10^{-6}\,t \tag{6.14}$$

$$C = -4.9535 \times 10^{-5} \tag{6.15}$$

At t = 25°C and S = 35, this equation gives $P_S = 2.7251$ kPa or 0.027251 bar. The appropriate humidity (h) and pressure (P_S) can be obtained from the conditions of the surface waters. Care must be taken, however, since solubility is slow to respond to changes in P_T, and the humidity near the water–air interface may be different from that observed on a ship (~5 m above the interface). For a water parcel that has left the surface, it is reasonable to assume $P_T = 1$ atm and h = 100%. In recent years, more accurate data have become available for the solubility of gases in seawater. These more accurate data allow examination of the departure of waters from equilibria. The supersaturation of N_2 and Ar, for example, can be related to entrapped bubbles. The super- or undersaturation of O_2 can be related to photosynthesis and respiration.

The solubility of gases (C is in μmol kg^{-1}) in seawater has been fit by Weiss (1971) to equations of the form

$$\ln C = B_1 + B_2\,S \tag{6.16}$$

which conforms to the Setchenow salting out equation and

$$\ln C = A_1 + A_2/T + A_3 \ln T \tag{6.17}$$

the integrated van Hoff equation. The final form used by Weiss (1971) is

$$\ln C = A_1 + A_2(100/T) + A_3 \ln(T/100) + S[B_1 + B_2(T/100) + B_3(T/100)^2] \quad (6.18)$$

The coefficients A_i are related to the solubility of the gas in water at various temperatures, while the coefficients B_i are related to the solubility of the gas in seawater. The effect of temperature on the salting coefficient B_2 is not of the proper van Hoff form (Equation 6.17). The B_2 and B_3 terms should be functions of 1/T and ln T, respectively. The values of A_i and B_i for various gases when [i] is in units of micromoles per kilogram are given in Table 6.3. Values of [i] expressed in these units for S = 35 seawater are given in Table 6.4. It is important to point out that the use of Equation 6.18 smoothes out the variability of gas

TABLE 6.3

Solubility of Gases in Seawater with the Constants for Equation 6.18 in Moles per Kilogram Relative to Air at 1 atm at 100% Relative Humidity

Gas	A_1	A_2	A_3	A_4
N_2	–173.2221	254.6078	146.3611	–22.0933
O_2	–173.9894	255.5907	146.4813	–22.2040
Ar	–174.3732	251.8139	145.2337	–22.2046
Ne	–166.8040	255.1946	140.8863	–22.6290
He	–163.4207	216.3442	139.2032	–22.6202
	B_1	B_2	B_3	
N_2	–0.054052	0.027266	–0.0038430	
O_2	–0.037362	0.016504	–0.0020564	
Ar	–0.038729	0.017171	–0.0021281	
Ne	–0.127113	0.079277	–0.0129095	
He	–0.44781	0.023541	–0.0034266	

Source: Data from Kester, D.R., Dissolved gases other than CO_2, in *Chemical Oceanography*, Vol. 1, 2nd ed., J.P. Riley and G. Skirrow, Eds., Academic Press, New York, 498–556, 1975.

TABLE 6.4

Solubility of N_2, O_2, Ar, Ne, and He in Seawater (S = 35) Equilibrated with the Atmosphere (P = 1 atm) at 100% Humidity

	μmol kg^{-1}			nmol kg^{-1}			
	N_2	O_2	Ar	Ne	He	Kr	Xe
0°C	616.4	349.5	16.98	7.88	1.77	4.1	0.66
5	549.6	308.1	15.01	7.55	1.73	3.6	0.56
10	495.6	274.8	13.42	7.26	1.70	3.1	0.46
15	451.3	247.7	12.11	7.00	1.68	2.7	0.39
20	414.4	225.2	11.03	6.77	1.66	2.4	0.33
25	383.4	206.3	10.11	6.56	1.65	2.2	0.29
30	356.8	190.3	9.33	6.36	1.64	2.0	0.25

solubility with respect to temperature and salinity (Kester, 1975). The solubility for O_2 has been replaced by the measurements of Benson and Krause (1984):

$$\ln C = -135.29996 + 1.572288 \times 10^5/T - 6.637149 \times 10^7/T^2 + 1.243678 \times 10^{10}/T^3 - 8.621061 \times 10^{11}/T^4 - S(0.020573 - 12.142/T + 2{,}363.1/T^2) \quad (6.19)$$

6.4 Air–Sea Exchange

Most of the gases in seawater originate from three sources: (a) the earth's atmosphere, (b) volcanic activity beneath the sea, and (c) chemical processes occurring in the sea (biological-photosynthesis and decomposition of organic matter, physical-radioactive decay). One of the most useful assumptions concerning the solubility of gases is that at one time, every parcel water was at the sea surface and at that time became equilibrated (or nearly so) with the atmospheric gases. In the course of oceanic circulation, the unreactive gases are distributed throughout the water column by advection and diffusion.

The exchange of gases across the air–sea interface has been examined by a number of workers using various models. The simplest model, which is a stagnant film model, is shown in Figure 6.1. The model considers three regions: (a) a turbulent atmospheric phase in which the partial pressure of each gas is uniform, (b) a turbulent liquid phase with a uniform partial pressure, and (c) a laminar layer that separates the two turbulent regions. The motion of the liquid in the laminar layer is parallel to the air–sea interface. It is assumed that the gas is transferred through the laminar layer by molecular diffusion and that the layer or film represents the major resistance to the gas transfer. The laminar or thin film is regarded as permanent and has a thickness of τ. The flux of gas across the interface can be examined using Fick's first law:

$$dC_i/dt = A\, D_i(dC_i/dz) \quad (6.20)$$

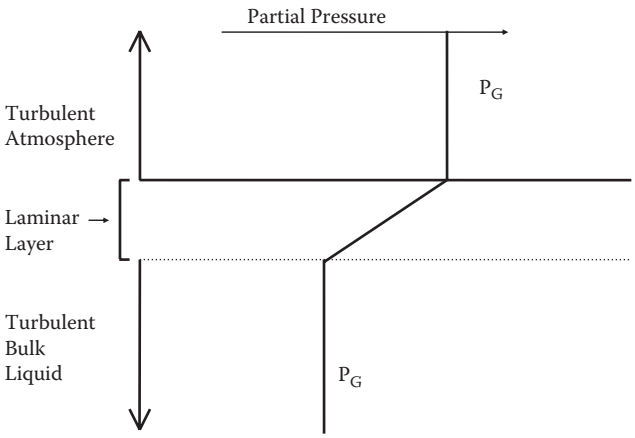

FIGURE 6.1
The laminar layer for the transport of gases across the air–sea interface.

where A is the interfacial area, C_i is the concentration of species i, t is the time, D_i is the diffusion coefficient or diffusivity of species i, and dC/dz is the gradient (z is the vertical distance). If this equation is combined with Henry's law ($P_i = k_i C_i$), we have

$$dC_i/dt = (A\ D_i/\tau\ k_i)[P_i(gas) - P_i(soln)] \tag{6.21}$$

where k_i is the Henry's law constant. This model assumes that the flux of the gas across the air–sea interface is directly proportional to the diffusion coefficient and inversely proportional to the Henry's law constant. The driving force of the gas exchange is proportional to the partial pressure difference of the gas between the liquid and the atmosphere. The molecular diffusion coefficients for various gases are given in Table 6.5. At a given temperature, the diffusion coefficients decrease with increasing molecular weight or size. An increase in temperature causes the diffusion coefficient to increase. The laminar layer model for various gases has led to observed boundary layers of $\tau = 0.002$ to 0.02 cm. The smaller thickness occurs with an increase in turbulence caused by an increase in the wind speed. Broecker and Peng (1982) compared wind tunnel measurements of τ to values obtained using ^{14}C and Rn measurements. The results shown in Figure 6.2 are in reasonable agreement. The values of τ range from 10 to 90 μm depending on the wind speed. The solid line is from wind tunnel measurements. The solid circles are based on radon measurements in the ocean, and the open squares represent global averages based on ^{14}C measurements. The laboratory results give lower film thickness than the direct measurements. This may be because of larger waves in the oceans than in the wind tunnel or problems in estimating the appropriate wind speed above the water (10 cm above water in the wind tunnel vs. 15 m above the water in the sea). Both studies demonstrate that the film thickness decreases at high wind speeds.

A more general equation for the rate of transfer of a gas across the air–sea interface is given by

$$dC_i/dt\ A(f_i/k_i)(P_i(gas) - P_i(soln)) \tag{6.22}$$

TABLE 6.5

The Rates of Molecular Diffusion of Various Gases in Seawater

		$D_i\ 10^{-5}$ ($cm^2\ s^{-1}$)	
Gas	**MW**	**0°C**	**20°C**
He	4.0	2.0	4.0
Ne	20	1.4	2.8
N_2	28	1.1	2.1
O_2	32	1.2	2.3
Ar	40	0.8	1.5
Kr	84	0.7	1.4
Xe	131	0.7	1.4
Rn	222	0.7	1.4
CO_2	44	1.0	1.9
N_2O	44	1.0	2.0

Source: Data from Broecker, W.S., and Peng, T.H., *Tracers in the Sea*, Eldigio Press, New York, 1982.

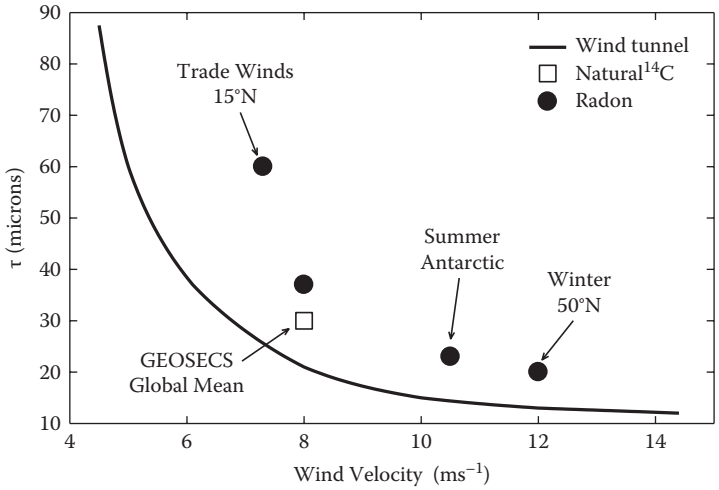

FIGURE 6.2
The thickness of the laminar layer as a function of the wind speed.

where $f_i\ D_i/\tau$ is called the exit coefficient or the transfer velocity. The laminar model equates f_i to D_i/τ. If one assumes that the rate-determining factor is the time θ, a volume element is at the air–sea interface:

$$f_i\ 2(D_i/\pi\theta)^{1/2} \tag{6.23}$$

The existence of a laminar layer at the air–sea interface has been supported by observations.

Fick's first law can also be expressed as

$$F = dC/dt = k\Delta C \tag{6.24}$$

where F is the flux (mol cm^{-2} s^{-1}), ΔC is the change in concentration across the air–sea interface (mol cm^{-3}), and k is called the transfer velocity (cm s^{-1}), permeability coefficient, mass transfer coefficient, absorption coefficient, exit coefficient, or piston velocity. If the thin-film layer model is used, k is proportional to D/τ, where D is the diffusion coefficient and τ is the boundary thickness. If the surface renewal model is used, k is proportional to $D^{1/2}$, and if a boundary layer model is used, k is proportional to $D^{2/3}$. The most popular model presently used in oceanography to describe the flux across the air–sea interface is the model of Liss (1975). This model is a stagnant film model with a two-layer boundary between the interfaces (see Figure 6.3).

As with the thin-film model, the air above and the liquid below the gas and liquid films are assumed to be well mixed. Gas transfer occurs by molecular diffusion, and the resistance to gas transport is diffusion across the gas–liquid interfacial layer. The value of k depends on the turbulence in the gas and liquid phases and the chemical reactivity of the gas. The reciprocal of the exchange coefficient is a measure of the resistance to transfer across the interface. This resistance is divided into the resistance of both the air and water phases:

$$1/k = R = R_g = R_l \tag{6.25}$$

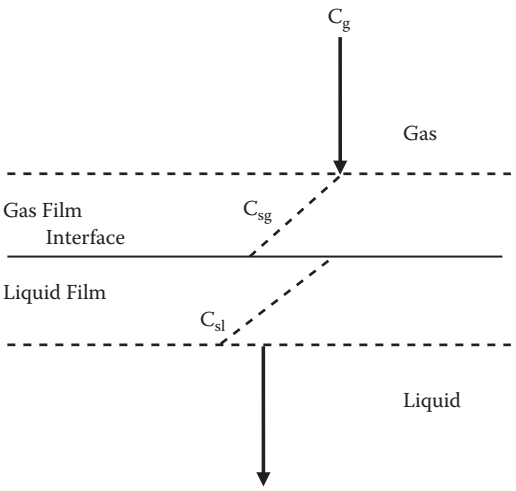

FIGURE 6.3
The gas film model for the transport of gases across the air–sea interface.

The total flux is equal to the values through the two boundaries

$$F = k_g(C_g - C_{sg}) = k_l(C_{sl} - C_l) \tag{6.26}$$

where C_g is the concentration of the gas in the gas phase, C_{sg} is the concentration of gas in the surface film, C_l is the concentration of the gas in the liquid phase, and C_{sl} is the concentration of the gas in the surface film. In the surface film,

$$C_{sg} = H\,C_{sl} \tag{6.27}$$

where H is the Henry's law constant. The substitution into Equation 6.26 gives

$$F = (C_g = H\,C_l)/(1/k_g + H/k_l)\ \ (C_g/H - C_l)(1/k_l + 1/H\,k_g) \tag{6.28}$$

If we define:

$$1/K_g = 1/k_g + H/k_l \tag{6.29}$$

$$1/K_l = 1/k_l + 1/H\,k_g \tag{6.30}$$

Equation 6.28 can be rewritten as

$$F = K_g(C_g - H\,C_l) = K_l(C_g/H - C_l) \tag{6.31}$$

The total resistance to transport across the air–sea interface R is given by

$$R = 1/K_A + 1/K_W \tag{6.32}$$

where $R_g = 1/K_g$ is the resistance of the gas phase and $R_l = 1/K_l$ is the resistance of the liquid phase. The value of R depends on the exchange constants of the gas and liquid phases

and the Henry's law constant for the gas. For most gases the resistance of one phase dominates and controls the total resistance.

For gases that can react chemically with water (CO_2 and SO_2), the transport is more complex. This is due to the existence of not only a gas gradient but also a gradient in the chemical species formed (HCO_3^- and HSO_3^-). To account for the increase in the flux caused by chemical reactions, workers have defined a term α. This gives

$$1/k_l = 1/k_l\alpha + 1/Hk_g = C_g/k_l\alpha H - C_l/k_l\alpha \tag{6.33}$$

For unreactive gases, α = 1.0, while for a gas like SO_2 α ≈ 2000. For gases like H_2O, HCl, SO_2, and HNO_3, which partition strongly into water (low H) or react rapidly, the $R_g >> R_l$. For gases like O_2, N_2, CO_2, inert gases, SF_6, and freons, which have high values of H and are nonreactive, $R_l >> R_g$. The α for CO_2, for example, is about 1.02 to 1.03. Thus, for most gases the R_l or k_l term will dominate.

Values of k_l at the air–sea interface have been estimated by a number of workers. Broecker and Peng (1982), using ^{14}C data, found a value of k_W = 20 cm h^{-1} with a probable error of 20%, or 5 cm h^{-1}. A number of workers have used O_2 measurements to estimate k_W. They found k_W = 5 to 15 cm h^{-1} in the summer and k_W = 40 to 50 cm h^{-1} in the winter. The higher values are probably related to the higher wind speeds in the winter. Broecker and Peng (1982) have also used the concentrations of radon ^{222}Rn near the interface to estimate values of k_W. These results give k_W = 12 to 15 cm h^{-1}, which corresponds to k_W = 15 cm h^{-1} for CO_2. The transfer velocity obviously depends on the wind velocity; however, as seen in Figure 6.2 and Figure 6.4, the relation is not straightforward.

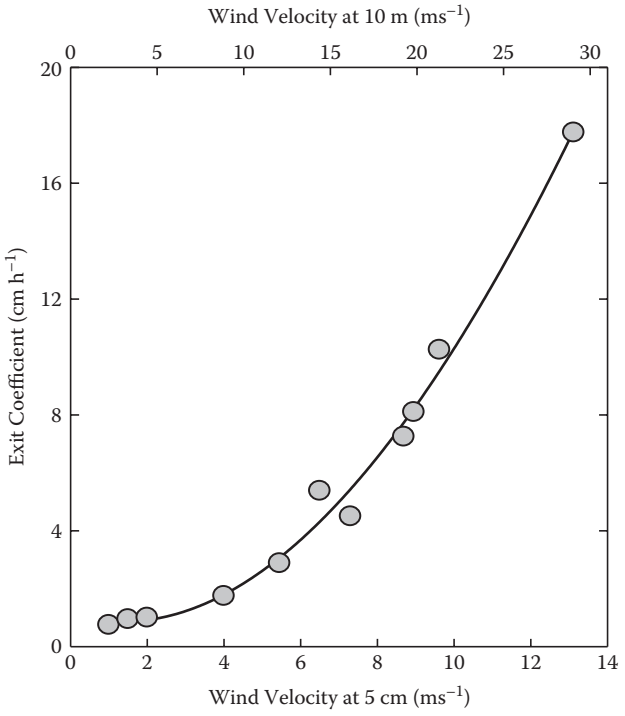

FIGURE 6.4
The exit coefficient (cm h^{-1}) across the air–sea interface as a function of wind speed.

Redfield (1948) used oxygen data in the Gulf of Maine to evaluate atmospheric exchange under natural conditions. In the spring, he found that O_2 was transferred from the sea to the atmosphere as a result of photosynthesis. In the summer, the warming of the waters produced further evolution of O_2. In the winter, O_2 was regained by the colder waters (40% to oxidize organic matter and 60% adsorbed). He determined the exchange coefficient, E = D/k f/k, was 3×10^6 cm^3 month^{-1} atm^{-1} from the oceans in the spring and l3×10^6 cm^3 month^{-1} atm^{-1} to the ocean in the winter.

The effect of wind speed on the exchange of O_2 across the air–water interface is shown in Figure 6.4. The exit coefficient is constant below a wind speed of 3 m s^{-1} (5 cm above the liquid). The coefficient is greatly increased above 3 cm s^{-1}, suggesting turbulent flow. The wind speeds of 5 cm are about half the value they are at the standard meteorological height of 10 cm. Although these early studies have been improved on, they do provide insight into some of the factors controlling gas transfer in natural waters. Broecker and Peng (1982) have compared wind tunnel measurements with calculated values using ^{14}C and radon measurements. The measured results (Figure 6.4) are in good agreement.

Air bubbles can also affect the exchange of gases across the air–sea interface. Hydrostatic pressure can affect the rate of solution and composition of air bubbles. The radius of the dissolving bubbles decreases linearly with time and depth. The composition of the air bubble becomes enriched with N_2 because of the larger Henry's law coefficient for O_2 compared to N_2. Free bubbles exhibited a diffusion coefficient twice as large as that for stationary bubbles. This difference is probably related to differences in the interfacial boundary between stationary and free bubbles and the liquid.

Air bubbles are carried to 20 m below the sea surface during a storm. The partial pressure of the gases in bubbles at this depth is three times the values at the sea surface. Gas exchange between a bubble and seawater is larger than across the air–sea interface because the laminar layer is thinner and the partial pressures are increased. Two populations of bubbles have been found: (a) those less than 40 μ in radius associated with atmospheric particles deposited on the sea surface and (b) those about 100 μ in radius formed at the sea surface by collapsing waves. Air bubbles can change the magnitude of the flux of a gas as much as barometric pressure changes of 2% in 12 h (the passage of a storm). The rate of exchange by bubbles could be several orders of magnitude greater than seasonal fluxes; thus, bubbles are an important mechanism for gas exchange.

At low film thickness (high wind speeds), the chemical effects are negligible, but waves can influence the gas transfer. The transfer rate is proportional to the mean square slope of the wave. For capillary waves, the enhancement was predicted to be a factor of nine. Waves produced in wave tunnels only show an enhancement of 10%. The wind tunnel results showed that the enhancement of the transfer rate varied as a function of the mean square slope of the waves divided by the friction velocity in the water. More work is needed to elucidate the many factors that control the transfer of gases across the air–sea interface.

6.5 Nonreactive Gases

Nitrogen and the noble gases are regarded as nonreactive. The distribution of nonreactive gases is affected by physical processes and the effects of temperature and salinity on solubility. Studies of the distribution of the nonreactive gases can be useful in separating the

effects of physical and biological processes on the distribution of reactive gases such as O_2 and CO_2. With the advent of better analytical techniques, recent advances have been and are being made in this area of research.

The variations of nonreactive gases are studied by examining the solubility at 1 atm total pressure and 100% relative humidity. The degree of saturation σ_i is given by

$$\sigma_i = [i]/[i]^* \times 100 \tag{6.34}$$

where [i]* is the solubility concentration at a given potential temperature and salinity, and [i] is the measured gas concentration. The saturation anomaly Δ_i is also used:

$$\Delta_i = ([i] - [i]^*)/[i]^*) \times 100 \tag{6.35}$$

The examination of σ_i and Δ_i permits one to follow the distribution without the bias of temperature and salinity. The physical processes that can cause nonreactive gases to depart from the expected concentration are

1. Departures from the standard pressure
2. Partial dissolution of air bubbles
3. Air injection
4. Differential heat and gas exchange
5. Mixing of waters of different temperatures
6. Radiogenic or primordial addition (He)

The radiogenic production of ^{40}Ar from ^{40}K in seawater is not significant. It would take 10^{11} years of ^{40}K decay to produce the amount of ^{40}Ar in the oceans.

Changes in barometric pressure and humidity affect all the gases by an equal percentage. At 30°, the Δ_i is increased by 0.9% when the humidity is decreased to 80%. To account for departures from the standard pressure and humidity, one must study at least two gases. When a bubble of air is submerged below the surface, it will dissolve as a result of hydrostatic pressure. If the bubble partially dissolves before it goes back to the surface, all the gases will partially dissolve and increase Δ_i. For partial dissolution, the composition of the gases in the bubble will remain unchanged. At a depth of 1 m, the Δ_i is increased by 10% for all the gases. If the air bubble completely dissolves, it is called air injection. Each gas is affected differently for air injection because of the differences in solubility. The differences in the variation of the solubility of gases with temperature are shown in Figure 6.5. This difference in composition produces large variation in Δ_i for different gases when air is injected or totally dissolved in seawater.

Since the solubility of gases varies differently with temperature, changes in temperature without an exchange with the atmosphere can cause Δ_i to vary. The mole fraction of each gas at equilibrium in solution is different from that of air (see Table 6.6). For example, at 15°C a 1°C decrease in temperature will cause Δ_i to vary from –0.24% for He to –2.5% for Xe (Kester, l975). When the heat exchange is more rapid than gas exchange (for example, in upwelling areas), saturation anomalies will occur. The mixing of waters of different temperatures will also produce saturation anomalies resulting from the nonlinear behavior of solubility with temperature. For example, the mixing of waters at 0 and 30°C will produce saturation anomalies of 1.3% for He and 18% for Xe.

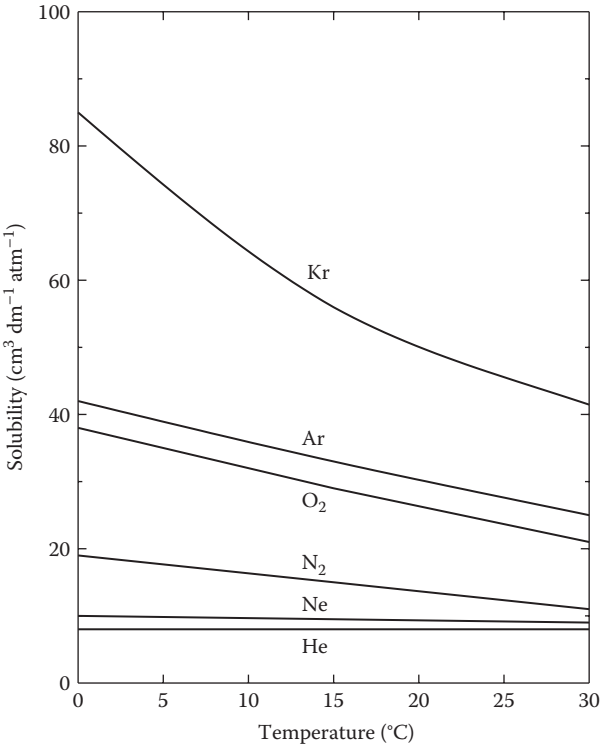

FIGURE 6.5
The effect of temperature on the solubility of gases in seawater.

TABLE 6.6

Comparison of the Mole Fraction (X_i) of Gases Dissolved in Saturated Seawater and in Dry Air and the Saturation Anomaly of Air Resulting from the Injection of 1 cm^3 of Air at STP per Kilogram of Seawater[a]

	N_2	O_2	Ar	CO_2	Ne	He	Kr	Xe
X_{air}	0.780	0.209	0.009	0.0003	18.2×10^{-6}	5.2×10^{-6}	1.1×10^{-6}	0.09×10^{-6}
X_{SW}	0.626	0.343	0.016	0.014	9.7×10^{-6}	2.3×10^{-6}	3.8×10^{-6}	0.54×10^{-6}
Air (%)	7.7	3.8	3.5	0.1	11.6	13.8	1.8	1.0

[a] All seawater values are based on 15°C and S = 35.

By studying several gases, it is possible to determine the magnitudes of these processes. Xe and Kr are not sensitive to air injection, so they can be used to examine temperature effects. He is sensitive to air injection but is not affected by temperature effects. Since Ar and O_2 are affected by nearly the same amounts, Ar is the best nonreactive gas for separating the biological and physical processes for O_2.

The saturation anomalies for N_2 have been studied by a number of workers. The results (Kester, 1975) are shown in Table 6.7. All the waters are within ±1.4% of the saturated values (which is within the standard error 3%). The high standard errors could be related to real variations caused by oceanic processes (air injection, etc.). Since biochemical processes are known that convert N_2 to organically bound nitrogen and N_2 can be produced from

TABLE 6.7

Saturation Anomalies for Nitrogen

	N_2	
Water Mass	**Mean**	**Standard Deviation**
All surface waters (z < 10 m)	–0.17%	3.4%
South Atlantic central water	–0.48%	1.3%
Antarctic intermediate water	–1.42%	3.0%
North Atlantic deep water	+0.32%	1.9%
Antarctic bottom water	–0.04%	2.2%

Source: Data from Kester, D.R., Dissolved gases other than CO_2, in *Chemical Oceanography*, Vol. 1, 2nd ed., J.P. Riley and G. Skirrow, Eds., Academic Press, New York, 498–556, 1975.

organic nitrogen under anoxic conditions, one may question the degree to which N_2 is conservative. Benson and Parker's measurements of the ratio of N_2 to Ar indicate that for most ocean waters N_2 can be considered to be conservative to ±1%. Richards and Benson's (1961) measurements of N_2/Ar in anoxic basins yielded ΔN_2 +2.3% for the Cariaco trench and +3.6% for the Damsfjord. Due to the different solubility data used and the method of reporting the results, it is difficult to make a detailed comparison of various N_2 studies at the 1% level. Most ocean waters are generally within 1 to 2% of the saturation values except in anoxic waters, which may be 2 to 4% supersaturated. As the analytical precision for N_2 has improved, the spread of Δ_{N2} has decreased.

The saturation anomalies of a gas can be attributed to three major components (Weiss, 1971):

$$\Delta_i = \delta_P + \delta_t + \delta_A \tag{6.36}$$

The factor δ_P is due to differences in the effective and standard atmospheric pressure:

$$\delta_P = \frac{[P_{atm} - (h/100)P_S]100}{1 - P_S} + \frac{Z}{10} \tag{6.37}$$

where Z is the depth in centimeters at which the air bubble is equated. Since δ_P does not depend on a specific property of a gas, it is not possible to determine the various terms separately. The factor δ_t is due to changes in temperature δ_t without gas exchange:

$$\delta_t = [-100\ d\ \ln[i]/d\ T]\ \Delta T \tag{6.38}$$

where ΔT is the observed potential temperature minus the temperature at the time of equilibration. This term applies to changes in temperature caused by radiative heating or cooling and geothermal heating (not mixing of waters of different temperature). The factor δA is the result of air injection and is given by

$$\delta A = X_i\ 100\ a/[i]\ 22{,}390 \tag{6.39}$$

where a is the cubic centimeters of air at STP injected per kilogram of SW and 22,390 is the molar volume of air in cubic centimeters at STP.

Kester (1975) has used these relations for Atlantic waters (t = 26°C and S = 36):

$$\Delta_{Ne} = 4.5 = \delta_P + 0.626\ \delta_t + 12.47\ \delta A \tag{6.40}$$

$$\Delta_{Ar} = 2.0 = \delta_P + 1.62\ \delta_t + 4.22\ \delta A \tag{6.41}$$

$$\Delta_{He} = 4.6 = \delta_P + 0.180\ \delta_t + 14.16\ \delta A \tag{6.42}$$

The solution gives $\delta_P = -2.8\%$, δ_t +1.7°C, and $\delta A = 0.50$ cm^3 air at STP per kilogram. The negative value of δ_P indicates that $P_{atm} < 1$ atm. A 1% increase in δ_P can be caused by an increase of 8 mm of Hg, an equilibration of air at 10 cm below the surface, or h = 65% at 25°C.

Deep ocean waters have been found to be injected by 0.5 to 1.0 cm^3 of air at STP per kilogram of seawater. Helium can also be injected into the deep oceans from the seafloor. The helium is produced by the radioactive decay of uranium and thorium in sediments and rocks. Direct injection of He has also been found to come from hydrothermal fluids. This excess helium injected into the deep oceans has been used by Craig (1969) to study the movement of waters in the deep sea (see Figure 6.6). Saturation anomalies for He, Ne, and Ar in North Atlantic deep waters (NADWs) can be attributed to air injection. In the Pacific, however, the ΔHe of 7 to 12% is partially (50%) due to excess helium. The He anomaly can be studied by examining the $^3He/^4He$ ratio. Observed values (Pacific) of this ratio greater than equilibrium values (Figure 6.7) can be attributed to helium coming from the interior of the earth from active ridges. Recent measurements of hydrothermal waters (Figure 6.8) gave ratios of $^3He/^4He = 1.08 \times 10^{-5}$ compared to expected air injection values of 1.38×10^{-6}.

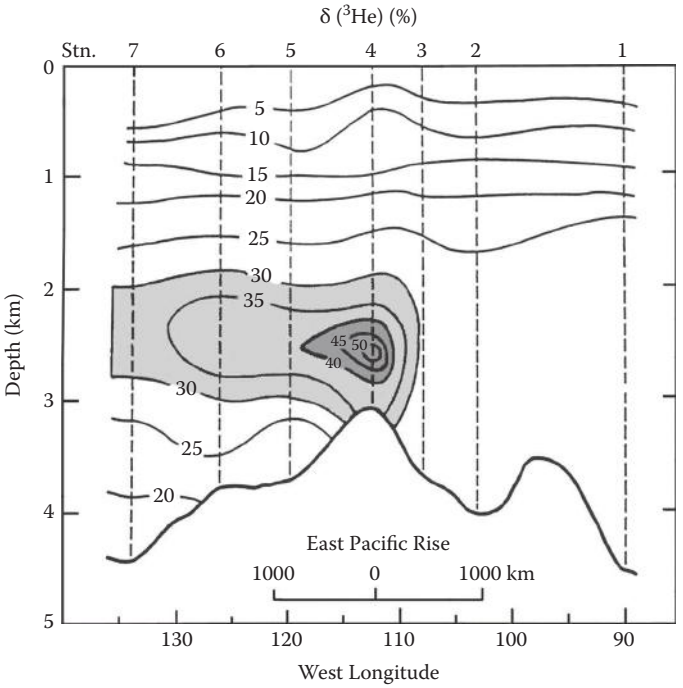

FIGURE 6.6
The concentration of helium-3 to helium-4 in the Pacific coming from active ridges.

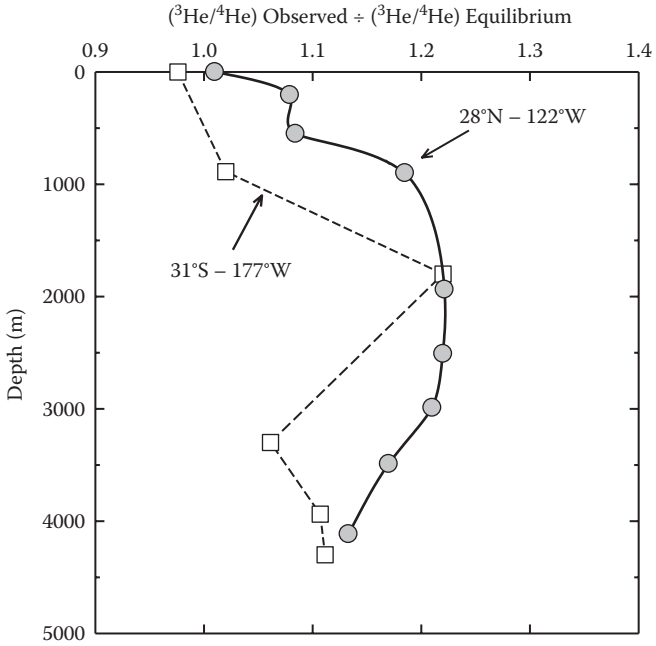

FIGURE 6.7
A profile of helium-3 to helium-4 in the Pacific Ocean showing the higher observed levels compared to equilibrium with the atmosphere.

6.6 Dissolved Oxygen in Seawater

By far the most studied gas (other than CO_2) in ocean waters is oxygen. This is largely because it is easy to measure and is of interest to oceanographers studying advective processes and biologists studying photosynthesis and the oxidation of plant material. The analysis of O_2 in natural waters is still made using the technique developed by Winkler in 1888 and modified by Carpenter in 1965. The collected sample is quickly fixed with $MnSO_4$ and NaOH. The reaction between NaOH and $MnSO_4$ forms manganous hydroxide:

$$Mn^{2+} + 2\ OH^- \rightarrow Mn(OH)_2 \tag{6.43}$$

The $Mn(OH)_2$ reacts with the O_2 to form a tetravalent manganous compound:

$$2\ Mn(OH)_2 + O_2 \rightarrow 2\ MnO(OH)_2 \tag{6.44}$$

This fixes the O_2. The solution is analyzed for O_2 after acidification in the presence of excess NaI. The manganous compound oxidizes the I^- to I_2:

$$MnO(OH)_2 + 4\ H^+ + 2\ I^- \rightarrow Mn^{2+} + I_2 + 3\ H_2O \tag{6.45}$$

The free I_2 formed is stabilized by the formation of I_3^- with the excess I^-:

$$I_2 + I^- \rightarrow I_3^- \tag{6.46}$$

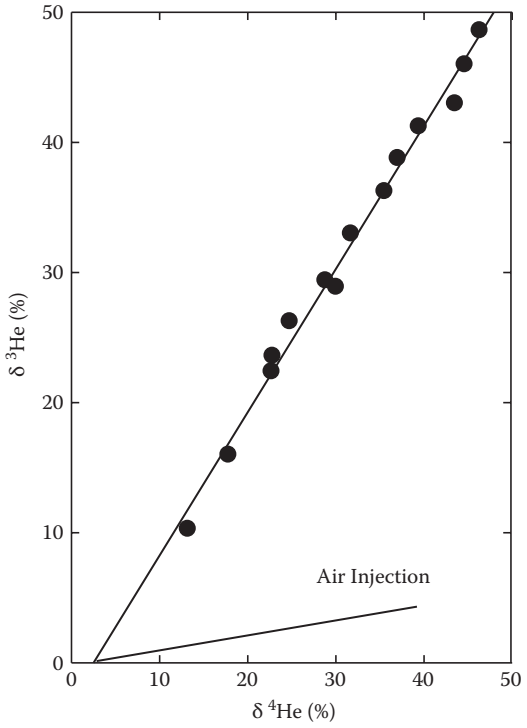

FIGURE 6.8
Values of helium-3 versus helium-4 for Pacific Ocean waters compared to expected values from air injection.

The amount of I_3^- formed is equivalent to the O_2 in the solution and is determined by titration with sodium thiosulfate:

$$I_3^- + 2S_2O_3^{2-} \rightarrow 3I^- + S_4O_6^{2-} \tag{6.47}$$

A starch solution that forms a blue complex with I_2 is used to determine the end point. The concentration of O_2 can also be measured using O_2 electrodes or by gas chromatography. The electrode system has been attached to conductivity-temperature-depth (CTD) systems to obtain continuous profiles of O_2 in ocean waters.

The vertical distribution of O_2 in the major oceans is shown in Figure 6.9. In surface waters, the O_2 concentrations in seawater are close to the expected values for the temperature and salinity of the waters. This is shown in Figure 6.10 for the measurements made during the Geochemical Oceans Sections Study (GEOSECS) program. The solid line represents the saturation value. The surface values are 7 μmol kg^{-1}, or about 3% supersaturated. This supersaturation can be attributed to bubble injection and photosynthesis. In the photosynthetic zone, the O_2 will go through a maximum because of photosynthesis (see Figure 6.11).

The most remarkable features of the O_2 profile in the major oceans are the minimum layer and the relatively high O_2 in deep waters. The minimum is the result of a balance between the biological oxidation of plant material and the advection of cold waters rich in O_2. The advection of oxygen-rich waters in the oceans is more clearly demonstrated in the sections of O_2 in the Atlantic, Pacific, and Indian Oceans given in Figure 6.12. The intrusion of Antarctic and Arctic intermediate waters is evident in the Atlantic, Pacific, and Indian

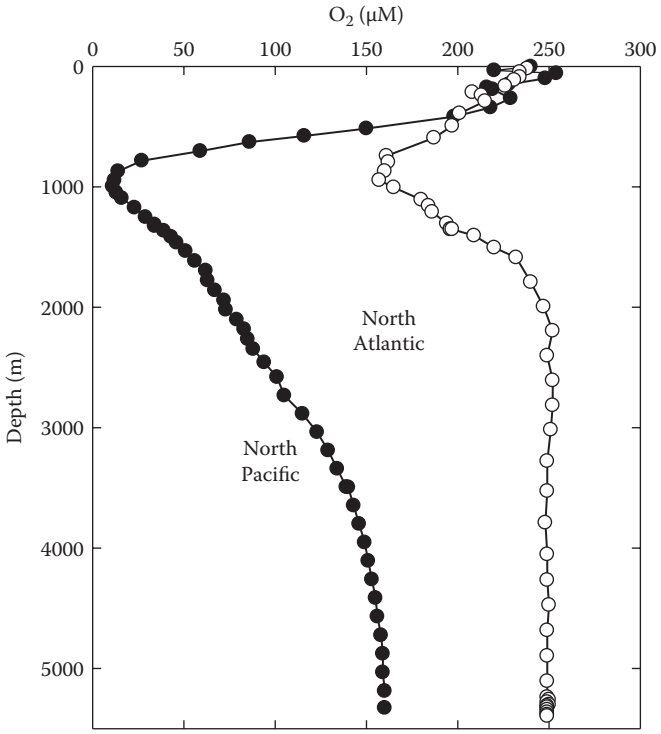

FIGURE 6.9
Profiles of oxygen in the North Atlantic and Pacific Oceans.

Oceans from the surface to about 900 m. The NADW is a region of high O_2 from 0 to 2000 m at 60° N to a maximum at 3000 m in the South Atlantic. This NADW gradually loses O_2 as it flows northward in the deep Pacific and Indian Oceans from the circumpolar waters. The contributions of Antarctic bottom waters are also seen from the high O_2 in the southern oceans. The intermediate waters of the North Pacific are much lower in O_2 than in the North Atlantic. The intense minimum off the coast of South America is related to the high productivity that occurs in the upwelled surface waters.

The distribution of O_2 in the oceans is the net result of

1. Near equilibration of atmospheric oxygen in the surface mixed layer
2. Biological production in subsurface waters caused by photosynthesis
3. Biological use of O_2 in respiration in all waters and oxidation of plant material in intermediate waters
4. Increases in O_2 in deep waters caused by the sinking of cold water rich in O_2

By examining the amount of O_2 that is utilized rather than the total concentration, it is easier to interpret the physical and biological effects. This eliminates the differences caused by conditions when the waters were in contact with the atmosphere. The contribution of processes such as air injection, thermal effects, and atmospheric pressure can be accounted for by the methods described previously. To do this properly, accompanying

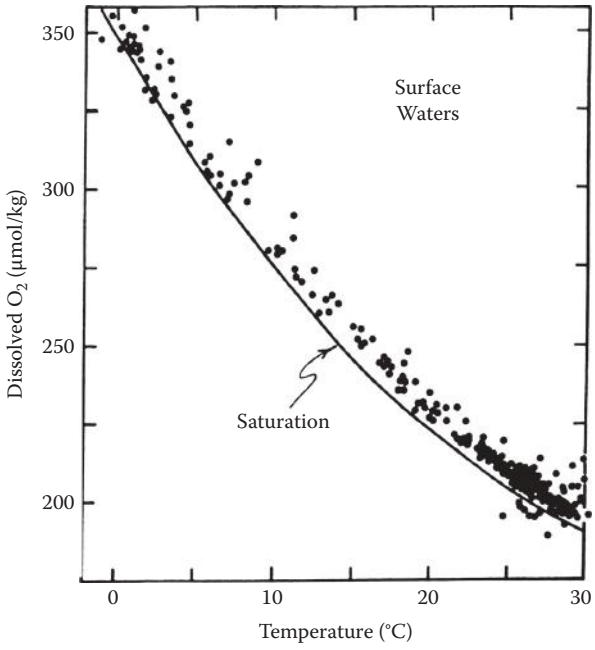

FIGURE 6.10
Comparison of the measured and calculated dissolved oxygen in surface seawaters as a function of temperature.

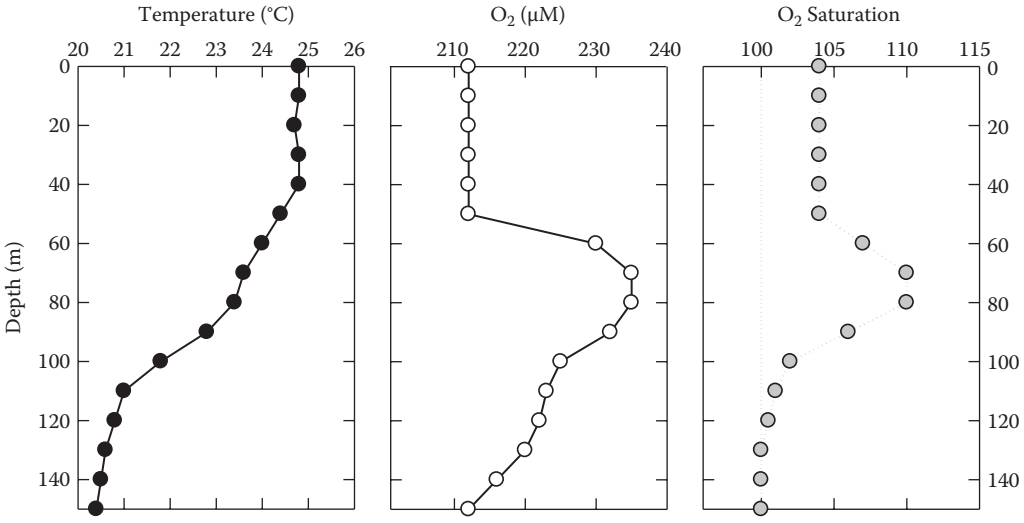

FIGURE 6.11
Profiles of temperature and oxygen in Pacific waters showing increases due to photosynthesis.

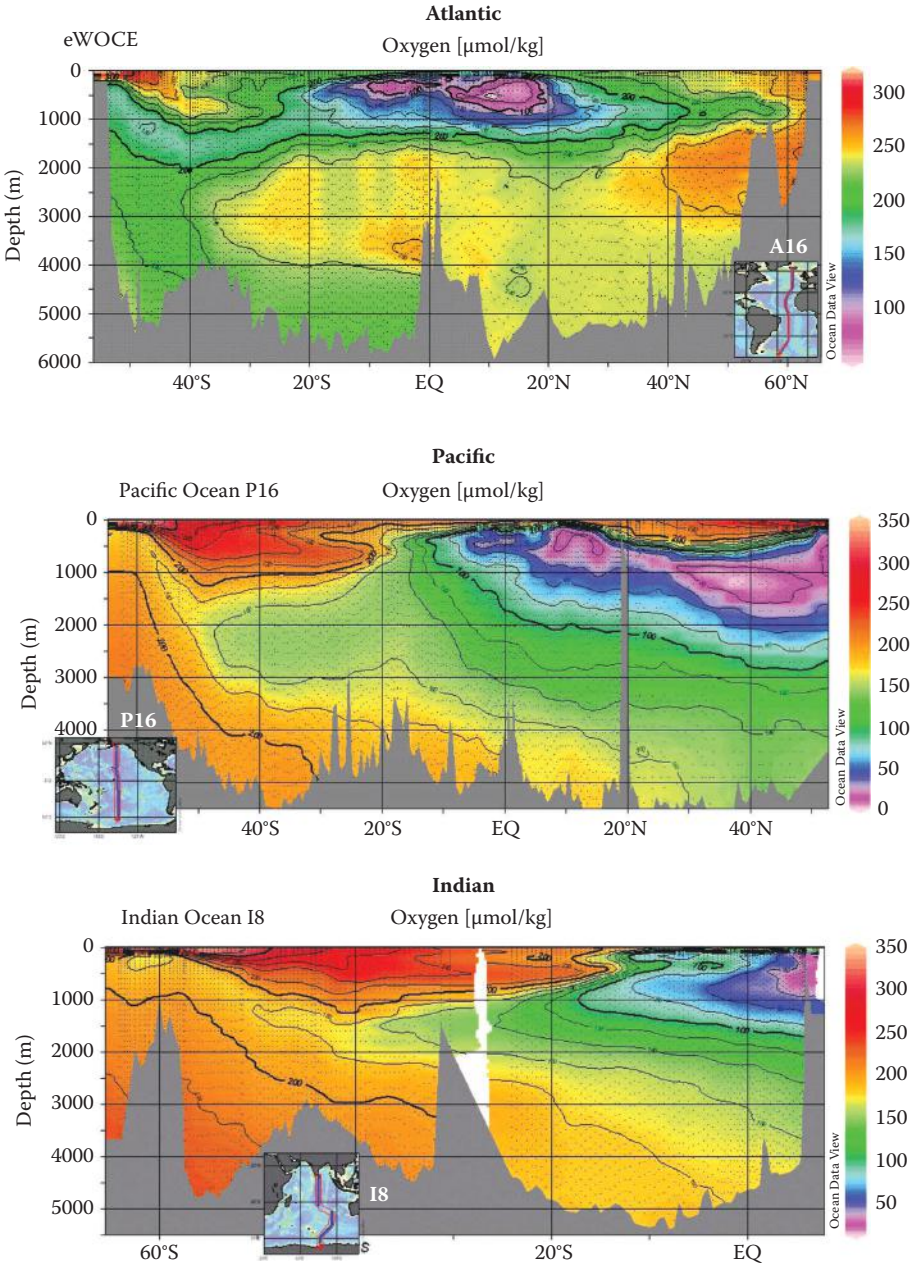

FIGURE 6.12
Sections of oxygen in the Atlantic, Indian, and Pacific Oceans.

information is needed for other inert gases. By using Ar as a reference gas, one can make a reasonable correction for the deviations caused by nonideal equilibria. The concentration of oxygen consumed since the waters left the surface is given by

$$[O_2]_{surf} - [O_2]_{meas} \quad [O_2]^* \times [Ar]_{meas}/\{[Ar]^* - [O_2]_{meas}\} \tag{6.48}$$

where [i]* is the predicted value at the given temperature and salinity and $[i]_{meas}$ is the measured value.

In the absence of Ar measurements, the apparent oxygen utilization (AOU) is determined from

$$AOU \quad [O_2]^* - [O_2]_{meas} \tag{6.49}$$

The AOU is used to recognize that the $[O_2]^*$ may depart from ideal values because of air injection and so on. As shown previously, surface waters are about 3% supersaturated. At upwelling areas, the surface O_2 concentrations can be 20% less than saturation. This is shown in Figure 6.13 for Pacific waters. The surface AOU values are 15 μmol kg^{-1} near the equator because of upwelling. This can be compared to values around –7 μmol kg^{-1} for other surface waters.

The distribution of O_2 and AOU at a depth of 4000 m is shown in Figure 6.14. The sinking bottom waters in the North Atlantic have high concentrations of O_2 (~300 μmol kg^{-1}) and low AOU (~50 μmol kg^{-1}). The older waters in the North Pacific have very low O_2 (~50 μmol kg^{-1}) and high AOU (~200 μmol kg^{-1}). The values of AOU and pCFC ages in the Pacific Ocean waters from the surface to 1000 m are shown in Figure 6.15. The equatorial upwelling waters have high values of AOU and are very old. The waters in the gyres in the north have AOU of about 150 μmol kg^{-1} and an age of 10 yr. This gives a loss of about 15 μmol kg^{-1} yr^{-1}. The ages of the upwelling or deeper waters cannot be accurately determined by the pCFC method since they have been around for about 50 yr. By examining the AOU at

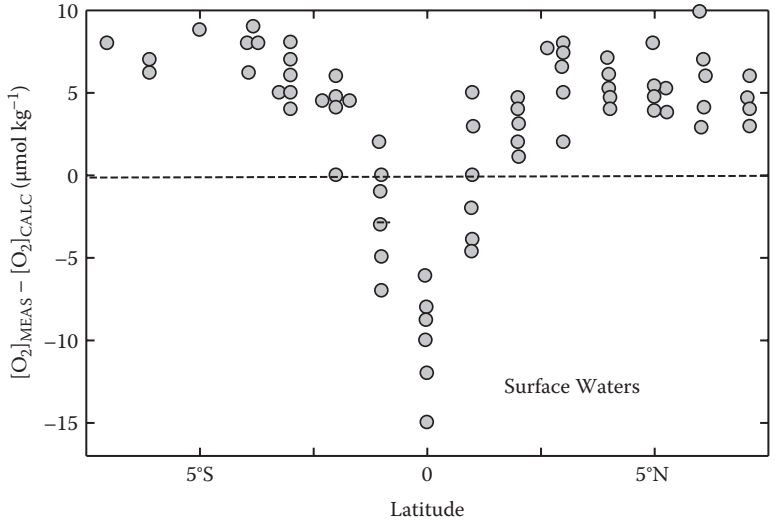

FIGURE 6.13
The differences in the measured and calculated dissolved oxygen concentrations in surface waters.

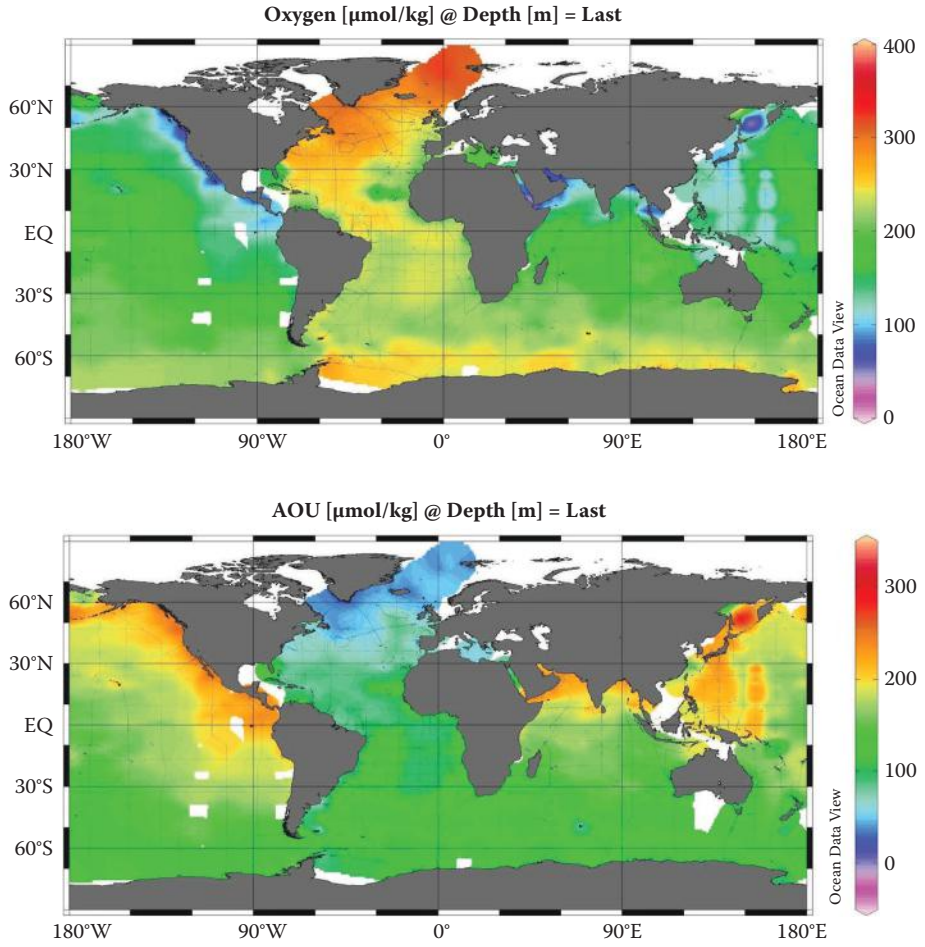

FIGURE 6.14
Oxygen and apparent oxygen utilization in deep waters of the world oceans.

different locations with the distribution of nutrients, it is possible to determine the causes of the increase. The slow increase in deep waters follows the increase in nutrient concentrations (discussed further in the chapter) and results from the oxidation of particulate organic material from the surface waters.

The O_2 levels in the world oceans at a depth of 200 m are shown in Figure 6.16. This figure clearly shows the very low concentration of O_2 in the waters off the coasts of North and South America, Northern Indian Ocean, and Africa. These upwelling zones have high primary production and, due to stratification, have lower O_2 levels due to the oxidation of plant material and stratification (Gruber, 2011). As shown in Figure 6.17 the O_2 levels in these regions are decreasing with time. The continued warming of these waters will probably continue to decrease the levels of O_2 in these regions. Similar decreases in the O_2 levels are occurring in other areas. For example, the so-called dead zone in waters off the coast of New Orleans has very low levels of O_2 due to the oxidation of plant material produced by the high concentration of nutrients from the Mississippi River. To the best of my knowledge, these waters have not lost enough O_2 to produce H_2S.

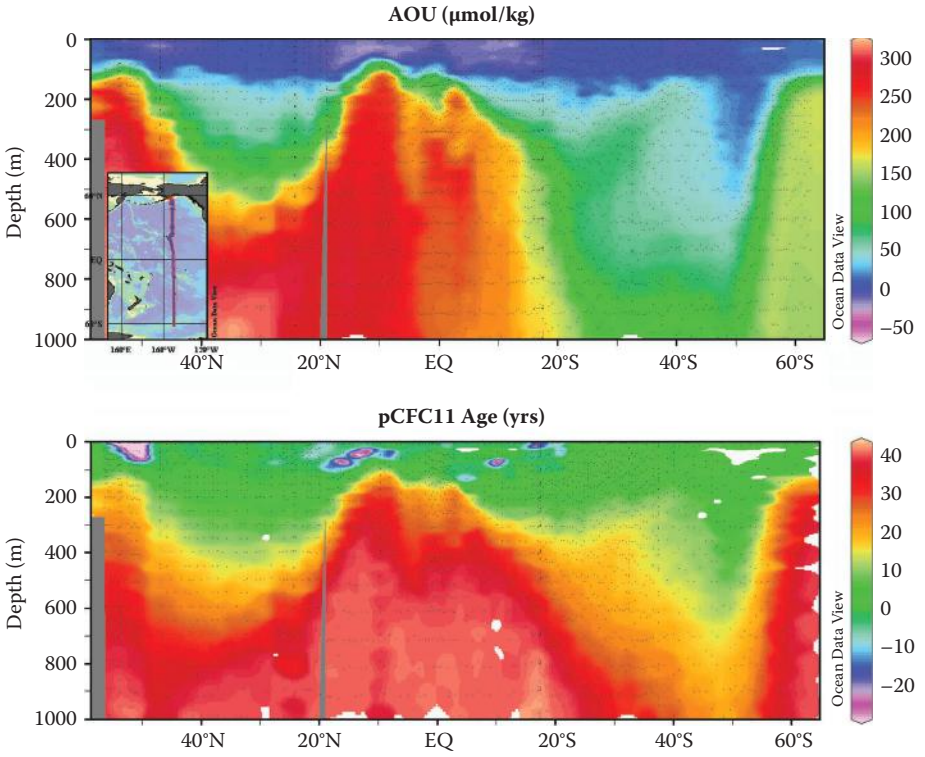

FIGURE 6.15
Apparent oxygen utilization and pCFC ages for Pacific Ocean waters.

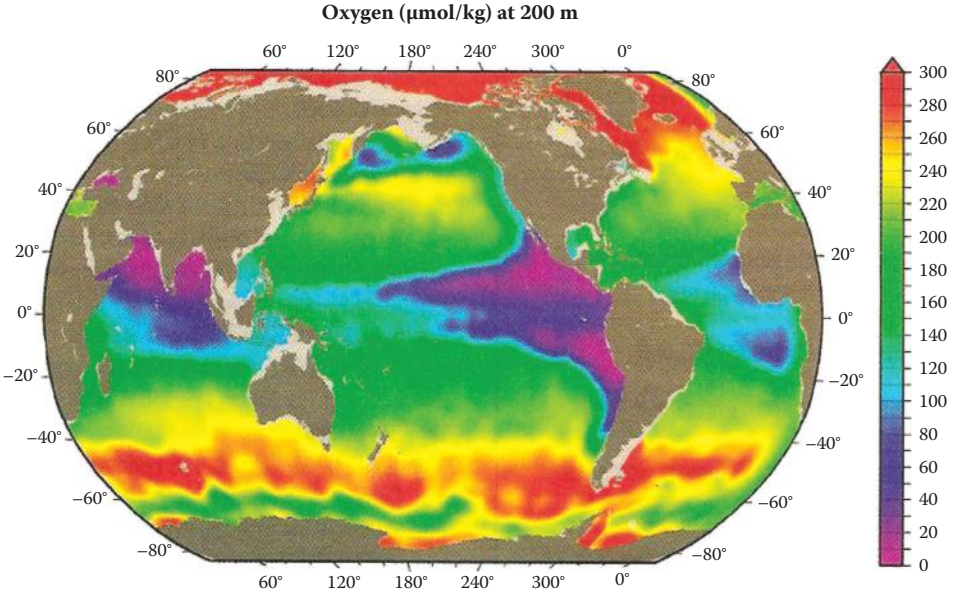

FIGURE 6.16
Oxygen levels for ocean waters at 200 m. (From Falkowski, P.G., et al., *EOS Trans.*, 92, 409–411, 2012. With permission.)

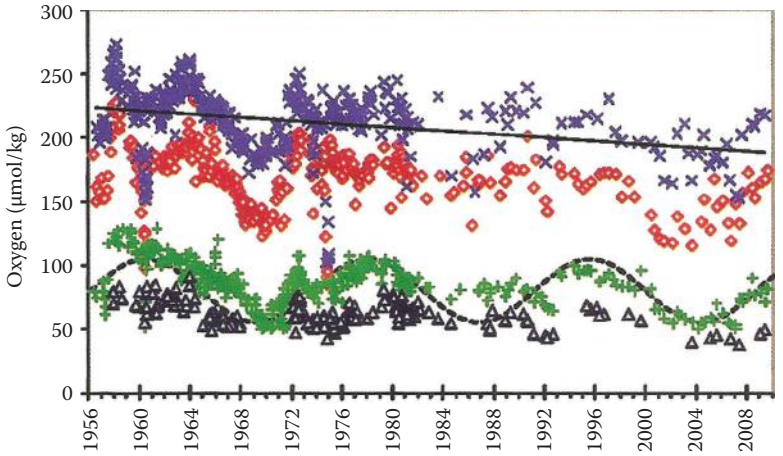

FIGURE 6.17
The decreases of the concentration of oxygen in surface waters. (From Falkowski, P.G., et al., *EOS Trans*., 92, 409–411, 2012. With permission.)

A number of workers have used advective diffusion models to analyze the O_2 minimum layer. The rate of the in situ oxygen consumption R is assumed to decrease exponentially with depth:

$$R = R_0 e^{-az} \tag{6.50}$$

where R_0 is the rate of O_2 utilization at the upper boundary of the model (~500 m), and α accounts for the rate at which R decreases with depth (z). Horizontal mixing is assumed to be zero, and the boundary values of O_2 are maintained by atmospheric exchange and horizontal transport. Wyriki (1962) applied this model to O_2 in the Indian Ocean and found the results shown in Figure 6.18. The rate R is given by

$$R = A_z (Z^2[O_2]/Z_z^2) - w(Z[O_2]/Z_z) \tag{6.51}$$

where A_z is the vertical eddy diffusion coefficient (independent of depth), and w is the vertical advection velocity. His results indicated that in situ consumption of O_2 was required to account for the O_2 minimum layer except for areas (off the western coast of South America and Africa) where the layer is near the surface; therefore, horizontal mixing is important. Craig (1969) and others have further developed this simple model. Culberson and Pytkowitz (1970), for example, showed that the derived values of R were in reasonable agreement with estimates of the oxidation rate of Packard (1969) obtained by using an enzyme analysis (see Figure 6.19).

This vertical model is an oversimplification of the real oceans. The ultimate description of the distribution must use three-dimensional models. The early work by Riley (1951) indicates that 90% of the oxidation of the organic matter produced by phytoplankton occurs in surface waters (<200 m). The remaining 10% is consumed in the deep oceans.

By examining the AOU distribution relative to other chemical parameters such as PO_4, NO_3, CO_2, and pH, Redfield (1948) developed a stoichiometric model. The oxidation of organic matter by O_2 can be represented by

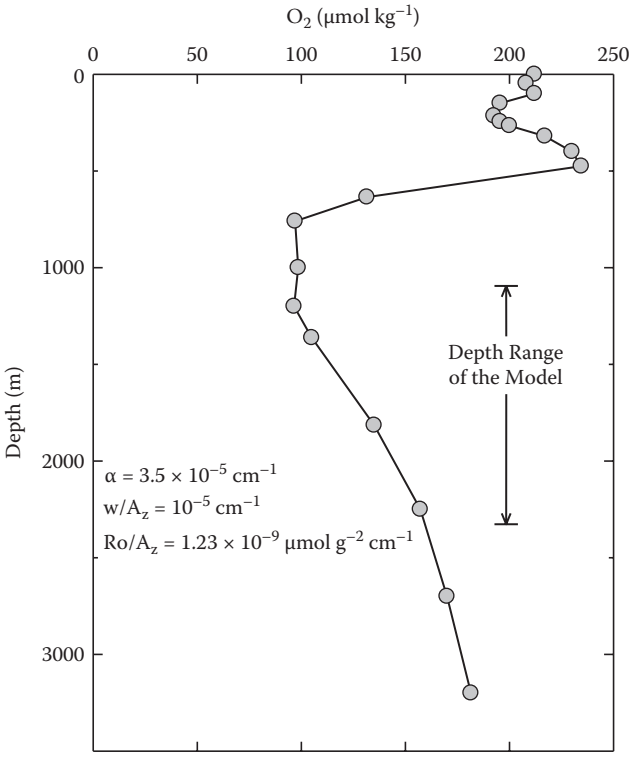

FIGURE 6.18
A comparison of the measured and calculated concentrations of oxygen using a one-dimensional mixing model.

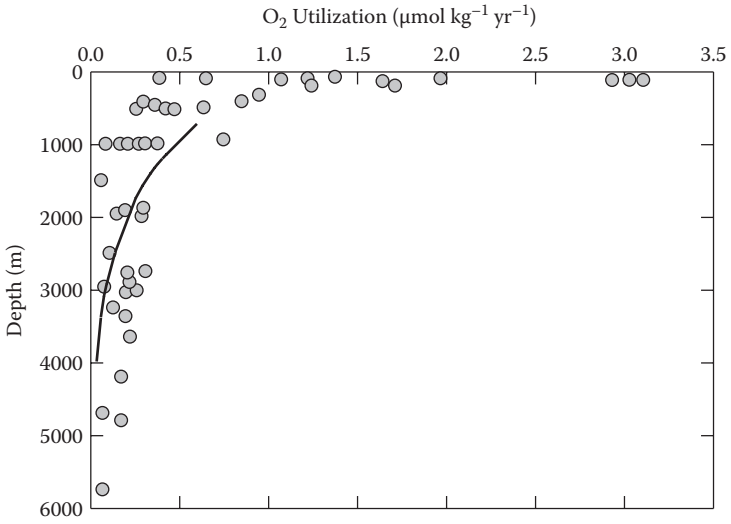

FIGURE 6.19
A profile of the measured (points) and calculated (line) oxygen utilization rates in the Atlantic Ocean.

$$(CH_20)_{106}\ (NH_3)16\ H_3PO_4 + 83\ O_2 \xrightarrow[\text{photosynthesis}]{\text{oxidation}} 106CO_2 + 16\ HNO_3 + H_3PO_4 + 122\ H_2O \qquad (6.52)$$

Details of using this simple model are discussed further in the chapter.

With the recent development of in situ O_2 instruments, one might expect future work to provide useful information on the details of the oxidation of organic material in the oceans. Kester (1975) has demonstrated how these instruments can be used to look at small changes of O_2 as a function of depth caused by mixing processes.

6.7 Other Nonconservative Gases

In recent years, other nonconservative gases such as CO, H_2, CH_4, and N_2O have been measured in seawater. A depth profile for CO in the eastern Atlantic is shown in Figure 6.20. The surface waters are supersaturated apparently from bacterial activity or photochemical processes. The increase at about 500 m is the location of water flowing out of the Mediterranean with its increase in microorganisms. The global cycle of CO is shown in Figure 6.21 (10^{14} g yr^{-1}). The oceans are a source of CO to the atmosphere.

A depth profile of H_2 in the Atlantic is shown in Figure 6.22. The values go through a maximum in the photosynthetic zone near the pycnocline apparently because of biological activity. The depth profile of CH_4 in seawater (Figure 6.23) also goes through a maximum in surface waters. As shown in the section of CH_4 (Figure 6.24), the source may be

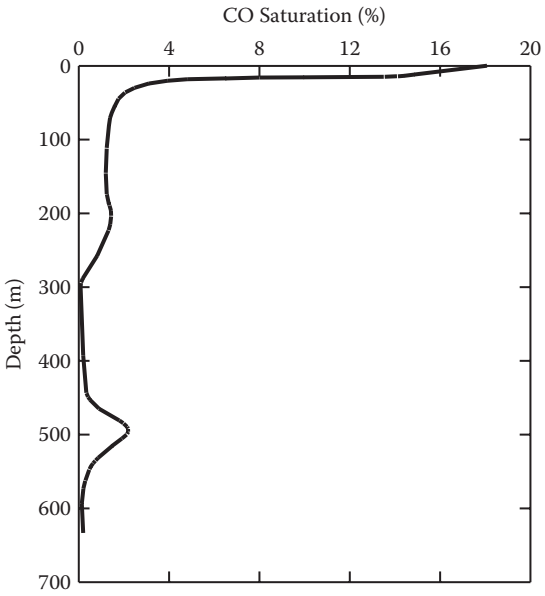

FIGURE 6.20
A profile of the saturation of carbon monoxide in the Atlantic Ocean.

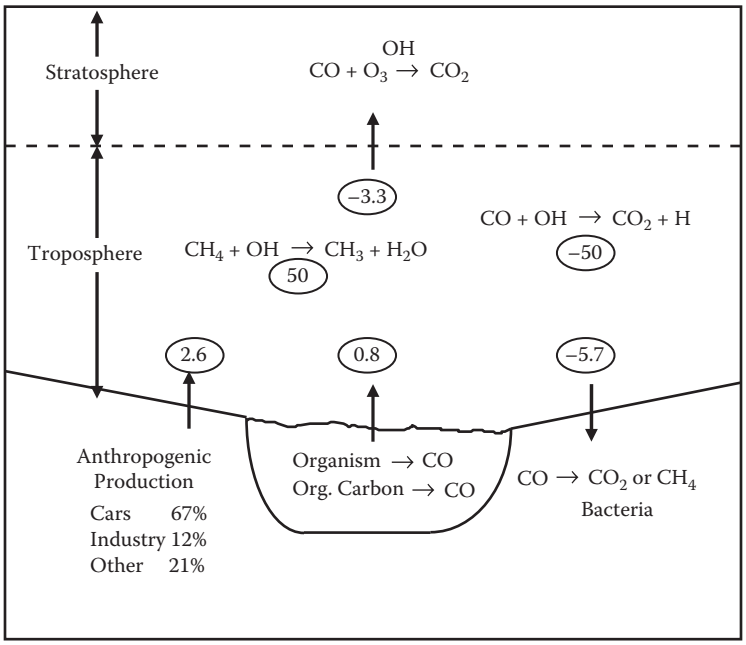

FIGURE 6.21
A sketch of the global cycle of carbon monoxide in the world.

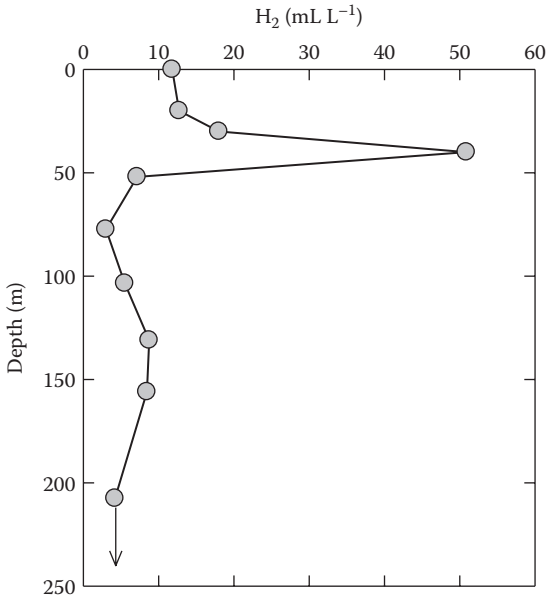

FIGURE 6.22
A profile of hydrogen in the Gulf of Mexico.

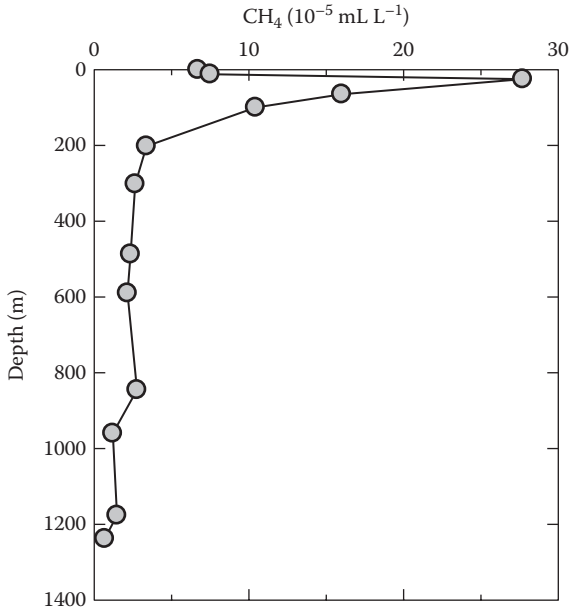

FIGURE 6.23
A profile of methane in the Gulf of Mexico.

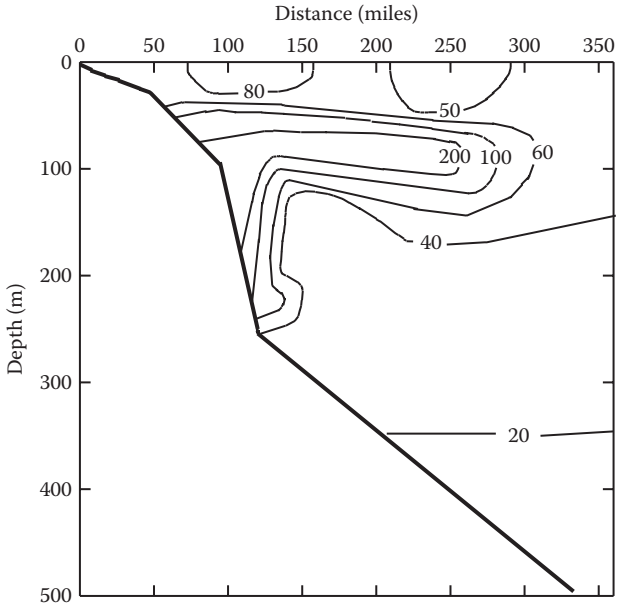

FIGURE 6.24
A section of methane off the Gulf Coast.

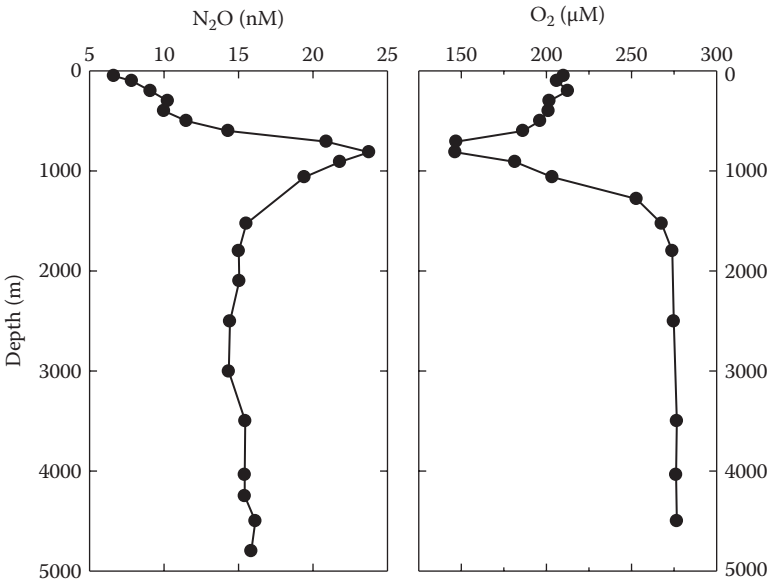

FIGURE 6.25
Profiles of nitrous oxide and oxygen in the Pacific Ocean.

from the shelf sediments. As will be discussed later, the profiles of N_2O in ocean waters (Figure 6.25) go through a maximum in the oxygen minimum layer.

6.8 Structural Aspects of the Solubility of Gases

Previously, we discussed the process of dissolving a charged ion in water and the energies involved. One might expect the dissolution of a gas molecule to involve very small energies and to be related entirely to packing or structural effects. Experimental studies of inert gases, however, indicate that ΔH_S and ΔS_S for the solution process are quite anomalous (see Table 6.8). The values of ΔH_S and ΔS_S are both negative. This is in contrast to the solution of these gases into other liquids, where the loosening of the solvent intermolecular forces results in an increase in entropy. These differences are normally interpreted in terms of changes in the structure of water in the vicinity of the dissolved gases. The dissolution process can be considered to be a two-step process: (a) the creation of a hole or cavity in the solvent and (b) the introduction of the gas molecule into the cavity. This accounts for the large negative ΔH_S that may be an indication of a chemical bond between the gas and water. Frank and Evans (1945), however, concluded that the addition of an inert gas or nonpolar molecule causes the water to appear to be more "ice-like"; that is, the water appears to be highly structured around an inert gas molecule. Others have suggested that the water structure does not build up around the solute but that the structure is already there. The introduction of the solute just causes the structure to shift locally. This local structure has been compared to crystalline hydrates and was suggested by Pauling (1960) to be some sort of clathrate. Many organic solutes

TABLE 6.8

Values of ΔH and ΔS for the Solution of Gases in Water (25°C)

Gas	ΔH (kcal mol^{-1})	ΔS (cal deg mol^{-1})
H_2	1.3	26
N_2	2.1	29
He	0.8	27
Ne	1.9	29
Ar	2.7	30
Kr	3.6	32
Xe	4.5	34
Rn	5.1	34
CO	3.9	30
O_2	3.0	31
NO	2.7	29
CO_2	4.7	31
COS	5.8	35
N_2O	4.8	32
CH_4	3.2	32

have similar thermodynamic properties, and the interaction is frequently called hydrophobic bonding.

The addition of an electrolyte to water interferes with the gas dissolution and the organization of water around the gas. This frequently results in a decrease in the solubility, or a "salting out." This salting out is frequently a linear function of the molar ionic strength:

$$\log C = \log C^\circ + k\, I_V \tag{6.53}$$

When k is negative, the result is a salting out, and when k is positive, the result is a salting in. Values of k for various gases in seawater are given in Table 6.9. The ratio of the solubility in water to the value in seawater is equal to the activity coefficient of the gas:

$$\gamma_g = C^\circ/C \tag{6.54}$$

Values of γ_g for various gases are also given in Table 6.10.

TABLE 6.9

Comparison of the Measured and Calculated Salting Coefficients of Gases in Seawater and NaCl at t = 25°C

	Seawater		NaCl	
Gas	Measured	Calculated	Measured	Calculated
He	0.092	0.099	0.090	0.100
Ne	0.102	0.099	0.106	0.100
Ar	0.122	0.123	0.131	0.122
O_2	0.122	0.135	0.142	0.134
N_2	0.132	0.144	0.141	0.143

TABLE 6.10

Activity Coefficients of Gases in Seawater (S = 35, t = 25°C)

Gas	γ_g
N_2	1.24
O_2	1.22
Ar	1.22
Ne	1.18
He	1.16
Kr	1.23
CO_2	1.17
CO	1.23
CH_4	1.24
H_2S	1.03

Masterton (1975) has shown that the salting out of gases in seawater can be accounted for using

$$k = k_a + k_b \tag{6.55}$$

This equation is derived from the scale particle theory. k_a results from the free energy of cavity formation, and k_b results from the free energy of interaction between the gas molecule and the surrounding water molecules and ions. The first term is calculated from the diameter of the gas and water molecules, the number of water molecules and ions per milliliter, and the diameter of the ion. The k_a term is always positive and leads to salting out. It increases as the diameter of the gas molecule increases and becomes a smaller positive number as the temperature rises.

k_b is related to the polarizability of the gas molecules and the ions, the total number of electrons in the ion, and the dipole movement of water. k_b is negative for all gases between 0 and 40°C and thus leads to salting in. The magnitude of k_b decreases with increasing temperature. A comparison of the measured and calculated values of k in NaCl and seawater is shown in Table 6.9. The agreement is quite good. A more thorough examination of the use of the scale particle model to gases in seawater has been given by Millero (2000).

References and Further Reading

Benson, B.B., and Krause, D., Jr., The concentration and isotopic fractionation of oxygen dissolved in fresh water and seawater in equilibrium with the atmosphere, *Limnol. Oceanogr.*, 29, 620 (1984).

Benson, B.B., and Parker, P.D.M., Nitrogen/argon and nitrogen isotope ratios in aerobic seawater, *Deep-Sea Res.*, 7, 237 (1961).

Broecker, W.S., and Peng, T.H., *Tracers in the Sea*, Eldigio Press, New York (1982).

Carpenter, J., The accuracy of the Winker method for the dissolved oxygen analysis, *Limnol. Oceanog*r., 10, 141 (1965).

Craig, H.H., Abyssal carbon and radiocarbon in the Pacific, *J. Geophys. Res.*, 74, 5491 (1969).

Culberson, C.H., and Pytkowicz, R.M., Oxygen-total carbon dioxide correlation in the eastern Pacific Ocean, *J. Oceanogr. Soc. Jpn*., 26, 15–21 (1970).

Falkowski, P.G., Algeo, T., Codispoti, L., Deutsch, C., Emerson, S., Hales, B., Huey, R.B., Jenkins, W.J., Kump, L.R., Levin, L.A., Lyons, T.W., Nelson, N.B., Schofield, O., Summons, R., Talley, L.D., Thomas, E., Whitney, F., and Pilcherm C.B., Ocean deoxygenation: past, present and future, *EOS Trans*., 92, 409–411 (2012).

Frank, H.S., and Evans, M.W., Free volume and entropy in condensed systems. III. Entropy in binary liquid mixtures; partial molal entropy in dilute solutions; structure and the thermodynamics in aqueous electrolytes, *J. Chem. Phy*s., 13, 507 (1945).

Gruber, N., Warming up, turning sour, losing breath: ocean biogeochemistry under global change, *Phil. Trans. Roy. Soc.*, 369, 1980–1996 (2011).

Kester, D.R., Dissolved gases other than CO_2, Chapter 8, *Chemical Oceanography*, Vol. 1, 2nd ed., Riley, J.P., and Skirrow, G., Eds., Academic Press, New York, 498–556 (1975).

Liss, P.S., Chemistry of the sea surface microlayer, Chapter 10, *Chemical Oceanography*, Vol. 2, 2nd ed., Riley, J.P., and Skirrow, G., Eds., Academic Press, New York, 193–243 (1975).

Masterton, W.L., Salting coefficients for gases in seawater from scaled particle theory, *J. Solution Chem*., 4, 523 (1975).

Millero, F.J., The activity coefficients of non-electrolytes in seawater, *Mar. Chem*., 70, 5 (2000).

Packard, T.T., The Estimation of the Oxygen Utilization Rate in Seawater from the Activity of the Respiratory Electron Transport System in Plankton, PhD thesis, University of Washington (1969).

Pauling, L., *The Nature of the Chemical Bond*, 3rd ed., Cornell Press, Ithaca, NY, Chapter 5 (1960).

Redfield, A.C., The exchange of oxygen across the sea surface, *J. Mar. Res*., 7, 347 (1948).

Richards, F.A., Dissolved gases other than carbon dioxide, in *Chemical Oceanography*, Vol. 1, Riley, J.P., and Skirrow, G., Eds., Academic Press, New York, 197–225 (1965).

Richards, F.A., and Benson, B.B., Nitrogen/argon nitrogen isotope rations in two anaerobic environments, the Carioca Trench in the Caribbean Sea and Damsfjord Norway, *Deep-Sea Res*., 7, 254 (1961).

Riley, G.W., Oxygen, phosphate, and nitrate in the Atlantic Ocean, *Bull. Bingham Oceanogr. Coll*., 13, 1–126 (1951).

Weiss, R., The effect of salinity on the solubility of argon in sea water, *Deep-Sea Res*., 18, 225 (1971).

Winkler, L.W., The determination of dissolved oxygen in water. *Ber. Dtsche. Chem. Ges.* 21, 2843–2854. (1888).

Wyriki, K., The oxygen minimum in relation to ocean circulation, *Deep-Sea Res*., 9, 11 (1962).

7

The Carbonate System

7.1 Introduction

The major portion of carbon in the oceans occurs as part of the carbonate system. This system involves the following equilibria:

$$CO_2(g) = CO_2(aq) \tag{7.1}$$

$$CO_2(aq) + H_2O = H^+ + HCO_3^- \tag{7.2}$$

$$HCO_3^- = H+ + CO_3^{2-} \tag{7.3}$$

$$Ca^{2+} + CO_3^{2-} = CaCO_3(s) \tag{7.4}$$

The carbonate system is very important since it regulates the pH of seawater and controls the circulation of CO_2 between the biosphere, the lithosphere, the atmosphere, and the oceans. Recent interest in the carbonate system in the oceans has resulted from the "greenhouse effect" of CO_2. As discussed in Chapter 5, the concentration of CO_2 in the atmosphere has increased in the twentieth century (see Figure 5.19). Since CO_2 can absorb infrared (IR) energy, this increase may cause the temperature of the earth to increase and could eventually melt the polar ice caps. The increase in CO_2 is related to the burning of fossil fuels (coal, petroleum, and natural gas) and the production of cement (see Figure 7.1). Once the CO_2 is in the atmosphere, it is available for primary productivity and weathering processes. The CO_2 can enter the ocean by physical processes called the solubility pump (Figure 7.1) and biological processes called the biological pump (Figure 7.2). Once the CO_2 enters the oceans across the air–sea interface and participates in the equilibrium processes outlined by Equation 7.1 to Equation 7.4, it also can be used by plants in primary productivity:

$$CO_2 + H_2O \rightarrow CH_2O + O_2 \tag{7.5}$$

These processes are far from simple since the rates of movement of CO_2 across the interface and from surface to deep waters vary with latitude, time, season, and biological processes. Diurnal and seasonal variations in the carbonate system are caused by the removal of CO_2 by photosynthesis and solar heating (see Figures 5.21 and 5.22). The natural and anthropogenic inputs of CO_2 also differ as a function of latitude (Figure 7.3). The uptake of CO_2 of the oceans is slow because of physical and chemical factors. The exchange involves the hydration of CO_2, which is a slow process relative to ionization. As discussed further

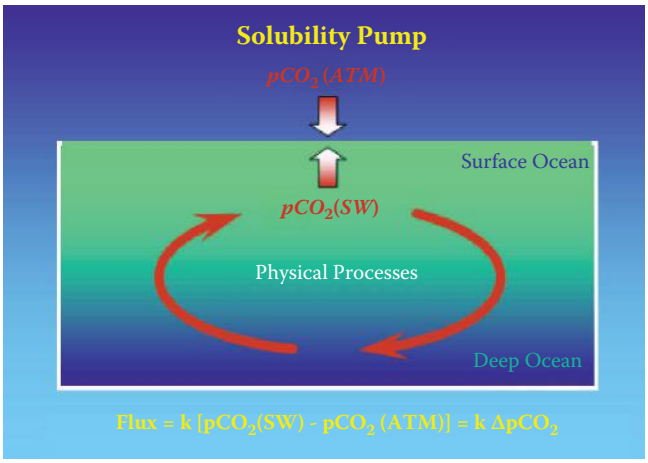

FIGURE 7.1
The solubility pump.

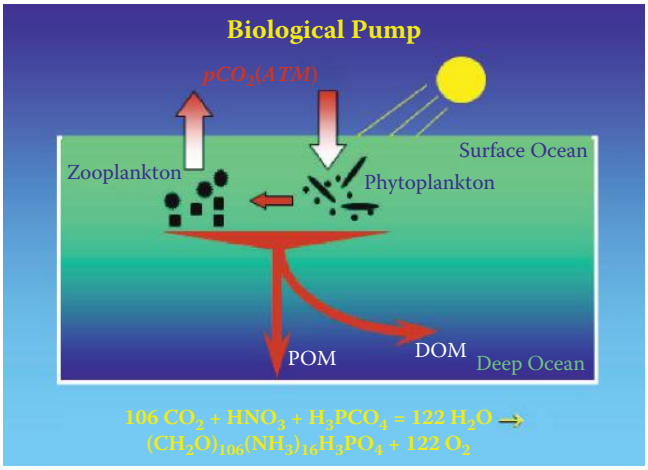

FIGURE 7.2
The biological pump. DOM = dissolved organic matter; POM = particulate organic matter.

in the chapter, the increased adsorption of CO_2 by the oceans will result in a decrease in the pH (ocean acidification). Approximate timescales for the mixing process can be determined using radioactive tracers to gain some idea of the mixing times. To use these estimates, it is necessary to have some idea of the total carbon in various reservoirs and the global carbon cycle. The most recent estimates are shown in Figure 7.4. The inorganic carbon estimates are reasonably accurate, but estimates for the carbon in the marine biosphere and humus are less precisely known. Most of the carbon in the oceans resides below the thermocline. The amount of carbon stored in carbonate rocks and sediments is a lot larger than the cycled CO_2 but is not important on short timescales (years).

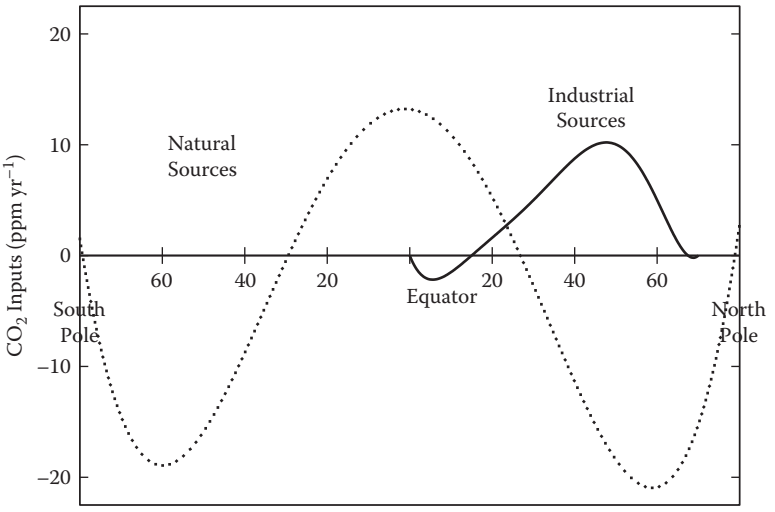

FIGURE 7.3
Anthropogenic inputs of carbon dioxide as a function of latitude.

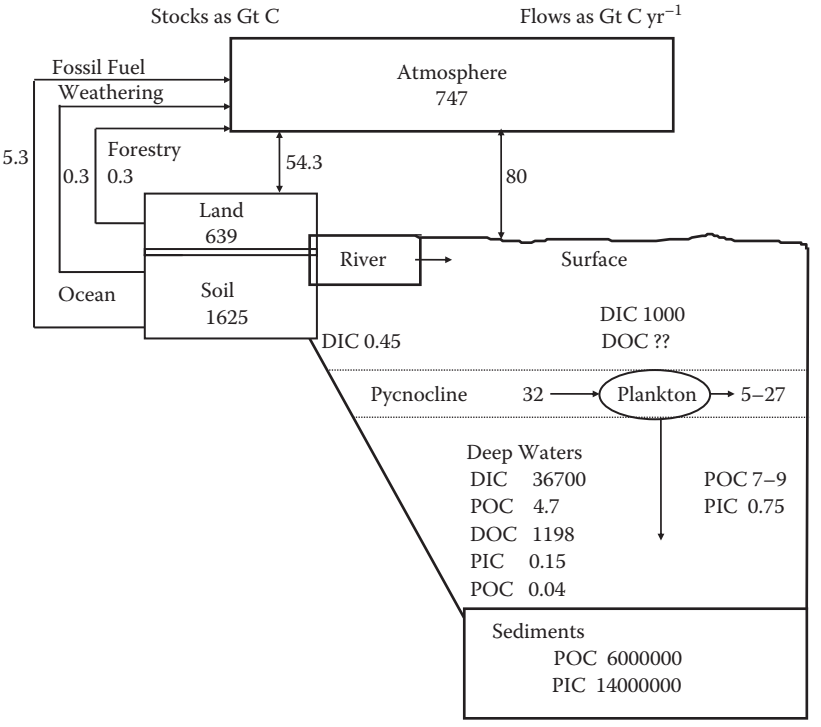

FIGURE 7.4
The global carbon cycle. DIC = dissolved inorganic carbon; PIC = particulate inorganic carbon.

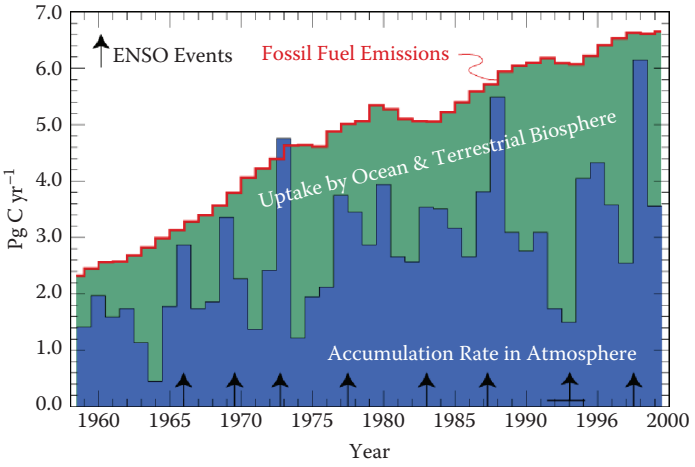

FIGURE 7.5
The annual input of fossil fuel CO_2 to the atmosphere compared to the measured CO_2 in the atmosphere during El Niño southern oscillation (ENSO) events (1955–1982).

The recent interest in the distribution of CO_2 in the oceans is related to the need to understand how the increase of CO_2 in the atmosphere and the expected increase in temperature will affect the climate. The partial pressures of CO_2 (pCO_2) in the atmosphere have been studied by a number of workers. The classical measurements of pCO_2 in the atmosphere were made by Keeling (Keeling and Whorf, 2004) at the Mauna Loa Observatory in Hawaii starting in 1958. More recent measurements have been made on the air trapped in ice cores. These measurements clearly demonstrate that the CO_2 in the atmosphere is increasing because of the burning of fossil fuels. Although the rates of increase are the same as the increase in the use of fossil fuels, the amounts in the atmosphere are only half of the expected values. This is shown in Figure 7.5, which compares the rates of fossil fuel emissions and rates accumulated in the atmosphere. The differences are related to the accumulation of CO_2 in the oceans and on land. The variations in the accumulation rates in the atmosphere are thought to be related to El Niño. During El Niño years, the ocean and land have lower accumulation rates. It should also be pointed out that the difference between the CO_2 produced and the amount put into the atmosphere has changed with time (see Figure 7.5), which means the natural sources and sinks have also changed. The estimates of the sources and sinks of CO_2 in the atmosphere are given in Table 7.1. The differences between the sources (7.0 Gt yr^{-1}) and sinks (5.4 Gt yr^{-1}) of 1.6 Gt yr^{-1} is close to the overall uncertainty (1.4 Gt yr^{-1}). The estimated ocean sink of 2 Gt yr^{-1} has been determined using ocean models and, more recently, by direct measurements. The value estimated from the penetration of ^{13}C into the oceans (Figure 7.6) by Quay et al. (1992) supports the newer estimates.

The fossil fuel carbon has a higher amount of ^{13}C than the atmospheric CO_2. Over time, this $^{13}CO_2$ penetrates into the deep ocean. The modeling of the changes in the $^{13}CO_2$ has been used to determine a penetration rate of 25 to 35 m yr^{-1} and an oceanic uptake of sink of 2.1 Gt yr^{-1}. We examine how the recent global survey has led to results that can shed more light on the magnitude of the ocean sink further in this chapter. As pointed out by Sarmiento (1993), the CO_2 added to the atmosphere will eventually come to equilibrium

TABLE 7.1

Budget for the Global CO_2 System (1980–1989)

	Average Perturbation (10^{15} g carbon yr^{-1})
Sources	
Fossil fuel combustion	5.4 ± 0.5
Deforestation	1.6 ± 1.0
Total	7.0 ± 1.2
Sinks	
Atmosphere	3.4 ± 0.2
Oceans (models)	2.0 ± 0.8
Total	5.4 ± 0.8
Unaccounted for sinks	1.6 ± 1.4

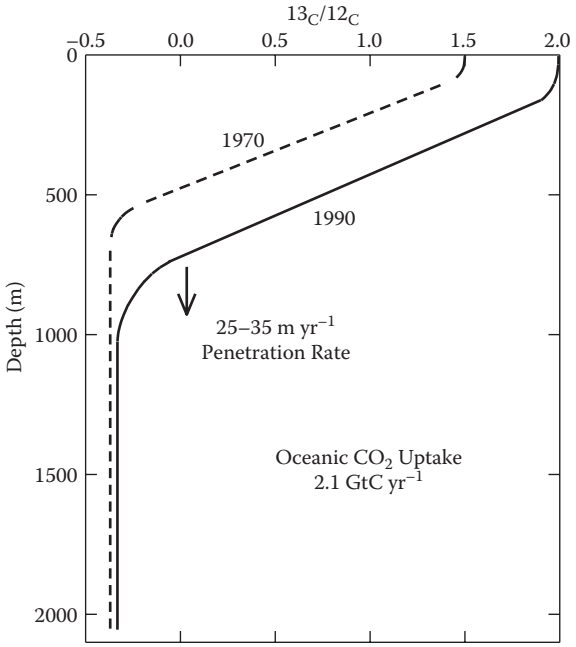

FIGURE 7.6

The changes in the ratio of $^{13}C/^{12}C$ as a function of depth. (Modified from Quay, P.D., Tilbrook, B., and Wong, C.S., *Science*, 256, 74, 1992.)

with seawater. Although this process is slow, Sarmiento's calculations indicate that the addition of 1095 molecules of CO_2 to the atmosphere will decrease to 15 molecules after 1000 yr (see Table 7.2). Most of the added CO_2 (985 molecules) will end up as part of the inorganic pool as bicarbonate and carbonate ions.

Before we examine the distribution of CO_2 in the oceans, the concepts needed to understand the carbonate system in the oceans are discussed.

TABLE 7.2

Fate of 1095 Molecules of CO_2 Added to the Atmosphere after 1000 Years

	Components	Totals
Inorganic Pool		
Atmosphere	15	15
Ocean		
CO_2	5	
HCO_3^-	875	
CO_3^{2-}	105	
	985	985
		1000
Organic Pool		
Terrestrial	54	
Oceanic	41	
	95	95
	Total	1095

7.2 Acid–Base Equilibria in Seawater

The equilibrium between acids and bases in seawater is important in controlling the carbonate system in the oceans. Before we discuss the equilibria of CO_2 in seawater, however, it is important to understand the concept of pH and how it is measured in seawater. Water is a weak electrolyte and dissociates according to

$$H_2O = H^+ + OH^- \tag{7.6}$$

This dissociation is defined by the equilibrium constant:

$$K_W = a_H a_{OH}/a_{H_2O} = [H^+][OH^-]\gamma_H\gamma_{OH}/a_{H_2O} \tag{7.7}$$

where a is activity, and γ is the activity coefficient. For dilute solutions, $a_{H_2O} = 1.0$, $\gamma_H = 1.0$, $\gamma_{OH} = 0$, and $K_W = 1 \times 10^{-14} = [H^+][OH^-]$ at 25°C. The pH is defined by

$$pH = -\log [H^+] = 7.0 \tag{7.8}$$

The thermodynamic dissociation constant varies as a function of temperature:

$$\ln K_W = 149.9802 - 13847.26/T - 23.6521 \ln T \tag{7.9}$$

K_W is also a function of pressure:

$$\ln(K_2P_W/K_W0) = -(\Delta V°/RT)\ P + (0.5\ \Delta K°/RT)\ P^2 \tag{7.10}$$

The volume $\Delta V°$ and compressibility $\Delta K°$ changes in water are given by

$$\Delta V° = -25.60 + 0.2324\ t - 3.6246 \times 10^{-3}\ (T - 273.15)^2 \tag{7.11}$$

$$10^3 \Delta K° = -7.33 + 0.1368\ t - 1.233 \times 10^{-3}\ (T - 273.15)^2 \tag{7.12}$$

The concentration of $H^+ + OH^-$ is also affected by the major components in seawater. The stoichiometric product for the dissociation is

$$K_W^* = K_W\ a_{H_2O}/\gamma_H\gamma_{OH} = [H^+]_T[OH^-]_T \tag{7.13}$$

The values of K_W^* in seawater can be determined from

$$\ln K_W^* = \ln K_W + A\ S^{0.5} + B\ S \tag{7.14}$$

$$A = -5.977 + 118.67/T + 1.0495 \ln T \tag{7.15}$$

$$B = -1.615 \times 10^{-2} \tag{7.16}$$

At 25°C and salinity of 35, K_W^* is equal to $10^{-13.19}$, or $pK_W^* = 13.19$. This increase in the pK_W^* from the value in freshwater is related to the interactions of H^+ with SO_4^{2-} and OH^- with Mg^{2+}:

$$H^+ + SO_4^{2-} \rightarrow HSO_4^- \qquad \beta_{HSO_4} = [HSO_4^-]/[H^+][SO_4^{2-}] \tag{7.17}$$

$$H^+ + F^- \rightarrow HF \qquad \beta_{HF} = [HF]/[H^+]\ [F^-] \tag{7.18}$$

$$OH^- + Mg^{2+} \rightarrow MgOH^+ \qquad \beta_{MgOH} = [MgOH^+]/[Mg^{2+}][OH^-] \tag{7.19}$$

As discussed, this causes the free H^+ and OH^- concentrations to decrease by 84% and 33%, respectively. The value of K_W^* is thus given by

$$K_W^* = K_W/\gamma_H\gamma_{OH} = 10^{-14} \times 0.981/(0.71 \times 0.22) = 10^{-13.20} \tag{7.20}$$

From this short discussion of the values of K_W, it is possible to understand the various definitions of pH used in oceanography. The original definition of pH was made by Sorensen in 1909. He defined pH as measured for the cell:

$$H_2(Pt)|Soln(X)||Salt\ bridge|Reference\ electrode| \tag{7.21}$$

The Nernst equation gives

$$E = E° + (2.303RT/F)\ pH(X) \tag{7.22}$$

The value of $E°$ was determined by measuring the electromotive force (EMF, E, or EO) in NaCl-HCl solutions of known $[H^+]$ determined using conductivity. Due to liquid junction differences between the solution-salt bridge-reference solutions, this method was not

satisfactory. Bates (1973) developed a practical pH scale at the National Bureau of Standards (NBS). The NBS pH is defined by

$$pH_{NBS} = -\log a_H \tag{7.23}$$

Since it is not possible to determine individual activities of ions, this scale is based on a conventional definition of activity coefficients. A number of buffers were developed that had fixed values of pH on this scale at a given temperature. The scale is generally used by measuring the EMF in a cell of the type

$$\text{pH Glass electrode} \mid \text{Solution(X)} \mid \text{KCl(aq)} \mid \text{Reference electrode} \tag{7.24}$$

where the reference electrode is normally a calomel electrode. The pH_{NBS} of a solution is determined from EMF measurements in (X) and the buffer. The values are determined from

$$pH(X) = pH(S) + [E(X) - E(S)]/(2.303RT/F) \tag{7.25}$$

In solutions of high ionic strength, this scale does not give reliable values because of differences in liquid junction potentials in the dilute buffers and the ionic media.

This difficulty has led various workers to develop pH scales that are defined using buffer solutions similar to those to be measured. The work in seawater is based on the total proton scale (where the subscripts T and F are, respectively, for total and free concentrations):

$$pH_T = -\log [H^+]_T \tag{7.26}$$

where

$$[H^+]_T = [H^+]_F + [HSO_4^-] \tag{7.27}$$

The two scales are related by

$$10 - pH_{NBS} = f_H[H^+]_T = f_H[H^+]_F (1 + \beta_{HSO_4} [SO_4^{2-}]_T + \beta_{HF}[F^-]_T) \tag{7.28}$$

where f_H is the apparent total proton activity coefficient (~0.7), β_i values are the association constants, and $[H^+]_F$ is the free proton concentration. Bates (1973) developed buffers that can be used to determine pH on the free and total scale:

$$pH_F = -\log [H^+]_F \tag{7.29}$$

The free and total pH scales are related by

$$pH_T = pH_F - \log(1 + \beta_{HSO_4} [SO_4^{2-}]) \tag{7.30}$$

The values of β_{HSO_4} can be determined from

$$\log \beta_{HSO_4} = 4276.1 - 141.328 + 23.093 \ln T + AI^{0.5} + BI + CI^{1.5} + DI^2$$

$$A = -324.57 + 13856/T + 47.986 \ln T$$

$$B = 771.54 - 35474/T - 114.723 \ln T \tag{7.31}$$

$$C = 2698/T$$

$$D = -1776/T$$

which can be used to convert from one scale to the other. The pH is also determined on the seawater scale, which is defined by

$$[H^+]_{SWS} = [H^+]_F + [HSO_4^-] + [HF] = [H^+]_F\,(1 + \beta_{HSO_4}[SO_4^{2-}] + \beta_{HF}\,[F^-]) \tag{7.32}$$

where

$$\log \beta_{HF} = 1590.2/T - 12.641 + 1.525\ I^{0.5} \tag{7.33}$$

The seawater scale is related to the total and free scales by

$$pH_{SWS} = pH_T - \log \{(1 + \beta_{HSO_4}\,[SO_4^{2-}] + \beta_{HF}\,[F^-])/(1 + \beta_{HSO_4}\,[SO_4^{2-}])\} \tag{7.34}$$

$$pH_{SWS} = pH_F - \log \{(1 + \beta_{HSO_4}\,[SO_4^{2-}] + \beta_{HF}\,[F^-])\} \tag{7.35}$$

At 25°C and S = 35, pH_{SWS} = 8.06, pH_T = 8.05, pH_F = 8.19, and pHa = 8.32.

Since variations in the liquid junction potentials of various reference electrodes are different, it is better to use pH_{SWS}, pH_T, or pH_F scales. Seawater buffers are available that can be used to calibrate electrodes on these scales at a given temperature and salinity.

The buffers are made up in a seawater media without carbonate and borate (see Table 7.3). Equal amounts of the acid and base form of the buffer are added to this seawater media. The pH of the buffers can be determined from equations derived by Dickson (1993) from the EMF data of Bates and Calais (1981) and Bates and Erickson (1986).

Although EMF measurements are normally used to measure pH, it is also possible to use indicators that absorb light to measure pH. An indicator is an acid or base whose ionized and un-ionized species absorb light differently. If the stoichiometric constant is known for the indicator, the pH is given by

$$pH = pK_{HA}^* + \log C_A/C_{HA} \tag{7.36}$$

where C_A and C_{HA} are the concentrations of the acid anion and un-ionized acid. The values of C_A and C_{HA} are directly proportional to the absorbance of light at a given wavelength. This method of measuring pH may prove useful for monitoring changes over long periods

TABLE 7.3

Composition of Synthetic Seawater Used to Study Acid–Base Equilibria

Salt	Molality
NaCl	0.42764
Na_2SO_4	0.02927
KCl	0.01058
$MgCl_2$	0.05474
$CaCl_2$	0.01075
NaF	0.00007

of time. Byrne and coworkers (Clayton and Byrne, 1993) have developed a number of indicators that can be used to measure the pH of seawater solution to a precision of 0.0004 and an accuracy of 0.003. One of the indicators used is m-cresol purple. The ratio R of the absorbance at 578 and 434 nm is used to determine the pH from

$$pH_T = 1245.69/T + 3.8275 + (2.11 \times 10^{-3})(35 - S) + \log\{(R - 0.00691)/(2.222 - R\ 0.1331)\} \quad (7.37)$$

where T is the temperature (K), S is the salinity, and the pH is on the total scale.

When a solution contains a weak acid and its salt (e.g., acetic acid and sodium acetate), the addition of H^+ or OH^- causes only a small change in the pH. The pH of this solution is given by Equation 7.33. Since $C_A = C_A^0 - \Delta H^+$ and $C_{HA} = C_{HA} + \Delta H^+$, the ratio of C_A/C_{HA} does not change:

$$C_A/C_{HA} = (C_A^0 - \Delta H^+)/C_{HA}^0 + \Delta H^+ \quad (7.38)$$

This buffering effect works best when $C_A^0 = C_{HA}^0$ or the desired pH = pK_{HA}^*. The buffer capacity of an acid or base is defined by

$$\beta = \Delta C_B/\Delta pH \quad (7.39)$$

For a dibasic acid H_2A, the buffer capacity is

$$\beta = 2.303[[K_1^* C_T C_H/(K_1^* + C_H)] + [K_2^* C_T C_{H^+}\ C_{H^+}\ C_{OH}(K_2^* + C_H)^2] \quad (7.40)$$

The maximum buffer capacity occurs where $C_A = C_{HA}$ and $C_{HA} = C_{H_2A}$.

To represent the concentrations of the components of an acid as a function of pH, one frequently uses a Bjerrum diagram. This diagram is simply a plot of the various forms of the acid (usually in percentage of the total) as a function of pH. For the ionization of a dibasic acid,

$$H_2A = H^+ + HA^- \quad (7.41)$$

$$HA^- = H^+ + A^{2-} \quad (7.42)$$

One has the following equations:

$$K_1^* = [H^+][HA^-]/[H_2A] \quad (7.43)$$

$$K_2^* = [H^+][A^{2-}]/[HA^-] \quad (7.44)$$

$$[H_2A]_T = [H_2A] + [HA^-] + [A^{2-}] \quad (7.45)$$

The fraction of the various forms can be obtained by solving these equations. The solution gives

$$\alpha_{H2A} = (1 + K_1^*/[H^+] + K_1^* K_2^*/[H^+]^2)^{-1} \quad (7.46)$$

$$\alpha_{HA} = (1 + [H^+]/K_1^* + K_2^*/[H+])^{-1} \quad (7.47)$$

$$\alpha_A = (1 + [H^+/K_2^* + [H^+]^2/K_1^* K_2^*)^{-1} \quad (7.48)$$

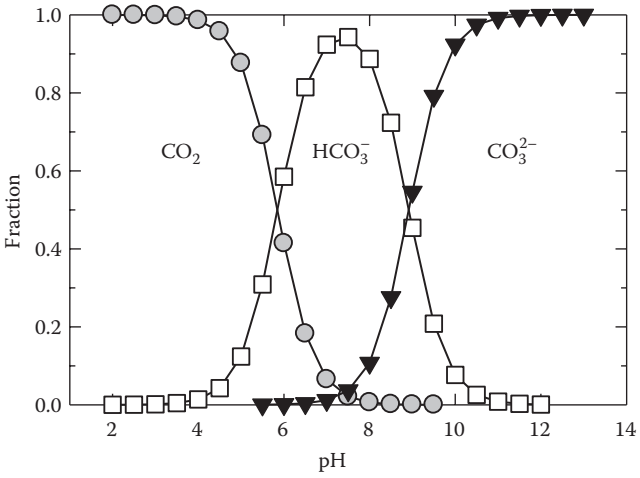

FIGURE 7.7
The fractions of carbonic acid as a function of pH.

From Equation 7.41 to Equation 7.45, the values of $[H_2A] = [HA^-]$ at pH = pK_1^* and $[HA^-] = [A^{2-}]$ at pH = pK_2^*. Thus, if the values of pK_1^* and pK_2^* are known, it is possible to sketch the Bjerrum diagram for a given acid that shows the fractions or concentrations of the acid–base species as a function of pH. The fractions of the components of carbonic acid are shown in Figure 7.7. The crossover points where $[CO_2] = [HCO_3^-]$ and $[HCO_3^-] = [CO_3^{2-}]$ occur, respectively, when pK_1 = pH and pK_2 = pH.

7.3 Equilibria of Carbonate Species

When CO_2 is in contact with water, equilibria as defined by Equation 7.1 to Equation 7.4 will be established. Kinetics can affect the features of these reactions. Equation 7.2 is first order with respect to CO_2 and has a first-order rate constant $k_1 = 0.03$ s or a half-time $t_{1/2} = \ln 2/k_1 = 23$ s. The reaction of $OH^- + CO_2 \rightarrow HCO_3^-$ is second order with respect to $[CO_2]$ and $[OH^-]$:

$$-d[CO_2]/dt = k_2[CO_2][OH^-] \tag{7.49}$$

where $k_2 = 8500\ M^{-1}\ s^{-1}$. This process is important at high values of pH. The dehydration reaction, $H_2CO_3 \rightarrow CO_2 + H_2O$, is first order with respect to $[H_2CO_3]$ with rate constant $k_{-1} = 20\ s^{-1}$ and $t_{1/2} = 0.03$ s. The values for the forward and backward reactions

$$CO_2 + H_2O \underset{k_{-1}}{\overset{k_1}{\rightarrow}} H_2CO_3 \tag{7.50}$$

can be used to determine the equilibrium ratio

$$K = k_1/k_{-1} = 0.03/20 = 1/670 \tag{7.51}$$

This indicates that at equilibrium the concentration of CO_2 is 670 times higher than H_2CO_3. This has led workers to use the so-called hydration convention to define the first ionization of carbonic acid (Equation 7.2). The thermodynamics of the carbonic acid system has been reviewed (Millero, 1995). The stoichiometric association constant for the first ionization is defined by

$$K_1^* = [H_+]_T\,[HCO_3^-]_T/[CO_2^*] \tag{7.52}$$

where $[CO_2^*] = [CO_2] + [H_2CO_3]$, and the subscript T is used to denote total concentrations. The concentration of dissolved CO_2 is related to the pressure by

$$[CO_2^*] = pCO_2\,K_0 \tag{7.53}$$

where K_0 is the Henry's law constant, similar to the values described for other gases in Chapter 6. The values of K_0 can be obtained from (Weiss, 1974)

$$\begin{aligned}\ln K_0 = {} & -60.2409 + 93.4517(100/T) + 23.3585\ln(T/100) + S[0.023517 \\ & - 0.023656(T/100) + 0.0047036(T/100)]\end{aligned} \tag{7.54}$$

where T = t°C + 273.15. The solubility of CO_2 decreases with increasing temperature and salinity as for other gases. The solubility of CO_2 is greater than that of O_2 or N_2. The air ratios are N_2:O_2:CO_2 = 240:630:1, and the solution ratios are 28:19:1. Henry's law is not obeyed at high pH because of the formation of HCO_3^- and CO_3^{2-}. The stoichiometric value of K_1^* is related to the thermodynamic value by

$$K_1 = a_H\,a_{HCO_3}/aCO_2\,a_{H_2O} = K_1^*\gamma_H\gamma_{HCO_3}/(\gamma_{CO_2}\,a_{H_2O}) \tag{7.55}$$

$\gamma_{CO_2} = [CO_2]^0/[CO_2]$, where the superscript zero denotes the solubility in pure water. The activity coefficients given are the total values and include the effects of the formation of ion pairs. The values of pK_1^* in seawater (K_1^* in moles per kilogram of seawater) can be calculated from (S = 0 to 45 and t = 0 to 50°C; Millero et al., 2006)

$$\begin{aligned}\ln K_1^* &= \ln K_1 + A\,S^{0.5} + B\,S + C\,S^2 \\ A &= 12.10 - 489.634/T - 1.881\ln T \\ B &= 0.022 - 2.635/T \\ C &= 0.0000474\end{aligned} \tag{7.56}$$

The thermodynamic values of pK_1 in water are given by

$$\ln K_1 = 290.9097 - 14554.21/T - 45.0575\ln T \tag{7.57}$$

The stoichiometric association constant for the second ionization of carbonic acid is defined by

$$K_2^* = [H+]_T[CO_3^{2-}]_T/[HCO_3^-]_T \tag{7.58}$$

which is related to the thermodynamic value K_2 by

$$K_2 = K_2^* \gamma_H \gamma_{CO_3} / \gamma_{HCO_3} \tag{7.59}$$

where the activity coefficients are total values that include the effect of ionic interactions. The values of K_2^* in seawater can be determined from (S = 0 to 45 and t = 0 to 50°C; Millero et al., 2006)

$$\ln K_2^* = \ln K_2 + A\, S^{0.5} + B\, S + C\, S^2 \tag{7.60}$$

$$A = 22.444 + 797.294/T - 3.558 \ln T$$

$$B = 0.148 - 26.687/T$$

$$C = 0.000369$$

where the thermodynamic value $\ln K_2$ is given by

$$\ln K_2 = 207.6548 - 11843.79/T - 33.6485 \ln T \tag{7.61}$$

The effect of pressure (p, bar) on K_1^* and K_2^* can be estimated from

$$\ln(K^P{}_i / K^0{}_i) = -(\Delta V_i / RT)\, P + 0.5 \Delta K_i\, P^2 \tag{7.62}$$

where

$$-\Delta V_1 = 25.50 + 0.151(S - 34.8) - 0.1271(T - 273.15) \tag{7.63}$$

$$-103 \Delta K_1 = 3.08 + 0.578(S - 34.8) - 0.0877(T - 273.15) \tag{7.64}$$

$$-\Delta V_2 = 15.82 - 0.321(S - 34.8) + 0.0219(T - 273.15) \tag{7.65}$$

$$-103 \Delta K_2 = -1.13 + 0.314(S - 34.8) + 0.1475(T - 273.15) \tag{7.66}$$

Since boric acid makes up one of the major constituents of seawater, it is necessary to consider its ionization:

$$HB = H^+ + B^- \tag{7.67}$$

where HB = $B(OH)_3$ and B– = $B(OH)_{4-}$. The dissociation constant is defined by

$$K^*_{HB} = [H^+]_T [B-]_T / [HB]_T \tag{7.68}$$

The values of pK_{KB}^* in seawater can be calculated from (Dickson, 1990)

$$\ln K_{HB}^* = \ln K_{HB} + B\, S^{0.5} + C\, S + D\, S^{1.5} + \ln (1 - S\, 0.001005) \tag{7.69}$$

$$A = -167.69908 + 6551.35253/T + 25.928788 \ln T$$

$$B = 39.75854 - 1566.13883/T - 6.171951 \ln T$$

$$C = -2.892532 + 116.270079/T + 0.45788501 \ln T$$

$$D = -0.00613142$$

where the thermodynamic value is given by

$$\ln K_{HB} = 148.0248 - 8966.90/T - 24.4344 \ln T \quad (7.70)$$

The effect of pressure on K_{HB}* can be determined from Equation 7.62, where

$$-\Delta V_{HB} = 29.48 - 0.295(S - 34.8) - 0.1622(T - 273.15) \quad (7.71)$$

$$-103\Delta K_{HB} = 2.84 - 0.354(S - 34.8) \quad (7.72)$$

The solubility of $CaCO_3$ in its two major forms, calcite and aragonite, is also needed when studying the carbonate system. The stoichiometric solubility product is given by

$$K_{SP}^* = [Ca^{2+}][CO_3^{2-}] \quad (7.73)$$

and is related to the thermodynamic value by

$$K_{SP}^* = K_{SP}/\gamma_T(Ca^{2+})\gamma_T(CO_3^{2-}) \quad (7.74)$$

The values in seawater are given by (Mucci, 1983)

$$\ln K_{SP}^* = \ln K_{SP}(i) + A\, S^{0.5} + B\, S + C\, S^{1.5} \quad (7.75)$$

where

$$A_{cal} = -0.77712 + 0.0028426\ T + 178.34/T$$

$$B_{cal} = -0.07711$$

$$C_{cal} = 0.0041249$$

$$A_{arag} = -0.068393 + 0.0017276\ T + 88.135/T$$

$$B_{arag} = -0.10018$$

$$C_{arag} = 0.0059415$$

The thermodynamic Ksp is given by

$$\ln Ksp(calcite) = -171.9065 - 0.077993\ T + 2839.319/T + 71.595 \log T \quad (7.76)$$

$$\ln Ksp(aragonite) = -171.945 - 0.077993\ T + 2903.293/T + 71.595 \log T \quad (7.77)$$

The effects of pressure on the solubility of calcite and aragonite are calculated from Equation 7.65, where

$$-\Delta V_{cal} = 48.76 - 0.5304(T - 273.15) \quad (7.78)$$

$$-\Delta V_{arag} = 46.0 - 0.5304(T - 273.15) \quad (7.79)$$

$$-10^3\Delta K_{cal} = 11.76 - 0.3692(T - 273.15) \quad (7.80)$$

$$-10^3\Delta K_{arag} = 11.76 - 0.3692(T - 273.15) \quad (7.81)$$

The pK's needed to calculate the parameters of the carbonate system in seawater (S = 35) at various temperatures are given in Table 7.4. It should be pointed out that all the carbonic acid constants are on the total scale. The values of the carbonate constants of seawater on the various pH scales are given in Table 7.5 (Millero, 2010).

The equation used to make conversions with the dissociation constants between pH scales is as follows (Millero, 2010):

$$pK_i - pK^0{}_i = A_i + B_i/T + C_i \ln(T)$$

where T is the absolute temperature, and A_i, B_i, and C_i are salinity-dependent constants. The values for $pK^0{}_1$ and $pK^0{}_2$ are fitted to the following equations (Millero et al., 2006):

TABLE 7.4

Dissociation Constants for Carbonate Calculations in Seawater (S = 35)

Temp. (°C)	pK_0	pK_1	pK_2	pK_B	pK_W	pK_{cal}	pK_{arg}
0	1.202	6.101	9.376	8.906	14.30	6.37	6.16
5	1.283	6.046	9.277	8.837	14.06	6.36	6.16
10	1.358	5.993	9.182	8.771	13.83	6.36	6.17
15	1.426	5.943	9.090	8.708	13.62	6.36	6.17
20	1.489	5.894	9.001	8.647	13.41	6.36	6.18
25	1.547	5.847	8.915	8.588	13.21	6.37	6.19
30	1.599	5.802	8.833	8.530	13.02	6.37	6.20
35	1.647	5.758	8.752	8.473	12.84	6.38	6.21
40	1.689	5.716	8.675	8.416	12.67	6.38	6.23

TABLE 7.5

Coefficients for the Fits of the Values pK_1 and pK_2 in Seawater as a Function of Temperature, Salinity, and Ionic Strength on the pH_F, pH_T, and pH_{SWS} Scales

		pK_1			pK_2		
		pH_F Scale	pH_T Scale	pH_{SWS} Scale	pH_F Scale	pH_T Scale	pH_{SWS} Scale
$S^{0.5}$	a_0	5.09247	13.4051	13.4038	11.0637	21.5724	21.3728
S	a_1	0.05574	0.03185	0.03206	0.1379	0.1212	0.1218
S^2	a_2	−9.279E-05	−5.218E-05	−5.242E-05	−3.788E-04	−3.714E-04	−3.688E-04
S0.5/T	a_3	−189.879	−531.095	−530.659	−366.178	−798.292	−788.289
S/T	a_4	−11.3108	−5.7789	−5.8210	−23.288	−18.951	−19.189
S0.5 ln T	a_5	−0.8080	−2.0663	−2.0664	−1.810	−3.403	−3.374
SE		0.0055	0.0053	0.0053	0.0105	0.0108	0.0109
Number		551	551	551	590	590	590

$$pK^0_1 = -126.34048 + 6320.813/T + 19.568224 \ln(T)$$

$$pK^0_2 = -90.81333 + 5143.692/T + 14.613358 \ln(T)$$

where the adjustable parameters A_i, B_i, and C_i are demonstrated by

$$A_i = a_0 S^{0.5} + a_1 S + a_2 S^2$$

$$B_i = a_3 S^{0.5} + a_4 S$$

$$C_i = a_5 S^{0.5}$$

The coefficients for all the fits of these equations are summarized in Table 7.5 for all of the pH scales.

7.4 Parameters of the CO_2 System in Seawater

To characterize the various components of the carbonate system in seawater, one must measure at least two of the four measurable parameters:

1. pH
2. Alkalinity, total alkalinity (TA)
3. Total CO_2 (TCO_2)
4. Partial pressure of CO_2, (pCO_2)

The pH can be measured using electrodes or indicators. If the electrodes are calibrated using seawater buffers, the accuracy is ±0.01, and the precision can be ±0.002 pH units. If the measurements are made at 25°C and 1 atm, it is necessary to determine the in situ values at a given depth in the ocean. The effect of temperature can be determined from

$$pH_t = pH_{25} + A + B\,t + C\,t^2 \tag{7.82}$$

where

$$A = -2.6492 - 0.0011019\,S + 4.9319 \times 10^{-6}\,S^2 + 5.1872\,X - 2.1586\,X^2 \tag{7.83}$$

$$B = 0.10265 - 0.20322\,X + 4431\,X^2 + 3.1618 \times 10^{-5}\,S \tag{7.84}$$

$$C = 4.4528 \times 10^{-5} \tag{7.85}$$

where $X = TA/TCO_2$. The effect of pressure can be estimated from

$$pH_t^P = pH_t^0 + A\,P \tag{7.86}$$

$$-10^3 A = 0.424 - 0.0048(S - 35) - 0.00282\,t - 0.0816(pH_t^0) \tag{7.87}$$

where pH_t^0 is the pH at temperature t°C and 1 atm.

TABLE 7.6

Contribution of Various Components to the Total Alkalinity of Seawater

Species	Percentage TA
HCO_3^-	89.8
CO_3^{2-}	6.7
$B(OH)_{4-}$	2.9
$SiO(OH)_{3-}$	0.2
$MgOH^+$	0.1
OH^-	0.1
HPO_4^{2-}	0.1

The TA of seawater is defined as the concentration of all the bases that can accept H^+ when a titration is made with HCl to the carbonic acid end point. The value of TA is given by

$$TA = [HCO_3^-] + 2[CO_3^{2-}] + [B(OH)_4^-] + [OH^-] - [H^+] + [SiO(OH)_3^-] + [MgOH^+] + 2[HPO_4^{2-}] + 3[PO_4^{3-}] \quad (7.88)$$

The percentage of TA from the various bases is shown in Table 7.6 for ocean waters with pH = 8 $[SiO(OH)_3^-] = 10^{-5.25}$, and $[HPO_4^{2-}] = 10^{-5.52}$. For most waters, $[HCO_3^-]$, $[CO_3^{2-}]$, and $[B(OH)_4^-]$ are the most important bases. For anoxic waters, HS^- and NH_3 can also contribute to the TA.

The carbonate alkalinity A_C is defined by

$$A_C = [HCO_3^-] + 2\,[CO_3^{2-}] \quad (7.89)$$

and is calculated from

$$A_C = TA - [B]_T \quad (7.90)$$

where $[B]_T = [B(OH)_{4-}] + \ldots$, the sum of all the bases other than HCO_3^- and CO_3^{2-}. The $[B(OH)_4^-]$ concentration, which is the largest source of $[B]_T$, can be calculated from

$$[B(OH)_4^-] = K^*_{HB}[B]_T/(K^*_{HB+}\,[H+]_T) \quad (7.91)$$

where $[B]_T = 1.2 \times 10^{-5}$ S (Lee et al., 2010). The contribution from other bases (phosphate, silicate, ammonium, and hydrogen sulfide) can be determined using the dissociation constants for the appropriate acid (Chapters 8 and 10, Appendix 4).

The TA of seawater is determined by titrating a given amount of seawater with HCl to the carbonic acid end point. The titration is followed by measuring the EMF of a glass pH and reference electrode. A typical titration of 234 cm^3 of S = 35 seawater with 0.25N HCl is shown in Figure 7.8. The titration shows two end points, V_1 and V_2. The value of A_T is determined from

$$TA = V_2 N_{HCl}/W \quad (7.92)$$

where N_{HCl} is the normality of the HCl solution, and W is the weight of the seawater titrated (W = Volume × Density). The difference between the first and second end point can be used to determine the TCO_2:

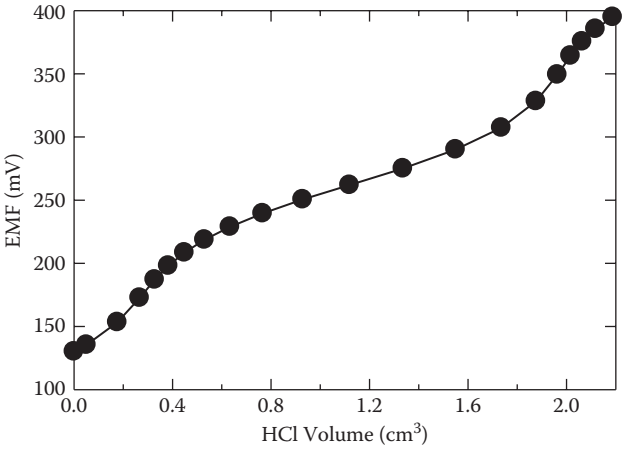

FIGURE 7.8
The changes in the EMF of a pH electrode during the titration of seawater with hydrochloric acid.

$$TCO_2 = (V_2 - V_1)N_{HCl}/W \tag{7.93}$$

The pH_{SWS} of the initial solution before the addition of HCl can be determined from

$$pH_{SWS} = -(E - E^*)/(2.303RT/F) \tag{7.94}$$

The quantities V_1, V_2, and E* are determined from the measured EMF (E) and the volume of added HCl (V) using an iteration technique. A reasonable approximation of V_1, V_2, and E* can be determined by calculating the $[H^+]_{SWS}$ from

$$[H^+]_{SWS} = 10[(E - 400)/k] \tag{7.95}$$

where k = 2.303 RT/F = 59.16 mV at 25°C.

Using the EMF data from 150 to 210 mV, the function F_2 is calculated from

$$F_2 = (V_0 + V)[H+]_{SWS} \tag{7.96}$$

where V_0 is the initial volume of seawater. The values of F_2 are then fit to the linear equation

$$V = a + b\,F_2 \tag{7.97}$$

(Figure 7.9). At $F_2 = 0$, the value of V equals V_2. The value of V_1 is determined from the initial EMF data (–15 to 50 mV) using the function

$$F_2 = (V_2 - V)[H^+]_{SWS} \tag{7.98}$$

The values of F_1 are fit to the equation

$$V = a + b\,F_1 \tag{7.99}$$

At $F_1 = 0$, the value of V equals V_1 (Figure 7.10). The value of E* is determined from the values of E past the second end point ($V > V_2$) using the equation

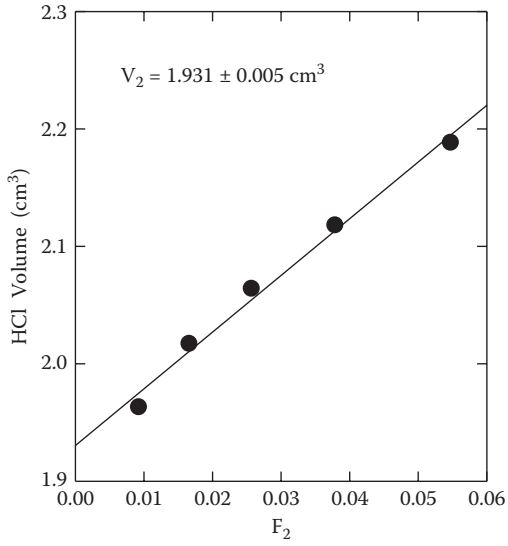

FIGURE 7.9
The Gran function F_2 as a function of the volume of HCl added during the titration of seawater.

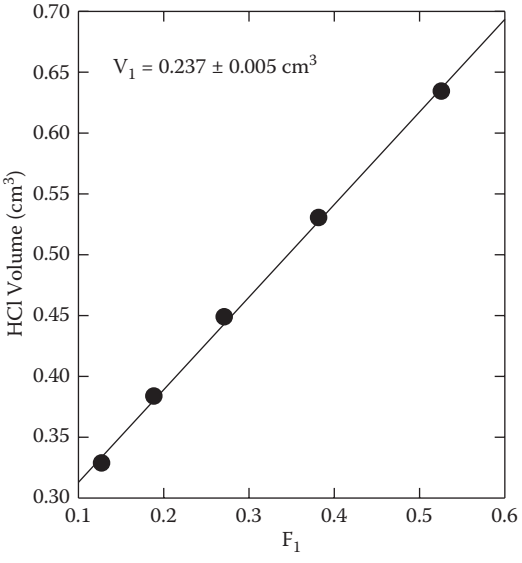

FIGURE 7.10
The Gran function F_1 as a function of the volume of HCl added during the titration of seawater.

$$E^* = E - k \log[\{(V - V_2)/(V_0 + V)\} N_{HCl}] \quad (7.100)$$

The average E* can be used to refine the calculations. For the data shown, TA = 2.237 ± 0.007 mmol kg^{-1}, TCO_2 = 2.023 ± 0.013 µmol kg^{-1}, pH_{SWS} = 7.731 ± 0.019, and E* = 407.6 ± 1.1 mV.

To make more accurate calculations, it is necessary to make corrections for side reactions. The modified F_2' is given by

$$F_2' = (V_0 + V)\{[H^+]_{SWS} + [HSO_4^-] + [HF] - [HCO_3^-]\} \quad (7.101)$$

$$F_1' = (V_2 - V)\{([H^+]2 - K_1^*K_2^*)/(K_1^*[H^+] + 2K_1^*K_2^*)\} + (V_0 + V)\{[H^+] + [HSO_4^-] + [HF]$$

$$- [B(OH)_4^-] - [OH^-] \times [H^+]^2 + K_1^*[H^+] + K_1^*K_2^*/N_{HCl}(K_1^*[H^+] + 2K_1^*K_2^*)\}$$

Computer programs make these calculations easier to do than one would expect from examining the complicated equation for F_1'.

Although it is possible to determine TCO_2 from a titration, more reliable values can be obtained by direct measurements. This is done by stripping the inorganic CO_2 with nitrogen after the addition of phosphoric acid. The CO_2 can be collected in a liquid air trap and analyzed by gas chromatography, infrared spectroscopy, or conductivity. By collecting the CO_2 in a DMSO (dimethyl sulfoxide) solution with ethylene amine, it can be coulometrically titrated with OH^- produced on a Pt electrode. Routine measurements of TCO_2 on 30 cm^3 seawater can be made to a precision of 1 μmol kg^{-1} and an accuracy of 2 μmol kg^{-1} using certified reference material prepared by Dickson (1993). This reference material is used to make TA and TCO_2 measurements in the laboratory and at sea.

The partial pressure of CO_2 in seawater is determined by equilibrating the sample with air or nitrogen. The CO_2 in the equilibrated gas is measured using gas chromatography or an IR analyzer. By passing seawater through a showerhead equilibrator, one can make continuous measurements on surface seawater (Weiss, 1981). The system can be calibrated using standard CO_2 gas mixtures and yield values of pCO_2 to a precision of 1 μatm.

As mentioned, any two combinations of the four observable parameters can be used to characterize the carbonate system. It is also possible to use three parameters. This gives a total of 10 combinations that can be used. The investigator must make a selection based on his or her needs after considering both the desired analytical precision and area of interest. Park (1969) has given all the equations needed to determine the carbonate parameters. The basic equations are for the commonly determined parameters pH, A_C, TCO_2, and A_C, where V_0 will be examined. For an input of pH and A_C, the equations are

$$[HCO_3^-] = A_C/[1 + 2K_2^*/[H^+] \quad (7.102)$$

$$[CO_3^{2-}] = A_CK_2^*/([H^+] + 2K_2^*) \quad (7.103)$$

$$[CO_2] = (A_C[H+]/K^*_1)/(1 + 2K^*_2/[H^+]) \quad (7.104)$$

$$TCO_2 = [HCO_3^-] + CO_3^{2-}] + [CO_2] \quad (7.105)$$

$$pCO_2 = [CO_2]/K_0 \quad (7.106)$$

Strictly speaking, the pCO_2 in Equation 7.106 should be the fugacity, which differs from the partial pressure because of interactions between CO_2 molecules in the gas phase. Since the difference is normally quite small (~3 μatm when pCO_2 is 360 μatm), the two can be equated without any serious errors. The values of K_1^*, K_2^*, K_0, and $[H^+]$ are determined for the in situ temperature, pressure, and salinity.

If the A_C and TCO_2 are determined, the various components of the carbonate system can be determined from

$$[CO_2] = TCO_2 - A_C + (A_CK_R - TCO_2K_R - 4A_C + Z)/2(K_R - 4) \quad (7.107)$$

$$[HCO_3^-] = (TCO_2\, K_2^* - Z)/(K_R - 4) \tag{7.108}$$

$$[CO_3^{2-}] = (A_C\, K_R - TCO_2\, K_R - 4\, A_C + Z)/2(K_R - 4) \tag{7.109}$$

where $K_R = K_1^*/K_2^*$, and Z is given by

$$Z = [4\, A_C + (TCO_2\, K_R - A_C\, K_R)^2 + 4(K_R - 4)A_C^2]^{1/2} \tag{7.110}$$

The value of $[H^+]$ needed to determine A_C from TA can be measured or calculated by solving the cubic equation

$$[H^+]^3 + [H+]^2\{[K_1^*(A - 1) + K_{HB}^*(A - B)]/A\} + [H^+]\{K_1^*K_{HB}^*(A - B - 1) + K_1^*K_2^*(A - 2)\}/A + K_1^*K_2^*K_{HB}^*(A - B - 2)/A = 0 \tag{7.111}$$

The values of A and B in this equation are given by

$$A = TA/TCO_2 \approx 1.05 \tag{7.112}$$

$$B = [B]_T/TCO_2 \approx 0.18 \tag{7.113}$$

If the value of TCO_2 is not measured, it is estimated using pH = 8.0 from the equation

$$TCO_2 = A_C(1 + [H^+]/K^*_{1+}K^*_2/[H^+])/(1 + 2K^*_2/[H^+]) \tag{7.114}$$

The cubic equation for $[H^+]$ can be solved by using the solution to a cubic equation or using iterative techniques. The process is repeated until self-consistent values of TCO_2 and $[H^+]$ are determined. The calculations of the components of the CO_2 with various inputs can be easily determined for seawater using an available QuickBasic program, CO2sys (Lewis and Wallace, 1998). Versions of this program in Excel and MATLAB® are also available (van Heuven et al., 2011).

To select the best parameters needed to study the carbonate system, we can examine how the system changes during the formation and breakdown of organic carbon and the dissolution or precipitation of $CaCO_3$. The largest changes in the CO_2 system in deep waters are due to the oxidation of organic carbon. This can be represented by the reaction

$$(CH_2O)_{106}(NH_3)_{16}H_3PO_4 + 138O_2 \rightarrow 106CO_2 + 122H_2O + 16HNO_3 + H_3PO_4 \tag{7.115}$$

This oxidation can be followed by considering the changes in the apparent oxygen utilization (AOU). The effect of changes in AOU of 0.13 and 0.26 m*M* is shown in Table 7.7. The largest change occurs in pCO_2 followed by TCO_2 and pH. A_C, the carbonate alkalinity, does not change. If one considers the present capabilities of measuring pCO_2 (±0.1%), TCO_2 (±0.17%), TA (±0.2%), and pH (±0.04%), the best selection would be $pCO_2 - TCO_2$, followed by $pH - TCO_2$ and $pCO_2 - TA$.

The changes in the CO_2 system caused by the dissolution of $CaCO_3$ in deep waters are shown in Table 7.8. The greatest change occurs in A_C, with pCO_2 and pH following. The best combination is $A_C - TCO_2$, followed by $pH - A_C$ and $A_C - TCO_2$, obtained by an acid titration. These represent the best approach for studying changes in the carbonate system caused by the precipitation or dissolution of $CaCO_3$.

TABLE 7.7

Changes in the CO_2 System Caused by the Oxidation of Plant Material

		ΔAOU (m*M*)		
	Initial[a]	**0.13**	**0.26**	**% Change**
ΔCO_2	0	0.10	0.20	—
TCO_2	2.200	2.300	2.400	9.1 ± 0.1
A_C	2.487	2.487	2.487	0
pCO_2	350	610	1.160	231 ± 1.0
pH	8.200	8.001	7.753	–5.5 ± 0.04
$[CO_2]$	0.012	0.021	0.040	233
$[HCO_3^-]$	1.889	2.072	2.234	18
$[CO_3^{2-}]$	0.299	0.208	0.126	–58

[a] All concentrations are millimolar.

TABLE 7.8

Changes in the CO_2 System Caused by the Dissolution of $CaCO_3$

		$\Delta CaCO_3$ (m*M*)		
	Initial[a]	**0.05**	**0.10**	**% Change**
ΔCO_2	0	0.05	0.10	—
TCO_2	2.200	2.250	2.300	4.5 ± 0.1
CA	2.487	2.587	2.687	72 ± 0.05
pCO_2	350	310	290	–17 ± 1.0
pH	8.200	8.264	8.321	1.5 ± 0.04
$[CO_2]$	0.012	0.011	0.010	–17
$[HCO_3^-]$	1.889	1.892	1.844	0.3
$[CO_3^{2-}]$	0.299	0.348	0.397	33

[a] All concentrations are millimolar.

If one combines the AOU and $CaCO_3$ effects, one finds

$$(CH_2O)_{106}(NH_3)_{16}H_3PO_4 + 138O_2 + 124CO_3^{2-} \rightarrow 16NO_3^- + HPO_4^{2-} + 230HCO_3^- + 16H_2O \quad (7.116)$$

The CO_3^{2-} ions formed from the dissolution of $CaCO_3$ react with the protons formed from the oxidation of plant material. If x μ*M* of $CaCO_3$ and y μ*M* of organics are decomposed, the changes in TA, TCO_2, and NO_3^- are given by

$$\Delta TA = 2x - 17y \quad (7.117)$$

$$\Delta TCO_2 = x + 106y \quad (7.118)$$

$$\Delta NO_3 = 16y \quad (7.119)$$

The changes in Ca^{2+} are given by

$$\Delta Ca = 0.463\Delta TA + 0.074\Delta TCO_2 = 0.5\Delta TA + 0.53\Delta NO_3 \quad (7.120)$$

This equation was first used by Chen (1978) to predict changes in Ca^{2+} as a function of depth in the Pacific that agree very well with the measured values. The changes in inorganic carbon to organic carbon are given by

$$\text{Inorg C/Org C} = x/106y = 16\Delta Ca/106\Delta NO_3 = (8TA + 8.5\Delta NO_3)/106\Delta NO_3 \quad (7.121)$$

This equation has also been shown by Chen to predict reasonable ratios of inorganic C to organic C in ocean waters.

If one uses these equations (Brewer, 1978; Chen and Millero, 1979) to examine the changes in TCO_2 in old deep waters and younger waters, it is possible to make an estimate of the changes caused by the increase of CO_2 in the atmosphere from the burning of fossil fuels. The estimated increases (≈260 ± 20 ppm for preindustrial values) are in reasonable agreement with the values (280 ppm) obtained from ice cores (see Figure 5.21). More will be said about estimating the penetration of fossil fuel into the oceans further in this chapter.

7.5 Distribution of Carbonate Species

The distribution of the various components of the CO_2 system in the oceans has been studied by many workers. Skirrow (1975) reviewed much of the earlier work. The earlier 1970s studies of the carbonate system during the GEOSEC (Geochemical Oceans Sections Study) program yielded the first global look at the CO_2 system. The more recent JGOFS (Joint Global Ocean Flux Study) CO_2 measurements made in the 1990s as part of the WOCE (World Ocean Circulation Experiment) hydrographic program yielded a much more reliable and global picture of the CO_2 system that will serve as a benchmark for the future. These results are available on the Web (http://cdiac.esd.ornl.gov). Over the last 10 yr repeat measurements of the oceans have and are still being studied as part of the Climate Variability and Predictability (CLIVAR) program. These results are discussed elsewhere in this chapter. In this section, we discuss the distribution of the CO_2 parameters.

7.5.1 pCO_2

Unfortunately, no historical data of sufficient accuracy are available for pCO_2 in surface waters of the oceans over time as in the atmosphere. An earlier comparison of the increase from 1957 to 1980 (Takahashi, Lamont Doherty Earth Observatory) is shown in Figure 7.11. Recent measurements at the time series stations were shown in this chapter (Figure 7.17). The repeat measurements over the last 20 yr give a hint of present changes in pCO_2 of surface waters. The most reliable recent measurements of pCO_2 as a function of time to 2007 are the results from the Bermuda and Hawaii Time Series stations, discussed elsewhere in this chapter. The measured increase in the surface waters appears to track the values in the atmosphere (2 ppm yr^{-1}). The changes in pCO_2 in surface waters can be caused by

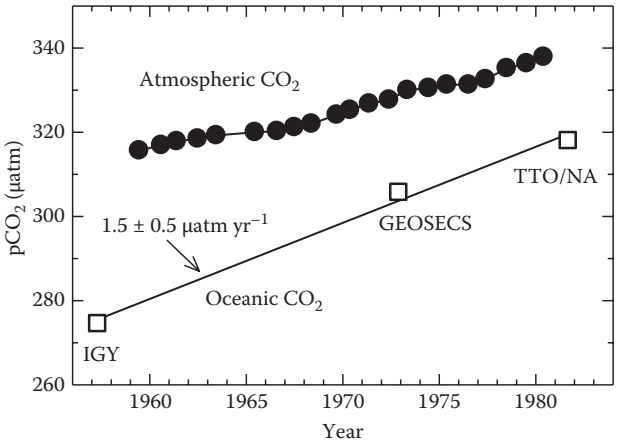

FIGURE 7.11
A comparison of the increase of the partial pressure of carbon dioxide in the atmosphere and the ocean from 1957 to 1980.

1. Removal by photosynthesis
2. Removal by dissolution of $CaCO_3$
3. Removal by solar heating
4. Addition by oxidation of plant material
5. Addition by formation of $CaCO_3$
6. Addition by increases in CO_2 in the atmosphere from fossil fuel burning

Unraveling all these effects is even more difficult because of the sluggish response of the oceans to changes in the level of CO_2 in the atmosphere. As with other gases, the driving force of CO_2 across the air–sea interface is the differences between the concentrations in the atmosphere and oceans given by

$$\text{Flux} = k\{pCO_2(SW) - pCO_2(ATM)\} = k\,\Delta pCO_2 \tag{7.122}$$

where the value k is called the transfer velocity. Liss (1975) divided this transfer velocity into two terms:

$$1/k = 1/\alpha k_W + 1/Hk_A \tag{7.123}$$

where k_w and k_A are transfer velocities in the water and air, respectively; H is the Henry's law constant (a unitless value, the ratio of air to water concentrations at equilibrium); and α is a factor that accounts for any enhancement of the transfer on the water side caused by chemical reactions between the gas and H_2O ($CO_2 + H_2O \rightarrow H^+ + HCO_3^-$). The value of α is 1.02 to 1.03 for CO_2. From ^{14}C measurements, values of k_w average about 6 mol m^{-2} yr^{-1} μatm^{-1} on a global basis. The transfer velocity increases with increasing wind speed (see Figure 7.12). The values of k determined in wind tunnel measurements are 3 to 4 mol m^{-2} yr^{-1} μatm^{-1}, much smaller than the value estimated from ^{14}C measurements, making it

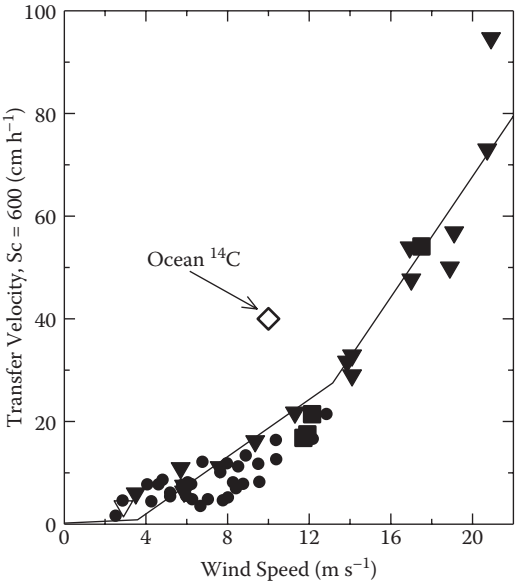

FIGURE 7.12
The transfer velocity of CO_2 at 20°C as a function of wind speed. The straight lines are based on the relationships of Liss and Merlivat (1986): $k = 0.17U_{10}$ for $U_{10} \leq 3.6$ m s^{-1}, $k = 2.85U_{10} - 9.65$ for 3.6 m s^{-1} < $U_{10} \leq 13$ m s^{-1} and $k = 5.9U_{10} - 49.3$ for $U_{10} > 13$ m s^{-1} (where U_{10} is the wind speed 10 m s^{-1} above the surface). The Schmidt number Sc = ν/D where ν is the kinematic viscosity (η/ρ) and D is the diffusion coefficient.

difficult to use Equation 7.122 to calculate global fluxes of CO_2. When ΔpCO_2 is positive, the oceans are a source of CO_2; when it is negative, the oceans are a sink for CO_2. To take up the missing CO_2, the value of ΔpCO_2 worldwide would have to be about 8 ppm.

As discussed for other gases, the value of k (the exit coefficient) is a function of the wind speed and is difficult to determine. If rapid exchange takes place, one would expect the pCO_2 in the atmosphere to be equal to the values in the surface waters. If the exchange is sluggish, the pCO_2 in surface waters will be higher in upwelling areas and lower in colder waters than the values in the atmosphere.

Measurements of pCO_2 in the Atlantic surface waters are shown in Figure 7.13.

The higher values of pCO_2 near the equator are the result of equatorial upwelling. The lower values of pCO_2 in the polar regions make these waters a sink for CO_2 As discussed by Broecker and Peng (1982), the levels of TCO_2 and pCO_2 in surface waters are related to the exchange of CO_2 across the air–sea interface. Sluggish exchange causes pCO_2 to be greater than the values in the atmosphere near the equator and lower in polar waters. A north-south section of pCO_2 in the surface waters in the Pacific shown in Figure 7.14 provides values similar to the values in the Atlantic Ocean.

A number of workers have attempted to separate the causes of the changes in the pCO_2 of surface waters from physical (temperature and salinity) and biological (chlorophyll) factors. An example of such a separation is shown in Figure 7.15 using the Atlantic data. The relative importance based on the magnitude of the changes is in the order temperature, chlorophyll, and salinity. This way of examining the importance of physical and biological process slopes neglects the importance of nutrients and the formation of phytoplankton blooms that can pull down the surface values of pCO_2.

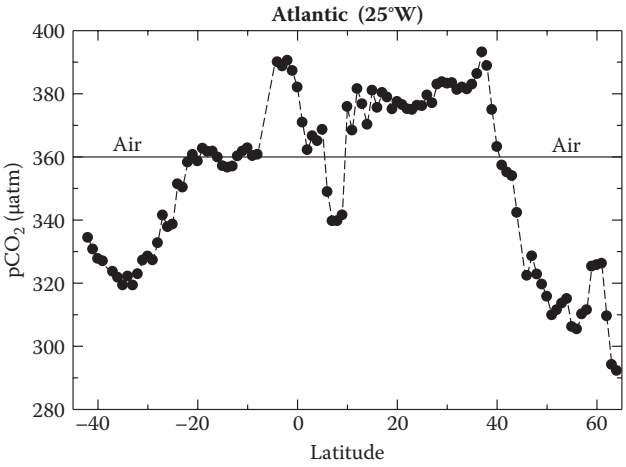

FIGURE 7.13
The partial pressure of carbon dioxide in the atmosphere (line) and surface waters (circles) of the Atlantic Ocean (Wanninkhof, AOML/NOAA, personal communication).

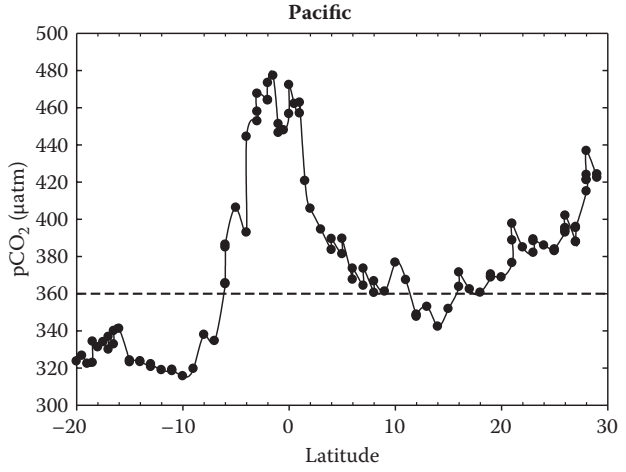

FIGURE 7.14
The partial pressure of carbon dioxide in the atmosphere (dotted line) and surface waters (solid line) of the Pacific Ocean (Goyet, WHOI, personal communication).

Values of pCO_2 in the surface waters of the oceans (Takahashi et al., 1999) are shown in Figure 7.16. The cold waters are a sink for CO_2 (pCO_2 less than 365 ppm), while the upwelling waters are a source of CO_2 (pCO_2 higher than 365 ppm) to the atmosphere. Recent measurements have been made at the Hawaii Ocean (HOT) and Bermuda Atlantic (BATS) time series stations. The results for BATS and HOT stations (Figure 7.17) show a large annual cycle of CO_2. The pCO_2 is lower in the winter and higher in the summer largely because of changes in the temperature of the waters. The annual cycle of pCO_2 is much greater in Bermuda than Hawaii because of the larger variations in temperature. The annual increases in the pCO_2 are 1.6 and 2.3, respectively, in Bermuda and Hawaii, which is the same order of magnitude as the increase in the atmosphere. The TA in the surface waters

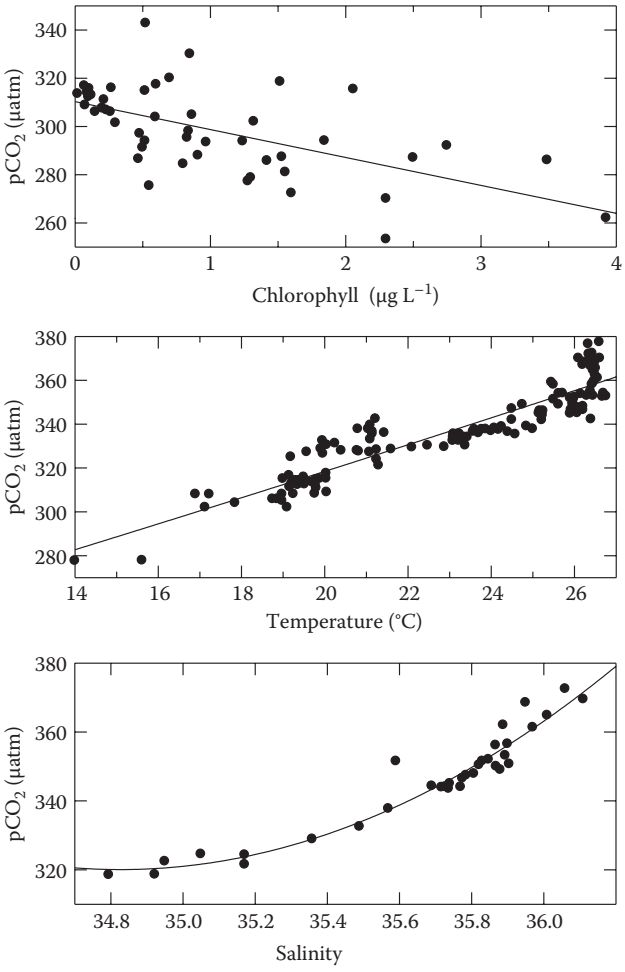

FIGURE 7.15
The relationship between the partial pressure of carbon dioxide in Atlantic surface waters to the concentrations of chlorophyll, the temperature, and the salinity. (Adapted from B. Schneider).

does not change significantly in these waters. The TCO_2 increases by 0.68 and 1.26 µmol kg^{-1} yr^{-1} and the $\delta^{13}C$ decreases by 0.024 and 027 ppm yr^{-1}, respectively, at the Bermuda and Hawaii time series stations.

The growth of phytoplankton blooms also affects the levels of pCO_2 in surface waters. The pull-down of surface pCO_2 by phytoplankton and delivery of the CO_2 to deep waters after decomposition is the so-called biological pump (Figure 7.2). Studies have shown that the pull-down of CO_2 by plankton occurs in the North Atlantic during the spring blooms. For this biological pump to take CO_2 permanently from the atmosphere, the organic carbon must sink below the thermocline and be oxidized back to CO_2 that will be stored for hundreds of years in deep waters.

The depth profiles of pCO_2 for the Atlantic and Pacific are shown in Figure 7.18. These values were calculated from TA and TCO_2, so they are not as accurate as direct measurements. The general trends, however, are real and as expected. The surface values are similar to atmospheric values. The values increase to a maximum (500 µatm in the North

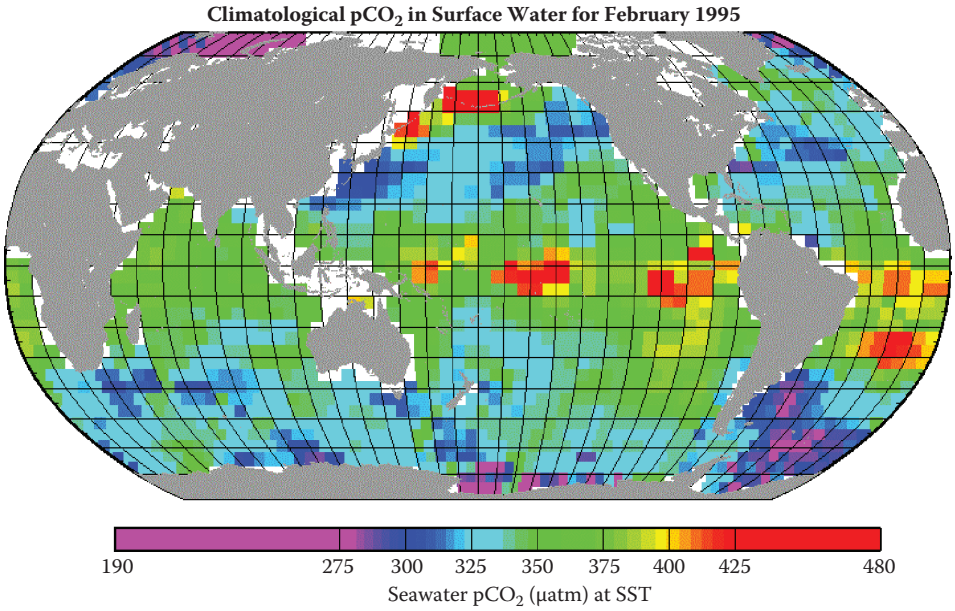

FIGURE 7.16
The global distribution of pCO_2 (µatm) for surface waters of the world oceans. (From Takahashi, T., et al., Net air–sea CO_2 flux over global oceans: an improved estimate based on sea–air pCO_2 differences, in *Proceedings of 2nd International Symposium on CO_2 in the Oceans*, CGER-1037-99, CGER/NIES, Tsukuba, Japan, 1999, pp. 9–15. With permission.)

Atlantic and 1200 µatm in the Pacific) at 1 km because of the oxidation of plant material. The higher values at 1 km in the Pacific are due to the higher productivity of the surface waters, resulting in the production of more organic carbon. The deep-water values in the Pacific are higher than in the Atlantic because of the fact that the waters are older and have accumulated more CO_2 from the oxidation of organic carbon as the waters make the trip from the North Atlantic to the North Pacific (600 yr). The deep waters originally formed at the surface have lower pCO_2 than the values at the oxygen minimum.

7.5.2 pH

The pH of most surface waters in equilibrium with the atmosphere is 8.2 ± 0.1. Recent measurements of pH in the surface waters of the Atlantic and Pacific Oceans are shown in Figure 7.19 and Figure 7.20, respectively. The gross trends in pH are those expected from the surface pCO_2 (the higher the pCO_2, the lower the pH and vice versa). The values are lower in upwelling waters in the equatorial regions and are proportional to temperature. In closed or small bodies of water, the pH can show diurnal variations and cycle between 8.2 and 8.9. The decrease occurs in the evening because of the respiration of organisms, and the increase occurs in the afternoon because of photosynthesis. Changes in the pH with depth in the Atlantic and Pacific Oceans are shown in Figure 7.21. Although it is difficult to see in this figure, the pH goes through a maximum in surface waters because of photosynthesis. The loss of CO_2 increases the pH. The pH then decreases because of the oxidation of plant material and goes through a minimum at about 1 km. This minimum coincides with the O_2 minimum and the maximum in pCO_2.

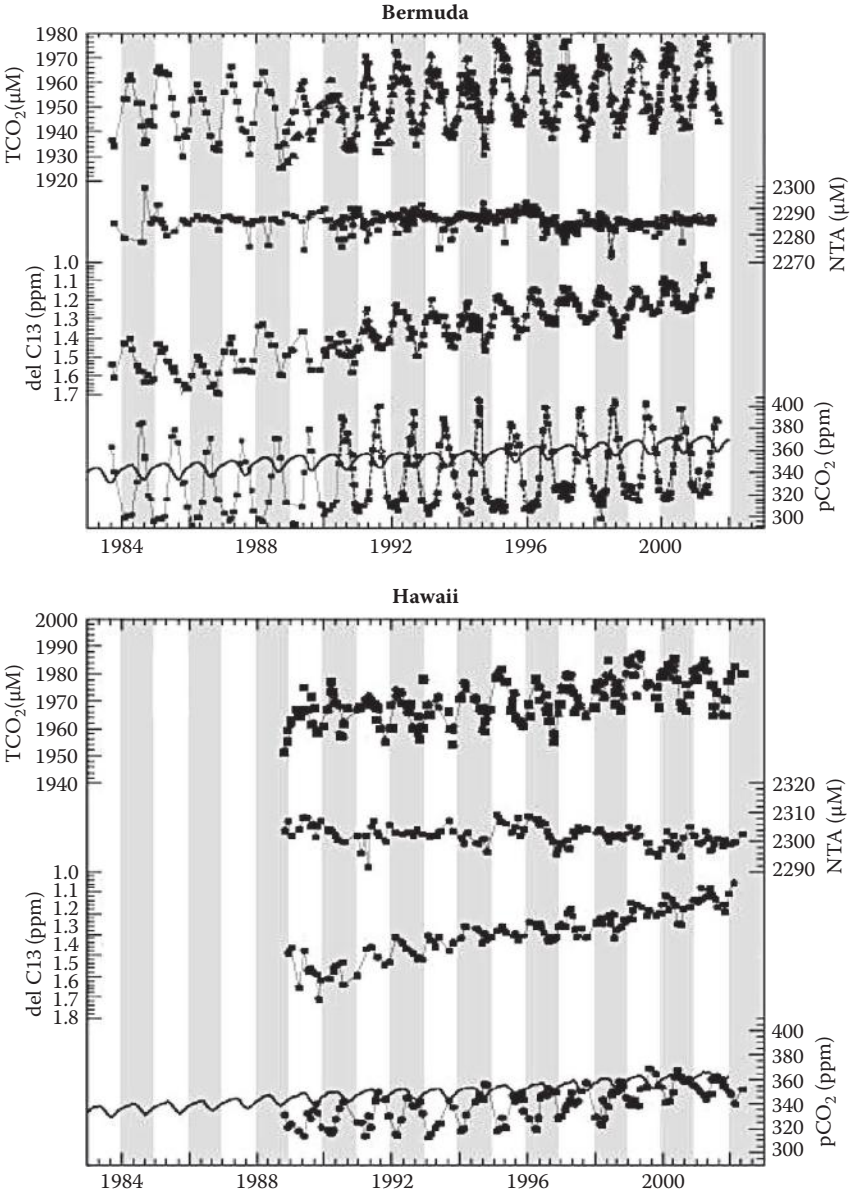

FIGURE 7.17
The variations of pCO_2, δC^{13}, TA, and TCO_2 at the Bermuda and Hawaii time series stations.

The pH increase in deep waters is due to the dissolution of $CaCO_3$. The pH of deep waters can be as low as 7.5 near 1000 m. In very deep waters, the pH can go through a maximum because of the effect of pressure on the ionization of carbonic acid. Park (1969) has used the Redfield et al. (1963) model to calculate the pH as a function of depth. He attributed the changes to two factors:

$$\Delta pH = \Delta pH(a) + \Delta pH(b) \tag{7.124}$$

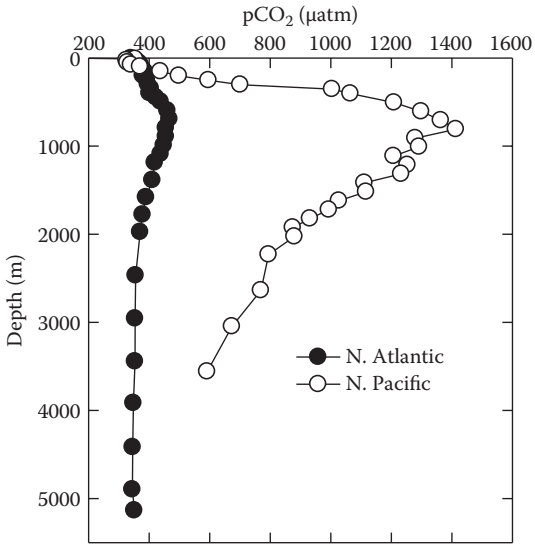

FIGURE 7.18
Depth profiles for the partial pressure of carbon dioxide in the Atlantic and Pacific Oceans.

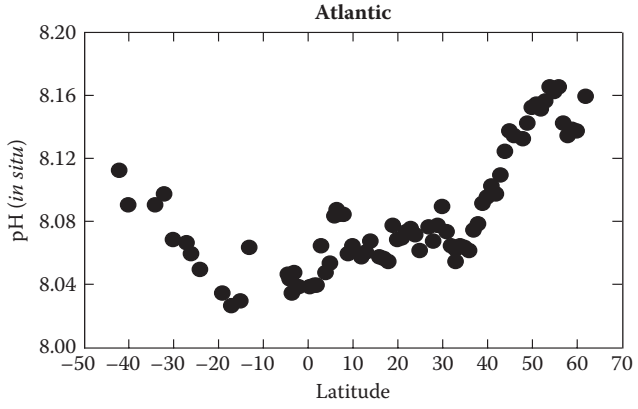

FIGURE 7.19
The pH of surface waters in the Atlantic Ocean.

where ΔpH(a) = –2.0 AOU, with the decrease caused by the oxidation of plant material, and ΔpH(b) = 2.4 ΔCa (where ΔCa is the change in Ca^{2+} caused by the dissolution of $CaCO_3$).

7.5.3 Total Alkalinity

The total alkalinity (TA) of surface and deep waters was measured extensively during the WOCE program and more recently as part of the CLIVAR studies. The surface values of temperature, salinity, and TA for surface waters in the Atlantic and Pacific Oceans are shown in Figure 7.22 and Figure 7.23, respectively. As is apparent from these figures, the TA of surface waters shows variations that are similar to salinity. This is shown more clearly when TA is plotted versus salinity for the North Atlantic (Figure 7.24). This linear behavior

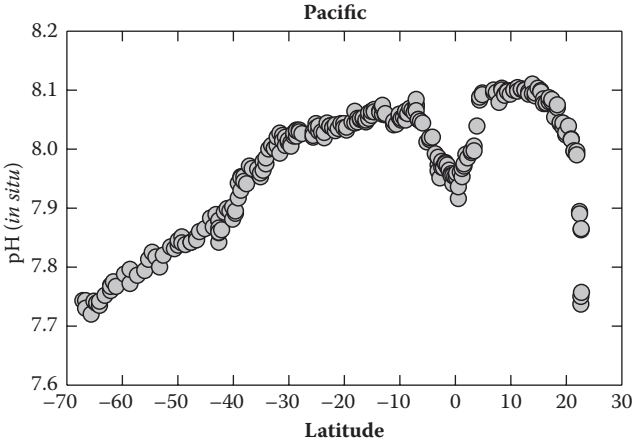

FIGURE 7.20
The pH of surface waters in the Pacific Ocean.

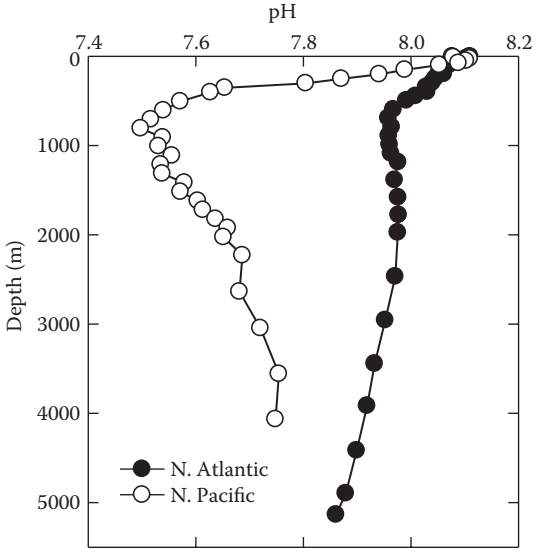

FIGURE 7.21
Depth profile of pH in the Atlantic and Pacific Oceans.

occurs because HCO_3^- is a major constituent of seawater and the ratio of HCO_3^- to salinity is nearly constant. The nonlinear behavior near salinity of 35 is due the upwelling of deep waters that have a higher TA because of the dissolution of $CaCO_3$. One can account for the changes in TA from changes in salinity by converting it to a constant salinity (S = 35). This is done by determining the normalized total alkalinity (NTA) given by NTA = TA × 35/S.

Values of NTA for open surface waters of the Atlantic and Pacific are all near 2300 μmol kg^{-1} (Figure 7.25). The values of NTA are higher in colder waters and nearly the same in the Atlantic and Pacific. This is related to the near-conservative behavior of HCO_3^- in seawater. The values are higher in polar waters (TA = 2380 μmol kg^{-1}). The higher values are related

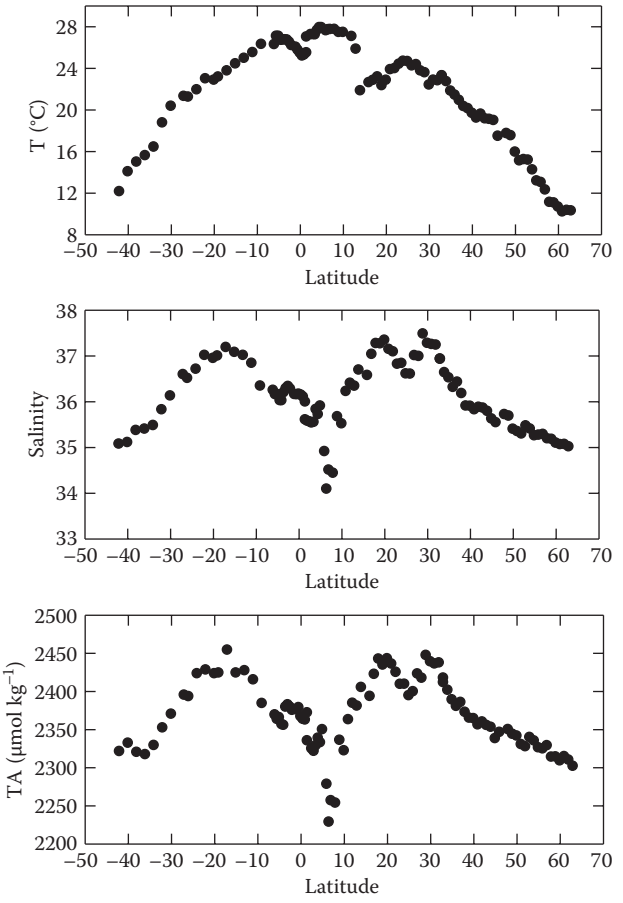

FIGURE 7.22
The temperature, salinity, and total alkalinity (TA) in the Atlantic Ocean.

to the upwelling of deep waters, which have higher NTA due to the dissolution of $CaCO_3$ shells (formanifera and pterpods).

Profiles of TA in the North Atlantic and North Pacific are shown in Figure 7.26. The surface values of TA in the Pacific are lower than in the Atlantic, while in the deep waters TA is lower in the Atlantic and higher in the Pacific. The surface differences are due to the higher salinities of the surface waters in the Atlantic caused by evaporation. If one normalizes the TA to a constant salinity (S = 35), the results are as expected (Figure 7.27). The surface values in both oceans are the same, and the NTA in deep waters is higher in the Pacific than in the Atlantic. The higher NTA in deep waters is related to the dissolution of $CaCO_3$. The deep Pacific alkalinity values are higher than those in the Atlantic because they are older and have accumulated more CO_3^{2-} from the dissolution of $CaCO_3$.

Sections of TA for the Atlantic and Pacific are not shown since they are similar to the salinity sections shown in the first chapter. Sections of TA in the major oceans are shown in Figure 7.28. The distribution of TA is very similar to the salinity distributions that follow the major water masses as shown for salinity in Chapter 1. The values of TA in deep waters increase from the North Atlantic (2330 μmol kg^{-1}) to the North Pacific (2430 μmol kg^{-1}) because of the dissolution of $CaCO_3$ in the waters.

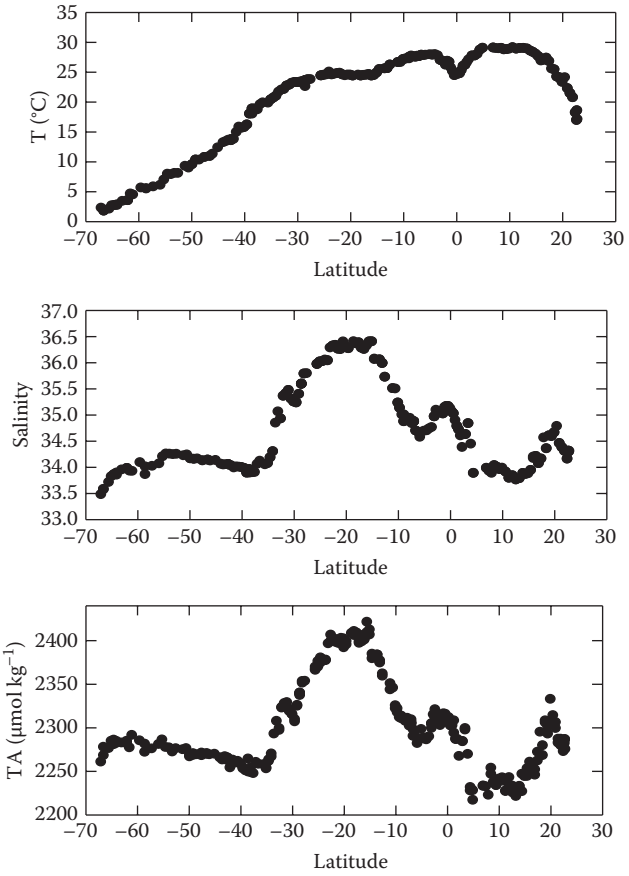

FIGURE 7.23
The temperature, salinity, and total alkalinity (TA) in the Pacific Ocean.

7.5.4 Total CO_2

The total dissolved inorganic carbon dioxide in the Atlantic and Pacific surface waters is shown in Figure 7.29. As with TA, the effect of salinity on TCO_2 can be corrected by normalizing the results to a constant salinity (normalized total CO_2 [$NTCO_2$] = $TCO_2 \times 35/S$). The values of $NTCO_2$ for the surface waters of the Atlantic and Pacific are shown in Figure 7.30. Unlike alkalinity, the TCO_2 in the equatorial waters shows a large increase. This is due to equatorial upwelling. The TCO_2 shows little latitudinal change. For rapid exchange, the pCO_2 in the water and air are similar, and the TCO_2 is higher in polar regions.

The depth profiles of TCO_2 in the Atlantic and Pacific are shown in Figure 7.31. The offset in surface waters is due to differences in the salinity. If the values of TCO_2 are normalized (Figure 7.32), the surface values are about 2.05 mmol kg^{-1} in both oceans. The values decrease to a minimum in surface waters because of photosynthesis. In deeper waters, the TCO_2 increases because of the oxidation of plant material. The TCO_2 values for deep Pacific waters are higher than those for the Atlantic because the waters are older and have had more time to accumulate CO_2 because of microbial oxidation.

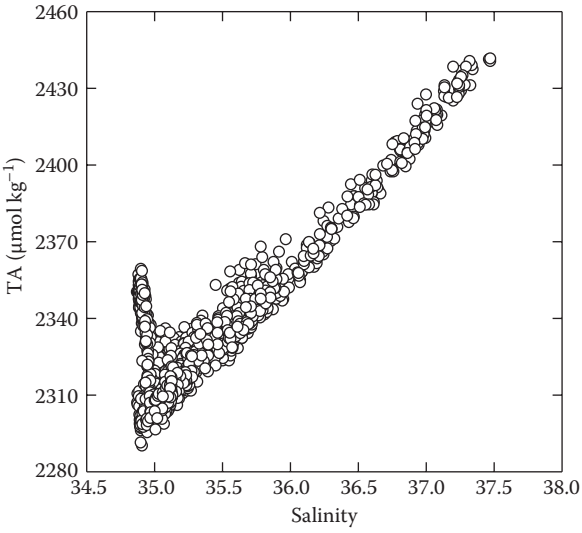

FIGURE 7.24
The total alkalinity as a function of salinity for surface waters in the Atlantic Ocean.

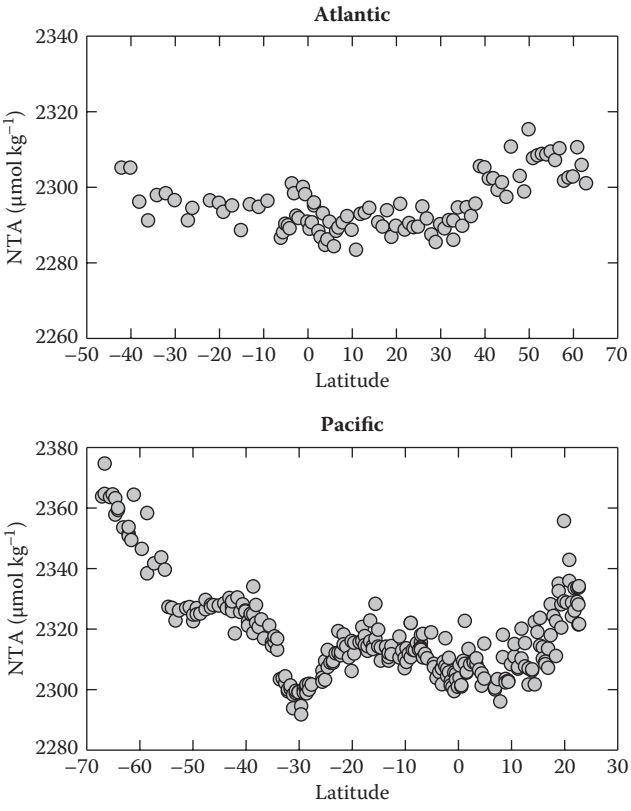

FIGURE 7.25
The normalized total alkalinity (NTA) in the Atlantic and Pacific Oceans.

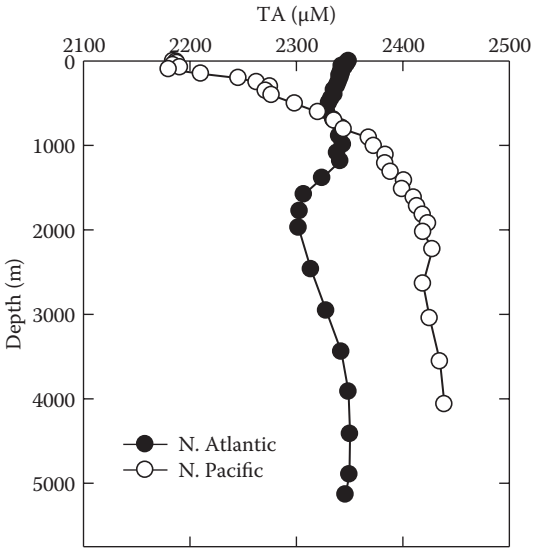

FIGURE 7.26
The total alkalinity (TA) as a function of depth in the Atlantic and Pacific Oceans.

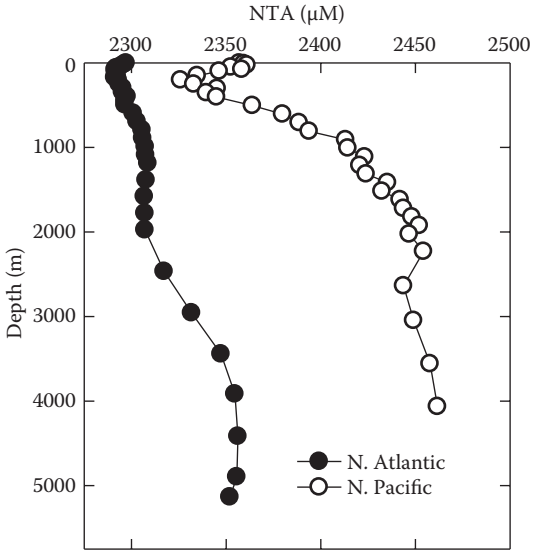

FIGURE 7.27
The normalized total alkalinity (NTA) as a function of depth in the Atlantic and Pacific Oceans.

The values in the deep waters increase from the North Atlantic (2180 μmol kg^{-1}) to the North Pacific (2380 μmol kg^{-1}) because of the oxidation of organic carbon and dissolution of $CaCO_3$. The values of TCO_2 and TA correlate very well with each other and can be used to characterize various water masses (see Figure 7.33).

Due to the buffering effect of seawater, only a small amount of CO_2 needs to be transferred to the oceans to restore the equilibrium between the atmosphere and surface. This buffering is called the Revelle factor (R). It is the ratio of the fractional change in the partial pressure of

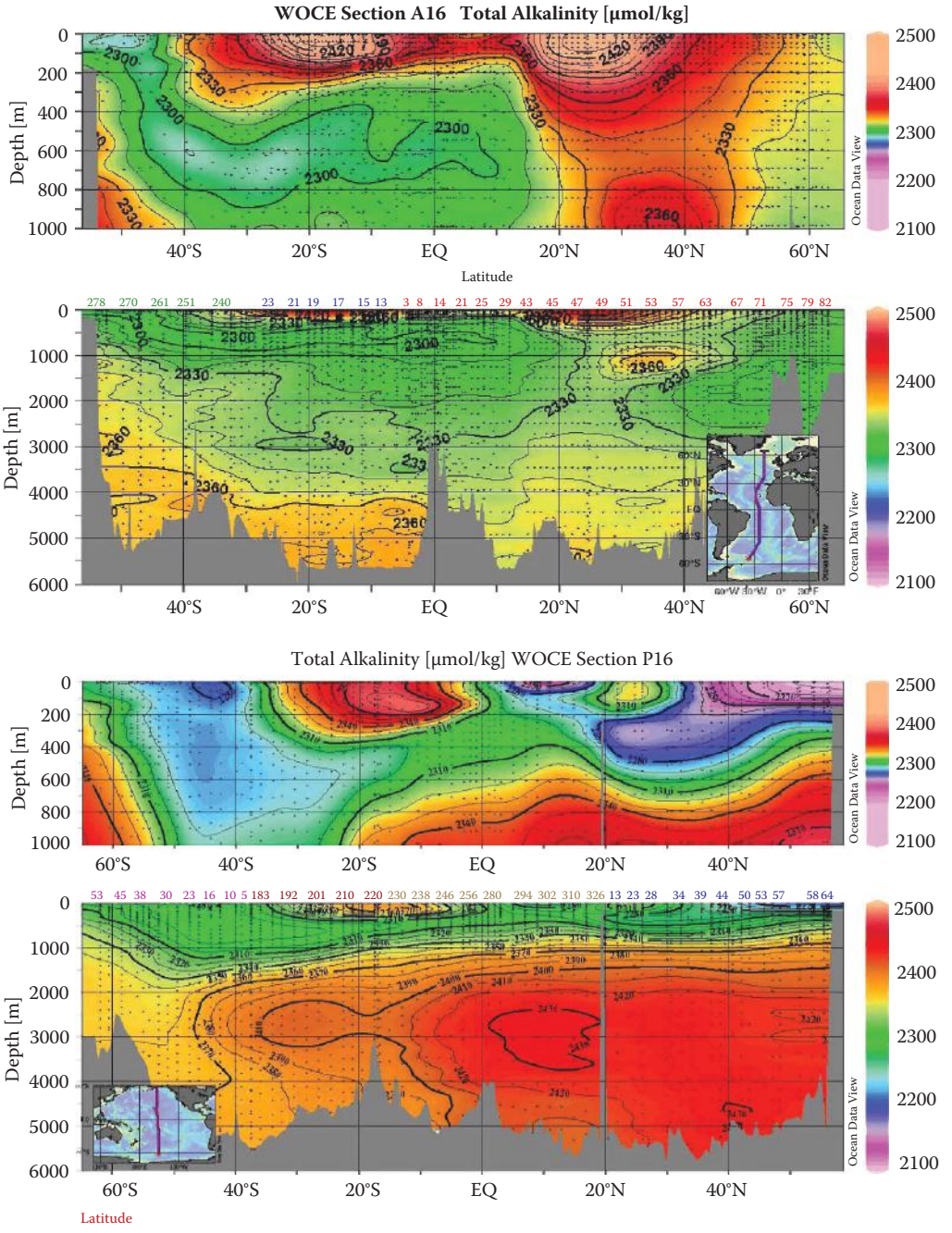

FIGURE 7.28
Sections of TA in the Atlantic and Pacific Oceans.

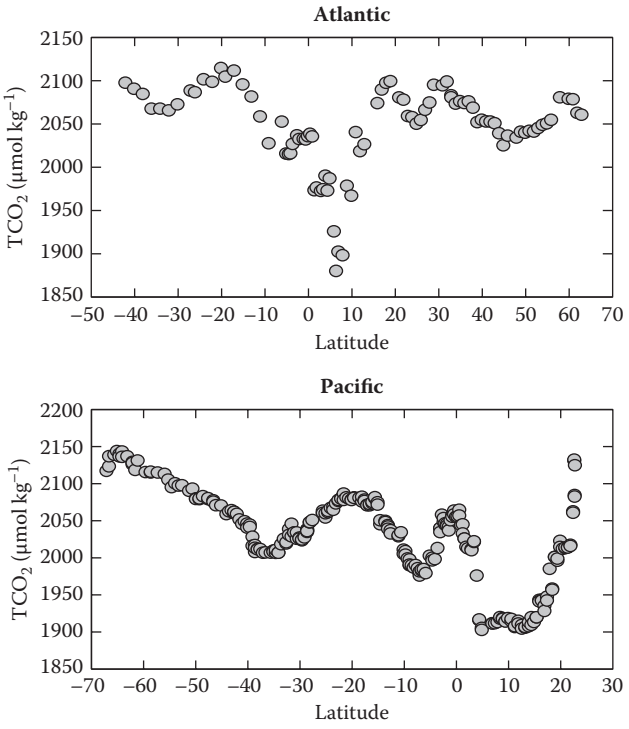

FIGURE 7.29
Surface values of the total carbon dioxide (TCO_2) in the Atlantic and Pacific Oceans.

carbon dioxide in the atmosphere to the fractional increase of the total carbon dioxide in the ocean. The increase in the TCO_2 near the equator is related to the Revelle factor:

$$R = (\Delta pCO_2/pCO_2)/(\Delta TCO_2/TCO_2) \tag{7.125}$$

This value is about 14 for cold waters and 8 for warmer waters (the average is about 10). Thus, a 10% change in pCO_2 results in only a 1% change in TCO_2. This factor is important when considering the effect that increases of CO_2 in the atmosphere have on the carbonate system.

Sections of TCO_2 in the Atlantic and Pacific are shown in Figure 7.34. The values in the deep waters increase from the North Atlantic (2180 μmol kg^{-1}) to the North Pacific (2380 μmol kg^{-1}) because of the oxidation of organic carbon and dissolution of $CaCO_3$.

7.6 $CaCO_3$ Dissolution in Seawater

The precipitation or formation of solid $CaCO_3$ in surface seawaters and the dissolution of solid $CaCO_3$ in deep waters is very important in transferring CO_2 from surface waters to deep waters. $CaCO_3$(s) is also present in pelagic sediments of the world oceans (see Figure 7.35).

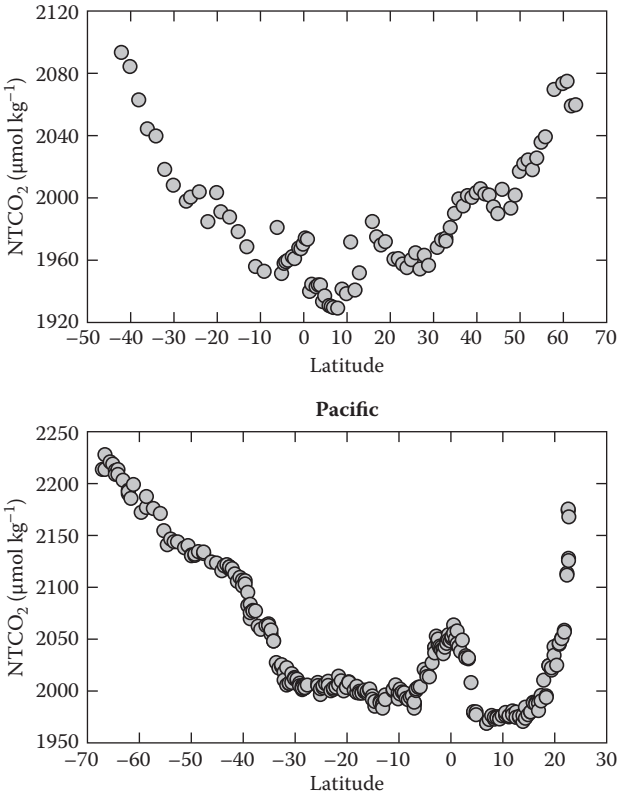

FIGURE 7.30
Normalized total carbon dioxide ($NTCO_2$) in the Atlantic and Pacific Oceans.

The saturation state of seawater with respect to $CaCO_3$ is determined from

$$\Omega = [Ca^{2+}][CO_3^{2-}]/Ksp^* \tag{7.126}$$

where $[Ca^{2+}][CO_3^{2-}]$ is the ion product of the concentration of Ca^{2+} and CO_3^{2-} and Ksp* is the solubility product at the in situ conditions of S, t, and P. Since Ca^{2+} is a major constituent of seawater (within 1%), its concentration (mol kg^{-1}) can be estimated from

$$[Ca^{2+}] = 2.934 \times 10^{-4}\ S \tag{7.127}$$

The solubility product for calcite formed by foramanifera and aragonite formed by pteropods can be determined from Equation 7.72 to Equation 7.80. The values of $[CO_3^{2-}]$ can be determined from the measured carbonate parameters (pH and TA or TA and TCO_2).

Profiles of Ω for calcite and aragonite for Atlantic and Pacific waters are shown in Figure 7.36 and Figure 7.37, respectively. The surface values of Ω for calcite are near 5.0 and decrease below 1.0 in deep water. The surface value of Ω for aragonite is 3.0. Aragonite is 1.5 times more soluble than calcite at a given S, t, and P. The waters of the Pacific become undersaturated ($\Omega < 1.0$) at shallower depths than those of the Atlantic.

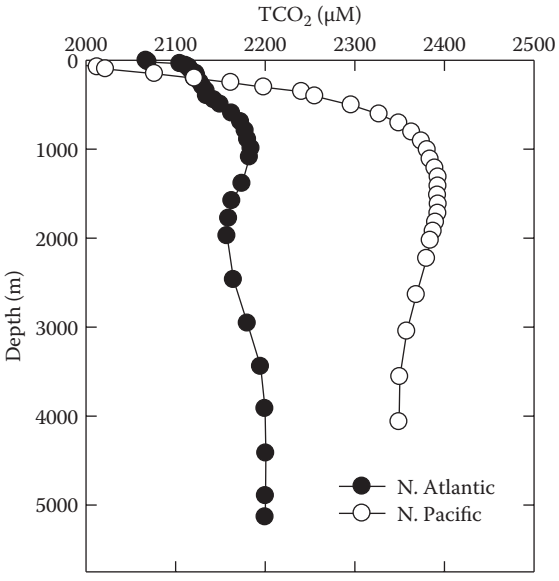

FIGURE 7.31
Depth profile of the total carbon dioxide (TCO_2) in the Atlantic and Pacific Oceans.

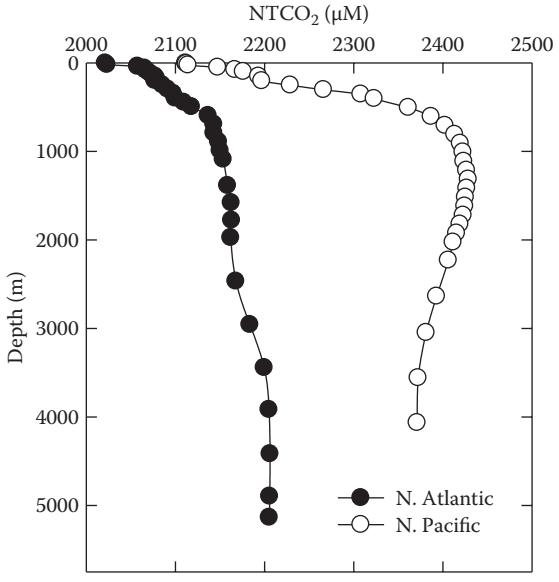

FIGURE 7.32
Depth profile of normalized total carbon dioxide ($NTCO_2$) in the Atlantic and Pacific Oceans.

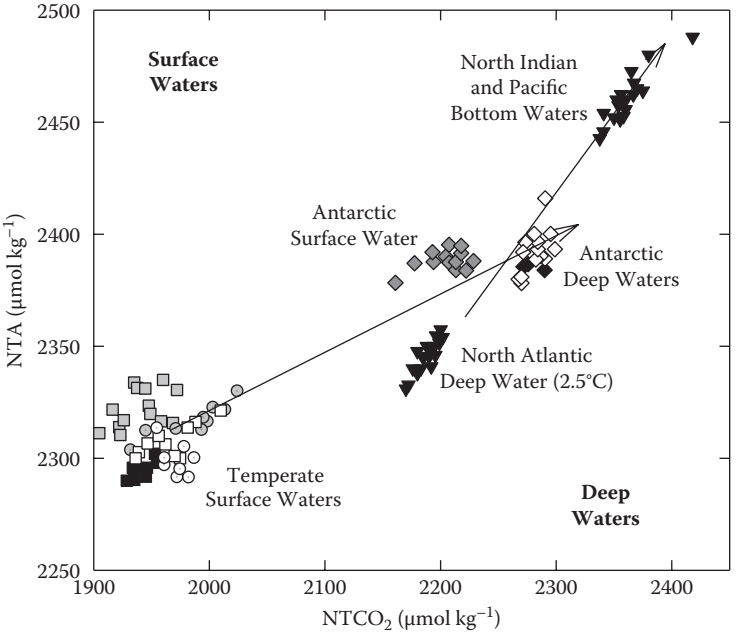

FIGURE 7.33
Values of the normalized total alkalinity and total carbon dioxide in various water masses.

Approximate saturation levels in North Atlantic and North Pacific waters are as follows:

	North Atlantic	North Pacific
Calcite	4300 m	750 m
Aragonite	1500 m	500 m

The greater solubility of these minerals in deep waters is related to the effect of pressure on the solubility of $CaCO_3$(s). Since two divalent ions are formed during the dissolution, the volume change is large and negative because of electrostriction. The Pacific deep waters become undersaturated at shallower depths because of the lower pH or higher CO_2 formed by the oxidation of plant material. This decreases the concentration of CO_3^{2-} caused by the shift in the equilibrium:

$$CO_3^{2-} + H^+ \rightarrow HCO_3^- \tag{7.128}$$

The differences in Ω in the two oceans become smaller in the deep oceans because of the effect of pressure controlling solubility. Although much of the deep oceans is undersaturated with respect to $CaCO_3$(s), large amounts of calcite are present in ocean sediments. Geologists call the layer where $CaCO_3$(s) is above 5% of the sediments the calcium carbonate compensation depth (CCD). As shown in Figure 7.38, the $CaCO_3$ compensation depth in the Atlantic is about 2 km below the saturation depth. These results indicate that the solubility of $CaCO_3$(s) in seawater is not controlled by equilibrium but by kinetic constraints.

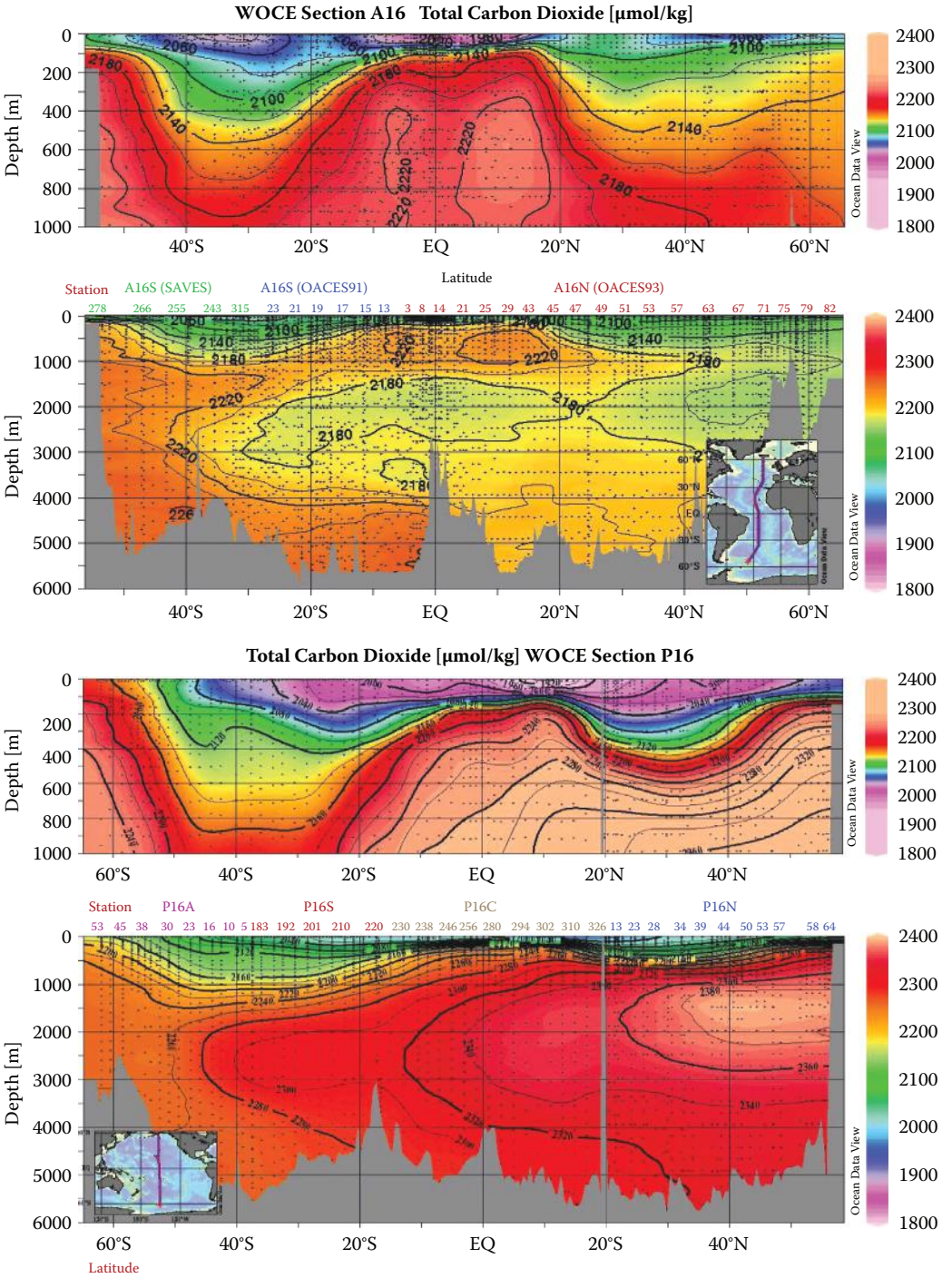

FIGURE 7.34
Sections of TCO_2 in the Atlantic and Pacific.

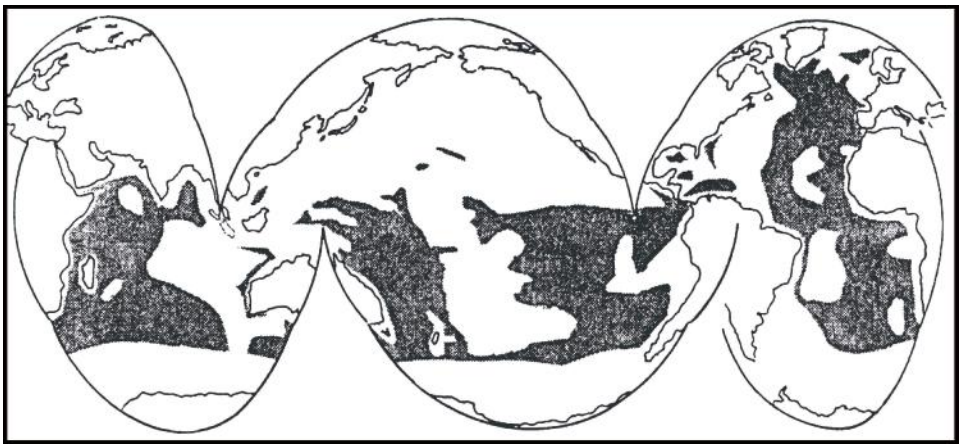

FIGURE 7.35
The areas of the oceans with sediments of calcium carbonate.

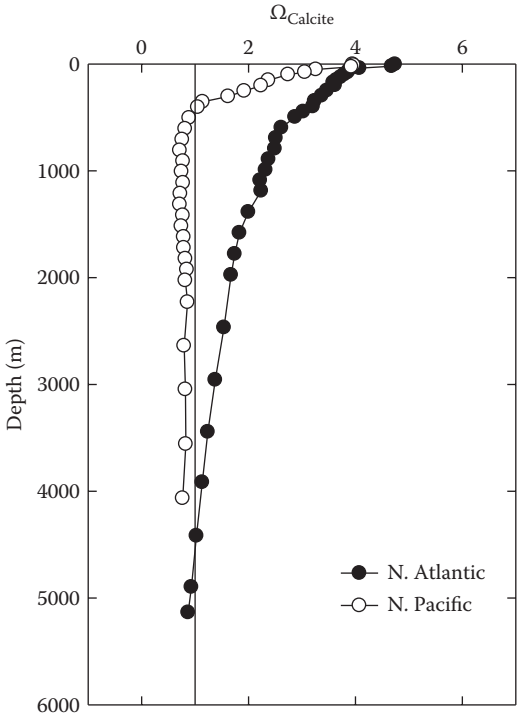

FIGURE 7.36
The depth profile of the calcite saturation state for the Atlantic and Pacific Oceans.

The first direct measurements to examine the rates of dissolution of $CaCO_3$(s) in the oceans were made by Peterson (1966). He suspended calcite spheres in the Pacific on deep-sea moorings for 250 days. His results are shown in Figure 7.39. At a depth of about 4000 m, the solution rate dramatically increased. This depth of rapid increase in the rate of dissolution is called the lysocline. Honjo (1975) suspended a number of $CaCO_3$ solids for 79 days

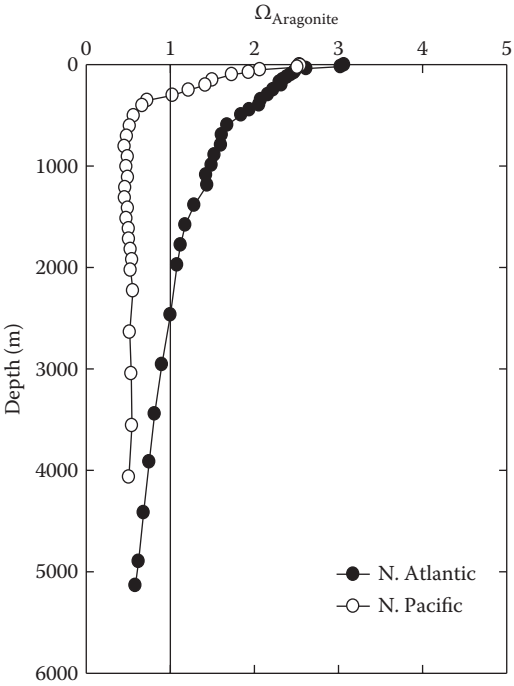

FIGURE 7.37
The depth profile of the aragonite saturation state for the Atlantic and Pacific Oceans.

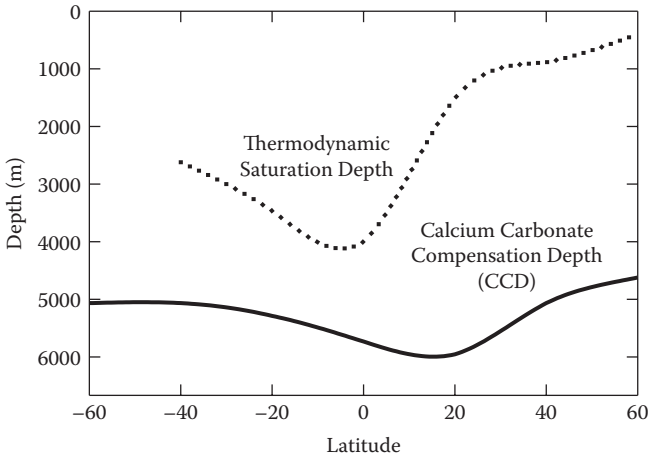

FIGURE 7.38
Comparisons of the thermodynamic saturation state Ω and calcium carbonate compensation depths (CCDs) in the Atlantic Ocean.

(coccoliths, foram shells, reagent calcite, and pteropod shells) in chambers through which seawater was drawn (Figure 7.39). The aragonite lysocline was found to be higher than the value for calcite in the water column. The depth of the lysocline found by suspending $CaCO_3$(s) agrees very well with the decrease in the mineral found in surface sediments at various depths in the same area (Figure 7.40). These results indicate that the lysocline

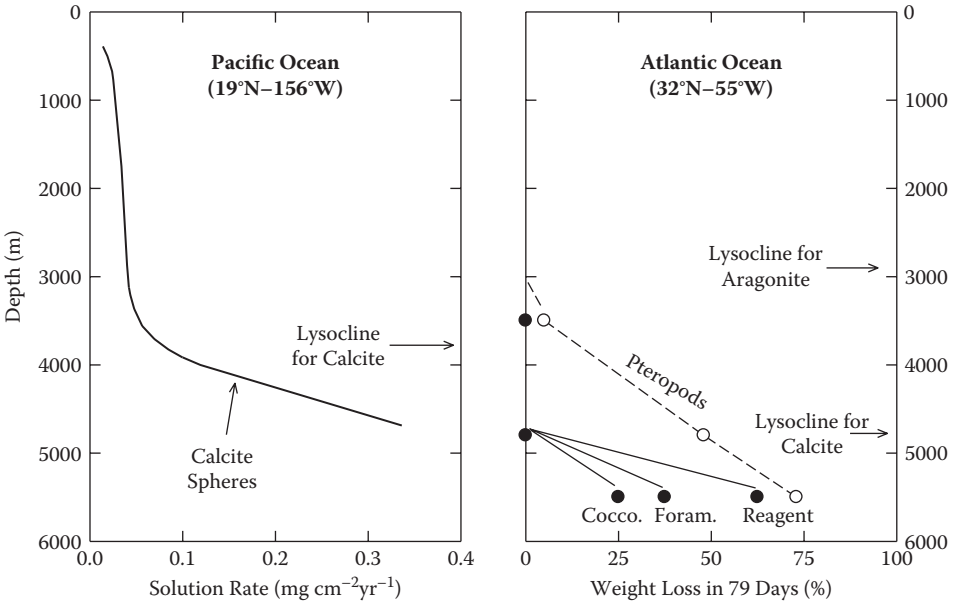

FIGURE 7.39
Depth profiles for the rates of solution of calcium carbonate in the Atlantic and Pacific Oceans.

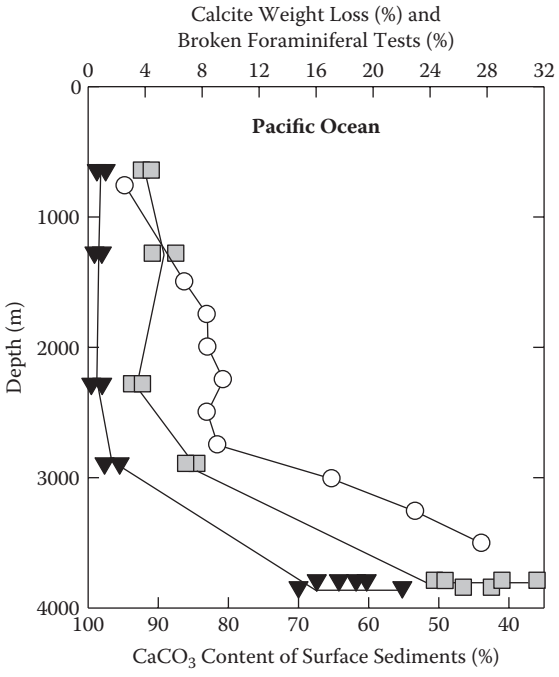

FIGURE 7.40
Depth profiles of the calcite loss and surface sediment concentration of $CaCO_3$ in the Pacific Ocean.

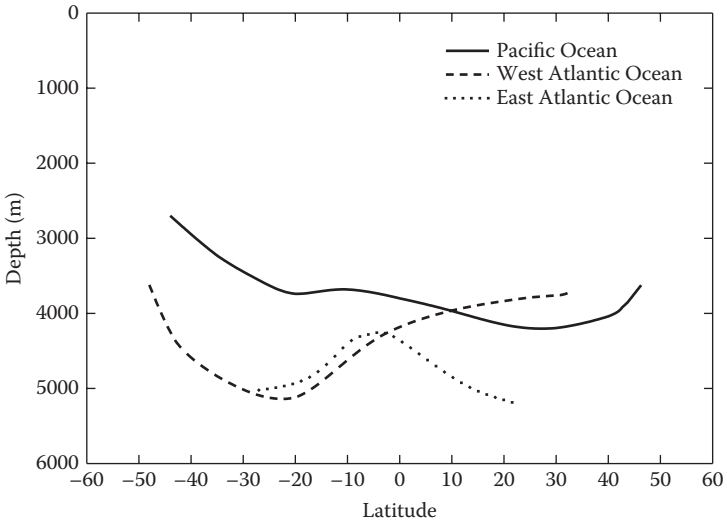

FIGURE 7.41
Depths of the lysocline in various oceans.

and $CaCO_3$ compensation depth in sediments are frequently at the same depth. Thus, the causes of the compensation depth being deeper than the saturation depth are the variable rates of dissolution of various forms of $CaCO_3$. If the sedimentation rates are high, it is possible that $CaCO_3$(s) could be preserved before it dissolves. This would cause the calcium CCD to be below the lysocline.

Values of the lysocline in the Atlantic and Pacific are shown in Figure 7.41. The lysocline is higher in the Pacific because of the greater undersaturation at lower depths. A comparison of the saturation horizon with the lysocline and calcium CCDs is shown in Figure 7.42. The values of the lysocline and the CCD are not affected by the saturation states. The CCD is close to the lysocline except in the equatorial region. This is due to the higher productivity of these waters. The higher the supply rate of $CaCO_3$(s), the deeper the CCD will be (see Figure 7.43).

Morse (1983) attempted to understand the causes of these increases in rates using laboratory studies. He has shown that when the saturation of waters gets to a critical value, $CaCO_3$(s) starts to dissolve. This critical value is about 30% undersaturation, or at $\Delta CO_3^{2-} - CO_3^{2-}(\text{sat}) = -10$ µmol kg^{-1} (i.e., the solution could absorb another 10 µmol kg^{-1} of $CaCO_3$). Broecker and Peng (1982) showed this critical $\Delta CaCO_3$ by the percentage of $CaCO_3$(s) in sediment core tops (see Figure 7.44). This so-called critical value is strongly dependent on the value selected for the solubility product of the $CaCO_3$(s). More recent studies by Byrne (University of South Florida) have concentrated on measuring solubility dissolution rates using minerals and waters collected in the oceans. He and his coworkers have found that the rates of dissolution of aragonitic $CaCO_3$(s) measured at sea can be described by

$$R = 130\ \{1 - [Ca^{2+}][CO_3^{2-}]/1.78\ K_{SP}(\text{cal})\}^{3.1} \tag{7.129}$$

where Ksp (aragonite) = 1.78 Ksp (calcite). The factor of $\rho = 1.78$ is slightly higher than the theoretical value of 1.5. This is related to the changes in Ksp (aragonite) and Ω_A for aragonite solubility as a function of time (see Figure 7.45).

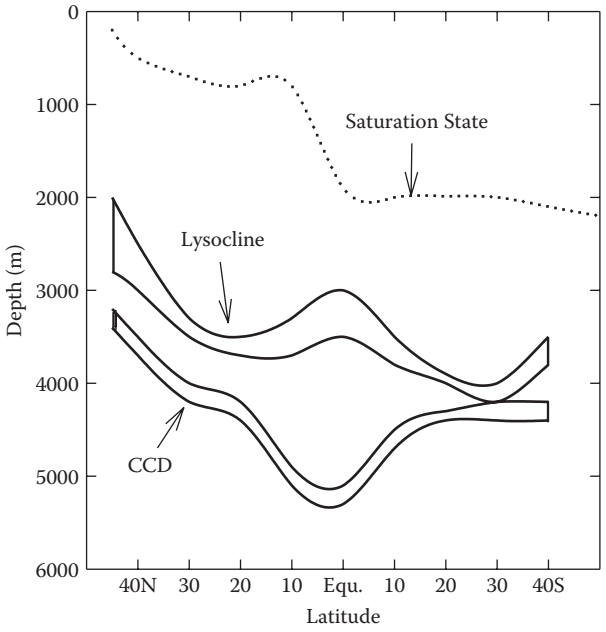

FIGURE 7.42
Comparisons of the saturation level, the carbonate compensation depth (CCD), and the lysocline at various latitudes.

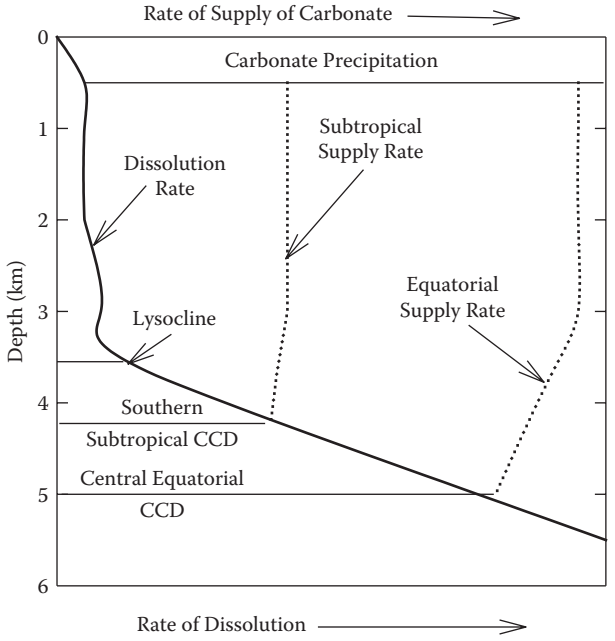

FIGURE 7.43
Depth profile of the dissolution rate and the rate of supply of carbonate to the oceans.

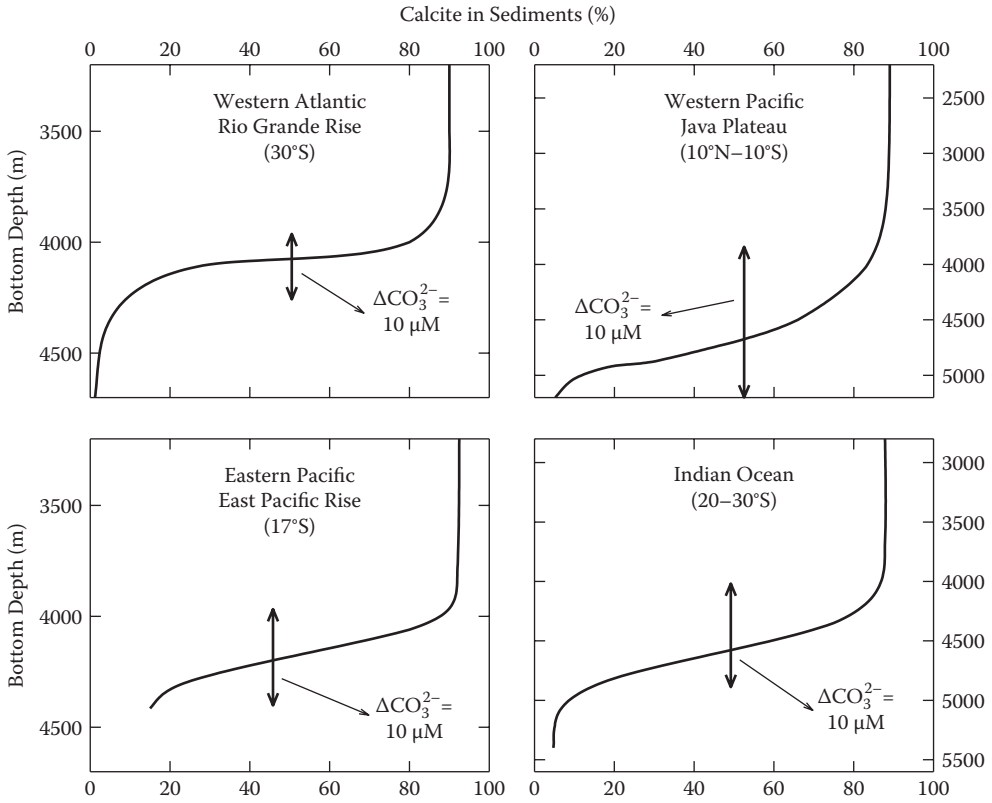

FIGURE 7.44
Calcium carbonate concentrations in the sediments of various oceans.

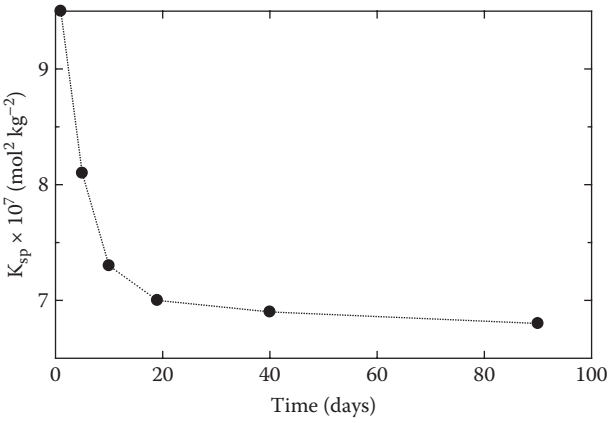

FIGURE 7.45
Values of the solubility product for aragonite in waters as a function of the equilibration times.

The dissolution rates in the laboratory studies of Morse (1983) and coworkers resulted in two equations. For $\Omega_A \leq 0.44$,

$$R(\%\text{ per day}) = 110(1 - \Omega)^{2.39} \tag{7.130}$$

and for $\Omega_A \leq 0.44$,

$$R(\%\text{ per day}) = 1318(1 - \Omega)^{7.27} \tag{7.131}$$

Although the equations are different, the calculated rates are in reasonable agreement. Since aragonite production appears to be high in the surface waters of the Pacific, and the deeper waters are undersaturated, the transport of the aragonite and dissolution could result in transporting carbon to deep waters. Betzer and coworkers (1984) have estimated that 90% of this aragonite flux would be dissolved in the upper 2.2 km of the water column. The values of aragonite precipitation of waters precipitating on the Bahamas Banks are quite similar to those shown in Figure 7.45 (Morse et al., 2010). The higher solubility in the beginning is thought to be high magnesium calcite that slowly precipitates to aragonite with time. Recent work has shown that fish produce a high magnesium calcite from drinking seawater (Wilson et al., 2009). The solubility of this high magnesium calcite like the material in the Bahamas is twice that of aragonite (Woosley, Millero, and Grosell, 2012). Much of the fish-produced high magnesium calcite is soluble enough to dissolve above the saturation horizon for aragonite.

Feely et al. (2004) examined the saturation state of calcite and aragonite in ocean waters and the rates of dissolution of $CaCO_3$ in the oceans. They determined the aragonite and calcite saturation states in the major oceans using the new carbonate data determined over the 10 yr on the WOCE cruises. These results are shown in Figure 7.46. The values ranged from 3000 and 4500 m in the North Atlantic to 500 and 700 m in the North Pacific, respectively, for aragonite and calcite. The effects of the anthropogenic CO_2 on the saturation levels are shown in Figure 7.47. The added CO_2 to the oceans has decreased the saturation levels by as much as 500 m. As will be discussed further, over the next 200 yr the surface waters of the oceans may be undersaturated with respect to aragonite. Feely et al. (2004) also determined the rates of dissolution of aragonite and calcite in the oceans. They determined the amount of $CaCO_3$ dissolved from the equation

$$\Delta CaCO_3 = 0.5[TA_{Meas} - TA^0] + 0.63(0.0941\ AOU) \tag{7.132}$$

The value of TA^0 is the preformed value of TA at the surface, and the last term corrects for changes in TA caused by the oxidation of plant material. By dating the waters using chlorofluorocarbons (CFCs) or ^{14}C, Feely et al. were able to estimate the rates of dissolution of $CaCO_3$ along constant density surfaces. The dissolution rates they found are presented in Table 7.9. The maximum values ranged from 0.5 μmol kg^{-1} yr^{-1} in the Atlantic to 1.2 μmol kg^{-1} yr^{-1} in the Pacific. Most of the dissolution occurred near the aragonite saturation. This is above the lysocline level and indicates that the dissolution may be occurring in microorganisms or particulate flocs of low pH or that the mineral may be high-magnesium calcite that is two times more soluble than aragonite. More work is needed to clarify these issues. The results indicate that about 50 to 70% of the calcium carbonate made in surface waters (0.8 to 1.4 Pg $CaCO_3$ yr^{-1}) is dissolved in the upper water column. More recently, Friis et al. (2006, 2007) suggested that the higher values of $TA - TA^0$ are due to ocean mixing. They also indicated that the normalization of TA should be relative to the extrapolated value when S = 0. I find it hard to believe that this is the case.

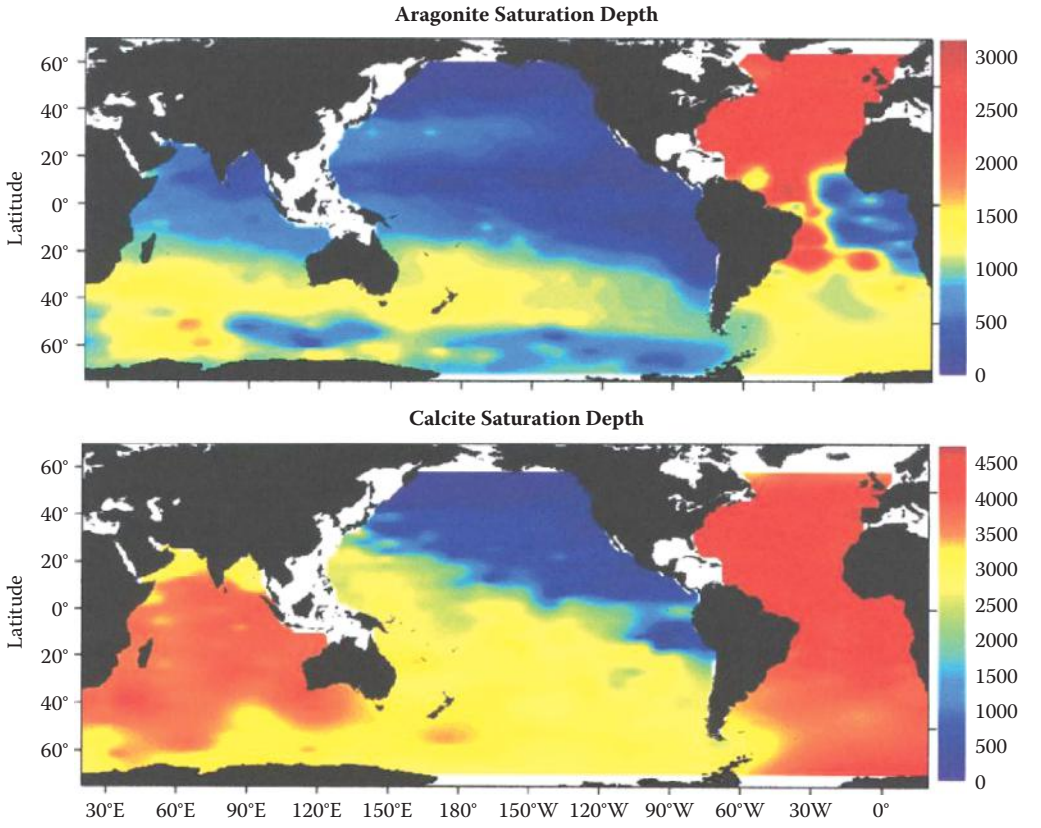

FIGURE 7.46
The saturation levels (Ω = 1.0) for aragonite and calcite in the oceans. (From Feely, R.A., Sabine, C.L., Lee, K., Berelson, W., Kleypas, J., Fabry, V.J., and Millero, F.J., *Science*, 305, 362, 2004. With permission.)

7.7 Fossil Fuel CO_2 Input to the Oceans

The input of fossil fuels into the oceans has been estimated by a number of methods. A summary of some of these estimates is given in Table 7.10:

1. Penetration of ^{13}C into the oceans (see Figure 7.4; Quay, Tilbrook, and Wong, 1992)
2. Penetration of CFCs into the oceans (McNeil et al., 2003)
3. Changes of pCO_2 in surface waters (Takahashi et al., 2002)
4. Correlations of O_2/CO_2 in the atmosphere (Battle et al., 2000)
5. Modeling (Xu et al., 2000)
6. Using measurements of TCO_2 as a function of time (Wallace, 2001)
7. Using measurements of TCO_2 and correcting for the amount added as a result of the oxidation of organic carbon and dissolution of $CaCO_3$ (Brewer, 1978; Chen and Millero, 1979; Gruber et al., 1996)

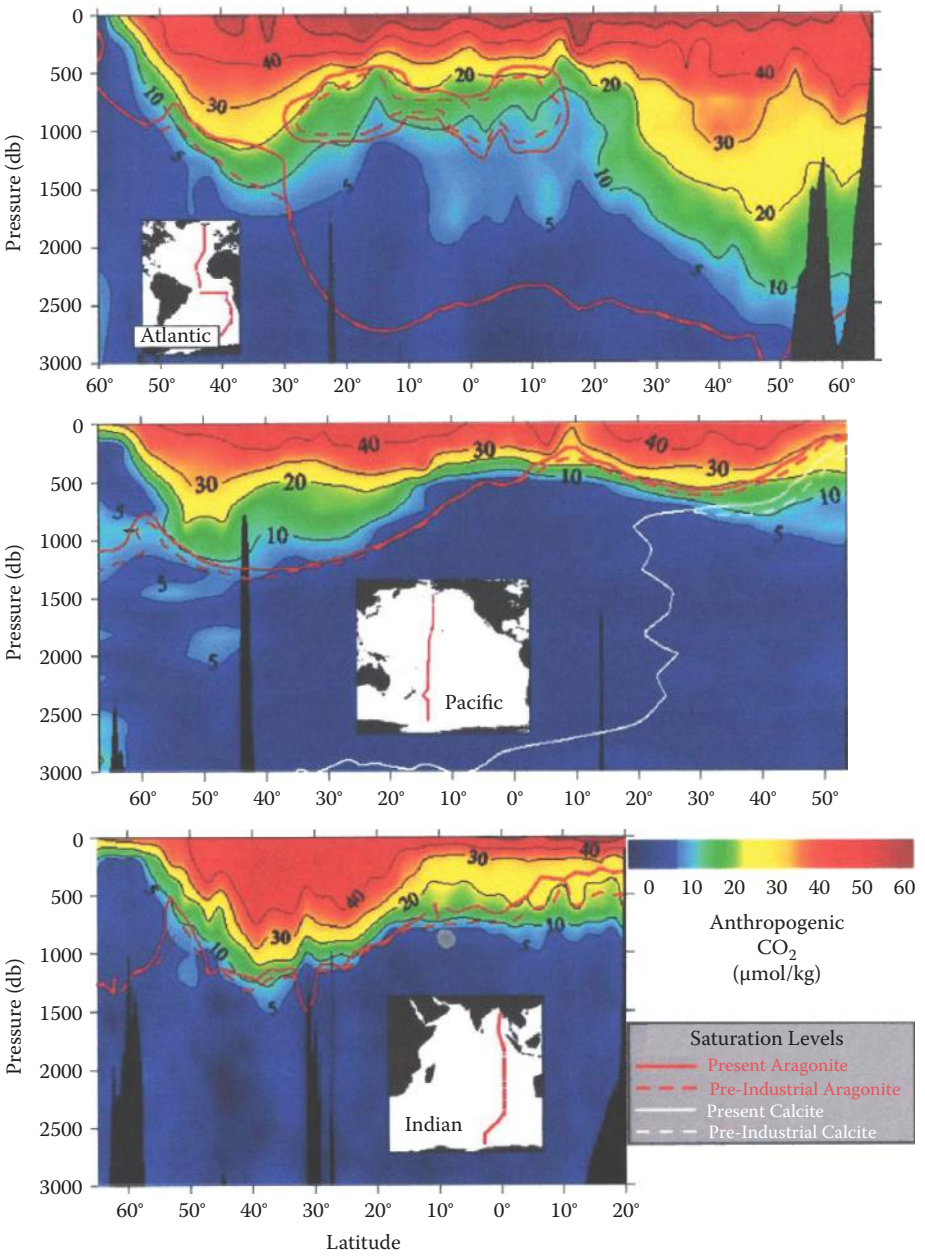

FIGURE 7.47
Effect of fossil fuel CO_2 on the saturation levels in the oceans. (From Feely, R.A., Sabine, C.L., Lee, K., Berelson, W., Kleypas, J., Fabry, V.J., and Millero, F.J., *Science*, 305, 362, 2004. With permission.)

TABLE 7.9

Maximum Dissolution Rates of $CaCO_3$ in the Oceans

Location	Depth (m)	Dissolution Rate ($\mu mol\ kg^{-1}\ yr^{-1}$)
North Atlantic	250–1000	0.40
South Atlantic	900	0.55
	250	0.22
North Indian	250	0.75
South Indian	750	1.2
North Pacific	500	1.2
South Pacific	1000	0.75

Source: Data from Feely, R.A., Sabine, C.L., Lee, K., Berelson, W., Kleypas, J., Fabry, V.J., and Millero, F.J., *Science*, 305, 362 (2004).

TABLE 7.10

Estimates of Ocean Uptake

Method	pgC/yr
^{13}C (1970–1990)	2.1 ± 0.8
^{13}C (1985–1995)	1.5 ± 0.8
Surface pCO_2 (1985)	2.8 ± 1.5
Inventory (1990)	1.6–2.7
Inventory (1990–2000)	1.9 ± 0.4

I discuss briefly the last two methods of determining the input of CO_2 into the oceans. The time series method simply examines the change in TCO_2 over a given time period.

$$\Delta(TCO_2)_{Anth} = [TCO_2(t = 1970) - TCO_2(t = 1990)]/20 \tag{7.133}$$

Direct measurements from 1990 can be compared to calculated values from a fit of the 1970 results to an empirical equation of the form

$$TCO_2\ (t = 1970) = a_0 + a_1\ S + a_2\ \Theta + a_3\ TA + a_4\ O_2 \tag{7.134}$$

where a_0 and so on are adjusted parameters. This method requires reliable measurements as a function of time. Unfortunately, the 1970 GEOSEC CO_2 data are not very accurate compared to the more recent WOCE results. This method, however, may be easier to do in the future.

The second method determined the TCO_2 entering the oceans using an equation of the form (Brewer, 1978; Chen and Millero, 1979)

$$\Delta(TCO_2)_{Anth} = (TCO_2)_{Meas} - \Delta(TCO_2)_{CaCO_3} - \Delta(TCO_2)_{Organic} \tag{7.135}$$

This method has been improved by Gruber et al. (1996) using

$$\Delta C^* = C_{Meas} - C_{Biol} - C_{280} \tag{7.136}$$

where C_{Biol} also corrects for the measured CO_2 from dissolution of $CaCO_3$ and oxidation of organic carbon. The change is compared to the preindustrial values of carbon (C_{280})

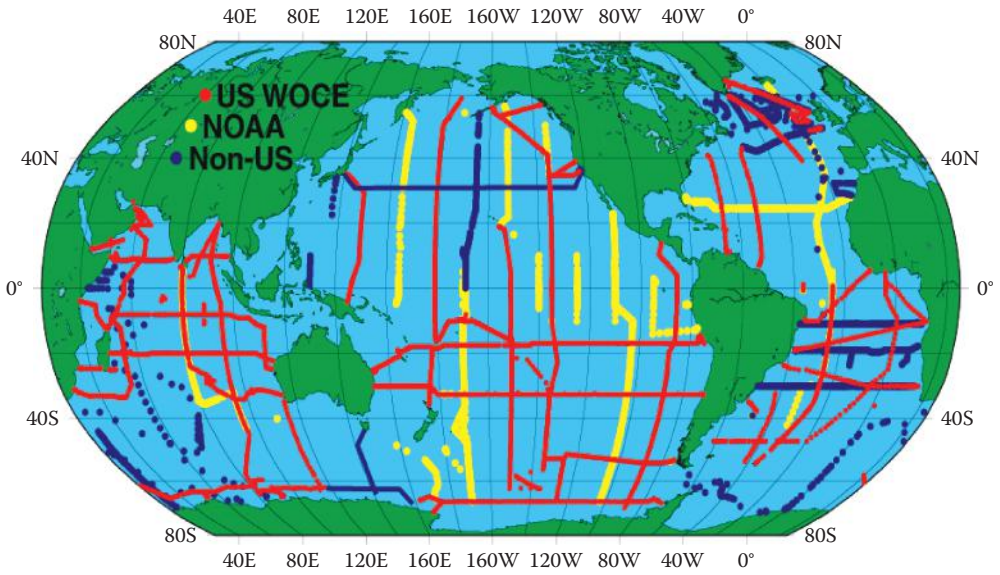

FIGURE 7.48
The cruise tracks occupied during the WOCE cruises. NOAA, National Oceanic and Atmospheric Administration.

calculated at pCO_2 = 280 µatm and the preformed TA (TA^0) in surface waters in 1800. The calculation of ΔC^* in surface waters is corrected for changes since leaving the surface and for the mixing of various water masses.

All of the CO_2 measurements made on the WOCE cruises (Figure 7.48) have been synthesized into a global database (http://cdiac.esd.ornl.gov). These results have led to reliable TA and TCO_2 values for all the major oceans and have been used to determine the input of fossil fuel into the world oceans (Sabine et al., 2004). The inventory of anthropogenic CO_2 into the oceans is shown in Figure 7.49. Most of the stored fossil fuel CO_2 is in the North Atlantic where deep water formation occurs. The penetration of fossil fuel CO_2 is shown in Figure 7.50. Except for the North Atlantic, the signal does not penetrate below 1500 m in the central gyres of the oceans. A summary of the anthropogenic budget for the various oceans compared to some model results is given in Table 7.11. The amounts stored in the Atlantic and Pacific Oceans are 71% of the total. The magnitudes in the Atlantic and Pacific are similar even though the volume of the Pacific is four times larger than the Atlantic. The calculated values for the major oceans are in reasonable agreement with estimates from models. A summary of the anthropogenic budget is given in Table 7.12**.** The oceans have taken up 48% of the anthropogenic CO_2 over the past 200 yr. In recent years, the rate of uptake has been 1.9 ± 0.4 Ptg/yr. Over the past 200 yr, the land has been a source of CO_2 to the atmosphere (39 Ptg), while in recent years it has become a sink (–15 Ptg). This uptake of CO_2 by terrestrial plants may be related to the regrowth of trees in North America. We are not certain if this trend will continue in the future.

At the present time, most CO_2 studies are part of the CLIVAR program. The cruise tracts in the world oceans presently being studied are shown in Figure 7.50. A number of countries are participating in the program. The recent studies by Sabine et al. (2008) demonstrate how the repeat measurements can be used to examine the changes of CO_2 over time. The study examines the change in two cruise tracts (P2, east-west and P16, north-south) in the Pacific Ocean (Figure 7.51). The TCO_2 values at the two sites are shown in Figure 7.52.

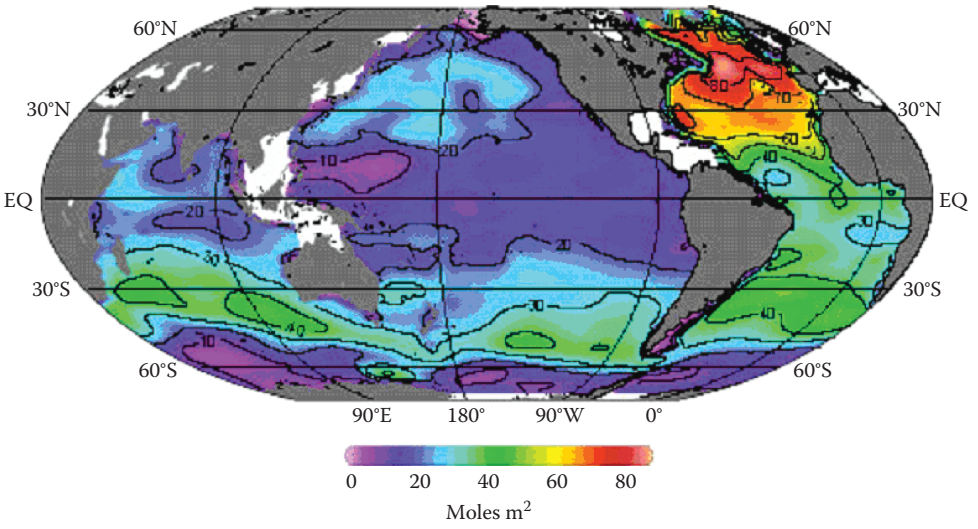

FIGURE 7.49
The inventory of fossil fuel CO_2 in the world oceans. (From Sabine, C.L., et al., *Science*, 305, 367–371, 2004. With permission. With permission.)

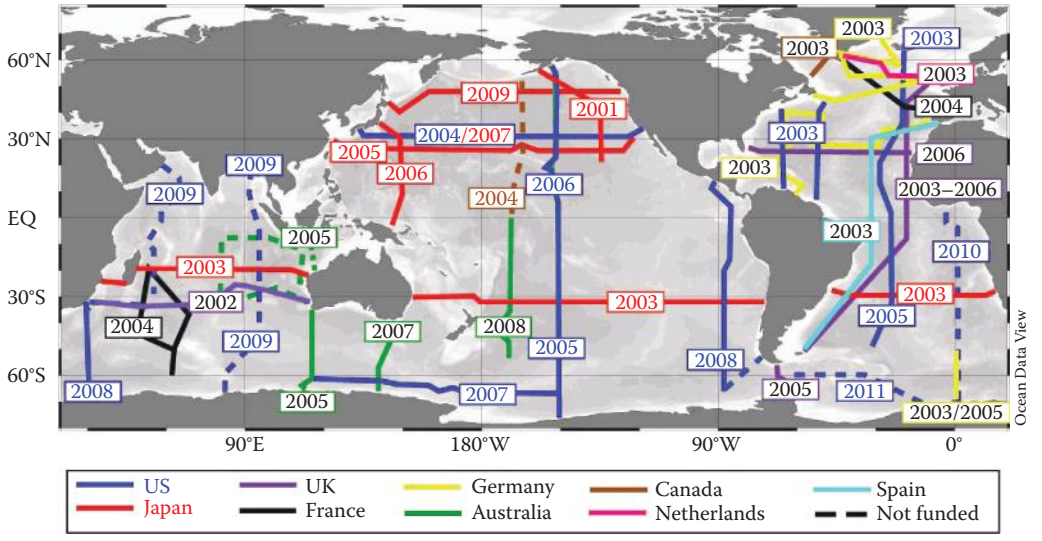

FIGURE 7.50
Cruise tracts for the CLIVAR CO_2 measurements.

The sections look very similar. The results at the two sections were fit to the empirical equation (Friis et al., 2005):

$$TCO_2 = \text{const.} + \mathbf{a}\,\sigma_\theta + \mathbf{b}\,\theta + \mathbf{c}\,S + \mathbf{d}\,SiO_2 + \mathbf{e}\,PO_4 \qquad (7.137)$$

where **a**, **b**, **c**, … are empirical constants. The differences between the equations for the two sections are shown in Figure 7.53. These methods do not work too well in the mixed layers

TABLE 7.11

Anthropogenic Fossil Fuel Input to the Oceans

Ocean	Location	Measurements	Models
Indian	>50 S–20 N	22 ± 2	22–27
Atlantic	>50 S–50 N	40 ± 5	30–40
Pacific	>50S–50 N	44 ± 5	47–62
Marginal seas	>65 N	12 ± 5	
Totals		118 ± 19	99–129

TABLE 7.12

Anthropogenic Budget

CO_2 Sources	1800–1994	1980–1999
Emissions	244 ± 20	117 ± 5
Storage in atmosphere	–165 ± 5	–65 ± 1
Uptake by oceans	–118 ± 19	–37 ± 8
Net terrestrial amount	39 ± 28	–15 ± 9

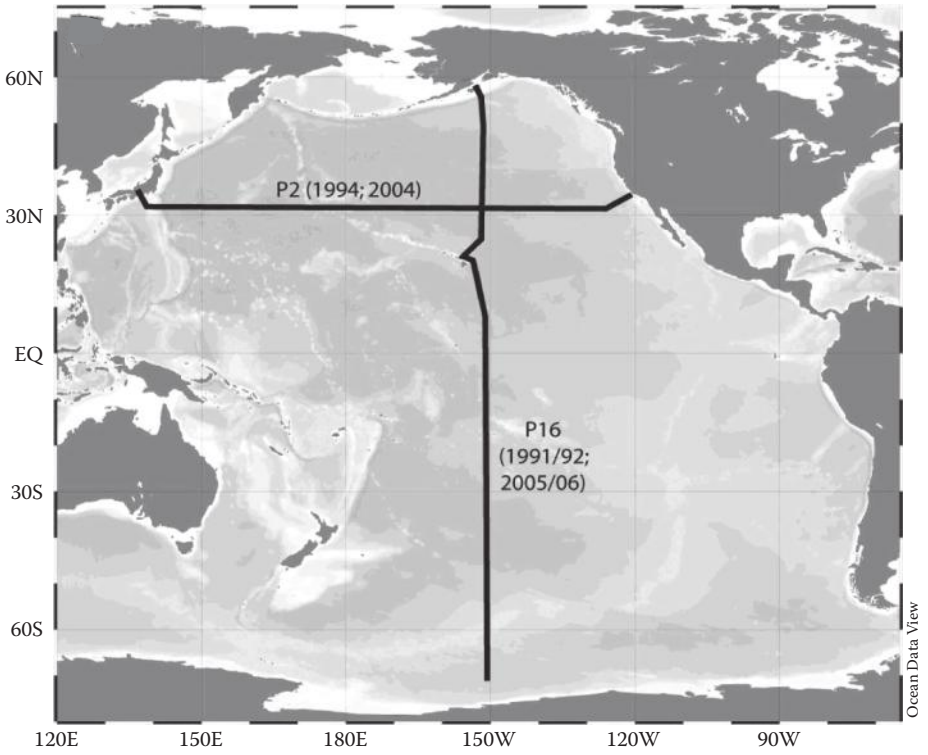

FIGURE 7.51
Cruise tracts P2 and P16 in the Pacific Ocean (From Sabine, C.L., et al., *J. Geophys. Res.*, 113, 2008. With permission.)

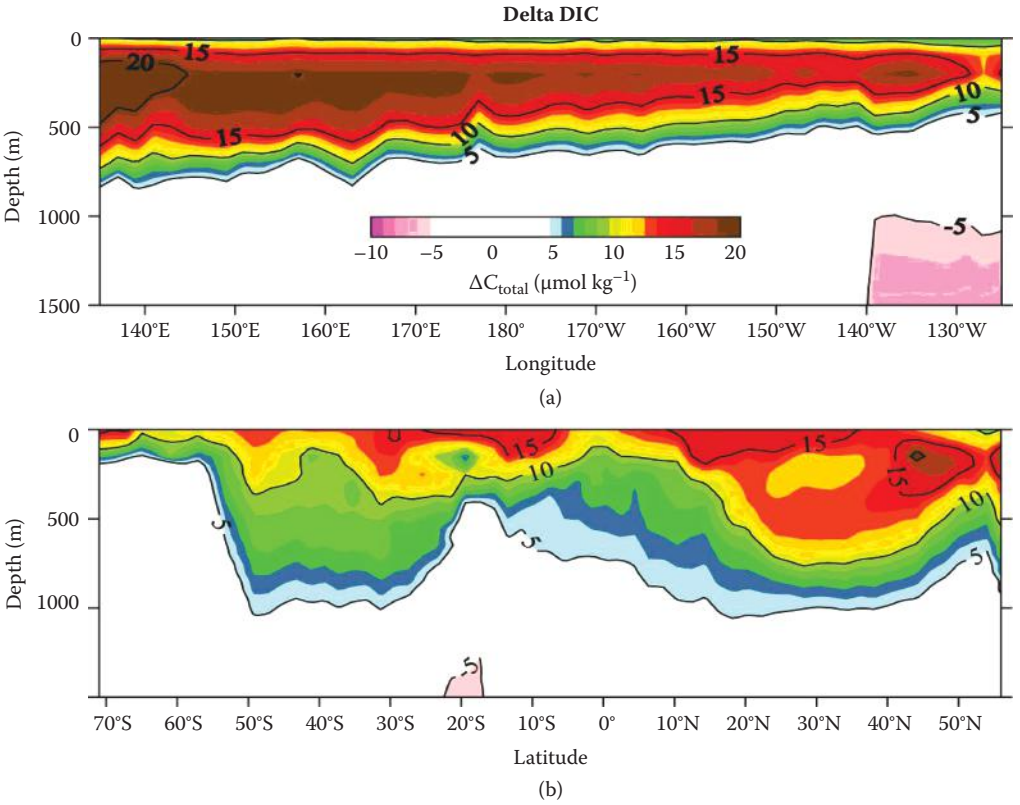

FIGURE 7.52
Changes in the measured CO_2 from the two stations in the Pacific Ocean. (From Sabine, C.L., et al., *J. Geophys. Res.*, 113, 2008. With permission.)

that are strongly affected by physical and biological processes. This is due, for example, to changes in the O_2 in the waters due to the oxidation of plant material and formation of CO_2 (Figure 7.54). If one subtracts the change in CO_2 due to the oxidation of plant material, the anthropogenic input of CO_2 is clearly shown (Figure 7.55). These results point out that care is needed when using this method to examine the changes in the uptake of CO_2 with time in ocean waters.

Most of the other studies resulting from CLIVAR repeat measurements are involved in changes in the pH and saturation state of ocean water due to the uptake of CO_2. Some of these results are discussed in the next section.

The effects of ocean acidification on the saturation state of the waters in the Pacific Ocean have been examined (Feely et al., 2012). The changes in the saturation states of aragonite and calcite in Pacific waters were examined on a number of cruises (Figure 7.56). The results for the changes in Ω for aragonite and calcite along the P16 north-south line are shown in Figure 7.57 and 7.58, respectively. The average change was 0.345 yr^{-1}. The upward migration of the saturation horizons was 1 to 2 m yr^{-1}. The shoaling in the South Pacific is larger due to the uptake of anthropogenic CO_2. If the CO_2 emissions continue over the next 100 yr, many coral reefs in the Pacific will be affected.

A number of recent studies have used the CLIVAR CO_2 measurements to examine the decadal changes in the pH of ocean waters (Byrne et al., 2010; Waters and Millero, 2011).

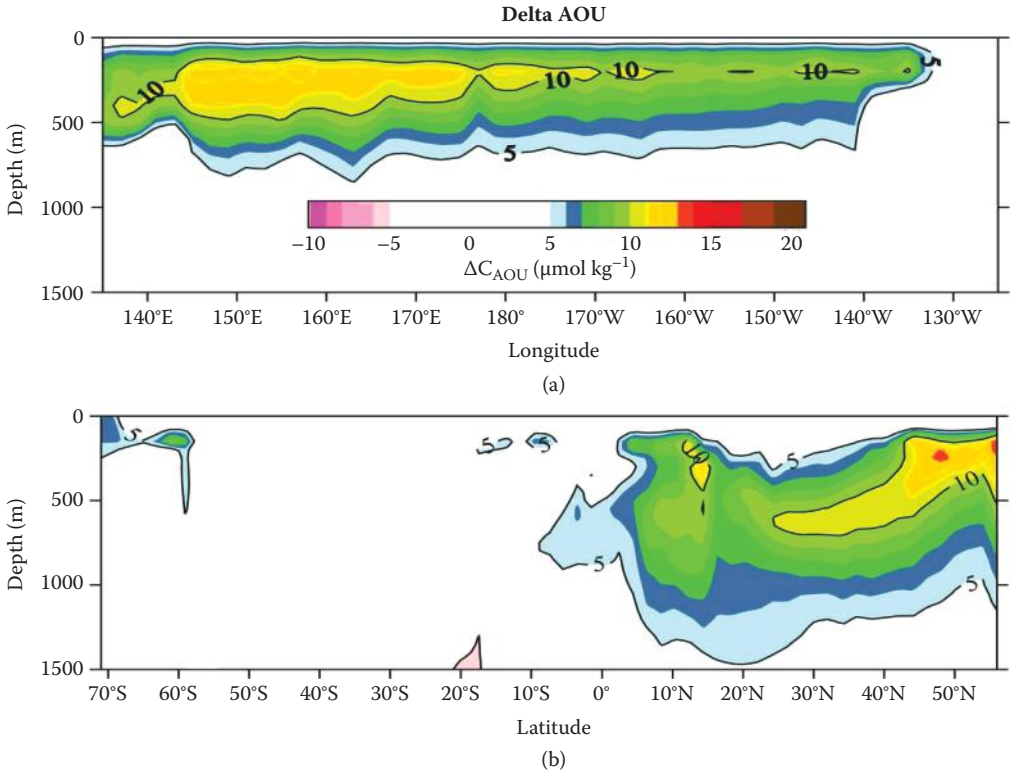

FIGURE 7.53
Change in the AOU in the two stations in the Pacific Ocean. (From Sabine, C.L., et al., *J. Geophys. Res.*, 113, 2008. With permission.)

They found pH changes of –0.0017 yr^{-1} and –0.0016 yr^{-1}, which are in excellent agreement with the directly measured values in the HOT station of –0.0018 yr^{-1} and the ESTOC (European Station for Time Series in the Ocean) Atlantic results of –0.017 yr^{-1} (Gonzalez et al., 2100). As shown in Figure 7.59 (Byrne et al., 2010), these changes in pH affect waters down to depths of ~ 700 m). Future CLIVAR measurements will see if this change in pH is similar to other regions of the ocean and does not change with time.

7.7.1 Ocean Acidification

The pCO_2 in the atmosphere will increase in the future because of the continued use of fossil fuels. The higher concentrations in the atmosphere cause the flux of CO_2 to increase and dissolve more CO_2 in the surface ocean waters. The CO_2 in the waters reacts with water to form carbonic acid:

$$CO_2(g) = CO_2(aq) \rightarrow CO_2(aq) + H_2O = H_2CO_3 \rightarrow H^+ + HCO_3^-$$

This increase in the concentration of the proton causes lowering of the pH. This process is called *ocean acidification*. One can estimate the past pH of the oceans by assuming that the TA of surface waters did not change and the pCO_2 of the atmosphere can be estimated from ice cores. The values of pCO_2 of surface waters calculated in this manner are shown in

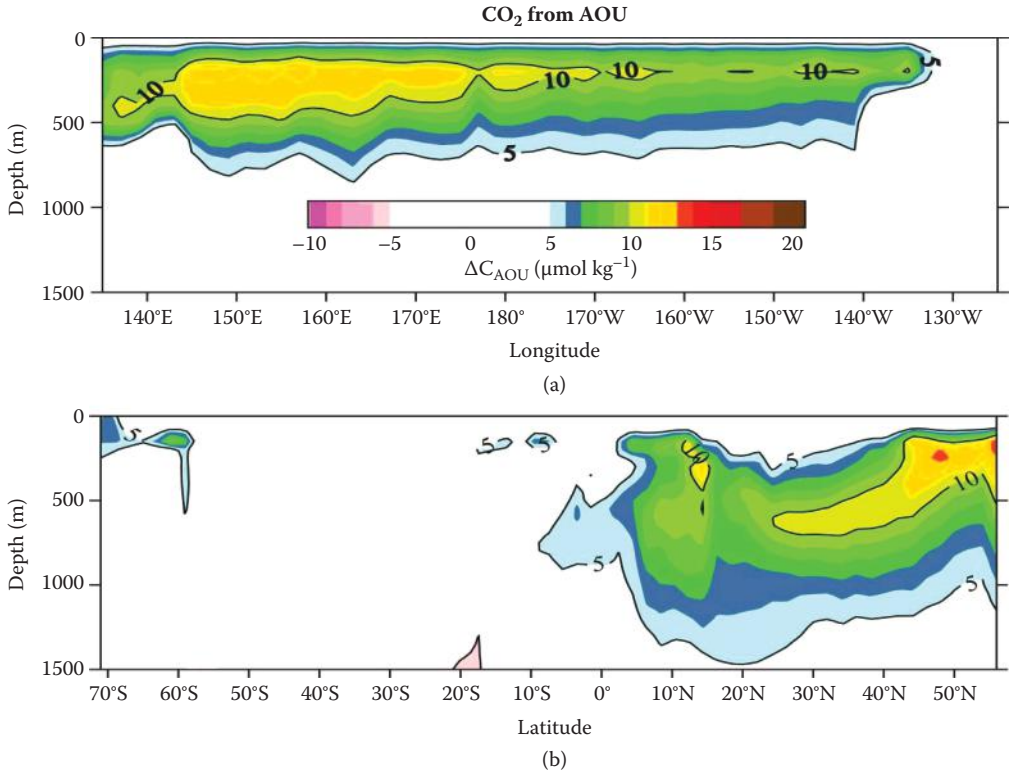

FIGURE 7.54
Change in the CO_2 due to the oxidation of plant material in the two stations in the Pacific Ocean. (From Sabine, C.L., et al., *J. Geophys. Res.*, 113, 2008. With permission.)

Figure 7.60 (Morel et al., 2010). The pH over the last 400,000 yr has oscillated between 8.2 and 8.3. Over the last 200 yr, the pH of the surface waters of the oceans has decreased from 8.2 to 8.1. The Intergovernmental Panel on Climate Change (IPCC, 2007) has estimated the possible increases in pCO_2 due to the burning of fossil fuels over the next 100 yr (Figure 7.61). The estimates are based on various estimates of the increase of CO_2 due to the burning of fossil fuels and lead to values of pH between 7.7 and 7.8 by the end of the century.

The pCO_2 over longer periods of time have been estimated by Caldeira and Wickett (2003). They have estimated the production of CO_2 (GtC/yr) due to the burning of all the fossil fuels and the resultant increase of pCO_2 in the atmosphere as a function of time (Figure 7.62). The pCO_2 is expected to reach levels of 2000 μatm. Since the uptake of the CO_2 is slow, the pCO_2 in the atmosphere will be high for hundreds of years. Table 7.13 summarizes all the expected changes in the CO_2 system over the next 1000 yr. The estimates of pH over the future have been made by assuming that TA was constant (2300 μmol kg^{-1}) and the surface waters are in equilibrium with the atmosphere. The resulting values of pH are shown in Figure 7.63 as a function of pCO_2 and time. At the maximum pCO_2 of 2000 ppm, the pH will be as low as 7.4.

The increases in pCO_2 in the atmosphere and the oceans are being measured at the HOT and BATS stations. The measurements at HOT are shown in Figure 7.64. The increase in the surface water follows the atmospheric values with a delay due to the slow uptake of CO_2 by the oceans. The changes in pH have also been measured in the waters. The

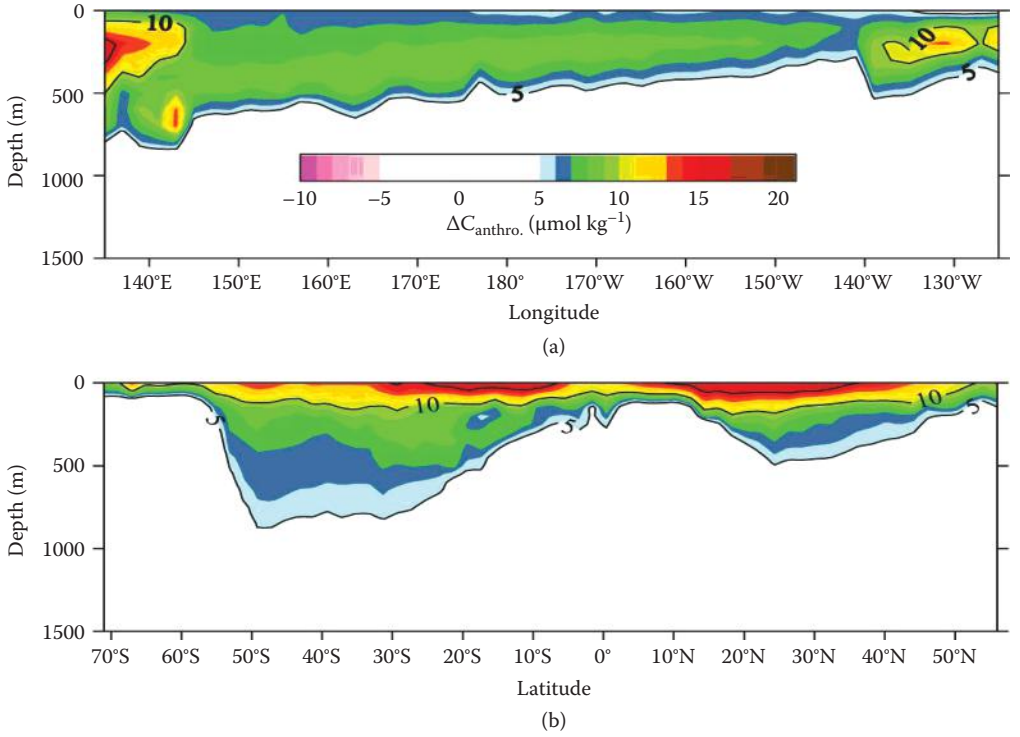

FIGURE 7.55
Change in the anthropogenic input of CO_2 derived from the change in CO_2 due to the oxidation of plant material in the two stations in the Pacific Ocean. (From Sabine, C.L., et al., *J. Geophys. Res.*, 113, 2008. With permission.)

results at Hawaii are shown in Figure 7.65 and indicate that the pH of the surface waters is decreasing by about 0.002 each year. Measurements of the pH at BATS and the ESTOC time series station also showed a similar decrease in the pH as a function of time. The long-term decrease in the pH of the surface ocean from 8.1 to 7.4 will increase the TCO_2 by 12%, decrease the CO_3^{2-} ion by 60%, and decrease the OH^- ion by 78%.

The expected higher pCO_2 over the next 1000 yr will decrease the CO_3^{2-} ion and the saturation state (Ω). The expected change in Ω is shown in Figure 7.66 (Millero et al., 2009). The decrease in Ω and the carbonate ion will make it much more difficult for calcifying organisms to make shells (Kleypas et al., 1999; Riebesell et al., 2000; Orr et al., 2005; Royal Society, 2005; Doney et al., 2009a). Most studies that have examined the effect of decreases of pH have been made on the changes in the saturation state of $CaCO_3$ in surface oceans (Doney et al., 2009a). The saturation state may be less than 1.0 in 200 yr and remain this low for a long time. This will result in difficulty of corals and other calcifiers to survive. The effect of lower saturation states on the growth of corals has been studied by Langdon and Anderson (2005); the results are shown in Figure 7.67. Most of the recent results for ocean acidification experiments for calcification, photosynthesis, nitrogen fixation, and reproduction are shown in Figure 7.68 (Doney et al., 2009a).

Photosynthesis and nitrogen fixation increase with lower pH. Most of the calcification and reproduction experiments have shown decreases with lower pH. The exception is for coccolithophores, which show a mixed behavior. The result for some show a decrease

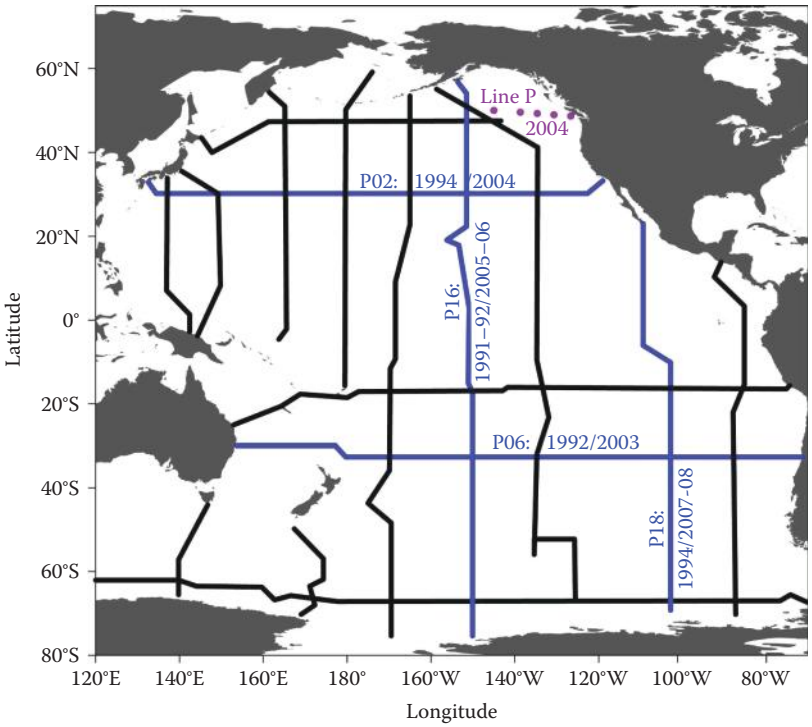

FIGURE 7.56
Cruise tracts in the Pacific Ocean used to determine the decadal changes in saturation horizons of aragonite and calcite.

in calcification (Riebesell et al., 2000; Delille et al., 2005) at low pH, and some show an increase or are not affected (Igeslas-Rodriguez et al., 2008; Shi et al., 2009) at low pH. Smith et al. (2012) have shown that coccolithophores (*Emiliania huxleyi*) show seasonality and are heavier under low-pH conditions. This is important since they contribute about 10% of primary production and dominate the carbonate flux in the oceans. The increase in nitrogen fixation and photosynthesis may be related to increased concentration of Fe at low pH. Future shocks to the system that may occur over the next 90 yr are based on results shown in Figure 7.69. One would expect that more will be said about these, and other types of experiments at low pH will be made in the future.

Feely et al. (2012) have shown that upwelling waters off the West Coast of America have low pH values (Figure 7.70). This low pH has already caused some problems in the rearing of oysters along the coast of Oregon (Service, 2012). Gruber et al. (2012) have used models to show that this problem will become more severe over the next 50 yr.

7.7.2 Effect of Ocean Acidification on the Speciation of Metals in Seawater

The decrease in the pH will also affect the speciation of metal in ocean waters (Millero et al., 2009). Most of the inorganic (OH^-, CO_3^{2-}) and organic (organic charged ligands, amino acids) ligands are a function of pH. The expected changes in concentrations of OH^- and CO_3^{2-} ions over the next 1000 yr are shown in Figure 7.71. The decrease in these ions

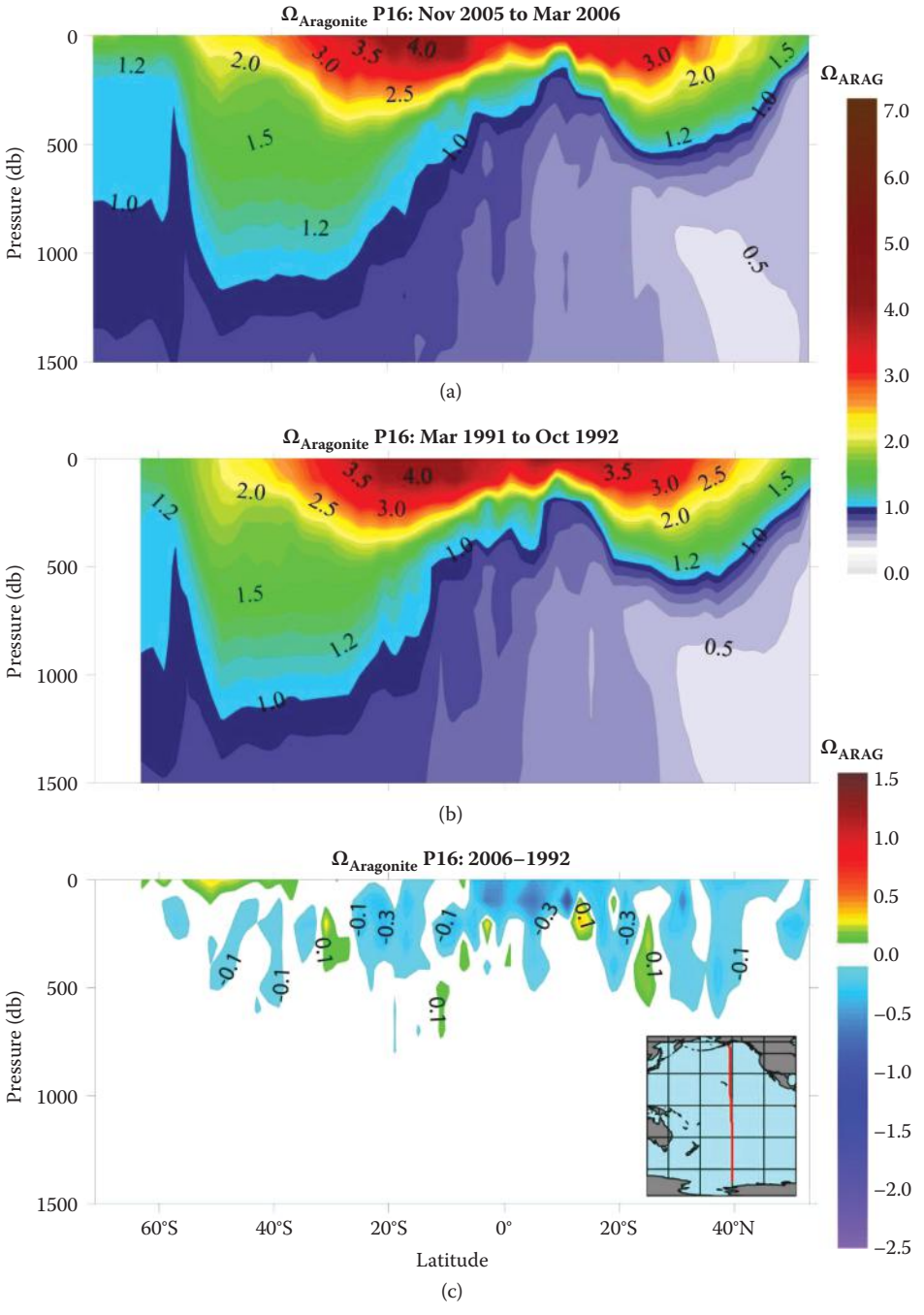

FIGURE 7.57
The changes in the saturation horizons of aragonite in the Pacific Ocean along the P16 cruise. (Feely, R.A., et al., *Global Biogeochem. Cycles*, 2012. With permission.)

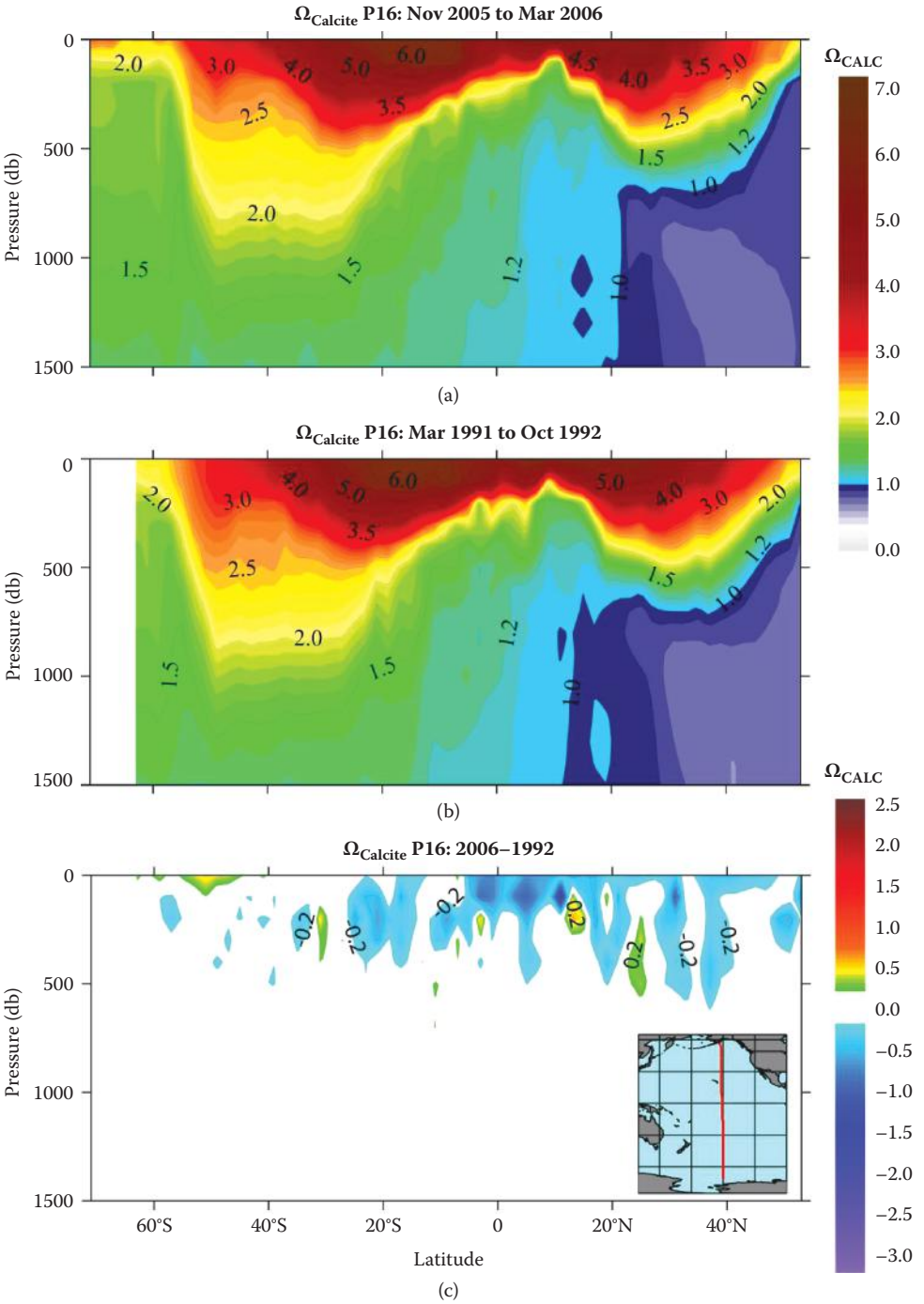

FIGURE 7.58
The changes in the saturation horizons of calcite in the Pacific Ocean along the P16 cruise. (Feely, R.A., et al., *Global Biogeochem. Cycles*, 2012. With permission.)

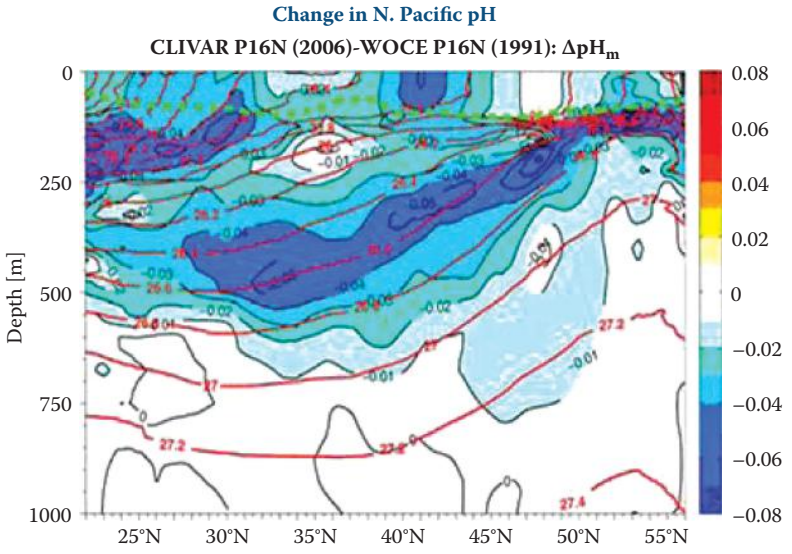

FIGURE 7.59
The decadal changes in the pH in the Pacific Ocean. (Byrne et al., *Geophys. Res. Lett.*, 37, L02601, 2010. With permission.)

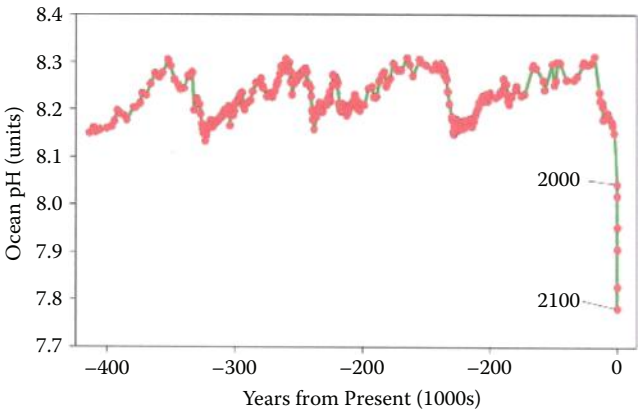

FIGURE 7.60
The estimated changes in the pH of seawater over the last 400,000 years. (From National Acad. Report, Morel et al., 2010. With permission.)

can increase the concentration of free metals in seawater. This is shown for the changes in the free Cu^{2+} in seawater as a function of time (Figure 7.72).

Similar calculations have been made for a number of divalent and trivalent ions (Millero et al., 2009). The percentage changes for the divalent ions are shown in Figure 7.73. The changes in the concentration of free metals can change the thermodynamic and kinetic behavior of metals in ocean waters. This can be demonstrated for two metals, Fe^{2+} and Cu^{2+}. Fe is need by plants to grow, and Cu at high concentrations is toxic to plankton and bacteria. At the present pH (8.1) of seawater, Fe^{2+} is oxidized quickly with O_2 or H_2O_2. The half-time with O_2 at the surface is about 2–4 min. As shown in Figure 7.74, the rate of

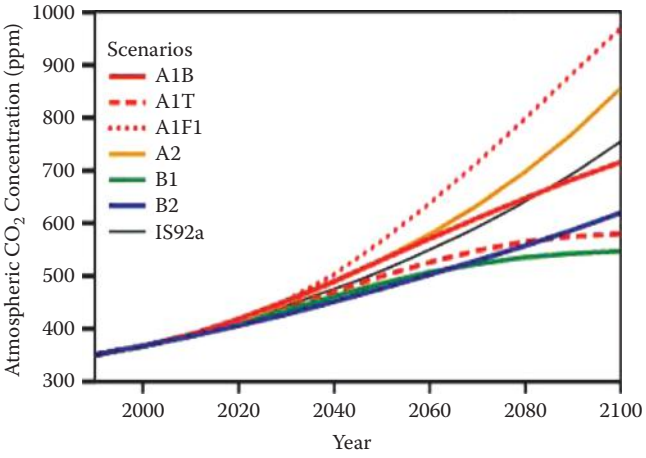

FIGURE 7.61
The International Panel on Climate Change estimates of the changes in pCO_2 over the next 100 years. (From ICPCC, 2007. With permission.)

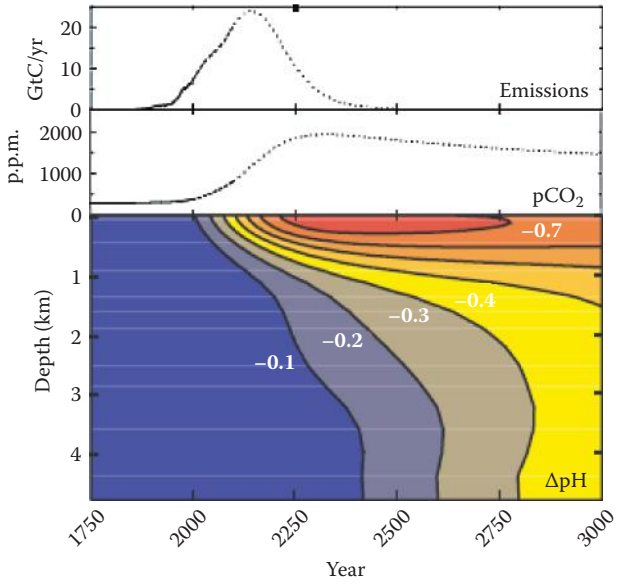

FIGURE 7.62
The expected change in TCO_2 in the atmosphere and resulting pCO_2 and pH over the next 1000 years. (From Caldeira, K., and Wickett, M.E., *Nature*, 425, 365, 2003. With permission.)

this reaction is slower at low pH. Fe^{3+} is more soluble in acidic solutions (Figure 7.75), so its concentration also increases at low pH. So, both processes increase the concentration of total Fe, which is good for primary production and nitrogen fixation. The lower pH can increase the concentration of Cu^{2+} and make it more toxic in seawater because the reduction of Cu^{2+} to Cu^{+} in surface waters with H_2O_2 is increased at low concentrations of CO_3^{2-}. As shown in Figure 7.76, the addition of borate has no effect on the reduction, while the

TABLE 7.13

Changes in the Carbonate System Caused by Increases of pCO_2 in the Atmosphere (S = 35, TA = 2300 µmol kg^{-1}, and t = 25°C)

Year	pCO_2 µtm	pH	TCO_2 µmol kg^{-1}	Ω (cal)	Ω (arg)	CO_3^{2-} µmol kg^{-1}
1800	280	8.16	1906	6.76	4.46	280.9
2000	370	8.07	1968	5.77	3.81	239.9
2040	570	7.92	2057	4.39	2.89	182.3
2080	770	7.80	2113	3.55	2.34	147.5
2120	970	7.72	2152	2.99	1.97	124.1
2160	1170	7.64	2182	2.58	1.70	107.1
2200	1370	7.58	2206	2.27	1.50	94.3
2240	1570	7.53	2226	2.03	1.34	84.2
2280	1770	7.48	3343	1.83	1.21	76.10
2320	1970	7.44	2258	1.67	1.10	69.40
2360	2170	7.40	2272	1.54	1.00	63.8
2400	2370	7.36	2284	1.42	0.94	59.1

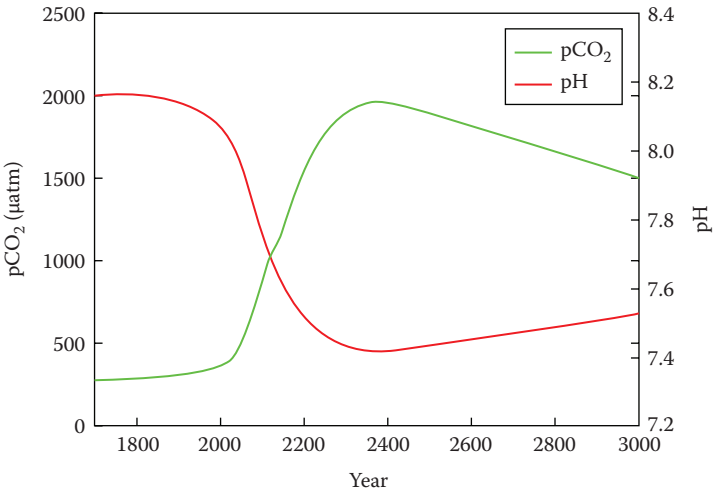

FIGURE 7.63
The expected pH of surface seawater over the next 1000 years. (From Millero et al., *Oceanography*, 22, 72–85, 2009. With permission.)

addition of carbonate decreases the reduction rate. A lowering of the carbonate ion at high pH will increase the rate of reduction. The surface waters may have higher concentrations of Cu^{+} that may be more toxic than Cu^{2+}. These are only two possible effects on metals; more examples will become apparent in the future since many chemical and biological processes are affected by pH.

In summary, the expected decrease in the pH of the ocean over the next 1000 yr will affect many chemical and biological processes in the oceans. Both good and bad effects may be the results of the future lower pH of ocean waters. As discussed in Chapter 3, most of the

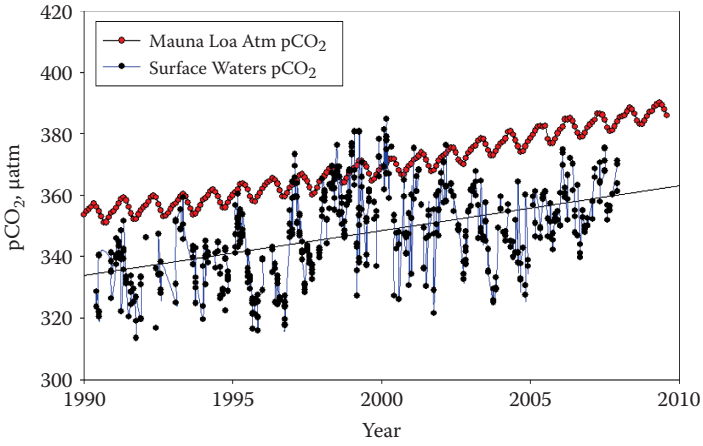

FIGURE 7.64
The increases in pCO_2 in the atmosphere and water at the Hawaii Ocean Time Series station.

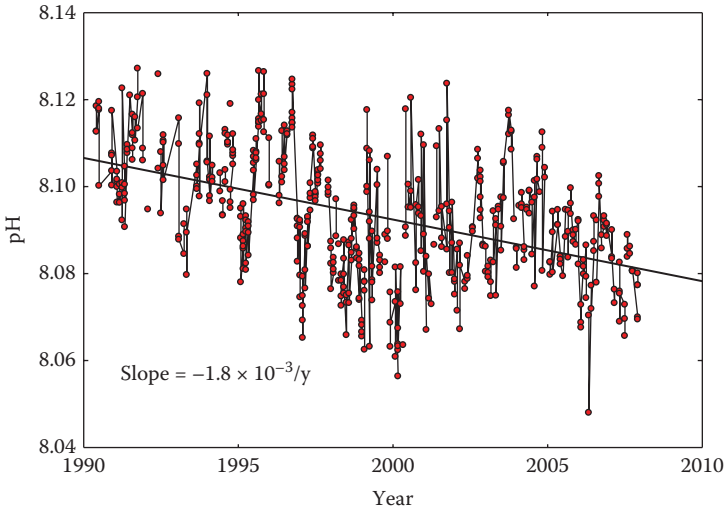

FIGURE 7.65
The decrease in pH in surface water at the Hawaii Ocean Time Series station.

divalent metals form very strong complexes with organic ligands in seawater. It is not clear at the present time how this speciation will be affected by low pH. The only study that I am aware of at present is the formation of Cu^{2+} complexes with natural organic ligands in seawater (Louis et al., 2009). These workers characterized the acid–base properties of the ligand (Figure 7.77). They found that the concentration of the ligand decreased when the pH range decreased from 8.0 to 7.0. As one might expect, a lower pH will decrease the formation of organic complexes of Cu^{2+}. It is hoped that over the next 10 yr more studies will be made on the effect of pH on the speciation of divalent metals with organic ligands in seawater.

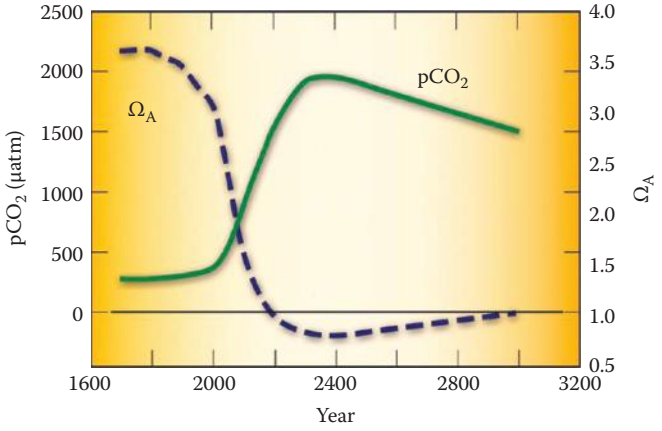

FIGURE 7.66
The expected change in the saturation state Ω over the next 1000 years. (From Millero, F.J., Woosley, R., DiTrolio, B., and Waters, J., *Oceanography*, 22, 72–85, 2009. With permission.)

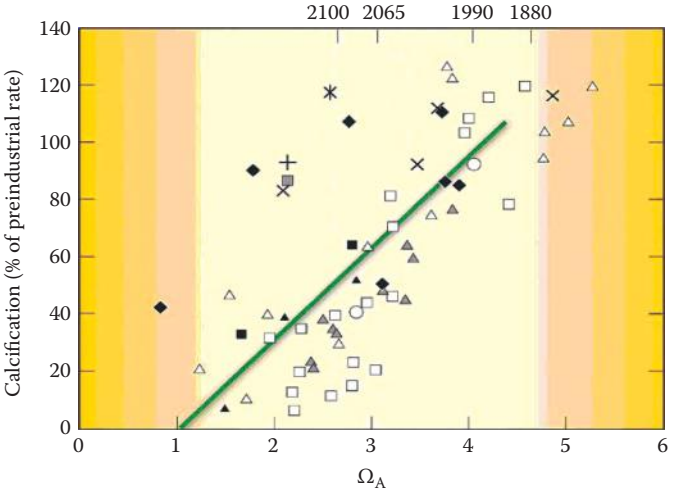

FIGURE 7.67
The effect of the decrease in the saturation state of aragonite on the growth of corals. (Adapted from Langdon and Atkinson, *J. Geophys. Res. Oceans*, 110, 1–16, 2005; Millero and DiTrolio, *Elements*, 6, 5, 299–303, 2010.)

Physiological Response	Major group	Response to increasing CO_2 a	b	c	d
Calcification					
	Coccolithophores	2–5	1	1	1
	Planktonic Foraminifera	2–5			
	Molluscs	>5		2–5	
	Echinoderms	2–5	1		
	Tropical corals	>5			
	Coralline red algae	1	1		
Photosynthesis					
	Coccolithophores		2–5	2–5	
	Prokaryotes		1	1	
	Seagrasses		2–5		
Nitrogen Fixation					
	Cyanobacteria		2–5	1	
Reproduction					
	Molluscs	2–5			
	Echinoderms	1			

FIGURE 7.68
Measured effects of ocean acidification on calcification, photosynthesis, nitrogen fixation, and reproduction of organisms. (From Doney, S.C., et al., *Oceanography*, 22, 16–25, 2009. With permission.)

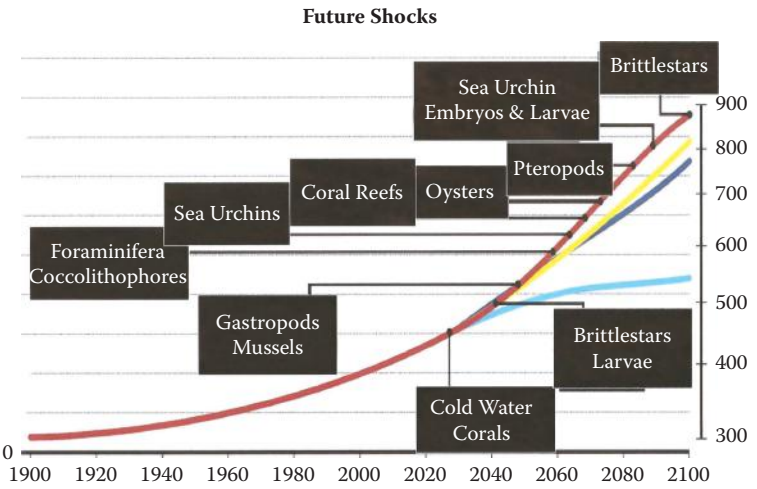

FIGURE 7.69
Future shocks on organisms over the next 100 years based on laboratory studies.

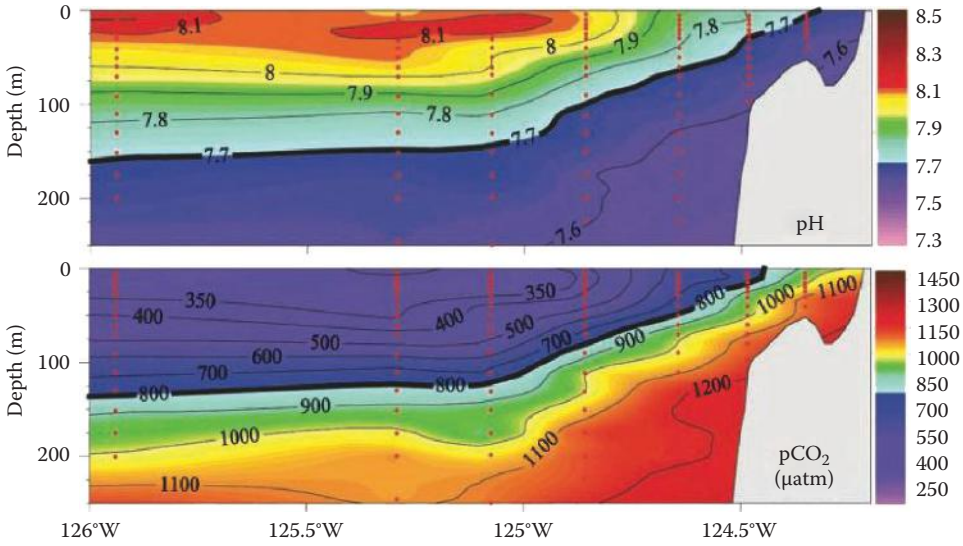

FIGURE 7.70
The increase in pCO_2 and decrease along the western coast of America. (From Feely et al., *Science*, 320, 1490–1492, 2008. With permission.)

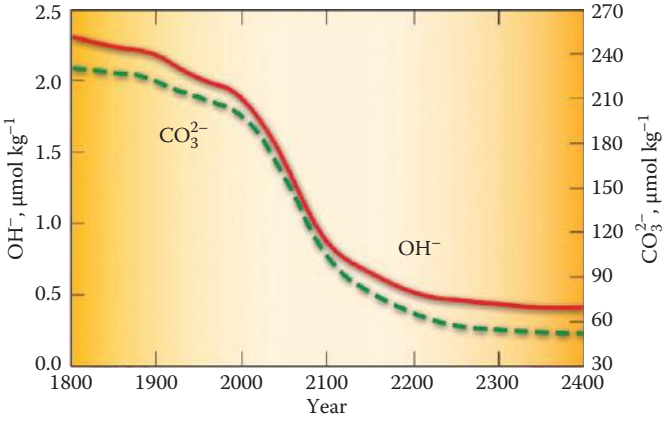

FIGURE 7.71
Expected decrease in the OH^- and CO_3^{2-} ions over the next 1000 years.

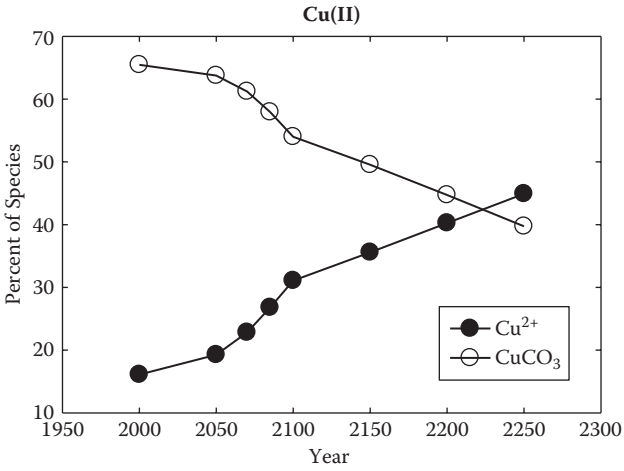

FIGURE 7.72
Expected decrease in fraction of free divalent ions in seawater over the next 1000 years.

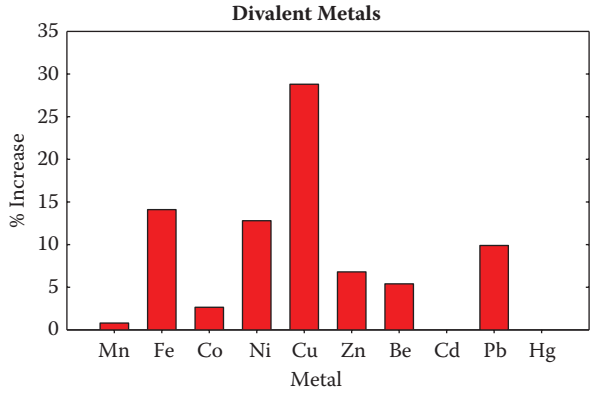

FIGURE 7.73
The percentage increase in the concentration of free divalent ions in seawater over the next 1000 years.

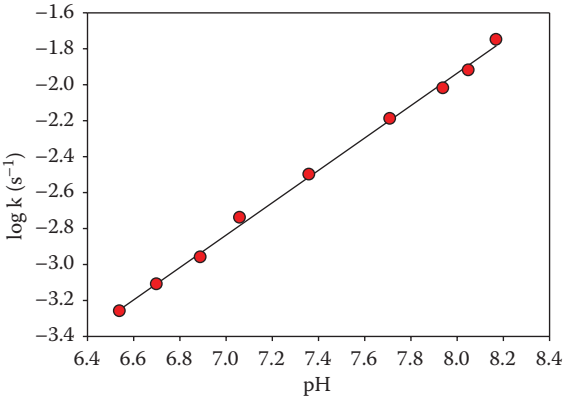

FIGURE 7.74
The effect of pH on the rate constant for the oxidation of Fe^{2+} with O_2 in seawater at 25°C.

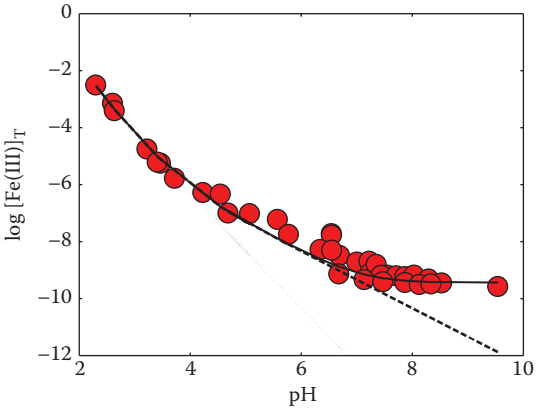

FIGURE 7.75
The effect of pH on the solubility of Fe^{3+} in seawater at 25°C.

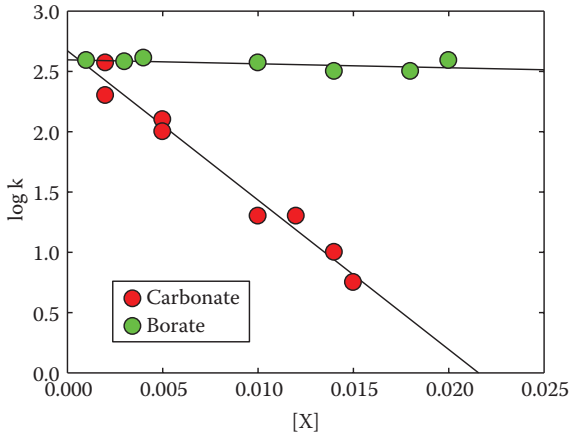

FIGURE 7.76
The effect of the concentration of CO_3^{2-} and $B(OH)_4^-$ on the rate constant for the reduction of Cu^{2+} with H_2O_2 in seawater at 25°C.

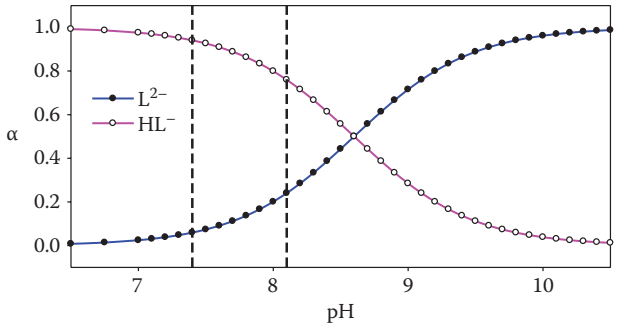

FIGURE 7.77
The effect of pH on the organic ligand that forms complexes with Cu^{2-} in seawater. (From Millero and DiTrolio, *Elements*, 6, 299–303, 2010.)

References and Further Reading

Barnola, J.M., et al., Vostok ice core provides 160,000-year record of atmospheric CO_2, *Nature*, 329, 408 (1987).

Bates, R.G., *Determination of pH Theory and Practice*, 2nd ed., Wiley, New York, 479 (1973).

Bates, R.G,. and Calais, J.G., Thermodynamics of the dissociation of Bis H^+ in seawater from 5 to 40 C. *J. Solution Chem*. 10, 269–279 (1981).

Bates, R.G., and Erickson, W.P., Thermodynamics of the dissociation of 2-minopyridinium ion in synthetic seawater and a standard for pH in marine systems. *J. Solution Chem.* 15, 891–901 (1986).

Battle, M., et al., Global carbon sinks and their variability inferred from atmospheric O_2 and $\delta^{13}C$, *Science*, 287, 2467 (2000).

Berger, W.H., Biogenous deep sea sediments: production, preservation, and interpretation, Chapter 29, *Chemical Oceanography*, Vol. 5, 2nd ed., Riley, J.P., and Chester, R., Eds., Academic Press, New York, 266–388 (1976).

Betzer, P.R., et al., The ocean carbonate system: a reassessment of biogenic controls, *Science,* 226, 1074 (1984).

Brewer, P.G., Direct observation of the oceanic CO_2 increase, *Geophys. Res. Lett.,* 5, 997–1000 (1978).

Broecker, W.S., and Peng, T.H., *Tracers in the Sea*, Eldigio Press, New York (1982).

Bustos, H., Morse, J.W., and Millero, F.J., The formation of whitings on the Little Bahama Banks, *Mar. Chem*., 113, 1–8 (2009).

Byrne, R.H., Mecking, S., Feely, R.A., and Liu, X., Direct observations of basin-wide acidification of the North Pacific Ocean, *Geophys. Res. Lett*., 37, L02601 (2010).

Caldeira, K., and Wickett, M.E., Oceanography: anthropogenic carbon and ocean pH, *Nature,* 425, 365 (2003).

Chen, C.-T.A., Decomposition of calcium carbonate and organic carbon in the deep oceans, *Science,* 201, 735 (1978).

Chen, C.-T.A., and Millero, F.J., Gradual increase of oceanic CO_2, *Nature,* 277, 205–206 (1979).

Clayton, T.D., and Byrne, R.H., Spectrophotometric seawater pH measurements: total hydrogen ion concentration scale calibration of m-cresol purple and at-sea results, *Deep-Sea Res.*, 40, 2115 (1993).

Cloud, P.E., Carbonate precipitation and dissolution in the marine environment, Chapter 17, *Chemical Oceanography*, Vol. 2, Riley, J.P., and Skirrow, G., Eds., Academic Press, New York, 127–158 (1965).

Coale, K.H., et al., Southern Ocean iron enrichment experiment: carbon cycling in high and low Si waters, *Science,* 304, 408 (2004).

Delille, B. et al., Response of primary production and calcification to changes pf pCO_2 during experimental blooms of the coccolithophorid Emiliania hyxley, *Globa. Biogeochem. Cycles*, 19, GB2023, doi:10.1029/2004GB002318 (2005).

Dickson, A.G., pH buffers for sea water media based on the total hydrogen ion concentration scale, *Deep-Sea Res*., 40, 107 (1993).

Doney, S.C., et al., Ocean acidification, a critical emerging problem for the ocean science, *Oceanography*, 22, 16–25 (2009a).

Doney, S.C., et al., Ocean acidification, the other CO_2 problem, *Annu. Rev. Mar. Sci*, 1, 169–192 (2009b).

Feely, R.A., et al., In situ calcium carbonate dissolution in the Pacific Ocean, *Global Biogeochem. Cycles*, 16, 1144 (2002).

Feely, R.A., Sabine, C.L., Lee, K., Berelson, W., Kleypas, J., Fabry, V.J., and Millero, F.J., The impact of anthropogenic CO_2 on the $CaCO_3$ system in the oceans, *Science,* 305, 362 (2004).

Feely, R.A., Sabine, C.L., Hernandez-Ayon, J.M., Ianson, D., and Hales, B., Evidence of upwelling of corrosive"acidified" water onto the Continental Shelf, *Science*, 320, 1490–1492 (2008).

Feely, R.A., Sabine, C.L., Byrne, R.H., Millero, F.J., Dickson, A.G., Wanninkhof, R., Murata, A., Miller, L.A., and Greeley, D., Decadal changes in the aragonite and calcite saturation state of the Pacific Ocean, *Global Biogeochem. Cycles*, 26 (2012).

Friis, K., et al., On the temporal increase of anthropogenic CO_2 in the subpolar North Atlantic, *Deep-Sea Res. Pt. I: Oceanogr. Res. Papers*, 52, 681–698 (2005).

Friis, K., et al., Possible overestimation of shallow-depth calcium carbonate dissolution in the ocean, *Global Biogeochem. Cycles*, 20, 1–11 (2006).

Friis, K., et al., Dissolution of calcium carbonate: observation and model result in the subpolar North Atlantic, *Biogeoscience* 4, 205-207 (2007).

Gledhill, D.K., Wanninkhof, R., Millero, F.J., and Eakin, M., Ocean acidification of the greater Caribbean region 1996–2006, *J. Geophys. Res*., 113, C10031 (2008).

González-Dávila, M., et al., Interannual variability of the upper ocean carbon cycle in the north-east Atlantic Ocean, *J. Geophys. Res. Lett.,* 34, L07608 (2007).

González-Dávila, M., et al., Oxidation of copper(I) in seawater at nanomolar levels, *Mar. Chem.,* 115(1–2), 118–124 (2009).

Gruber, N., et al., An improved method for detecting anthropogenic CO_2 in the oceans, *Global Biogeochem. Cycles*, 10, 809 (1996).

Gruber, N. et al., Rapid progression of ocean acidification in the California current system, *Science*, 337, 220–223 (2012).

Honjo, S., Dissolution of suspended cocoliths in the deep-sea water column and sedimentation of cocoliths ooze, in *Dissolution of Deep-Sea Carbonates,* Sliter, W., Be, A.W.H., and Berger, W.H., Eds., Cushman Foundation Foraminifera Res, Spec. Pub. No. 13, pp. 115–128 (1975).

Igellas-Rodriguez et al. Plankton calcification in a high-CO2 World, *Science*, 320, 336–340 (2008).

IPCC Report, Contribution of Working Groups I, II and III to the Fourth Assessment Report of the Intergovernmental Panel on Climate Change, Core Writing Team, Pachauri, R.K. and Reisinger, A. (Eds.) IPCC, Geneva, Switzerland. 104 pp. (2012).

Keeling, C.D., and Whorf, T.P., Atmospheric CO_2 records from sites in the SIO air sampling network. in *Trends: A Compendium of Data on Global Change,* Carbon Dioxide Information Analysis Center, Oak Ridge, TN (2004).

Kleypas, J.A., et al., Geochemical consequences of increased atmospheric carbon dioxide on coral reefs, *Science*, 284(5411), 118–120 (1999).

Langdon, C., and Atkinson, M., Effect of elevated pCO_2 on photosynthesis and calcification of corals and interactions with seasonal change, *J. Geophys. Res.*, 110(C9) (2005).

Lewis, E., and Wallace, D.W.R., Program developed for CO_2 system calculations, Report 105, Oak Ridge National Laboratory, Carbon Dioxide Inf. Anal. Cent. (1998).

Liss, P.S., Chemistry of the sea surface microlayer, Chapter 10, *Chemical Oceanography*, Vol. 2, 2nd ed., Riley, J.P., and Skirrow, G., Eds., Academic Press, New York, 193–243 (1975).

Louis, Y., et al., Characterisation and modelling of marine dissolved organic matter interaction with major and trace cations, *Mar. Environ. Res*., 67, 100–107 (2009).

Marion, G.M., Millero, F.J., Camões, M.F., Spitzer, P., Feistel, P., and Chen, C-T. A., pH and acidity of natural waters, *Mar. Chem.,* 126, 89–95 (2011).

Marion, G.M., Millero, F.J., and Feistel, R., Precipitation of solid phase calcium carbonates and their effect on application of seawater S_A–T–P models, *Ocean Sci*., 5, 285–291 (2009).

McNeil, B.I., et al., Anthropogenic CO_2 uptake by the ocean based on the global chlorofluorocarbon data set, *Science*, 299, 235 (2003).

Millero, F.J., The marine inorganic carbon cycle, *Chem. Rev.*, 107(2), 308–341 (2007).

Millero, F.J., Thermodynamics of carbon dioxide system in the oceans, *Geochim. Cosmochim. Acta*, 59, 661 (1995).

Millero, F.J., Carbonate constants for estuarine waters, *Mar. Freshwater Res.*, 61, 130–143 (2010).

Millero, F.J., and DiTrolio, B., Use of thermodynamics in examining the effects of ocean acidification, *Elements*, 6(5), 299–303 (2010).

Millero, F.J., et al., Dissociation constants of carbonic acid in seawater as a function of salinity and temperature, *Mar. Chem.*, 100, 80–94 (2006).

Millero, F.J., DiTrolio, B., Suarez, A.F., and Lando, G., Spectroscopic measurements of pH for NaCl brines from I = 0.1 to 5.7 m, *Geochem. Cosmochim. Acta*, 73, 3109–3114 (2009).

Millero, F.J., Woosley, R., DiTrolio, B., and Waters, J., The effect of ocean acidification on the speciation of metals in natural waters, *Oceanography*, 22, 72–85 (2009).

Morel, F.M., et al., *Ocean Acidification: A National Strategy to Meet the Challenges of a Changing Ocean*, National Academies Press, Washington, DC (2010).

Morse, J.W., The kinetics of calcium carbonate dissolution and precipitation, in *Review in Mineralogy: Carbonates—Mineralogy and Chemistry*, Reeder, R.J., Ed., Mineralogical Society of America, Bookcrafters, Chelsea, MI, 227–264 (1983).

Morse, J.W., and Mackenzie, F.T., *Geochemistry of Sedimentary Carbonates*, Elsevier, New York (1990).

Morse, J.W., Mucci, A., and Millero, F.J., The solubility of calcite and aragonite in seawater of 35‰ salinity at 25°C and atmospheric pressure, *Geochim. Cosmochim. Acta*, 44, 85–94 (1980).

Morse, J.W., Gledhill, D.K., and Millero, F.J., $CaCO_3$ precipitation kinetics in waters from the Great Bahama Bank, *Geochim. Cosmochim. Acta*, 67, 2819–2826 (2003).

Mucci, A., The solubility of calcite and aragonite in seawater at various salinities, temperatures and one atmosphere total pressure, *Am. J. Sci*., 283, 780 (1983).

Mucci, A., Millero, F.J., and Morse, J.W., Comment on "The Solubility of Aragonite in Seawater," *Geochim. Cosmochim. Acta*, 46, 105–107 (1982).

Orr, J.C., et al., Anthropogenic ocean acidification over the twenty-first century and its impact on calcifying organisms, *Nature*, 437(7059), 681–686 (2005).
Park, K., Oceanic CO_2 system: an evaluation of ten methods of investigation, *Limnol. Oceanogr.*, 14, 179 (1969).
Peng, T., and Wanninkhof, R., Increase in anthropogenic CO_2 in the Atlantic Ocean in the last two decades, *Deep-Sea Res. Pt. I: Oceanogr. Res. Papers*, 57(6), 755–770 (2010).
Peterson, M.N., Calcite: rates of dissolution in a vertical profile in Central Pacific, *Science*, 154, 1542 (1966).
Pierrot, D., Lewis, E., and Wallace, D.W.R., *MS Excel Program Developed for CO_2 System Calculations*, Rep. ORNL/CDIAC-105a, Carbon Dioxide Information Analysis Center, Oak Ridge National Laboratory, U.S. Department of Energy, Oak Ridge, TN (2006).
Quay, P.D., Tilbrook, B., and Wong, C.S., Oceanic uptake of fossil fuel CO_2: carbon 13 evidence, *Science*, 256, 74 (1992).
Redfield, A.C., et al., The influence of organisms on the composition of sea-water, in *The Sea*, Hill, M.N., Ed., Wiley-Interscience, New York, 26–77 (1963).
Riebesell, U., et al., Reduced calcification of marine plankton in response to increased atmospheric CO_2, *Nature*, 407(6802), 364–367 (2000).
Royal Society, *Ocean Acidification due to Increasing Atmospheric Carbon Dioxide*, Royal Society, London (2005).
Sabine, C.L., et al., Anthropogenic CO_2 inventory of the Indian Ocean, global and biogeochemical cycles, *Global Biogeochem. Cycles*, 13(1), 179–198 (1999).
Sabine, C.L., et al., Distribution of anthropogenic CO_2 in the Pacific, *Global Biogeochem. Cycles*, 16, 1083 (2002).
Sabine, C.L., et al., The oceanic sink for anthropogenic CO_2, *Science*, 305, 367–371 (2004).
Sabine, C.L., et al., Decadal changes in Pacific carbon, *J. Geophys. Res.*, 113, C07021 (2008).
Sarmiento, J.L., Ocean carbon cycle, *Chem. Eng. News*, May 31, 30–43 (1993).
Service, R.F., Rising acidity brings an ocean of trouble, *Science*, 337, 146–148 (2012).
Shi et al., Effects of pH/pCO_2 control method on medium, *Biogeoscience*, 6, 1199–1207 (2009).
Skirrow, G., The dissolved gases—carbon dioxide, Chapter 9, *Chemical Oceanography*, Vol. 2, 2nd ed., Riley, J.P., and Skirrow, G., Eds., Academic Press, New York, 1–192 (1975).
Smith, E.K., et al., Predominance of heavily calcified Coccolithophores at low $CaCO_3$ saturation during winter in the Bay of Biscay, *Proceedings Natl. Acad. Sci.* , doi/10.1073/pnas.1117508109 (2012).
Solomon, S., et al., *Contribution of Working Group 1 to the Fourth Assessment Report of the Intergovernmental Panel on Climate Change*, Cambridge University Press, Cambridge, UK (2007).
Takahashi, T., et al., Net air–sea CO_2 flux over global oceans: an improved estimate based on sea–air pCO_2 differences, in *Proceedings of Second International Symposium on CO_2 in the Oceans*, CGER-1037-99, 9–15, CGER/NIES, Tsukuba, Japan (1999).
Tans, P.P., et al., Observation constraints on the global atmospheric CO_2 budget, *Science,* 247, 1431 (1990).
van Heuven, S., et al., *MATLAB Program Developed for CO_2 System Calculations*, Carbon Dioxide Information Analysis Center, Oak Ridge National Laboratory, U.S. Department of Energy, Oak Ridge, TN (2011).
Wallace, D.W.R., Storage and transport of excess CO_2 in the oceans: the JGOFS/WOCE Global CO2 survey in *Ocean Circulation and Climate,* Siedler, G., Church, J., and Gould, W.J., Eds., Academic Press, San Diego, CA, 489–521 (2001).
Waters, J., and Millero, F.J., The free proton concentration scale for seawater pH (2011).
Waters, J., Millero, F.J., and Sabine, C.L., Synthesis and analysis of the carbonate parameters in the Pacific Ocean, *Global Biogeochem. Cycles*, 25 (2011).
Weiss, R., Carbon dioxide in water and seawater, the solubility of a non-ideal gas, *Mar. Chem.*, 2, 203 (1974).
Weiss, R., Determinations of carbon dioxide and methane by dual catalyst flame ionization chromatography and nitrous oxide by electron capture chromatography, *J. Chromatogr. Sci.*, 19, 611 (1981).
Wilson, R.W., et al., Contribution of fish to the marine inorganic carbon cycle, *Science*, 323, 359–362 (2009).

Woosley, R.J., Millero, F.J., and Grosell, M. The solubility of fish produced high magnesium calcite in seawater, *Geophys. Res. Lett.*, 117, C04018 (2012).

Xu, Y., et al., Simulation of storage of anthropogenic carbon dioxide in the North Pacific using an ocean general circulation model, *Mar. Chem.*, 72, 221 (2000).

Zeebe, R.E., and Wolf-Gladrow, D., *CO_2 in Seawater: Equilibrium, Kinetics, Isotopes*, Elsevier Oceanographic Series 65, Elsevier, New York (2001).

8

Micronutrients in the Oceans

8.1 Introduction

Marine phytoplankton require certain trace elements for growth. These nutrients are used until they become limiting and further growth is inhibited. A crude way of assessing the availability and need of marine plants for various elements can be made by examining the composition of phytoplankton compared to the concentration in average seawater. Such a comparison is shown in Table 8.1. The most important micronutrients are nitrogen and phosphorus. Some organisms (diatoms) have siliceous frustules and require silica. Although other elements such as Fe, Mn, Cu, Zn, Co, and Mo are also essential for growth, it is generally thought that growth is not inhibited or limited by the concentration of these metals. An exception for certain waters may be Fe and Mn. In addition, certain organic compounds, such as vitamins, are necessary for growth. This chapter discusses the major micronutrients P, N, and Si.

8.2 Phosphorus in Seawater

Phosphorus occurs in seawater in dissolved and particulate forms. In surface waters, dissolved and particulate organic phosphates occur due to the decomposition of plants. These dissolved organic phosphorus compounds make up a significant but variable portion of dissolved P in surface waters. Although the compounds have not all been identified, they are undoubtedly related to the decomposition and excretion products of marine organisms.

Sugar phosphates, phospholipids, phosphonucleotides, and their hydrolyzed products occur. Phosphate esters (O–P bonds) and more stable aminophosphonic acids (C–P bonds) may also make up a considerable portion of the organic-phosphorus compounds. At present, the details of the cycling of these compounds in surface waters are largely unknown. Dissolved inorganic phosphorus exists entirely as the ionized products of H_3PO_4.

$$H_3PO_4 \rightarrow H^+ + H_2PO_4^- \tag{8.1}$$

$$H_2PO_4^- \rightarrow H^+ + HPO_4^{2-} \tag{8.2}$$

$$HPO_4^{2-} \rightarrow H^+ + PO_4^{3-} \tag{8.3}$$

TABLE 8.1

Distribution of Elements in Organisms (N) and Seawater (A): A Measure of Availability to Need

Element	N (g/100 g)	A (g/m³)	A/N
H	7	—	—
Na	3	10,750	3600
K	1	390	390
Mg	0.4	1300	300
Ca	0.5	416	830
C	30	28	1
Si[a]	0.5	0.50	1
Si[b]	10	0.50	0.05
N	5	0.30	0.06
P	0.6	0.030	0.05
O (O_2 + O_2)	47	90	2
S	1	900	900
Cl	4	19,300	4800
Cu	0.005	0.010	2
Zn	0.00125	0.005	4
B	0.002	0.005	2500
V	0.003	0.0003	0.1
As	0.0001	0.015	150
Mn	0.002	0.005	2.5
F	1	1.4	1400
Br	0.0025	66	26,000
Fe[a]	0.001	0.00005	0.05
Fe[b]	0.000	0.050	1.3
Co	0.00005	0.0001	2
Al	1	0.120	120
Ti	0.100	—	—

[a] Phytoplankton.
[b] Diatoms.

The fractions of these forms are controlled by the pH and the composition of the waters. The ionization constants for the three-step dissociation are defined by

$$K_1 = [H^+][H_2PO_4^-]/[H_3PO_4] \quad (8.4)$$

$$K_2 = [H^+][HPO_4^{2-}]/[H_2PO_4^-] \quad (8.5)$$

$$K_3 = [H^+][PO_4^{3-}]/[HPO_4^{2-}] \quad (8.6)$$

The pK's (–log K) for H_3PO_4 in water, NaCl (0.7m), and seawater (salinity [S] = 35) at 25°C are given in Table 8.2. The increase in the ionization as one goes from NaCl to seawater is related to the increase in ionic strength ($H_2O \rightarrow$ NaCl) and the formation of strong ion pairs (NaCl $\rightarrow$ seawater) of Ca^{2+} and Mg^{2+} with phosphate ions. For $M^{2+} = Mg^{2+}$ or Ca^{2+} we have

TABLE 8.2

Values of the pK_i for H_3PO_4 in Water, NaCl, and Seawater

Media	pK_1	pK_2	pK_3
H_2O	2.15	7.20	12.34
NaCl (0.7)	1.73	6.38	11.13
Seawater (S = 35)	1.57	5.86	8.69

TABLE 8.3

Values of Log K_{MX} for the Formation of Mg^{2+} and Ca^{2+} Phosphate Ion Pairs

Species (X)	log β_{MgX}	log β_{CaX}
$H_2PO_4^-$	0.14	–0.15
HPO_4^{2-}	1.23	0.97
PO_4^{3-}	3.36	4.51

$$M^{2+} + H_2PO_4^- \rightarrow MH_2PO_4^+ \tag{8.7}$$

$$M^{2+} + HPO_4^{2-} \rightarrow MHPO_4^0 \tag{8.8}$$

$$M^{2+} + PO_4^{3-} \rightarrow MPO_4^- \tag{8.9}$$

The association constants K_i^* for the formation of Mg^{2+} and Ca^{2+} phosphate ion pairs at I = 0.7 and 25°C are given in Table 8.3.

$$K_1^* = [MH_2PO_4^+]/[M^{2+}][H_2PO_4^-] \tag{8.10}$$

$$K_2^* = [MHPO_4^o]/[M^{2+}][HPO_4^{2-}] \tag{8.11}$$

$$K_3^* = [MPO_4^-]/[M^{2+}][PO_4^{3-}] \tag{8.12}$$

The fractions of the various forms of phosphate in a given medium can be calculated from

$$\alpha(H_3PO_4) = \{1 + K_1/[H^+] + K_1K_2/[H^+]^2 + K_1K_2K_3/[H^+]^3\} \tag{8.13}$$

$$\alpha(H_2PO_4^-) = \{1 + [H^+]/K_1 + K_2/[H^+] + K_3/[H^+]\} \tag{8.14}$$

$$\alpha(HPO_4^{2-}) = \{1 + [H^+]/K_2 + [H^+]^2/K_1K_2 + K_2K_3/[H^+]^3\} \tag{8.15}$$

$$\alpha(PO_4^{3-}) = \{1 + [H^+]/K_3 + [H^+]2/K_2K_3 + [H^+]^3/K_1K_2K_3\} \tag{8.16}$$

The dissociation constants for phosphoric acid are given by

$$\ln K_1 = 115.54 - 4576.752/T - 18.453 \ln T + (0.069171 - 106.736/T)\, S^{0.5} + (-0.01844 - 0.65643/T)\, S \tag{8.17}$$

$$\ln K_2 = 172.1033 - 8814.71/T - 27.927 \ln T + (1.3566 - 160.340/T)\, S^{0.5} + (-0.05778 + 0.37335/T)\, S \tag{8.18}$$

$$\ln K_3 = -18.126 - 3070.75/T + (2.81197 + 17.27039/T)\, S^{0.5} + (-0.09984 - 44.99486/T)\, S \tag{8.19}$$

The calculated percentage of the various forms of phosphate in H_2O, NaCl, and seawater as a function of pH are shown in Figure 8.1. At pH 8.1, the percentage of each species is given in Table 8.4.

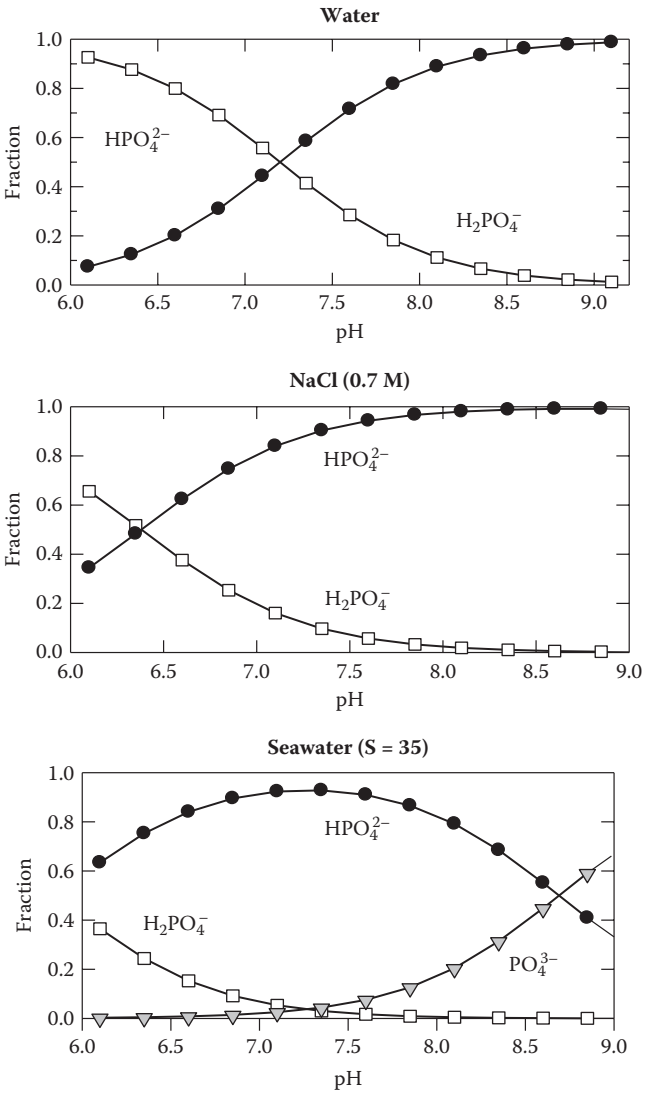

FIGURE 8.1
The various forms of phosphoric acid in water, NaCl (0.7 *M*), and seawater (S = 35).

TABLE 8.4

Percentage of Total Phosphate Species at 25°C and pH 8.1

Species	H_2O	NaCl	Seawater
H_3PO_4	0	0	0
$H_2PO_4^-$	11.2	1.9	0.5
$H_2PO_4^{2-}$	88.8	98.0	79.2
PO_4^{3-}	0	0.1	20.4

TABLE 8.5

The Effect of Pressure (P) on the Ionization Constants of H_3PO_4 in Seawater (25°C)

	K_1^P/K_1^0	K_2^P/K_2^0	K_3^P/K_3^0
0 bar	1.00	1.00	1.00
500	1.36	1.65	1.98
1000	1.78	2.61	3.64

TABLE 8.6

Percentage of the Various Forms of Phosphate in Seawater (S = 35, 25°C) as a Function of Pressure (bar)

Species	P = 0	P = 500	P = 1000
H_3PO_4	0	0	0
$H_2PO_4^-$	0.5	0.2	0.1
HPO_4^{2-}	79.2	66.1	51.6
PO_4^{3-}	20.4	33.7	48.3

TABLE 8.7

Percentage of the Various Forms of H_3PO_4 in Seawater at 25°C

X	Free X	Mg X	Ca X
$H_2PO_4^-$	92.3	7.0	0.7
HPO_4^{2-}	49.3	45.8	4.9
PO_4^{3-}	0.2	26.6	73.2

As one increases the pressure (or depth), the various forms of H_3PO_4 change because of the negative volume change that occurs for the ionization process. The ionized species are more highly charged and have a smaller molar volume. An increase in the pressure forces the equilibria to the smallest volume, and the dissociation constants become larger. The effect of pressure on the ionization of H_3PO_4 is given in Table 8.5. At pH 8.1, the various forms in seawater change as shown in Table 8.6. In deep waters, the PO_4^{3-} ion becomes a more important form (~50% at P = 1000 bar or 10,000 m). In all the calculations shown, the fractions of H_3PO_4 refer to the total concentrations. The speciation of the various forms of H_3PO_4 can be calculated from the ion-pairing constants given in Table 8.3. The results are given in Table 8.7. The $H_2PO_4^-$ is largely free (92%); the HPO_4^{2-} is 49% free, 46% as $MgHPO_4$ and 5% as $CaHPO_4$; PO_4^{3-} is 27% as $MgPO_4^-$ and 73% as $CaPO_4^-$.

Little is known of the nature of particulate phosphorus in seawater. One might expect particulate forms of inorganic P to regulate the maximum concentration of H_3PO_4 in seawater. The solubility product of $Ca_3(PO_4)_2$ has been estimated to be about 10^{-32}. This value can be used to estimate the equilibrium concentration of PO_4^{3-} in seawater:

$$K_{SP} = [Ca^{2+}]_T^3[PO_4^{3-}]_T^2\,\gamma_T^3(Ca^{2+})\,\gamma_T^2(PO_4^{3-}) \tag{8.20}$$

using $[Ca^{2+}] = 0.0108$, $\gamma_T(Ca^{2+}) = 0.28$, $\gamma_T(PO_4^{3-}) = 3.7 \times 10^{-5}$, this gives $[PO_4^{3-}]_T = 0.02 \times 10^{-6}$ M. One would also expect particulate organic phosphorus compounds from the breakdown of plants in surface waters. Since PO_4^{3-} can be absorbed on various surfaces, it may be associated with detrital material and clay minerals. In $CaCO_3$ environments, much of the phosphate is absorbed to carbonate minerals. Although one would expect concentrations of PO_4^{3-} in pore waters of sediments receiving organic matter, the concentrations are nearly undetectable in carbonate sediments (for example, in the Bahama islands sediments).

8.2.1 Determination of Phosphate

The determination of phosphate is carried out by treating an aliquot of seawater with an acidic molybdate reagent containing ascorbic acid and a small amount of potassium antimonyl tartrate. The resulting phosphomolybdic acid is reduced to give a blue-purple complex. The absorbance is measured at 885 nm with a spectrophotometer. The reduced heteropoly acid has a ratio of 1:12:1 for P:Mo:Sb. Polyphosphates do not react but can be determined after hydrolysis in acid media at 100°C. Before total P is determined, the organic compounds must be broken down by oxidation. This can be done by treating the sample with hydrogen peroxide and irradiating it for a few hours with high-intensity UV (ultraviolet) radiation. Organic phosphorus concentrations are determined by difference. Particulate P can be determined by filtration through a 0.45-μm filter.

The chemical reactions for the analysis are given by two steps. The formation of a yellow ammonium molybdiphosphate complex is indicated by

$$H_2SO_4 + (NH_4)_2MoO_4 \cdot 4H_2O + PO_4^{3-} \rightarrow NH_4P(Mo_3O_{10})_4 \tag{8.21}$$

On treatment with a reducing agent, such as ascorbic acid, the complex yellow acid is reduced to molybdenum blue.

The amount of molybdenum blue formed is proportional to the concentration of phosphorus present in the seawater as orthophosphate. The intensity of the color can be measured with a spectrophotometer that relates concentration to light absorbance. Arsenate ions can interfere with the analyses. The PO_4^{3-}, as well as other nutrients, is normally measured with an autoanalyzer. This system allows precise measurements in a short period of time. Johnson and Petty (1982) have described a flow injection technique to measure PO_4^{3-}. The precision of the technique is 1.5% at 3 μ*M*, and the detection limit is 0.05 μ*M*. The rate of analysis can be 90 samples per hour.

8.2.2 Distribution of Phosphate

The distribution of the various forms of phosphate in ocean waters is controlled by biological and physical processes. The phosphate cycle for the oceans is shown in Figure 8.2. In surface waters, PO_4^{3-} is taken up by phytoplankton during photosynthesis. Phosphorus compounds such as ATP (adenosine triphosphate) and nucleotide coenzymes play key roles

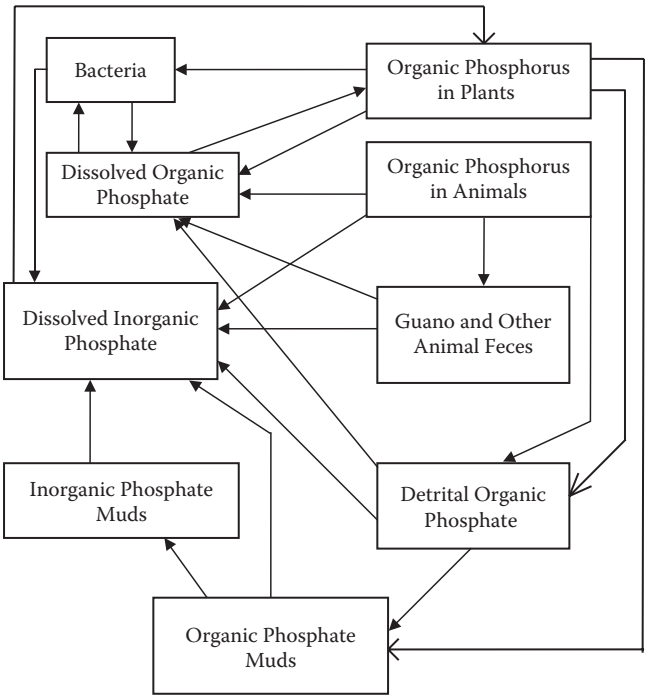

FIGURE 8.2
The phosphate cycle in ocean waters.

in photosynthesis and other processes in plants. Absorption and conversion to organic P compounds proceed even in the dark. Above a concentration of 0.3 μ*M*, the rate of growth of many species of phytoplankton is independent of the concentration of P. Below 0.3 μ*M*, cell division becomes inhibited, and P-deficient cells are produced. This probably does not occur in the oceans since NO_3^- is usually exhausted before PO_4^{3-} falls to a critical level.

When phytoplankton die, the organic P is rapidly converted to PO_4^{3-}. Much of the phytoplankton is consumed by zooplankton, which obtain PO_4^{3-} in the process. The unassimilated material is lost in fecal pellets, which contain appreciable amounts of organic P. Hydrolysis of organic P occurs rapidly through the action of phosphorylases. The excretion of P by zooplankton is minimal when phytoplankton are abundant and maximal when phytoplankton are not abundant. The low rate of excretion when food is abundant arises because phospholipids are being stored or used for egg production. When food is scarce, these trends are reversed, and P is excreted.

Typical profiles of total and inorganic P in the English Channel are shown in Figure 8.3. In the summer, nearly 50% of the P in surface waters is organic. In deeper waters, most of the P is in an inorganic form. In the winter, almost all the P is inorganic. The variations in coastal waters are the result of upwelling and phytoplankton blooms. Surface mixing in the winter can cause linear profiles of P in nearshore waters. After spring and summer blooms, the PO_4^{3-} is decreased considerably. In the Chesapeake Bay, phosphate decreases from 0.4 to 0.1 μ*M* can occur at 3:00 p.m. After sunset, the values rapidly increase to a maximum at 2:00 a.m.

Typical profiles of PO_3^{3-} in the Atlantic and Pacific (from World Ocean Circulation Experiment [WOCE] measurements) are shown in Figure 8.4. The surface values are nearly

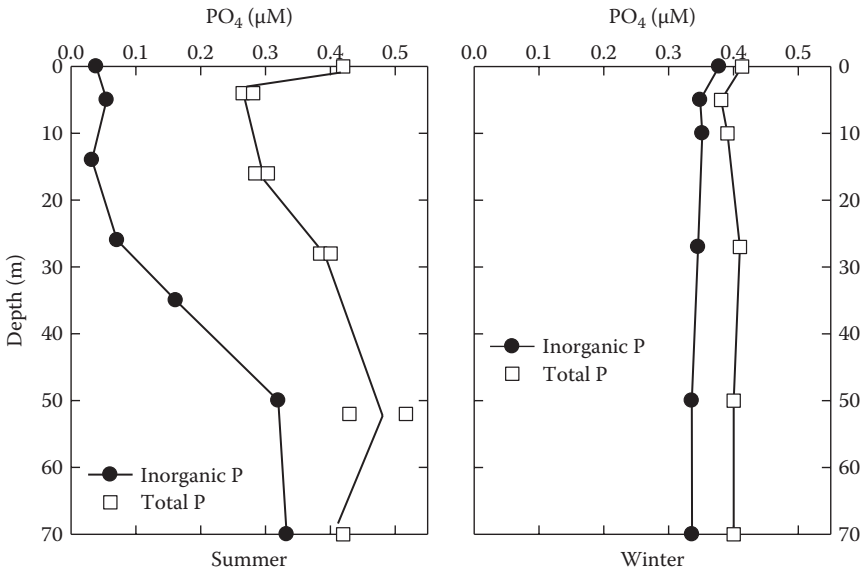

FIGURE 8.3
Typical profiles of total and inorganic phosphate in the English Channel.

zero. As phytoplankton and other organisms die, the PO_4^{3-} is regenerated in the water column. A maximum occurs in both oceans near 1000 m, which is the same depth as the O_2 minimum layer. The maximum values in the Atlantic are about 1.5 μ*M*, while in the Pacific, values of about 3.2 μ*M* occur. The higher values in the Pacific (and Indian) Ocean compared to the Atlantic are due to the waters being older (thus accumulating more oxidized plant material). Sections of PO_4^{3-} in the Atlantic, Pacific, and Indian Oceans are shown in Figure 8.5. The values generally follow the movement of the major water masses. The values in deep waters increase from the North Atlantic to the North Pacific and Indian Oceans.

8.3 Nitrogen Compounds in Seawater

In addition to N_2, the sea contains small amounts of inorganic and organic nitrogen compounds (about 1/10 the concentration of N_2). The forms can be dissolved or particulate and subdivided into organic and inorganic. The principal inorganic forms are NO_3^- (1 to 500 μ*M*), NO_2^- (0.1 to 50 μ*M*), and $NH_3 + NH_4^+$ (1 to 50 μ*M*). Small amounts of nitrous oxide, hydroxylamine, and hyponitrite ion also occur. The difficulty with nitrogen compounds is that they can exist in nine oxidation states (see Table 8.8).

The ammonia ion can exist in two forms depending on the pH. The dissociation of NH_4^+ is given by

$$NH_4^+ + H^+ + NH_3 \tag{8.22}$$

and has a pK of 9.5 at 25°C in seawater. At a pH of 8.1, 95% of the total ammonia is NH_4^+, and 5% is NH_3. The dissociation constant of ammonia (NH_4^+) can be determined from

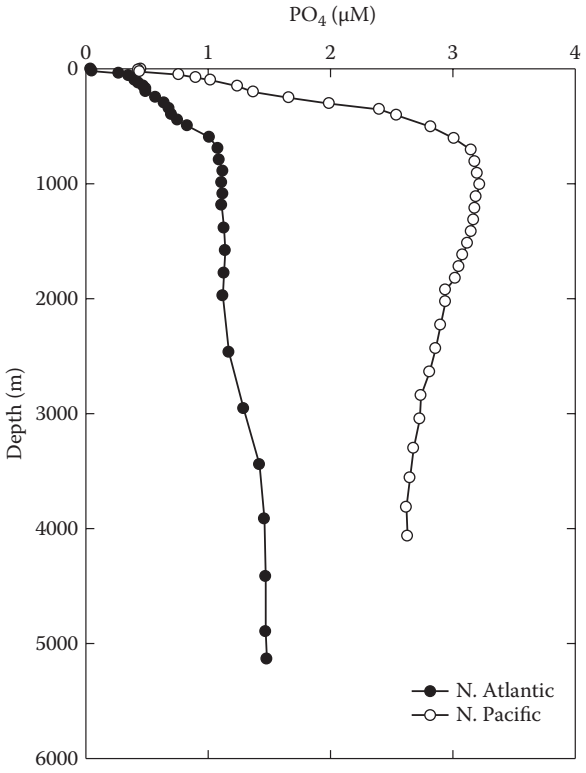

FIGURE 8.4
Profile of phosphate in the Atlantic and Pacific Oceans.

$$\ln K_{NH_4} = -6285.33/T + 0.0001635\,T - 0.25444 + (0.46532 - 123.7184/T)\,S + (-0.01992 + 3.17556/T)\,S \tag{8.23}$$

8.3.1 Determination of Nitrogen Compounds

Before looking at nitrate cycles in the oceans, it is of value to briefly mention the methods used to determine NO_3^-, NO_2^-, and NH_4^+. The inorganic forms of N are normally determined by colorimetric methods using an auto analyzer. NO_2^- is determined by treating the water sample with a solution of sulfanilamide. The resultant diazonium ion is coupled with N-(1 naphthyl)-ethylenediamine to give a pink azo dye. The absorbance is measured at 543 nm with a spectrophotometer. The reactions are as follows:

$$\underset{}{NH_2{-}C_6H_4{-}SO_2NH_2} + NO_2^- + 2H^+ \rightarrow \underset{\text{Diazonium ion}}{{}^+N{\equiv}N{-}C_6H_4{-}SO_2NH_2} + \underset{\text{Sulfanilamide}}{} H_2O \tag{8.24}$$

$$\underset{\text{Naphthyl-ethylenediamine}}{NH_2CH_2CH_2NH{-}C_{10}H_7} + \underset{\text{Diazonium ion}}{{}^+N{\equiv}N{-}C_6H_4{-}SO_2NH_2} \rightarrow$$

$$\rightarrow \underset{\text{Pink azo dye}}{NH_2CH_2CH_2NH{-}C_{10}H_6N{=}N{-}C_6H_4{-}SO_2NH_2} + H^+ \tag{8.25}$$

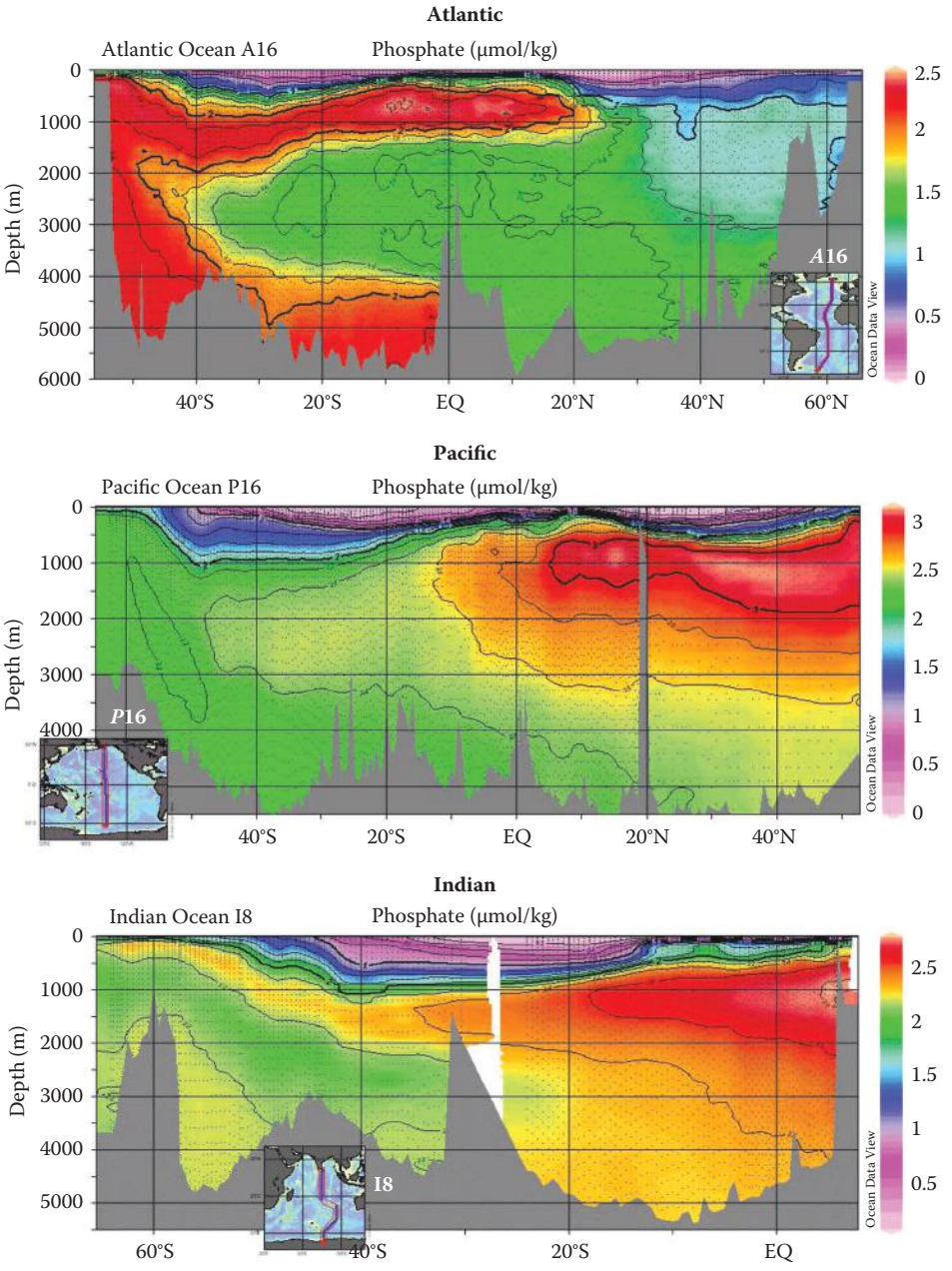

FIGURE 8.5
Sections of phosphate in the Atlantic, Pacific, and Indian Oceans.

NO_3^- is determined by reducing it to NO_2^-, which is analyzed as given. The reduction is carried out by treating the sample with NH_4Cl or EDTA (ethylenediamine N,N,N,N′ tetraacetic acid) and passing it through a glass column packed with amalgamated or copper-coated cadmium filings. No completely satisfactory method exists for the routine analysis of NH_3 and NH_4^+, which are at very low concentrations in oxygenated

TABLE 8.8

The Various Oxidation States of Nitrogen

Oxidation State	Compound
+5	NO_3^-, N_2O_5
+4	NO_2
+3	HONO[a], NO_2^-, N_2O_3
+2	HONNOH[b], $HO_2N_2^-$, $N_2O_2^{2-}$
+1	N_2O
0	N_2
–1	H_2NOH, HN_3, N_3^-, NH_2OH
–2	H_2NNH_2
–3	RNH_4, NH_3[c], NH_4^+[c]

[a] pK = 3.35.
[b] $pK_1 = 7.05$, $pK_2 = 11.0$.
[c] $pK_B = 4.75$, $pK_A = 9.48$.

seawater. At present, two methods are being used (certain organic N compounds can cause interference):

1. NH_3 is oxidized to NO_3^- by alkaline hypochlorite. The excess hypochlorite is then reduced with arsenite and the NO_2^- determined as presented.
2. NH_3 is oxidized in an alkaline citrate medium with Na hypochlorite and phenol in the presence of catalytic amounts of Na nitroprusside. A blue indophenol dye is produced and is measured with a spectrophotometer (Catalano, 1987).

Johnson and Petty (1983) have described an inexpensive and reliable flow injection method that can be used to determine nitrate and nitrite in seawater. The chemistry is similar to that described, and the system is automated. It can make 75 determinations per hour, has a detection limit of 0.1 μ*M*, and has a precision of 1% at levels above 10 μ*M*.

8.3.2 Distribution of Nitrogen Compounds

The nitrogen cycle in the oceans is shown in Figure 8.6. There are three major inputs of nitrogen to ocean waters:

1. Volcanic activity (NH_3)
2. Atmospheric (NO_2 from nitrogen fixation)
3. Rivers (fertilizers)

The components of the nitrogen cycle involve a number of oxidation and reduction processes. Nitrates are taken from surface waters during primary productivity. When the plants die and decompose, nitrogen compounds are regenerated to the water column. Marine birds can also cause a loss of nitrogen as $NaNO_3$ in guano. The large deposits of $NaNO_3$ in Chilean deserts could also have been formed by bacteria fixation or volcanism. Nitrogen can be lost back to the atmosphere as N_2O. As discussed, this gas can react with ozone. The assimilation of fixed nitrogen (NH_3, NO_2^-, and NO_3) by phytoplankton takes place in the euphotic zone during photosynthesis. The NH_3 or NH_4^+ form is usually

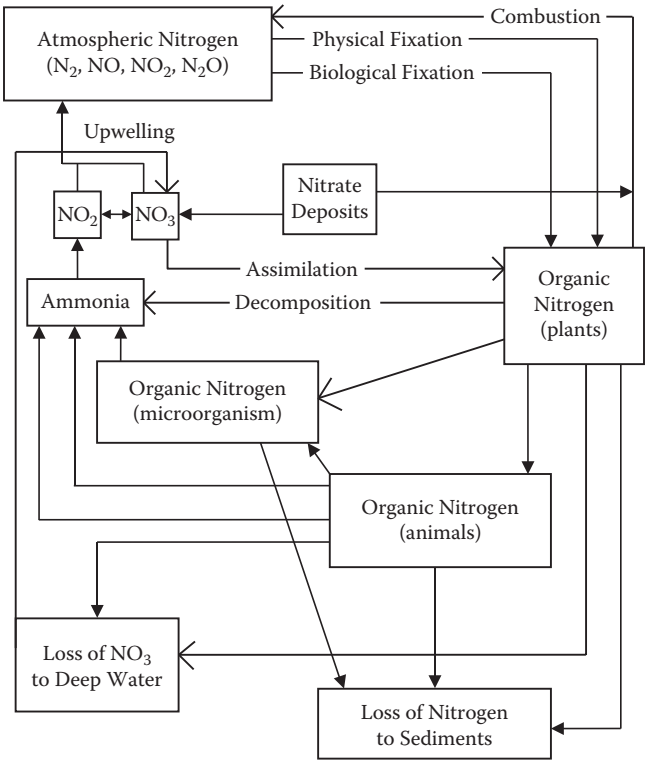

FIGURE 8.6
The nitrogen cycle in ocean waters.

preferred. The uptake shows a direct hyperbolic behavior that increases to a maximum rate at a given nutrient concentration. When nitrate is below 0.7 μ*M*, nitrogen-deficient cells are produced before cell division stops. These cells can take up NH_3 and NO_3^-, but not NO_2^-, in the dark. Some phytoplankton can utilize amino acids, as can some diatoms with the help of bacteria. In polluted waters, a significant amount of NO_3^- can be obtained from organic nitrogen. Urea is also used in restricted coastal and estuarine areas.

The conversion of NO_3^- to amino acids requires the formation of NH_3:

$$NO_3^- + 2H^+ + 2e \rightarrow NO_2^- + H_2O \tag{8.26}$$

$$2NO_2^- + 4H^+ + 4e \rightarrow N_2O_2^{2-} + 2H_2O \tag{8.27}$$

$$N_2O_2^{2-} + 2H^+ + 2e \rightarrow NH_3 + H_2O \tag{8.28}$$

where $N_2O_2^{2-}$ is hyponitrite, and NH_2OH is hydroxylamine. The first step is catalyzed by coenzyme II. The NH_3 is converted to glutamic acid by

$$\begin{aligned} &HOOC^-CO^-(CH_2) + NH_3 + 2NADPH \\ &\rightarrow HOOC^-CH(NH)_2CH_2CH_2COOH + 2NADP + H_2O \end{aligned} \tag{8.29}$$

The acid reacting with NH_3 is called ketoglutaric acid. Twenty other amino acids are formed from glutamic acid by transamination. The formation of alanine, for example, is formed from pyruvic acid:

$$\begin{aligned} &CH_3COCOOH + HOOC^-CH(NH_2)CH_2CH_2COOH \\ &\rightarrow CH_3CH(NH_2)COOH + HOOC^-CO(CH_2)_2COOH \end{aligned} \tag{8.30}$$

Proteins are formed by the linking of the various amino acids by reactions involving RNA and DNA and using energy from ATP.

NO_3^- is regenerated mainly by bacterial oxidation of organic nitrogen. When cells die, they undergo rapid autolysis, releasing NH_3 and PO_4^{3-}. The decomposition of organic nitrogen compounds to NO_3^- takes place in a number of steps. This is shown in Figure 8.7 for the bacterial oxidation of dead organisms. A small percentage of the particulate organic nitrogen is resistant to bacterial attack and can be accumulated in the sediments.

Details of the biogeochemical processes that involve nitrogen compounds are shown in Figure 8.8. The processes shown in the figure by number include

1. *Anammox*. The Anammox process has recently been added to the cycling of nitrogen in surface ocean waters with low concentrations of O_2. This process was first discovered in sanitation plants. It is the reaction of nitrite and ammonia to form nitrogen:

$$NO_2^- + NH_4 \rightarrow N_2$$

2. *Nitrogen fixation*. Nitrogen fixation is the conversion of nitrogen gas to ammonium ($N_2 \rightarrow NH_4$). Bacteria on land plants and blue-green algae, molds, and yeast

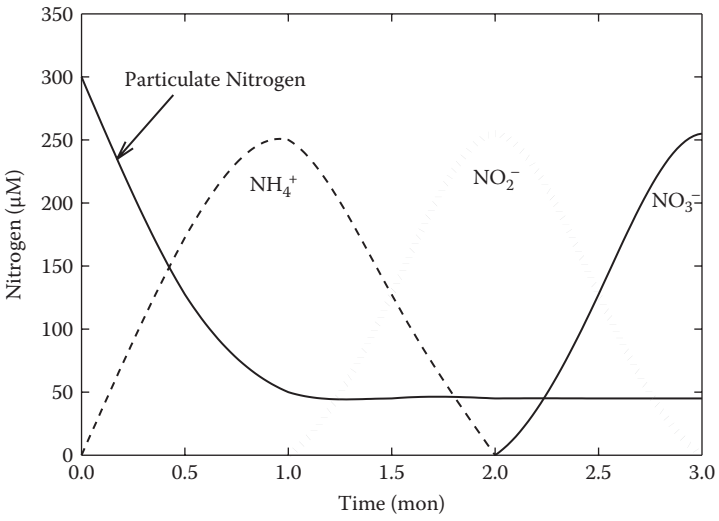

FIGURE 8.7
The decomposition of organic nitrogen by bacterial oxidation.

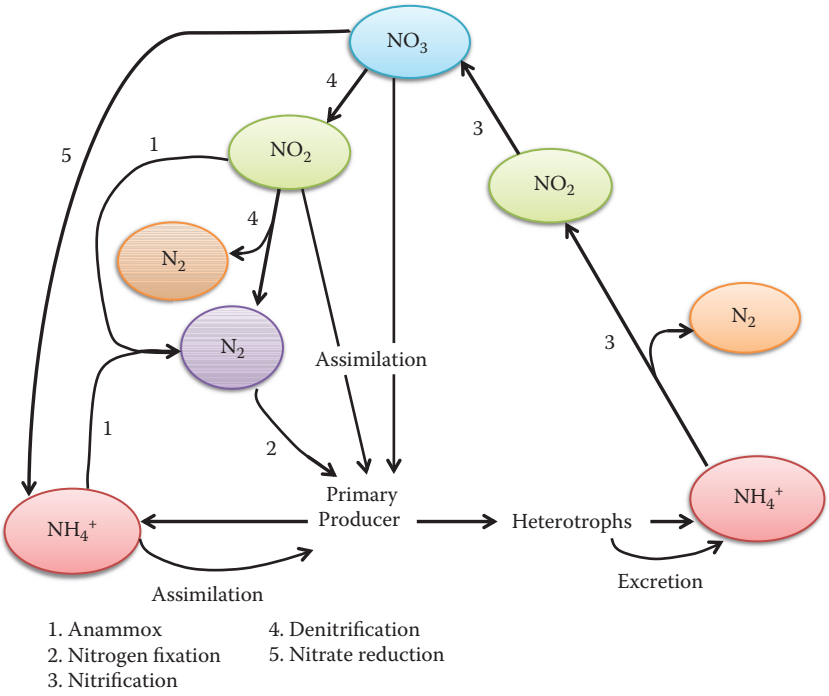

FIGURE 8.8
The biochemical cycles of nitrogen in ocean waters.

can fix nitrogen. In the oceans, blue-green algae, or more correctly cyanobacteria, are the main nitrogen fixers (Howells and Geesey, 2010). The major species is *Trichodesmium* (Capone, 1997). Since Fe is needed by the enzyme, it was thought that the fixation was higher in the Atlantic (due to Fe from African dust), but it appears to be higher in the Pacific (Howells and Geesey, 2010).

3. *Nitrification*. Nitrification is the oxidation of NH_3 to NO_3^-. This process yields NO_2^- as an intermediate and is carried out by bacteria in the water column and in the sediments. It may lead to NO_2^- in upwelled waters off Peru. Bacteria are also capable of reducing NO_3^- to NO_2^-. This reduction was thought to occur in waters with high organic levels, but it is now thought to occur in low-oxygen waters.

$$NH_4^+ \rightarrow NO_2^- \rightarrow NO_3^-$$

4. *Denitrification*. Most denitrification ($NO_3^- \rightarrow NO_2^- \rightarrow N_2O$ or N_2) occurs by bacterial growth in anoxic waters. The NO_3^- is used as an electron acceptor instead of O_2. This process can also occur in waters with O_2 less than 2 μ*M*. It is hard to detect changes in the concentrations of N_2 in ocean waters due to the large dissolved N_2 from the dissolution in the oceans.
5. *Nitrate Reduction*. Nitrate reduction ($NO_3^- \rightarrow NH_4^+$) occurs in low-oxygen areas of the ocean by bacteria. The reduction stops at NH_4^+. As will be discussed, the generated ammonium may help the anammox process.

Typical profiles of NO_3^- in the Atlantic and Pacific Oceans are shown in Figure 8.9. Surface waters have very low levels; the deep waters have significant concentrations.

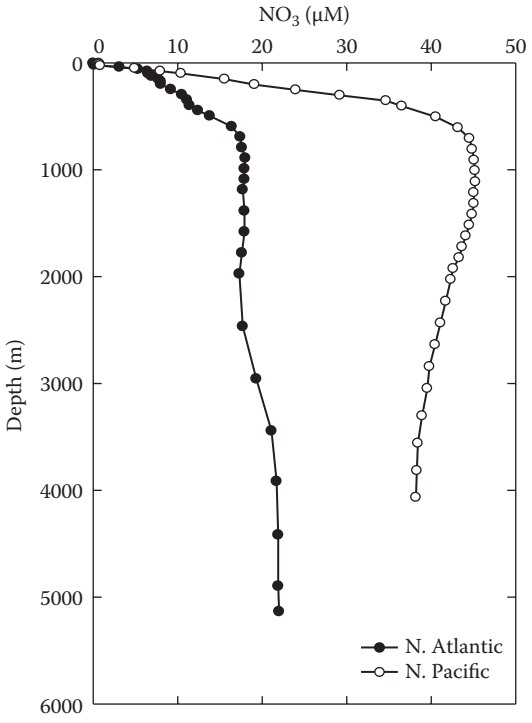

FIGURE 8.9
Profiles of nitrate in the Atlantic and Pacific Oceans.

The higher concentrations in the deep Pacific are the result of the waters being older and accumulating more NO_3^-. Sections of NO_3^- in the Atlantic, Pacific, and Indian Oceans are shown in Figure 8.10. As with PO_4^{3-}, the values follow the major water masses and increase in the deep waters from the North Atlantic to the North Pacific and North Indian Oceans. In coastal areas, there is frequently a seasonal variation of inorganic nitrogen (see Figure 8.11). In the spring, rapid removal occurs because of phytoplankton growth. The phytoplankton are consumed by zooplankton and fish, returning the NH_4^+ and NO_3^- to the water. In the summer, the thermocline prevents vertical mixing or replenishment of surface waters. This can deplete the nutrients enough to prevent further primary productivity. In upwelling areas, NO_3^- is not limiting. The oxidation of plant material causes the NO_3^- to maximize just below the oxygen minimum. The changes in the nitrate plus nitrite in surface waters at the Bermuda Atlantic Time Series (BATS) station over the years are shown in Figure 8.12. This figure clearly shows the cyclic variations of nitrate in surface waters caused by winter mixing. The variations in the nitrate result in similar variation in the primary production that occurs in these waters.

The distribution of NO_2^- in the low ocean waters (100 to 300 m) shows two maxima in the Arabian Sea (Figure 8.13), one just below the photosynthetic compensation depth and the other in the oxygen minimum zone. The first maximum is due to the oxidation of NH_3 ($NH_3 \rightarrow NO_2^- \rightarrow NO_3^-$). The second maximum that occurs in the Arabian Sea and certain areas of the Pacific is caused by the bacterial reduction of NO_3^-. When the O_2 levels are low, the bacteria use NO_3^- as a source of oxygen.

Recent studies have contrasted the nitrogen cycles in the Arabian Sea and Eastern Tropical South Pacific (ETSP) as shown in Figure 8.14. In the Arabian Sea at the low oxygen

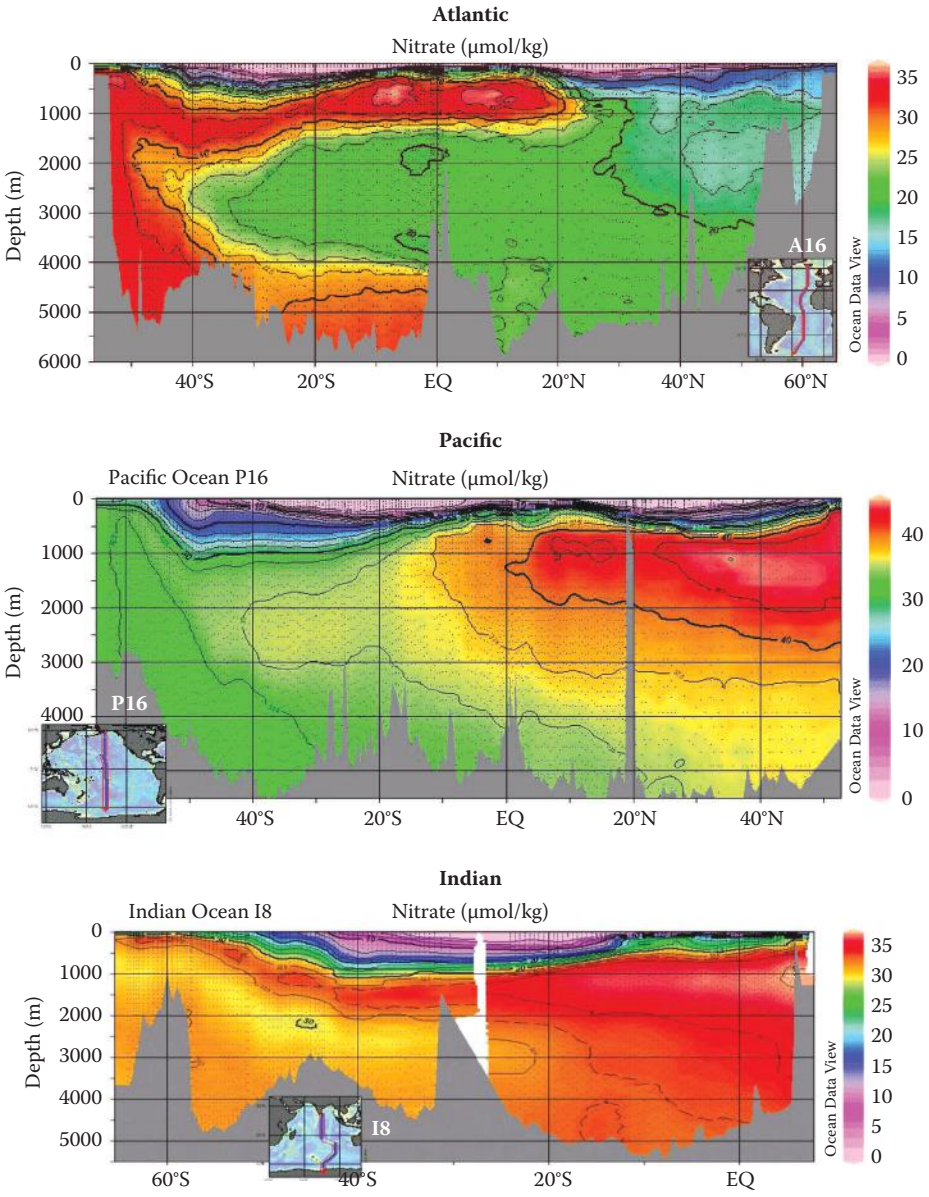

FIGURE 8.10
Sections of nitrate in the Atlantic, Pacific, and Indian Oceans.

levels, denitrogenation is more important than anammox. In the ETSP, anammox is an important way N_2 is formed. The anammox is fueled by the NH_4 from dissimilatory nitrate reduction to anammox (DNR).

As discussed, N_2O is formed in the oxygen minimum layer. This is shown in Figure 8.15, where the estimated concentration of NO_3^- is compared to the values calculated from the concentration of PO_4^{3-} and assuming N/P = 16. This deficiency in NO_3^- is due to the amount used by bacteria to oxidize organic carbon in water with low oxygen. The nitrate is reduced to N_2O as is shown in Figure 8.15. The excess N_2O

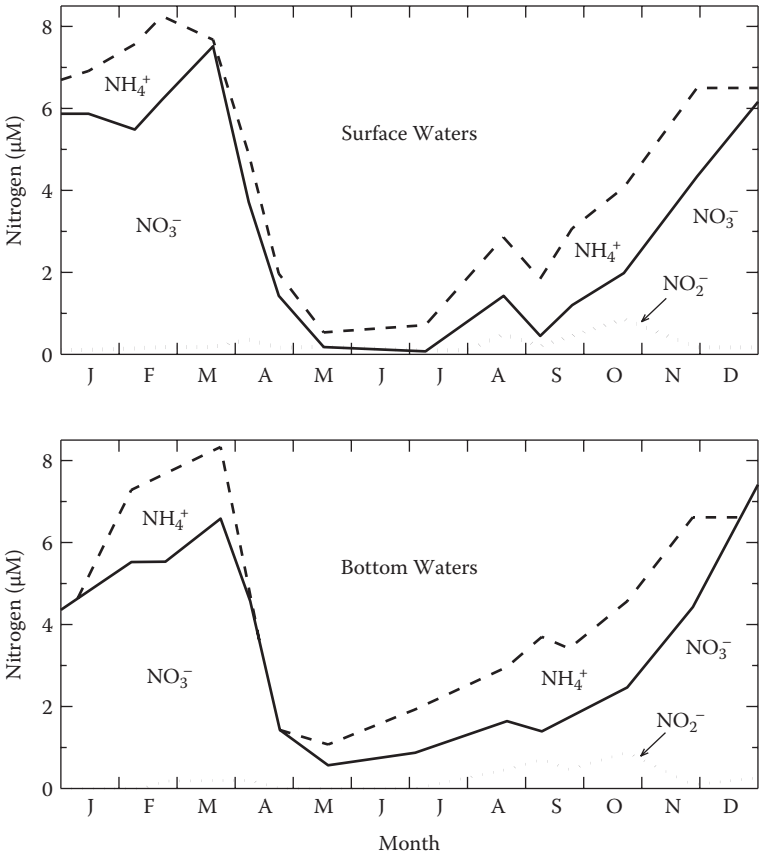

FIGURE 8.11
Seasonal distribution of nitrogen species in the English Channel.

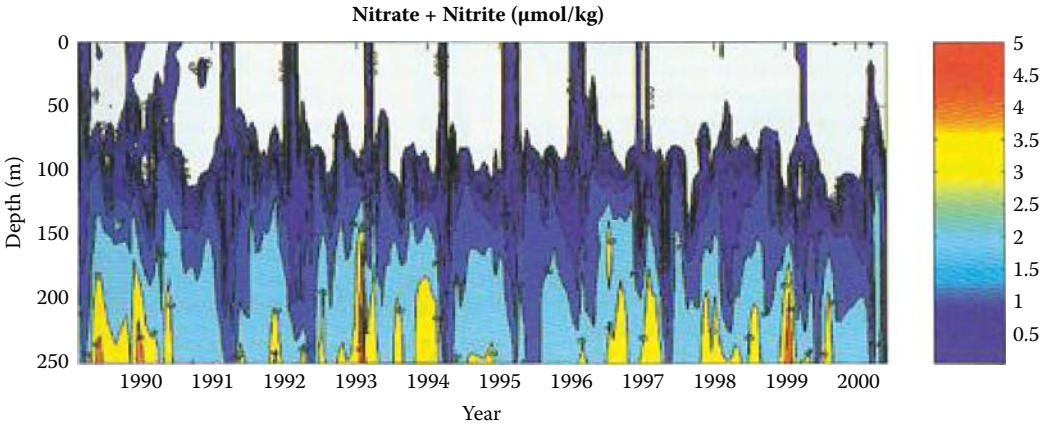

FIGURE 8.12
The variations of NO_3^- + NO_2^- at the Bermuda Time Series station.

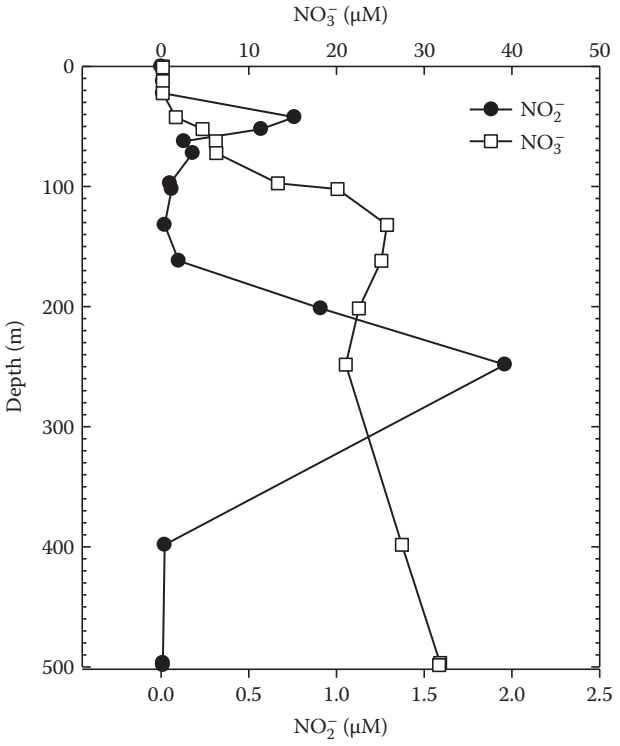

FIGURE 8.13
Profiles of nitrite and nitrate in the Arabian Sea.

produced is proportional to the AOU (apparent oxygen utilization). One molecule of N_2O is produced for every 10,000 molecules of O_2 utilized by NO_3^-. When the waters have low concentrations of oxygen, the relationship between N_2O and O_2 is broken (see Figure 8.16). This is caused by the utilization of N_2O as a source of oxygen when O_2 levels are very low.

8.3.3 Dissolved Organic Nitrogen and Phosphate

As shown previously (Figure 8.3), the total organic phosphate in ocean waters is defined as the differences between the total and inorganic value. Total organic nitrate can be described in a similar manner.

$$TOP = [PO_4]_T - [PO_4]$$

$$TON = [NO_3]_T - [NO_3]$$

It should be pointed out that the dissolved organic nitrogen (DON) and phosphate (DOP) are the values after filtration. The differences are small for most waters. Abell, Emerson, and Renaud (2000) examined the distribution of TOP, TON, and TOC in a North Pacific subtropical gyre. The Abell, Emerson, and Renaud (2000) surface water results are summarized in Figure 8.17. The values of TOP and TON in surface waters are 83 and 98%,

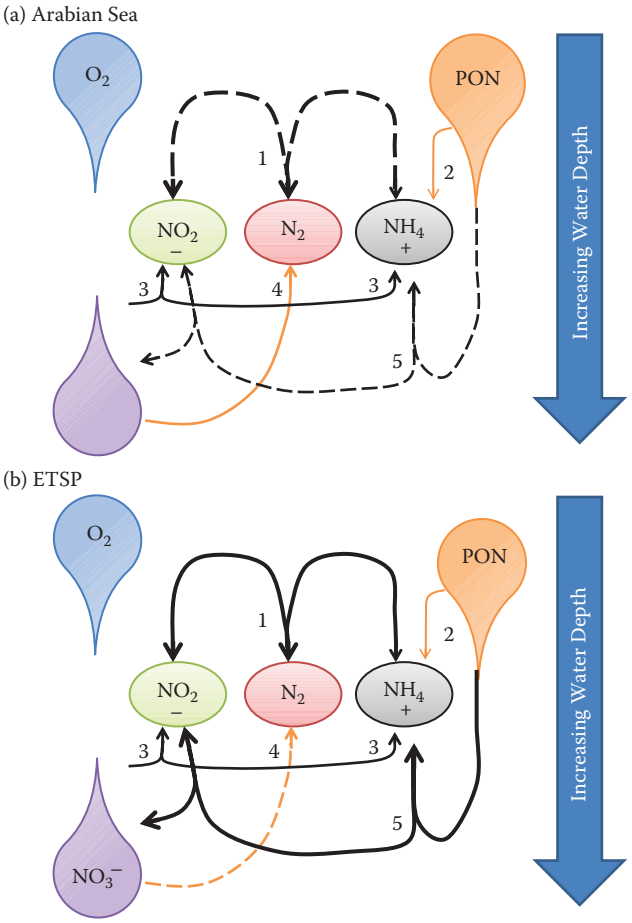

FIGURE 8.14
Nitrogen cycles in the (a) Arabian Sea and (b) Eastern Tropical South Pacific (ETSP). PON, particulate organic nitrogen.

respectively, of the total dissolved PO_4 and NO_3. The TOP values are higher than the PO_4 concentrations over most of the surface with the exception of the subarctic, where PO_4 is higher due to the outcropping of deep waters. The TOP in the surface waters is higher over the entire range of studies. These values of TON and TOP may be an important source of NO_3 for plants. The N/P ratios of TON to TDN (total dissolved nitrogen) vary between 15 and 42 over this range. As discussed in the next sections, this is a much larger range than the ratios for inorganic nitrogen and phosphate.

Knapp et al. (2005) have shown that the nitrogen isotopic composition ($^{15}N/^{14}N$) of DON in the Atlantic can better constrain the dynamics of DON pool and nitrogen fixation at the BATS station. The bulk and higher molecular weight DON have a $^{15}N/^{14}N$ that is higher than the suspended particulate organic nitrogen. Knapp et al. (2011) have more recently examined the $^{15}N/^{14}N$ of DON in the Atlantic and Pacific surface waters (0 to 300 m). The average DON in the upper 100 m in both oceans was similar (4.5 to 5.0 μ*M*). This indicates that DON was participating in the nitrogen cycle in both regions. The average $\delta^{15}N$ of DON is different from N_2 in air (3.9% in the Atlantic and 4.7% in the Pacific). They have developed a model to explain these results. The DON is produced from particulate organic

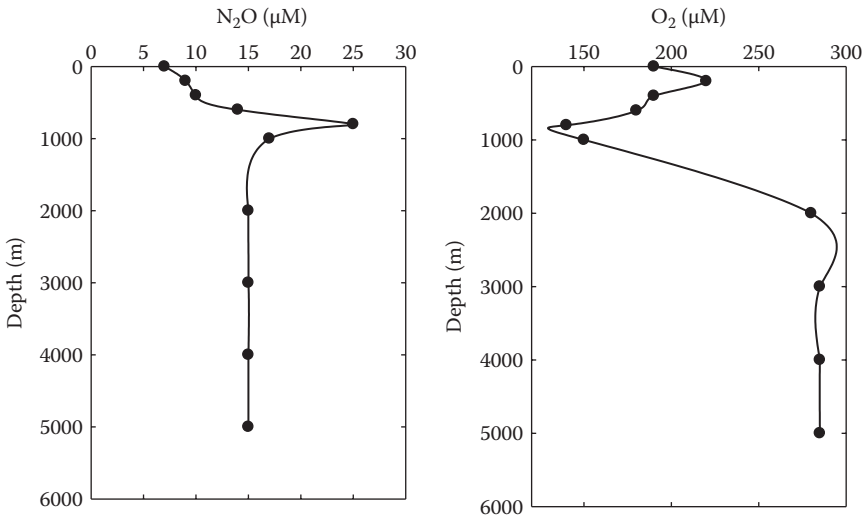

FIGURE 8.15
Profiles of nitrogen oxide and oxygen in the Atlantic Ocean.

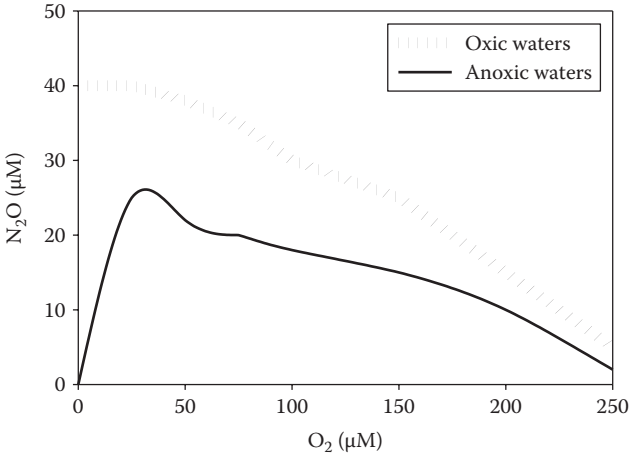

FIGURE 8.16
The relationship between nitrogen oxide and oxygen in Pacific Ocean waters.

matter without fractionation, and DON removal is by fractionation. The NH_4 produced and organic nitrogen compounds are taken up by plankton. In summary, the measurements of $^{15}N/^{14}N$ can be useful in understanding the complications that control nitrogen in the surface oceans.

8.3.4 Nitrogen–Phosphorus Ratio

The N:P ratio assimilated from seawater by phytoplankton as they grow is about 15:1. Lower values are found in coastal waters. For example, in the English Channel, winter values are 10.5:1, while in the summer they are 19:1. The P:N:C ratio in phytoplankton is 1:16:106 (Redfield, 1958). From Liebig's law of minimum (the concentration present in

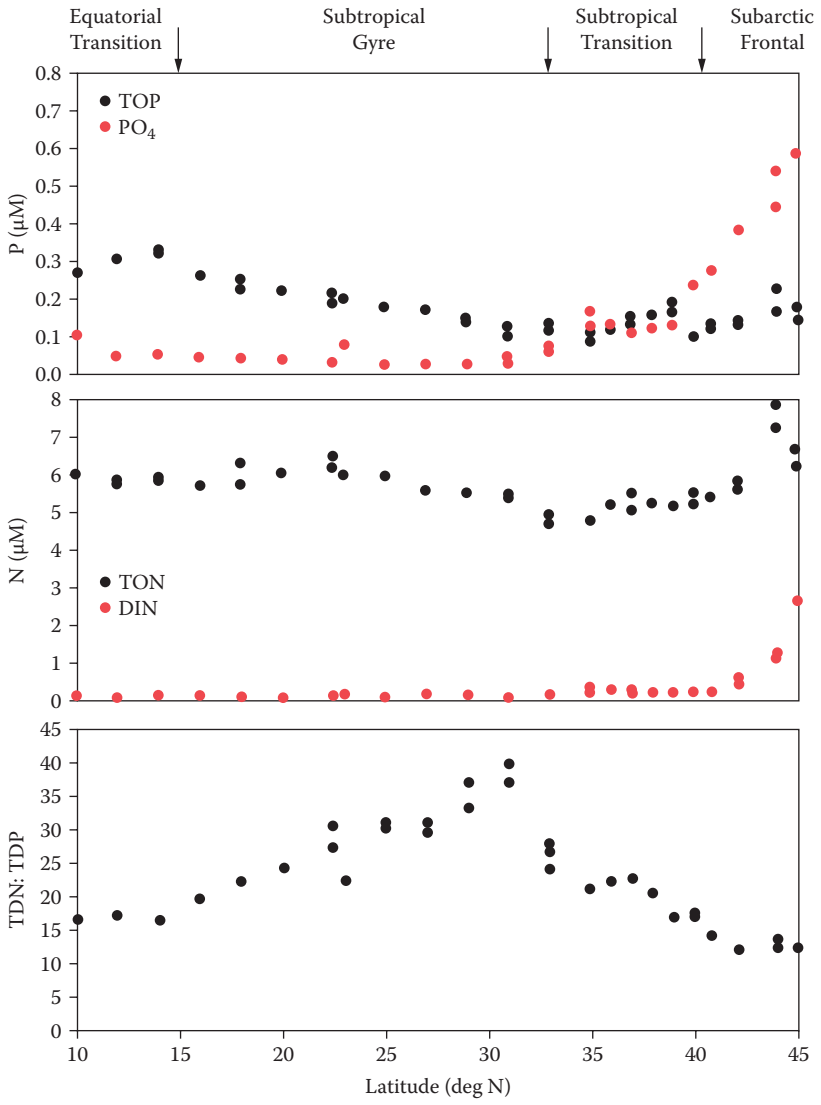

FIGURE 8.17
The distribution of TOP, TON, and TOC in North Pacific waters. TDP = total dissolved phosphorus. (Adapted from Abell et al., *J. Mar. Res.* 58, 203–222, 2000.)

the smallest quantity relative to the requirement for growth of an organism will be the limiting factor), it is clear that the P:N is limiting compared to carbon (the actual P:C ratio is ~1000). Typical values of N:P in the North Atlantic and Pacific Oceans are shown in Figure 8.18. The ratios of the waters in the Atlantic vary from 16:1 at the surface to 15:1 in deep waters. The deep waters in the Pacific are also close to 15:1, but the waters in the O_2 minimum layer are as low as 14:1. This is due to the conversion of NO_3^- to N_2O in these low-oxygen waters as discussed previously.

The higher values of the N and P in the North Atlantic may be due to nitrogen fixation. The values of N and P from the WOCE studies on some cruises in the Atlantic (A16), Pacific (P16), and Indian Oceans (I8) are shown in Figure 8.19. The least-square values of the ratios

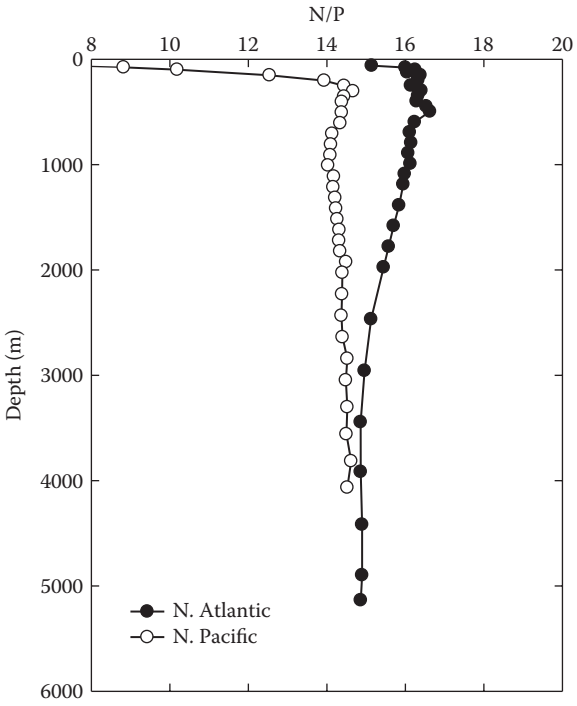

FIGURE 8.18
The nitrogen-to-phosphate molar ratios in the North Atlantic and Pacific Oceans.

are 15.3 ± 0.7, 15.3 ± 0.9, and 15.3 ± 0.8, respectively, for the Atlantic, Pacific, and Indian Oceans. The values in the Atlantic show a reasonable distribution around the fitted line. The values of NO_3^- at low ratios of N:P in the Pacific and Indian Oceans go to zero before PO_4^{3-}. This clearly shows that nitrate is limiting to growth in these surface waters. At high values of N and P the values show a negative deviation from the regression line. This is related to the use of NO_3^- as an oxidant by bacteria when the oxygen levels are very low.

The differences in the N:P ratio in the surface waters in the Atlantic and Pacific from the BATS and Hawaii Ocean Time Series (HOT) stations are shown more clearly in Figure 8.20. The high values of N and P in the waters off Bermuda are due to nitrification ($N_2 \rightarrow NH_3 \rightarrow NO_3^-$) by cyanobacteria, while the low values off Hawaii are due to denitrification ($NO_3^- \rightarrow N_2O$ or N_2) by bacteria.

In 1934, Redfield examined the relationship between the concentrations of O_2, CO_2, NO_3^-, and PO_4^{3-} in seawater based on the average chemical composition of plankton. This relationship predicts the ratio of oxygen consumption to nutrient production caused by biological oxidation. In the North Atlantic, he found an N:P ratio of 20:1. He also found an apparent O_2 utilization to NO_3^- of 6:1. He found variations that he attributed to preformed concentrations in the deep waters that originated before the waters sank. He estimated an N:C ratio of 1:7. He proposed an oxidation ratio of P:N:C of 1:20:140 accompanied by 120 units of O_2. These ratios supported the plankton sample ratios of 1:18:137. Redfield, Ketchum, and Richards (1963) proposed a revised ratio of 1:16:106:138 for P:N:C:O. These results led to the following equation for the oxidation of plant material:

$$(CH_2O)_{106}(NH_3)_{16}(H_3PO_4) + 138O_2 \rightarrow 106CO_2 + 122H_2O + 16HNO_3 + H_3PO_4 \qquad (8.31)$$

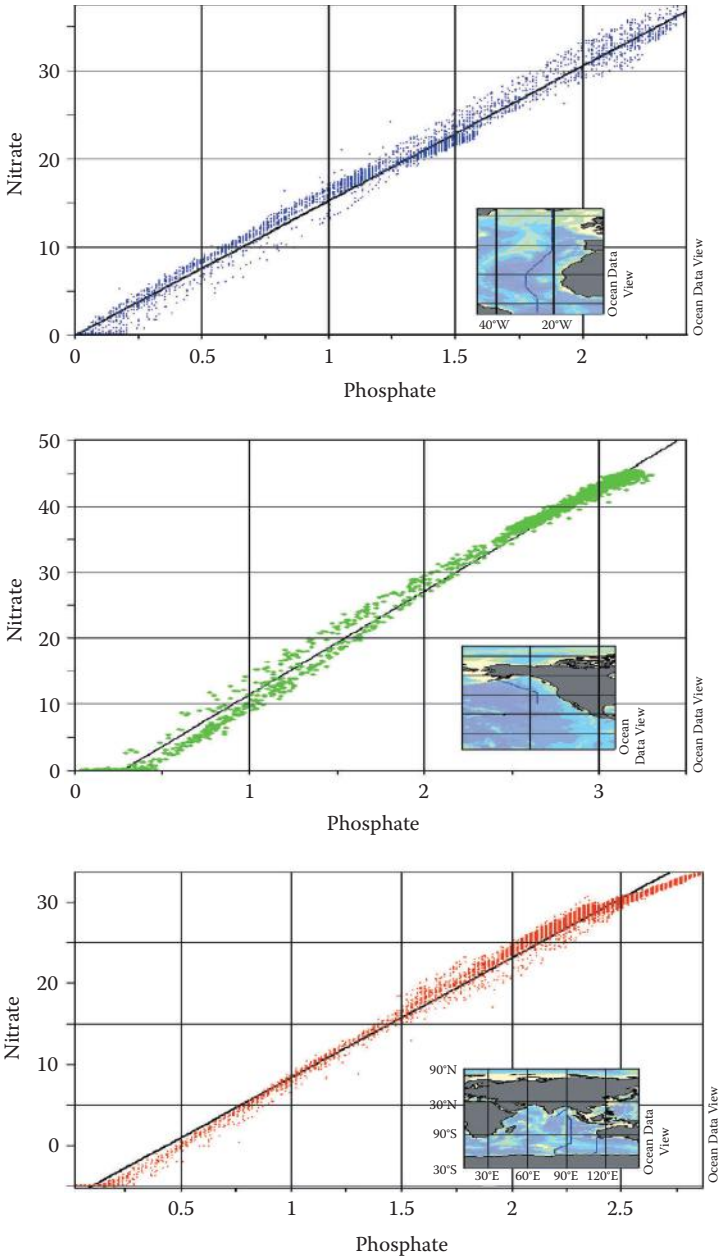

FIGURE 8.19
Correlations of the molar ratio of nitrogen to phosphate for the three major oceans.

where the first compound is a hypothetical organic molecule containing the C:N:P ratio of average plankton. This equation assumed a C:O_2 ratio of 1:1, an N:O_2 ratio of 1:2, and a computed P:O_2 ratio of 1:138. The O_2 rate was not based on observations made in the oceans.

To test the Redfield (1958) model (Redfield et al., 1963), one normally examines a plot of AOU versus the concentrations of nutrients arising from the oxidation. A number of workers have tested this model by examining values of O_2:PO_4^{3-} and O_2:NO_3^- in the Atlantic and

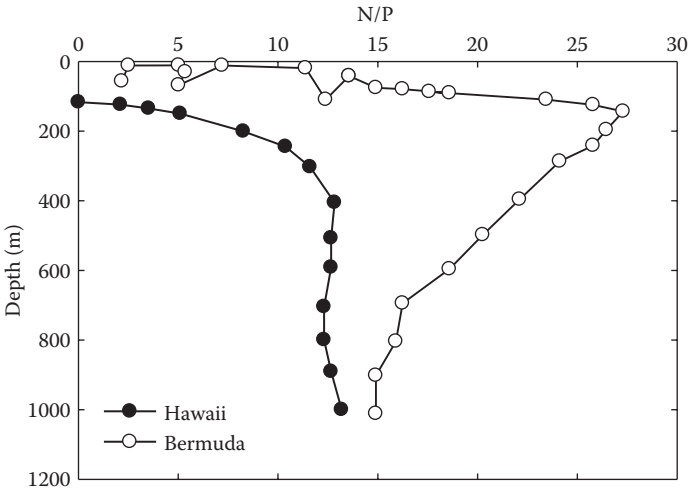

FIGURE 8.20
The nitrogen-to-phosphate molar ratio at the Bermuda and Hawaii time series stations.

TABLE 8.9

Molecular Ratios of P, N, C, O_2, and $CaCO_3$ Changes in the Atlantic and Indian Oceans

Location	Surface	P	N	CO_2	$(O_2\text{-}2N)$	O_2	$CaCO_3$
North Atlantic	27	1	17.6 ± 0.6	97 ± 9	130 ± 6	165 ± 7	15 ± 4
	27.2	1	16.8 ± 0.5	88 ± 6	139 ± 6	173 ± 6	8 ± 3
South Atlantic	27	1	16.7 ± 0.7	102 ± 7	131 ± 6	165 ± 6	8 ± 2
	27.2	1	16.7 ± 1.2	95 ± 10	150 ± 2	182 ± 9	8 ± 4
Mean Atlantic		1	17 ± 0.4	96 ± 6	138 ± 9	171 ± 8	10 ± 4
South Indian	27	1	15.2 ± 0.6	112 ± 6	138 ± 7	169 ± 8	15 ± 4
	27.2	1	14.5 ± 0.5	125 ± 7	145 ± 5	174 ± 6	19 ± 6
Mean Indian		1	14.9 ± 0.4	119 ± 5	142 ± 5	172 ± 5	17 ± 4
Overall mean		1	16.3 ± 1.1	103 ± 14	140 ± 8	172 ± 7	12 ± 5

Pacific. These studies showed that the ratios were consistent with the Redfield model. The variations found with depth, latitude, and time were attributed to mixing between different water types with different preformed concentrations of O_2, PO_4^{3-}, and NO_3^-. They were unaware at the time of the conversion of NO_3^- to N_2O in O_2 minimum zones.

Takahashi, Broecker, and Langer (1985) used GEOSEC data to examine the Redfield ratio along isopycnal (constant-density) surfaces in the Atlantic and Indian Oceans. Their values corrected for mixing are given in Table 8.9. The authors attempted to correct the CO_2 values for the dissolution of $CaCO_3$. The mean values of P:N:C:O_2 were found to be 1:17:100:165 at σ_T = 27.0 and 1:17:92:178 at σ_T = 27.2. The small differences between horizons cannot be explained. They suggest values of 1:16:103:172. If the C value is assumed to be represented by the oxygen utilization minus the O_2 used for oxidation of NH_3 with 2 moles of O_2, a ratio of 1:16:140:172 is obtained. The P:O_2 ratio lies between 1:103 and 1:140. This difference may be due to the increase of CO_2 caused by the anthropogenic CO_2 or an excess

TABLE 8.10

Molecular Ratios of N, P, C, and O_2 during the Growth of Diatoms during the IRONEX II Study in the Pacific Ocean

Ratio	Redfield	Takahashi et al.	Steinberg et al.
N:P	16.0	14.9 ± 0.4[a]	14.3 ± 0.2
C:N	6.6	6.3 ± 0.9	6.2 ± 0.2
C:P	106	103 ± 14	90 ± 5
C:O_2	–0.77	–0.6 ± 0.2	0.66 ± 0.07

Source: Data from Takahashi, T., Broecker, W.S., and Langer, S., *J. Geophys. Res.*, 90, 6907 (1985); Steinberg et al. (1998).

[a] Indian Ocean value.

demand for oxidation of organic molecules without N. The decomposition of fatty acids would require more O_2:

$$C_2H_4 + 3O_2 \rightarrow 2CO_2 + 2H_2O \tag{8.32}$$

rather than what Redfield assumed:

$$C + O_2 \rightarrow CO_2 \tag{8.33}$$

These results lead to the following equation for the oxidation of phytoplankton-derived organic carbon:

$$\begin{aligned}&(CH_2O)_{103}(CH_2)_3(NH_3)_{16}(H_3PO_4) + 135O_2\\ &\rightarrow 103CO_2 + 119H_2O + 16HNO_3 + H_3PO_4\end{aligned} \tag{8.34}$$

During the IRONEX II experiment in the equatorial Pacific, the N:P, O:P, and C:P ratios were determined during the growth of diatoms in waters with added Fe(II) (Steinberg et al., 1998). These results are shown in Table 8.10 and lead to the following stoichiometry for the formation of diatoms:

$$\begin{aligned}&90CO_2 + 104H_2O + 14HNO_3 + H_3PO_4 + 18SiO_2\\ &\rightarrow (CH_2O)_{76}(CH_2)_{14}(NH_3)_{14}(H_3PO_4) + 125O_2\end{aligned} \tag{8.35}$$

8.4 Silicon in Seawater

Silicon in seawater can be both dissolved and particulate. The solubility of solid $SiO_2(s)$ gives

$$SiO_2(s) + 2H_2O \rightarrow Si(OH)_4(aq) \tag{8.36}$$

Since $Si(OH)_2$ is a weak acid, it can dissociate in aqueous solutions.

$$Si(OH)_4 \rightarrow H+ + Si(OH)_3O^- \tag{8.37}$$

The pK_{Si}^* is 9.47 and pK_2^* is 12.60 for the ionization of $Si(OH)_4$ in 0.6 *M* NaCl at 25°C. At a pH of 8.1 in seawater, these pK's give:

$$[Si(OH)_4]/[SiO_2]_T = \{1 + K_{HA}/[H+]\}^{-1} = 95.9\% \tag{8.38}$$

$$[Si(OH)_3O^-]/[SiO_2]_T = \{1 + [H+]/K_{HA}\}^{-1} = 4.1\% \tag{8.39}$$

Polymerized forms of $Si(OH)_4$ and $Si(OH)_3O^-$ are not important for seawater solutions. This is due to the low concentrations of SiO_2 in natural waters. If Mg^{2+} or Ca^{2+} ions form strong complexes with $Si(OH)_3O^-$, the charged forms could be in higher concentrations.

The dissociation constant for silicic acid can be determined from

$$\ln K_{Si} = 117.40 - 8904.2/T - 19.334 \ln T + (3.5913 - 458.79/T)\, I^{0.5} + (-1.5998 + 188.74/T)\, I\, (0.07871 - 12.1652/T)\, I^2 \tag{8.40}$$

Seawater contains a wide variety of finely divided siliceous material. Much of this material is produced by the weathering of rocks and is transported to the oceans by rivers and by the wind. The materials include quartz, feldspar, and clay minerals. As these minerals sink through the water column to the sediments, they can react with the components of seawater to form secondary minerals. Recent studies have shown that hydrothermal vents can also contribute a considerable amount of SiO_2 to the oceans. In surface waters, when diatoms and radiolarians, which have skeletons composed of opal (a noncrystalline form of hydrated SiO_2), die, they sink to the sediments, forming diatom oozes. These diatom oozes are quite prevalent in Antarctic waters. The concentration of suspended material is variable. On average, 50% is inorganic, and Si can make up 15 to 60% of the inorganic material (the remainder being mostly $CaCO_3$). Concentrations as high as 100 μg L^{-1} of biogenic particulate SiO_2 is present in Antarctic surface waters during diatom blooms. Since ocean waters are undersaturated with respect to SiO_2, the sinking particulate silica will dissolve in deep waters. The breakdown of the diatoms in deep waters contributes to this increase of SiO_2 to the water column. This leads to depth profiles given in Figure 8.21. Since the release of SiO_2 is a slow process, the profiles of dissolved SiO_2 do not show the maximum at 1000 km seen in the NO_3^- and PO_4^{3-} profiles. The values of SiO_2 are higher in the deep Pacific than the Atlantic because the waters are older and have had a longer time to accumulate SiO_2.

8.4.1 Determination of Silicon

The determination of silicon dissolved in seawater is made by forming a yellow silicomolybdic complex. Other molybdate complexes are formed with phosphate and arsenate. These interfering complexes are decomposed by the addition of oxalic acid. The silicomolybdate complex is reduced by the addition of a solution containing metal (p-methylaminophenol sulfate). This forms a blue compound that is determined spectrophotometrically at 812 nm. It is generally reduced to a stable and more absorbent molybdenum blue complex measured at 812 mm. The reduction can be carried out with metol (p-methyl-amino-phenol sulfate) and Na sulfite. Phosphate produces similar blue complexes, but its formation is prevented by incorporating oxalic or tartaric acid in the reducing reagent. Thomsen, Johnson, and

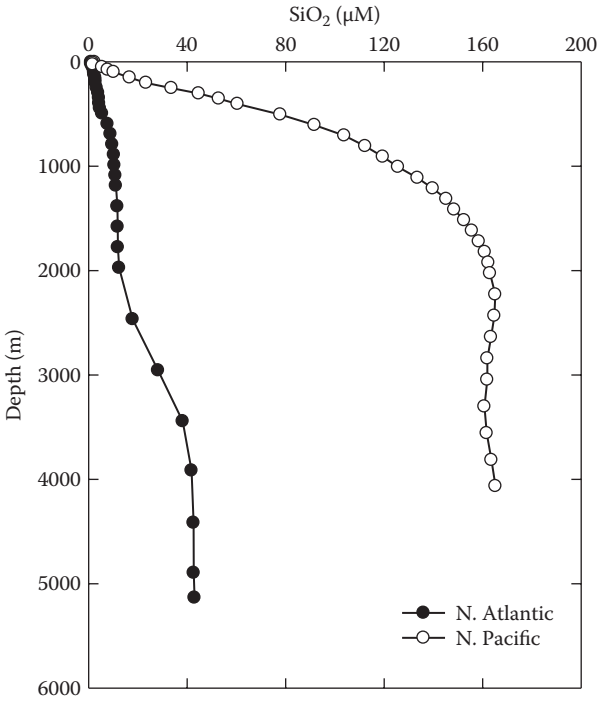

FIGURE 8.21
Profile of silicate in the Atlantic and Pacific Oceans.

Petty (1983) have described a flow injection method that can be used to quickly and accurately determine silicate in seawater. As with the system described previously for phosphate and nitrate, it is automatic and can measure 30 samples per hour. The precision is 1% and has a lower detection limit of 0.1 μ*M*.

The values of SiO_2 vary from 0 to 200 μ*M* in seawater. It is an essential part of the solid structure of diatoms, radiolarians, and sponges. Up to 60% of the inorganic material in diatoms is SiO_2. These plants can completely exhaust the dissolved SiO_2 in surface waters. This process is the principal stripping process of SiO_2 from seawater. The great majority is deposited as diatomaceous oozes in Antarctica. The SiO_2 coming into the oceans from rivers can be removed in estuaries before the waters reach the oceans. This is thought to be due to diatom production, but interactions with other minerals could be important. Much of the particulate SiO_2 coming in from rivers is deposited at the river mouths. The finely suspended minerals, however, can remain in the water column for years. These suspended clay minerals can affect the concentration of trace organic and inorganic species as the result of absorption and ion-exchange processes. As much as 70 to 99% of the particles have diameters less than 10 μm.

Not a lot is known about how diatoms take up SiO_2 and deposit it as hydrated silica. Proteins are involved in the absorption of Si on the cytoplasmic membrane. The process is fast, and it spreads from particular centers. As much as 50% of the dry weight of a diatom can be SiO_2 depending on the species. If diatoms are grown in depleted media, the cells become Si deficient. Such cells are viable for several weeks. They will take up added Si even

in the dark. If deficient cells are illuminated, they photosynthesize for a limited period, but they soon die. The silica in diatoms is insoluble when living but dissolves rapidly when they die. An organic or inorganic (Al or Fe) skin may protect them when they are alive. The treatment of dead cells with EDTA has been shown to accelerate the dissolution.

8.4.2 Distribution of Dissolved SiO_2

The distribution of SiO_2 in coastal waters is generally higher than in the open oceans because of river runoff. In regions where diatom blooms occur, the seasonal variations are similar to PO_4^{3-}. The concentrations decrease in the spring and increase in the summer when growth slackens and then increase to a maximum in early winter. The concentrations in surface waters are low except in upwelling areas. A typical depth profile is shown in Figure 8.21. A section of the distribution of SiO_2 in the Atlantic, Pacific, and Indian Oceans is shown in Figure 8.22. The lateral distribution follows the general water mass circulation. The high values in the Antarctic region are from the large diatom production in the surface waters. The SiO_2 is also added to the deeper waters from the flux from the sediments. The glacial weathering may also lead to higher concentrations of SiO_2 in these regions. The high concentration of SiO_2 in the Antarctic bottom waters can be used to trace this water mass. The vertical section in the Pacific (Figure 8.22) shows that the values in the deep waters increase toward the north and reach concentrations of 220 μ*M* in the Bering Sea.

8.5 Use of Nutrients as Water Mass Tracers

Traditionally, temperature and salinity have been used as a tracer of water masses. More recently, isotopes such as tritium have been used. From time to time, a number of workers have used nutrients to follow various water masses. To use nutrients, it is necessary to make a correction to the amount of nutrients added because of the oxidation of plant material. The concentration of a nutrient present in the water when it was at the surface is called the preformed value. This preformed value should be conservative if other processes are not involved in the addition or subtraction from the water mass. Although both PO_4^{3-} and NO_3^- have been used to trace water masses, only NO_3^- is discussed in this section. As shown by Broecker (1974), the combination of O_2 and NO_2^- can lead to a conservative water mass tracer. The oxidation that occurs is estimated from the AOU. The oxidation of plant material is given by

$$CH_2O + O_2 \rightarrow CO_2 + H_2O \tag{8.41}$$

$$NH_3 + OH^- + 2O_2 \rightarrow NO_3^- + 2H_2O \tag{8.42}$$

The change in the moles of oxygen used is given by

$$\Delta O_2 = -(2\,\Delta NO_3^- + \Delta CO_2) \tag{8.43}$$

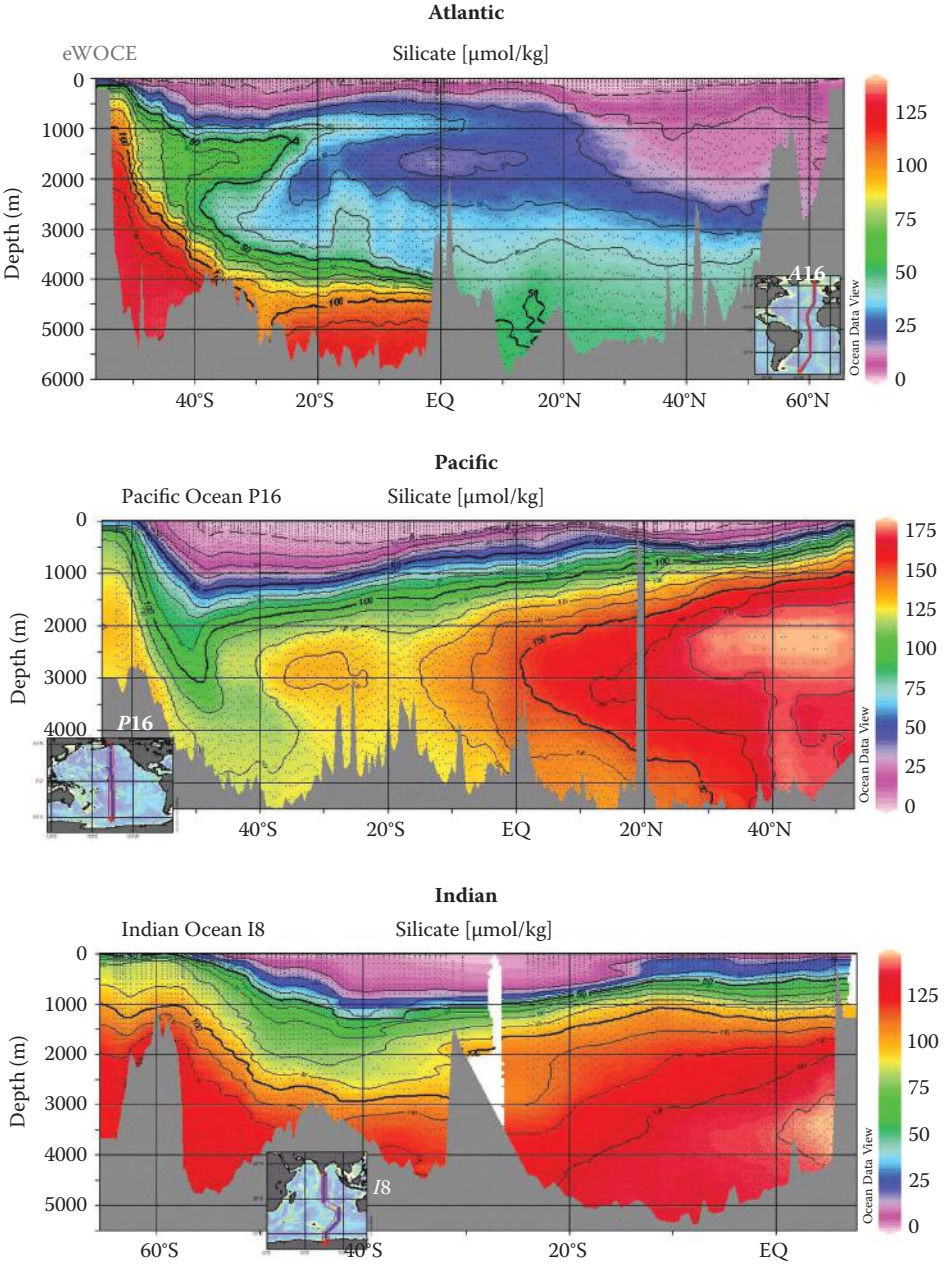

FIGURE 8.22
Sections of silicate in the Atlantic, Pacific, and Indian Oceans.

The change in the NO_3^- to CO_2 can be estimated from the Redfield ratio:

$$\Delta NO_3^-/\Delta CO_2 = 16/106 \tag{8.44}$$

The substitution into Equation 8.42 gives

$$-\Delta O_2 = (2 + 106/16)\,\Delta NO_3^- = 9\Delta NO_3^- \tag{8.45}$$

The preformed NO_3^- concentration is thus related to the measured value by

$$[NO_3^-]_P = [NO_3^-]_{MEAS} - 1/9\ AOU \tag{8.46}$$

Substituting $AOU = [O_2]_{CALC} - [O_2]_{MEAS}$ into Equation 8.45 gives, on rearrangement,

$$\text{“NO”} = 9[NO_3^-]_{MEAS} + [O_2]_{MEAS} = 9[NO_3^-]_P + [O_2]_{CAL} \tag{8.47}$$

where “NO” is a conservative tracer. By a similar argument, it is possible to describe a conservative tracer using phosphate:

$$\text{“PO”} = 135\,[PO_4^{3-}]_{meas} + [O_2]_{meas} \tag{8.48}$$

where “PO” is a conservative tracer. Since the concentration of NO_3^- is higher and can be measured more accurately than the PO_4^{3-}, “NO” is a better conservative tracer than “PO.”

The use of “NO” as a tracer for the mixing of North Atlantic deep water (NADW) and Antarctic intermediate water (AAIW) is shown in Figure 8.23. The concentrations of O_2 and NO_3^- show a nonlinear variation as a function of salinity. The quantity of “NO,” however, is a linear function of salinity or a conservative tracer of the mixing of the two water masses. The values of “NO” vary from 440 μ*M* for NADW to 510 μ*M* for AAIW. A plot of “NO” for various water masses is shown in Figure 8.24.

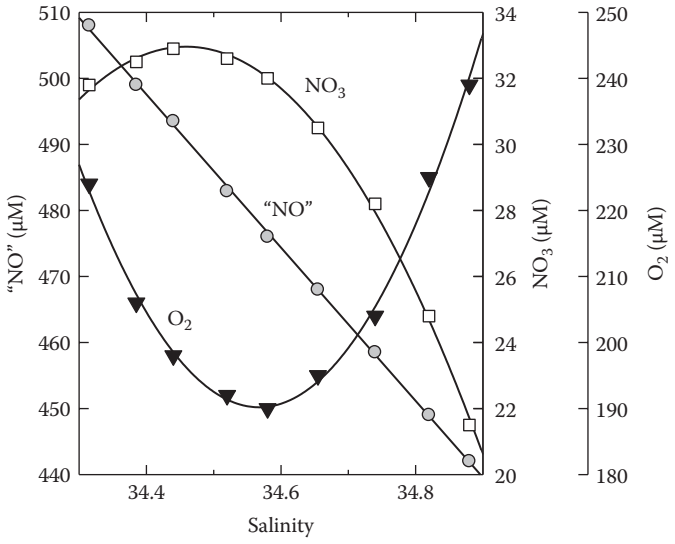

FIGURE 8.23
Values of “NO,” NO_3, and O_2 in the Atlantic Ocean.

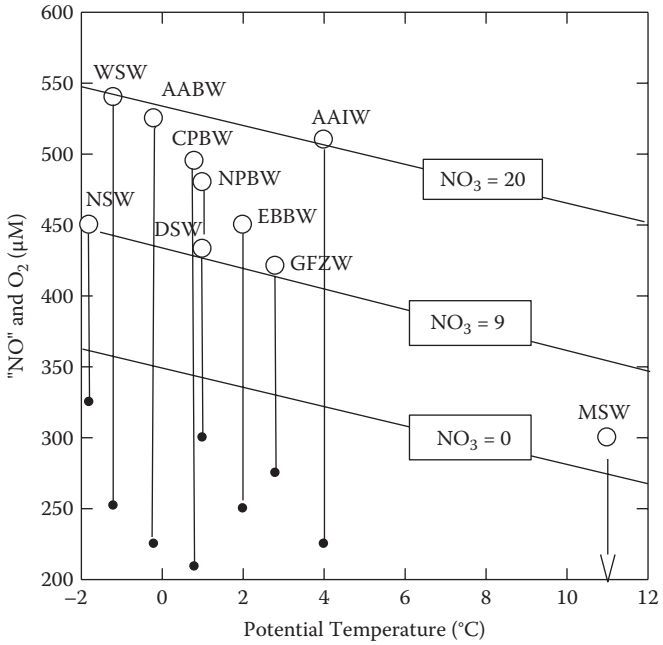

FIGURE 8.24
Values of "NO" and O_2 for various water masses as a function of potential temperature. WSW = Weddell Sea Water; AAIW = Antarctic Intermediate Water; AABW = Antarctic Bottom Water; CPBW = Circpolar Bottom Water; NPBW = North Pacific Bottom Water; DSW = Denmark Straits Overflow Water ; NSW = Norwegian Sea Surface Water; GFZW = Gibbs Fracture Zone Water; MSW = Mediterranean Overflow Water; EBBW = Eastern Basin Bottom Water (Atlantic).

References and Further Reading

Spencer, C.P., The micronutrient elements, Chapter 11, *Chemical Oceanography,* Vol. 2, 2nd ed., Riley, J.P., and Skirrow, G., Eds., Academic Press, New York, 245–300 (1975).

Phosphorus

Abell, J., Emerson, S., and Renaud, P., Distributions of TOP, TON and TOC in the North Pacific subtropical gyre: implication for nutrient supply in the surface ocean and remineralization in the upper thermocline, *J. Mar. Res*. 58, 203–222 (2000).

Armstrong, F.A.J., Phosphorus, Chapter 8, *Chemical Oceanography*, Vol. 1, Riley, J.P., and Skirrow, G., Eds., Academic Press, New York, 323–364 (1965).

Johnson, K.S., and Petty, R.L., Determination of phosphate in seawater by flow injection analysis with injection of reagent, *Anal. Chem.,* 54, 1185 (1982).

Torres-Valdes, S., et al., Distribution of dissolved organic nutrients and their effect on export production over the Atlantic Ocean, *Global Biogeochem. Cycles*, 23 (2009).

Nitrogen

Capone, D.G., *Cyanobacterium trichodesmium*, a globally significant marine bacteria, *Science* 276, 1221 (1997).

Catalano, G., An improved method for determination of ammonia in seawater, *Mar. Chem.,* 20, 289 (1987).
Howells, A., and Geesey, G., Nitrogen fixation in the ocean: the role of cyanobacteria, *Appl. Environ. Microbiol*., March (2010).
Johnson, K.S., and Petty, R.L., Determination of nitrate and nitrite in seawater by flow injection analysis, *Limnol. Oceanogr.,* 28, 1260 (1983).
Kim, Tae-W., et al., Increasing N abundance in the Northwestern Pacific Ocean due to atmospheric nitrogen deposition, *Science,* 334, 505–509 (2011).
Redfield, A.C., Ketchum, B.H., and Richards, F.A., The influence of organisms on the composition of sea-water, in *The Sea,* Hill, M.N., Ed., Interscience, New York, 26–77 (1963).
Steinberg, P.A., Millero, F.J., and Zhu, X.R., Carbonate system response to iron enrichment, *Mar. Chem.,* 62, 31 (1998).
Takahashi, T., Broecker, W.S., and Langer, S., Redfield ratio based on chemical data from isopycnal surfaces, *J. Geophys. Res.,* 90, 6907 (1985).
Thomsen, J., Johnson, K.S., and Petty, R.L., Determination of reactive silicate in seawater by flow injection analysis, *Anal. Chem.,* 55, 2378 (1983).
Vaccaro, R.F., Inorganic nitrogen in sea water, Chapter 9, *Chemical Oceanography,* Vol. 1, Riley, J.P., and Skirrow, G., Eds., Academic Press, New York, 365–408 (1965).

Silicon

Armstrong, F.A.J., Silicon, Chapter 10, *Chemical Oceanography,* Vol. 1, Riley, J.P., and Skirrow, G., Eds., Academic Press, New York, 409–432 (1965).

Use of Nutrients

Anderson, L.A., and Sarmiento, J.L., Redfield ratios of remineralization determined by nutrient data analysis, *Global Biogeochem. Cycles*, 8, 65–80 (1994).
Broecker, W., "NO," a conservative water-mass tracer, *Earth Planet. Sci.,* 23, 100 (1974).
Broecker, W.S., Glacial to interglacial changes in ocean chemistry, *Prog. Oceanogr*., 2, 151–197 (1982).
Codispoti, L.A., in *Productivity of the Ocean: Past and Present*, Berger, W.H., Smetacek, V.S., and Weber, G., Eds., Wiley, New York, 377–394 (1989).
Falkowski, P.G., Rationalizing elemental ratios in unicellular algae, *J. Phycol*., 36, 3–6 (2000).
Geilder, R.J., and La Roche, J., Redfield revisited: variability of C:N:P in marine microalgae and its biochemical basis, *Eur. J. Phycol*., 37, 1–17 (2002).
Kim, R.-W., Lee, K., Najjar, R.G., Jeong, H.-D., and Jeong, H.J., Increasing N abundance in the northwestern Pacific Ocean due to atmospheric nitrogen deposition, *Science,* 334, 505–508 (2011).
Knapp, A.N., Sigman, D.M., and Lipschultz, F., N isotopic composition of dissolved organic nitrogen and nitrate at the Bermuda Atlantic Time-Series Study site, *Global Biogeochem. Cycles,* 19, GB1018 (2005).
Knapp, A.N., et al., Interbasin isotopic correspondence between upper-ocean bulk DON and subsurface nitrate and its implications for marine nitrogen cycling, *Global Biogeochem. Cycles*, 25, GB4004 (2011).
Quigg, A., et al., The evolutionary inheritance of elemental stoichiometry in marine phytoplankton, *Nature*, 425, 291–294 (2003).
Redfield, A.C., The biological control of chemical factors in the environment, *Am. Sci*., 46, 205–221 (1958).
Steinberg, P.A., The Carbonate System Response to Iron Enrichment, Master Thesis, University of Miami, Coral Gables Florida (1998).
Takahashi, T., Broecker, W.S., and Langer, S., Redfield ratio based on chemical data from isopycnal surfaces, *J. Geophys. Res*, 90, 6907–6924 (1985).
Weber, T.S., and Deutch, C., Ocean nutrient ratios governed by plankton biogeochemistry, *Nature*, 467, 550–554 (2010).

9

Primary Production in the Oceans

9.1 Primary Production

The various sources of organic compounds in the oceans are shown in Figure 9.1 and tabulated in Table 9.1. As is apparent from Table 9.1, the major source of organic compounds to the ocean is from the primary production of marine plants (Falkowski, 2012). This primary production is the result of the growth of these organisms as a result of photosynthetic processes. It provides the basis of the marine food chain that culminates in fish and mammals. The plants remove CO_2 and micronutrients from the water and, using solar energy, convert them to complex organic compounds. The simple reaction for the formation of carbohydrates is

$$CO_2 + H_2O \xrightarrow{\text{light}} CH_2O + O_2 \tag{9.1}$$

Phytoplankton are the microorganisms responsible for the greatest primary production in the sea. Attached algae are important in shallow waters. Phytoplankton are free-floating microscopic plants with only limited mobility and are distributed by ocean currents. They can be divided by size into

Microplankton: 50 to 500 μm
Nanoplankton: 10 to 50 μm
Ultraplankton: 0.5 to 10 μm

Since they live primarily by photosynthesis, they are *phototrophic organisms.* Photosynthesis is a complicated process: Solar energy is absorbed by phytoplankton cells and converted to biological energy stored in the form of organic compounds. The stages are as follows:

1. Absorption of photons of light by photosynthetic pigments that are contained in the chromatophores. The principal pigments are chlorophylls. The structure of chlorophyll-a is shown in Figure 9.2. The resonating system of double bonds stabilizes the molecule and provides electrons that are easily excited to orbitals of higher energy when light is absorbed.
2. Part of the energy absorbed by these excited electrons is converted to chemical energy through a cyclic series of enzymatic reactions involving cytochrome I, which leads to the production of high-energy adenosine triphosphate (ATP) from adenosine diphosphate (ADP) and orthophosphate (P):

$$ADP + P \rightarrow ATP \tag{9.2}$$

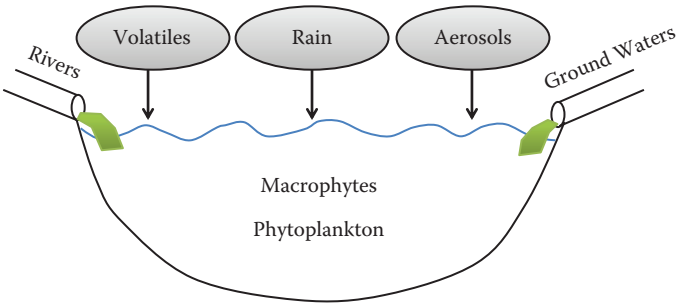

FIGURE 9.1
Sources of organic compounds to the oceans.

TABLE 9.1

The Sources of Organic Compounds to the Oceans

Method of Input	Amount (10^{15} gC/yr)	% of Total	
Primary Production			
Phytoplankton	23.1	84.4	
Macrophytes	1.7	6.2	90.6
Liquid Input			
Rivers	1.0	3.65	
Groundwaters	0.08	0.3	3.95
Atmospheric Input			
Rain	1.0	3.65	
Dry deposition	0.5	1.8	5.45
Total	27.4		

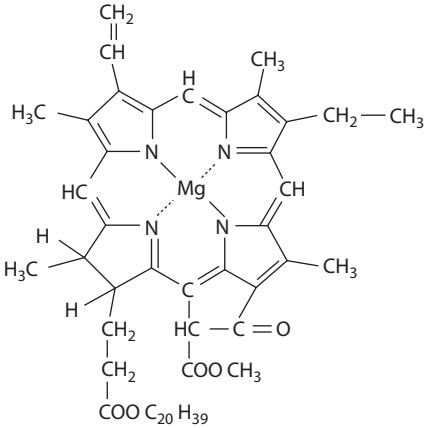

FIGURE 9.2
Sketch of chlorophyll-a.

The rest of the energy of the excited electrons is used in a series of enzymatic reactions of riboflavin phosphate and nicotinamide adenine dinucleotide phosphate (NADP).

$$4NADP + 2H_2O + 2ADP + 2P \rightarrow 4NADPH + O_2 + 2ATP \quad (9.3)$$

The protons are from water, and the excited electrons are from the reduced form of NADP. The hydroxide from the water yields molecular oxygen and donates electrons to chlorophyll via the cytochrome I chain.

3. The CO_2 is assimilated in a cyclic series of reactions utilizing the reducing action of NADPH (protonated form of NADP) and the phosphorylating power of ATP. These reactions, which can take place in the dark, lead to the production of carbohydrates (CH_2O).

$$CO_2 + 4NADPH + ATP \rightarrow CH_2O + H_2O + 4NADP + ADP + P \quad (9.4)$$

Combining Equation 9.1 to Equation 9.3 gives

$$CO_2 + H_2O \rightarrow CH_2O + O_2 \quad (9.5)$$

Labeled $^{14}CO_2$ finds its way very quickly into compounds other than carbohydrates. Compounds such as fats and amino acids are synthesized from intermediates in the carbon cycle in addition to being produced from CH_2O.

The photosynthetic quotient (PQ = molecules of O_2 liberated/molecules of CO_2 assimilated) differs from 1.0 because of the production of other classes of compounds. The PQ is 1.4 if only lipids are formed; the PQ is 1.05 when amino acids are formed using NH_3 and 1.6 using NO_3^-. Values of 1.20 to 1.39 are common for natural populations provided there are adequate nutrients. At low light intensities, heterotrophic utilization of compounds such as acetate may take place. This may be advantageous because it requires less energy than to fix CO_2.

The energy required for metabolic processes is obtained by the oxidation of the photosynthesized organic compounds. This process is known as *respiration*. The simple overall reaction is

$$CH_2O + O_2 \rightarrow CO_2 + H_2O \quad (9.6)$$

The respiration quotient (RQ; molecules of CO_2 liberated/molecules of O_2 assimilated) lies close to 1.0. Thus, fats and protein are not normally used. Respiration takes place in the light and dark at approximately the same rate. The rate is about 5 to 10% of the maximum rate of photosynthesis of cells grown under optimal conditions. The respiration that occurs in the light is assumed to be the same as in the dark.

9.1.1 Phytoplankton Production

Both the amount and the rate at which phytoplankton are produced are important to consider with respect to the availability of organic carbon to the food chain. The *standing crop* is the amount of living phytoplankton at a given time in a given amount of seawater (mg C m^{-3} of seawater) or beneath a given surface of seawater (mg C m^{-2}). The *rate of primary production* (P) is defined as the weight of inorganic carbon fixed photosynthetically

per unit time per unit volume (mg C m^{-3} h^{-1}) or under unit surface area (g C m^{-2} day^{-1}). The primary production is normally determined from measurements performed at depths of 100, 10, and 1 m.

$$P = (1/5)(2P_{100} + 2P_{10} + P_1)(D/2)\,N\,K \tag{9.7}$$

where D is the depth at which light is 1% of surface, N is the number of hours to sunset, and K is the fudge factor (1.0 in the tropics).

The *new production* is defined as the primary production associated with newly available nitrogen (NO_2^-, NO_3^-, NH_3). The new production plus the *regenerative production* (the primary production associated with recycled nitrogen) is equal to the total primary production.

$$P_T = P_{NEW} + P_{REG} \tag{9.8}$$

These definitions are based on the systems being in steady state. The ratio of the new production to the total production is called the f ratio:

$$f = P_{NEW}/P_T \tag{9.9}$$

The f ratio is useful in describing the fraction of organic nitrogen and carbon exported from the surface waters of the oceans into the deep ocean. The oxidation of these organic compounds returns NO_3^- and CO_2 to the deep waters. It also represents the capacity of the system to sustain secondary and higher levels of production.

9.1.2 Standing Crop or Biomass

The biomass is concentrated by centrifugation or filtration, and the cells are counted by eye, with a Coulter counter, or by analyzing a chemical component of the cell. The concentration of chlorophyll-a, determined by spectroscopic and fluorometric methods, is often used as an indicator of the levels of biomass. The rate of consumption of micronutrient elements is also used to obtain integrated values of primary productivity over fairly lengthy periods. Since NO_3^- and PO_4^{3-} can be regenerated and recycled several times a year, these values will tend to be minimal levels.

A number of methods have been used to determine the primary productivity (see Table 9.2). A brief discussion of the most popular methods used to determine primary production are given in the next two sections.

9.1.3 The O_2 Liberation Method of Measuring Primary Productivity

A series of 300-ml glass-stoppered bottles are filled with seawater collected using clean techniques (Teflon-lined bottles on Kevlar line). The bottles are suspended at various depths throughout the photic zone or in a water bath under various light levels. Dark or "light-tight" bottles filled with the same seawater are suspended at the same depths. After 3 to 8 h, the water is analyzed for O_2. The increase of O_2 in the light bottles is a measure of the net photosynthesis. The gross productivity is obtained from the difference in the O_2 in the light and dark bottles (the loss of O_2 from respiration). Some problems with the method are as follows:

TABLE 9.2

Methods Used to Determine Primary Productivity

In Vitro	Component	Timescale
^{14}C assimilation	$P_T = P_N$	Hours to 1 day
O_2 evolution	P_T	Hours to 1 day
$^{15}NO_3$ assimilation	P_{NEW}	Hours to 1 day[a]
$^{15}NH_4$	P_T	Hours to 1 day[a]
$^{18}O_2$ evolution	$P_{NEW} = P_C$	Hours to 1 day[b]
Physical transport		
Sediment traps	$P_{NEW} = P_C$	Days to months
Bulk properties		
NO_3 flux to photic zone	P_{NEW}	Hours to days
O_2 utilization	P_{NEW}	Seasonal to annual
Net O_2 accumulation	P_{NEW}	Seasonal to annual
$^{238}U/^{234Th}$	P_{NEW}	Days to year[c]
$^3H/^3He$	P_{NEW}	Seasonal to annual[d]
Upper and lower limits		
Photons absorbed	P_T	Instantaneous to annual
Depletion of winter NO_3	P_{NEW}	Seasonal
Remote sensing	P_T, P_{NEW}	Days to annual

Note: P_T, total primary production ($P_{NEW} + P_R$); P_{NEW}, new production; P_N, net primary production; P_R, regenerative production; P_C, community production.

[a] Altabet, M., and Deuser, W., *Nature*, 315 (1985).

[b] Bender, M., et al., *Limnol. Oceangr.*, 32, 1085 (1987).

[c] Coale, K., and Bruland, K., *Limnol. Oceangr.*, 32, 189 (1987).

[d] Jenkins, W., *Nature*, 300, 246 (1982).

1. There is insufficient sensitivity (~3 mg C m^{-2} h^{-1}) in low-productivity oligotrophic waters.
2. It cannot be used in polluted waters because the oxidation of organic pollutants can result in the loss of O_2.
3. Results will be low when lipids or proteins are photosynthesized products (e.g., diatoms).
4. Bacteria adsorbed to the bottle wall can cause problems.
5. The growth may be affected by confinement in the bottles.

Bender and coworkers (1987) have developed a method to measure gross primary production using the stable isotope ^{18}O. The sample is artificially enriched with ^{18}O in H_2O, and the ^{18}O in O_2 is produced by the reaction

$$H_2{}^{18}O + CO_2 \rightarrow CH_2O + {}^{18}O^{16}O \tag{9.10}$$

The rate of O_2 production is measured using a mass spectrophotometer. The fractionation of oxygen isotopes during photosynthesis does not affect the measurement significantly. The $\delta(O^{18}/^{16}O) = [(O^{18}/^{16}O_{sample}/O^{18}/^{16}O_{standard}) - 1]10^3$ is raised by 2000 to 3000. The changes caused by respiration affect the rate to a much smaller degree than the ^{14}C method. This method measures the gross production; the ^{14}C method measures the difference between

net and gross production. The method is thus useful in separating the gross and net productivity. It has been shown to yield values for the gross production that agree with the changes in total oxygen. The ^{14}C production is 65% or less of the gross production (Grande et al., 1989).

9.1.4 Uptake of CO_2 Method of Measuring Primary Productivity

The most common method of measuring primary productivity is using carbon-14. The 300-ml bottles are filled with seawater and 2 cm^3 of bicarbonate solution with labeled ^{14}C (1 to 25 μCi depending on productivity expected). The bottles are suspended at various depths or placed in a thermostatic bath and illuminated with light from fluorescent lamps filtered to give the intensities and spectral distribution of a given depth. After 2 to 6 h, the seawater is gently filtered through a 0.45-μm filter. The filters are washed with seawater or HCl vapor to remove calcareous inorganic carbon. The radiocarbon flux is counted with a scintillation counter to determine the activity. About 1 to 2% of the CO_2 may be exchanged in the dark (10% in tropical waters). The productivity is given by

$$\text{Productivity (mg C m}^{-3}\text{ h}^{-1}) = 1.05\,(C_S - C_D)W/C\,N \tag{9.11}$$

where W is the total CO_2 in the sample (mg C m^{-3}); N is the number of hours exposed; 1.05 compensates for slow uptake of alga cells of $^{14}CO_2$ compared to $^{12}CO_2$; C_S and C_D are counting rates of light and dark bottles, respectively; and C is the normalized counting rate of ^{14}C that has been added to the bottles. Strickland and Parson (1968) gave the full details of using this technique. Some problems with the method are as follows:

1. It is important to measure net production (60 to 90% of gross production).
2. Extracellular metabolites may not be retained by the filter (30%).
3. Sample enclosure may cause changes.
4. Diurnal effects may be missed.
5. Measures only fixation of inorganic C.

Laboratory measurements with cultures show reasonable agreement between estimates of primary productivity based on O_2 production, CO_2 assimilation, uptake of P, and the volume of packed cells obtained after centrifugation. The O_2 method gives more meaningful results for longer than 24-h sampling and highly productive waters. ^{14}C is best for oligotrophic waters—after correcting for extracellular products.

9.1.5 Determining New Production

In recent years, the new production has been determined by a number of chemical and physical methods. Since nitrogen is thought to limit the production of phytoplankton in the oceans, it is frequently used to define and measure new production. New production can thus be estimated as the rate of transport of nitrate into the photic zone of the oceans or the rate of organic nitrogen that leaves this area. This role of nitrogen-fixing organisms still remains to be fully elucidated. The in vitro techniques that can be used to determine new production are the assimilation of $^{15}NO_3^-$ and the evolution of $^{18}O_2$. The collection of organic nitrogen in surface sediment traps can also be used to determine the new production. Other methods that measure bulk properties include the determination of the flux of

NO_3^- to the photic zone and the accumulation of oxygen in the photic zone. Other methods that have been used in recent years are based on the use of tracers. These include

1. The measurement of the consumption of O_2 that results from the production in surface waters and export of organic carbon from the photic zone. The vertical integration of the oxygen utilization rates (OURs) can be used to estimate new production. This method gives long-term (seasonal-to-decadal) and large-scale (1000-km) averages of new production.
2. The measurement of the production rates of O_2 in the photic zone.
3. The flux of nitrate into the euphotic zone, which can be estimated by examining the balance between the upward flux of ^3He from the thermocline and the loss to the atmosphere.
4. The thorium deficiency method, which has been used in recent years to estimate the primary production. The ratio of $^{234}Th/^{238}U$ should be 1.0 at equilibrium. As shown in Figure 9.3, this is the case for surface and deep waters but not for waters in the photosynthetic zone. The deficiency of ^{234}Th is due to its adsorption to organic particulate material (living and dead). By integrating the area of this deficiency, one can get an estimate of the total primary production in the photosynthetic zone at a given location over a period of days. The method is calibrated by using estimated primary production by other methods (^{14}C).

The OURs have been determined by measuring the AOU (apparent oxygen utilization) as a function of time using tritium-^3He, ^{228}Ra, or chlorofluorocarbons (CFCs) to determine the age of the water. The ^3H-^3He dating method (Jenkins, 1987) has been widely used to determine the OUR. The values as a function of depth are shown in Figure 9.4. The oxygen

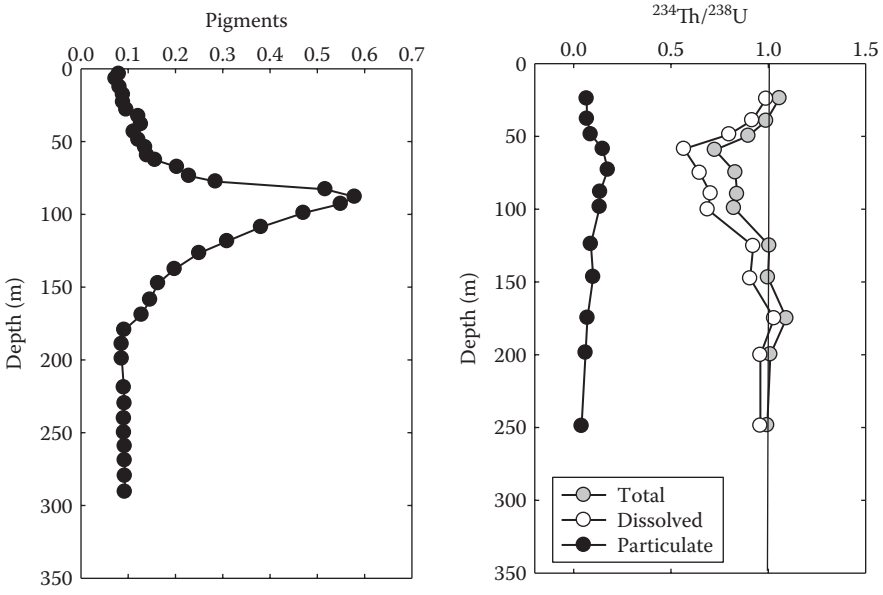

FIGURE 9.3
The thorium deficiency method of determining primary production.

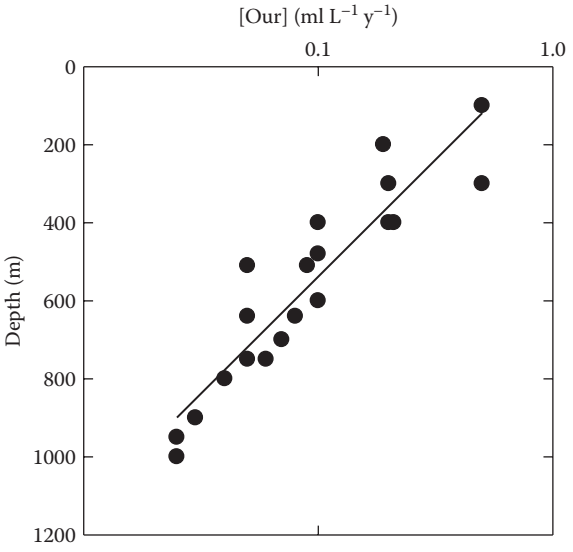

FIGURE 9.4
The values of the oxygen utilization rates (OURs) as a function of depth. (From Jenkins, *Nature*, 300, 246, 1982. With permission.)

demand found by this method is about 5 to 6 mol (O_2) m^{-2} yr^{-1}. Using a Redfield O/C ratio of 1.65, the vertically integrated oxygen demand corresponds to a new productivity of 3 to 3.5 mol C m^{-1} yr^{-1} in the North Atlantic. This is in good agreement with the values estimated from the value determined from oxygen production (5 mol m^{-2} yr^{-1}) in the same area. These estimates are for long time scales (seasonal to decadal) and are much larger than estimates made by in vitro bottle estimates and short deployments of sediment traps. These estimates imply that the upward flux on nitrate is 0.6 mol m^{-2} yr^{-1} compared to calculated values that are 5 to 10 times lower. One possible cause of this discrepancy is that isopycnal transport of NO_3^- is due to small-scale eddy processes. These episodic events have been shown to occur at the Bermuda Atlantic Time Series station (BATS; see Figure 8.12).

9.1.6 Factors Affecting the Growth of Phytoplankton

A number of physical and chemical factors can affect the growth of phytoplankton in the oceans. Some are given next.

9.1.6.1 Light

Two factors that influence light must be taken into consideration:

1. Factors controlling the intensity and the spectral composition in the sea
2. Species' preference for a given intensity and wavelength

The amount of light reaching the surface oceans is controlled by

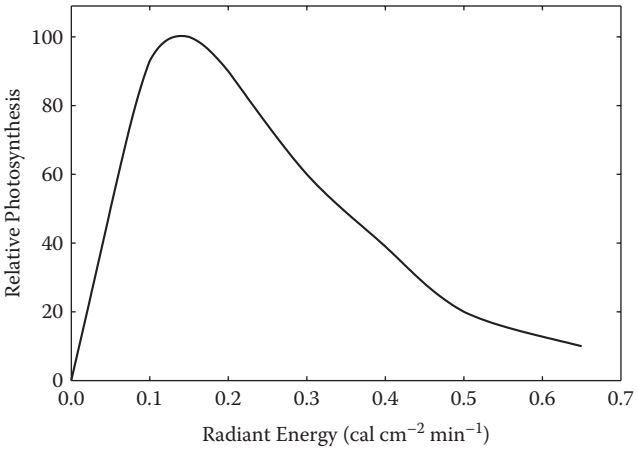

FIGURE 9.5
Relative photosynthesis as a function of the radiant energy.

1. The sun's altitude
2. Cloud cover
3. Wavelength (370 to 720 nm)
4. Reflection, absorption, and scattering

The rate of photosynthesis increases in proportion to the light intensity at low intensities (see Figure 9.5). Light saturation is reached at moderate intensities. At high intensities, inhibition occurs, perhaps as a result of the inhibition of chlorophyll production. Permanent inhibition occurs as a result of photo-oxidation at high light intensities.

9.1.6.2 Temperature

The temperature range in the open oceans is –2 to 30°C. Phytoplankton is rapidly killed at temperatures 10 to 15°C above the temperature at which they are adapted to live. Lowering the temperature slowly has less of an effect. Phytoplankton is best cultured at 5 to 10°C higher than natural conditions. The combined effects of temperature and light may determine the pattern of succession at a given latitude.

9.1.6.3 Salinity

Marine phytoplankton will grow at salinities as low as 15, some more successfully than at 35. Stenohaline organisms will only thrive in a limited range of salinity, for example, *Peridinium balticum* at salinity of 8 to 12 (Baltic). Euryhaline organisms can live over a wide range of salinities.

9.1.6.4 Micronutrients and Trace Metals

Organisms need N and P for healthy growth. A few organisms (e.g., cyanobacteria) can fix molecular N. Others need NH_3, NO_2^-, and NO_3^-; heterotrophs can use organic N, and

some can use dissolved or particulate organic P. Most species can grow at NO_3^- and PO_4^{3-} levels 29 times the maximum values in the oceans. The minimum level of PO_4^{3-} needed is about 0.3 µ*M* but may vary with different species. This does not occur in the oceans since N is exhausted before P falls to a critical level. Heavy blooms in enclosed areas can be caused by excess amounts of NO_3^- and PO_4^{3-} from sewage or fertilizer runoff. SiO_2 is needed for the growth of diatoms; the minimum levels needed are about 1.8 µ*M* (which may occur in subtropical waters). Trace metals (Fe, Mn, Mo, Zn, Cu, Co, V) are required for the healthy growth of phytoplankton. These metals are needed for proteins and enzymes, for example:

Ferrodoxin (Fe protein)
Enzymes (Mn, Mo, Cu, Zn, Co)

Phytoplankton can assimilate chelated forms of many elements. EDTA (ethylenediamine N,N,N,N′ tetraacetic acid) is frequently added to cultures to permit nontoxic forms of metals to be available without the risk of the precipitation of hydroxides. Recent work has indicated that shortages of Fe may limit the production of plankton in waters that have high levels of nutrients (N, P, and Si), for example, the North Pacific and Southern Ocean waters. The input of Fe from atmospheric sources could control the primary production in these regions. This is discussed further in the chapter.

9.1.6.5 Organic Factors

Phytoplankton growth will not take place unless minute amounts of specific organics are available. Some organics, however, also inhibit the growth of algae. Vitamin B_{12} and B_1 (thiamine) are growth promoters. Ascorbic acid and cysteine may also be needed. Bacteria may produce some of these compounds. A shortage of vitamin B_{12} appears to limit the rates of photosynthesis by stopping cell division, causing a loss of pigmentation and cell size.

9.1.7 Growth and Distribution of Phytoplankton in the Sea

The rates of plankton growth are similar to bacteria that have been extensively studied. An idealized growth curve is given in Figure 9.6. This simple growth curve does not occur in the oceans because of physical and chemical factors as well as biological (grazing) and hydrographic (horizontal and vertical water movement) factors. Discussion of the various phases follows.

1. **Lag phase:** This delay of growth is thought to be due to a lack of balance in the enzymatic reactions in the cell caused by growth promoters.
2. **Exponential phase:** This is the linear exponential growth phase, where the number of cells (N) increases according to

$$\ln(N/N_0) = k\,t \tag{9.12}$$

where N_0 is the initial number of cells, and k is related to the nature of the organism and conditions of growth. The half-time of growth $t_{1/2} = \ln 2/k$. In a culture, the value of k = 0.1 to 1.0 h^{-1}, while in the sea, k = 0.09 to 0.015. This gives an average $t_{1/2}$ = 8 to 46 h at sea.

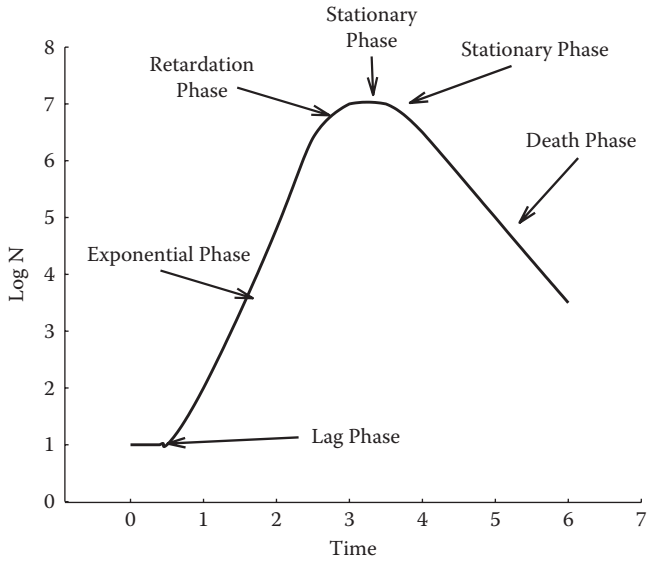

FIGURE 9.6
Idealized phytoplankton growth curve.

3. **Retardation phase:** This is due to the reduction of the growth rate caused by the depletion of nutrients, inhibition caused by growth inhibitors, and reduction in photosynthesis caused by shading.
4. **Stationary phase:** This is when there is no net increase in living cells, but metabolic activity still is not limited.
5. **Death phase:** This is when cells die at an exponential rate. Not all of the cells die; some go into a resting state and survive for long periods. In the oceans, a bloom will dissipate due to grazing by zooplankton, sinking below the photic zone, horizontal movement, and toxins.

The seasonal variation of primary productivity is shown in Figure 9.7. The productivity peaks in the spring and fall and is related to the availability of N and P from mixing and the appropriate light intensity. The smaller peaks in the summer are due to the recycling of nutrients by zooplankton grazing. The relative rates of photosynthesis as a function of depth in the summer and winter are shown in Figure 9.8. The springtime primary production in the North Atlantic has been studied by a number of workers over the years. The springtime blooms fix carbon and export it to deep waters. These blooms were thought to be triggered by stratification of the surface waters due to springtime warming. This stratification reduces the grazing of zooplankton and resultant growth of phytoplankton. Mahadevan et al. (2012), using observations and modeling, have indicated that the stratification and resulting blooms are caused by surface currents due to density gradients. This results in the blooms occurring 20–30 days earlier than could be due to warming.

The *compensation depth* is defined as the depth at which photosynthesis is equal to respiration. This is when the AOU is equal to 0. In the summer, the maximum photosynthesis occurs at a depth where the transmission of light is between 25 and 50%. The low rates of photosynthesis that occur in the winter result in a compensation depth near the surface. In the open oceans, the photosynthetic compensation depth is related to the availability

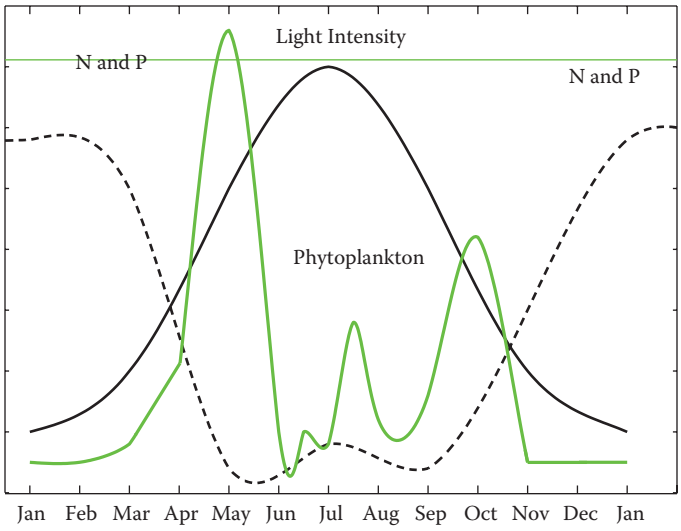

FIGURE 9.7
Seasonal variation of phytoplankton, nutrients, and light in a typical northern temperate sea.

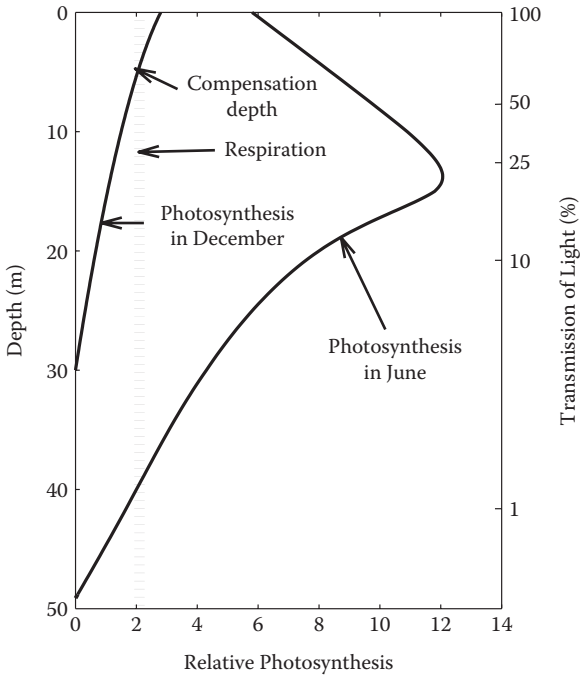

FIGURE 9.8
Integrated daily rate of primary productivity as a function of depth.

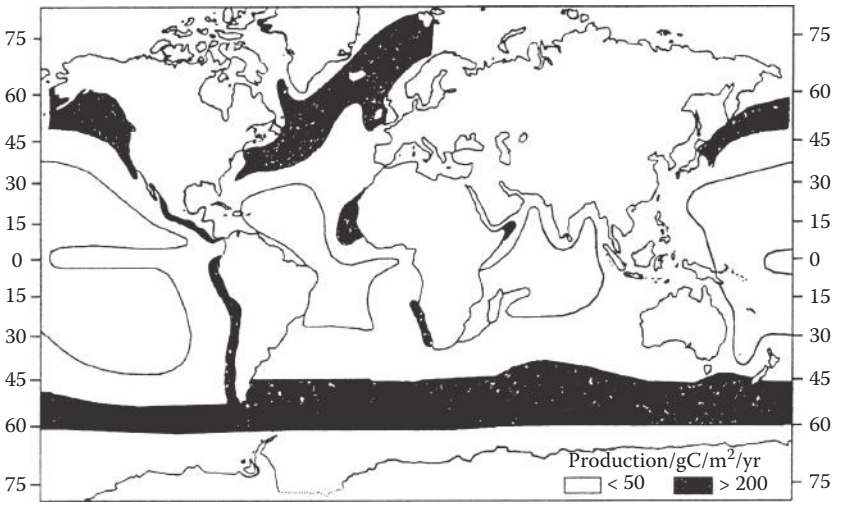

FIGURE 9.9
Geographical distribution of primary productivity in the oceans (g carbon m^{-2} yr^{-1}).

TABLE 9.3
Primary Productivity in Ocean Waters

Area	gC m^{-2} $year^{-1}$
Open ocean	18–55
Equatorial Pacific Ocean	180
Equatorial Indian Ocean	73–90
Upwelling areas	180–3600
Saragasso Sea	72 (18–168)
Continental Shelf, New York	120
Continental Shelf, North Sea	50–80
Kuroshio	18–36
Arctic	1
Mean of all oceans	50–370

of nitrogen from deeper waters. The geographical distribution of primary productivity is shown in Figure 9.9. It is highest in upwelling coastal regions and in the southern oceans. Some typical values for various regions are given in Table 9.3. The totals for the oceans range from mean values of 50 to 370 g C m^{-2} yr^{-1} (4 to 31 mol C m^{-2} yr^{-1}), with the higher values coming from O_2 utilization estimates. The annual values of 3 to 15 × 10^{10} metric tons of carbon can be compared to land estimates of 2 to 3 × 10^{10} metric tons of carbon.

In recent years, a number of workers have questioned the validity of the values of primary productivity determined by the carbon-14 technique. The earlier measurements are uncertain because of possible trace metal contamination. The uncertainty of whether the technique is measuring net or gross primary production was also considered. Recent studies indicated that reliable gross production measurements can be made using the ^{14}C method using trace metal collection techniques, and that it provides an upper limit for net production.

The OUR measurement of Jenkins (1982) using the $^{3}H/^{3}He$ ratio gave primary production rates in the North Atlantic of 4.5 mol C m^{-2} yr^{-1} or 55 g C m^{-2} yr^{-1}. If this represents 80 to 90% of the amount being produced, the amount of primary productivity would be at least 60 g C m^{-2} yr^{-1}. This is a lot higher than the expected values for open oceans.

9.1.8 Remote Sensing Techniques

Current estimates of global production are biased by sampling errors. The tracer techniques integrate over seasonal to annual time scales, while the ^{14}C and O_2 techniques are short in duration (hours). Recent work indicates that the oceans are perturbed over short time scales, which can result in large transients in the carbon fixation. The distributions of phytoplankton revealed from ships are quite scattered and poorly sampled. Since photosynthesis depends on chlorophyll, the concentration of chlorophyll in seawater can be taken as an index of photosynthetic potential. This method is approximate since it is hard to distinguish between active and inactive chlorophyll in dead material. This has led to the development of remote sensing methods to estimate the pigment biomass (Gordon et al., 1988). By using satellites (Figure 9.10), the chlorophyll in the waters can be used to get an idea of the primary productivity occurring over a wide area. If the satellite data are calibrated using direct measurements, one can improve the correlations between color and production. Most of the chlorophyll is in coastal and upwelling areas of the oceans, where nutrients are available for primary production.

Remote sensing techniques have advanced our understanding of the global productivity of the surface oceans (upper 25% of the euphotic zone). The use of satellites to determine primary production is not simple and is an evolving technology. A complete understanding of primary production in the oceans will require measurements over different time and space scales. This will require different methods of measurement (e.g., ships, moorings, and satellites). To determine primary production from satellites, one needs to know the light field, the pigments and their adsorption properties, and so on. To convert the concentration of pigments to primary production, a number of workers have developed

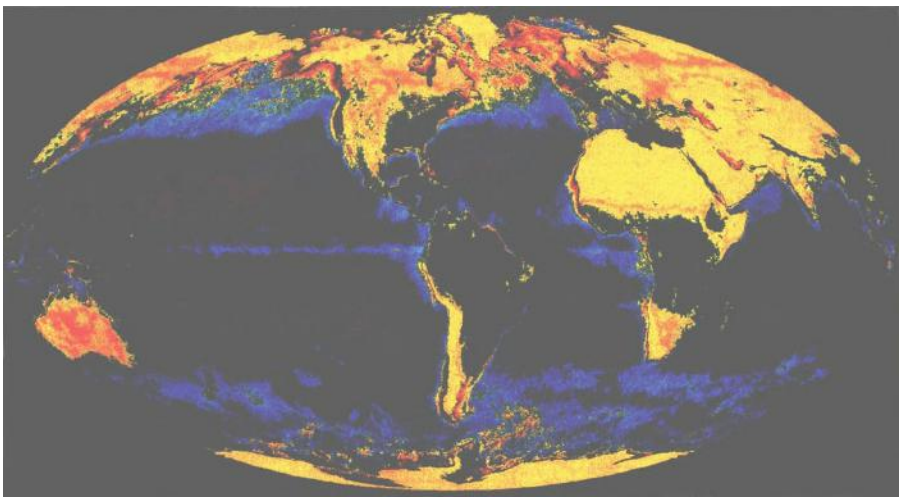

FIGURE 9.10
The world pigment map produced by NASA Goddard Space Flight Center and the University of Miami from the color zone satellite.

semiempirical models (Bidigare et al., 1992). The simplest model for the integral photosynthesis ∑P constructed by Talling (1969) is given by

$$\sum P(\text{hourly}) = \frac{[\text{Chi}] \times \left(P_{max}/[\text{Chi}]\right)}{K_{Qpar}} \ln\left[\frac{Q_{par}(0\text{-})}{0.5\ I_k}\right]\Bigg\} \tag{9.13}$$

where [Chl] is the concentration of chlorophyll, $P_{max}/[Chl]$ is the chlorophyll-specific maximum rate of photosynthesis, $Q_{par}(0)$ is the downwelling photosynthetic active radiation (par) measured below the surface, K_{Qpar} is the diffuse attenuation coefficient for $Q_{par,}$ and I_k is the saturation parameter for photosynthesis (the minimum irradiance to sustain light-saturated rates of photosynthesis). The half-saturation constant for photosynthesis ($0.5\ I_k$) is comparable to the K_m ($–0.5\ V_{max}$) for enzyme saturation kinetics and links the natural variability in the photophysiological state to the surrounding light.

Rodhe (1965) simplified the model by assuming that the depth corresponding to $0.5\ I_k$ is equal to the depth of the 10% light level ($Z_{0.1Qpar(0–)} = 0.1$):

$$\sum P(\text{hourly}) = Z_{0.1}[\text{Chl}](P_{max}/[\text{Chl}]) \tag{9.14}$$

These equations assume that the chlorophyll is uniformly distributed in the water column and the photosynthetic irradiance (P-I) parameters do not vary with light depth.

Ryther and Yentsch (1957) developed a model based on P-I relationships of phytoplankton cultures.

$$\sum P(\text{daily}) = (R/K_{Qpar})[\text{Chl}](P_{max}/[\text{Chl}]) \tag{9.15}$$

The factor R is a relative photosynthesis parameter that varies as a function of the total dial surface radiation. The depth dependence of primary production has been determined. The most widely used equation was developed by Jassby and Platt (1976):

$$P(z) = [\text{Chl}(z)](P_{max}/[\text{Chl}])\ \tanh[\text{Qpar}(z)/I_k] \tag{9.16}$$

More complicated spectral models have also been developed (Bidigare et al., 1992) that take into account the depth- and wavelength-dependent variation in irradiance and phytoplankton adsorption properties. Balch, Platt, and Sathyendranath (1993) compared a number of the models with directly measured values of primary production. All of them seem to have some defects.

The concentration of phytoplankton in surface waters can affect the color as seen from satellites. The ability to obtain a global view of phytoplankton pigments at high spatial resolution can be used to examine primary production, the flux of carbon between the atmosphere and oceans, and effects on the heat budget by the formation of clouds (from DMS [dimethylsulfide]) and may absorb solar radiation at visible frequencies. Phytoplankton have a short life span (1 to 10 days) and spatial scale (1 to 5 km), so only satellite measurements can give reliable temporal and spatial resolution. The satellite ocean color instruments like the SeaWIFS (sea-viewing wide field-of-view sensor) measure radiance entering the aperture of the sensor in space. The radiance must be corrected to obtain optical and biological properties of the surface of the oceans. Algorithms for making the appropriate corrections are still in development. Since 95 to 99% of the radiance observed by the satellite is derived from scattered light, corrections must be made for scattering by the atmosphere. This scattering is a function of the wavelength, viewing angle relative to the surface, and the sun. The scattering correction has three components: (a) molecular (Rayleigh) scattering,

(b) aerosol scattering, and (c) the diffuse transmittance of the atmosphere, all of which must be computed to propagate the signal leaving the water and reaching the level of the satellite. Once these corrections are made, one can estimate the water leaving radiance. Bio-optic algorithms must be used to calculate the relevant quantities, such as chlorophyll and primary production. This must be done by correction for the optical properties of the surface waters. This is normally done using empirical equations that attempt to link the upwelling radiance Lw and the concentration of pigments (Gordon et al., 1988):

$$C = 1.15\ (Lw(443)/Lw(569)^{-1.42}, \quad C < 1\ mg\ m^{-3}\ (Green\ water)$$
$$C = 3.64\ (Lw(500)/Lw(560)^{-2.62}, \quad C < 1\ mg\ m^{-3}\ (Blue\ water)$$

The occurrence of blooms of phytoplankton with shells of $CaCO_3$ can lead to high reflectance because of the milky waters (Balch et al., 1993). The calculation of the integrative total productivity uses complicated equations that depend on the surface irradiance and parameters related to bio-optical properties of the waters. The estimation of new production and the carbon flux across the air–sea interface are more difficult to determine. As more global data become available, these parameterizations will be improved.

The global primary production of the world oceans is shown in Figure 9.11. The highest levels occur in coastal upwelling areas. The oceanic values of primary production are compared to land production in Table 9.4.

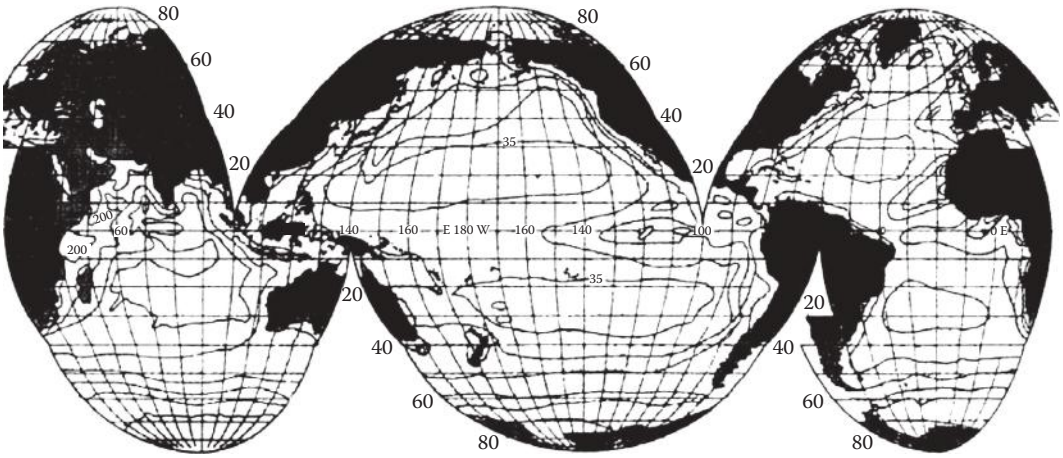

FIGURE 9.11
Global primary productivity in the oceans (mg carbon m^{-2} day^{-1}).

TABLE 9.4

Comparative Global Primary Production

Theoretical Algal Maximum	**27 gC m^{-2} day^{-1}**
Rice field	4
Pine forest	2
Upwelling ocean	2
Antarctic ocean	1
Neritic ocean	0.2 (e.g., 20 mgC m^{-3} per 10 m photic zone)
Oceanic	0.1 (e.g., 1.3 mgC m^{-3} per 77 m photic zone)

9.2 The Iron Hypothesis

Nitrate, phosphate, and silicate are needed for phytoplankton to grow in the surface waters of the oceans. The limiting nutrient is thought to be nitrate in most ocean waters. Over 10% of the world's ocean surface waters, however, are replete with the major plant nutrients (nitrate, phosphate, and silicate) and light, while standing stocks of phytoplankton remain low. These areas include the North Pacific, the equatorial Pacific, and the Southern Ocean waters around Antarctica. The surface concentrations of nitrate in the surface waters of the Pacific waters from the south to the north are shown in Figure 9.12. The factors that limit phytoplankton growth and biomass in high-nutrient, low-chlorophyll (HNLC) areas have been vigorously debated (Chisholm and Morel, 1991). Some have suggested that increasing the growth of plants in HNLC areas could remove significant amounts of carbon dioxide from the atmosphere (Martin, Gordon, and Fitzwater, 1990).

The cause of the lack of growth of plants in some HNLC areas has been attributed to the following:

1. Zooplankton grazing may contribute to the maintenance of low chlorophyll levels (Banse, 1990).
2. Strong turbulence at high latitudes might mix phytoplankton below the critical depth and result in light limitation (Mitchell et al., 1991).
3. Lack of needed micronutrient elements such as iron may limit the growth (Brand, 1991).

The limitation of metals for the growth of phytoplankton can be demonstrated by examining the relative concentrations of metals to phosphate (Brand, 1991) in ocean waters

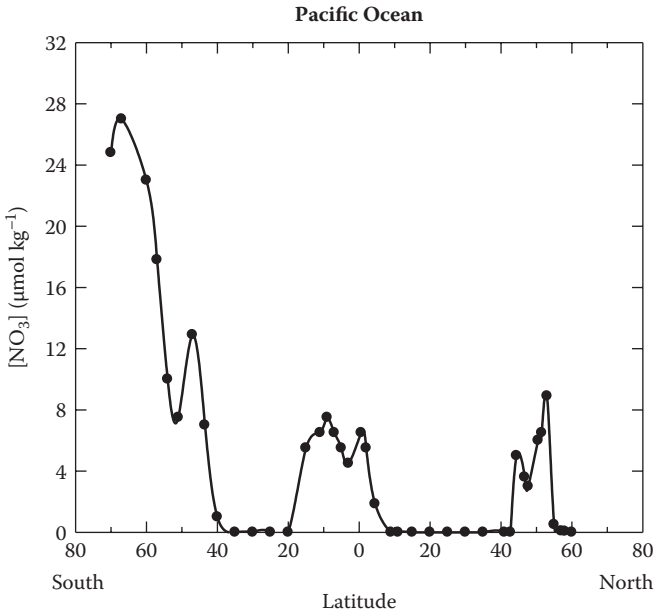

FIGURE 9.12
The concentration of nitrate in the surface waters of the North Pacific, Equatorial Pacific, and Antarctic Oceans.

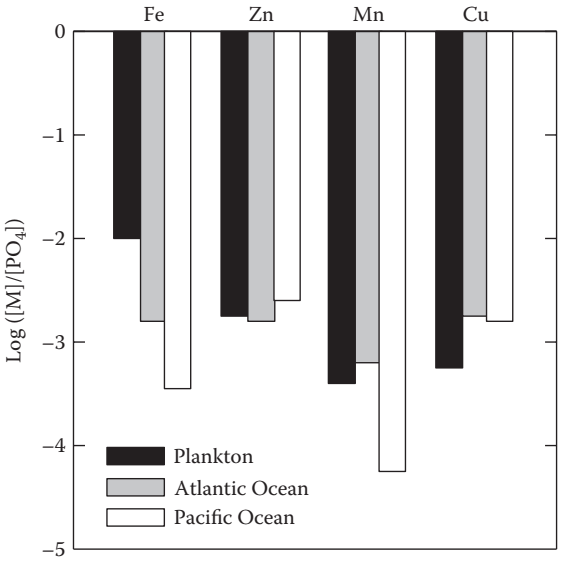

FIGURE 9.13
The relative concentrations of metals to phosphate in ocean waters compared to the ratio in phytoplankton.

compared to the ratio in phytoplankton (see Figure 9.13). The relative concentrations of iron in phytoplankton are higher than the levels in the waters, suggesting that it may be limiting to growth. Mn is the only other metal that is lower in Pacific waters relative to the concentration in phytoplankton.

Since iron is an essential trace element used in electron transport and enzyme systems, Martin (1992) has suggested that the concentration of Fe is most important. This led him to the following iron hypothesis:

> Iron availability limits specific rates of phytoplankton growth in HNLC areas of the world's oceans.

Two corollaries to this hypothesis are

1. The uptake of nutrients and carbonate by phytoplankton is limited by iron availability.
2. Since iron limitation controls the growth of phytoplankton that removes CO_2 from the atmosphere, the levels of atmospheric CO_2 vary as a function of iron transport to the surface of the oceans.

A number of preliminary studies were made that support the iron hypothesis, including

1. Measured iron levels are quite low (Figure 9.14) and may not support high phytoplankton biomass at maximum growth rates (Martin and Gordon, 1988). The use of trace metal clean sampling techniques has shown that open ocean iron concentrations in surface waters are present at picomolar levels that are insufficient to support the growth of phytoplankton.
2. The addition of Fe to uncontaminated seawater from the HNLC areas has been shown to stimulate the growth of phytoplankton, especially diatoms (Martin and Fitzwater, 1989; Martin et al., 1991). This is demonstrated in a comparison of the

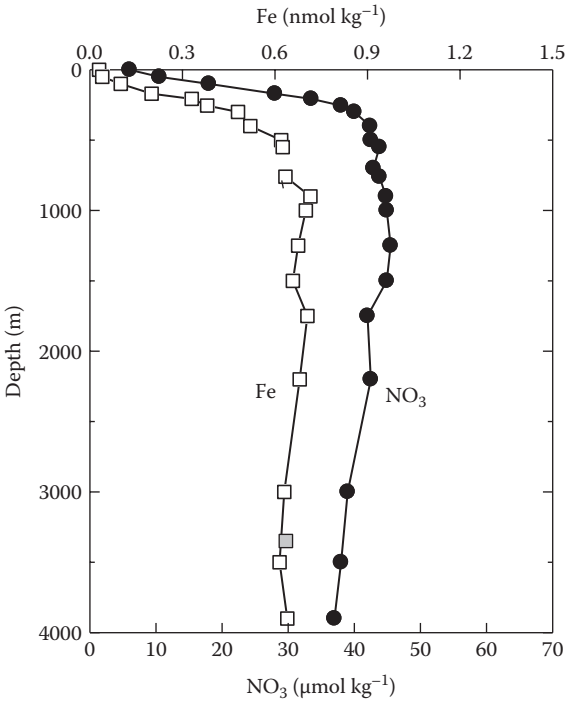

FIGURE 9.14
Profile of Fe in North Pacific waters compared to the nitrate and oxygen.

doubling times of phytoplankton in waters with and without the addition of iron in waters collected near the North Pacific (Alaska), the South Pacific (Antarctica), and the Equatorial Pacific (equator) in Figure 9.15.

3. Laboratory experiments have also shown that low levels of iron can limit the growth of phytoplankton (Sunda et al., 1991; Hudson and Morel, 1990; Brand, 1991). Coastal phytoplankton have optimum ratios of Fe:P of 10^{-2} to $10^{-3.1}$, while most ocean species have ratios less than 10^{-4}, an indication that the latter have adapted to low levels of Fe in the open oceans. New production of cyanobacteria is Fe limited, while algal biomass is not. By controlling the concentration of iron by the addition of the complexing ligand EDTA, it can be shown that low levels of Fe decrease the growth of coastal and oceanic cyanobacteria.
4. Fluorometry with a fast repetition rate has shown that the photochemical energy conversion efficiency in phytoplankton is less than maximum in HNLC areas and is significantly increased with the addition of nanomolar levels of iron (Greene, Geider, and Falkowski, 1991).

These experiments suggested that iron availability and supply may regulate ocean production in HNLC areas. The historical record of atmospheric CO_2, dust deposition, and non-sea-salt aerosols (from the growth of phytoplankton) in the Vostok ice core suggests that iron deposition may be related to ocean productivity (see Figure 9.16). The supply of iron-rich dust to the oceans may cause an increase in ocean productivity and decrease the atmospheric concentration of CO_2 (Martin, 1990).

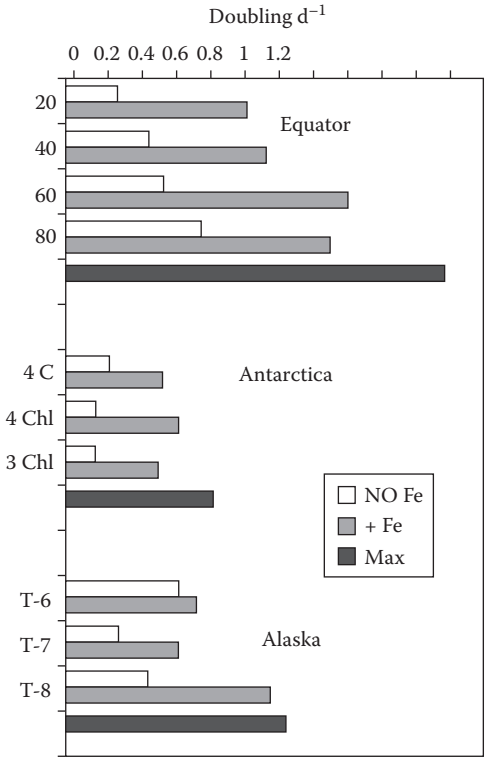

FIGURE 9.15
The effect of the additions of Fe on the doubling times of the growth of phytoplankton in the North Pacific, Equatorial Pacific, and South Pacific.

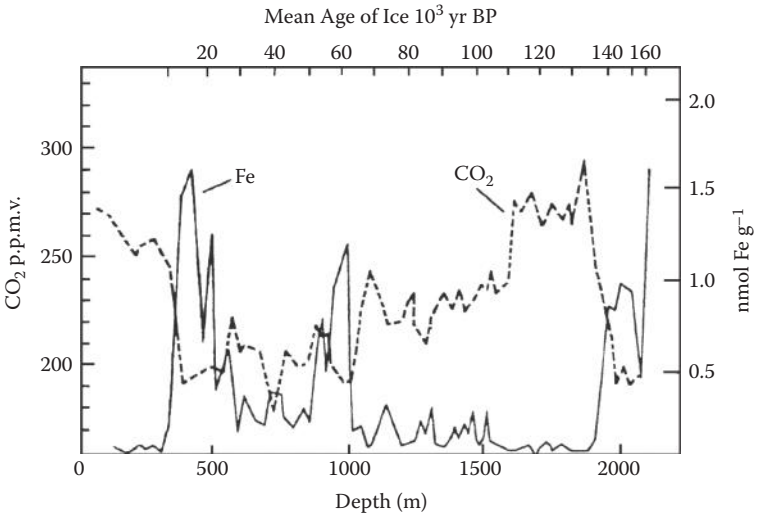

FIGURE 9.16
The historical record of atmospheric CO_2, dust deposition, and non-sea-salt aerosols.

The extrapolation of these shipboard and laboratory experiments to whole ecosystems has, however, been strongly criticized (Banse, 1990). Bottle experiments, by design, do not accurately represent the community response to nutrients since some components of the community are excluded. The effects of iron on phytoplankton growth in HNLC areas can only be resolved by actual mesoscale enrichments of ocean waters to see the effect on the entire ecosystem. Two natural iron enrichment studies (IRONEX I and II) have been conducted in the waters south of the Galapagos Islands in the Equatorial Pacific (Martin et al., 1991; Coale et al., 1996). The locations were selected as favorable spots since they are in an HNLC area, and the Galapagos plume off the western coast of the island provides a proximal comparison as a possible natural iron enrichment experiment. More recently, an iron addition experiment (SOFeX, Southern Ocean Iron Experiment) was carried out in the southern oceans (Coale et al., 2004). These experiments were undertaken to examine the connection between iron availability, phytoplankton productivity, and atmospheric carbon dioxide. The results of these studies are discussed next. More details are available in the numerous articles describing these experiments.

9.2.1 IRONEX I Study

In mid-October 1993, the research vessel *Columbus Iselin* occupied an area approximately 500 km south of the Galapagos Islands to begin the enrichment experiment. A scientific paper summarizing the results of the experiment by Martin et al. (1991) has been published. The initial iron concentrations in the area of the experiment were approximately 0.1 n*M*. To be sure that the changes in the patch could be attributed to the addition of iron, the area was surveyed over a period of 2 days to determine its biological, chemical, and physical heterogeneity (see Table 9.5). The surface waters to about 35 m had uniform properties. The temperature and salinity of the surface waters to about 40 m were quite uniform (t = 22 ± 0.08°C and S = 35.36 ± 0.01). The carbonate parameters were also quite uniform in the surface waters (pH = 8.008 ± 0.009, NTA [normalized total alkalinity] = 2309 ± 2 µ*M*, $NTCO_2$ [normalized total carbon dioxide] = 2044 ± 2 µ*M*, fCO_2 = 408 ± 6 µatm). The surface water levels were higher than the atmospheric levels (360 µatm) in this region. The oxygen levels were constant and in near equilibrium with the atmosphere (216 ± 1 *M*).

TABLE 9.5

Maximum Changes in Chemical Parameters Observed during Iron Enrichment Experiments, SOFeX, IRONEX I, IRONEX II, SOIREE, EisenEx, and This Study

	IRONEX I[a] Day 3	IRONEX II[b] Day 8	SOIREE[c] Day 13	EisenEx[d] Day 18	North Patch Day 39	South Patch Day 20
NO_3 (µmol kg^{-1})	–0.68 ± 0.2	–3.9 ± 0.2	–2.9 ± 0.3	–1.57 ± 0.1	–1.4 ± 0.1	–3.5 ± 0.1
PO_4 (µmol kg^{-1})	–0.02 ± 0.02	–0.24 ± 0.02	–0.19 ± 0.02	–0.16 ± 0.01	–0.09 ± 0.02	–0.21 ± 0.02
$Si(OH)_4$ (µmol kg^{-1})	–0.02 ± 0.2	3.9 ± 0.2	–2.4 ± 0.4	–0	–1.1 ± 0.1	–4.0 ± 0.1
NTA (µmol kg^{-1})	–2.0 ± 2	–1.0 ± 3	—	—	0 ± 4	0 ± 4
$NTCO_2$ (µmol kg^{-1})	–6 ± 2	–27 ± 2	–18 ± 3	–15 ± 2	–14 ± 4	–23 ± 4
pH_{sws} (25°C)	—	—	—	0.025 ± 0.001	0.032 ± 0.01	0.057 ± 0.01
fCO_2 (µatm)	–13 ± 6	–73 ± 6	–38 ± 2	23 ± 2	–26 ± 3	–36 ± 3
O_2 (µmol kg^{-1})	2.8 ± 1.0	32 ± 1.0	—	10 ± 1	23 ± 2	11 ± 2

[a] Data from Coale et al. (1996); Martin et al. (1991).
[b] Data from Cooper, Watson, and Nightingale (1996); Steinberg, Millero, and Zhu (1998).
[c] Data from Bakker, Watson, and Law (2001); Boyd et al. (2000).
[d] Data from Bozec et al. (2004).

The concentrations of nitrate, phosphate, and silicate were 10.8 ± 0.4 μ*M*, 0.92 ± 0.02 μ*M*, and 3.9 ± 0.1 μ*M*, respectively, and the chlorophyll concentrations were 0.24 ± 0.02 μg L^{-1}, typical of the equatorial HNLC region. The low chlorophyll conditions were substantiated by overflights of the NASA airborne optical laboratory prior to the experiment. The primary production (15 to 25 μg C L^{-1} day^{-1}) for surface waters is typical for this region.

An area of approximately 64 km^2 (8 × 8 km) was enriched by adding 455 kg (7800 moles) of iron as $FeSO_4$ (0.5 *M*) in acidic seawater (pH = 2) to the prop wash of the ship. Along with the iron, sulfur hexafluoride, SF_6, was added as an inert tracer. The SF_6 solution (Ledwell et al., 1993) was prepared by dissolving 0.35 moles of SF_6 in seawater in a 2500-L steel tank. The SF_6 was pumped (1.4 min^{-1}) together with the iron solution (12 L min^{-1}) into the prop wash as the ship steamed at about 9 km h^{-1}. The goal was to increase the iron concentration to 4 n*M* (a level, in bottle experiments, that was sufficient to cause large increases in chlorophyll and complete depletion of the available major nutrients within 5 to 7 days). This enriched patch was tracked for 10 days and monitored for changes in biological, chemical, and physical parameters. The iron hypothesis required that we detect increased rates of growth in the patch relative to water outside the patch. The increased growth in the patch should reduce major nutrient concentrations and decrease the fugacity of carbon dioxide. Three tracking strategies were employed to maintain contact with the iron-enriched area. The iron deployment and initial sampling were performed about a central Lagrangian reference point located by a buoy equipped with a global positioning system (GPS) receiver interfaced to a VHF (very-high-frequency) packet radio transmitter and receiver. The GPS buoy was interrogated every 5 min to determine the location of the ship relative to this central point. In addition, four World Ocean Circulation Experiment (WOCE) drifter buoys equipped with ARGO floats buoy positions could be received. All of these buoys had a holey sock drogue set at 10 m to reduce slippage relative to the enriched patch.

The inert chemical tracer SF_6 also added to the patch was detected continuously by electron capture gas chromatography (GC) at detection limits of less than 10^{-16} *M*. A flow-through pumping system with the intake set at 3 m on the ship's bow was used to sample surface seawater. SF_6 measurements were used to determine the position of the enriched iron patch relative to the GPS buoy. The concentration of iron in the patch was also determined every 8 min by both colorimetric and chemiluminescent analyses based on flow injection techniques. Surface seawater was supplied for iron analyses through the Teflon pumping system with the intake on the ship's bow. Samples were acidified to pH = 3 before analyses, resulting in the detection of dissolved iron, freshly precipitated colloidal iron, and much of the aged colloidal iron (total dissolvable iron).

The patch was sampled for 3 days in a star-shaped pattern using the surface pumping systems while the ship steamed at approximately 9 km h^{-1}. Each day, one major hydrographic station was occupied within the patch and one outside the patch at a time near local noon. Samples were collected at these stations for primary productivity, species composition, chlorophyll, pigments, nutrients, POC (particulate organic carbon), PON (particulate organic nitrogen), DOC (dissolved organic carbon), DMS, dimethylsulfonium propionate (DMSP), dissolved and particulate trace metals, halocarbons, and CO_2 system parameters. The concentrations of the SF_6 tracer, together with the ship's position relative to the GPS buoy, were used to distinguish inside from outside stations. Overflights of the NASA P-3 *Orion* optical laboratory were performed on four additional occasions during the experiment to assess the large-scale effects of iron on surface water chlorophyll. The aircraft flew legs of approximately 180 km in length in a star pattern centered on the GPS buoy.

The core of the patch was subducted beneath a low-salinity front that passed through the area from east to west late on the fourth day after the iron addition, to a depth of 30 to

35 m, where it was confined in a 5- to 10-m layer at the top of the thermocline. After subduction, the patch could still be detected by its distinct salinity and low light transmission. Hydrographic sampling of these areas confirmed the presence of SF_6 by direct chemical analysis. SF_6 concentrations did not decrease after subduction. The highest values found each day were a constant 40 to 50 f*M* over the entire 9-day duration of the experiment. The constancy of the SF_6 suggests that unfertilized waters did not penetrate into the core of the patch even after subduction.

Dissolvable iron concentrations (DFe) as high as 6.2 n*M* were determined in the core of the patch 4 h after fertilization. These values decreased rapidly when the water column mixed, with the highest values on the subsequent day being 3.6 n*M*, in good agreement with predicted concentrations (3.8 n*M* Fe). The concentrations of DFe in the core of the patch decreased by about 15% each day. Despite this decrease, contour plots of iron and SF_6 in the surface layer were still in good spatial agreement 3 days after fertilization. Iron dropped below the detection limit in the subducted layer after the fourth day. Remnants of the patch also remained on the surface, as demonstrated by SF_6 measurements. The iron concentrations extrapolated from the amount of SF_6 that was found at the surface would have been too low to detect at sea.

Three distinct pools of iron were formed on injection. Most of the Fe(II) injected into the patch was oxidized in minutes to Fe(III), and colloidal iron oxyhydroxides should have precipitated with a first-order rate constant of 0.1 h. Of the three, colloidal Fe(III) is not thought to be bioavailable. Laboratory experiments, however, indicated that these colloids would remain suspended where they could be photoreduced and rendered bioavailable.

The changes in the chlorophyll in the patch became apparent within a day after the addition of Fe. Changes in chlorophyll (Figure 9.17) and primary productivity (Figure 9.18) as a function of depth in the water column were quite apparent a few days after the addition of Fe. The chlorophyll increased from values of 0.24 μg L^{-1} to a maximum of about 0.65 μg L^{-1}, a factor of 3 increase. The maximum primary production values in the mixed layer were initially 15 to 25 μgC L^{-1} day^{-1} and increased to values of 48 μgC L^{-1} day^{-1}. This two- to threefold productivity increase was seen in both small and large phytoplankton.

Microscopic examination of the water collected from within the patch indicated an increase in the biomass of all classes counted. Total autotrophic biomass calculated from cell numbers and volumes increased from 16 to 33 μgC L^{-1}, a 100% change. The largest contributors to the plankton biomass were *Synechococcus*, a red fluorescing picoplankton, and autotrophic dinoflagellates. Diatoms were a small fraction of the initial total plankton biomass (17%) yet showed increases similar to the other groups. Heterotrophic biomass increased from 4.7 to 7.3 μg C L^{-1} and was associated with heterotrophic dinoflagellates followed by ciliates.

Photosynthetic energy conversion efficiency (Fv/Fm) was the first biological response detected (Kolber et al., 1994). Values of Fv/Fm increased by 60% on the first sampling transect through the patch, indicating a large physiological response within the first 24 h (the period required to fertilize the patch). This parameter increased from 0.3 to 0.60 by day 2 of the experiment, approaching the maximum value attainable for phytoplankton grown under nutrient-replete conditions (0.65). The distributions of Fv/Fm and chlorophyll were also coincident with the area enriched in iron (Figure 9.19). The rapid increases in photosynthetic energy conversion efficiency in all sizes of phytoplankton in the patch confirm that the ambient populations in all size classes are physiologically limited by lack of available iron.

The changes in the chemical constituents that occurred in the surface waters are shown in Figure 9.20. The nutrients showed little or no systematic differences in nitrate,

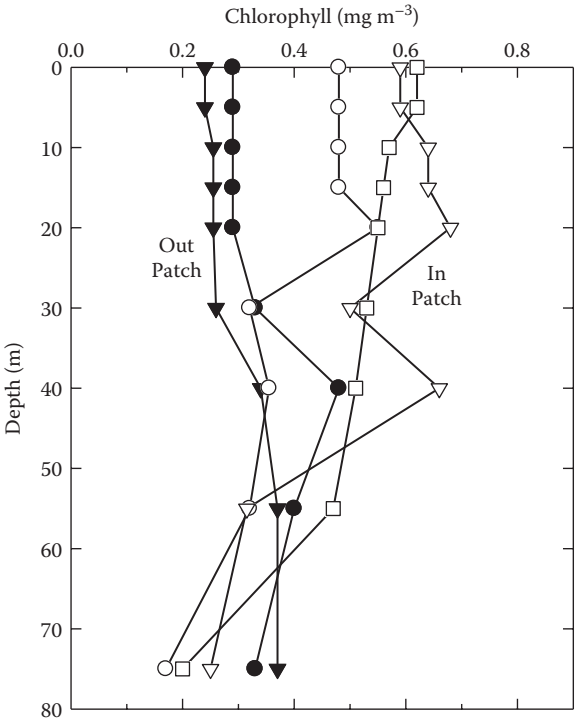

FIGURE 9.17
Changes in chlorophyll as a function of depth 3 days after the addition of Fe to the patch.

phosphate, and silicate concentrations within the mixed layer between inside and outside stations. The ratio of nitrate uptake to chlorophyll production in incubated Fe experiments is approximately 1 mole NO_3^- g^{-1} Chl. A chlorophyll increase of 0.5 µg L^{-1} should be accompanied by a nitrate change of about 0.5 µ*M*. Initial nitrate concentrations were 10.8 µ*M*. The day-to-day precision of the nitrate measurements (±0.4 µ*M*) was insufficient to detect a 0.5-µ*M* decrease. Phosphate and silicate also showed no definitive change over this time period inside the patch.

Ammonia, however, showed a consistent difference between the inside and outside stations. After fertilization, the mean ammonia concentrations measured inside the patch after 3 days were 0.1 ± 0.07 µ*M* lower than the values observed outside the patch. An ammonia maximum with values near 0.45 µ*M* was regularly found near the base of the mixed layer outside the patch. This maximum disappeared within the fertilized patch, and, with one exception, no ammonia concentrations higher than 0.12 µ*M* were found inside the patch. Preferential uptake of ammonia would be expected as physiological rates increased.

The measurements of CO_2 fugacity and total CO_2 in the patch (Table 9.6) were significantly lower (3 to 12 µatm and 6 µ*M*) than those observed outside the patch (Watson et al., 1994). These changes were apparent within 2 days of the iron release. Biomass increase estimated from microscopic counts of cells was 20 µg C L^{-1}. If the inorganic carbon decreased by the same amount, the fugacity of CO_2 in the mixed layer should decrease by 3 µatm per day in the fertilized patch. If the CO_2 fugacity decrease were four times larger (upper range measured) than that predicted from the observed increase in biomass, then a large amount of the carbon may have been lost from the patch.

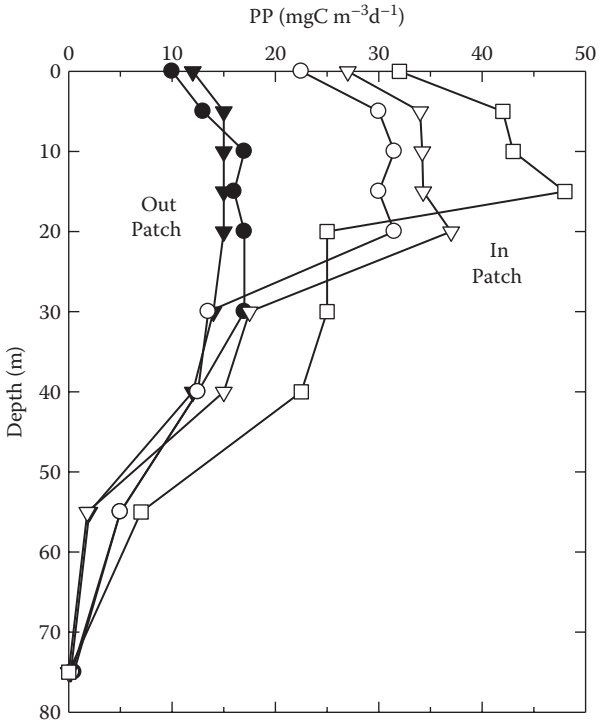

FIGURE 9.18
Changes in the primary production as a function of depth 3 days after the addition of Fe to the patch.

Particulate DMSP showed a significant increase (50 to 80%) in the fertilized patch. DMSP is produced by phytoplankton and decays to produce DMS. There were no clear changes in DMS concentration in surface water (2.5 n*M* ± 0.4), which is not surprising considering the duration of the study versus the time needed to degrade DMSP to DMS.

Fertilization studies by Smetacek et al. (2112) in the Southern Ocean have produced diatom-dominated blooms. They found a pull down of surface CO_2 and nutrients as in earlier studies. However, unlike the earlier studies, they were able to track the sinking particles. They found that as much of 50% of the particles sank below 1000 m.

9.2.2 Galapagos Plume Study

The Galapagos Islands lie near a sharp equatorial front that separates low-nutrient, oligotrophic waters to the north from high-nutrient waters to the south. There are strong horizontal gradients as a result. Satellite studies show a plume of high-chlorophyll water off the west of the Galapagos Islands (Figure 9.21) that is associated with the nutrient-rich, westerly flowing, south equatorial current. Hydrographic surveys show anomalously high chlorophyll concentrations and depleted nitrate concentrations over the Galapagos Platform and downstream of the islands. It has been suggested that these elevated chlorophyll levels are produced by the addition of iron derived from the island platform. As part of the IRONEX study, a series of stations were occupied both upstream (to the east) and downstream (to the west) of the Galapagos Islands (Figure 9.22). Measurements of trace metals as well as onboard analysis for the same parameters as measured in the patch

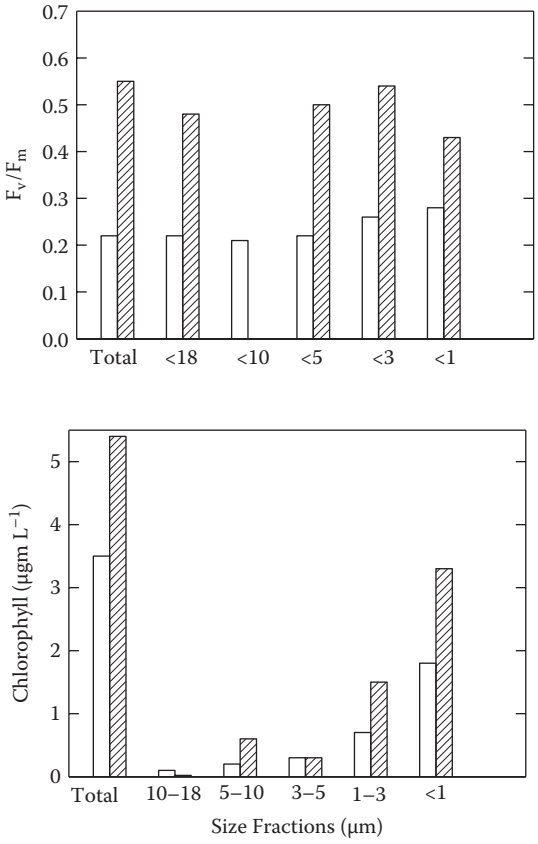

FIGURE 9.19
Changes in the photosynthetic energy conversion efficiency (Fv/Fm) and chlorophyll after the addition of Fe.

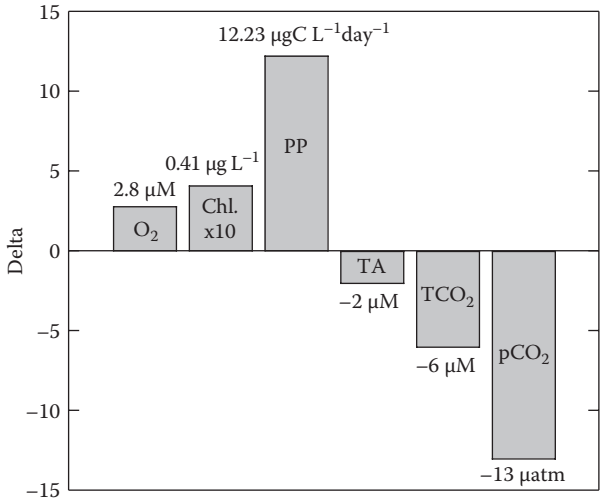

FIGURE 9.20
Changes in the chemical parameters in the surface waters 3 days after the addition of Fe.

TABLE 9.6

Maximum Changes in Chemical Parameters Observed during the Last Occupation of the North Patch and the South Patch during the SOFeX Study

	North Patch Day 39	South Patch Day 20
NO_3 (μmol kg^{-1})	–1.4 ± 0.1	–3.5 ± 0.1
PO_4 (μmol kg^{-1})	–0.09 ± 0.02	–0.21 ± 0.02
$Si(OH)_4$ (μmol kg^{-1})	–1.1 ± 0.1	–4.0 ± 0.1
NTA (μmol kg^{-1})	0 ± 4	0 ± 4
$NTCO_2$ (μmol kg^{-1})	14 ± 4	–23 ± 4
pH_{sws} (25°C)	0.032 ± 0.01	0.057 ± 0.01
fCO_2 (μatm)	–26 ± 3	–36 ± 3
O_2 (μmol kg^{-1})	23 ± 2	11 ± 2

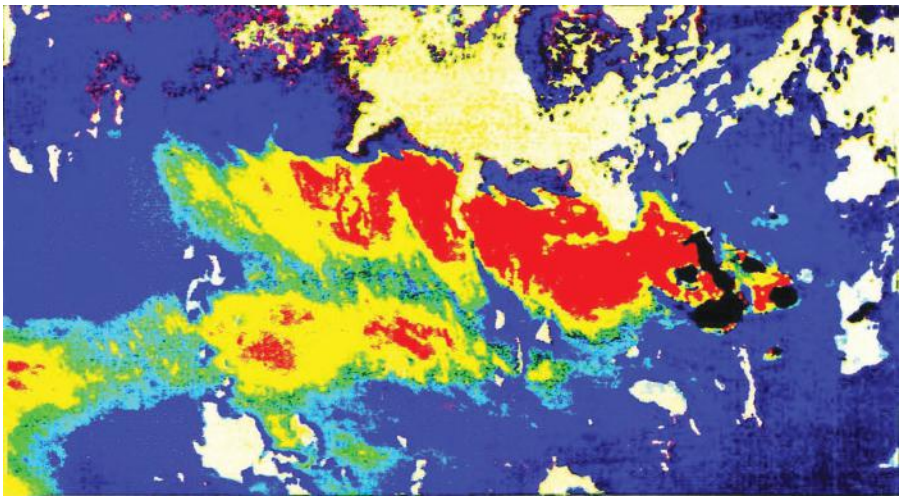

FIGURE 9.21
Color satellite view showing the plume of high chlorophyll on the western coast of the Galapagos Islands.

were performed. Surface water iron, nitrate, fCO_2, and fluorescence were also performed on transits between stations (Sakamoto et al., 1998; Millero et al., 1998). The surface values of temperature, nitrate, and fCO_2 around the islands showed the strong upwelling that occurs off the western coast (see Figure 9.23).

The nitrate concentrations around the islands were greater than 10 μ*M* at the surface. Chlorophyll concentrations and rates of primary production were significantly elevated at stations downstream when compared to upstream. Iron was not detected (<0.2 n*M*) with the surface mapping system on transits upstream of the islands. Iron concentrations as high as 1.3 n*M* were detected on a transect from 1°30′ S to 0° along 91°45′ W. The areas with elevated iron concentrations are within 10 km of Isla Isabella. These high concentrations appeared to be associated with upwelled water that had higher salinity and lower temperature than the surrounding surface water masses. Elevated chlorophyll fluorescence signals were also associated with the high iron concentrations. Even higher iron concentrations

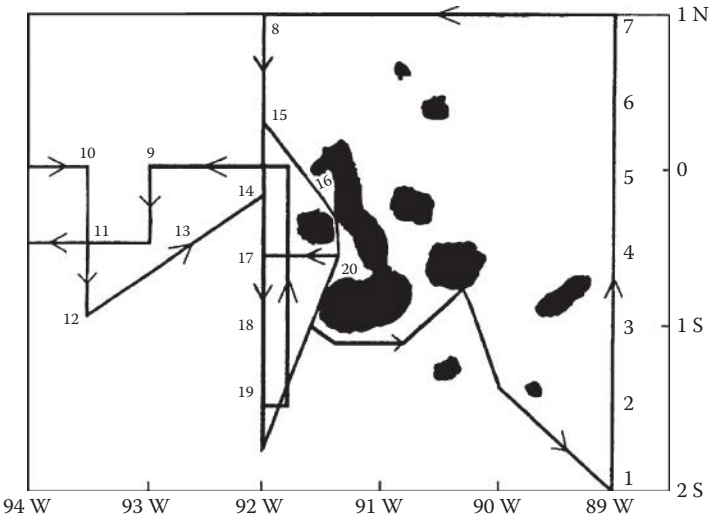

FIGURE 9.22
Hydrographic stations around the Galapagos Islands.

(3 n*M*) were found in the Bolivar Canal. These concentrations were associated with chlorophyll levels in excess of 13 μg L^{-1} and nearly complete depletion of nitrate and decreases of pCO_2 of as much as 200 μatm (see Figure 9.24; Sakamoto et al., 1998).

Chlorophyll concentrations in the downstream plume were typically near 0.7 μg L^{-1} or three times higher than in the upstream water mass. High fluorescence signals were regularly associated with frontal features characterized by lower temperatures, higher salinities, and higher nitrate and pCO_2 concentrations (see Figure 9.23). The highest fluorescence signals always occurred at the contact between these upwelled water masses and the surrounding water.

Concentrations of chlorophyll and primary productivity rates increased by three to four in the downstream plume. Chlorophyll-specific rates of primary production showed a smaller change. This is not surprising as enclosed enrichment experiments have consistently shown that iron-deficient cells will preferentially synthesize chlorophyll, resulting in a decrease of the cellular carbon:chlorophyll ratio.

Increased grazing pressure must have exerted some control on the rate of biomass increase. However, it does not seem to be a likely mechanism for preventing phytoplankton from completely consuming the available major nutrients in the waters downstream of the Galapagos Islands. Complete utilization of the available nitrate was observed only in the Bolivar Canal station. Other investigators have also seen significant depletion of major nutrients at stations over other regions of the Galapagos Platform. Grazing can be a significant limitation on nutrient consumption only if there is a large reduction in grazing pressure in waters over the Galapagos Platform and in bottle experiments. Although reduced grazing in bottle experiments is likely, there is no reason to expect an equivalent reduction in grazing pressure over shelf regions. While vertically migrating zooplankton might be excluded over a continental shelf, microheterotrophs should be unaffected over shelf regions.

This suggests that nutrient consumption and phytoplankton growth are limited in the patch and downstream of the Galapagos Islands because of a loss term that occurs in open

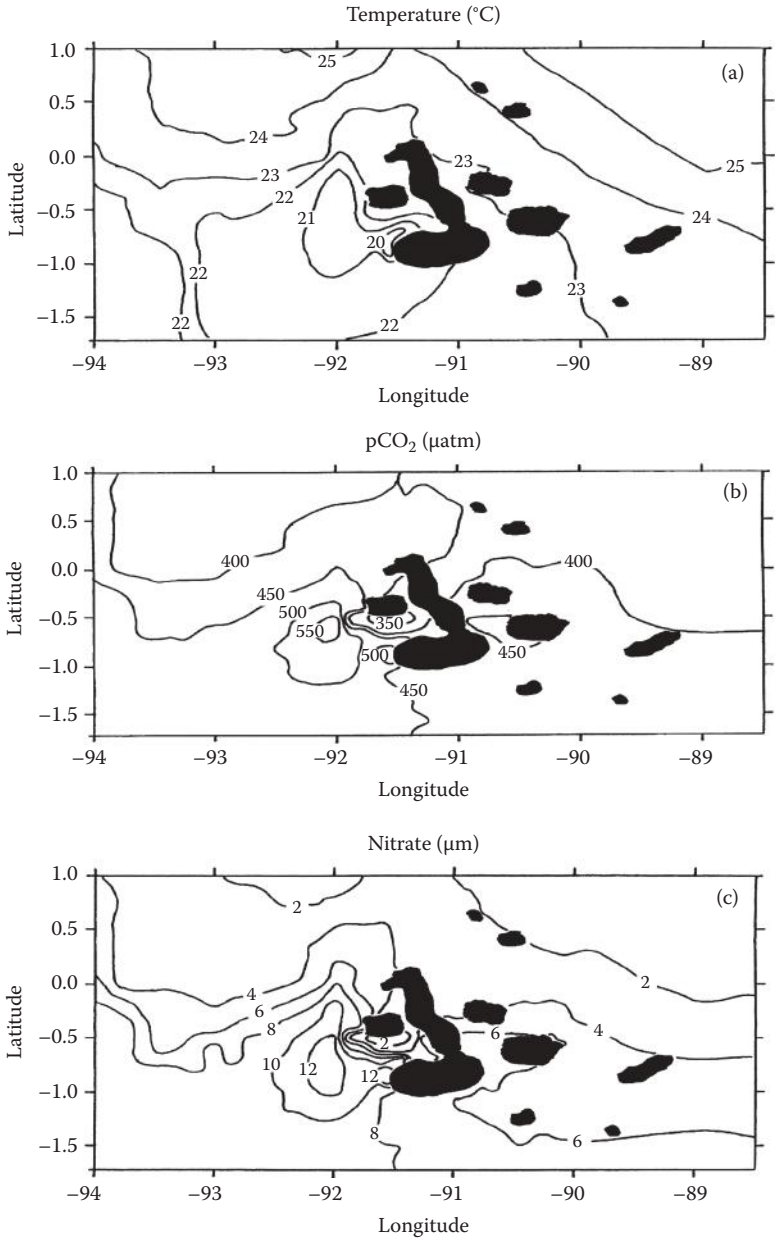

FIGURE 9.23
Surface values of temperature, NO_3^-, and pCO_2 in surface waters around the Galapagos Islands.

waters but not in bottles or in shallow shelf regions. This loss term might be sinking of large diatoms. If sinking keeps the diatom population low, then the absolute rates of nutrient uptake will be limited because phytoplankton growth is a first-order process.

Iron would also be lost much more rapidly from open ocean systems than from bottles or shallow waters. Iron cannot be lost from a bottle. In shallow waters, sinking iron

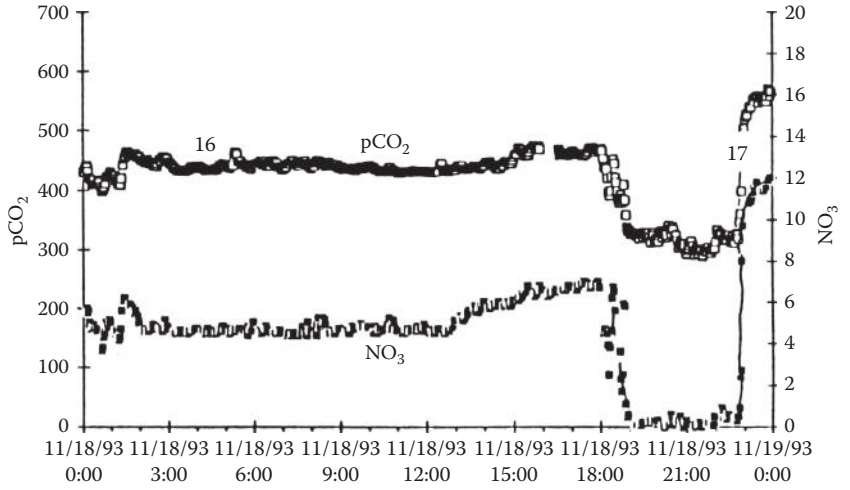

FIGURE 9.24
Changes in the surface NO_3^- and pCO_2 in the waters in the Western Galapagos Islands.

is trapped in a nepheloid layer near the bottom. Concentrations of Fe in the nepheloid layer along continental margins can be greater than 10 n*M*, and these enriched waters from the nepheloid layer will continually resupply the euphotic zone with iron. This probably accounts for the iron concentrations greater than 1 n*M* observed near the islands. The biological similarity of shipboard iron enrichment experiments and stations over the Galapagos Platform and Bolivar Canal suggests that it is the elimination of the loss term for iron that may be responsible for complete utilization of nutrients.

Upwelling in deep water along the equator is not nearly as effective at supplying iron to the mixed layer. The highest dissolved iron values found in the equatorial Pacific are only 0.55 n*M* at depths of 2400 m. Iron concentrations at 150 m are less than 0.2 n*M* and thus are unable to supply the levels of Fe needed to decrease the levels of nutrients much. Since the upwelling of waters from the equatorial undercurrent could not produce the large iron concentrations found, the enrichment of iron must come from the island platform. It has also been suggested that atmospheric transport and deposition of island-derived aerosol particles may be responsible for increased iron in the plume. Since the prevailing winds do not have the proper orientation of the plume to supply the Fe, ocean currents may transport the island-derived materials to the plume.

The residence time of bioavailable iron added to surface waters must be very short. Iron was not detected far from the source region downstream of the islands. This indicates that both systems reflected a transient addition of iron rather than a sustained addition characteristic of bottle enrichments and shallow shelf stations. With a transient addition, only a few cell divisions are possible before the iron is removed from the system. Continual supply must occur to sustain production. The factors controlling the cycling of Fe in ocean waters are shown in Figure 9.25. The oxidation of Fe(II) to Fe(III) is quite fast (two to three half-times). Fe(III) is not very soluble at the high pH of seawater and can form colloidal Fe oxides that eventually come out of solution by coagulation. The colloids can be stabilized by organics that also can form strong complexes with Fe(III). The rapid removal of Fe added to seawater prevents the complete removal of nutrients. The continual addition of Fe from coastal sediments can serve as a source of Fe that can completely use up the nutrients in bottles and shallow waters near the Galapagos.

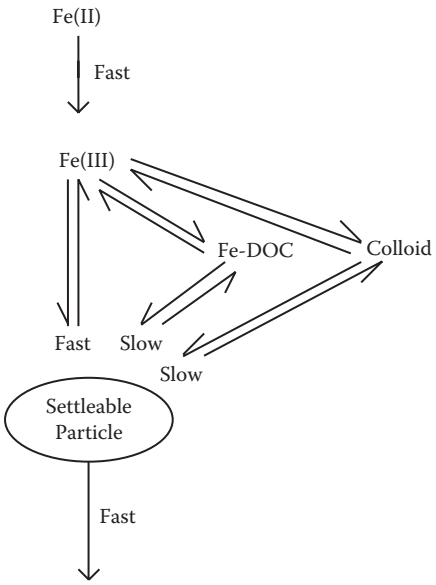

FIGURE 9.25
Cycling of iron in the marine environment—the processes controlling the state of Fe in seawater.

9.2.3 IRONEX II Study

Although the results of the IRONEX I experiment were encouraging, many questions remained. It was not clear that the modest increase in productivity and negligible loss of nitrogen and phosphate resulted from the loss of Fe or an increase in zooplankton grazing. In May 1995, the IRONEX II study was conducted in Equatorial Pacific to attempt to answer some of these questions. During this experiment, the patch was repeatedly fertilized with Fe and studied for 19 days. The response of the system to an initial 2-n*M* iron infusion and two subsequent 1-n*M* reinfusions to the surface water were measured several times a day during the study. The results led to a significant decrease in nutrients and carbon dioxide (Coale et al., 1996). A summary of the decreases in the nutrients and carbon dioxide parameters during the IRONEX II study is given in Table 9.5. The decreases in NO_3^-, PO_4^{3-}, $Si(OH)_4$, TCO_2 (total carbon dioxide), and pCO_2 were much larger in the IRONEX II study. The maximum changes of the carbonate parameters within the patch relative to outside measurements were –27 μmol kg^{-1} in TCO_2, –73 μatm in pCO_2, and +0.058 in pH on days 8 and 9 of the experiment. The total alkalinity (TA) did not change within the experimental error of the measurements (±3 μmol kg^{-1}). In addition to the daily measurements, three transects were made across the patch that showed a spatial biochemical response to the influence of iron and correlations between nutrients and the various carbonate parameters. The changes in the concentration of the pCO_2, nitrate, and fluorescence in and out of the fertilized patch are shown in Figure 9.26. The silicate concentrations in the patch decreased to zero during the experiment, making the system limiting in this nutrient. A diel study of the patch showed daytime decreases of 27 μatm in pCO_2 and 16 μmol kg^{-1} in TCO_2.

The changes in carbon to nutrients during the experiment gave $\Delta NO_3/\Delta PO_4 = 14.3 \pm 0.7$, $\Delta C/\Delta NO_3 = 6.2 \pm 0.2$, $\Delta C/\Delta PO_4 = 90 \pm 5$, $\Delta C/\Delta O_2 = -0.66 \pm 0.07$, $\Delta C/\Delta SiO_2 = 5.05 \pm 0.3$. Corrections for the flux of gases across the air–sea interface during the experiment affected

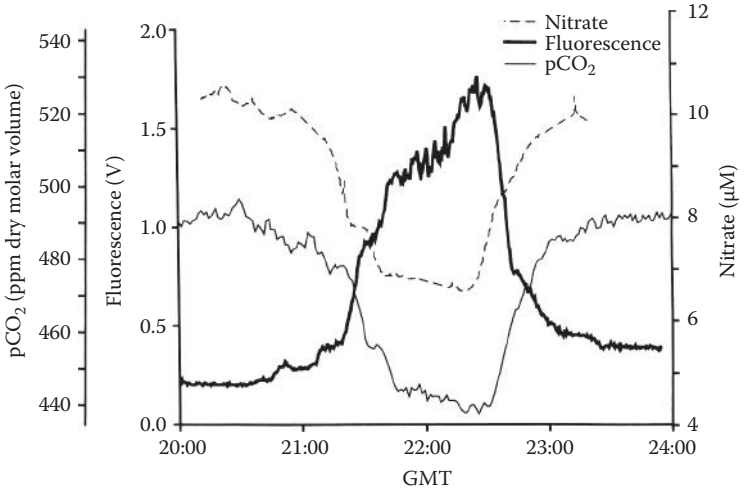

FIGURE 9.26
The values of pCO_2, NO_3^-, and fluorescence across the iron-enriched waters during the IRONEX II study, specifically Transect 3, Day 154 (1996).

the oxygen changes, giving $\Delta C/\Delta O_2 = -0.72$. The slightly lower ratios than those predicted from the Redfield model have been attributed to the predominant production of diatoms that have high concentrations of lipids. These results suggest the following stoichiometry (Steinberg, Millero, and Zhu, 1998):

$$90CO_2 + 104H_2O + 14HNO_3 + H_3PO_4 + 18SiO_2$$

$$\rightarrow (CH_2O)_{76}(CH_2)_{14}NH_3)_{14}(H_3PO_4)(SiO_2)_{18} + 125O_2$$

for the production of phytoplankton in the iron-enriched patch.

The results of these experiments should lead to a better understanding of the interactions between the effect of nutrients and metals on the growth of phytoplankton and the resultant grazing of zooplankton. The issue of whether Fe additions can sequester substantial quantities of atmospheric CO_2 will lead to further debates. The IRONEX experiments, however, demonstrated that open ocean manipulative experiments are possible, and ecological studies in the open ocean are no longer limited to passive observations. This will change significantly the way geochemical and ecological studies are performed in the ocean.

9.2.4 SOFeX Study

During the 2002 austral summer, two *in situ*, mesoscale iron fertilization experiments were conducted (Coale et al., 2004) in two distinct silicic acid regimes of the Southern Ocean (SOFeX) (see Figure 9.27). The properties of the surface waters on the transit from the south and back are shown in Figure 9.28. The concentration of the nutrients and carbon dioxide parameters all increase from the north to the south. This is due to the outcropping of deep waters rich in nutrients and CO_2. The silica concentrations are quite low in the north and increase in the south. The iron was added to the low $Si(OH)_4$ concentrations of the

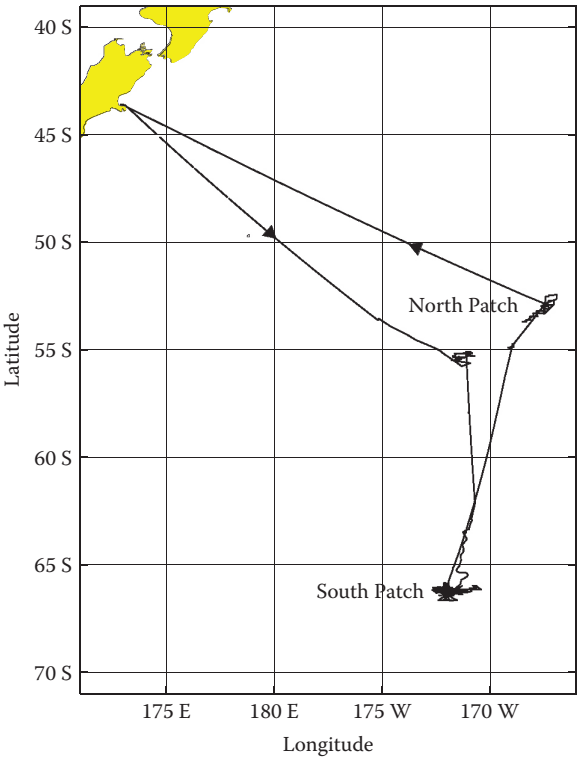

FIGURE 9.27
The cruise track of the transit and locations of the northern and southern patches.

subantarctic (<3 μmol kg^{-1}, north patch) and the high $Si(OH)_4$ concentrations poleward of the Antarctic circumpolar current (ACC), (~63 μmol kg^{-1}, southern patch). The limited iron availability in these two regimes of the Southern Ocean prevents complete biological utilization of the ambient nutrients and influences phytoplankton species composition. The uptake of the macronutrients silicic acid, phosphate, nitrate, and nitrite were measured along with simultaneous measurements of the carbonate parameters TA, total inorganic carbon (TCO_2), and pH from water sampled both inside and outside the iron-enriched waters (Hiscock and Millero, 2005).

A summary of the change in nutrients and carbonate parameters is given in Table 9.5. The observed maximum changes in the northern and southern patches were $\Delta NTCO_2$ = –14, –23 μmol kg^{-1}; ΔNTA = 0 μmol kg^{-1}; ΔpH = –0.032, –0.057; ΔfCO_2 = –26, –36 μatm; ΔPO_4 = –0.09, –0.21 μmol kg^{-1}; $\Delta Si(OH)_4$ = –1.1, –4.0 μmol kg^{-1}; and ΔNO_3 = –1.4, –3.5 μmol kg^{-1}, respectively. The changes in the southern patch were much greater than in the north patch. The changes during SOFeX were the same order of magnitude as found during the IRONEX II study. SOIREE (Southern Ocean Iron Release Experiment) and EisenEx (experiment of the addition of iron to seawater) were preformed in the intermediate silica concentrations of 9.5 μmol kg^{-1} and 14.2 μmol kg^{-1}, respectively. SOIREE was south of the Antarctic polar front (APF) in the Australian sector (Boyd et al., 2000), and EisenEx (iron experiment) within the Antarctic polar frontal zone (APFZ) of the Atlantic sector (Bozec et al., 2004). The north patch results were in reasonable agreement with the results of the SOIREE and EisenEx studies made at intermediate levels of Si.

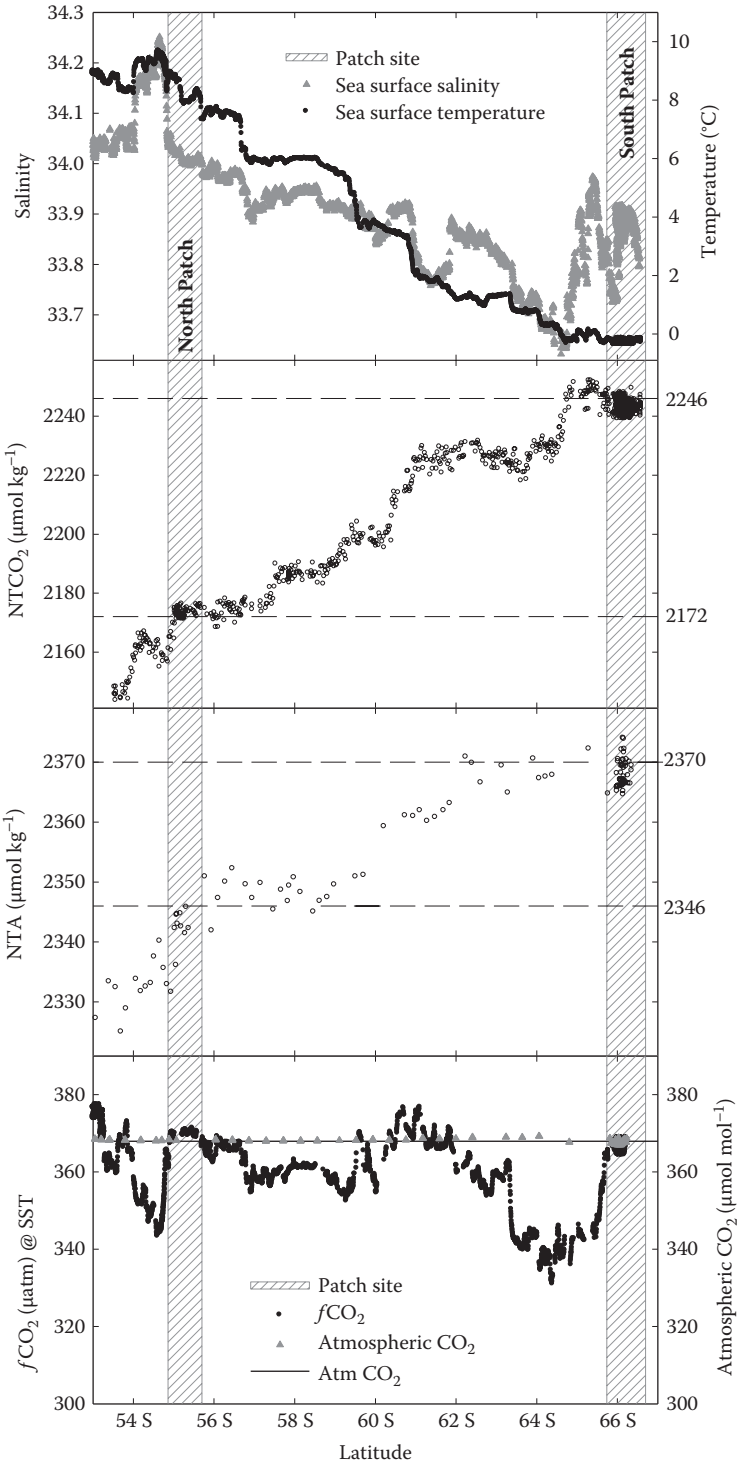

FIGURE 9.28
Surface values of S, t, NTA, $NTCO_2$, and pCO_2 on the transit from the north to the south and back.

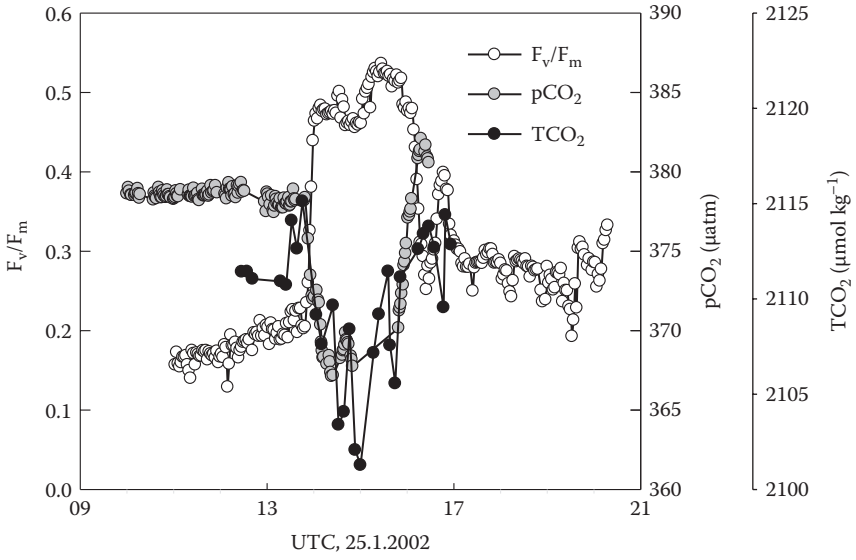

FIGURE 9.29
The value of NO_3^-, fluorescence, and pCO_2 across the southern patch.

The changes in the values of NO_3^-, fluorescence, and pCO_2 across the southern patch are shown in Figure 9.29. A comparison of the surface values of pCO_2 in the north patch and the chlorophyll is shown in Figure 9.30. The southern patch was studied over a period of 20 days, allowing examination of the pull-down of pCO_2 as a function of time. This is shown in Figure 9.31 along with the value in the atmosphere. The large variability of pCO_2 in the waters was partly due to the strong winds in the area during the study. The maximum pull-down at the southern patch was 36 µatm.

The changes in the molar ratios in the northern and southern patches, respectively, were $\Delta N/\Delta P = 13.8 \pm 0.2$ and 13.9 ± 0.1; $\Delta C/\Delta N = 8.8 \pm 0.9$ and 6.7 ± 0.2; $\Delta C/\Delta P = 104 \pm 18$ and 98.4 ± 2.3; $\Delta C/\Delta Si = 8.2 \pm 0.9$ and 5.7 ± 0.2; $\Delta C/\Delta O_2 = -0.73 \pm 0.02$ and -0.74 ± 0.04. The results in the northern and southern patches are compared to the results during the IRONEX I, EisenEx studies in Table 9.7. The N/P ratios in the northern and southern patches are close to the Redfield ratio, while the results of IRONEX II and EisenEx are lower.

The ratios found are different from those found in the earlier Fe experiments in the eastern Equatorial Pacific and the Redfield ratios. They yield different average compositions for the diatoms formed after the addition of Fe given by (Hiscock and Millero, 2005)

$$104CO_2 + 118H_2O + 14HNO_3 + H_3PO_4 + 13SiO_2$$
$$\rightarrow (CH_2O)_{82}(CH_2)_{22}(NH_3)_{14}(H_3PO_4)(SiO_2)_{13} + 143O_2$$
$$98CO_2 + 112H_2O + 14HNO_3 + 17SiO_2$$
$$\rightarrow (CH_2O)_{82}(CH_2)_{16}(NH_3)_{14}(H_3PO_4)(SiO_2)_{17} + 134O_2$$

in the northern and southern patches, respectively.

Both investigations in the Southern Ocean produced notable increases in biomass and associated decreases in dissolved inorganic carbon and macronutrients, a result of the iron

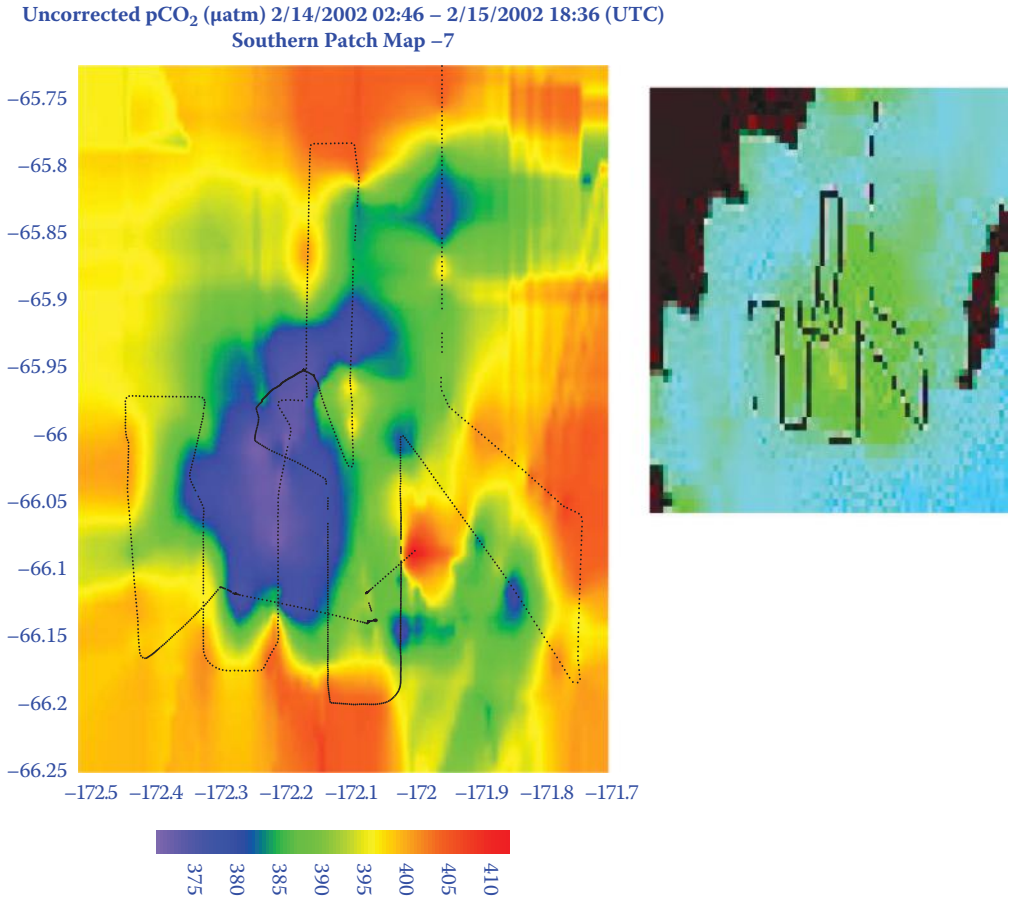

FIGURE 9.30
Comparison of the pCO_2 measured in the northern patch and the chlorophyll from satellite measurements.

enrichment. The SOIREE bloom was observed for only 13 days and the EisenEx bloom for 18 days.

In contrast to the intermediate silica environments examined in previous iron fertilization experiments, the Southern Ocean includes the low-silica region (<3 µmol kg^{-1}) of the subantarctic zone and the high silica concentrations (~63 µmol kg^{-1}) of the subpolar region. The detailed frontal structure of the Southern Ocean (Orsi, Whitworth, and Nowlin, 1995) is directly related to the strong meridional gradients of hydrographic, carbonate, and nutrient parameters. Only a small fraction of the dissolved organic carbon is thought to make it to deep waters and indirectly take CO_2 from the atmosphere to deep waters. A recent study (Smetacek et al., 2012) suggests that as much as 50% is removed to waters at a depth of 1000 m. In summary, most feel that adding Fe to ocean waters with high nutrients is not going to sequester CO_2 from the atmosphere.

Recent observations of the effect of [Fe] on the elemental composition of phytoplankton in HNLC regions of the Southern Ocean document stoichiometric utilization ratios in the euphotic zone that differ from the classical Redfield values (Hiscock and Millero, 2005). A comparison of the SOFeX results to other Fe addition experiments made by other studies

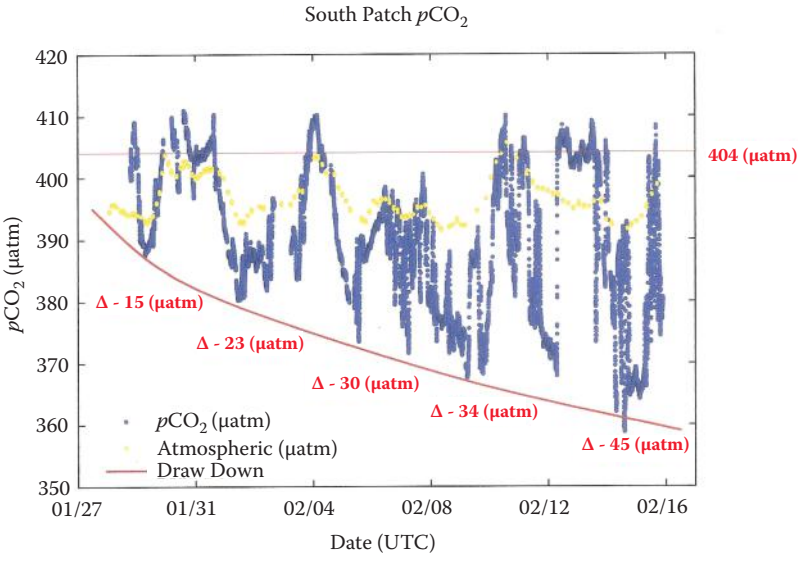

FIGURE 9.31
The decrease in the surface pCO_2 as a function of time in the southern patch.

TABLE 9.7

Slopes of Linear Regressions and Standard Error of Slope for Nutrients Observed during IRONEX II, EisenEx, and SOFeX Compared to Redfield Proportions

Ratio	IronEx II[a]	EisenEx[b]	North Patch	South Patch	Redfield[c]
ΔC:ΔP	90 ± 5	82 ± 5	104 ± 18	98.4 ± 2.3	106
ΔC:ΔN	6.2 ± 0.2	5.9 ± 0.2	8.8 ± 0.9	6.7 ± 0.2	6.6
ΔC:ΔSi	5.1 ± 0.3	2.9 ± 0.3	8.2 ± 0.9	5.7 ± 0.2	7.3
$\Delta C:\Delta O_2$	–0.72 ± 0.07	—	–0.73 ± 0.02	–0.74 ± 0.04	–0.77
ΔN:ΔP	14.3 ± 0.2	12 ± 0.2	13.8 ± 0.15	13.9 ± 0.08	16
ΔSi:ΔN	1.2 ± 0.1	2.0 ± 0.4	1.04 ± 0.02	1.11 ± 0.01	0.9

[a] Data from Steinberg, Millero, and Zhu (1998).
[b] Data from Bozec et al. (2004).
[c] Data from Redfield, Ketchum, and Richards (1963).

in the Pacific (Coale et al., 1996; Martin et al., 1991) and the Southern Oceans (Bakker et al., 2001; Boyd et al., 2000; Bozec et al., 2004; Coale et al., 2004) is shown in Table 9.7.

9.3 Microbial Transformations

Microorganisms in the marine environment can be divided into two types: (a) *eukaryotes* (10 to 100 µm), which have a complete cell structure and include algae (photosynthetic), protozoa (predators of bacteria) and fungi, yeast, and molds (nonphotosynthetic); and (b) *prokaryotes* (1 to 10 µm), which eat single cells and include bacteria (0.5 to 10 µm),

blue-green algae, and perhaps viruses. The latter groups, especially bacteria, are import agents in the transformation of organic matter into a large range of organic breakdown products and eventually CO_2. They are frequently associated with microbial biomass and are quite active at discontinuities in the marine environment. Their small size gives them a high surface-to-volume ratio. They frequently live in microenvironments (marine snow, the guts of animals, etc.) that have a different pH, p, O_2, and composition than that of bulk seawater. These microenvironments are created by particles, diffusion barriers, and the metabolic activity of the microorganisms.

It is difficult to study these microorganisms because of the lack of methods that can be used to accurately access their biomass, metabolic activity, and growth rates. For example, cell numbers and biomass may be misleading in determining the potential for biochemical transformations. Nongrowing cells may have a greater chemical impact than efficient and rapidly growing cells. Many of the earlier studies of microorganisms neglected to sample at ocean discontinuities caused by physical (bubbles, thermoclines, pycnoclines, and water mass boundaries); chemical (nutriclines, oxic–anoxic interfaces, digestive tracts); and physiochemical (air–sea interface, sediment–sea interface, aerosols, particles, sea–ice interface, and animal burrows) properties.

The uptake of organic compounds by bacteria follows Michaelis-Menten kinetics shown in Figure 9.32. The velocity v or rate of uptake increases as the concentration of the substrate S increases to a maximum level v_{max}. This can be represented by the equation

$$v = v_{max}\, S/(k_S + S) \tag{9.17}$$

where K_S is the half-saturation constant (the concentration of S at $v_{max}/2$). This equation can be rearranged to give the linear equation

$$S = v_{max}(S/v) - k_S \tag{9.18}$$

A plot of S versus S/v can be used to determine the intercept $-k_S$ and slope v_{max}.

Some of the methods that have been used to determine the biomass of microorganisms include direct microscopy (light, phase contrast, epifluorescence, immunofluorescence, and electron beam). By culturing the marine organism, it is possible by enrichment to isolate specific physiological or metabolic groups that can be used as biochemical indices (chlorophyll a, ATP, lipopolysaccharide, muramic acid). The physiological potential of

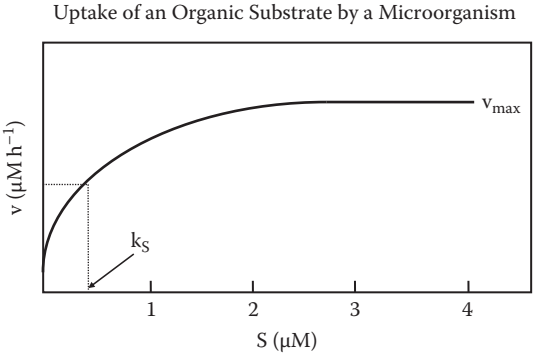

FIGURE 9.32
The rate of the uptake of dissolved organic carbon as a function of the concentration (Michaelis-Menton kinetics).

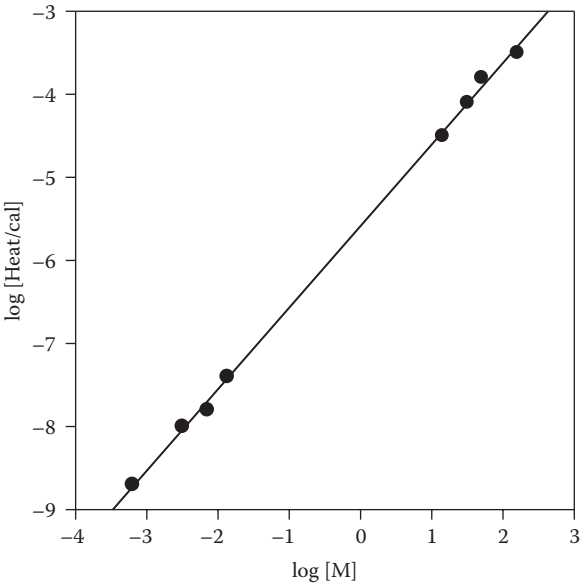

FIGURE 9.33
The heat of catabolism of glucose by bacteria.

microorganisms can be accessed by measuring the adenylate energy charge or looking for specific enzymes (dihydrogenase, alkaline phosphates, nitrogenase, and glutamine synthetase). The metabolic activity of microorganisms can be determined by measuring the end products (O_2, CO_2, and CH_4) or measuring the uptake of ^{14}C- or ^{3}H-labeled substrates (glucose, glutamate, amino acids). Oxygen respirometry and microautoradiography can also be used to determine the metabolic activity of microorganisms. Microcalorimetry is also useful in measuring the rates of metabolic activity. We have used this method to study the uptake of glucose by bacteria (Gordon and Millero, 1980). We found that the total output of heat caused by catabolism was directly proportional to the glucose used (Figure 9.33).

The growth rate of biomass and related production during an incubation of a microorganism can be determined by measuring a product of the growth (chlorophyll a, ATP, POC, protein, RNA). The rate of incorporation of labeled precursors into stable macromolecules (lipids, proteins, cell walls, RNA) can also be measured. The use of elemental composition ratios (C:N:P, GTP:ATP) can also be useful in following the growth rate of a microorganism. The rate of cell division can be studied by measuring the rate of incorporation of labeled precursors into DNA. It is also possible to make direct observations of cell divisions through a microscope. The measured increase of cell numbers as a function of time during an incubation can also be used to examine the cell division rate.

9.4 Dissolved and Particulate Organic Compounds in Seawater

Although the concentration of organic matter in the oceans is less than 0.01% of the total amount of salts, these compounds are important modifiers of many of the biological and

chemical reactions that take place in the sea. They provide a nutritional and energy base for micro- and macroorganisms, have a major impact on the speciation of many metals by such processes as complexation and adsorption, and are precursors of fossil fuels such as petroleum and oil shale. These organic compounds can also provide growth promoters and inhibitors that may control phytoplankton succession. Much research activity has been directed toward identifying the specific components of organic matter in the seas and toward untangling the complex web of biogeochemical relationships between dissolved and particulate compounds associated with microbial processes (amino acids, carbohydrates, fatty acids, etc.).

The source of most of the organic compounds in seawater is primary production in the euphotic zone (Table 9.1). Part of the organic matter from photosynthesis is partially metabolized to satisfy the energy requirements of phytoplankton. The other fraction is assimilated by zooplankton and released into the water column by the autolysis of dead cells or is excreted by organisms. Bacteria eventually break down most of the organic compounds to carbon dioxide. In coastal waters, a significant proportion of the organic matter can also come from the land via rivers and coastal sediments. The various sources of organic compounds in the oceans are discussed in the next section.

9.4.1 Sources of Organic Matter

Primary production by marine phytoplankton has been estimated to be responsible for the production of approximately 2×10^{16} gC yr^{-1}. Much of this organic matter is consumed by organisms, but a significant amount is decomposed at the surface, while 1 to 12% of the annual production (0.2 to 2.4×10^{15} gC yr^{-1}) remains as a refractory fraction, quite resistant to biological and chemical transformations. The residence time of this residual DOC in the sea has been estimated by Williams and Druffel (1987) to be 1310 years for surface and 6240 years for deep dissolved organic matter (DOM). Most of this residual organic carbon consists of humic substances.

The other sources of input of organic matter to seawater, in addition to primary productivity by marine plankton, include terrestrial input by rivers and by the atmosphere, excretion by marine organisms, and the resuspension of organic matter from marine sediments. The direct addition of organic matter from oil spills is an additional source.

9.4.1.1 Terrestrial Input by Rivers

The typical concentration of DOC in estuaries (Figure 9.34) shows that rivers can be a source of DOC to the oceans. Based on levels of POC and DOC of major river systems, it has been estimated by Meybeck (1987) and others that the amount of total organic carbon (TOC) transported to the seas by river systems amounts to about 33×10^{12} mol C yr^{-1}. Approximately half of this carbon comes from POC and the other half from DOC. Terrestrially derived carbon is often referred to as allochthonous carbon (which means that it is derived from outside the system being considered—the oceans). In freshwater systems, the two major sources of organic carbon are plant- and soil-derived carbon. Rainwater that penetrates soils can leach organic soil and plant debris, as well as inorganic constituents, into dissolved and suspended phases.

Numerous studies on the leaching of plant organic matter into streams have shown that within 24 h as much as 40% of the organic matter of fresh plant litter can be solubilized by water. At least half of the DOC of the leachates from plant debris consists of carbohydrates. The remaining DOC consists of a mixture of substances that are either contributors or

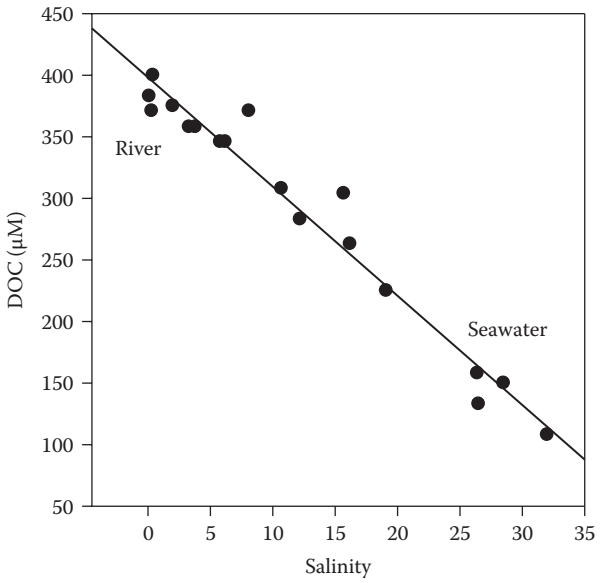

FIGURE 9.34
The dissolved organic carbon (DOC) as a function of salinity in a typical estuary.

precursors of fulvic acids. The major portion of organic matter leached from soils consists of humic substances that may account for as much as 70% of the organic matter of soil. Other terrestrial plant and animal decomposition products are also transported from the soil into streams and rivers and eventually into the marine environment. Most studies of the organic matter of the deep ocean basins indicate that virtually all of it is derived from autochthonous (within the system) sources. Most of these data are based on carbon isotope ratios that are significantly different for terrestrial than marine vegetation. The ^{13}C value of dissolved marine organic matter was found to range from –21 to 24.0‰, while that of the Amazon River was evaluated at –28 to 25‰. Various studies have indicated that the flocculation and subsequent precipitation of organic matter in freshwaters occurs on mixing with higher-salinity waters in estuaries. This apparent "salting out" of organic matter results in the restriction of allochthonous river-transported organic matter largely to coastal regions.

In addition to naturally derived terrigenous sources of organic matter, streams and rivers deliver an increasing amount of organic substances derived from sewage and industrial effluents. Although these forms of pollution have not yet caused any open-ocean disasters, their introduction into freshwater and estuarine environments has caused significant changes in population diversities of microorganisms, invertebrates, and vertebrates and has resulted in negative changes in water quality.

9.4.1.2 Terrestrial Input from the Atmosphere

The introduction of organic matter to seawater from the atmosphere takes place at the air–sea interface, which has been the subject of much recent research (Peltzer and Gagosian, 1989). It has been well known for many years that the chemistry of the sea surface microlayer is very different from that of bulk seawater. For example, the DOC of this interfacial layer, which is less than a micrometer thick, can be as much as 10 times the DOC concentration

in surface seawater below the microlayer. The chemical composition of the organic matter in the seawater microlayer is not yet well known, but appreciable quantities of macromolecule species similar to humic substances constitute a major fraction of the DOC and POC at this interface. Mono- and polysaccharides as well as fatty acids have also been isolated from surface microlayers.

The transfer of organic material across the air–sea interface can be accomplished by either wet (liquid) or dry (gas or solid) deposition, although these categories are sometimes difficult to effectively separate from each other. For example, when liquid deposition takes place (rainwater), the dissolved gases and particulate material in rainwater are simultaneously deposited. Williams (1975) has estimated that 2.2×10^{14} gC yr^{-1} is a reasonable estimate for the amount of organic carbon contributed to the oceans by rainfall. This figure is similar in value to the amount of organic carbon input by rivers (3.3×10^{13} moles C $yr^{-1} \times$ 12 gC L^{-1} mole C = 4.0×10^{14} gC yr^{-1}). Hunter and Liss (1977) pointed out that this flux of organic carbon into the oceans may not represent a net input because of the input of marine organic matter into the atmosphere by the bursting of bubbles in whitecaps and breaking waves. Bubble bursting ejects a significant amount of organic matter from the seawater microlayer into the atmosphere, and rising bubbles also harvest organic matter from subsurface waters. Thus, it is possible that a significant portion of the organic matter transferred to the sea from the atmosphere by rain is organic matter recycled from seawater. Much of this organic material is lipid material that is concentrated in surface seawaters.

Other recent studies of marine aerosols have found that the organic matter in the aerosols was dominated by waxes of terrestrial origin. Peltzer and Gagosian (1989) reported that four lipid compound classes (aliphatic hydrocarbons, fatty alcohols, fatty acid esters, and fatty acid salts) all indicate a terrestrial vascular plant source for organic matter isolated from atmospheric samples collected from the tropical North Pacific. Their results indicated that these aerosol lipids originate from wind erosion of soils and direct emission from vegetation, and that the major fluxes to seawater result from rain rather than from dry deposition.

However, definite net fluxes of organic matter from the atmosphere to seawater have been established for anthropogenic substances such as DDT and polychlorinated biphenyls (PCBs). DDT is a chlorinated hydrocarbon pesticide that was used extensively following World War II. It is no longer used in the United States because it is extremely persistent and tends to accumulate in food chains. PCBs are also very persistent in the environment, and until the manufacture of these compounds was discontinued in 1977, they were used industrially as plasticizers, in paints, and as coolants and transformers. Hunter and Liss (1977) estimated that 10% and 0.5% of the total annual production of PCBs and DDT, respectively, are transported into the world's oceans through atmospheric–seawater fluxes. PCBs and DDT are extremely widespread in the marine environment and have been found in the tissues of many marine organisms.

9.4.1.3 Additional Sources of Organic Matter

In addition to the sources of organic matter described, marine organisms are often considered an "internal source" of organic matter by the excretion of metabolites and the release of substances on the death and decay of cells. However, marine organisms, except for the case of primary producers, are not really sources of organic matter but are essentially transformers that modify the organic substances that enter the marine environment by the processes discussed. Another internal source of marine organic matter that must be con-

sidered is marine sediments (Simoneit, 1978). Although marine sediments act as a sink for organic matter, in local situations they may act as an important source due to resuspension.

9.4.2 Dissolved and Particulate Organic Matter

In aquatic systems, it is traditional to divide organic matter into the two major categories of dissolved and particulate (DOM and particulate organic matter [POM]). POM includes those species that will be retained by a 0.45-µm glass fiber filter. When seawater is passed through a 0.45-µm filter, some colloids are retained as well as suspended matter. Various workers have used filters with pore sizes ranging from 0.40 to 1.0 µm to achieve this separation.

The DOC is determined on the filtered sample by first acidifying and bubbling with nitrogen to remove the inorganic CO_2. The sample is then treated with a strong oxidizing agent (such as potassium peroxydisulfate, $K_2S_2O_8$), sealed, and heated to 130°C for 1 h. The CO_2 produced is removed using a carrier gas such as He or N_2. The released CO_2 is determined by an infrared analyzer or by GC. The addition of H_2O_2 before the UV (ultraviolet) irradiation of the sample can also be used to oxidize the organic carbon to CO_2. In recent years, the DOC has been determined using a high-temperature catalyst (Pt) to oxidize the sample. The CO_2 produced is analyzed using an IR (infrared) detector. The dissolved organic nitrogen (DON) and phosphate (DOP) can be determined on the oxidized sample by measuring the total inorganic NO_3^- and PO_4^{3-} and subtracting the inorganic nutrient in the sample prior to oxidation (e.g., DON = $[NO_3]_T - [NO_3]$).

DOC is about 50% of the DOM, and POC is about 50% of the value of POM. The concentration of DOC in seawater is typically significantly greater than that of POC (see Table 9.8). While the typical range of DOC concentrations in surface seawater is 75 to 170 µ*M*, the average concentration of POC in surface seawater is only 8 µ*M* (range of 1 to 17 µ*M*). Typical profiles of dissolved and particulate carbon in the oceans are shown in Figure 9.35. Seasonal variations in DOC and POC occur primarily in shallow waters and are similar to the variations in primary productivity. At depths below a few hundred meters, the average DOC is 40 µ*M*; the average POC is 0.8 µ*M*. The POC frequently goes through a

TABLE 9.8

Levels of Dissolved and Particulate Organic Material in Natural Waters

Source	Dissolved (µ*M*)	Particulate (µ*M*)
Seawater		
Surface	75–150	1–17
Deep	4–75	0.2–1.3
Coastal	60–210	4–83
Estuarine	8–833	8–833
Drinking water	17	
Groundwater	58	
Precipitation	92	
Oligotrophic lake	183	80
River	420	170
Eutrophic lake	830–4170	170
Marsh	1250	170
Bog	2500	250

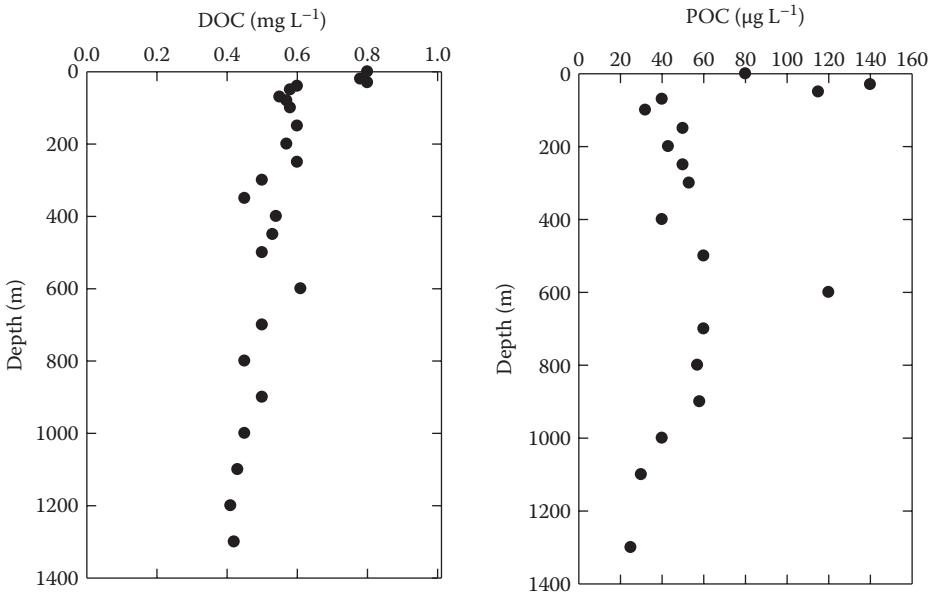

FIGURE 9.35
Profile of dissolved and particulate organic carbon in the oceans.

TABLE 9.9

Comparison of Dissolved and Particulate Organic Carbon, Nitrogen, and Phosphorus

	Carbon (μ*M* C)		Nitrogen (μ*M* N)		Phosphorus (μ*M* P)	
Location	**Diss.**	**Part.**	**Diss.**	**Part.**	**Diss.**	**Part.**
Surface	75–150	12.5	4–10	2.1	0.1–0.6	0.06
Oxygen min.	10	3–5	0.6	0.03		
Deep	4–75	1.7	0.9	0.03		
Coastal	60–210	4–83	4–60	0.6–1.6		

Note: Diss., dissolved; Part., particulate.

maximum in the oxygen minimum zone. Some have suggested that this is the result of sinking particulate material having a density similar to waters at a depth of 500 to 1000 m (σ_T = 26.4). The oxygen minimum is thus a result of bacteria oxidizing this material in this zone. The dissolved and particulate organic carbon, nitrogen, and phosphorus levels in surface, deep, and coastal waters are compared to the levels at the oxygen minimum in Table 9.9. The coastal levels are higher than those in surface waters of the oceans. The levels of dissolved and particulate concentrations of all the organic compounds are much lower in deep waters than in surface waters.

The DOC measurements in ocean waters have been made by a number of workers using the high-temperature oxidation method and are in agreement with the earlier results obtained using the wet methods. The results at the Hawaii Ocean Time Series (HOTS) station of Karl and coworkers are shown in Figure 9.36. The surface values are about 80 μ*M*, while the deep waters have values of 40 μ*M*. The values of DOC in the deep water from the North Atlantic to the North Pacific are shown in Figure 9.37. The semilabile DOC is

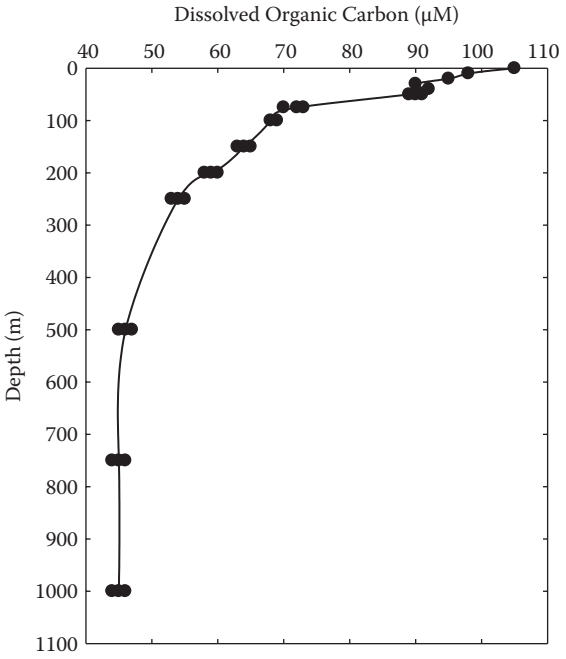

FIGURE 9.36
Dissolved organic carbon as a function of depth at the Hawaii Ocean Time Series station.

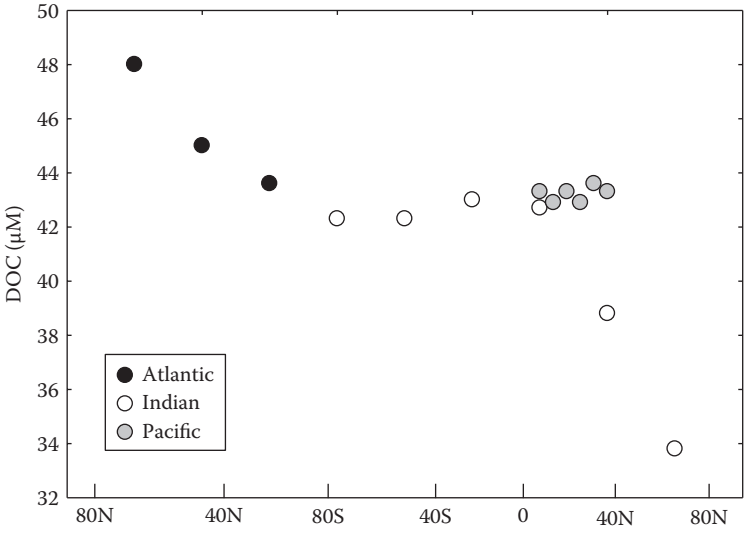

FIGURE 9.37
Values of DOC in deep water from the North Atlantic, Indian Ocean, and North Pacific.

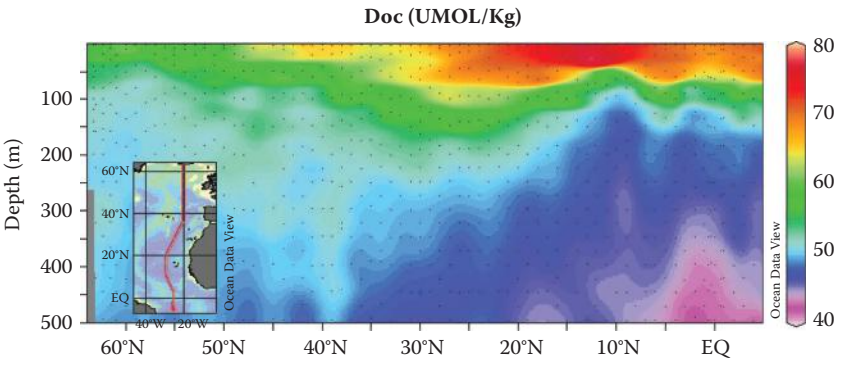

FIGURE 9.38
Section of dissolved organic carbon in the North Atlantic (A16). (From Hansell, D.A., personal communication.)

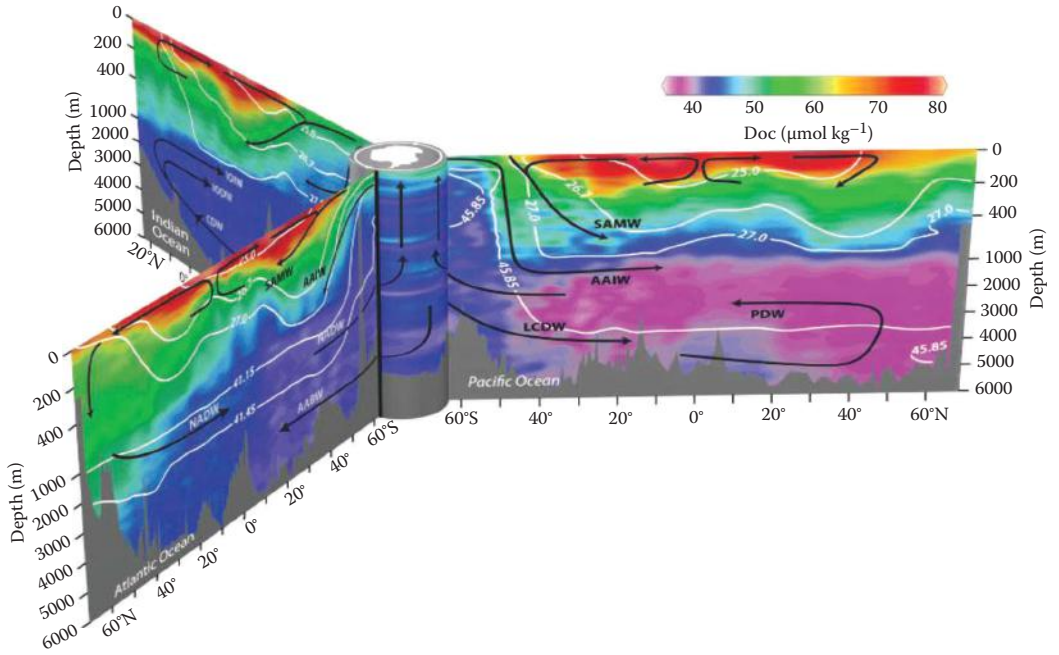

FIGURE 9.39
The global distribution of DOC in the world oceans. (From Hansell, D.A., et al., *Oceanography*, 12, 203–211, 2009. With permission.)

rapidly removed; the refractory DOC is slowly lost with time. The values decrease from 40 to 36 *M* in the deep waters as the waters move from the North Atlantic to the North Pacific over a period of about 500 yr. A section of the DOC in the surface waters of the Atlantic Ocean from the surface to 500 m is shown in Figure 9.38. The highest values are in the surface waters. The upwelling off the coast of Africa brings up lower waters of DOC from the deep. The global distribution of DOC in the world oceans is shown in Figure 9.39. The deep values of DOC follow the circulation of the deep waters. The deep Pacific waters have

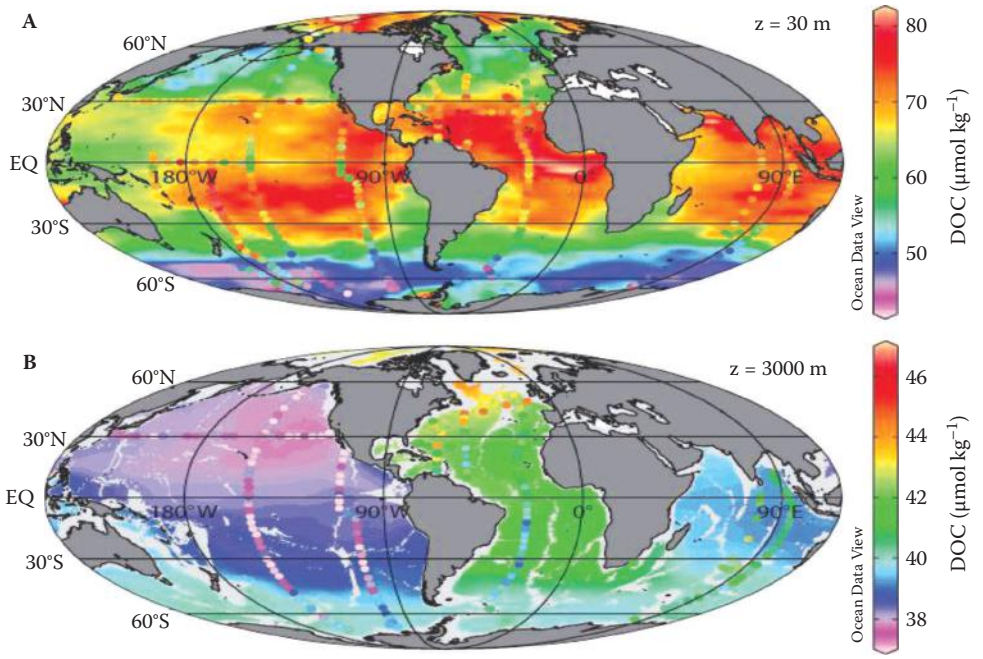

FIGURE 9.40
The surface and deep-water concentration of DOC. (From Hansell, D.A., et al., *Oceanography*, 12, 203–211, 2009. With permission.)

the lowest DOC. These older waters have a loss of DOC due to bacterial oxidation over time. The DOC concentration of surface and deep waters in the world oceans is shown in Figure 9.40. As particulate material falls from the surface to deep waters, POC is converted to DOC. The modeled downward flux of DOC (PgC yr^{-1} black line) and DOC/POC export flux ratio (gray line) are shown in Figure 9.41. Most of the changes occur in the surface waters. The global export of POC is shown in Figure 9.42. The concentration of DOC in surface waters varies by season (Carson et al., 1994). In the North Atlantic, the values are higher during the spring bloom.

9.4.2.1 Dissolved Organic Matter

Dissolved marine organic matter is extremely complex and is a mixture of compounds with only 10 to 20% fully characterized. Measurements of DOC, DON, and DOP compounds are standard measurements used to obtain an understanding of the major types of organic compounds present in the oceans (Table 9.9). Measurements of individual organic compounds are few. Since the concentration of the individual compounds rarely exceeds 1 μ*M* C, it is frequently necessary to concentrate the sample from several liters of seawater (as well as remove the salts). Specific concentration methods will depend on the class of compound being measured. For example, solvent extraction is used to determine fatty acids and insecticides, adsorption on carbon is used to determine carbohydrates, and the concentration of polystyrene beads is used to determine vitamin B and humic materials.

Much of the data on individual organic compounds in seawater has been obtained by GC and mass spectrometry (MS) or by capillary GC. In all current chromatographic methods, much of the total DOM appears as an undifferentiated peak on the chromatogram

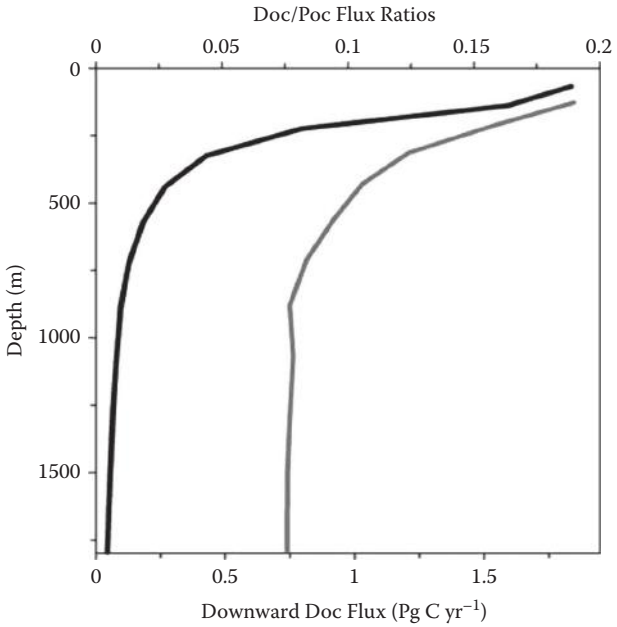

FIGURE 9.41
DOC and POC flux ratios to the deep oceans. (From Hansell, D.A., et al., *Oceanography*, 12, 203–211, 2009. With permission.)

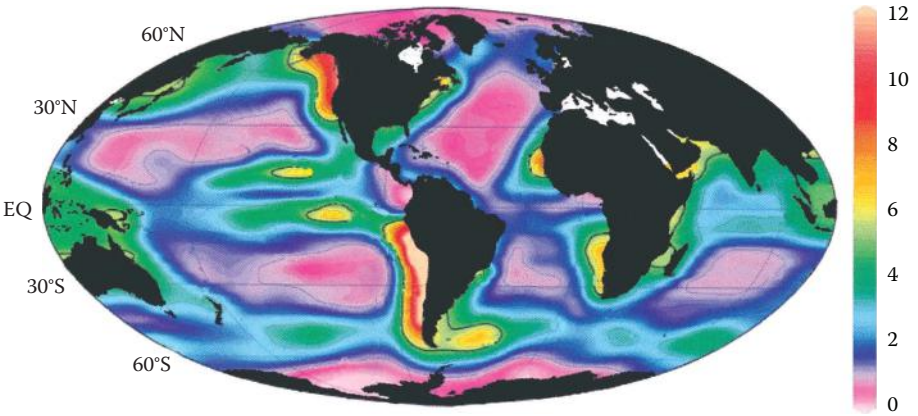

FIGURE 9.42
POC and DOC export to the world oceans. (From Hansell, D.A., et al., *Oceanography*, 12, 203–211, 2009. With permission.)

that is often referred to as an "unresolved complex mixture." Thin-layer chromatography coupled to flame ionization detection (FID) is a promising new technique that can be used to separate the DOM from seawater into compound classes such as lipids and base mobile (amines, alcohols, ketones) and acid mobile fractions. The large number of unidentified organic compounds as seen on a chromatogram is indicative of how much we still have to learn before we can hope to begin to form realistic models of the organic chemistry of the oceans. Mopper and Stahovec (1986) used HPLC (high-performance

liquid chromatography) to determine low molecular weight organic compounds in seawater. The organic compounds are reacted with fluorescence compounds that react with specific functional groups (acids, aldehydes, amines, etc.) and are detected using a fluorescence detector.

The DOM in seawater consists largely of humic substances and more labile compounds from the major biochemically important compound classes such as carbohydrates, steroids, alcohols, amino acids, hydrocarbons, and fatty acids (as well as fatty acid esters and waxes).

9.4.2.2 Particulate Organic Matter

Of the TOC in the oceans, it has been estimated that POC constitutes only 1 to 10%. Frequently, POM is evaluated from measurements of POC made by carbon analyses or organic-free glass fiber filters (0.45-μm pore size) used to separate POM and DOM. POM is obtained by multiplying POC by a factor of two, based on the approximation that carbon constitutes roughly 50% by weight of marine organic matter. PON and particulate organic phosphorus (POP) compounds are much less than the POC (see Table 9.9).

POM consists of a mixture of living and dead phytoplankton and zooplankton, and bacteria and their degradation and exudation products and macroscopic aggregates often termed "marine snow." The distribution and nature of POM have been found to be quite variable geographically, vertically, diurnally, and seasonally and are influenced by a complex set of equilibria between sources, sinks, and circulation patterns. In the euphotic zone, the major portion of the POM comes from phytoplankton, the chemical composition of which will vary with species as well as with environmental conditions, hence leading to significant variations in the nature of the POM. The metabolic products of phytoplankton can vary with changes in temperature, light intensity, and nutrient availability. Much less is known about the chemical content and biogeochemistry of POM than is known about DOM. In the euphotic zone, the majority (90%) of POC comes from living matter, while at depths of 2400 m and more, less than 1% of the POC comes from living organisms.

Much research activity has focused on the vertical flux of POM from the surface waters of the ocean to the seafloor (Lee and Wakeham, 1989). The chemical and biochemical changes that occur as particles sink through the water column significantly affect the composition of both the sediments and the overlying water. Thus, the physical and biogeochemical processes that affect the composition of sinking particulate matter also affect biological productivity in the water column as well as modify the organic matter that reaches the ocean floor and serve in turn as a major source of nutrition for benthic organisms and as a source of precursors to marine-derived fossil fuels.

Sediment trap experiments conducted at various depths have recently yielded valuable information on the chemical content and fluxes of marine POM. Sediment traps are large cones fitted with a number of baffles, and they collect the particulate material in bottles containing brine and sodium azide to retard the growth of bacteria. The downward flux of POC appears to be dominated by rapidly sinking particles, that is, particles with diameters greater than 62 μm. The organic components of these particles consist largely of zooplankton fecal pellets, zooplankton and phytoplankton remains, and humic substances. The chemical content of these particles is affected by a very complex set of reactions, including degradation and transformation processes that result in the increased removal of some labile organic compounds with depth, while other labile organic compounds (often unsaturated), as reported by Wakeham et al. (1984), were found at depths as great as 5068 m (see Figure 9.43 and Figure 9.44). The feeding activity of meso- and bathypelagic zooplankton on these rapidly sinking particles was invoked by Wakeham et al. to explain the selective

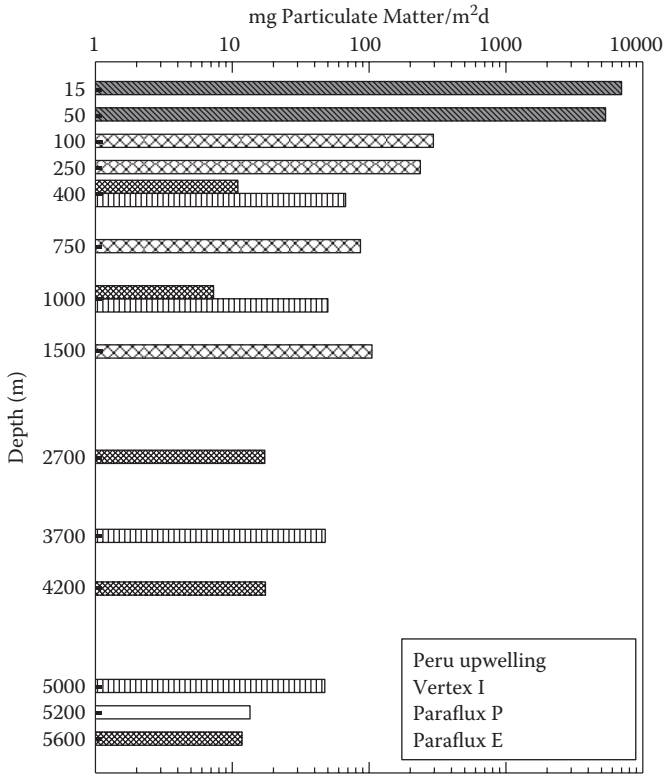

FIGURE 9.43
Particulate matter off the coast of Peru.

removal of some labile organic compounds from sinking POM and the selective incorporation of other labile organic matter into sinking POM as fecal material excretion products. The fraction of POC is much less at other parts of the ocean (Figure 9.45) and depends on the growth of calcareous and siliceous phytoplankton and the input of atmospheric aerosols.

Much of the work on the biogeochemistry related to sinking marine particles has focused on lipids (fats, oils, and fat-soluble compounds). Lipids constitute a minor but important fraction of the DOC and POC because of their involvement in energy storage and use, reproduction, regulation of metabolic processes, membrane structure, and so on. The particulate lipids are much more complex than the dissolved lipids. Although the major components of dissolved and particulate lipids are similar (n-alkanes, pristane, phytane, and fatty acid esters), particulate lipids include a substantial amount of unresolved compounds as well as olefins, alkylated benzenes, quinones, and minor contributors not found in the dissolved samples.

9.4.3 Kinds of Organic Compounds in Seawater

One can imagine that almost all the possible organic compounds could exist in seawater because of the breakdown. It is difficult to determine the individual compounds in seawater because of their low levels and the problems with their concentration in a large amount of seawater with changing composition. The simple organic compounds can be broken down into a number of major groups (Table 9.10), briefly discussed next.

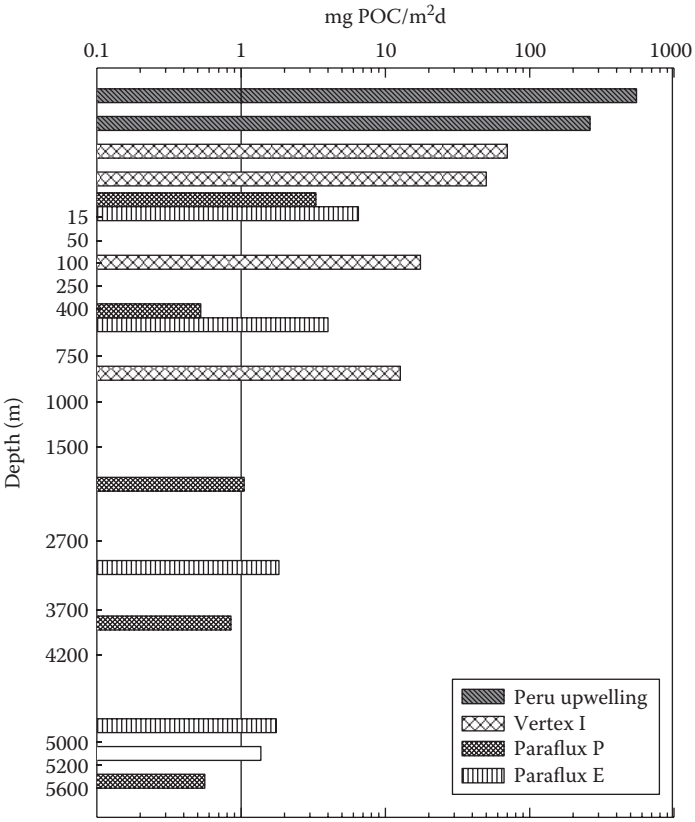

FIGURE 9.44
Organic carbon off the coast of Peru.

9.4.3.1 Carbohydrates

Carbohydrates are a major class of naturally occurring organic compounds. Plants are composed of 50 to 90% carbohydrates. Carbohydrates are the central source of energy for mechanical work and chemical reactions in all living cells. The derivatives of carbohydrates (ATP and nucleic acids) control energy transformations and the transfer of genetic material. The general formula for carbohydrates is $C_n(H_2O)_m$. They are classified by the number of carbon chains per molecule:

Monosaccharide: a single continuous chain of carbon atoms

Disaccharides: two monosaccharide units per molecule

Polysaccharides: composed of many mono- or disaccharide units per molecule

The term *sugar* (or saccharide) refers to monosaccharides, disaccharides, or lower oligosaccharides (simple sugar is D-glucose). Monosaccharides are classified by the number of carbon atoms per chain. For example, a monosaccharide with six carbons is called hexose (where -ose is used to denote that it is a carbohydrate). Cellulose, the main structural component of the cell wall, is a linear sequence of glucose units linked by bonds formed from the acetal carbonyls. It consists of a linear sequence of glucose units linked by acetal

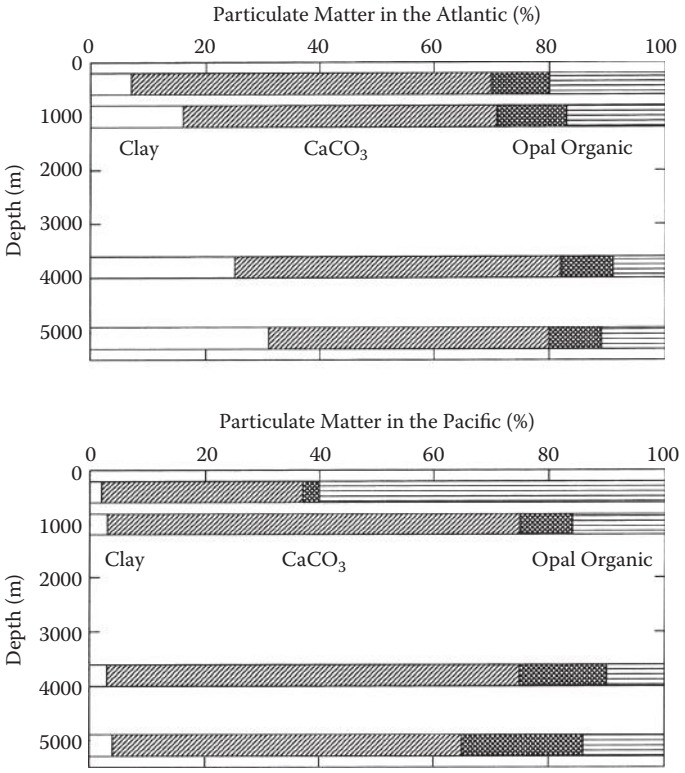

FIGURE 9.45
Particulate matter in the Atlantic and Pacific Oceans.

TABLE 9.10

Some Organic Compounds Found in the Oceans

Compound	Formula
Carbohydrates	$C_n(H_2O)_m$
Amino acids	R–CH–COOH | NH_2
Hydrocarbons	C_nH_m
Carboxylic acids	R–COOH
Humic substances	Phenolic?
Steroids	

carbonyl bonds. Glucose and fructose were found to be the dominant monosaccharides in seawater (Mopper and Stahovec, 1986). Carbohydrates are also an important component of POM in the oceans.

Benner et al. (1992) have used tangential-flow ultrafiltration to recover milligrams of DOM with a molecular weight greater than 1000 from 10, 765, and 4000 m in the North Pacific. The sample represented 22 to 33% of the DOM and included essentially all the colloidal material. They found that the isolates were quite high in polysaccharides (50%) in

surface waters and decreased to 25% in deep waters. These results indicate that carbohydrates are more abundant and reactive in the oceans than previously thought.

9.4.3.2 Amino Acids and Proteins

Proteins are present in all living cells and often account for over 50% of the bulk weight of organisms. They serve as a component of the structure of the cell and as metabolic regulators and are instrumental in motion and defense. Proteins are made up of amino acids linked by peptide (amide) bonds. Although a wide variety of proteins exists, they are composed of a rather small number of amino acids. Since the nitrogen composition of proteins is nearly constant (16%), the nitrogen concentrations are used as a way of determining the protein content of living material. The concentration of amino acids in seawater ranges from 20 to 250 μg L^{-1} and makes up 2 to 3% of the DOC. Amino acids are organic acids in which the alpha carbon of the –COOH group is replaced by an $–NH_2$ group. They have the general formula ($RCHNH_2COOH$), where R is a functional group that differs for each amino acid. Free amino acids make up a small fraction of the organic carbon compounds present in living cells. Combined amino acids are found in dissolved, colloidal, and particulate matter. Free amino acids are also produced enzymatically by the hydrolysis of peptides and proteins in seawater by bacteria.

9.4.3.3 Hydrocarbons

Hydrocarbons make up less than 1% of the DOC in seawater and contain carbon and hydrogen in the chemical formula C_nH_m. They have concentrations between 1 and 50 μg L^{-1}, with an average of 10 μg L^{-1}. Hydrocarbons are frequently classified as low ($<C_{14}$) and high ($>C_{14}$) molecular weight. Methane (CH_4) is the simplest hydrocarbon and is found in all natural waters. Its concentrations range from 10 to 100 μgL^{-1}. The biological production of methane is of interest because it is a useful fuel and also a greenhouse gas that has doubled in the atmosphere since 1900.

Hydrocarbons are classified as saturated, unsaturated, and aromatic. Saturated hydrocarbons (paraffins or alkanes) are quite stable. Unsaturated hydrocarbons contain one or more double bonds (C=C). The most common found in seawater are alkenes or olefins. An unsaturated hydrocarbon with two double bonds is called a diene, with three it is called a triene, and so on. Isoprene is a diene that is a component of many plants and animals and is often referred to as one of nature's building blocks. Many complex hydrocarbons can be broken down into isoprene units, which is called the "isoprene rule." Terpenes are isoprenoids that are found in the essential oils of plants. They have a regular head-to-tail arrangement of isoprene units. Aromatic hydrocarbons contain at least one benzene ring (six carbon atoms arranged in a ring with alternating single and double bonds, e.g., C_6H_6). They are considered to be derived mainly from abiotic processes such as the pyrolysis of organic matter at high temperatures (e.g., forest fires and fossil fuel combustion).

9.4.3.4 Carboxylic Acids

Carboxylic acids have at least one carboxylic group (–COOH). Amino acids discussed previously and fulvic and humic acids also contain a –COOH group but are discussed separately because of their unique behavior. The other carboxylic acids of importance in the marine environment include fatty acids such as stearic acid [$CH_3(CH_2)_{16}$–COOH] and palmitic acid [CH_3–$(CH)_2$–COOH]. Fatty acids are found as fats in animals and waxes

in plants and have 4 to 36 carbon anions. The term *fat* is normally applied to solid glycol esters and oils and liquid glycol esters. Fats and oils are esters (–COOR) of glycerol ($HO–CH_2–CHOH–CH_2–OH$) and fatty acids (RCOOH). The term *lipid* refers to fats, oils, and fat-soluble compounds. Nonvolatile fatty acids have concentrations between 10 and 200 μg L^{-1} and typically account for 1% of the DOC. Less is known about the concentrations of hydroxy [RC(OH)COOH], dicarboxylic [RCOOH], and aromatic acids (C_6H_6–COOH) in the marine environment. Most of the fatty acids arise from the hydrolysis of triglycerides (triacylglycerols) during the degradation of detrital organic matter. Triglycerides comprise a major fraction of the lipid component of plant and animal storage tissue, and the fatty acids account for approximately 90% of the weight of triglycerides. Thus, fatty acids are a major component of lipids derived from the degradation of organic matter.

9.4.3.5 Humic Substances

Humic substances are complex mixtures of individual compound classes and tend to be quite resistant to extensive microbial degradation. They are precursors of the geopolymeric material known as kerogen (dispersed organic matter found in sedimentary rocks and insoluble in organic solvents, mineral acids, and bases). Petroleum is produced from the geochemical maturation of kerogen derived primarily from aquatic organisms. Since humic substances consist of a mixture of plant and animal debris at various stages of decomposition, the chemical composition will vary with source of input and environment of deposition. Humic substances have been studied by soil and water chemists for many years because of the important roles they play with respect to water quality, soil fertility, and soil porosity and their association with both inorganic and organic nutrients and pollutants through complexation and adsorption processes. In seawater, the concentration of humic substances ranges from 60 to 600 μg C/L, which accounts for 10 to 30% of the DOC of seawater.

Early studies of marine humic substances described the isolation of "gelbstoff," a yellowish-brown acid material that could be extracted from seawater with organic solvents. Humin is both acid and base insoluble. Humic and fulvic acids are typically extracted together into a basic solution (0.5 *M* NaOH), and the humic acids are precipitated out by acidification of the solution (addition of HCl to a pH of 2.0 or the use of an ion-exchange resin in the H^+ form), leaving the acid-soluble fulvic acid fraction in solution. Humin is chemically very similar to humic acid but is more tightly bound to the inorganic soil and sediment constituents. Humic substances consist of approximately 40 to 60% carbon, 30 to 45% oxygen, 1 to 5% nitrogen, and 2% or less sulfur. Humic acids tend to be richer in carbon and poorer in oxygen than fulvic acids. Historically, the chemical compositions of humic substances from various environments were studied by wet chemical and instrumental methods of analysis. The major structural components include aliphatic chains with varying degrees of branching, aromatic rings, phenolic, hydroxyl, methoxyl, and carboxylic acid groups.

9.4.3.6 Steroids

Steroids are related to the terpenoids, which are built of five carbon atom isoprene units ($CH_2CHCH_3CHCH_2$). Steroids (Table 9.10) are classified according to their principal functional groups. Cholesterol, for example, is classified as a sterol because it contains an alcohol group (ROH). All steroids have the same carbon skeleton (Table 9.10), typically have 27

to 29 carbon atoms, and are only slightly soluble in seawater. Sterols are divided into subgroups such as stanols (saturated steroid), stenols (monounsaturated sterols), and distenols (diunsaturated steroids). Steranes (saturated aliphatic steroids) and stanones (ketone-containing steroids) are also of interest to geochemists. Due to the stable steroid structure and the numerous variations in the basic structure, they have been useful as biological and geochemical markers. The marine biogeochemistry of steroids has been extensively studied by scientists who have used the reduction of sterols to the saturated analogs, the stanols (Wakeham et al., 1984; Lee and Wakeham, 1989). In the Black Sea, they found conversion of sterol to stanol in the anoxic waters. In the waters above the oxic–anoxic interface, a rapid metabolism of stenols and stanols was observed. These decompositions occur much more rapidly than do the stenol-to-stanol reactions in the water column. Stanols and stanones (intermediates in the stenol-to-stanol reaction) were isolated in sediments.

References and Further Reading

Primary Productivity

Altabet, M., and Deuser, W., Seasonal variations in natural abundance of 15N in particle sinking to the deep Sargasso Sea, *Nature*, 315, 218–219 (1985).

Balch, W., Platt, T., and Sathyendranath, S., Comment on "The Remote Sensing of Ocean Primary Productivity Use of a New Compilation to Test Satellite Algorithms," *J. Geophys. Res*., 98, 16, 583 (1993).

Bender, M., et al., A comparison of four methods for determining planktonic community production, *Limnol. Oceanogr*., 32, 1085 (1987).

Bidigare, R.R., Prezelin, B.B., and Smith, R.C., Bio-optical models and the problems of scaling in *Primary Productivity and Biogeochemical Cycles in the Sea*, Falkowski, P.G. and Woodhead, A.D., Eds., Plenum Press, New York, 175–212 (1992).

Coale, K., and Bruland, K., Oceanic stratified euphotic zone as elucidated by ^{234}Th:^{238}U disequilibria, *Limnol. Oceanogr*., 32, 189 (1987).

Falkowski, P.G., and Woodhead, A.D. (Eds.) *Primary Productivity and Biogeochemical Cycles in the Sea*, Plenum Press, New York (1992).

Fogg, G.E., Primary productivity, Chapter 14, *Chemical Oceanography*, Vol. 2, 2nd ed., Riley, J.P., and Skirrow, G., Eds., Academic Press, New York, 386–453 (1975).

Gordon, H., Brown, O., Evans, R., Brown, J., Smith, R., Baker, K., and Clark, D., A semi-analytic radiance model of ocean color, *J. Geophys. Res*., 93, 10, 909 (1988).

Grande, K., et al., Primary production the North Pacific gyre: a comparison of rates determined by ^{14}C, O_2 concentration and ^{18}O methods, *Deep-Sea Res*., 36, 1621 (1989).

Jassby, A.D., and Platt, T., Mathematical formulation of the relationship between photosynthesis and light for phytoplankton, *Limnol. Oceanogr*., 21, 540 (1976).

Jenkins, W., Oxygen utilization rates in North Atlantic subtropical gyre and primary production in oligotrophic systems, *Nature*, 300, 246 (1982).

Jenkins, W.J., ^{3}H and ^{3}He in the Beta Triangle: Observations of gyre ventilation and oxygen utilization rates. *J. Phys. Oceanogr*., 17, 763–783 (1987).

Mahadeva, A. et al., Eddy-driven stratification initiates North Atlantic spring phytoplankton blooms, *Science*, 337, 54–58 (2012).

Platt, T., Harrison, W., Lewis, M., Sathyendranath, S., Smithe, R., and Vecina, A., Biological production of the oceans: the case for a consensus, *Mar. Ecol. Prog. Ser*., 52, 77 (1990).

Platt, T., and Sathyendranath, S., Oceanic primary production: estimation by remote sensing at local and regional scales, *Science*, 241, 1613 (1988).
Rodhe, H., Standard correlations between pelagic photosynthesis and light, in *Primary Productivity in Aquatic Environments*, Goldman et al., Eds., University of California Press, Berkeley and Los Angeles, CA, 464 pp. (1966).
Ryther, J., and Yentsch, C., The estimation of phytoplankton production in the ocean from chlorophyll and light data, *Limnol. Oceanogr.*, 2, 281 (1957).
Strickland, J.D.H., Production of organic matter in the primary stages of the marine food chain, Chapter 12, *Chemical Oceanography*, Vol. 1, Riley, J.P., and Skirrow, G., Eds., Academic Press, New York, 478–610 (1965).
Strickland, J.D.H., and Parson, T.R.S., A practical handbook of sea water analysis, *Fish Res. D. Can. Bull.*, 167, 311 pp. (1968).
Talling, J.F., The incidence of vertical mixing, and some biological and chemical consequences in tropical African Lakes, *Verhandlungen der Internationale Vereinigung fur Limonologie*, 17, 998–1012 (1969).

Iron Limitation

Bakker, D.C.E., Watson, A.J., and Law, C.S., Southern Ocean iron enrichment promotes inorganic carbon drawdown, *Deep-Sea Res. II*, 48, 2483 (2001).
Banse, K., Does iron really limit phytoplankton production in the offshore subarctic Pacific? *Limnol. Oceanogr.*, 35, 772 (1990).
Boyd, P.W., et al., A mesoscale phytoplankton bloom in the polar Southern Ocean stimulated by iron fertilization, *Nature*, 407, 695 (2000).
Bozec, Y., et al., The CO_2 system in a Redfield context during an iron enrichment experiment in the Southern Ocean, *Mar. Chem.*, 95, 89–105 (2004).
Brand, L., Minimum iron requirements of marine phytoplankton and the implications for the biogeochemical control of new production, *Limnol. Oceanogr.*, 36, 1756 (1991).
Chavez, F., The iron hypothesis: ecosystem test in Equatorial Pacific waters, *Nature*, 371, 123 (1994).
Chisholm, S.W., and Morel, F.M.M., What controls phytoplankton production in nutrient rich areas of the open sea? *Limnol. Oceanogr.*, 36, 1507 (1991).
Coale, K.H., et al., The IronExII mesoscale experiment produces massive phytoplankton bloom in the equatorial Pacific, *Nature*, 383, 495 (1996).
Coale, K.H., et al., Southern Ocean iron enrichment experiment: carbon cycling in high- and low-Si waters, *Science*, 304, 408 (2004).
Cooper, D.J., Watson, A., and Nightingale, P., Large decrease in ocean surface CO_2 fugacity in response to in situ iron fertilization, *Nature*, 381, 511 (1996).
Greene, R., Geider, R., and Falkowski, P., Effect of iron limitation on photosynthesis in a marine diatom, *Limnol. Oceanogr.*, 36, 1772 (1991).
Hiscock, W., and Millero, F.J., Nutrient and carbon parameters during the Southern Ocean Iron Experiment (SOFeX), *Deep-Sea Res. I*, 52, 2086–2108 (2005).
Hudson, R.J.M., and Morel, F.F.M., Iron transport in marine phytoplankton: kinetics of cellular and medium coordination reaction, *Limnol. Oceanogr.*, 35, 1002 (1990).
Kolber, K., et al., Iron limitation of phytoplankton photosynthesis in the Equatorial Pacific Ocean, *Nature*, 371, 145 (1994).
Ledwell, J., Watson, A., and Law, C., Evidence for slow mixing across the pycnocline from an open-ocean tracer-release experiment, *Nature*, 364, 701 (1993).
Martin, J.H., Glacial–interglacial CO_2 change: the iron hypothesis, *Paleoceanography*, 5, 1 (1990).
Martin, J.H., Iron as a limiting factor in oceanic productivity in *Primary Productivity and Biogeochemical Cycles in the Sea*, Falkowski, P.G., and Woodhead, A., Eds., Plenum, New York, 123–137 (1992).
Martin, J.H., and Fitzwater, S.E., Iron deficiency limits phytoplankton growth in the northeast Pacific subarctic, *Nature*, 331, 341 (1989).

Martin, J.H., and Gordon, R.M., Northeast Pacific iron distributions in relation to phytoplankton production, *Deep-Sea Res*., 35, 177 (1988).
Martin, J.H., Gordon, M., and Fitzwater, S., Iron deficiency limits phytoplankton growth in the Antarctic waters. *Global Biogechem. Cycles*, 4, 5–12 (1990).
Martin, J.H., et al., The case for iron, *Limnol. Oceanogr*., 36, 1793 (1991).
Millero, F.J., Yao, W., Lee, K., Zhang, J.-Z., and Campbell, D.M., Carbonate system in the waters near the Galapagos Islands, *Deep-Sea Res*. *II*, 45, 1115 (1998).
Mitchell, B.G., Brody, E.A., Holm-Hansen, O., McClain, C., and Bishop, J., Light limitation of phytoplankton biomass and micronutrient utilization in the Southern Ocean, *Limnol. Oceanogr*., 36, 1662 (1991).
Orsi, A.H., Whitworth, T., and Nowlin, W.D., On the meridional extent and fronts of the Antarctic Circumpolar Current, *Deep-Sea Res*., 42, 641 (1995).
Redfield, A.C., Ketchum, B.H., and Richards, F.A., The influence of organisms on the composition of sea-water, in *The Sea*, Hill, M.N., Ed., Interscience, New York, 26–77 (1963).
Sakamoto, C.M., Millero, F.J., Yao, W., Friederich, G.E., and Chavez, F.P., Surface seawater distributions of inorganic carbon and nutrients around the Galapagos Islands: results from the PlumEx experiment using automated chemical mapping, *Deep-Sea Res*. *II*, 45, 1055 (1998).
Smetacek, V., et al., Deep carbon export from a Southern Ocean iron-fertilized diatom bloom, *Nature*, 487, 313–319.
Steinberg, P.A., Millero, F.J., and Zhu, X.R., Carbonate system response to iron enrichment, *Mar. Chem*., 62, 31 (1998).
Sunda, W.G., Swift, D., and Huntsman, S.A., Iron growth requirements in oceanic and coastal phytoplankton, *Nature*, 351, 55 (1991).
Watson, A.J., Law, C.S., Van Scoy, K., Millero, F.J., Yao, W., Friederich, G., Liddicoat, M.I., Wanninkhof, R.H., Barber, R.T., and Coale, K., Minimal effect of iron fertilization on sea-surface carbon dioxide concentrations, *Nature*, 371, 143 (1994).

Organics in Seawater

Benner, R., Pakulski, D., McCarthy, M., Hedges, J., and Hatcher, P., Bulk chemical characteristics of dissolved organic matter in the ocean, *Science*, 255, 1561 (1992).
Carlson, C.A., Ducklow, H.W., and Michaels, A.F., Annual flux of dissolved organic carbon from the euphotic zone in the northwestern Sargasso Sea, *Nature*, 371, 405 (1994).
Degens, E.T., and Mopper, K., Factors controlling the distribution and early diagenesis of organic material in marine sediments, Chapter 31, *Chemical Oceanography*, Vol. 6, 2nd ed., Riley, J.P., and Chester, R., Eds., Academic Press, New York, 60–113 (1976).
Duursma, E.K., The dissolved organic constituents of sea water, Chapter 11, *Chemical Oceanography*, Vol. 1, Riley, J.P., and Skirrow, G., Eds., Academic Press, New York, 433–475 (1965).
Duursma, E.K., and Dawson, R., *Marine Organic Chemistry*, Elsevier, New York (1981).
Falkowski, P., The power of plankton, *Nature*, 483, S17–S20 (2012).
Gordon, A., and Millero, F.J., Use of microcalorimetry to study the growth and metabolism of marine bacteria, *Thallassia Jugoslav.*, 16, 405–424 (1980).
Hansell, D.A., and Carlson, C.A., Eds., *Biogeochemistry of Marine Dissolved Organic Matter*, Academic Press, New York (2002).
Hansell, D.A., et al. Dissolved organic matter in the ocean, *Oceanography*, 12, 203–211 (2009).
Hunter, K.A., and Liss, P., The input of organic material to the oceans: air-sea interactions and the organic chemical composition of the sea surface, *Mar. Chem*., 5, 361 (1977).
Lee, C., and Wakeham, S.G., Organic matter in sea-water: biogeochemical processes, Chapter 49, *Chemical Oceanography*, Vol. 9, 2nd ed., Riley, J.P., Ed., Academic Press, New York, 1–52 (1989).
Meybeck, M., Global chemical weathering of surficial rocks estimate from river dissolved loads, *Am. J. Sci*., 287, 401 (1987).

Mopper, K., and Stahovec, W., Sources and sink of low molecular weight organic carbonyl compounds in seawater, *Mar. Chem*., 19, 305 (1986).

Parsons, T.R., Particulate organic carbon in the sea, Chapter 13, *Chemical Oceanography*, Vol. 2, 2nd ed., Riley, J.P., and Skirrow, G., Eds., Academic Press, New York, 365–383 (1978).

Peltzer, E., and Gagosian, R., Organic geochemistry of aerosols over the Pacific Ocean, Chapter 61, *Chemical Oceanography*, Vol. 10, Riley, J.P., and Chester, R., Eds., Academic Press, New York, 282–339 (1989).

Sackett, W.M., Suspended matter in sea-water, Chapter 37, *Chemical Oceanography*, Vol. 7, 2nd ed., Riley, J.P., and Chester, R., Eds., Academic Press, New York, 127–172 (1978).

Simoneit, B.R.T., The organic chemistry of marine sediments, Chapter 39, *Chemical Oceanography*, Vol. 7, 2nd ed., Riley, J.P., and Chester, R., Eds., Academic Press, New York, 233–311 (1978).

Thurman, E.M., *Organic Geochemistry of Natural Waters*, Martinus Nijhoff/W. Junk, Dordrecht, The Netherlands (1985).

Wakeham, S., Lee, C., Farrington, J., and Gagosian, R., Biogeochemistry of particulate organic matter in the oceans: results from sediment trap experiments, *Deep-Sea Res*., 31, 509 (1984).

Williams, P.J. le B., Biological and chemical aspects of dissolved organic material in sea water, Chapter 12, *Chemical Oceanography*, Vol. 2, 2nd ed., Riley, J.P., and Skirrow, G., Eds., Academic Press, New York, 301–363 (1975).

Williams, P.M., and Druffel, E.R.M., Radiocarbon in dissolved organic matter in the central North Pacific Ocean, *Nature*, 330, 246 (1987).

10

Processes in the Oceans

10.1 Photochemical Processes in Seawater

There has been increasing interest in the photochemical processes that occur in the surface waters of the oceans and other natural waters. Much of this work has been stimulated by the pioneering work of Zika and coworkers (at the University of Miami, 1981, 1982, 1985), Zafiriou (at Woods Hole Oceanographic Institution [WHOI], 1983, 1990), and Zepp (at the Environmental Protection Agency [EPA]), who applied state-of-the-art photochemistry to ocean systems. This chapter briefly discusses the principles of photochemistry and the application of these principles to some ocean systems.

10.1.1 Principles

A photochemical process is a chemical reaction that takes place only under the influence of light. Photochemistry is concerned with the interaction of electromagnetic radiation and matter; it is at the crossroads of physics and chemistry. The light for photochemical processes includes wavelengths (λ) in the visible (400- to 700-nm), near-ultraviolet (UV) (100- to 400-nm), and near-infrared (700- to 1000-nm) ranges. This light is considered to be made up of individual photons of energy $E = h\nu$ (where h is Planck's constant, 6.63×10^{-34} J; ν is the frequency of light, $\nu = c/\lambda$; and c is the velocity of light).

Only the light that is absorbed can cause a photochemical effect (Grotthus–Draper law). Although this may seem obvious, it has been known as the first law of photochemistry for a long time. The primary photochemical reaction can be written in the form

$$M + h\nu \rightarrow M^* \tag{10.1}$$

where M is a molecule that can absorb light (a chromophore), $h\nu$ is the photon of light, and M* is the molecule in an "excited state." The extra energy ($h\nu$) and the properties of M* result in the photochemical process. The second law of photochemistry (Stark–Einstein law) states that an atom or molecule undergoing a photochemical process absorbs only a single photon.

$$\text{Reactants} + n\,h\nu \rightarrow \text{Products} \tag{10.2}$$

It is necessary to consider the yield of a photochemical reaction in terms of the amount of light absorbed by the sample. For long irradiations, it is often possible to obtain nearly quantitative yields like common chemical reactions (which can be characterized in terms

of the yield of products formed or reactants used). The yield of a photochemical reaction can be limited by four factors:

1. The occurrence of competitive reactions:

$$M^* + h\nu \rightarrow A \tag{10.3}$$

$$h\nu \rightarrow B$$

each with its own yield.

2. The occurrence of further photochemical reaction products:

$$M^* \rightarrow A \tag{10.4}$$

$$A + h\nu \rightarrow A^* \tag{10.5}$$

$$A^* \rightarrow B \tag{10.6}$$

The maximum yield of A will thus depend on the wavelength of irradiation, quantum yield, and so on.

3. The existence of true photochemical equilibrium:

$$M \overset{h\nu}{=} A \tag{10.7}$$

This equilibrium will depend on the irradiation wavelength.

4. The existence of a dark reverse reaction:

$$M \underset{\text{dark}}{\overset{h\nu}{=}} A \tag{10.8}$$

The quantum yield or efficiency of a photochemical reaction is defined as the number of molecules of product formed for each photon absorbed.

$$\phi = \{\text{Number of product molecules formed}\}/\{\text{Number of photons absorbed}\} \tag{10.9}$$

This is the quantum yield of product formation. It is also possible to define the quantum yield of the disappearance of the reactant:

$$\phi = \{\text{Number of reactant molecules that disappear}\}/\{\text{Number of photons absorbed}\} \tag{10.10}$$

The values of ϕ are generally less than 1.0 but can be greater than 1.0 for chain reactions.

The sequence of a photochemical reaction takes place in two steps. The first step starts with the absorption of light:

$$M + h\nu = M^*(\text{Absorption}) \tag{10.11}$$

The excited molecule can react by rearrangement:

$$M^* \rightarrow P \tag{10.12}$$

or by reaction with another species N:

$$M^* + N \rightarrow P \tag{10.13}$$

These steps involving M* are called the primary photochemical process. The products P may undergo further reactions that lead to final, stable products. The excited molecule can lose its energy by the loss of heat:

$$C^* \rightarrow C + \text{Heat} \tag{10.14}$$

by the loss of light energy:

$$C^* \rightarrow C + h\nu \tag{10.15}$$

or by ionization:

$$C^* \rightarrow C^+ + e^- \tag{10.16}$$

where e^- is an electron. Secondary reactions of the primary photoproducts can frequently occur with the components of the solution. For example, when the solutions contain O_2, the free radical O_2^- can be formed. This radical can react as both an oxidizing and a reducing agent.

Before we discuss various photochemical reactions important in seawater, it is useful to briefly review the energy states of molecules. The types of excited molecules depend on the amount of energy absorbed. Rotational excitation of a molecule requires the smallest amount of energy. This results in a spinning of the molecule around a preferred axis; however, the molecule is not changed chemically. With higher energies, the molecule may be promoted to a vibrationally excited state. The energy is in the form of vibrations of various parts of the molecule; again, the molecule is not changed chemically. With higher energies, the molecule can be excited to an electronically excited state. One or more electrons can be promoted to higher-energy orbitals.

Photochemical reactions occur from such electronically excited states of molecules. If a very high amount of energy is absorbed, a continuum is reached, and the molecule is ionized or dissociated:

$$M \xrightarrow{h\nu} M^+ + e^- \tag{10.17}$$

$$M \xrightarrow{h\nu} X + Y \tag{10.18}$$

The electronic states of polyatomic molecules are shown in Figure 10.1. In the electronic ground state and various electronically excited states, there are sublevels ν containing various vibrational states, and each vibrational state can have various rotational sublevels.

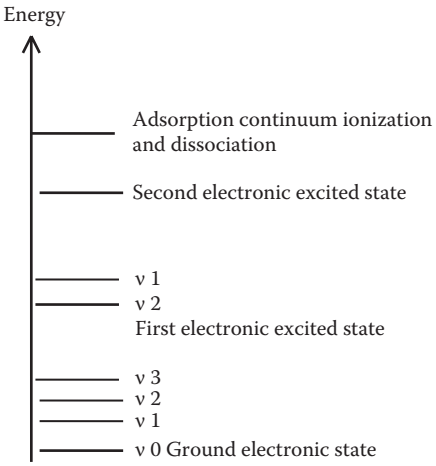

FIGURE 10.1
Distribution of electronic, vibrational, and rotational states in polyatomic molecules.

The energy of an atom or molecule is given in units of electron volts, kilocalories, or kilojoules. One electron volt is equal to 9.65×10^4 J. The frequency ν of electromagnetic radiation is equivalent to a given energy ($E = h\nu$). Spectroscopists often use the wave numbers rather than the frequency (wave number = ν/c, where $c = 3 \times 10^8$ m s^{-1}, the speed of light). The wavelength is related to the frequency by

$$\lambda = c/\nu \tag{10.19}$$

The wavelength is given in units of angstroms (1 Å = 10^{-8} cm) or the preferred unit of the nanometer (1 nm = 10^{-9} m = 10 Å).

The relationship between energy and the various types of excitation are shown in Figure 10.2. These energies can be compared (see Figure 10.3) to the energy of thermal agitation (RT = 144 J mol^{-1}), which is the same order of magnitude of translational and rotational energy. Although some of the low vibrational levels (ν = 0) can be occupied, electronically excited states cannot normally be obtained from the application of heat.

The absorption of a photon of electromagnetic radiation is possible if the energy corresponds to the energy separation between orbitals. Emission of a quantum of energy by an atom takes place when an electron jumps back from an outer orbital to an inner orbital. The frequencies of the light emitted are the same as the frequencies of the light absorbed. In the ground state, all the electrons fill the available orbitals in order of increasing energy. An excited state has one or several electrons occupying higher-energy orbitals, leaving one or several vacancies of lower orbitals. A ground state can only absorb light. An excited state can emit light and go to a lower or ground state. It can also absorb light and go upward in energy to a higher excited state.

A schematic diagram of the photophysical process and its relationship to the various electronic states of an atom or molecule is shown in Figure 10.4. The absorption of light excites the molecule from the ground state S_0 to an excited state Sν. The excited molecule loses some of its energy and can be transferred to a lower singlet (spin-paired) state. For an isolated atom, the emission wavelength is the same as the absorption wavelength. The emission from molecules is almost exclusively observed from the lowest excited state. The lifetime of this emission is usually very short (10^{-8} s). The emission process of an

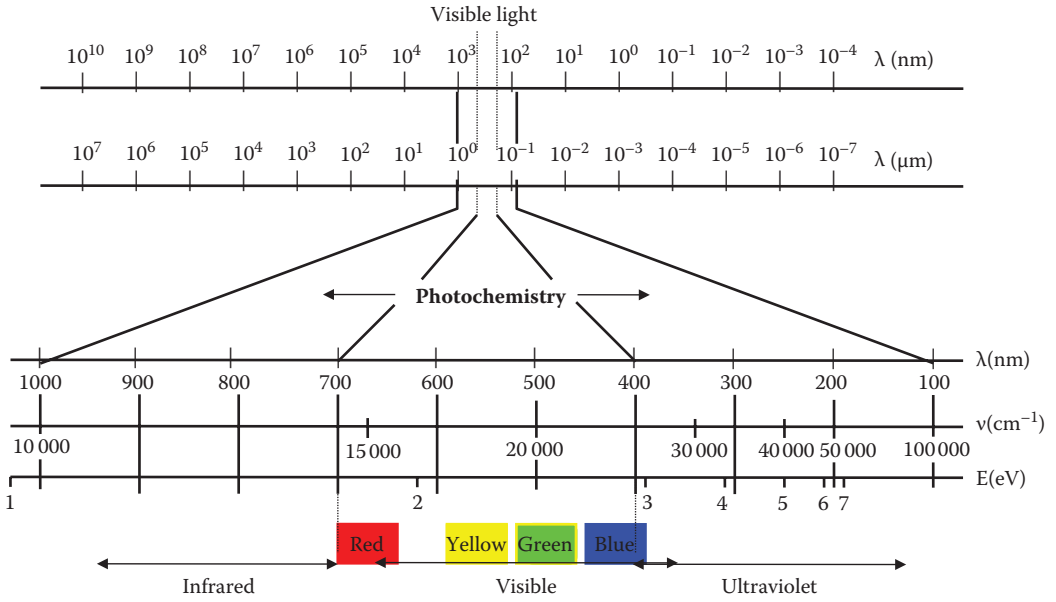

FIGURE 10.2
The electromagnetic radiation.

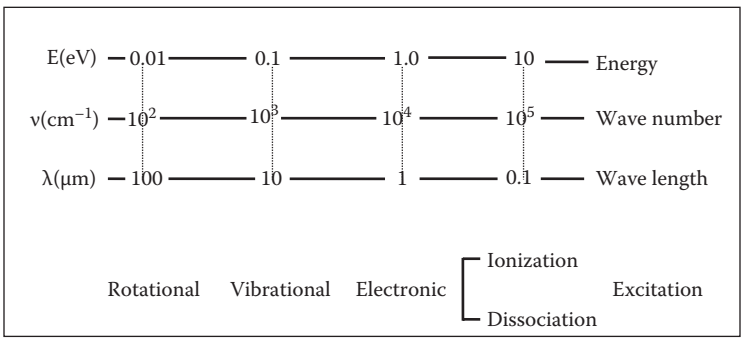

FIGURE 10.3
The energies of states and characteristics of radiation.

excited molecule from a singlet state to the ground state is called *fluorescence*. The emission of many molecules is shifted to longer wavelengths (lower energy). This is shown for anthracene in Figure 10.5. Many molecules show a longer-lived emission at longer wavelengths. This emission can last for seconds. It comes from a special type of excited state known as a triplet (unpaired).

Two electrons can share the same orbital only if they have different spin quantum numbers (↑↓). In an excited state, one electron is a singly occupied higher orbital, while it has left a vacancy in the lower orbital, which is also singly occupied. These two electrons in different orbitals are quite independent and can have their spins antiparallel, as in the ground state, or parallel (↑↑ or ↑↓). When the spins are parallel, the excited state is called the triplet state. The emission from a molecule in the triplet state is called *phosphorescence*. Delayed fluorescence arises from the production of an excited singlet state from the triplet

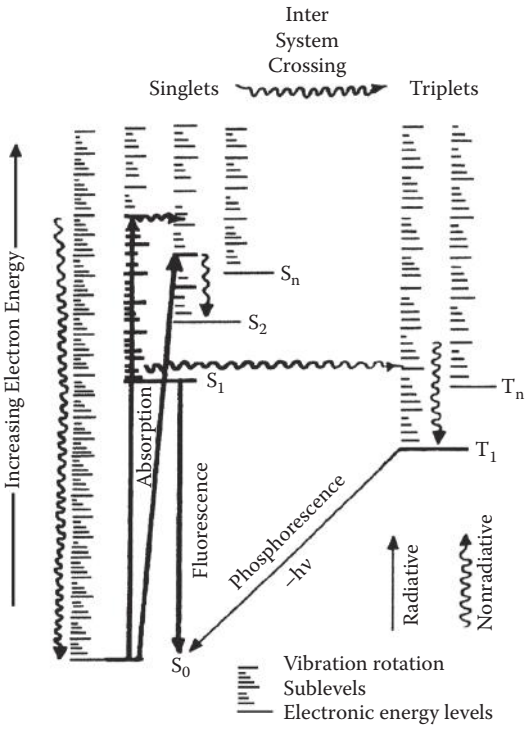

FIGURE 10.4
The photophysical processes and electronic states.

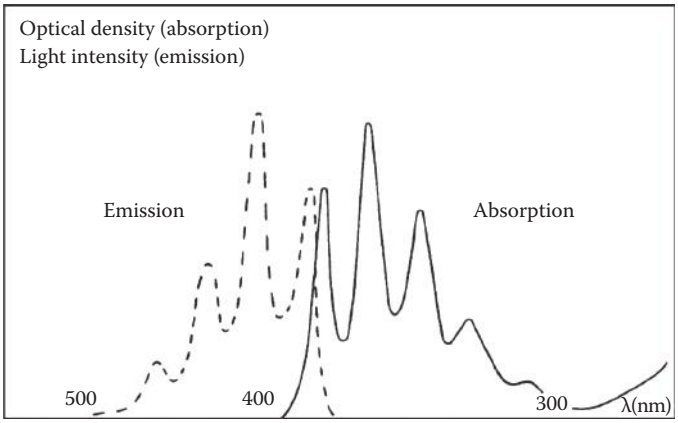

FIGURE 10.5
The fluorescence emission and absorption spectra of anthracene in solution.

or by chemical reactions. Singlet excited states can also be formed by triplet–triplet annihilation. This can result in delayed fluorescence if the diffusion of the excited molecules is rapid. An excited state that occurs by chemical effects can also have a delayed fluorescence called *chemiluminescence*.

Photochemical processes in the surface waters of the oceans can be important because they can generate various redox transients. One, however, cannot rule out the formation of

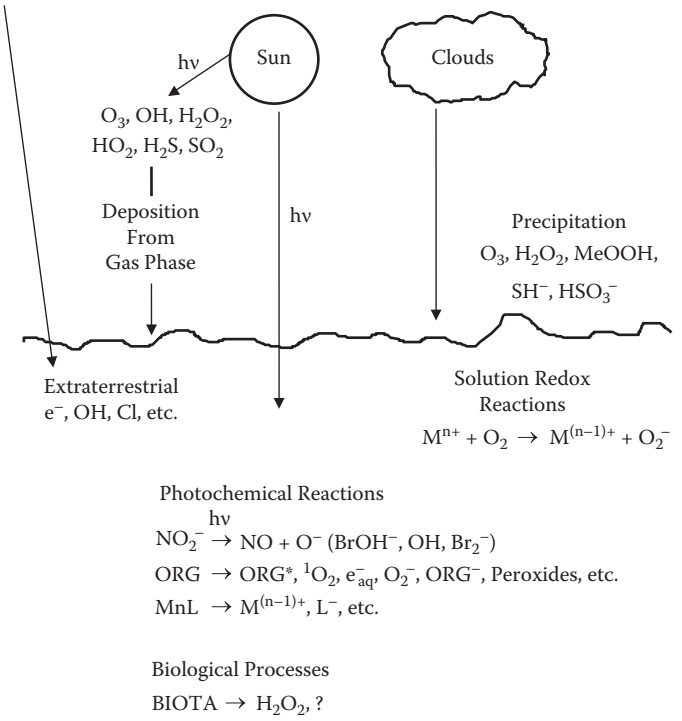

FIGURE 10.6
The primary sources of redox transients in the oceans.

redox transients from precipitation (rainout) or gas phase deposition as well as biological processes (see Figure 10.6). For photochemical processes to occur, it is necessary to have light of sufficient energy (usually UV). As shown in Figure 10.7, below a depth of 100 m little or no UV light is available for photochemical processes. For photochemical processes to occur, chromophores must be available to absorb the light. Some of the photochemical processes that occur in natural waters are given in Table 10.1. The chromophores responsible for the initial absorption of light are thought to be humic and fulvic materials. A number of other organic and inorganic molecules may also be important chromophores and are given in Table 10.2 and Table 10.3.

10.1.2 Formation of Hydrogen Peroxide

The initial findings of hydrogen peroxide (H_2O_2) in surface seawaters (see Figure 10.8) strongly support the notion that photochemical processes occur in the oceans. The sources of the H_2O_2 can result from three major processes:

1.
$$\text{Org} + h\nu \rightarrow \text{Org}^* \tag{10.20}$$
$$\text{Org}^* \rightarrow \text{Org}^+ + e^- \tag{10.21}$$
$$O_2 + e^- \rightarrow O_{2-} \tag{10.22}$$
$$O_2^- + H^+ \rightarrow HO_2 \tag{10.23}$$
$$HO_2 + HO_2 \rightarrow H_2O_2 + O_2 \tag{10.24}$$

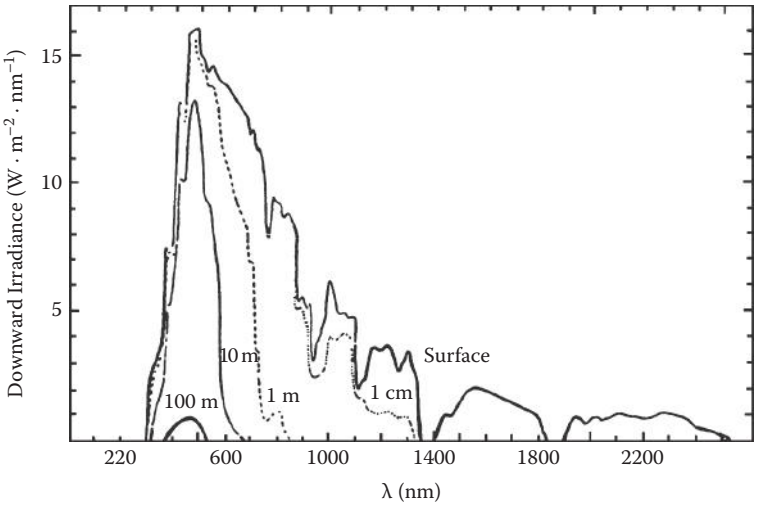

FIGURE 10.7
The spectra of light in the surface of the ocean.

2. $$Org^* + O_2 \rightarrow Org^+ + O_2^- \quad (10.25)$$

$$Org^* + sub \rightarrow Org^- + sub^+ \quad (10.26)$$

$$Org^* + sub \rightarrow Org^+ + sub^- \quad (10.27)$$

$$Org^+ + sub \rightarrow Org + sub^+ \quad (10.28)$$

$$Org^- + O_2 \rightarrow Org + O_2^- \quad (10.29)$$

$$sub^- + O_2 \rightarrow sub + O_2^- \quad (10.30)$$

3. $$M^{n+} + h\nu \rightarrow M^{(n-1)} + L^- \quad (10.31)$$

$$M^{(n-1)} + O_2 \rightarrow Mv+ + O_2^- \quad (10.32)$$

Studies by Zika and coworkers (1982) indicate that the formation of H_2O_2 is higher in coastal waters with higher humic concentrations than in oligotrophic waters (see Figure 10.9). The production rates also appear to be directly related to the concentration of the humic material in the waters (see Figure 10.10) as measured by absorbance at 300 nm. These results support the notion that abiotic photochemical processes are responsible for the production of hydrogen peroxide in the surface waters of the oceans. The biological (Palenik and Morel, 1988) and nonphotochemical processes known to form hydrogen peroxide are generally insignificant, except in oligotrophic waters. The portion of the sunlight responsible for most of the formation of H_2O_2 is below 400 nm.

Since steady-state levels of H_2O_2 of 10 to 200 n*M* are found in surface waters, the decay rates of H_2O_2 must be slower than the production rates. The diurnal variation of H_2O_2 is from 60 to 180 n*M* (see Figure 10.11). The half-times of H_2O_2 in Gulf Stream waters are

TABLE 10.1

The Diversity of Natural Water Photoprocesses

Environment	Substrates	Products	Probable Mechanisms
Marine and fresh	Natural org.	C• + HO_2	H atom transfer to O_2
	Chromophores	C• + AH•	or A
		$C^+ + O_2^-$	Energy transfer to O_2
		HOOH	Disproportionation of HO_2
	NO_2^-	NO + OH	Direct photolysis
	Br^-, CO_3^{2-}, RH	Br_{2-}, CO_3^{2-}, R•	OH radical redox and abstraction
	R•	ROO•	O_2 addition
Marine	CH_3I	CH_3^+	Direct photolysis
	MnO_2 (colloidal)	Mn^{2+}	Unknown
	Cu(II)	Cu(I)Cl	H_2O_2/O_2 – reduction of Cu(II)
	Cu(II)L	Cu(I)Cl	Charge transfer to metal
	Fe(II)	Fe(III) + H_2O_2	OH radicals (?)
Freshwater	Fe(III)L	Fe(II)	O_{2-} (?)
Surface films	I^-	HOI, oxidized organics	
Polluted waters	RH, ArH, R_2	R˙O, RCO_{2-}	Free radicals, direct
		R_2SO	Photolysis, singlet O_2

TABLE 10.2

Photoreactions of Organic Compounds

Chromophore	Products or Effects
Humic, fulvic	1. Bleaching of absorption and fluorescence
	2. Production of singlet oxygen
	3. Fe(III) reduction
	4. Release of soluble P
	5. Oxidation of cumene via ROO and OH radicals
	6. Oxidation of phenolic groups to ArO and formation of e^- and O_2^-
	7. CO formation
	8. H_2O_2 formation (via O_2^-)
Chlorophyll	Loss of chlorophyll
Vitamins	Loss of bioassay activity
Amino acids	?
Glycine	COOH C^{14} loss, HCHO formation
$CH_3SSCH_3CH_3S$	
CH_3ICH_3	
Fatty acids	Particles, absorbed, hydroperoxides
Aldehydes	RCO, R, CO

about 120 h and about 12 h in coastal waters. Studies also indicate that the lifetimes are much longer in deep waters (1900 h at 250 m). These results suggest that the rates of decay of H_2O_2 may be controlled by particles or biological processes. The effect of particles on decay is shown in Figure 10.12. Filtration through a 0.2-μm filter slows the rate of decay of H_2O_2.

TABLE 10.3

Photoreactions of Inorganic Compounds

Compounds	Products or Effects
Fe^{2+}	$Fe^{3+} + H_2$ (Precambrian)
Cu^{2+} complexes	NH_3 and HCHO
Fe-humates	1. Fe^{2+}, CO_2, O_2
	2. Fe^{2+}, PO_4^{3-}
I^-	$I + e^-$
NO_2^-	1. NO + OH•
	2. Methionine destruction
NO_3^-	NO_3^- loss, NO_2^-

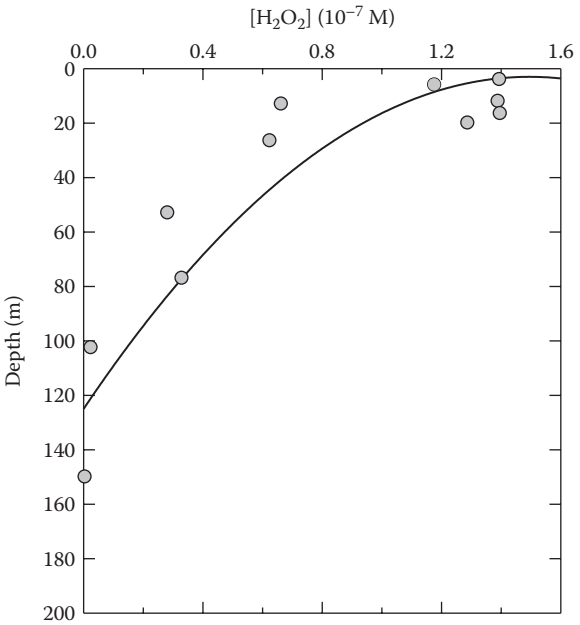

FIGURE 10.8
Profile of hydrogen peroxide in the Gulf of Mexico.

Since autoclaving the seawater has a similar affect (see Figure 10.13), the decay appears to be partly related to biological particles (living and dead cells). Further work is needed to elucidate the decay mechanism of H_2O_2 and the effect cells have on the formation and destruction of H_2O_2. The decomposition is not affected by light and occurs in a matter of days. Enzymes as well as particles may be important in the destruction of H_2O_2 in natural waters. Although abiotic decomposition processes are small, they may be important in the open oceans. Two major enzymes in organisms that control intracellular H_2O_2 are catalases and peroxidase. Moffett and Zafiriou (1990), using ^{18}O-labeled H_2O_2 and O_2, found that in coastal waters 65 to 80% of the decomposition of H_2O_2 was due to catalase.

The superoxide anion (O_2^-) is a key intermediate in the formation of H_2O_2. Thus, all the reactions that lead to O_2^- will increase the concentration of H_2O_2. The aqueous chemistry of superoxide has been studied extensively by Bielski (1978). The superoxide radical (HO_2)

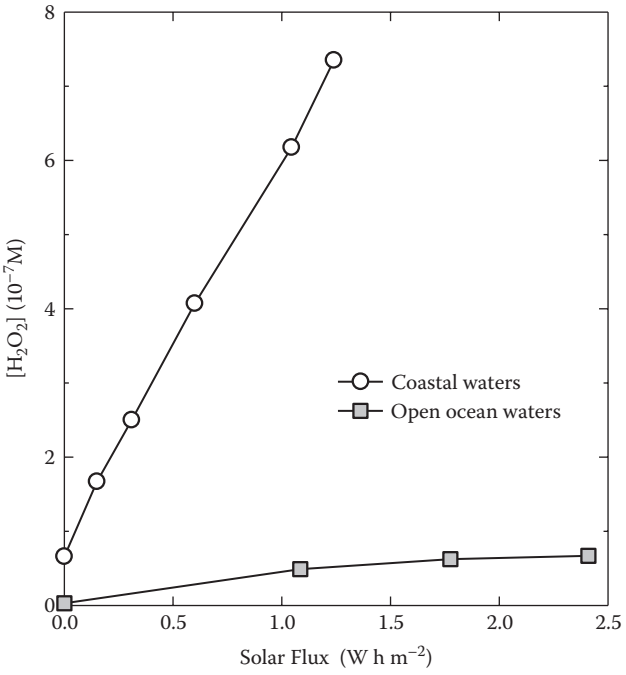

FIGURE 10.9
The photochemical accumulation of hydrogen peroxide in seawater.

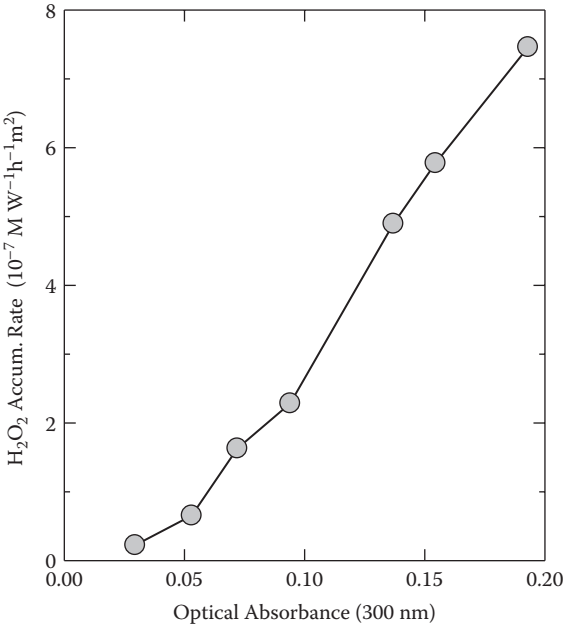

FIGURE 10.10
The accumulation rates for different seawaters as a function of the optical absorbance.

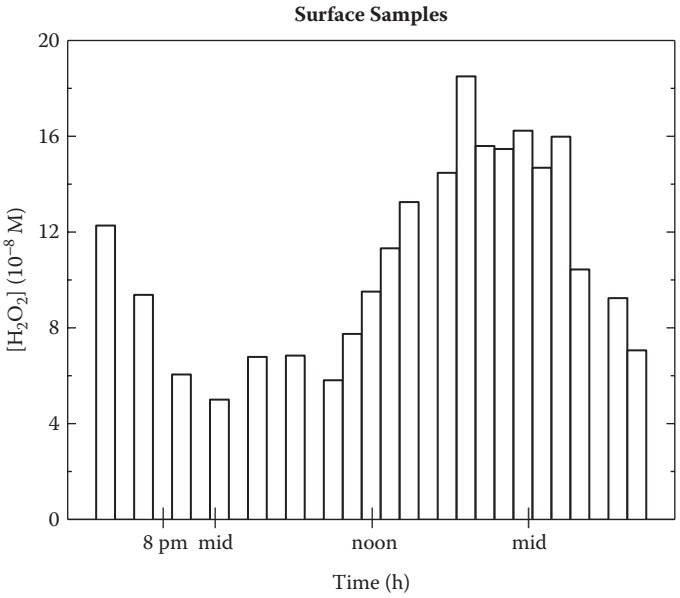

FIGURE 10.11
The diurnal variations of hydrogen peroxide in surface waters in the Bahamas.

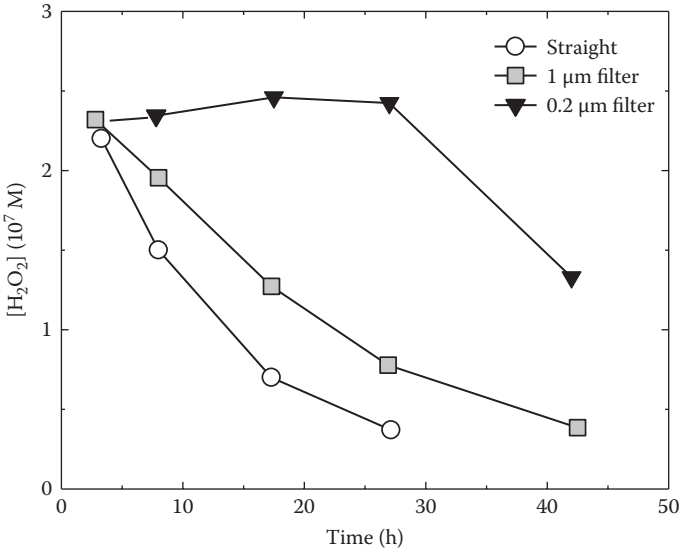

FIGURE 10.12
The effect of filtering on the decay of hydrogen peroxide in seawater.

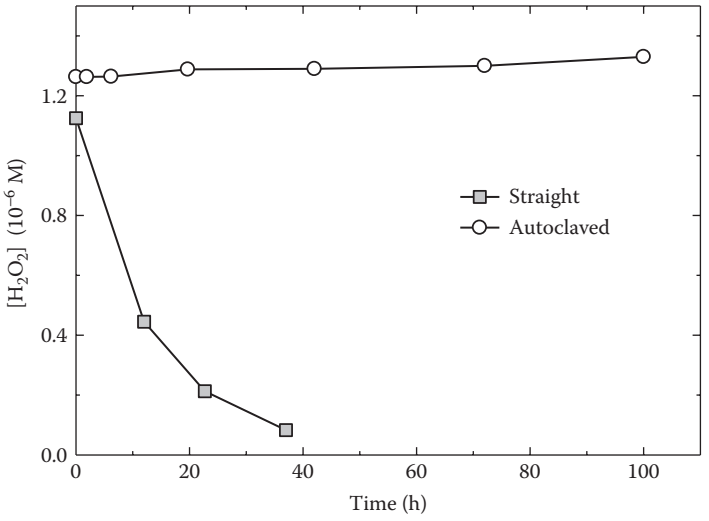

FIGURE 10.13
The effect of autoclaving on the decay of hydrogen peroxide in seawater.

is an acid and can dissociate to H^+ and O_2^- with a pK of 4.8 in pure water. The disproportionation reaction can take place by

$$HO_2 + HO_2 \rightarrow H_2O_2 + O_2 \tag{10.33}$$

$$HO_2 + O_2^- + H_2O \rightarrow H_2O_{2+}\ O_2 + OH^- \tag{10.34}$$

The second-order rate equation for these reactions is given by

$$-d[HO_2]/dt = k_2[HO_2]_T \tag{10.35}$$

where $[HO_2]_T$ is the total concentration of superoxide, and k_2 is the second-order rate constant. At a low pH, Reaction 10.33 is important, and above a pH of 6, Reaction 10.34 dominates (Millero, 1987). The second-order rate constant dominates over the pH range of most natural waters (7 to 9); the values of k_2 in water can be estimated from $\log k_2 = 12.68 - 1.0$ pH. The half-time for the disappearance of HO_2 is given by

$$t_{1/2} = 1/2k_2[HO_2]_T \tag{10.36}$$

At a pH of 8 and a level of $[HO_2]_T = 100$ n*M* (the levels of H_2O_2 in surface waters), the lifetime of O_2^- in water should be about 100 s—if it decays only to form H_2O_2. The lifetimes of O_2^- in seawater based on measurements in sea salts (at high concentrations of O_2^-) were thought to be higher (three to five times longer) because of the formation of MgO_2^+ and CaO_2^+ complexes. However, measurements made by Zafiriou (1990) indicated that the rate and lifetimes in seawater are the same order as in pure water. These differences may be related to the higher levels of O_2^- used in the earlier experiments analyzed by Millero. These lifetimes are long enough to make O_2^- an important reductant and oxidant in surface waters of the oceans. Measured formation rates of O_2^- in natural seawater by Petasne and Zika (1988) suggested that about 40% of the loss is from a second pathway. Thus, in

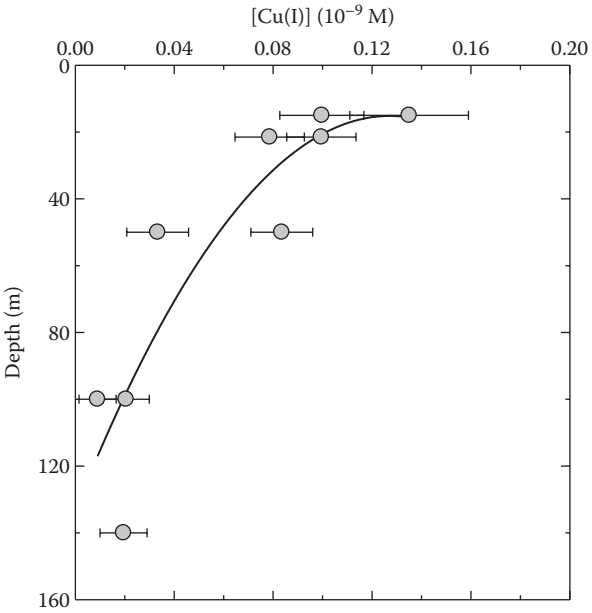

FIGURE 10.14
Profile of copper(I) in the surface waters of the Sargasso Sea.

some waters the uncatalyzed dismutation may not be the major reactant of O_2^-. Reactions of O_2^- with metals (Cu^{2+}) and organic compounds such as superoxide dismutases released by biota may also be an important sink in surface waters. This anion is a strong reductant and can result in the formation of reduced metals:

$$Fe^{3+} + O_2^- \rightarrow Fe^{2+} + O_2 \tag{10.37}$$

$$Cu^{2+} + O_2^- \rightarrow Cu^{+} + O_2 \tag{10.38}$$

Since Cu^+ has been measured in surface seawaters (Figure 10.14) by Moffett and Zika (1988), this reduction process may result in this transient species. The oxidation of Cu^+ to Cu^{2+} is prevented by the formation of chloro complexes that are resistant to oxidation (Sharma and Millero, 1988).

$$Cu^{+} + Cl^- \rightarrow CuCl \tag{10.39}$$

$$CuCl + Cl^- \rightarrow CuCl_{2-} \tag{10.40}$$

$$CuCl_2^{-} + Cl^- \rightarrow CuCl_3^{2-} \tag{10.41}$$

Our entire view of redox processes in the surface waters of the oceans has changed as a result of these photochemically generated redox species. This has been demonstrated by King, Lounsbury, and Millero (1995) for the redox chemistry of iron in natural waters. The proposed mechanism of oxidation is described by the reactions

$$Fe(II) + O_2 \rightarrow Fe(III) + O_2^- \tag{10.42}$$

$$Fe(II) + O_2^- \rightarrow Fe(III) + 2H^+ + H_2O_2 \tag{10.43}$$

$$Fe(II) + H_2O_2 \rightarrow Fe(III) + OH + OH^- \quad (10.44)$$

$$Fe(II) + OH \rightarrow Fe(III) + OH^- \quad (10.45)$$

The Fe(III) generated by the oxidation can be converted back to Fe(II) by photoreduction.

At the levels of iron in coastal waters (20 n*M*), this photoreduction can produce a steady-state concentration of 8 n*M* of Fe(II) with a turnover time of 29 h^{-1} and Fe(II) flux of 230 n*M* h^{-1}. At a pH of 8, the steady-state concentrations of H_2O_2 and O_2^- are, respectively, 46 and 0.42 n*M*. These calculations represent the upper limits of the production of H_2O_2 and O_2^- by iron redox cycling. Since the photolysis of natural organics dominates the production of O_2^- and H_2O_2, the iron cycling may not be important in surface waters but could be important at oxic–anoxic interfaces and at low oxygen levels at the O_2 minimum in the oceans.

10.1.3 The •OH Radical

The •OH radical (discussed in Chapter 5) is the most reactive photochemically produced free radical in the atmosphere. Its role in aqueous systems is less clearly understood. Flash photolysis studies by True and Zafiriou (1987) have demonstrated that it is formed in seawater. The •OH radical formed in seawater is thought to be controlled by reactions with the bromide ion via the reactions

$$\bullet OH + Br^- \rightarrow BrOH^- \quad (10.46)$$

$$BrOH^- \rightarrow Br + OH^- \quad (10.47)$$

$$BrOH^- + Br^- \rightarrow Br_2^- + OH^- \quad (10.48)$$

$$Br + Br \rightarrow Br_2^- \quad (10.49)$$

The $BrOH^-$ in seawater at pH 8 can react to Br_2^- directly by Equation 10.48 or by Equation 10.47 and Equation 10.49. At the low Br^- levels in seawater (0.8 m*M*), Equation 10.47 is about 1000-fold faster than Equation 10.48. True and Zafiriou (1987) generated the Br radical in seawater by flash photolysis,

$$Br^- + hv \rightarrow Br + e^- \quad (10.50)$$

and pulse radiolysis that produced the •OH radical in seawater without photooxidizing Br^-. The disappearance of the Br_2^- in seawater is quite fast because of reactions with the major components of seawater. The decay proceeds by parallel first- and second-order reactions:

$$-d[Br_{2\_}]/dt = k_1 [Br_2^-] + k_2 [Br_2^-]^2 \quad (10.51)$$

where k_1 and k_2 are rate constants. The first-order decay k_1 appears to be with carbonate ions:

$$Br_2^- + CO_3^{2-} \rightarrow 2Br^- + CO_3^- \quad (10.52)$$

From the speciation of carbonate in seawater, the reactive carbonate species appear to be CO_3^{2-}, $MgCO_3$, $NaCO_3$, and $CaCO_3$.

Mopper and Zhou (1990) measured the production and steady-state concentrations of •OH in sunlight-irradiated seawater. They determined the •OH radical by reaction with methanol:

$$CH_3OH + \bullet OH \rightarrow CH_2OH + H_2O \quad (10.53)$$

$$CH_2OH + O_2 \rightarrow CH_2O + HO_2 \quad (10.54)$$

and the reaction with aromatic ring Ar of benzoic acid:

$$H\text{-}Ar + \bullet OH \rightarrow H\text{-}Ar\text{-}OH \quad (10.55)$$

$$H\text{-}Ar\text{-}OH + O_2 \rightarrow HO\text{-}Ar + HO_2 \quad (10.56)$$

The products (formaldehyde) from the reaction are determined using high-performance liquid chromatography (HPLC) techniques.

The possible sources of the •OH radical in seawater are NO_3^-, NO_2^-, H_2O_2, Fe^{2+}, and dissolved organic material (DOM). A summary of their results for various waters is given in Table 10.4. The reactive wavelengths were found to be 280 to 320 nm (UV B region of solar spectrum). The concentrations of •OH formed in seawater were lower than those formed in freshwaters. The steady-state concentrations were much higher in upwelling and coastal waters than in open ocean waters. The •OH productions from NO_3^-, NO_2^-, and H_2O_2 in sunlight in seawater were found, respectively, to be 3.0×10^{-13}, 2.3×10^{-11}, and 4.1×10^{12} mol s^{-1}. The production from NO_3^- and NO_2^- are only important in upwelling areas and some coastal waters. By far the most important source of the •OH radical is the DOM in seawater. The low concentrations of H_2O_2 and dissolved Cu(I) and Fe(II) in surface waters make the Fenton-type reactions a poor source of •OH radicals. The photolysis of the light by the hydroquinolic and phenolic parts of humic substances is thought to be responsible for the formation of the •OH radical. The major sink of the •OH radical was found to be Br^- (93%), with approximately 7% available to react with DOM. The BrOH formed can also react with DOM. The reactions of DOM with •OH can result in the formation of more labile low molecular weight organics. Mopper and Zhou (1990) have estimated the first-order rate constant at steady-state levels of •OH:

$$d[DOM]/dt = -k[DOM] \quad (10.57)$$

of $k = 1 - 2 \times 10^4$ for surface waters, $4 - 5 \times 10^4$ for deep waters, and $5 - 8 \times 10^4$ for coastal waters. The lower reactivity for surface waters may be due to photobleaching (loss of reactivity from absorption of sunlight). The reaction of DOM with the •OH radical and resultant formation of low molecular weight organics may result in the long-term transformation of DOM in ocean waters.

TABLE 10.4

Formation of the OH Radical for Different Waters

		Production		Source (%)		
Water	**[OH•] 10^{18}**	**Rate (n*M*/h) 10^{12}**	**NO_3**	**NO_2**	**H_2O_2**	**DOM**
Sargasso Sea (surface)	1.1	2.8	<1	<4		>95
Sargasso Sea (700 m)	6.3	15.9	19	1	3	77
Biscayne Bay	9.7	24.4	2		2	96
Everglades	840	420				

10.2 Hydrothermal Vent Chemistry

In April 1979, scientists aboard the submersible *Alvin* discovered hot springs coming from the seafloor in areas of active volcanism near the Galapagos Islands. The area around the black smokers had deposits of metal-rich minerals and unique biological communities. A cartoon of a typical cluster of organisms around a hydrothermal vent is shown in Figure 10.15. Large clams, crabs, mussels, and worms are fed by the hydrothermal fluids. These vent communities are thought to persist only for years to decades. Since the initial discovery in the Galapagos, more vent systems have been found along the East Pacific rise and more recently along the mid-Atlantic ridge (see Figure 10.16). Two types of vents have been found: (a) warm vents with maximum exit temperatures of 5 to 23°C and flow rates of 0.5 to 2 cm s^{-1} and (b) hot vents with maximum exit temperatures of 270 to 380°C and flow rates of 1 to 2 m s^{-1}. Hot vents include white smokers (≈300°C) and black smokers (350 ± 2°C).

Bacteria use the geothermal energy from the vents through the process of bacterial chemosynthesis. Like photosynthesis, the process involves the biosynthesis of organic carbon compounds from CO_2, with the source of energy being chemical oxidation (rather than light). The energy used to produce organic compounds in these vent systems is the bacterial oxidation of hydrogen sulfide (Figure 10.17). Chemoautotrophy is the assimilation of CO_2 by bacteria with the ability to use reduced inorganic compounds as a source of energy (chemolithotroph). The following equations illustrate the relationships between the two processes. For nonoxygenic photoautolithotrophy, purple and green bacteria:

$$2CO_2 + H_2S + 2H_2O \xrightarrow{h\nu} 2[CH_2O] + H_2SO_4 \qquad (10.58)$$

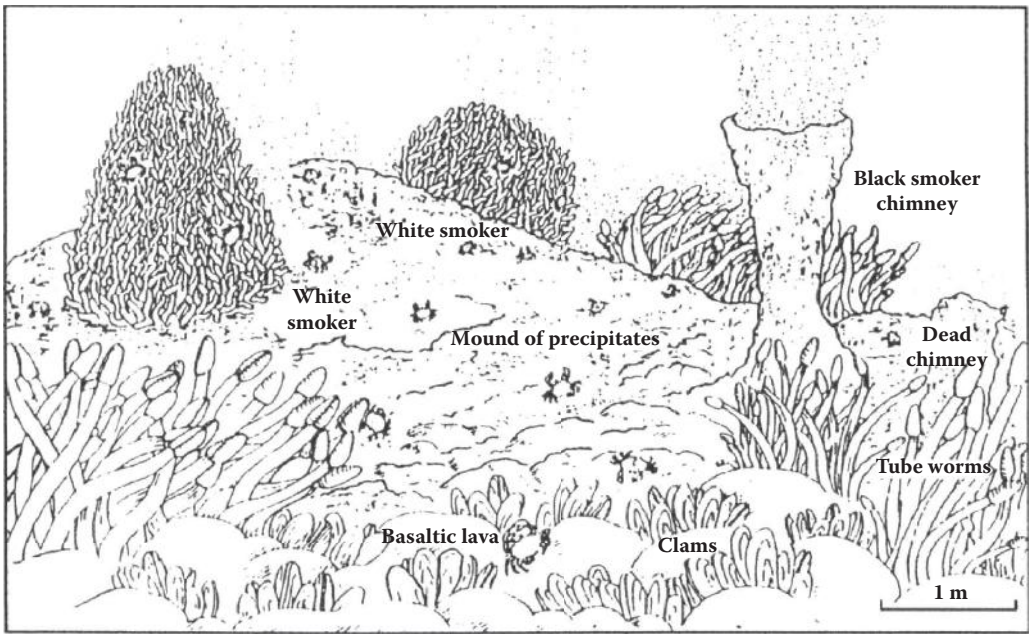

FIGURE 10.15
A typical hydrothermal cluster of structures.

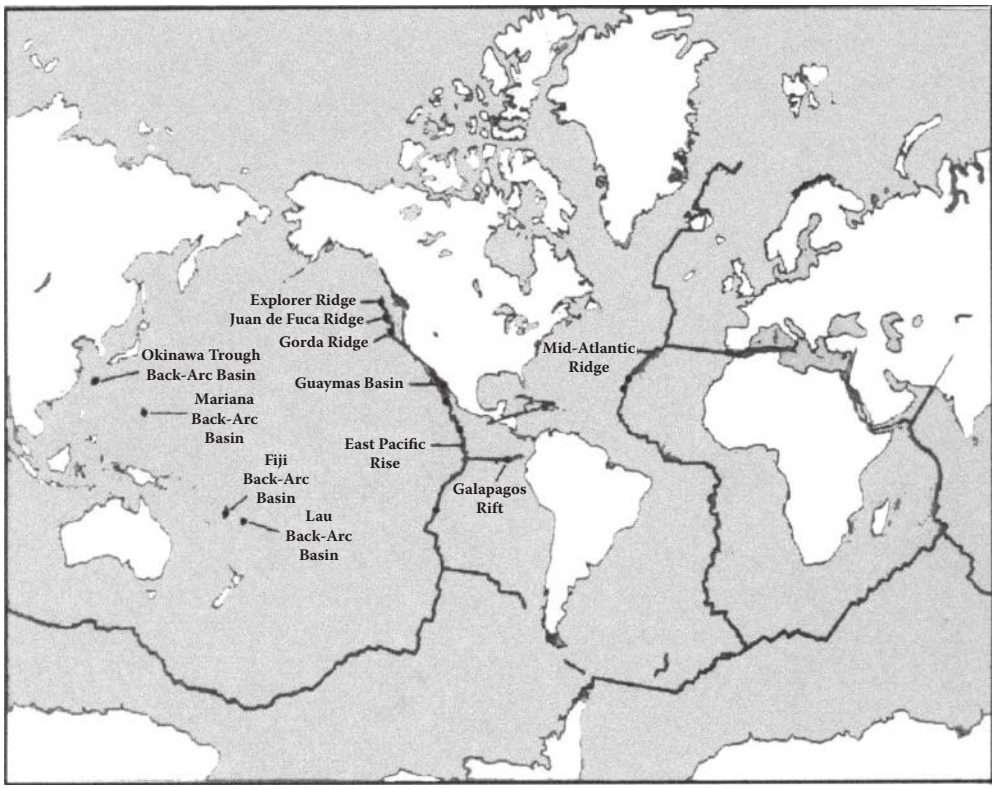

FIGURE 10.16
Hydrothermal vent sites.

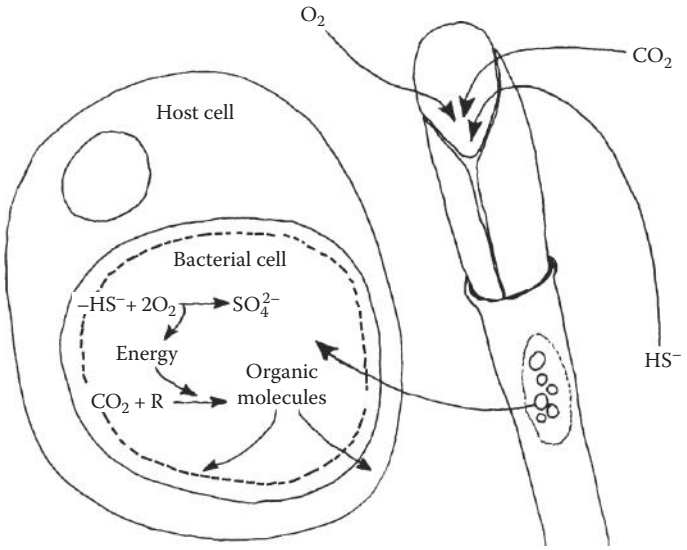

FIGURE 10.17
Sketch of the host bacterial cell that oxidizes H_2S for energy to make organic compounds.

For oxygenic photoautolithotrophy, green plants:

$$CO_2 + H_2O \xrightarrow{h\nu} [CH_2O] + O_2 \quad (10.59)$$

For aerobic chemoautolithotrophy, bacteria:

$$CO_2 + H_2S + O_2 + H_2O \rightarrow [CH_2O] + H_2SO_4 \quad (10.60)$$

For anaerobic chemoautolithotrophy, bacteria:

$$2CO_2 + 6H_2 \rightarrow [CH_2O] + CH_4 + 3\,H_2O \quad (10.61)$$

The possible electron donors used by bacteria are shown in Table 10.5. Some are the same as those used in anaerobic chemosynthesis (NO_3^-, SO_4^{2-}, or CO_2). The inorganic sources of energy are used to produce adenosine triphosphate (ATP).

A diagram of the chemical processes occurring at vent systems is shown in Figure 10.18 and Figure 10.19. The seawater permeates into the top of a crustal magma chamber (1 to 3 km) and reacts with the molten basalt. As the temperature of the seawater increases toward the mantle, $CaSO_4$ may precipitate en route. The sulfate in seawater is converted at high temperatures to hydrogen sulfide. The bicarbonate is converted into carbon dioxide and methane. Magnesium reacts with the basalt to form a new mineral phase, releasing a proton. Some of the protons released exchange with the basalt and release a number of trace metals to the fluid. The hydrothermal fluid permeates back to the surface and exits at low (2 to 23°C) and high (350°C) temperatures.

Reactions between metals and sulfide can occur along the route of precipitating sulfides. H_2S, as the reduced compound coming from the vents, is the major electron donor. It is formed by the reduction of SO_4^{2-} from seawater, coupled with the oxidation of Fe^{2+} in basalt to Fe^{3+}. The H_2S may also be leached from crystal basalts. Both mechanisms have been found in laboratory experiments at 300°C. The concentration of HS^- (25 m*M*) is nearly the same as SO_4^{2-} in seawater (28 m*M*). This indicates that seawater circulating through the hydrothermal system reacts with an amount of rock nearly equal to its own mass. Since seawater can lose SO_4^{2-} as $CaSO_4$ (anhydrite), little of the seawater SO_4^{2-} may get to the hotter parts of the system where it can be reduced. Sulfur isotope work on the vent waters

TABLE 10.5

Electron Sources and Types of Chemolithotrophic Bacteria Potentially Occurring at Hydrothermal Vents

Electron Donor	Electron Acceptor	Organisms
S^{2-}, S^0, $S_2O_3^{2-}$	O_2	Sulfur-oxidizing bacteria
S^{2-}, S^0, $S_2O_3^{2-}$	NO_3^-	Denitrifying and sulfur-oxidizing bacteria
H_2	O_2	Hydrogen-oxidizing bacteria
H_2	NO_3^-	Denitrifying hydrogen bacteria
H_2	S^0, SO_4^{2-}	Sulfur- and sulfate-reducing bacteria
H_2	CO_2	Methanogenic and acetogenic bacteria
NH_4^+, NO_2^-	O_2	Nitrifying bacteria
Fe^{2+}, Mn^{2+}	O_2	Iron- and manganese-oxidizing bacteria
CH_4, CO	O_2	Methylotrophic and carbon monoxide-oxidizing bacteria

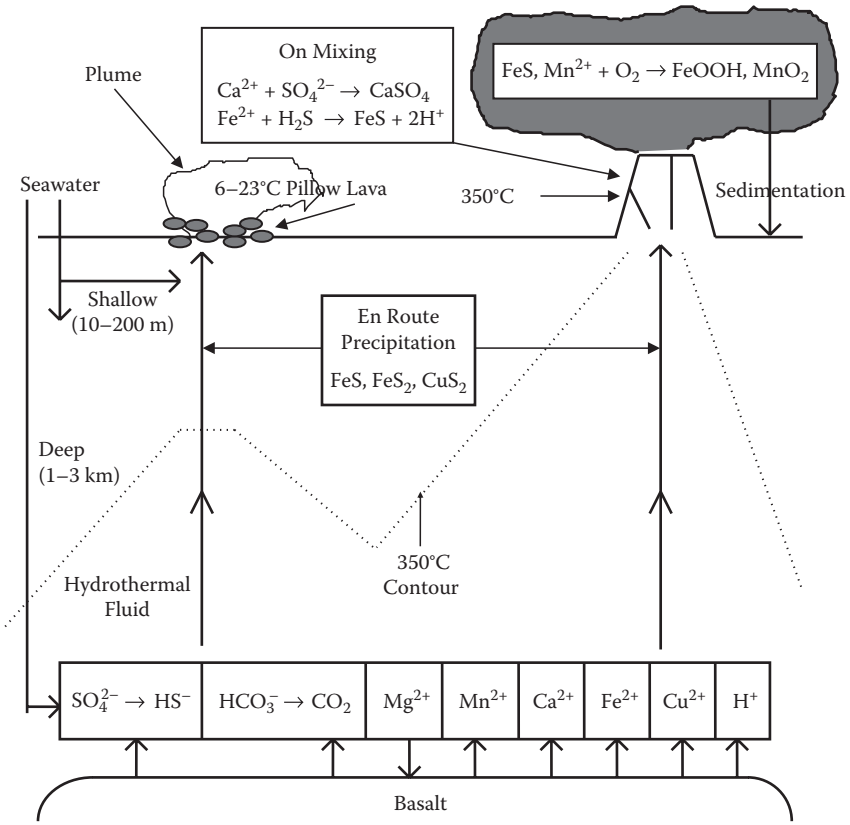

FIGURE 10.18
Schematic diagram showing the inorganic processes occurring at a vent site.

indicates that H_2S is mainly derived from the basalt. The hydrothermal reactions associated with the fluid flow are shown in Figure 10.19. As the hot black smokers exit, the precipitation of sulfides and $CaSO_4$ results in the formation of chimneys (Figure 10.20). The Fe(II) released results in the formation of metalliferous sediments.

Before we examine the chemistry of the hydrothermal fluids, we will examine the suggested evidence for hydrothermal fluxes before they were discovered. The first evidence came from geophysical observations. Heat flow measurements, for example, were lower than the theoretically predicted values (see Figure 10.21) as one approached the active ridges. The lost heat is attributed to the amount carried away by circulating seawater. Other geophysical evidence for hydrothermal fluxes comes from metalliferous sediments and ^3He anomalies in the water column (see Figure 6.6).

The second source of evidence for hydrothermal fluxes comes from experimental laboratory measurements. These laboratory measurements were made between basalt and seawater mixtures (at water:rock ratios of 10:1) in steel bombs. The measurements were made at low temperatures (70°C), high temperatures (150 to 300°C), and very high temperatures (300 to 350°C). The low-temperature measurements showed losses of Mg^{2+}, Na^+, and K^+ from seawater and a release of Cu^{2+} and SiO_2 from the basalt. The higher-temperature measurements (water:rock ratio of 50:1 or 62:1) showed a loss of Mg^{2+}, SO_4^{2-}, and Na^+ from seawater and a release of Ca^{2+}, H_2S, CO_2, SiO_2, K^+, and H^+ from the basalt. The release of the

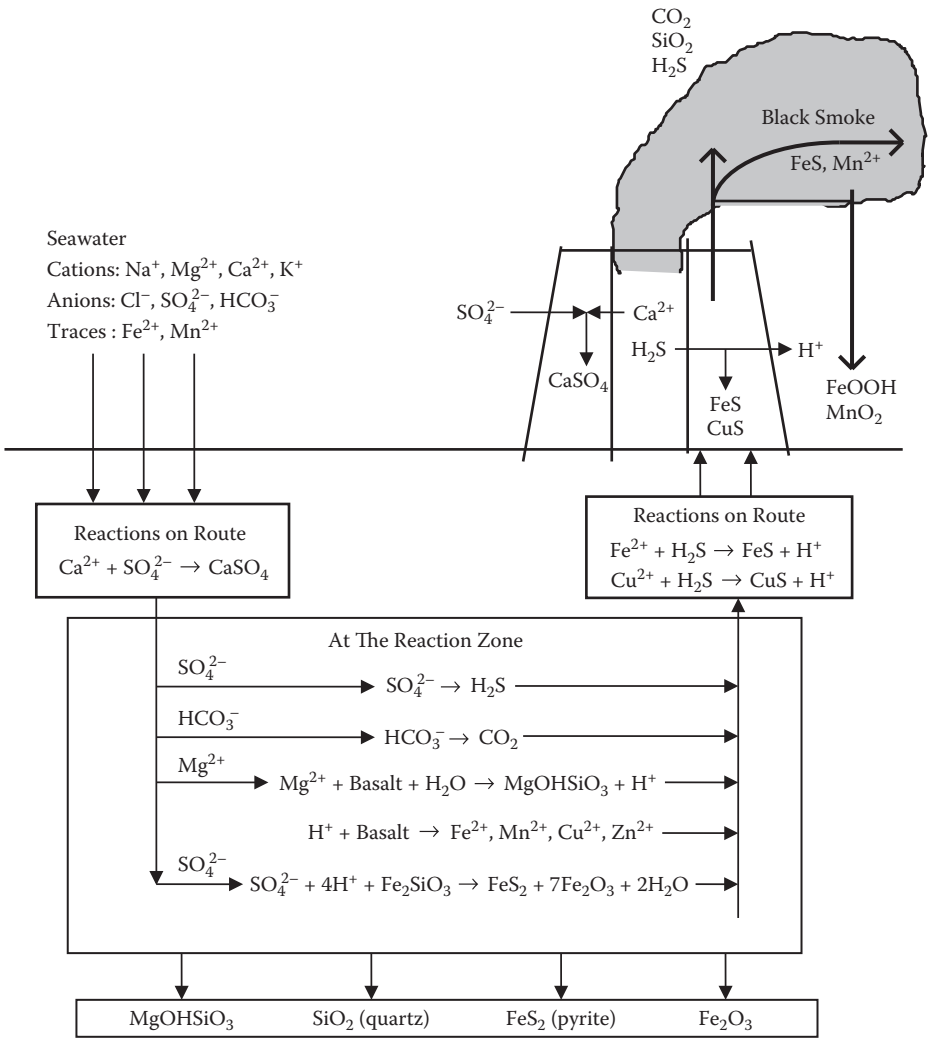

FIGURE 10.19
The hydrothermal chemical reactions.

H^+ causes the pH to decrease to values near 5.0. Slight increases of Fe^{2+}, Mn^{2+}, Ba^{2+}, Al^{3+}, and Cu^{2+} were also found. In the very-high-temperature measurements (water:rock ratio of 50:1 or 62:1), higher concentrations of trace metals were found.

The third source of evidence for hydrothermal fluxes comes from geochemical field measurements. This evidence includes finding altered basalts, sulfide deposits, and hydrothermal precipitates. The iron- and manganese-rich hydrothermal precipitates found by Bonatti and Joensuu (1966) on active ridge systems were a strong indication that high-temperature reactions were occurring. Earlier studies on Red Sea hot brines also demonstrated that circulating seawater is heated by molten basalt.

The discovery of hot springs in the Galapagos and on the East Pacific rise demonstrated that hydrothermal processes were occurring in the oceans. More recent studies of hydrothermal vents have been made in a number of sites (Figure 10.16). The Galapagos vent

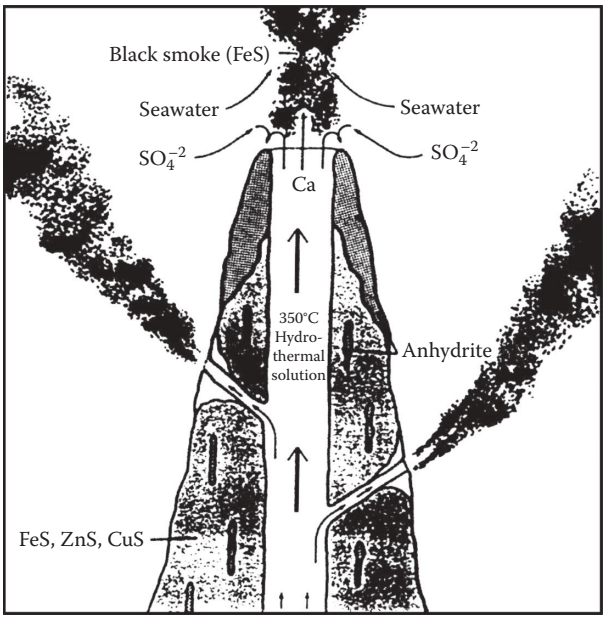

FIGURE 10.20
Sketch of a chimney formed by a black smoker.

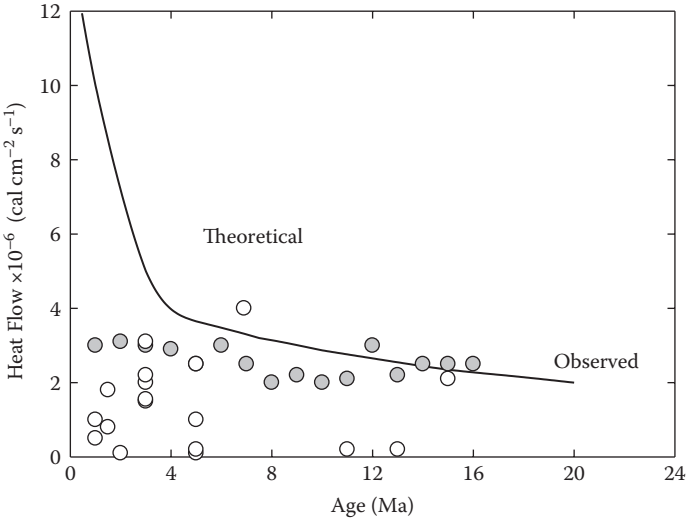

FIGURE 10.21
Comparison between the measured and theoretical heat flow as a function of the crustal age for slow- and fast-spreading centers.

studies showed a linear increase of SiO_2 with temperature (Figure 10.22). As the SiO_2 increases, the Mg^{2+} decreases (Figure 10.23). The Mg^{2+} concentration is inversely proportional to the temperature (Figure 10.24). This has led to the use of Mg^{2+} as a measure of the mixing of the hot hydrothermal fluids with seawater. The concentrations of Li^+, K^+, and Rb^+ coming from the Galapagos vents are shown in Figure 10.25 to Figure 10.27, respectively.

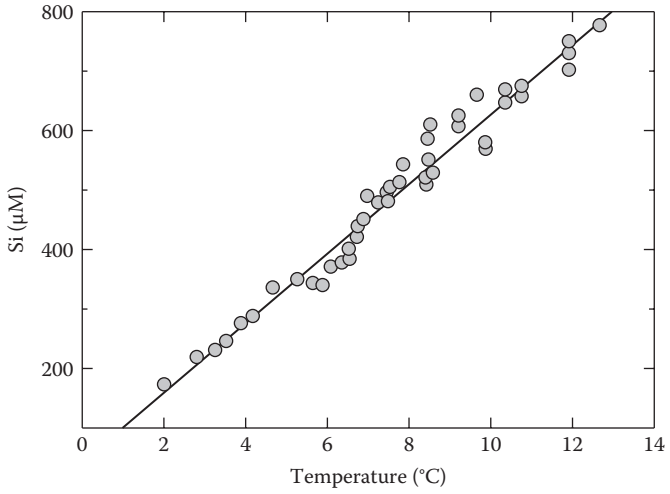

FIGURE 10.22
Concentration of SiO_2 as a function of the temperature for the Galapagos vent waters.

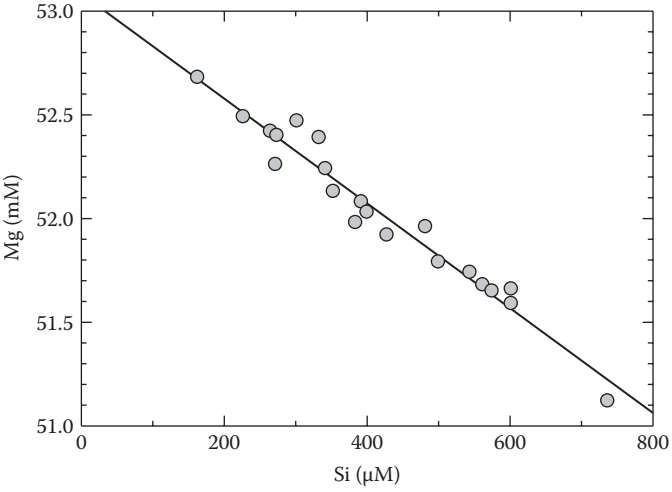

FIGURE 10.23
Concentration of magnesium as a function of the silica concentration.

The extrapolated values to [Mg] = 0 can be used to estimate the concentrations at high temperature. The concentrations of Ca^{2+} and Sr^{2+} coming from the vents are shown in Figure 10.28 and Figure 10.29, respectively.

The extrapolated pH of the hydrothermal waters is close to 4.0 (see Figure 10.30). The SO_4^{2-} ion shows a loss in the hydrothermal waters as expected (see Figure 10.31). The trace metals Mn^{2+}, Fe^{2+}, and Zn^{2+} show increases as the Mg decreases (Figure 10.32 to Figure 10.34). The measurements of Na^+ and Cl^- versus Mg^{2+} are not as conclusive (see Figure 10.35 and Figure 10.36, respectively). The loss of Na^+ and Cl^- may occur at the triple point of seawater (~350°C, liquid and vapor are in equilibrium). A comparison of the estimated composition

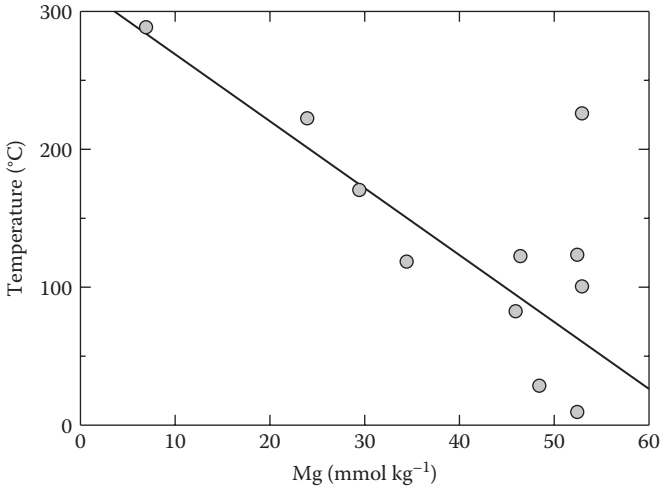

FIGURE 10.24
Magnesium concentration as a function of the temperature of vent waters.

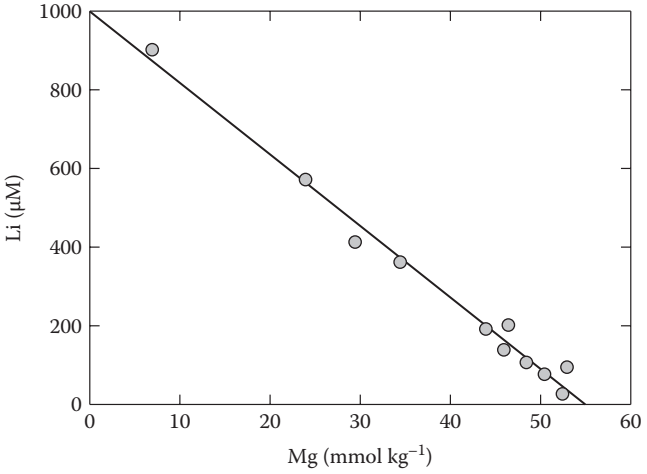

FIGURE 10.25
Lithium concentration as a function of magnesium in vent waters.

of the 350°C end member and in seawater is given in Table 10.6. A comparison of the hydrothermal and river fluxes of elements is shown in Table 10.7. These comparisons indicate that for some elements the hydrothermal flux is the same order as the river flux.

Coale et al. (1991) made direct measurements of Fe(II) and H_2S coming from vent systems. Measurements of Fe(II) and temperature across a vent system are shown in Figure 10.37. Fe(II) levels as high as 40 n*M* were found in the vent fluids. Measurements have also been made of H_2S before and after clear-cutting the plants and organisms in the region (see Figure 10.38). Before clear-cutting the area, the levels of H_2S were quite low because of its oxidation by bacteria living in tube worms. The measurements of H_2S showed a good

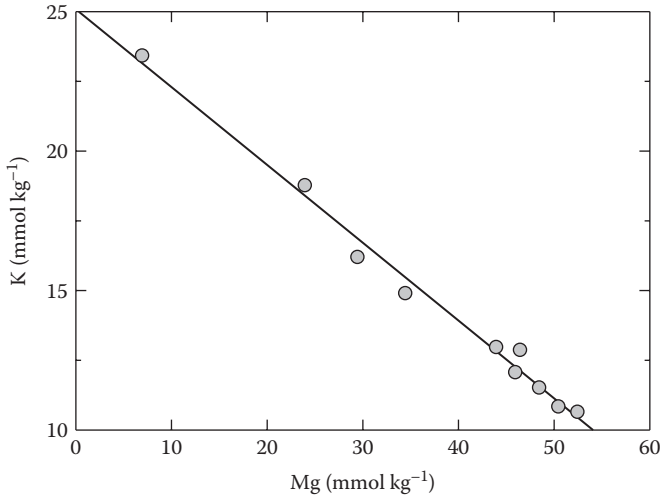

FIGURE 10.26
Potassium concentration as a function of magnesium in vent waters.

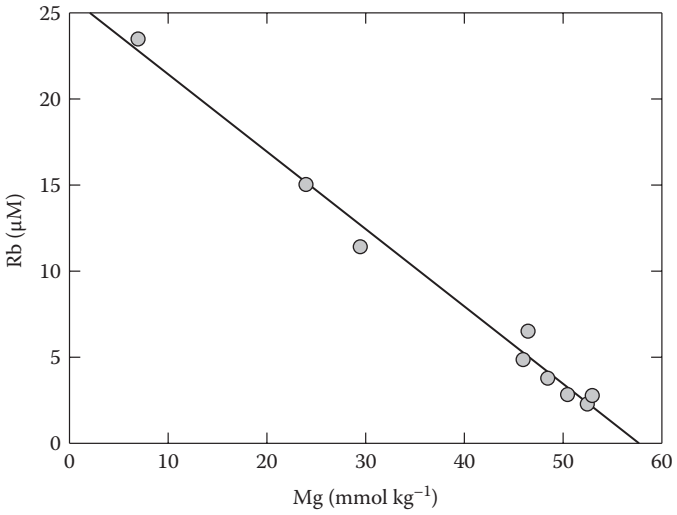

FIGURE 10.27
Rubidium concentration as a function of magnesium in vent waters.

linear correlation with SiO_2 and reached levels as high as 100 μ*M* in seawater when the area was clear-cut of the tube worms and other organisms.

The scanner system developed by Johnson, Beehler, and Sakamoto-Arnold (1986) has been used to measure the properties of the plumes coming from the vent systems. Their results for temperature, light attenuation, iron, and manganese are shown in Figure 10.39. They have used the measurements of Fe(II) and Mn(II) in the waters as a way of dating the plume. The Fe was rapidly removed from the system because of oxidation with oxygen, while the Mn(II) was stable in its reduced form. From the known rates of oxidation of Fe(II)

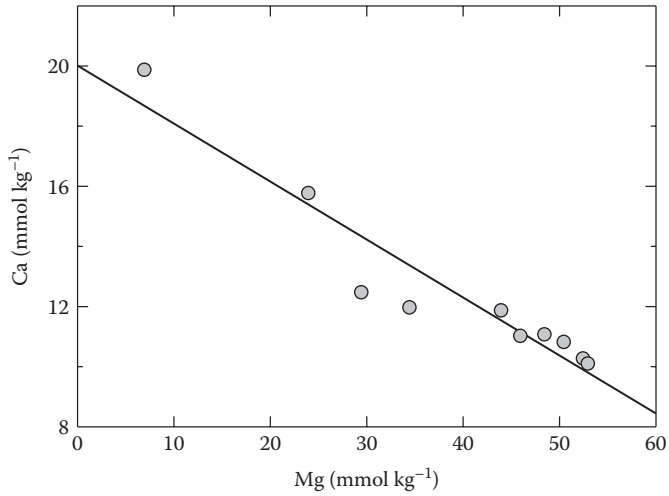

FIGURE 10.28
Calcium concentration as a function of magnesium in vent waters.

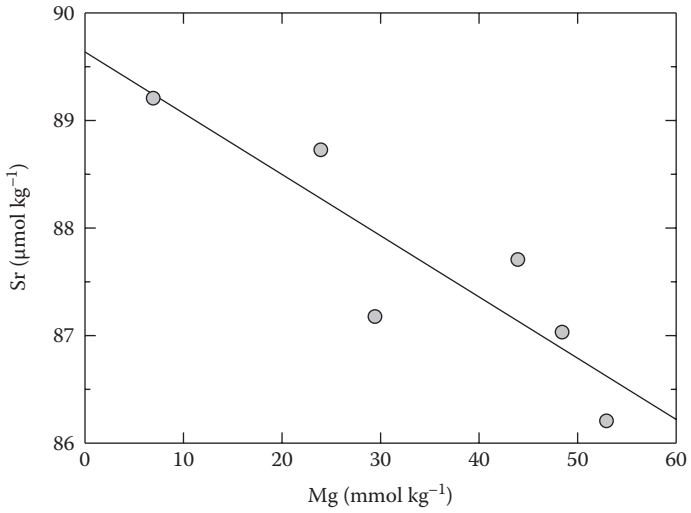

FIGURE 10.29
Strontium concentration as a function of magnesium in vent waters.

to Fe(III), Johnson, Beehler, and Sakamoto-Arnold determined the age of the plume waters at a specific distance from their source. Most of the Fe was lost by precipitation of Fe(III) within a few days. Studies by German et al. (1991) of the chemistry of hydrothermal vents have concentrated on the formation of particulate matter largely from the precipitation of Fe^{2+} from the vents. The formation of reactive iron oxides results in the scavenging of metals and nonmetals (phosphate) from seawater and removal to the sediments. By measuring the concentration of various elements on the particles formed from the oxidation of Fe(II), it is possible to study the uptake and removal of elements from seawater. The mixing lines for some metals as a function of particulate iron are shown in Figure 10.40 and

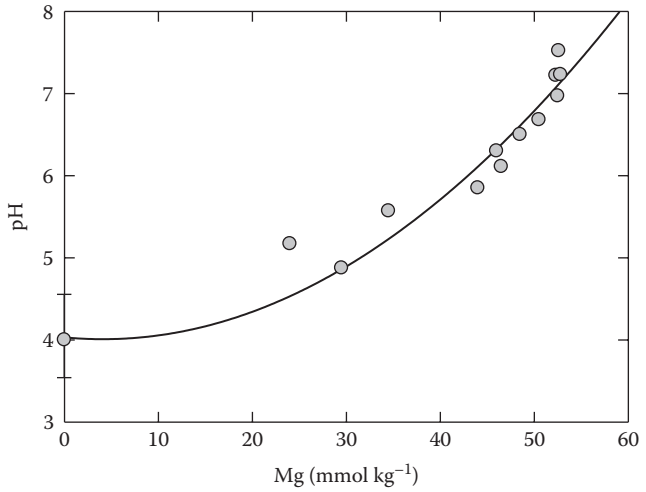

FIGURE 10.30
pH and total alkalinity as a function of magnesium in vent waters.

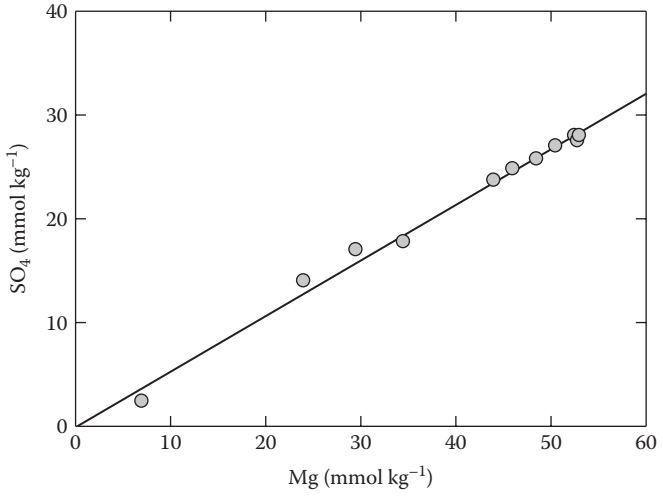

FIGURE 10.31
Sulfate concentration as a function of magnesium in vent waters.

Figure 10.41. The ratio of the concentration of an element in the particulate phase to that in seawater (Figure 10.42) can be used to examine metals scavenged by particulate iron at vent systems.

It was shown (Foustoukos and Seyfried, 2004) that low molecular weight hydrocarbons (methane, CH_4, ethane, C_2H_6, and propane (C_3H_8) may be generated in hydrothermal fluids. The process that results in the formation of these hydrocarbons is given by

$$CO_2(aq) + [2 + (m/2n)[H_2(aq) \rightarrow (1/n)\ C_nH_m + 2H_2O \qquad (10.62)$$

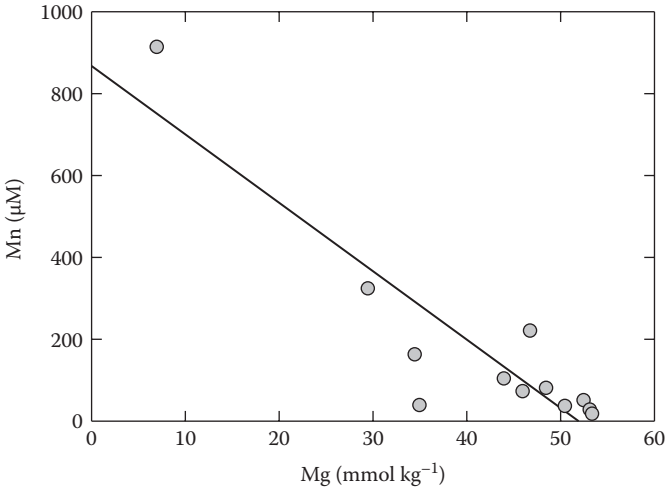

FIGURE 10.32
Manganese concentration as a function of magnesium in vent waters.

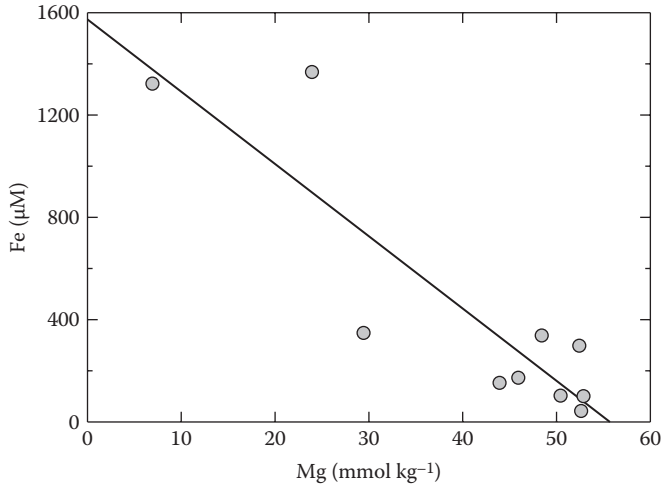

FIGURE 10.33
Iron concentration as a function of magnesium in vent waters.

Iron- and manganese-rich rocks with chromium are thought to catalyze the reactions that occur at high temperatures (390°C) and pressures (400 bars). If microbes can use these hydrocarbons as substrates, chemolithotrophic life may be possible in these systems on Earth and elsewhere. Further work is needed to demonstrate whether deep-sea microbes can utilize these hydrocarbons. Evidence has shown the inputs of dissolved cobalt, iron, and manganese from the South Atlantic Ocean (Figure 10.43) (Noble, 2012).

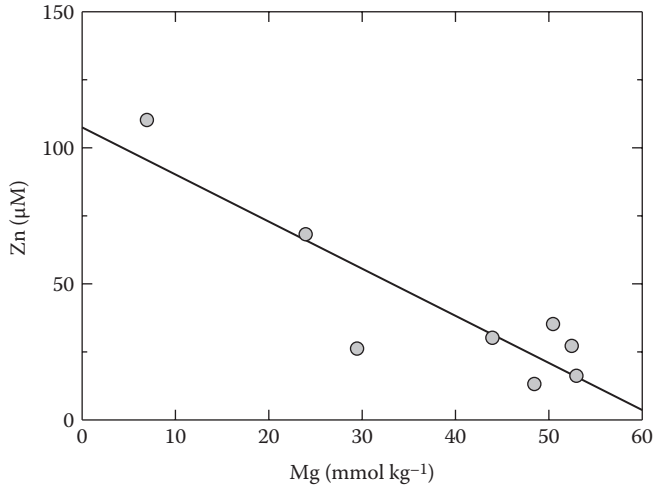

FIGURE 10.34
Zinc concentration as a function of magnesium in vent waters.

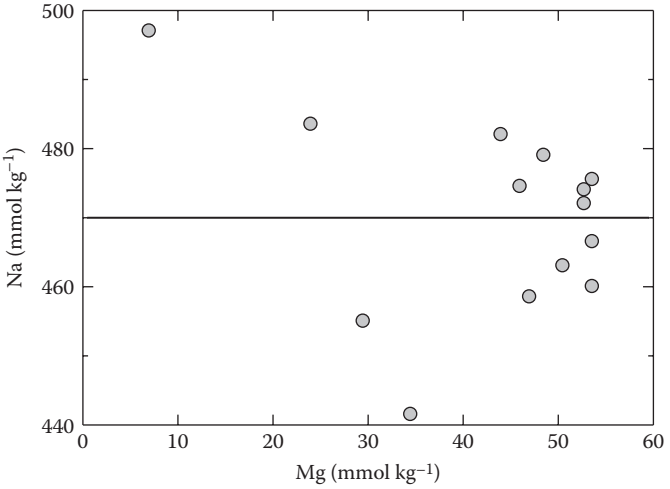

FIGURE 10.35
Sodium concentration as a function of magnesium in vent waters.

10.3 Anoxic Waters

Anoxic basins were first described in detail by Richards in 1965. He defined anoxia as a condition in which no dissolved oxygen is available. This condition can arise in natural waters when the consumption rate of oxygen exceeds the supply. The consumption is linked to the oxidation of organic matter by bacteria at a greater rate than the oxygen supply from the atmosphere. The supply of O_2 below the photic zone is dependent on diffusion and

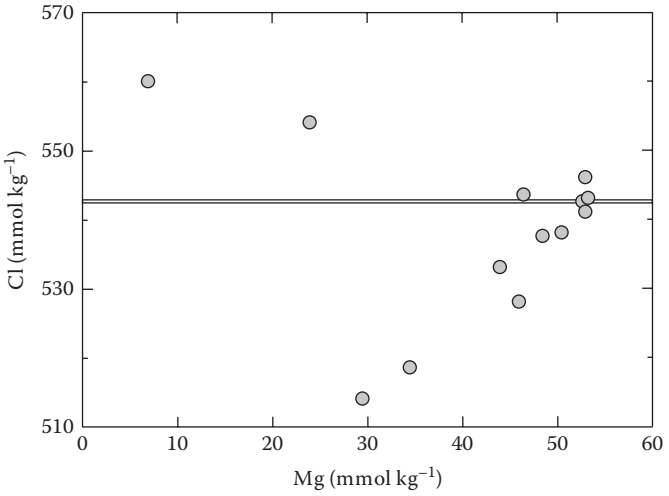

FIGURE 10.36
Chloride concentration as a function of magnesium in vent waters.

TABLE 10.6

Comparison of the Estimated Composition of the Galapagos and 21° N Vents and Seawater

	Galapagos	21° N	Seawater
Li (μmol kg^{-1})	1142–689	820	28
K (mmol kg^{-1})	18.8	25.0	10.1
Rb (μmol kg^{-1})	20.3–13.4	26.0	1.32
Mg (mmol kg^{-1})	0	0	52.7
Ca (mmol kg^{-1})	40.2–24.6	21.5	10.3
Sr (μmol kg^{-1})	87	90	87
Ba (μmol kg^{-1})	42.6–17.2	95–35	0.145
Mn (μmol kg^{-1})	1140–360	610	0.002
Fe (μmol kg^{-1})	+[a]	1800	–[a]
Si (mmol kg^{-1})	21.9	21.5	0.160
SO_4^{2-} (mmol kg^{-1})	0	0	28.6
H_2S (mmol kg^{-1})	+[a]	6.5	0

Source: From Edmond et al. 1982.
[a] +, nonconservative to subsurface mixing; –, seawater concentration not accurately known.

advection. Anoxia normally occurs in enclosed basins where physical barriers (sills) and density stratification limit the advection of O_2 to the deep waters. There are two types of anoxic basins. The most common occurs because of a strong halocline (salinity gradient), which is the result of a net outflow of low-salinity water from a positive estuary. The halocline prevents low-salinity oxic waters from mixing with the high-salinity deep waters. Examples of this type of basin are the Black Sea, the Baltic Sea, and many fjords such as the Framvaren in Norway. The second type of basin arises because of a strong thermocline that prevents the mixing of surface and deep waters. The Cariaco Trench off the coast of Venezuela is an example of this type of basin. It is a deep trench with a maximum depth of

TABLE 10.7

Comparison of Hydrothermal and River Fluxes of Elements into the Oceans[a]

	21° N	GSC[b]	River[c]
Li	$1.2 \rightarrow 1.9 \times 10^{11}$	$9.5 \rightarrow 16 \times 10^{10}$	1.4×10^{10}
Na	$-8.6 \rightarrow 1.9 \times 10^{12}$	+, –4	6.9×10^{12}
K	$1.9 \rightarrow 2.3 \times 10^{12}$	1.3×10^{12}	1.9×10^{12}
Rb	$3.7 \rightarrow 4.6 \times 10^{9}$	$1.7 \rightarrow 2.8 \times 10^{9}$	5×10^{6}
Be	$1.4 \rightarrow 5.3 \times 10^{6}$	$1.6 \rightarrow 5.3 \times 10^{6}$	3.3×10^{7}
Mg	-7.5×10^{12}	-7.7×10^{12}	5.3×10^{12}
Ca	$2.4 \rightarrow 15 \times 10^{11}$	$2.1 \rightarrow 4.3 \times 10^{12}$	1.2×10^{13}
Sr	$-3.1 \rightarrow +1.4 \times 10^{9}$	0	2.2×10^{10}
Ba	$1.1 \rightarrow 2.3 \times 10^{9}$	$2.5 \rightarrow 6.1 \times 10^{9}$	1.0×10^{10}
F	$-1.0 \rightarrow 2.3 \times 10^{9}$	$2.5 \rightarrow 6.1 \times 10^{9}$	1.0×10^{10}
Cl	$0 \rightarrow 1.2 \times 10^{13}$	$-31 \rightarrow 7.8 \times 10^{12}$	6.9×10^{12}
SiO_2	$2.2 \rightarrow 2.8 \times 10^{12}$	3.1×10^{12}	6.4×10^{12}
Al	$5.7 \rightarrow 7.4 \times 10^{8}$	n.a.	6.0×10^{10}
SO_4	-4.0×10^{12}	-3.8×10^{12}	3.7×10^{12}
H_2S	$9.4 \rightarrow 12 \times 10^{11}$	+	
S	$-2.8 \rightarrow 3.1 \times 10^{11}$	–	
Mn	$1.0 \rightarrow 1.4 \times 10^{11}$	$5.1 \rightarrow 16 \times 10^{10}$	4.9×10^{9}
Fe	$1.1 \rightarrow 3.5 \times 10^{11}$	+	2.3×10^{10}
Co	$3.1 \rightarrow 32 \times 10^{6}$	n.a.	1.1×10^{8}
Cu	$0 \rightarrow 6.3 \times 10^{9}$	–	5.0×10^{9}
Zn	$5.7 \rightarrow 15 \times 10^{9}$	n.a.	1.4×10^{10}
Ag	$0 \rightarrow 5.4 \times 10^{6}$	n.a	8.8×10^{7}
Cd	$2.3 \rightarrow 26 \times 10^{6}$	–	
Pb	$2.6 \rightarrow 5.1 \times 10^{7}$	n.a.	1.5×10^{8}
As	$0 \rightarrow 6.5 \times 10^{7}$	n.a.	7.2×10^{8}
Se	$0 \rightarrow 1.0 \times 10^{7}$	n.a.	7.9×10^{7}

Note: +, gain; –, loss; n.a., not analyzed.

[a] All numbers are in mol yr^{-1}.

[b] GSC data are from Edmond et al. (1979a, 1979b).

[c] River concentrations and fluxes are from either Edmond et al. (1979a, 1979b) or Broecker and Peng (1982).

1400 m. The water is isohaline and isothermal from 600 m to the bottom. It is permanently anoxic below a depth of 350 m. The appearance of H_2S above the thermocline is caused by mixing. Both basins have a physical obstacle that prevents horizontal mixing of various water masses. In a fjord-type basin, a shallow sill prevents the salty seawater rich in O_2 from entering the basin and sinking to the bottom.

In recent years, estuarine systems with deep basins like the Baltic and Chesapeake have experienced periodic anoxic behavior. The Mississippi plume also becomes nearly anoxic at certain times of the year. This has been attributed to higher productivity in the surface waters caused by increases of nutrients used as fertilizers and perhaps by acid rain. Some examples of anoxic basins are given in Table 10.8.

The loss of oxygen in a basin or sediment pore waters causes a series of reactions to occur in a given sequence that is shown in Figure 10.44. Biogeochemical cycles of C, N, P, and S are linked because they are all involved in the photosynthesis and respiration

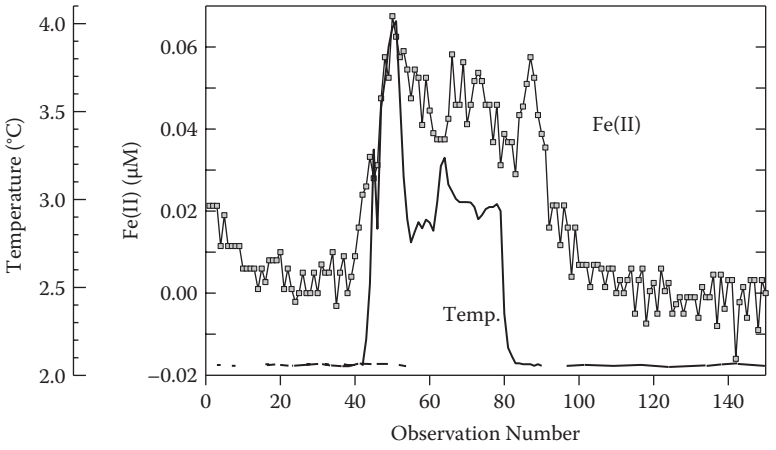

FIGURE 10.37
Temperature and Fe(II) over a vent system.

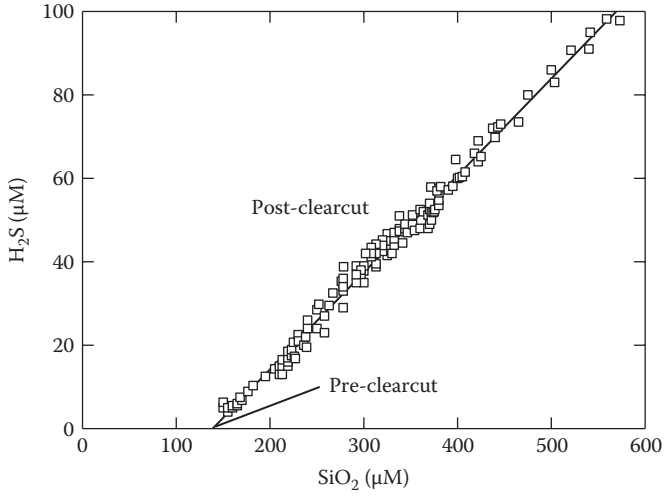

FIGURE 10.38
H_2S concentration as a function of silicate.

(decay) of plants in a nearly fixed stoichiometric ratio. The decomposition of organic matter and the associated release of nutrients proceed by aerobic respiration in the presence of oxygen. Denitrification occurs when oxygen is depleted, by sulfate reduction when nitrate and nitrite are depleted, and by fermentation when sulfate is depleted. Richards (1965) developed stoichiometric models for these processes using a C:N:P ratio of 106:16:1, the Redfield ratios for average plankton material for the world ocean.

In an aerobic environment, O_2 is the electron acceptor; aerobic respiration occurs according to

$$(CH_2O)_{106}(NH_3)_{16}H_3PO_4 + 138O_2 \rightarrow 106CO_2 + 122H_2O + 16HNO_3 + H_3PO_4 \quad (10.63)$$

After the oxygen is depleted, denitrification occurs, with NO_3^- being the electron acceptor. The denitrification can be described by

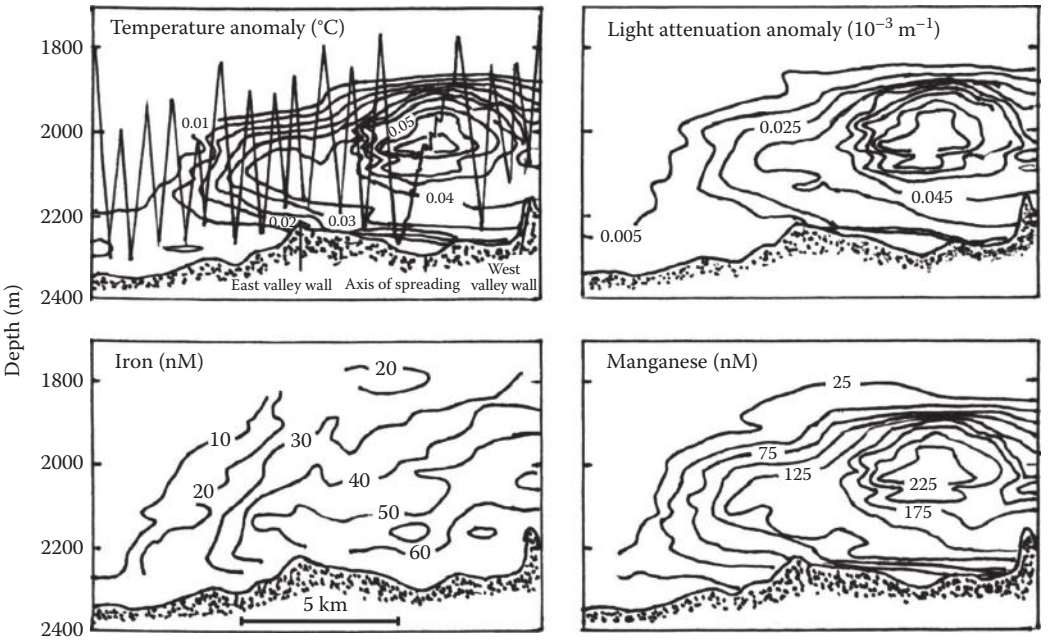

FIGURE 10.39
Temperature anomaly, light attenuation, Fe(II), and Mn(II) in a hydrothermal plume.

$$(CH_2O)_{106}(NH_3)_{16}H_3PO_4 + 84.8HNO_3 \rightarrow 106CO_2 + 42.4N_2 + 148.4H_2O + 16NH_3 + H_3PO_4 \quad (10.64)$$

and

$$(CH_2O)_{106}(NH_3)_{16}H_3PO_4 + 94.4HNO_3 \rightarrow 106CO_2 + 55.2N_2 + 177.2H_2O + H_3PO_4 \quad (10.65)$$

MnO_2 reduction occurs next, with Mn^{4+} being the electron acceptor, followed by NO_3^- reduction to NH_4^+ and reduction of Fe^{3+} to Fe^{2+}. Since the concentrations of these electron acceptors are not very high, these processes do not dominate the oxidation of organic material. The next electron acceptor is SO_4^{2-}, and sulfate reduction occurs according to

$$(CH2O)_{106}(NH_3)_{16}\ H_3PO_4 + 53SO_4^{2-} \rightarrow 53CO_2 + 53HCO_3^- + 53HS^-$$
$$+ 16NH_3 + 53H_2O + H_3PO_4 \quad (10.66)$$

No oxidation of NH_3 occurs, and the ratio of changes in H_2S to NH_3 is 3.3.

The decomposition can also occur with CO_2 as the electron acceptor and the resultant formation of CH_4:

$$(CH_2O)_{106}(NH_3)_{16}\ H_3PO_4 \rightarrow 53CO_2 + 53CH_4 + 16NH_3 + H_3PO_4 \quad (10.67)$$

These equations can be used to predict the steady-state concentrations of C, N, P, and S in anoxic systems. There are some deficiencies in this approach because it does not account for mixing or the rates at which the system is driven to a steady state. According to the model, carbon, nitrogen, and phosphate are released in the atomic ratio of 106:16:1. There

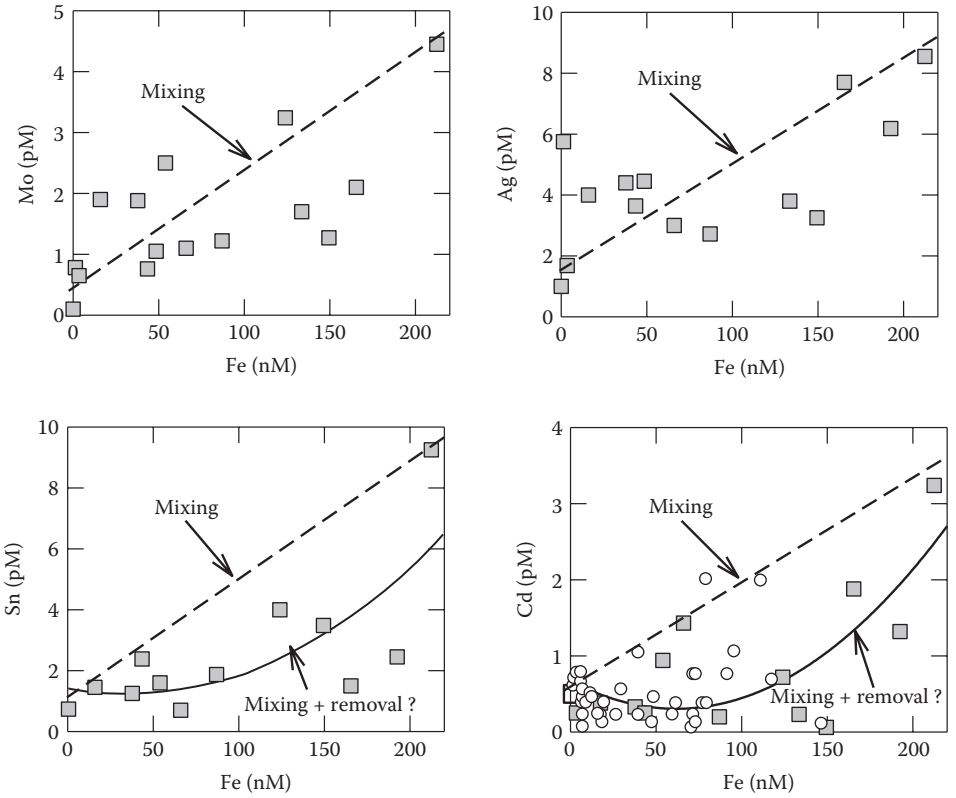

FIGURE 10.40
Concentrations of Mo, Ag, Sn, and Cd in vent particles as a function of Fe.

are a number of processes that can alter this ratio. Under aerobic conditions, the regenerated phosphate can be absorbed on iron and manganese (hydr)oxides. Denitrification, occurring at oxic/anoxic interfaces, can alter the ratio of combined nitrogen (nitrate + nitrite + ammonium) to carbon dioxide and phosphate by producing N_2O and N_2. It is also possible that the organic matter has a C:N:P ratio different from 106:16:1 when lipids rather than carbohydrates are formed or degraded. As discussed in Chapter 9, phytoplankton can also incorporate C:N:P in ratios different from 106:16:1 depending on the availability of these elements.

The decomposition of organic matter in anoxic basins, based on a theoretical organic molecule with the composition $(CH_2O)_{106}(NH_3)_{16}(H_3PO_4)$ given by Equation 10.65, can be used to examine the stoichiometry in these basins (keeping in mind the problems described). According to this model, during sulfate reduction, sulfide, ammonia, phosphate, and total CO_2 should accumulate in a ratio of 53 moles of sulfide to 16 moles of ammonia, to 1 mole of phosphate, and to 106 moles of total CO_2 in the anoxic water column. The changes in waters below the oxic–anoxic interface should be in the ratios

$$\Delta NH_3/\Delta H_2S = 16/53 = 0.33 \Delta PO_4/\Delta H_2S = 1/53 = 0.019$$

$$\Delta TCO_2/\Delta H_2S = 106/53 = 2.0$$

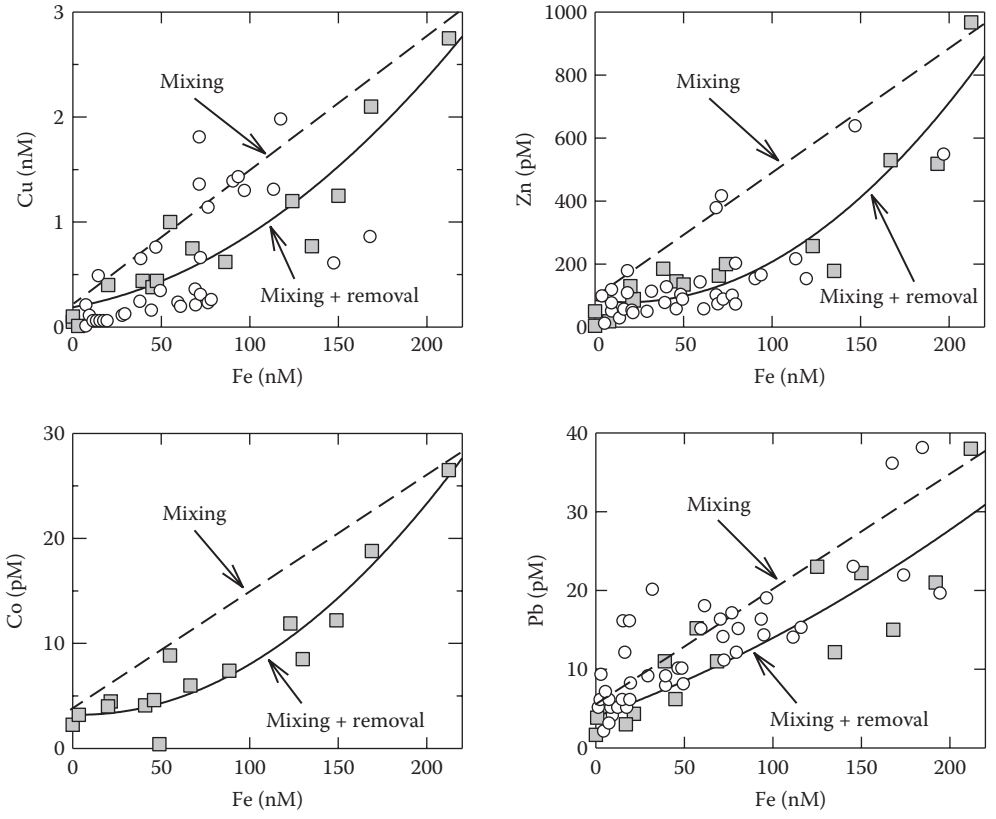

FIGURE 10.41
Concentrations of Cu, Zn, Co, and Pb in vent particles as a function of Fe.

The changes in total alkalinity (TA) relative to H_2S are given by

$$\Delta TA/\Delta H_2S = (106 + 16 - 2)/53 = 2.3$$

The changes between TA and TCO_2 (total carbon dioxide) are given by

$$\Delta TA/\Delta TCO_2 = (106 + 16 - 2)/106 = 1.13$$

These relationships allow one to examine the chemistry of anoxic basins. In the next sections, the distribution of various chemicals is examined for some anoxic basins.

10.3.1 The Black Sea

The Black Sea is the largest and most studied anoxic basin (Figure 10.45). The present anoxic conditions began about 1500 to 2000 years after the influx of saline Mediterranean seawater into the basin. It is an estuarine basin with an area of 413,500 km^2, where precipitation and river runoff exceed evaporation. There is a net outflow (12,600 $m^3\ s^{-1}$) of low-salinity water compared to the inflow (6100 $m^3\ s^{-1}$) from the Mediterranean. This

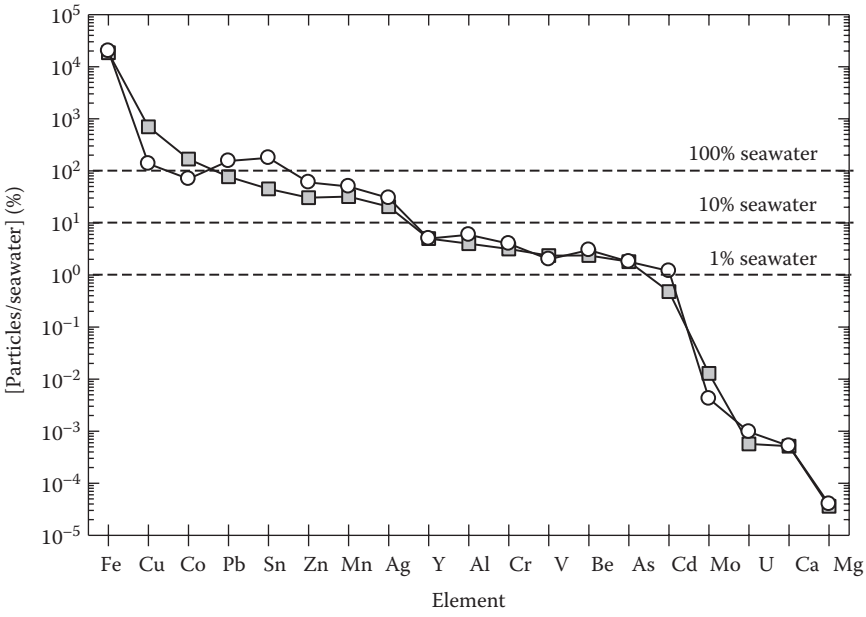

FIGURE 10.42
Ratio of the concentration of elements in vent particles and seawater.

results in a permanent halocline as in the Baltic Sea with a thickness of 100 to 240 m. The anoxic waters extend to a maximum depth of 2234 m. The oxygenated water from the Mediterranean Sea is unable to displace the anoxic bottom water. The low-salinity surface waters leaving the basin are also unable to penetrate the more saline anoxic deep waters.

The depth of the transition zone between the oxic and anoxic waters varies from 100 to 250 m. Past studies showed an upper boundary of 150 m with a 50-m layer that contained both O_2 and H_2S. More recent studies in the summer of 1988 showed that the interface had moved up to 100 m and showed a depth zone of 50 m without O_2 and H_2S (see Figure 10.46). This change in the interface was related to changes in the salinity and temperature of the waters. When the concentrations of oxygen and hydrogen sulfide are plotted versus the density, the interface does not change significantly with time.

A number of workers have examined the balance of waters in the Black Sea. The annual estimates made by Fonselius are given in Figure 10.47. Complete renewal of the deep waters has been estimated to take 2500 years. Carbon measurements yield shorter lifetimes of about 800 years, presumably due to lateral mixing of salty waters from the Mediterranean through the Bosporus. A large portion of the exchange between the surface and deep waters occurs along the edge of the Black Sea.

The 1988 expedition to the Black Sea resulted in numerous measurements of a number of chemical parameters (Friederich et al., 1988). Some of the measurements were made to depths of 400 m with a pump system in real time. The resulting profiles of temperature, salinity, and sigma-t for a central station are shown in Figure 10.48. The salinities increase from 18 in surface waters to 22 in the deep waters, while the temperature decreases from 15°C in surface waters to 19.5°C in deep waters. The increase in density in the deep waters is largely related to the increase in salinity. The nutrients are shown in Figure 10.49 for a station in the center of the Black Sea. The phosphate increase in the surface waters is due

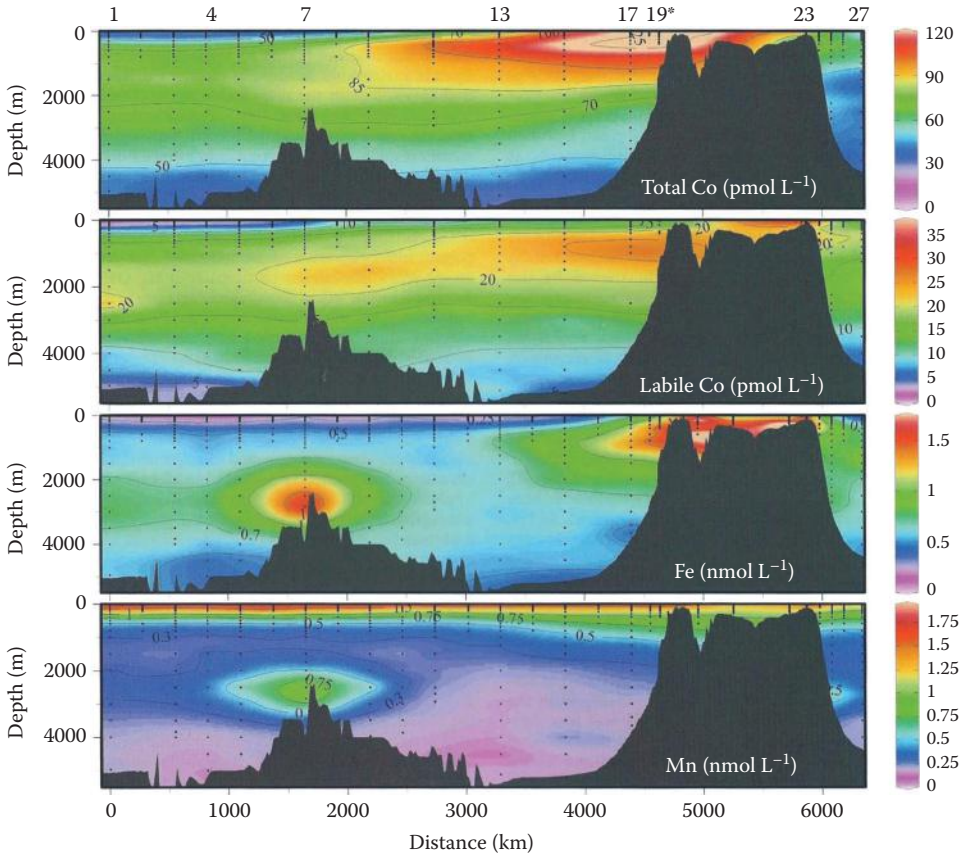

FIGURE 10.43
Basin-scale inputs of Co, Fe, and Mn from hydrothermal vents.

TABLE 10.8

Anoxic Basins

Name	Location	Bottom (m)	Sill (m)	Maximum H_2S (μ*M*)
Goteland Deep	Baltic Sea	249	60	20
Cariaco Trench	Caribbean Sea	1390	150	160
Lake Nitinat	British Columbia	250	4	250
Saanich Inlet	British Columbia	236	65	250
Black Sea	Europe	2243	40	350
Framvaren	Norway	350	2	6000

to the oxidation of organic carbon with O_2. At the interface, the phosphate levels decrease dramatically and increase below the interface in the anoxic waters. This is due to the adsorption of PO_4^{3-} to MnO_2(s) and $Fe(OH)_3$(s) in the oxic waters and release in the anoxic waters caused by the reactions of the oxides with H_2S and formation of reduced Fe(II) and Mn(II). These adsorption and dissolution processes occur at the interface of most anoxic basins. The nitrate levels increase in the oxic waters because of the oxidation of NH_3 with

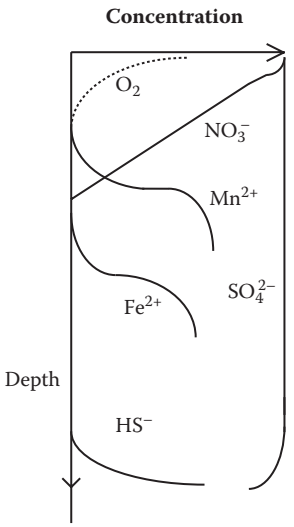

Processes	Electon Acceptor	Eh Range (mv)
Aerobic Respiration	O_2	200 to 800
Denitrification	NO_3^-	50 to 750
Mn^{2+} Reduction	Mn^{4+}	150 to 600
Fe^{2+} Reduction	Fe^{3+}	−500 to 50
Sulfate Reduction	SO_4^{2-}	−650 to −200

FIGURE 10.44
Schematic representation of chemical profiles in a stratified water column.

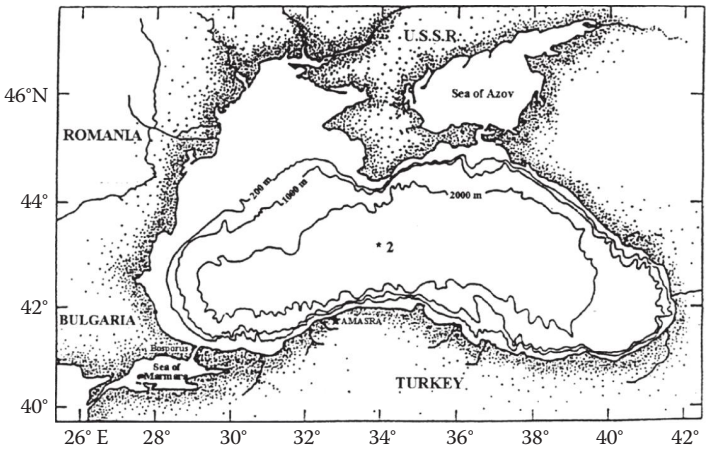

FIGURE 10.45
Sketch of the 1988 Black Sea expedition.

O_2. In the anoxic waters, the nitrate is reduced to NH_3 by bacteria using nitrate to oxidize organic carbon. The nitrite levels go through a maximum in the oxic waters as part of the oxidation of $NH_3 \rightarrow NO_2^- \rightarrow NO_3^-$, and the nitrite is formed again because of the use of NO_3^- as an oxidant ($NO_3^- \rightarrow NO_2^- \rightarrow NH_3$) in anoxic waters.

Measurements of trace metals at another station in the Black Sea have been made by Haraldsson and Westerlund (1988). Their results for the Black Sea are shown in Figure 10.50 and Figure 10.50. The metals Mn(II), Co(II), and Fe(II) go through a maximum below the interface because of the reduction of Mn(IV), Co(III), and Fe(III). The reduction of MnO_2 to Mn^{2+} and $Fe(OH)_3$ to Fe^{2+} are chemical reactions with H_2S. The reduced metals diffuse back to oxic waters, where Mn^{2+} is oxidized to MnO_2 assisted by bacteria, and Fe^{2+} is chemically oxidized to $Fe(OH)_3$ with O_2. The resulting cycle of oxidation and reduction

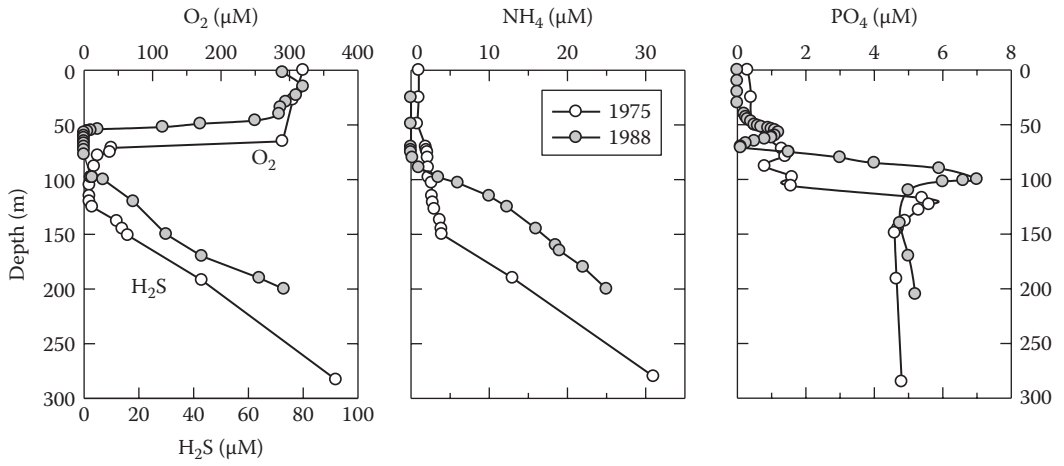

FIGURE 10.46
The changes in the oxic–anoxic interface in the Black Sea. Open circles are older studies; closed circles are more recent studies.

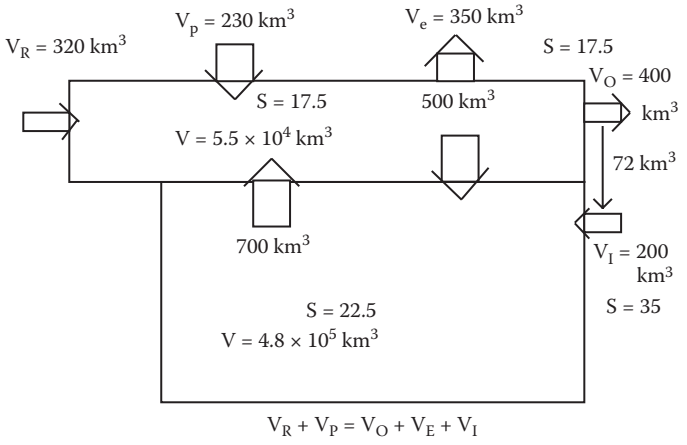

FIGURE 10.47
Box model of the Black Sea.

at the interface leads to the maximum of the reduced Fe(II) and Mn(II). Cu(II), Cd(II), and Pb(II) and other metals are adsorbed in the oxic water to $Fe(OH)_3$ and MnO_2 solids and increased below the interface when the solids react with H_2S. The concentrations of the metals decrease in the deeper waters because of the low solubility of the sulfides of these metals. Ni(II) shows little change across the interface because it does not appear to be adsorbed on $Fe(OH)_3$ and MnO_2, and the concentrations are below the saturation levels in sulfidic waters.

Schijf et al. (1991) measured the rare earths in the Black Sea. Their results for La^{3+} are shown in Figure 10.52. The concentrations of the rare earths go through a minimum at a depth of 100 m (σ_θ = 16.1) in the suboxic zone (no O_2 or H_2S) and increase to a maximum at about 400 m. The Ce concentrations show redox changes, unlike the other rare earths (Figure 10.52). All the rare earths are involved in the redox cycling that occurs across the

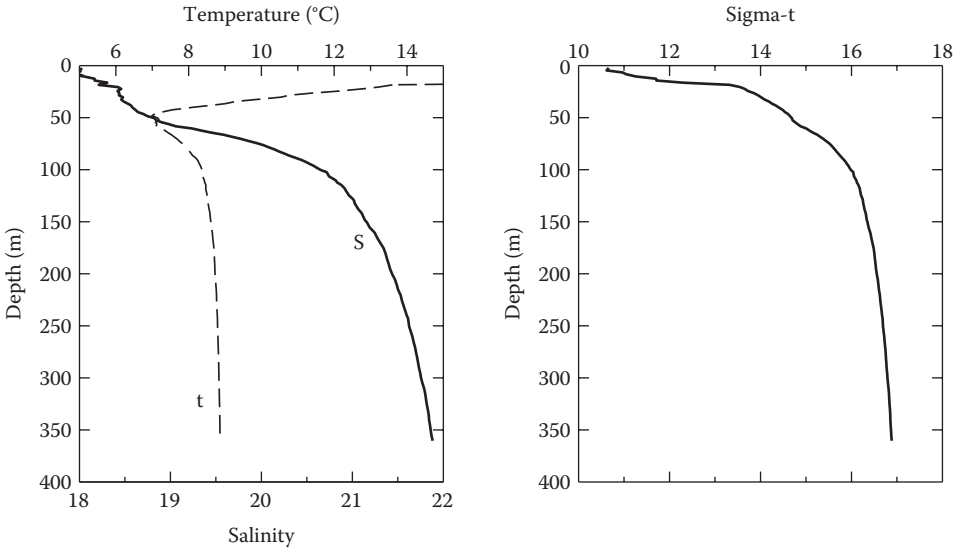

FIGURE 10.48
Profiles of temperature, salinity, and sigma-t in the Black Sea.

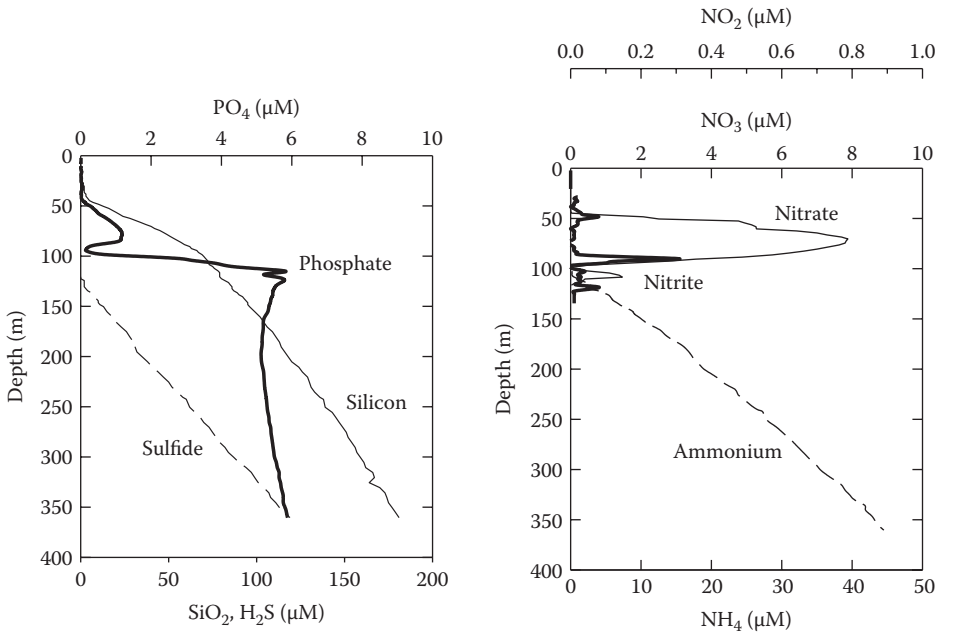

FIGURE 10.49
Profiles of nitrate, nitrite, ammonia, silicate, phosphate, and hydrogen sulfide in the Black Sea.

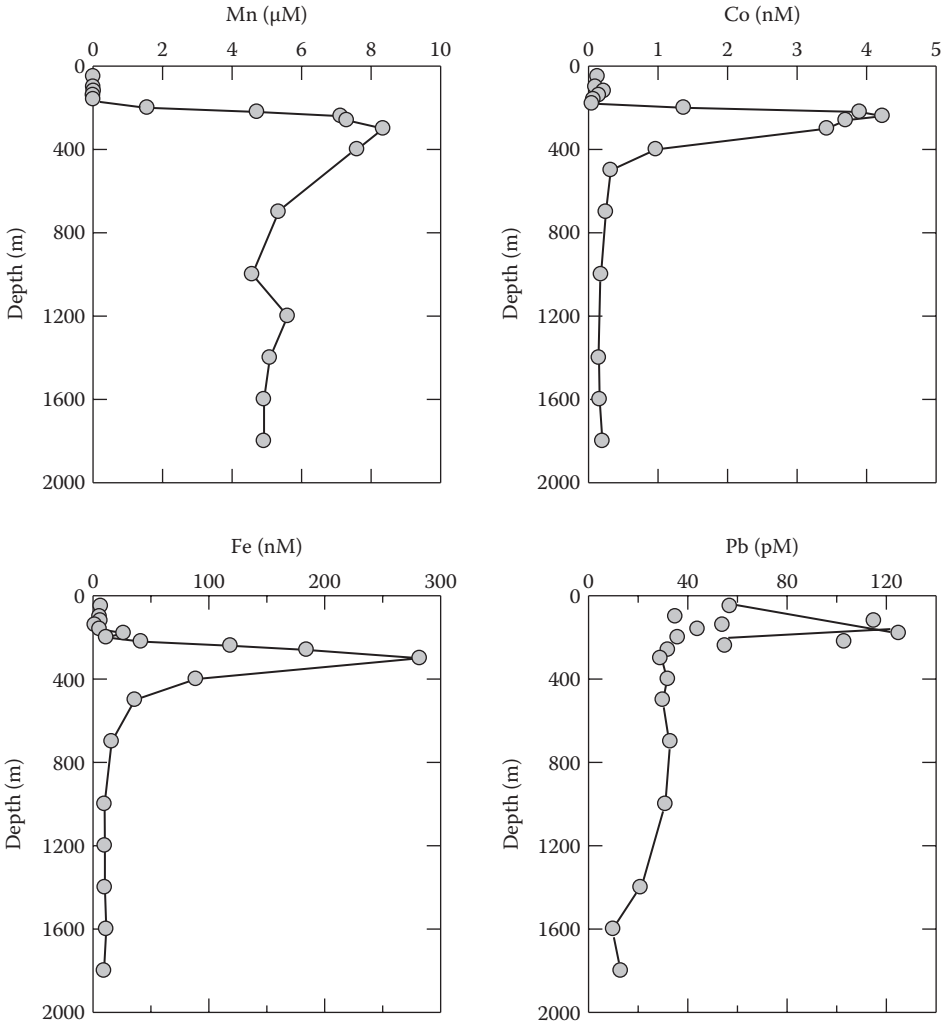

FIGURE 10.50
Profiles of Mn, Co, Fe, and Pb in the Black Sea.

suboxic–anoxic interface (where bacteria are abundant). Most metals behave in a similar manner in other anoxic basins discussed further in this chapter.

More recent studies of the Black Sea were carried out in 2001 (Hiscock and Millero, 2006). Unlike our earlier study in 1988 (Millero, 1991a), the cruise concentrated on the eastern area of the Black Sea near the Sea of Marmara. On this cruise, we made measurements of the TA and nutrients. The nutrient measurements allowed us to examine how they affected the TA and gave us a better understanding of the CO_2 system in the Black Sea. Since a pumping system was used, near-continuous measurements were made across the O_2–H_2S interface. The results for H_2S, NH_4, PO_4, $Si(OH)_4$, NO_3, and TA are shown in Figure 10.53. The results for CA, TCO_2, and Ω for calcite and aragonite are shown in Figure 10.54. The concentrations of NO_3 and PO_4 increase in the oxygenated waters due to the bacterial oxidation of plant material. In the anoxic waters, the oxidation with SO_4 converts the NO_3

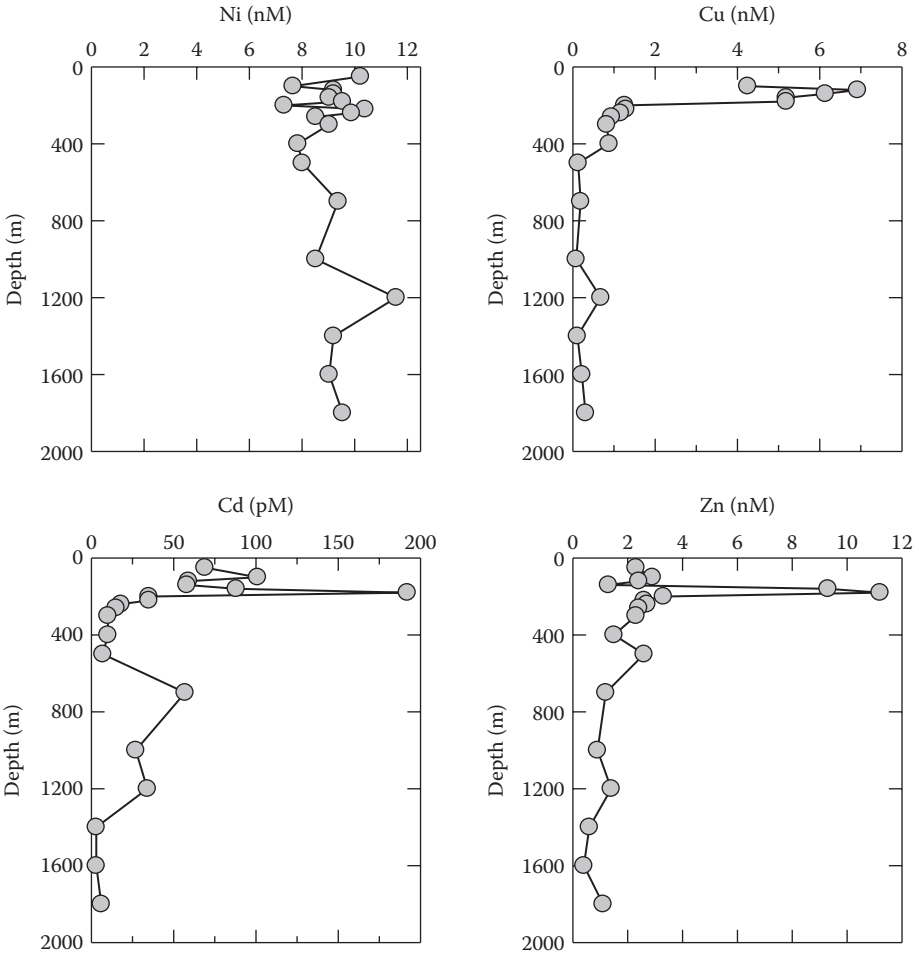

FIGURE 10.51
Profiles of Ni, Cu, Cd, and Zn in the Black Sea.

to NH_4, which increases in the deeper anoxic waters. The PO_4 is adsorbed to FeO_2 and MnO_2 at the interface. In the anoxic waters, FeO_2 and MnO_2 are reduced to Fe^{2+} and Mn^{2+} by the H_2S. This releases the adsorbed PO_4 to the anoxic waters. The diffusion of Fe^{2+} and Mn^{2+} to the oxygenated waters results in the formation of FeO_2 and MnO_2, and the cycle is repeated. The FeO_2 is formed by reaction of O_2 with Fe^{2+}; while the Mn^{2+} is converted to MnO_2 by Mn-oxidizing bacteria.

10.3.2 Cariaco Trench

The Cariaco Trench (Figure 10.55) is located in the Caribbean Sea off the continental shelf north of Venezuela. It is about 200 km long and 50 km wide with a maximum depth of about 1400 m. The basin is separated from the rest of the Caribbean Sea by a 146-m sill (Richards, 1965). The surface waters of the trench can exchange freely with the offshore water. The deep part of the basin is divided by a saddle at 900 m into two subbasins, the

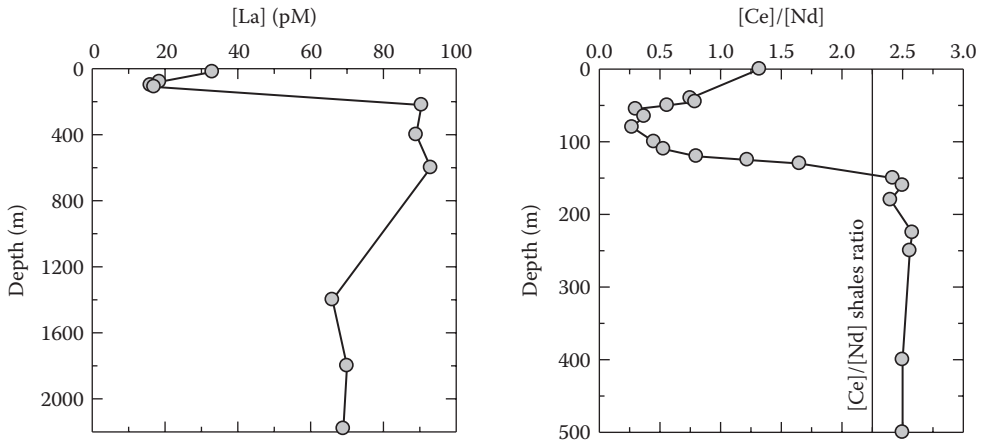

FIGURE 10.52
Profiles of La^{3+} and the ratio of Ce/Nd in the Black Sea.

eastern basin and the western basin. The vertical mixing below the mixed layer in the Cariaco Trench is prevented by the presence of a strong pycnocline. The salinity decreases with depth, and the stability of the basin water is caused by the temperature gradient. Coastal upwelling causes the high productivity in the surface waters and contributes the organic matter to the deep waters of the Cariaco Trench. Because the horizontal and vertical exchange is limited, the dissolved oxygen used to oxidize the organic matter is not rapidly replenished, and the deep waters have become anoxic. The sedimentary record suggests that anoxic conditions have prevailed in the deep waters for the past 1100 years, probably punctuated by deep-water renewal (Richards, 1965).

The Cariaco Trench has been widely used as a natural laboratory for the study of anaerobic processes since its deep waters were found to be anoxic in 1954. From the oceanographic data accumulated over three decades to the 1990s, it became increasingly clear that the anoxic portion of the Cariaco Trench is not in steady state, and that the values of a number of properties have been changing systematically with time (Scranton et al., 1987). Although uncertainty exists about the accuracy of each data set, increases in temperature and the concentration of sulfide have been reported by several workers (Richards, 1965; Bacon et al., 1980).

Zhang and Millero (1993a) measured a number of chemical parameters in the Cariaco Trench. These results have been used to examine its temporal changes in the hydrography and chemistry. Water samples were collected at two stations (see Figure 10.55). Temperature and salinity data obtained for both the eastern and western basins of the Cariaco Trench are presented in Figure 10.56. The maximum temperature occurs at the surface and decreases smoothly with depth, approaching a nearly constant value of about 17.2°C below 600 m. The temperature below 200 m shows no significant differences between the two basins. The maximum salinities occurred at 60 m in both basins, 36.86 in the western basin and 36.90 in the eastern basin. These maxima disappeared during the dry season (January to May), probably because of mixing brought about by the stronger winds and lower air temperatures typical of that season. Below the maxima, the salinities decrease smoothly with depth and become almost constant at about 36.21 below 500 m in both basins. The changes in temperature between the surface and deep waters result in the density gradient that separates the oxic and anoxic waters.

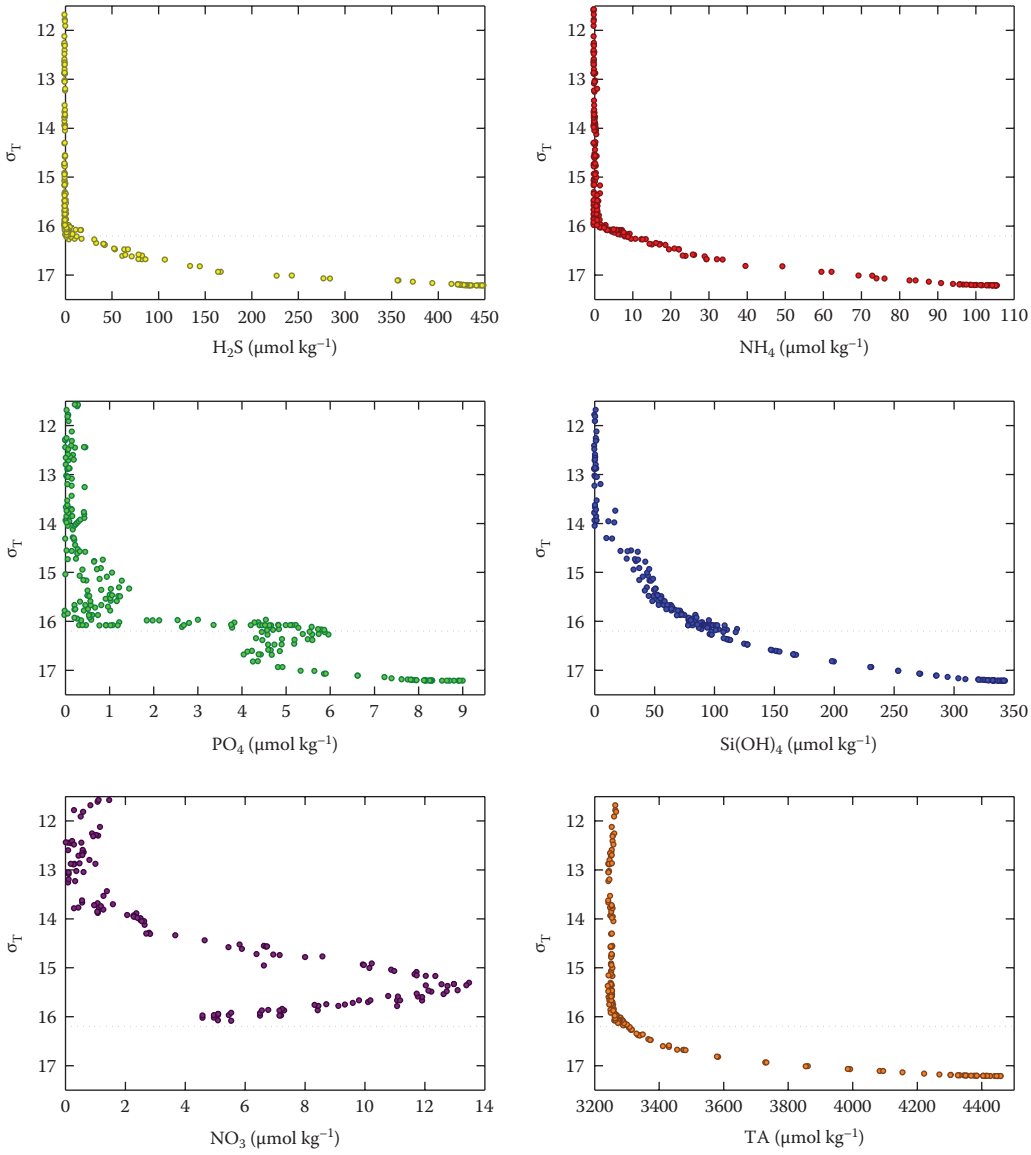

FIGURE 10.53
Profiles of H_2S, NH_4, PO_4, $Si(OH)_4$, NO_3, and TA across the O_2–H_2S interface in the Black Sea.

Profiles of oxygen and hydrogen sulfide are shown in Figure 10.57 for the two basins. The maximum oxygen occurred at the surface in both basins (211 μ*M* in the western basin and 208 μ*M* in the eastern basin). The oxygen concentrations decreased sharply with depth and became undetectable at 330 m, where hydrogen sulfide appeared in both basins. The concentrations of hydrogen sulfide increased rapidly below the interface to maximum values of 58 μ*M* in the eastern basin and 55 μ*M* in the western basin at 1300 m.

The depth of the oxic–anoxic interface in the Cariaco Trench has fluctuated between 250 to 375 m since the first expedition in 1956 (Table 10.9). The depth of the interface is controlled by changes in the density or the flux of organic matter, which is produced by

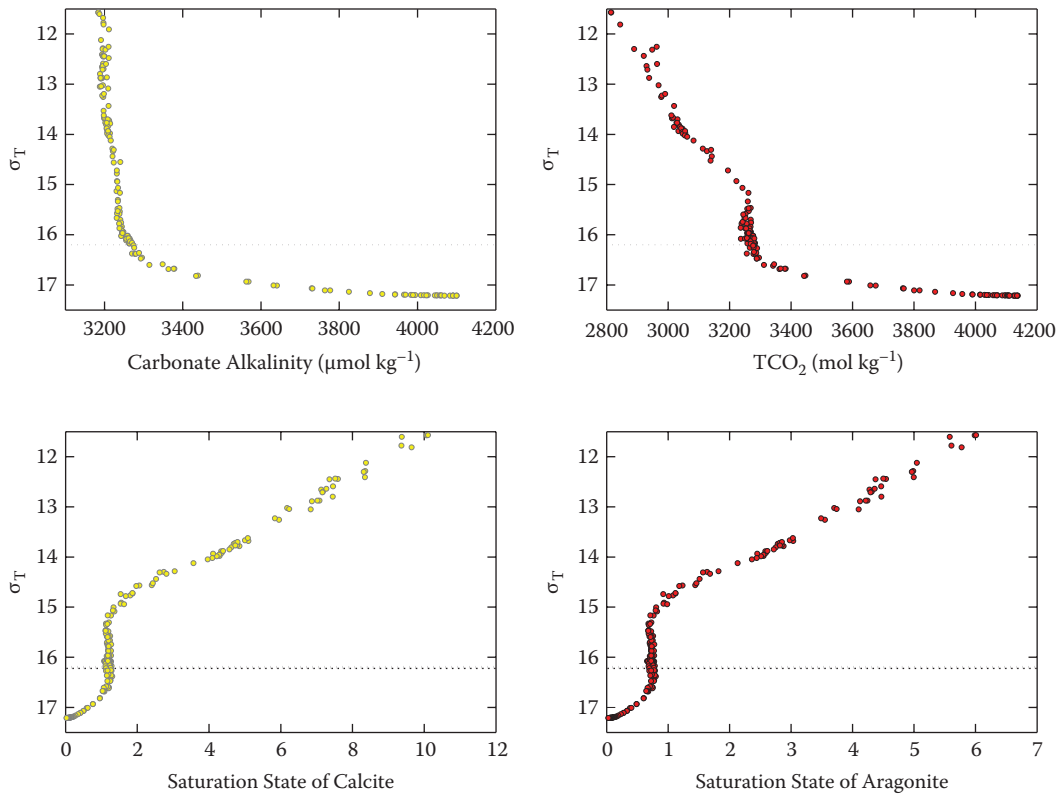

FIGURE 10.54
Profiles of the carbonate alkalinity, total CO_2, and the saturation state of calcite and aragonite across the O_2–H_2S interface in the Black Sea.

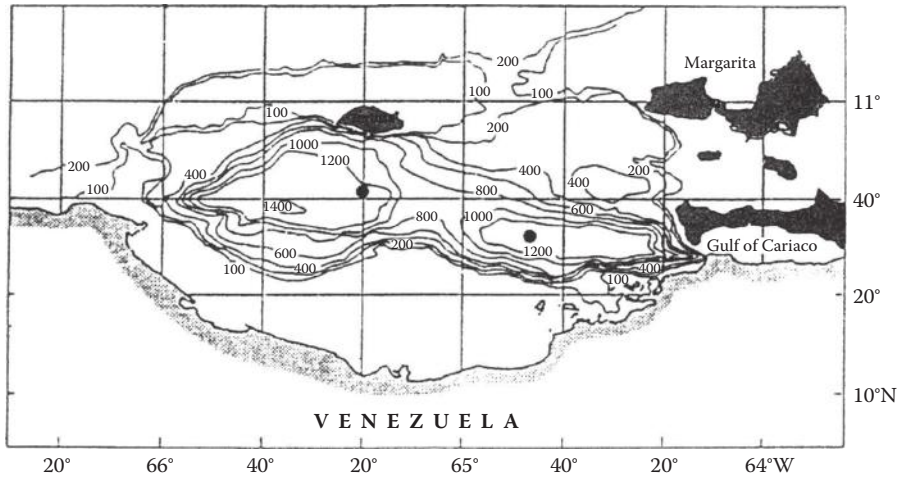

FIGURE 10.55
Sketch of the Cariaco Trench in the Caribbean Sea.

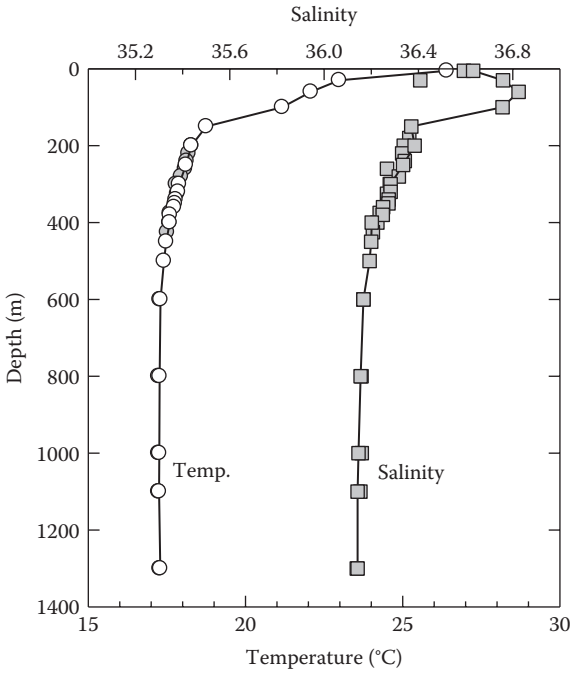

FIGURE 10.56
Salinity and temperature in the eastern (closed symbols) and western (open symbols) basins of the Cariaco Trench.

photosynthesis in the surface water and sinks into the deep-water column. A shallower oxic–anoxic interface is found during the upwelling season because of the high productivity in the surface water.

The concentrations of ammonia, phosphate, and silicate in the eastern basin are shown in Figure 10.58. In surface waters, about 1 μ*M* of ammonia was present in the euphotic zone at 30 m and was undetectable below 60 m. The ammonia increases rapidly below the oxic–anoxic interface to 20.2 μ*M* at 1300 m. The concentrations of phosphate in the surface waters are below 0.4 μ*M*, increase rapidly with depth to 2.3 μ*M* at the oxic–anoxic interface, and reach a value of 3.7 μ*M* at 1300 m. The concentrations of silicate in the surface waters are less than 2 μ*M*, increase rapidly with depth to about 42 μ*M* at the oxic–anoxic interface, and reach values of 86 μ*M* at 1300 m. The sampling across the interface was not close enough to see the detailed changes in NO_3^- and PO_4^{3-} as seen in the Black Sea.

The profiles of sulfite and thiosulfate are presented in Figure 10.59. The levels of sulfite and thiosulfate were undetectable in the oxic waters but were found in micromolar levels in the deep waters (1.8 μ*M* at about 600 m for sulfite and 1.0 μ*M* for thiosulfate). The sulfite and thiosulfate may be caused by the oxidation of H_2S from oxygenated waters that periodically sink below the oxic–anoxic interface. The tritium measurements made by Goto Ostlund (University of Miami, personal communication) on waters collected at the same time support the idea that the deep waters had been renewed with detectable levels of tritium found in the bottom waters. The work of Holmen and Rooth (1991) supports the episodic injection of water into the mid-depth of the waters in the trench. The thiosulfate increases gradually as one approaches the bottom and shows no maximum near 600 m. The higher values in the deep waters suggest a sediment source for the thiosulfate. A

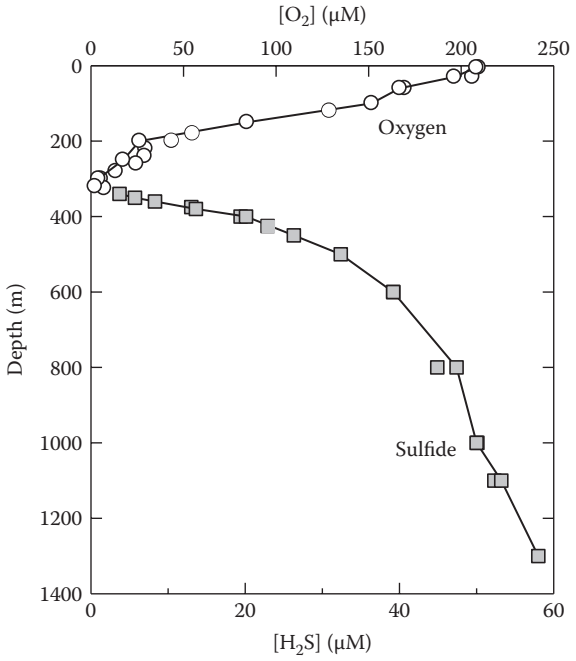

FIGURE 10.57
Profiles of oxygen and hydrogen sulfide in the eastern (closed symbols) and western (open symbols) basins of the Cariaco Trench.

TABLE 10.9

Depth of the Oxic–Anoxic Interface in the Cariaco Trench

Date	Depth (m)	$[H_2S]$, μ*M*	Author[a]
1955	375	30	Richards and Vacacaro
1957	340	24	Richards and Benson
1958	320	22	Richards
1965	300	26	Richards
1968	297	28	Fanning and Pilson
1970	300	30	Richards
1971	270	32	Spencer and Brewer
1973	250	35	Bacon et al.
1982	300	47	Hastings and Emerson
1986	270	63–71	Casso et al.
1990	330	58	Zhang and Millero

[a] References to earlier work were given by Zhang, J.-Z., and Millero, F.J., *Deep Sea Res.*, 40, 1023, 1993.

concentration of 178 μ*M* thiosulfate was found in the pore waters of the sediments in the Cariaco Trench, but this may be the result of oxidation of the sediments during collection. The formation of thiosulfate in the sediments could result from the reaction of MnO_2 and FeOOH minerals with H_2S or possibly from the reduction of sulfate.

The pH measurements made during the cruise are shown in Figure 10.60. The maximum value of pH (8.26 to 8.30) occurred between 5 and 30 m depth in both basins. The pH

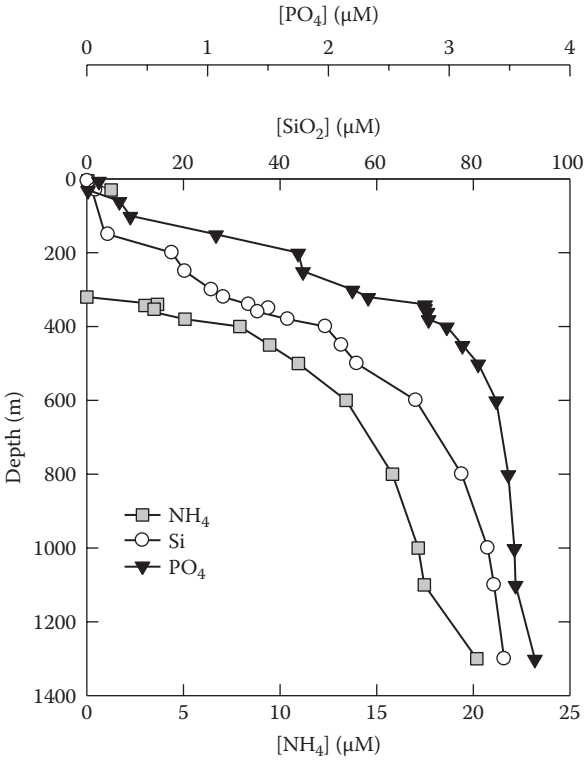

FIGURE 10.58
Profiles of ammonia, phosphate, and silicate in the Cariaco Trench.

decreases to 7.9 below the oxic–anoxic interface. A profile of TCO_2 in the eastern basin is also shown in Figure 10.60. The minimum value of 2.0 m*M* appeared at the surface, and the value became constant below 1000 m (2.40 m*M*). The TA was calculated based on the known pH and total CO_2. The profile of TA is also shown in Figure 10.60. The maximum in the surface water at a depth of 60 m is consistent with the salinity maximum. The salinity-corrected TA does not show this effect. The TA increases with depth below the oxic–anoxic interface because of the bacterial anaerobic respiration of organic matter to bicarbonate and simultaneous reduction of sulfate to sulfide. The dissolution of $CaCO_3$ may also be part of the cause of the increase in the deep waters.

The rates of oxidation of H_2S in surface waters (with added NaHS), deep waters, and mixtures of surface and deep waters were measured on the cruise. A comparison of the rates in the different waters is shown in Figure 10.61 along with the half-times for these runs. The cause of the acceleration of the rates of oxidation of H_2S is the high concentrations of Fe^{2+} and Mn^{2+}. At the maximum levels of Fe^{2+} in the Cariaco Trench, one would expect the rates of oxidation to be 17 times faster. These estimates are the same order as found in our direct measurements. The calculated half-times ($t_{1/2}$ = 17.2, 2.7, and 1.5 h, respectively, for the surface, mixed, and deep waters) are in good agreement with the measured values ($t_{1/2}$ = 17.2, 3.0, and 1.6 h).

The intermediates SO_3^{2-} and $S_2O_3^{2-}$ were determined, along with the disappearance of H_2S, during the course of the oxidation of sulfide in the waters of the Cariaco Trench. The results are shown in Figure 10.62. The decrease of H_2S and resultant increase of

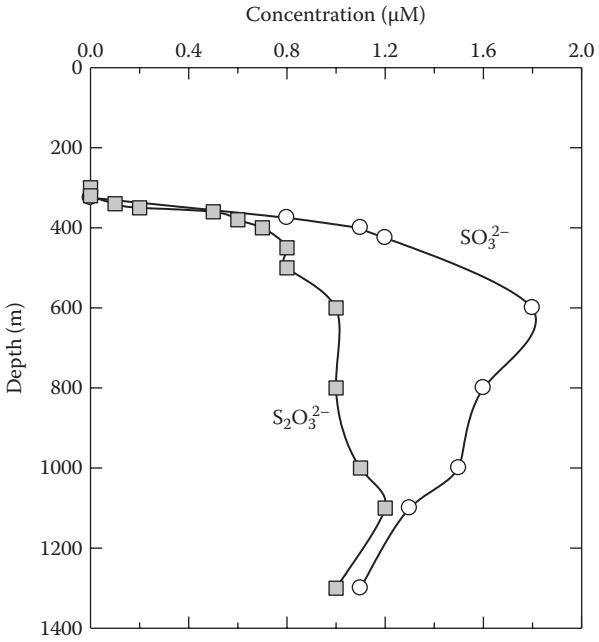

FIGURE 10.59
Profiles of sulfite and thiosulfate in the eastern (closed symbols) and western (open symbols) basins of the Cariaco Trench.

SO_3^{2-}, $S_2O_3^{2-}$, and SO_4^{2-} occurring during the oxidation are similar to laboratory studies and measurements in other anoxic basins. Plots of the concentration of NH_4^+, PO_4^{3-}, and ΔTCO_2 versus H_2S in the anoxic waters of the Cariaco Trench are shown in Figure 10.63. Good linear correlations were found with slopes of 0.33 ± 0.07 for NH_4^+, 0.0191 ± 0.0014 for PO_4^{3-}, and 2.25 ± 0.10 for TCO_2. These slopes are in good agreement with the theoretical values (0.30 for NH_4^+, 0.0189 for PO_4^{3-}, and 2.00 for TCO_2). Corrections for total sulfur to include sulfite and thiosulfate slightly improved the values of the ratios (0.31 ± 0.06 for NH_4^+, 0.0182 ± 0.0014, and 2.01 ± 0.07 for total CO_2). Since decreases in the concentration of sulfide could also occur due to reactions with MnO_2 and FeOOH, we cannot rule out that this effect may be responsible for the slightly larger slopes found without any corrections.

A plot of the concentration of silicate versus H_2S in the anoxic water is also shown in Figure 10.63. The linear correlation between sulfide and silicate in the anoxic water gives a slope of 0.91 ± 0.07. There is no theoretical ratio of H_2S to Si from the oxidation of biogenic organic matter because of its dependence on the relative abundance of siliceous organisms (e.g., diatoms) in the phytoplankton population of the surface water. The population of siliceous organisms varies temporally and spatially. From the profile of silicate, it can be estimated that about 50% of the silicate is regenerated above the oxic–anoxic interface. Another 50% of the silicate is released in the anoxic waters below the interface. Small amounts of silicate may be released from the sediments as sulfide is produced. Little is known about the effect of anoxic environments on the dissolution of silicate.

Scranton et al. (1987) suggested that the physical and chemical properties of the deep waters of the Cariaco Trench are increasing. For example, there has been a significant change in the temperature distribution over 35 years since the first expedition in 1955. There has been a distinct increase in the temperature of the waters below 1000 m as well as

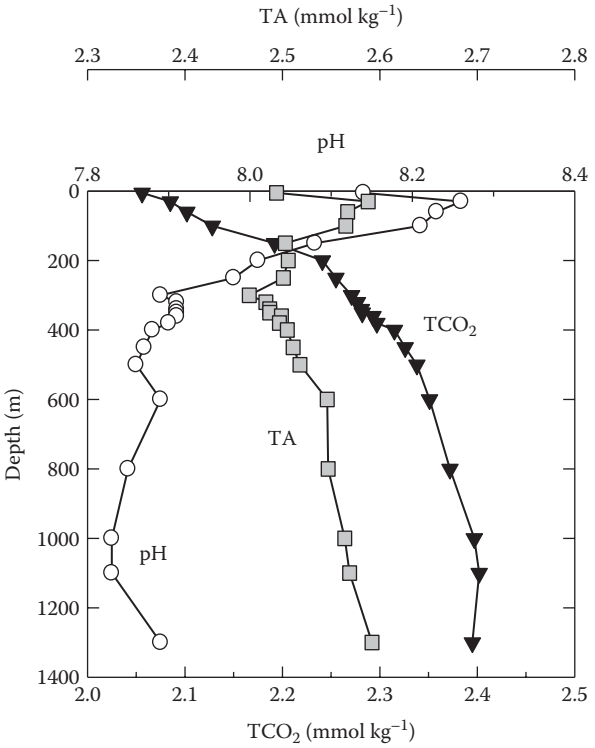

FIGURE 10.60
Profiles of the pH, TCO_2, and TA in the Cariaco Trench (1982–1990).

a much larger increase at shallower depths. Temperature data available from other Cariaco Trench expeditions together with our data are plotted in Figure 10.63. Between 1955 and 1982, an average increase of 0.006°C per year occurred, while a much faster rate of increase, 0.028°C per year, occurred in the past 8 years. At 300 m, a much larger increase in the rate of change of temperature was found. Richards (Zhang and Millero, 1993a) found values of 17.08°C in 1965, and Scranton et al. (1987) found values of 17.55°C in 1982 compared with our values of 17.79°C in the western basin and 17.89°C in the eastern basin in 1990. Further measurements are needed to verify the recent increase in temperature of the deep basin. Since the temperatures we reported were made with reversing thermometers rather than a CTD (conductivity temperature depth) system, our results may be too high because of errors in the calibration of the thermometers.

The concentrations of hydrogen sulfide in deep waters of the Cariaco Trench have increased with time as suggested by Richards (1965) and Scranton et al. (1987). The increase (Figure 10.65) in the concentration at 1300 m between 1982 and 1990 (1.58 μM yr^{-1}) is consistent with the increases observed between 1965 and 1982 (1.42 μM yr^{-1}). The average rate of increase over a 40-year span from the 1950s to the 1990s is 1.11 μM yr^{-1}. The sulfide enrichment of the deep waters in the eastern basin relative to the western basin reported by Richards in 1975 was also observable in our data (at 1300 m, 58 μM in the eastern basin and 55 μM in the western basin).

Salinity variations in the deep portion of the Cariaco Trench are harder to trace than the temperature variations. Scranton et al. (1987) found that the salinity increased by 0.008

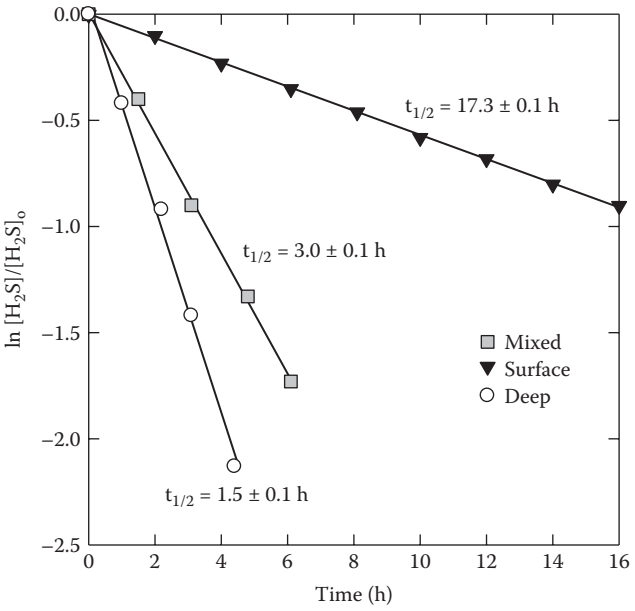

FIGURE 10.61
Comparison of the rates of oxidation of H_2S in different waters of the Cariaco Trench.

over a period of 9 yr. This variation is small relative to the analytical error, and it is hard to confirm the increasing pattern. The continuous decrease of salinity with depth in our data suggests that the upward salt flux from the sediments is insignificant.

The concentrations of ammonia, phosphate, and silicate in the deep waters of the Cariaco Trench have increased with time since the first measurements were made in the 1950s. These temporal changes are also shown in Figure 10.65. The rates of increase are 0.282 μ*M* yr^{-1} for ammonia, 0.0372 μ*M* yr^{-1} for phosphate, and 0.854 μ*M* yr^{-1} for silicate. These increases are consistent with the increase of H_2S with time in the deep waters of the Cariaco Trench. If these compounds behave conservatively, they should have accumulated in the anoxic water column in fixed ratios as predicted. The ratio of the rate of increase for ammonia to that of sulfide is equal to 0.25. Considering that these rates of increase are average values taken over four decades, the ratio of the rates of increase for ammonia and sulfide are in reasonable agreement with the value of 0.30 predicted from the model. The ratio of the rate of increase for phosphate to that of sulfide is equal to 0.0335, while the theoretical value is 0.0189. The larger increase for phosphate suggests other sources besides the decomposition of organic particulate materials such as the incorporation of PO_4^{3-} on Fe and Mn oxides that sink below the interface. The dissolution of phosphate minerals in the anoxic water or diffusion from sediment pore waters might also provide the input of the phosphate in the anoxic waters. The flux of silicate from the pore water of the sediment into the water column has been suggested as the cause of the high concentrations of silicate in the deep waters of the Cariaco Trench (Fanning and Pilson, 1972; Scranton et al., 1987).

By extrapolating the concentrations of H_2S and NH_4^+ to zero, it is possible to estimate the last time that the trench was oxic. The earlier rate of increase (1955 to 1969) in the H_2S with time extrapolated to zero gives a date of 1916. A similar extrapolation for NH_4^+ gives a date of 1914. These estimations, from two independent chemical compounds, are in good agreement for the last occurrence of a complete turnover of the trench waters. It is interesting to

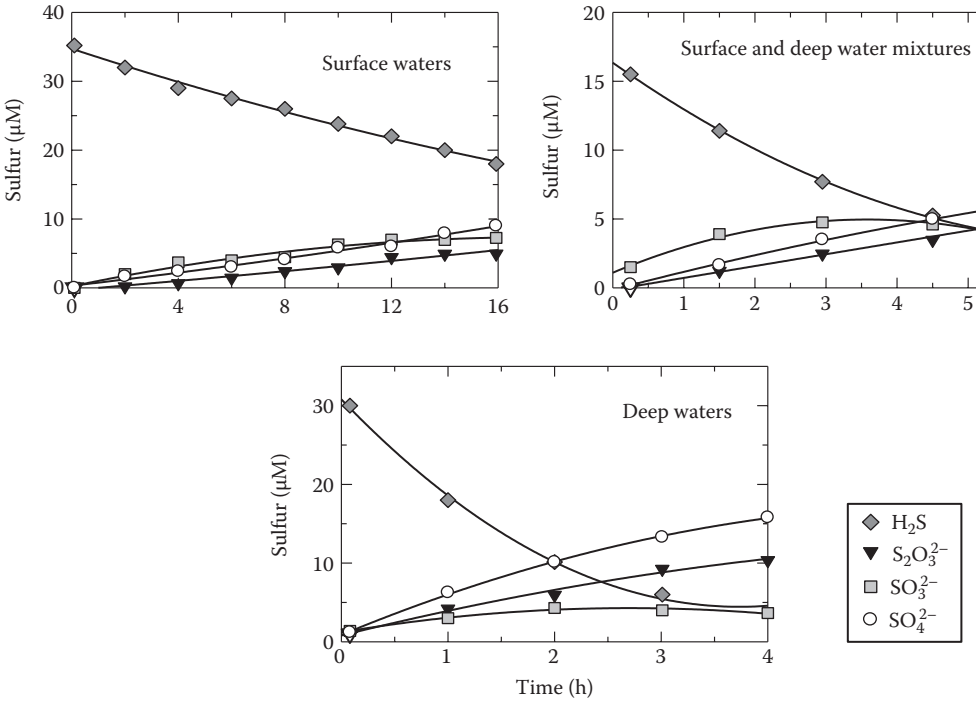

FIGURE 10.62
The formation of intermediates during the oxidation of H_2S in different waters of the Cariaco Trench. Top: surface waters; and surface and deep-water mixtures. Bottom: deep waters. The smooth curves were calculated from the kinetic model.

note that the ^{210}Pb dating of the sediments (Hughen et al., 1996) indicate that some disturbance of the sediment water interface occurred around 1932 and 1897, apparently due to earthquakes around 1900 and 1929. These events could also have influenced the turnover of the waters in the trench that we estimate occurred around 1920. The concentrations of PO_4^{3-} and SiO_2 were estimated to be 1 and 2 μ*M*, respectively, at the time of turnover based on their rates of increase. These concentrations are in good agreement with the concentration of these compounds in the Caribbean Sea (e.g., silica is 25 μ*M* in the deep Caribbean Sea).

The increase in the rates of oxidation of H_2S by Fe(II) at low concentrations is truly a catalytic effect. This is presumably caused by the oxidation of Fe(II) (Millero et al., 1987):

$$Fe(OH)_2 + O_2 \rightarrow Fe(OH)_2^+ + O_2^- \tag{10.68}$$

The oxidation products O_2^- and $Fe(OH)_2^+$ may also oxidize H_2S. The reaction of dissolved or particulate Fe(III) with H_2S can regenerate Fe(II) to complete the catalytic cycle. The overall reaction is given by

$$2\ FeOOH + HS^- + 5\ H^+ \rightarrow 2\ Fe^{2+} + S_0 + 4\ H_2O \tag{10.69}$$

The kinetic measurements made on the formation of intermediates during the oxidation of H_2S in Cariaco Trench waters give some support to our contention about the source of the SO_2^{2-} and $S_2O_3^{2-}$ found in the anoxic waters of the trench.

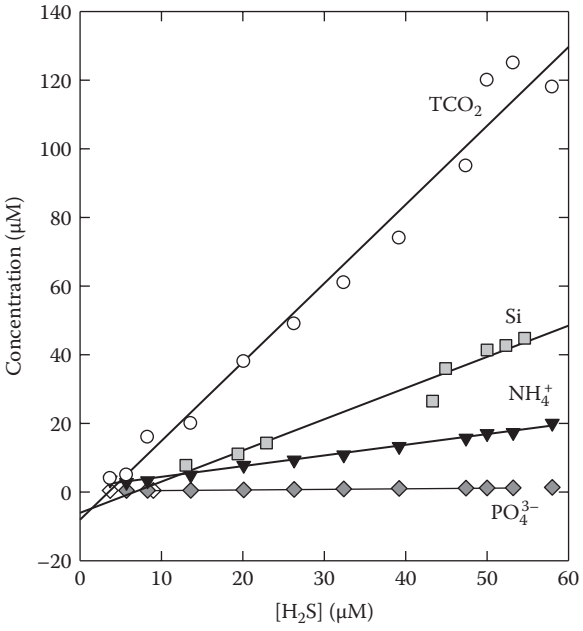

FIGURE 10.63
Plots of the changes in concentration of ammonia, phosphate, silicate, and total carbon dioxide in anoxic waters versus the concentration of H_2S.

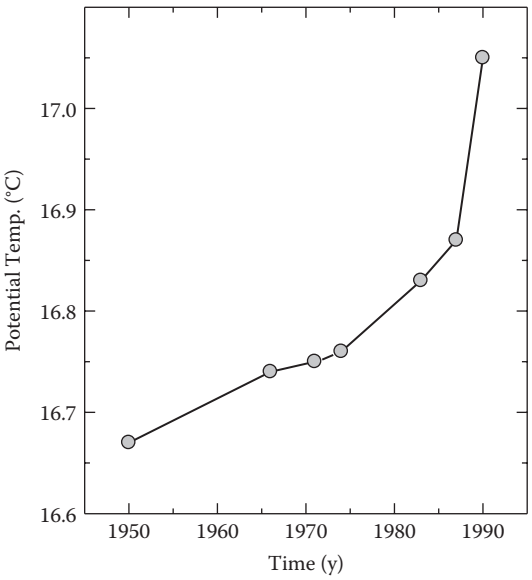

FIGURE 10.64
The temporal changes of potential temperature of water below 1200 m in the Cariaco Trench.

10.3.3 Framvaren Fjord

The Framvaren Fjord, located in southern Norway (Figure 10.66) is a permanent superanoxic fjord that has the highest levels of H_2S (6 μ*M*) reported for an open anoxic basin. The catchment area (31 km^2) is dominated by granitic rock. The rock consists of quartz (20%), microcline perthite (35%), oligoclas (36%), hornblende (5%), and accessory minerals. The fjord (Figure 10.67) has a shallow 2-m sill that separates the outer Hellevikfjord (80 m) from the basin, which is 183 m deep (Skei, 1988a). A major river entering the Lyngdalsfjord causes a flow of freshwater through the canal into the Framvaren. In 1993, we conducted chemical studies of the Framvaren Fjord (Yao and Millero, 1995). The large salinity gradient (Figure 10.68) accounts for the large pycnocline that separates the surface and deep water. The surface waters have a salinity of 12, while the deep waters have salinities as high as 24. The salinity gradient prevents vertical mixing and results in the formation of H_2S below a depth of about 18 m. The temperatures of the surface waters (Figure 10.68) fluctuate from 0°C in the winter to 19°C in the summer. The deep waters have a uniform temperature of 7 to 8°C. Based on the hydrography, the water masses can be divided into four major layers: the low-salinity surface layer (0 to 2 m) above the sill depth; the intermediate oxygenated layer down to about 18 m; the deep water, where steep gradients in the chemistry occur (18 to 90 m); and the bottom water below 90 m, where changes in salinity and chemistry are small.

The deep basin has been anoxic for about 8000 years. The sill was dredged in 1850, resulting in the formation of a new layer of H_2S (Figure 10.69). A vertical section of O_2 and H_2S in the central basin is shown in Figure 10.70. A surface maximum is observed in O_2 resulting from the photosynthesis of phytoplankton. The O_2 goes to zero at about 18 m,

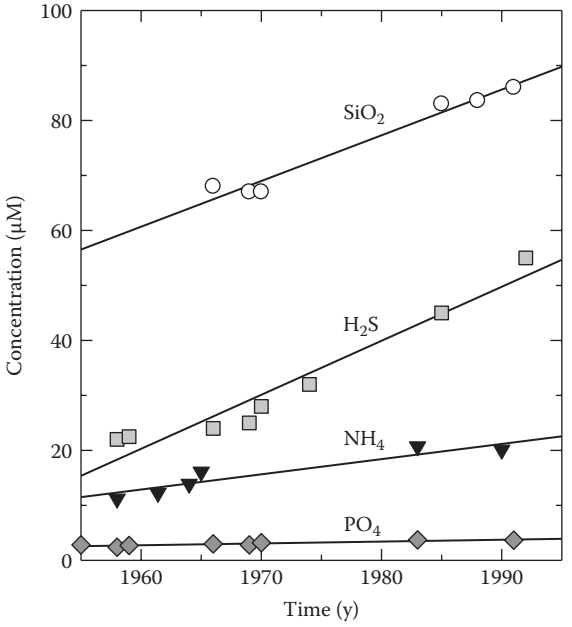

FIGURE 10.65
The temporal changes of the maximum concentration of ammonia, phosphate, silicate, and H_2S in water below 1200 m in the Cariaco Trench.

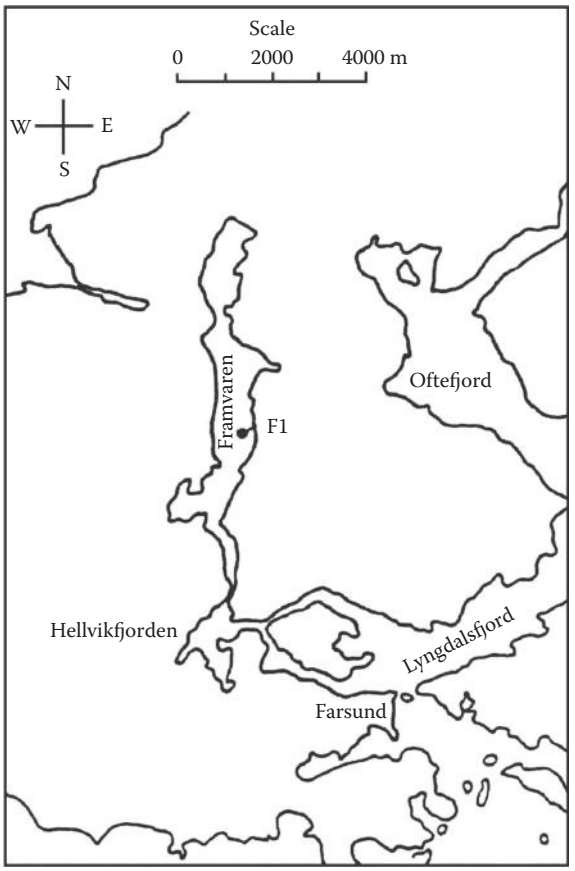

FIGURE 10.66
Sketch of the site of the Framvaren Fjord in Norway.

and the H_2S increases to concentrations as high as 6 m*M* or 6000 μ*M*. These values are the highest levels of H_2S found in any anoxic basin.

The concentration of metals in the Framvaren has been determined by a number of workers. The results from Haraldsson and Westerlund (1988) for some metals are shown in Figure 10.71 and Figure 10.72. The results are similar to those shown earlier for the Black Sea. Mn^{2+}, Fe^{2+}, Co^{2+}, and Pb^{2+} concentrations have the characteristic maximum near the oxic–anoxic interface; Ni^{2+} shows no changes across the interface. The concentrations of Cu^{2+}, Zn^{2+}, and Cd^{2+} show slight maximum concentrations near the interface and large decreases in the deeper waters caused by the low solubility of their metal sulfides. The oxidation of H_2S with O_2 in the Framvaren has been shown to be greatly enhanced by the high content of Fe and Mn. Only low levels of the intermediates SO_3^{2-} and $S_2O_3^{2-}$ were found near the interface.

The dissolved Mn and Fe together with O_2 and H_2S near the interface are shown in Figure 10.73 (Yao and Millero, 1995). The concentrations of dissolved Mn increased rapidly below 15 m, corresponding to the rapid decrease of O_2, and reached a maximum at 21 m, where the concentration of H_2S was 12 μ*M*. The maximum dissolved Mn found in this study, 18.0 μ*M*, was higher than previous values of 10.5 μ*M* (Jacobs, Emerson, and

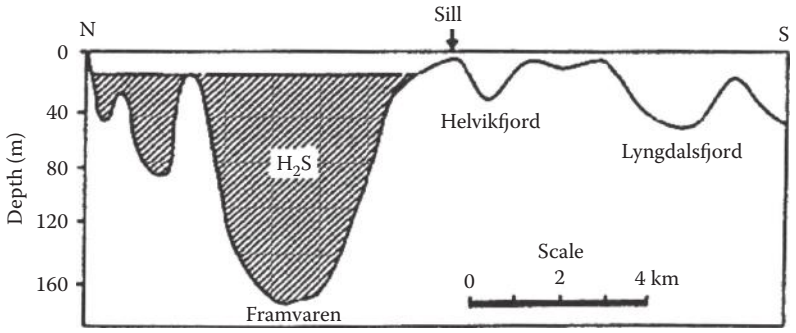

FIGURE 10.67
A longitudinal profile of the Framvaren Fjord.

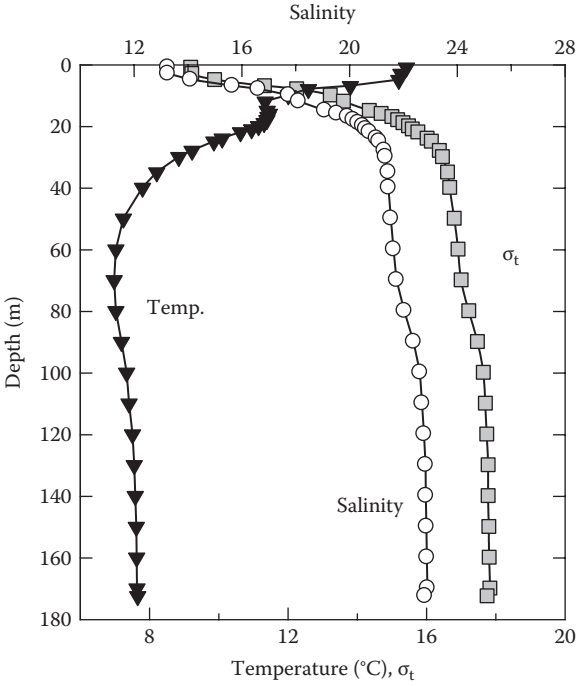

FIGURE 10.68
Profile of salinity, temperature, and sigma-t in the Framvaren Fjord.

Skei, 1985) and 15.3 μ*M* (Haraldsson and Westerlund, 1988). Our higher value might be due to the better sampling resolution with the submersible pumping system. It might also reflect the continuing accumulation of Mn in the transition zone. The concentrations of dissolved Mn decreased rapidly below the maximum peak at 21 m and reached nearly constant values (less than 1 μ*M*) below 100 m.

The concentrations of dissolved Fe started increasing just below the O_2–H_2S interface (Figure 10.73) to a sharp maximum at 21 m. The maximum value found in this study, 2.85 μ*M*, is higher than earlier values of 2.0 μ*M* (Haraldsson and Westerlund, 1988). Again, these differences could be caused by various sampling depths or fluctuation of

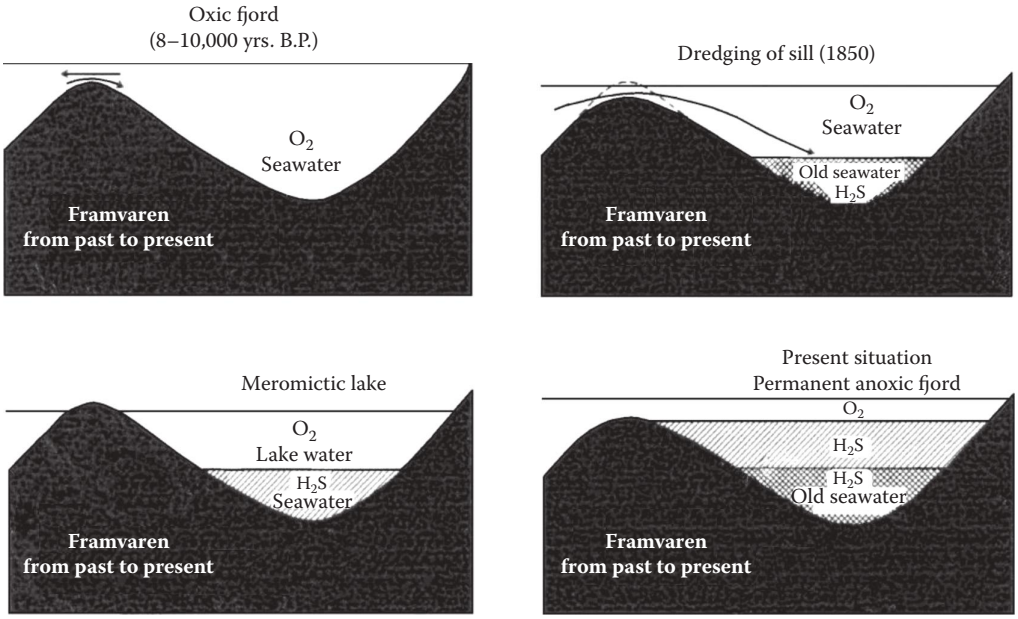

FIGURE 10.69
The historical development of the Framvaren Fjord.

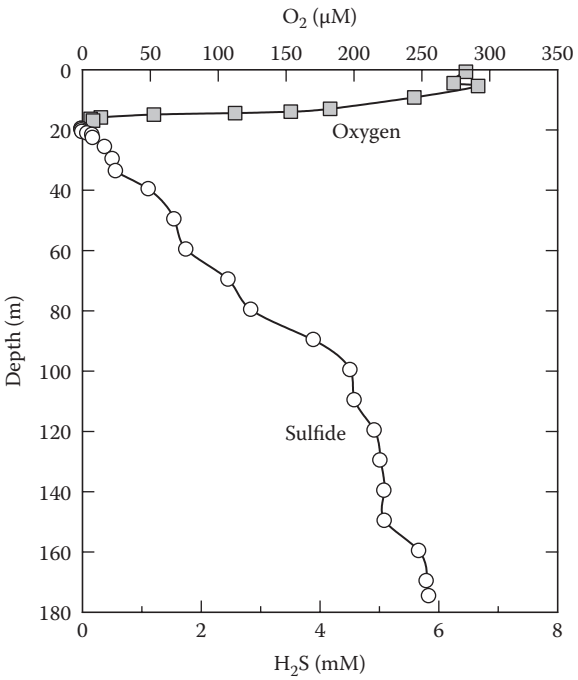

FIGURE 10.70
Profiles of oxygen and hydrogen sulfide in the Framvaren Fjord.

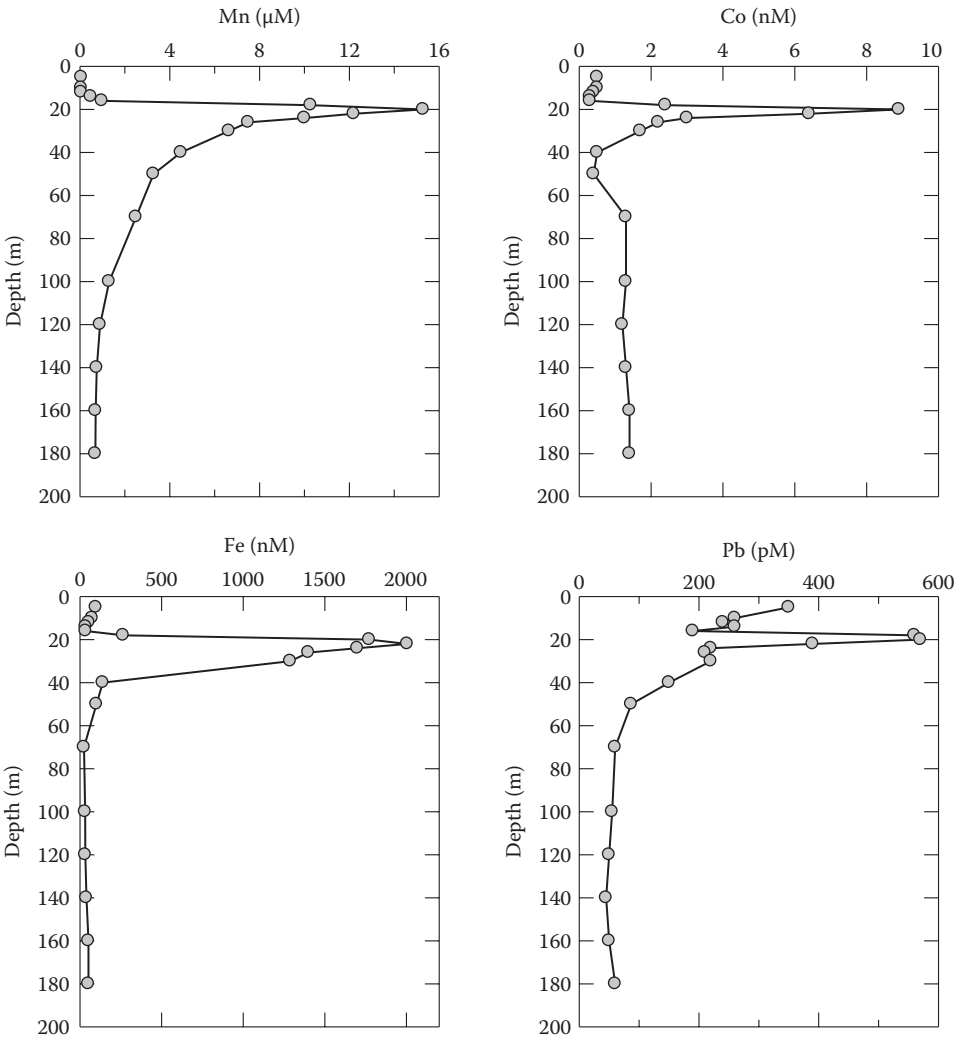

FIGURE 10.71
Profiles of Mn, Co, Fe, and Pb in the Framvaren Fjord.

Fe(II) concentration with time. The lower value of 0.89 μ*M* found in the winter might have resulted from the oxidation of Fe(II) near the interface by O_2 caused by the enhanced water mixing in this season. The concentrations of dissolved Fe(II) decreased rapidly below the maximum to less than 40 n*M* in the bottom water, probably due to the formation of iron sulfide minerals (Skei, 1988a,b).

Due to the unusual chemical and microbiological properties, the Framvaren has been widely used as a natural laboratory to study anaerobic processes since the 1930s. Earlier studies on the hydrography, currents, trace metals, isotopes, microbiology, sedimentation, and seismology of the fjord have been reviewed (Skei, 1988a,b). Unlike most other anoxic basins, the O_2–H_2S interface (~18 m) in the Framvaren is at a depth of significant light penetration. Dense populations of photosynthetic bacteria were present at the redox boundary (Skei, 1988a,b), as indicated by the measurements of ATP (Figure 10.74) near the interface. There is also a concentration of particles at the interface, as shown by the vertical

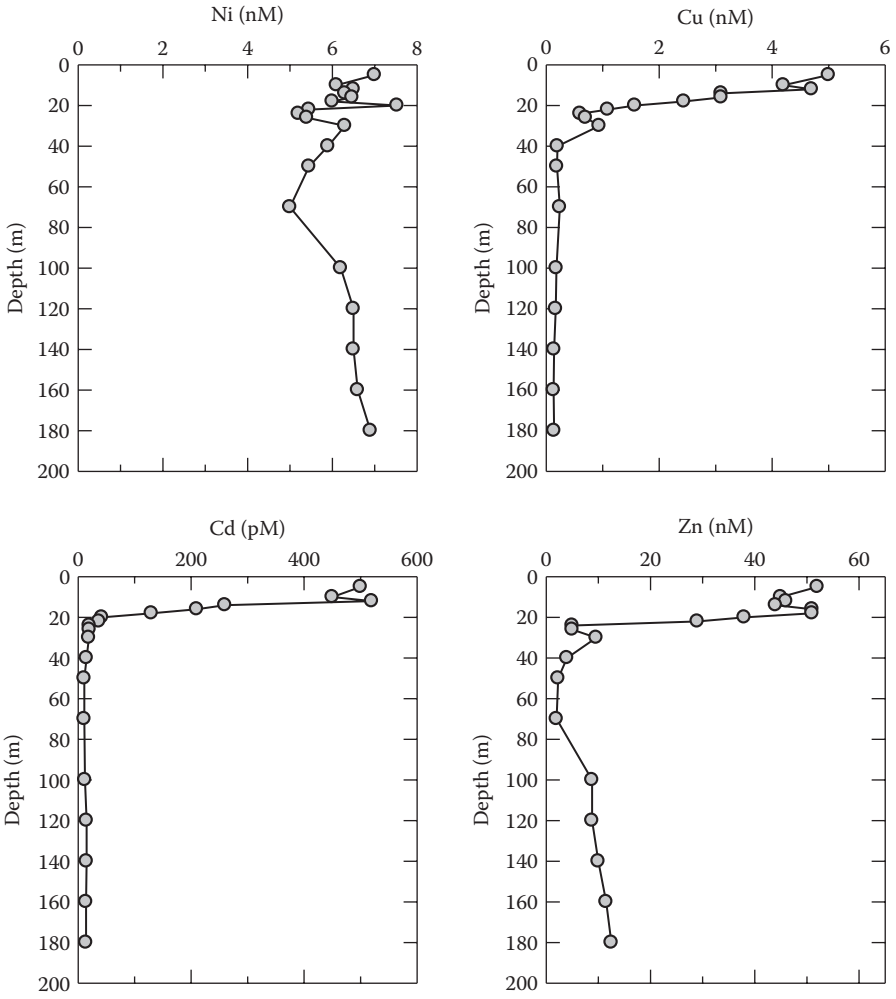

FIGURE 10.72
Profiles of Ni, Cu, Cd, and Zn in the Framvaren Fjord.

distribution of the transmission of light (see Figure 10.75). This high biological activity can effectively control the biogeochemistry of metals and nonmetals. The increase in the particles in the deep waters is related to the formation of metal sulfides and polysulfides. Framboidal pyrite (FeS_2) has been found in the deep waters (see Table 10.10).

Much of our understanding of anaerobic microbial decomposition of organic matter has come from studies of these systems (Richards, 1965; Grasshoff, 1975). Dyrssen (1989) has used a stoichiometric model of the organic matter based on available data to show that more sulfate was reduced than sulfide found in the Framvaren. Yao and Millero (1995) examined the distribution of chemicals at a central station of the Framvaren. The maximum temperature occurred at the surface and decreased sharply with depth to 14 m (Figure 10.68). The temperature slightly increased in the middle of the intermediate layer and reached a submaximum at 16.5 m (Figure 10.67). This temperature structure might have been due to the intrusion of the surface water of Hellvikfjord through the sill, which may also have contributed to the renewal of the upper 10- to 20-m waters. There was a steep salinity

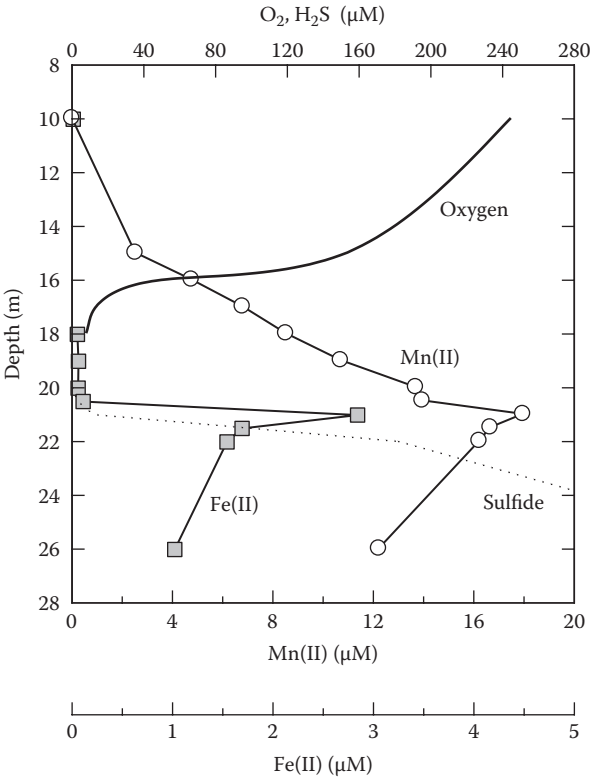

FIGURE 10.73
Concentrations of oxygen, hydrogen sulfide, Mn(II), and Fe(II) near the interface in the Framvaren Fjord.

increase from the surface down to the bottom of the intermediate layer (~20 m), which contributed to the large pycnocline. A secondary halocline was also observed at about 90 m. The salinity in the surface waters was about 13.26, which is much higher than the value found during the 1989 cruise. Both cruises were at the same time of the year. These results suggest that the local freshwater supply to the Framvaren may vary annually.

The dissolved oxygen in the surface water was 283 μ*M*, which is close to the saturated value (285 μ*M*). The maximum value of 292 μ*M* in the subsurface (6 m) is the result of photosynthesis. The oxygen concentration decreased sharply from 15 m and became undetectable below 18 m (Figure 10.68). The H_2S appeared at 20 m (0.4 μ*M*), which corresponded to the σ_T = 15.8 isopycnal surface. The interface at 18 m showed no overlap in the levels of O_2 and H_2S within the sampling scale (1 m). The interface was located at 18 m (σ_T = 16.52) in 1979, at 18 m (σ_T = 15.8 to 15.9) in 1985, and at 19 m (σ_T = 15.60) in 1989. The oxic–anoxic interface has been relatively stable during the past 20 years based on the depth resolution of Niskin bottles. Small fluctuations, however, are expected to be caused by changes in the exchange of water with outside basin and internal waves. The concentrations of H_2S in the bottom water were found to be as high as 5.8 m*M*, which is in reasonable agreement with the results of Landing and Westerlund (6.1 m*M*; 1988) and Millero (5.7 m*M*; 1991b). The gradient of H_2S in the bottom water (below 100 m) was much smaller than that in the deep water (20 to 100 m) (Millero, 1991b). This may have been due to the separation of the older water and more recent anoxic water (Skei, 1988a,b). The distributions of nutrients TA and TCO_2 (shown below) show the same pattern.

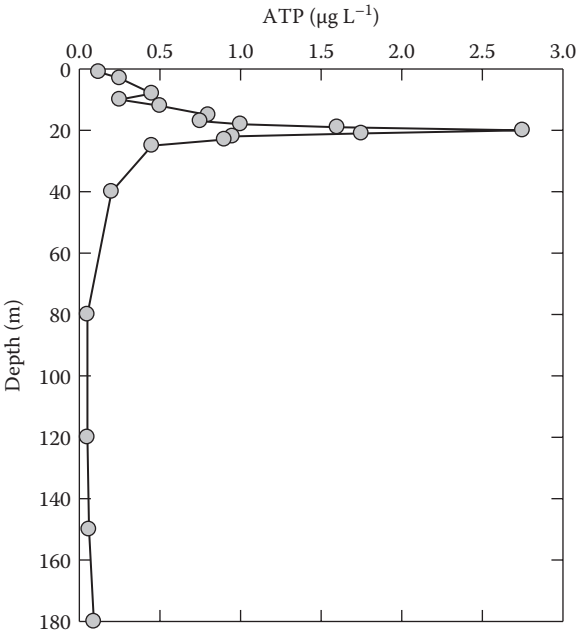

FIGURE 10.74
The vertical distribution of ATP in the Framvaren Fjord.

The concentration of phosphate in the surface water was about 0.4 μ*M* and reached a minimum (0.18 m*M*) between 16 and 18 m, which may have been due to the high productivity at this region or absorption onto Mn and Fe particles. Maximum values of particulate Mn and Fe are usually found at or above the O_2–H_2S interface. The PO_4^{3-} increased rapidly below the interface and reached a maximum of 100 to 102 μ*M* in the bottom water (Figure 10.76). Ammonia was present in the oxic euphotic zone at about 5.0 μ*M*. It increased rapidly below the interface and reached a maximum of 1.6 μ*M* in the bottom waters (Figure 10.76). Relatively high (~20 μ*M*) silicate was found in the oxic waters, and the concentrations increased rapidly below the interface to a maximum of 640 μ*M* in the bottom water (Figure 10.76). The concentrations of phosphate, ammonium, and silicate in the bottom water were all close to the results of earlier studies (Skei, 1988a,b).

The distributions of pH, TA, and TCO_2 are plotted in Figure 10.77. The pH in the surface waters was about 7.89 and decreased to a minimum (6.98) at 15 m. The low pH at 15 m is difficult to explain, although it agrees with the calculated value using TA and TCO_2. The pH decreased below the interface and was constant (about 6.90) below 90 m.

The TA increased with depth from the surface to the interface, corresponding with the increase in salinity. The average normalized (to S = 35) TA (NTA) was 2.41 m*M* in the surface water, which is slightly higher than the value in ocean surface water (about 2.35), probably because of the impact of freshwater with high NTA. Below the interface, the TA increased rapidly because of the bacterial anaerobic respiration of organic matter to bicarbonate and simultaneous reduction of sulfate to hydrogen sulfide. The TA was 19.8 μ*M* in the bottom water, which was about 1 m*M* lower than earlier results (Skei, 1988).

The TCO_2 in the water samples was determined after poisoned samples were returned to the laboratory. Due to the extremely high TCO_2 in the anoxic waters (the pCO_2 in the bottom water was as high as 38,000 μatm), a large amount of CO_2 in samples (about 2 m*M* in

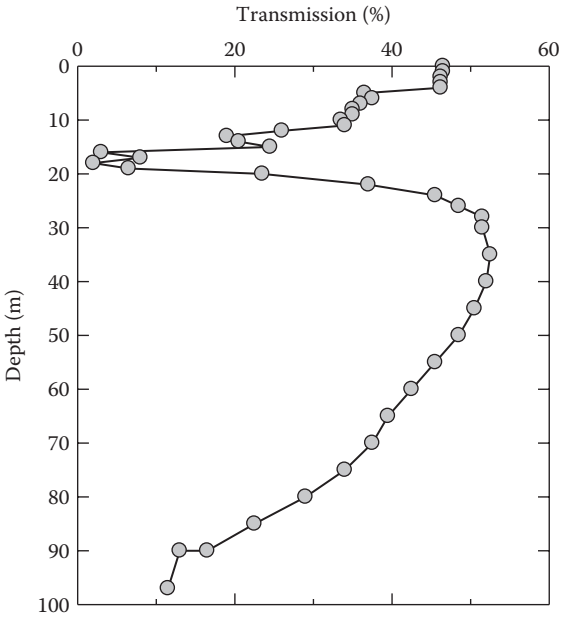

FIGURE 10.75
Transmission of the waters in the Framvaren Fjord.

TABLE 10.10

Framboidal Pyrite Composition
(Average of 22 Framboids)

Element	Wt%	Standard Deviation
Cu	0.5	0.08
Zn	0.3	0.11
Mn	1.0	0.16
Ni	0.03	0.03
Co	0.03	0.04
Fe	33.5–40.3	
S	36.2–45.5	

the bottom samples) was lost to the headspace in the sample bottles. We thus give the calculated values of TCO_2 (Figure 10.77) for the samples below the interface. The values of TCO_2 were calculated based on the pH and TA. The TCO_2 increased rapidly below the interface because of the oxidation of organic matter to inorganic carbon. The concentration of TCO_2 in the bottom water was 17.3 m*M*, which was 1 m*M* lower than earlier values (Skei, 1988).

Salinity increased sharply from the surface to the interface, while the temperature showed an inflection at 14 m (σ_t = 14.19) and reached a submaximum at 16.6 m (σ_t = 14.87). The same temperature structure was observed in previous studies. However, the extent of the increase of temperature has varied (Figure 10.77). It was most significant in 1984 (ΔT = 4.7°C). The depth of the temperature inflection varied from 9 to 14 m (σ_T = 13.2 to 16.0). This "submaximum temperature layer" might originate from the warm surface water of the Helvikfjord as discussed. The extent of the temperature anomaly and the depth of the submaximum temperature layer depend on the extent of the water exchange

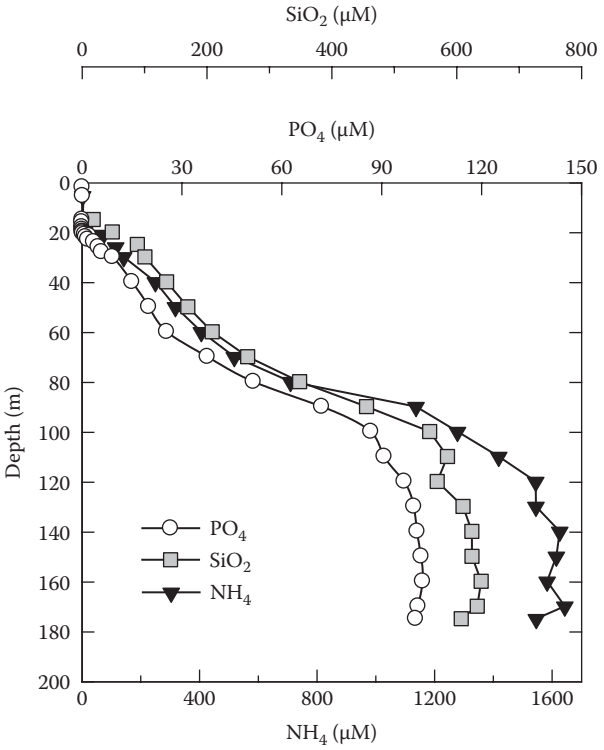

FIGURE 10.76
Profiles of ammonia, phosphate, and silicate in the Framvaren Fjord.

and the difference in the hydrographic properties of the two basins. This water intrusion caused the nonlinear relationship between temperature and salinity across the interface. This suggests that horizontal transport might be an important process near the interface, which has to be considered in explaining the vertical profiles of chemical species.

In the deep water, the salinity increased slightly from the interface down to 80 m, while temperature decreased sharply down to 60 m and was almost constant between 60 and 80 m. Both temperature and salinity increased from 80 to 100 m. There was no linear T-S relationship in the deep water (Figure 10.79). The nature of the curvature in the bottom water suggested an additional source of heat flow. As discussed, chemical species showed large gradients through the region between 80 and 100 m. The hydrographic properties and the concentrations of chemical species changed very slightly below 100 m. The interface between 80 and 100 m may reflect the separation between the older and more recent anoxic waters that occurred after a channel was dug in 1850, allowing water to enter from the outside basin. This water input might have caused some deep-water renewal. The extent of this renewal and its effect on the seawater at the bottom is not known. Skei (1988a,b) argued that the renewal was likely to be complete because only 50% of the sulfate in the bottom water is reduced.

Anderson, Dyrssen, and Hall (1988) assumed that a total water exchange took place. This opinion was based on sediment data that showed a dramatic change from light-colored to black at a depth corresponding to about 1850 m. Due to the existence of the chemical gradients at this interface, the renewal might only be partially complete. One would expect this renewal to continue slowly at the slight step in the hydrographic properties at the top of

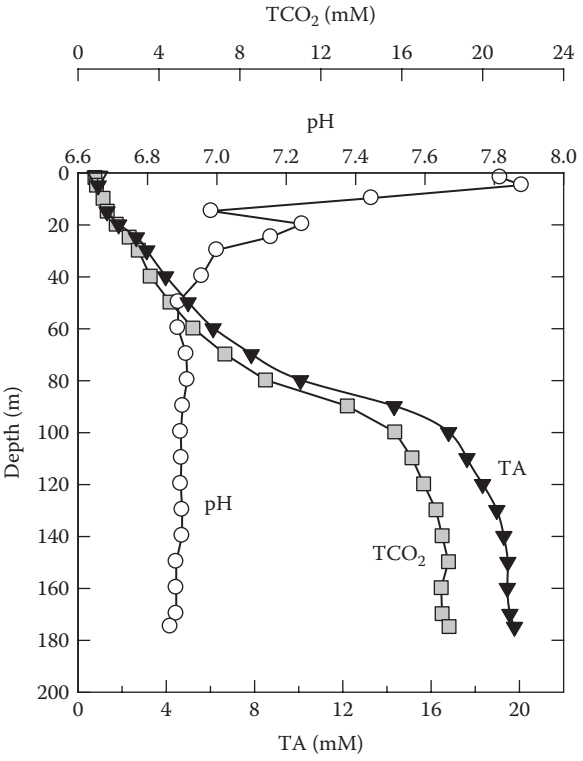

FIGURE 10.77
Profiles of pH, TCO_2, and TA in the Framvaren Fjord.

the bottom layer and be smoothed out by diffusion. The uniform properties in the bottom layer suggested that it was produced and maintained by convection, probably driven by geothermal heat from the sediments. The temperature and salinity both increased slightly below 80 m, so the vertical transport is possibly controlled by double diffusion. Double diffusion takes place when the gradients of temperature and salinity have the same sign and thus have opposite effects on density.

The temperature of the bottom water showed a significant decrease of 1.1°C from the 1930s to the present (Figure 10.80). This suggests that the heat flow to the bottom water, probably geothermal heating from sediments, was decreasing. The salinity in the bottom water also showed a decreasing trend. This decrease in salinity implies that the renewal of the bottom water was with the lighter water above by vertical diffusion. Vertical diffusion might also account for the decrease of temperature in the bottom water.

At present, it is not possible to establish a complete balance of sulfur in the Framvaren because of the incomplete measurements of sulfur species, especially the particulate sulfur (such as S^0 and FeS_2) and organic sulfur compounds. The ratio of thiols (mercaptans) to H_2S was found to be 0.036 in the Framvaren (Dyrssen, 1989). The difference between the initial sulfate concentration, $([SO_4]_{init})$, as calculated from salinity, and the measured sulfate concentration was significantly higher (1 to 3 m*M*) than the measured sulfide in bottom water. This discrepancy is explained by the removal of sulfide by oxidation and formation of iron sulfides (FeS and FeS_2), in addition to the possible diffusion of H_2S. If the major product of the oxidation of H_2S is sulfate (Millero, 1991a), the discrepancy may have

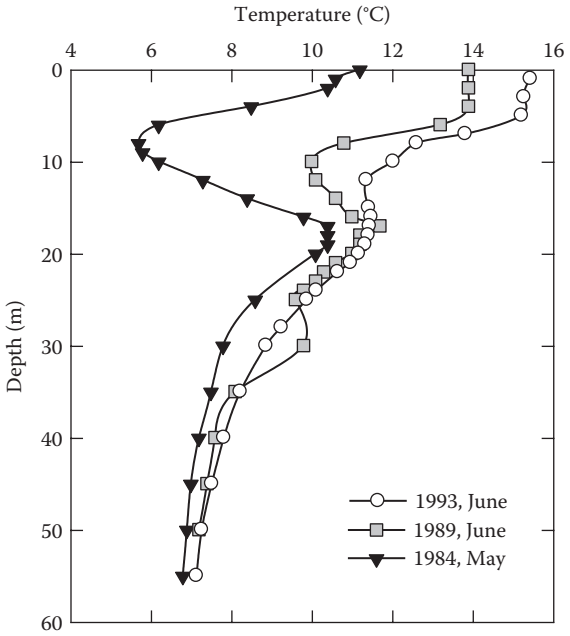

FIGURE 10.78
Profiles of temperature in the upper 60 m in recent years in the Framvaren Fjord.

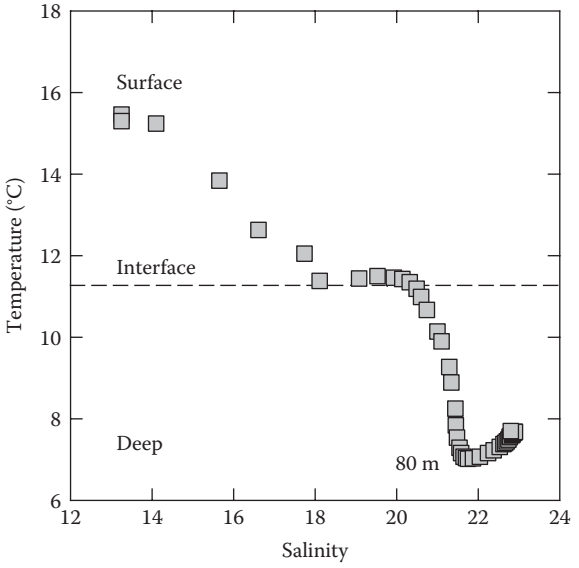

FIGURE 10.79
The T-S diagram for the water in the Framvaren Fjord.

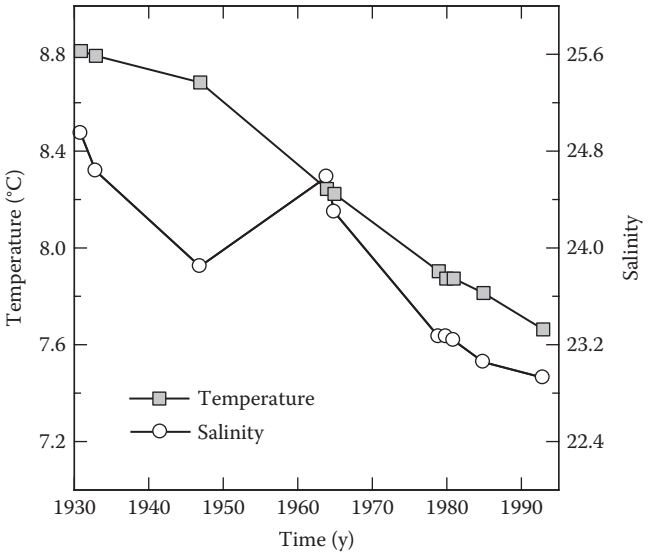

FIGURE 10.80
Temporal changes of temperature and salinity in the bottom waters of the Framvaren Fjord.

been even greater. The removal of sulfide by formation of iron sulfides is restricted to a continuing supply of iron. At pH 7.0, about 30% of the total hydrogen sulfide is in H_2S(aq). Diffusion might be a pathway for H_2S to escape into upper oxic water and be oxidized. In addition, there is evidence of the early diagenetic incorporation of inorganic sulfur into organic compounds.

Like other anoxic basins, the evolution of anoxic conditions in the Framvaren started from the bottom because of the restricted supply of dissolved oxygen. The hydrogen sulfide concentration is mainly controlled by the supply of organic matter and its encounter with oxygen—either through the injection of fresh seawater over the sill or by vertical exchange through the oxic–anoxic interface. A simple vertical advection–diffusion model is commonly used to examine the flux of chemical species and explain the sequence of redox reactions occurring across the interface (Brewer and Murray, 1973). One difficulty of this approach is that horizontal transport might be important because diffusion and mixing are more rapid along, rather than across, isopycnal surfaces. As discussed, the lateral mixing is significant near the interface in the Framvaren.

The upward sulfide electron gradient (140×10^{-3} mol e^- m^{-4}) was about three times greater than the downward O_2 electron gradient (58.4×10^{-3} mol e^- m^{-4}). The extremely steep gradient of sulfide in the Framvaren results from the high content of sulfide in the water column and the shallow depth of the basin. This deficiency of an oxygen gradient suggests that the downward flux of O_2 cannot account for the oxidation of upward sulfide. There are three possible alternatives for sulfide oxidation. First, oxidized metals such as MnO_2 and FeOOH could serve as oxidants (Millero, 1991a). The sharp maximum peaks of Mn(II) and Fe(II) (Figure 10.73) just below the interface result from the reductive dissolution of Mn and Fe oxides by sulfide. One difficulty with this metal oxide hypothesis is that the sum of the vertical electron gradients of Mn(II) and Fe(II) is much less than that of sulfide. This problem can be overcome if the particulate oxides are mainly transported horizontally into the intermediate layer through the sill. A second possible explanation is that photosynthetic sulfide oxidation by phototrophic sulfur bacteria takes place in the

chemocline. Dense populations of the phototrophic bacteria are present at the interface in the Framvaren (Sørensen, 1988). It is not clear whether there are specific species among them that can oxidize sulfide anaerobically. The third alternative process is horizontal ventilation, which results from the water intrusion through the sill as discussed. Dissolved oxygen in these ventilating injections could oxidize sulfide. Traces of the oxidation intermediates SO_3^{2-} and $S_2O_3^{2-}$ were found near the anoxic interface (Millero, 1991a). Such ventilation could account for the imbalance in the gradients of oxygen and sulfide.

The NTA (= TA × 35/S) and normalized TCO_2 ($NTCO_2$ = TCO_2 × 35/S) in the bottom water of the Framvaren are about 12 times more than in the open ocean, suggesting an enormous production of both TA and TCO_2 from oxidation of organic matter through the reduction of sulfate. The value of NTA in the Framvaren surface water was 2.41 m*M*, which is only slightly higher than the typical value of the open ocean (2.35 m*M*), while the $NTCO_2$ was much higher (2.31 m*M*) than the value of the open ocean (2.05 m*M*). Much higher values of both NTA (6.34 m*M*) and $NTCO_2$ (5.80 m*M*) were found in the surface water of the Black Sea (Goyet, Bradshaw, and Brewer, 1991). As discussed by Dyrssen (1986), these high values cannot result from the low salinity and high NTA of the river water mixing with Mediterranean seawater. The lower NTA in the Framvaren surface water indicates that the impact of freshwater was minor. The cause of the higher values of $NTCO_2$ in the surface waters may be the oxidation of organic matter in oxic water or diffusion from below the interface.

Plots of ΔTA and ΔTCO_2 versus H_2S are shown in Figure 10.81. The linear correlation between these properties demonstrates that hydrogen sulfide is produced proportionately to the formation of both TCO_2 and TA. However, the values of $\Delta TA/\Delta H_2S = 3.42 \pm 0.1$ and $\Delta TCO_2/\Delta H_2S = 3.00 \pm 0.12$ are both higher than the model values. Based on previous data, Dyrssen (1989) obtained a value of $\Delta TCO_2/\Delta H_2S = 2.54$. These ratios are also higher than the model values in the Black Sea (Goyet, Bradshaw, and Brewer, 1991); they are in good

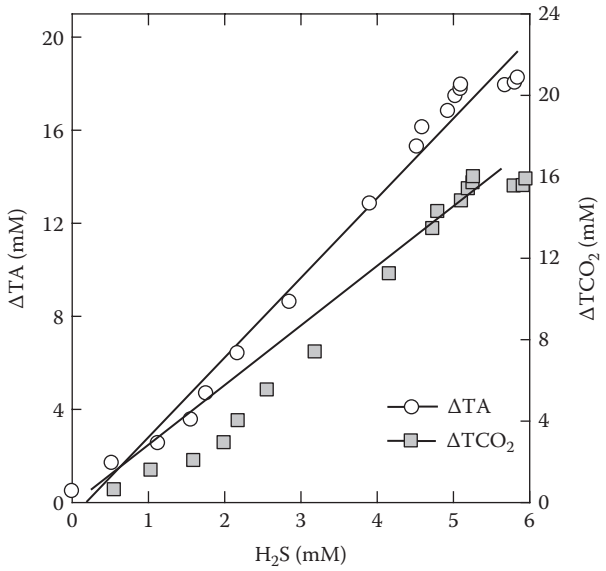

FIGURE 10.81
Plots of the changes of TCO_2 and TA versus the concentration of H_2S in the anoxic waters of the Framvaren Fjord.

agreement with the theoretical values in the Cariaco Trench (Zhang and Millero, 1993a,b). The ratio of ΔTA to ΔTCO_2 in anoxic waters of the Framvaren was 1.14 and equal to the model value. The same value of $\Delta TA/\Delta TCO_2$ (1.15) was found by Dyrssen (1989). This ratio was higher (1.32) than the model value in the Black Sea. As suggested by Dyrssen (1985), the differences between the observed ratios and the model values may be attributed to a combination of high values of TA and TCO_2 and the low values of H_2S. One possible explanation of low H_2S concentration is that a small fraction of hydrogen sulfide is removed by formation of Fe sulfides (Goyet, Bradshaw, and Brewer, 1991):

$$2\ FeOOH + 3\ H_2S = FeS + FeS_2 + 4\ H_2O \tag{10.70}$$

without changing TA and TCO_2. Goyet, Bradshaw, and Brewer (1991) argued that the capacity of this reaction must be small because of the low dissolved iron concentrations and cycling rates in the Black Sea.

Inflow of O_2-containing water through the sill may cause the removal of H_2S in the deep waters of the Framvaren, such as the renewal of the bottom waters when the channel was dug in 1850. To keep the same deviations in the ratios of TA/H_2S and TCO_2/H_2S, the removal process of H_2S should not change the TA. In other words, sulfide should be removed from the water column as FeS_2 and elemental sulfur or polysulfides:

$$2\ H_2S + O_2 = 2\ S^0 + 2\ H_2O \tag{10.71}$$

$$(x - 1)\ S^0 + HS^- = HS_x^- \tag{10.72}$$

again, without altering both TA and TCO_2. If the product is SO_4^{2-} instead of S^0, the alkalinity will be lowered. Millero et al. (1987) found that the main reaction product between H_2S and O_2 was SO_4^{2-} when O_2 was in excess. Experimental errors in the measurements of TA and H_2S, and the presence of organic acids that are not taken into account in this simple chemical theory, are also likely to contribute to the difference.

The calculated pCO_2 in the surface water in June 1993 was 250 μatm. This low pCO_2 was mainly due to the low temperature (15.41°C) and low CO_2 content (875 μ*M* due to low salinity) in the surface water. If the pCO_2 in the atmosphere is assumed to be 350 μatm, the surface water of the Framvaren serves as a sink of CO_2 for the atmosphere.

Ammonium started increasing below the interface because of the anaerobic decomposition of organic matter. Based on the model, a plot of NH_4^+ versus H_2S should give a slope of 0.30. Our experimental result gave the same value, 0.30 (±0.01) for all data from 20 to 175 m (Figure 10.82). A lower value of $NH_4^+/H_2S = 0.25$ (±0.02) was found for data from 30 to 80 m. The ratio of NH_4^+ to H_2S in the Cariaco Trench (0.31; Zhang and Millero, 1993a,b) agreed with the model value, while it was lower (0.23) in the Black Sea (Table 10.11). Due to the possible removal of H_2S as discussed, the real ratio of NH_4^+ to H_2S must be lower than the model value. One explanation for this is that the C:N ratio in organic matter was higher than 106:16. The detailed discussion follows.

Compared with nitrogen, phosphorus transformations are simple in terms of redox chemistry because of its single oxidation state. However, phosphate can absorb onto particles such as reactive Fe and Mn hydroxides, which results in a lower recycling efficiency than C and N, especially in upper oxidizing sediments. The rapid increase of concentrations of phosphate below the interface also results from the anaerobic respiration of organic matter. The ratio of PO_4^{3-} to H_2S should be 0.019. Our experimental result gave exactly the same value, 0.0191 (±0.0004), for all data from 20 to 175 m (Figure 10.82). A

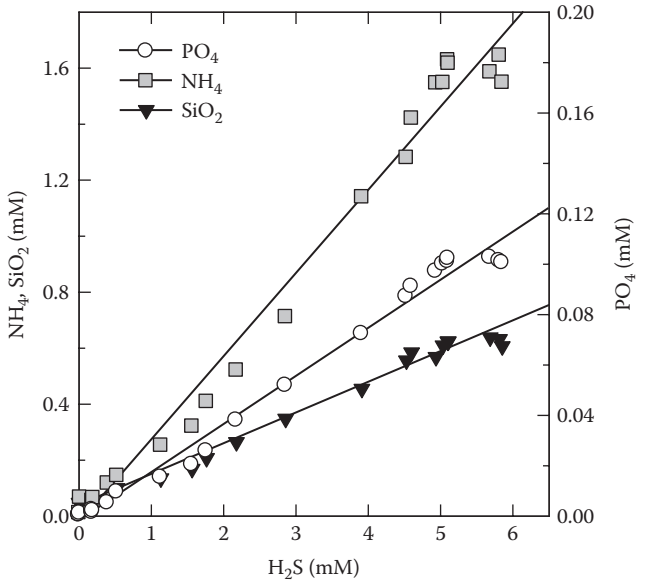

FIGURE 10.82
Plots of the changes in ammonia, phosphate, and silicate versus the concentration of H_2S in the anoxic waters of the Framvaren Fjord.

TABLE 10.11

Stoichiometric Ratios in Anoxic Waters of Different Basins

Basin	TCO_2:H_2S	TA:H_2S	PO_4:H_2S	NH_4:H_2S	Si:H_2S	C:N:P
Framvaren	3.00	3.42	0.019	0.30	0.11	155:16:1
Black Sea	2.30	3.05	0.009	0.23	0.61	255:25:1
Cariaco Trench	2.01	2.43	0.018	0.31	0.91	112:17:1
Model value	2.00	2.30	0.019	0.30	—	106:16:1

similar value of 0.0188 (±0.0021) was found for 30 to 80 m. The ratio of PO_4^{3-} to H_2S in the Cariaco Trench (0.018; Zhang and Millero, 1993a,b) agreed fairly well with the predicted value, while it was only half of the model value (0.009) in the Black Sea. This low recycling efficiency of PO_4^{3-} in the Black Sea might partially be due to the removal of PO_4^{3-} by adsorption onto particles. Again, the good agreement between the measured ratio of PO_4^{3-} to H_2S in the Framvaren and the model value might be incidental when we consider the possible removal of H_2S produced by sulfate reduction.

The linear correlation between sulfide and silicate in the anoxic waters of the Framvaren gave a slope of 0.11 (±0.01) (Figure 10.82), indicating that silicate was also released proportionately to the production of hydrogen sulfide. There is no theoretical ratio of Si to H_2S from the oxidation of biogenic organic matter because it depends on the relative abundance of siliceous phytoplankton (e.g., diatoms). The ratios were 0.61 and 0.91 for the Black Sea and Cariaco Trench, respectively. The concentration of silicate in the Framvaren was relatively low compared to the sulfide level. Little is known about the effect of anoxic environments on the dissolution of silicate.

The classic work of Redfield introduced the concept of nearly parallel C, N, and P changes in aquatic ecosystems. Nutrients are taken up by phytoplankton and released during organic matter degradation according to a simple and constant stoichiometry. The Redfield model gives a nitrate:phosphate ratio of 16:1 and suggests that the nitrogen and phosphorus are incorporated into living plankton and released from decomposing plankton in the same ratio. However, the ratio of C:P in marine detritus has been suggested by Peng and Broecker (1987) to be 127 instead of 106. Based on chemical data from isopycnal surfaces of the Atlantic and Indian oceans, Takahashi, Broecker, and Langer (1985) yielded a C:N:P ratio of 103:16:1 if the carbon value was represented by the observed increase in the TCO_2 concentration and a ratio of 140:16:1 if the carbon value was assumed to be represented by the oxygen utilization minus the oxygen used for oxidation of NH_3 with 2 moles of O_2 per nitrogen atom. The C:P and N:P ratios are more variable for lake particles but generally higher than the Redfield ratio of 106:16:1. Terrestrial soils and vegetation are rich in C and N with high C:N, C:P, and N:P ratios. One could expect that C, N, and P in those marine environments such as basins and fjords, which are influenced by terrestrial input, might not have Redfield behavior.

The major input of terrestrial origin organic matter is tree leaves, which have high C:N and C:P ratios. Part of these tree leaves are difficult to decompose. The C:N:P ratio of bacteria is unknown, and the bacteria might contribute significantly to the carbon flux. The linear correlation between concentrations of NH_4^+ and concentrations of PO_4^{3-} for samples collected below the oxic layer give an N:P slope of 16.0 (±0.3), which is the same as the Redfield ratio. A plot of concentrations of TCO_2 versus NH_4^+ in deep anoxic waters gives a C:N slope of 9.6 (±0.2) (Figure 10.83), which is higher than the Redfield value of 6.6. A similar value of C:N = 10.0 (±0.6) has been found for 30 to 80 m. Based on measurements of organic carbon and nitrogen in the suspended material collected from sediment traps, Naes and Skei (1988) reported the average C:N ratio was 8 in the sedimenting material. The

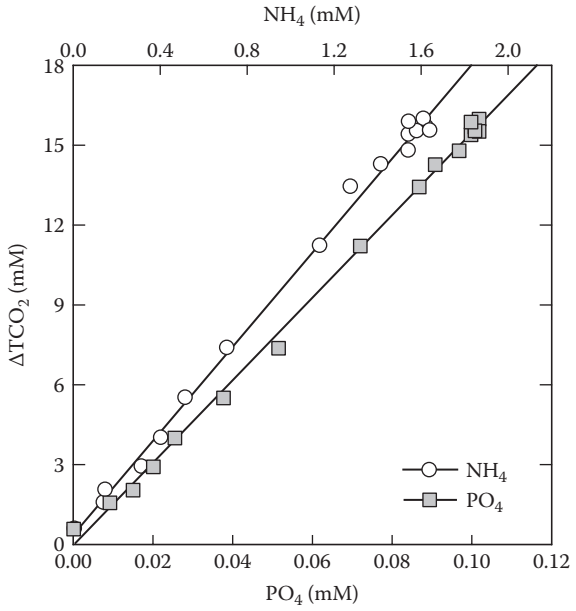

FIGURE 10.83
Plots of the changes in TCO_2 versus the changes in the concentrations of ammonia and phosphate.

particulate C:N ratios in the surface waters were found to be about 10 in June 1993 (McKee and Skei, 1999).

A plot of concentrations of TCO_2 versus PO_4^{3-} in the anoxic waters (20 to 175 m) of the Framvaren shows a C:P slope of 155 (±2) (Figure 10.83), which is much higher than the Redfield ratio of 106 and is also higher than the value of 127 for ocean waters suggested by Peng and Broecker (1987). These results indicate that the nutrients (N, P) show Redfield behavior in the Framvaren, while ratios of C:N and C:P are higher. Dyrssen (1989) suggested that the excess of carbohydrates could easily be explained by the addition of tree leaves and other terrestrial matter. It has also been proposed that phytoplankton can incorporate C, N, and P in ratios different from 106:16:1, depending on the availability of these elements. The high C:N and C:P ratios might result from the excess supply of inorganic carbon compared to N and P.

If we assume the C:N:P ratio of the organic matter in the Framvaren to be 155:16:1 based on the average value for all the data (20 to 175 m), Equation 10.65 can be rewritten as

$$(CH_2O)_{155}(NH_3)_{16}(H_3PO_4) + 77.5SO_4^{2-} = 155HCO_3^- + 77.5H_2S + 16NH_3 + H_3PO_4 \quad (10.73)$$

The increase of C:N and C:P ratios does not change the value of 2.0 for $\Delta TCO_2/\Delta H_2S$, while the ratio of $\Delta TA/\Delta H_2S$ decreases slightly from 2.3 to 2.2. The ratios of NH_4^+ and PO_4^{3-} to H_2S both decrease, from 0.30 to 0.20 and 0.019 to 0.013, respectively. We further assume that total inorganic carbon, ammonia, and phosphate in the anoxic waters of the Framvaren are produced only through the decomposition of organic matter based on Equation 10.72, and there are no significant removals for them. This assumption is supported, but not proved, by the fact that the correlations between C, N, and P are better than the correlations between C, N, P, and H_2S. To rebalance the measured NH_4^+:H_2S and PO_4^{3-}:H_2S ratios (0.30 and 0.019, respectively) to the new model values (0.20 and 0.013, respectively), the initially formed H_2S should equal

$$[H_2S]_{initi.} = (77.5/53) \times [H_2S]_{meas.}$$

In other words, about 30% of the H_2S produced from sulfate reduction has been removed, which corresponds to 2.8 m*M* SO_4^{2-} anomalies in the bottom water. This is equal to the estimate (about 3 m*M* in the bottom water) made by Dyrssen (1986) and Anderson, Dyrssen, and Hall (1988) by calculating the SO_4^{2-} balance (see Figure 10.84). As discussed, the removal of sulfide includes the processes such as oxidation, formation of FeS_2, diffusion, and incorporation into organic matter.

If we take the initially formed H_2S ($[H_2S]_{initi.}$) instead of the measured values, the ratios of TCO_2:$[H_2S]_{initi.}$ and TA:$[H_2S]_{initi.}$ are 2.04 and 2.33, respectively, which are close to the model values. The C:N ratio was 10 in the Black Sea, which is the same value as in the Framvaren. The extremely high value of C:P may be due to the anomalous behavior of phosphate, as discussed previously. Higher C:N and C:P ratios in the Black Sea may also have resulted from the large influence of terrestrial inputs. The C:N:P ratio in the Cariaco Trench, which is a typical open ocean with little terrestrial input, was 107:15:1 and agrees well with the Redfield value.

10.3.4 The Kinetics Oxidation of Hydrogen Sulfide in Natural Waters

The production of H_2S that occurs in stagnant basins (seas, lakes, rivers, and fjords) also occurs in the pore water of sediments because of biological processes and in hydrothermal systems because of geochemical processes. Molecular oxygen is the most important and

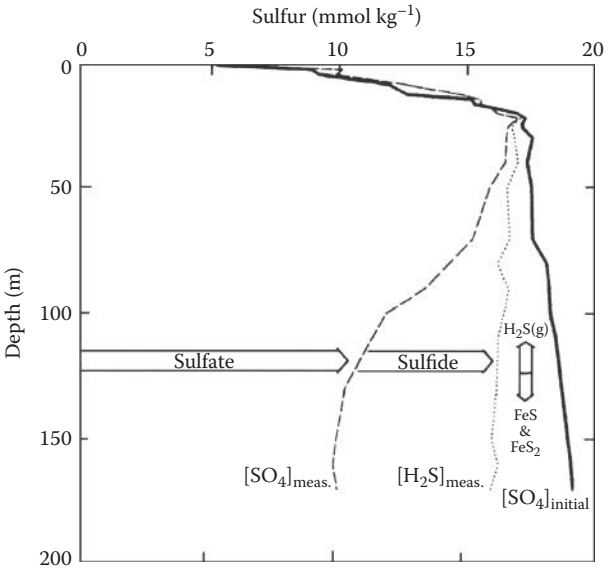

FIGURE 10.84
Plots of the various sulfur species in the Framvaren Fjord. The initial concentrations were calculated from the salinity using $SO_4/S = 28.28/35$ m*M*. (From Dyrssen, *Sci. Total Environ*., 5, 199, 1986. With permission.)

abundant oxidant for hydrogen sulfide in natural waters, followed by MnO_2 and Fe_2O_3. This oxidation involves a complex mechanism that results in the formation of several reduced sulfur species (i.e., thiosulfate, sulfite, elemental sulfur, and polysulfide) as well as sulfate. A number of studies of the oxidation of H_2S (Millero et al., 1987; Zhang and Millero, 1993a,b) and H_2SO_3 (Zhang and Millero, 1991) with O_2 in natural waters have been conducted in the laboratory and in the field. My research group has attempted to characterize how the rates and distributions of products are affected by trace metals and developed a kinetic model that can be used to predict the rates of oxidation and formation of products. The results of these studies are briefly reviewed in this section.

The overall rate equation for the oxidation of sulfide can be represented by

$$-d[H_2S]/dt = k[H_2S][O_2] \tag{10.74}$$

where the brackets represent concentrations. When oxygen is in excess, the rate of disappearance of H_2S can be simplified to

$$-d[H_2S]/dt = k'[H_2S] \tag{10.75}$$

where $k' = k[O_2]$. Plots of $\ln[H_2S]$ versus time during the oxidation will give a straight line with a slope of k′ (Figure 10.61). At a pH of 8.0, the rate constant (k, kg H_2O mol^{-1} h^{-1}) is given by (T, K)

$$\log k = 11.78 - (3.0 \times 10^3)/T + 0.44\, I^{1/2} \tag{10.76}$$

At 25°C, the half-time for the oxidation of H_2S with O_2 was found to be $t_{1/2} = \ln 2/k' = 50 \pm 16$ h in water and 26 ± 9 h in Gulf Stream seawater. The effect of pH in water is given by

$$k = (k_0 + k_1 K_1/[H+])/(1 + K_1/[H^+]) \quad (10.77)$$

where k_0 = 80 kg H_2O mol^{-1} h^{-1} for the oxidation of H_2S and k_1 = 344 kg H_2O mol^{-1} for the oxidation of HS^-:

$$H_2S + O_2 \xrightarrow{k_0} \text{Products} \quad (10.78)$$

$$HS- + O_2 \xrightarrow{k_1} \text{Products} \quad (10.79)$$

The value of K_1 is the dissociation constant for the ionization of H_2S. The effects of temperature and ionic strength on the rate constants k_0 and k_1 have been given by

$$\log k_0 = 9.22 - (2.4 \times 10^3)/T \quad (10.80)$$

$$\log k_1 = 10.50 + 0.16\ pH - (3.0 \times 10^3)/T + 0.44\ I^{1/2} \quad (10.81)$$

These equations are valid from pH = 4 to 8, t = 5 to 65°C, and I = 0 to 6 *M*.

Field measurements made on the oxidation of H_2S in the Black Sea (Millero, 1991c), the Framvaren Fjord (Millero, 1991a), the Chesapeake Bay (Millero, 1991b), and the Cariaco Trench (Zhang and Millero, 1993a,b) yielded half-times that were much faster than those determined in the laboratory on Gulf Stream seawater (see Figure 10.61). To determine if this increase was due to trace metals, we measured the rates of oxidation of H_2S in seawater with added transition metals (Vazquez, Zhang, and Millero, 1989). These studies show that at concentrations below 300 n*M*, the rates were only affected by Fe^{2+}, Cu^{2+}, and Pb^{2+}. At higher metal concentrations, the rates of oxidation of H_2S increased for all the metals except Zn^{2+}. The order of the increase in the rates at higher concentrations for these metals is $Fe^{2+} > Pb^{2+} > Cu^{2+} > Fe^{3+} > Cd^{2+} > Ni^{2+} > Co^{2+} > Mn^{2+}$.

Only Fe^{2+} and Mn^{2+} have levels in anoxic basins high enough to affect the oxidation of H_2S. The effect of metals on the oxidation of H_2S with oxygen can be estimated from (Figure 10.85)

$$\log(k/k_0) = a + b \log[M] \quad (10.82)$$

where

a = 6.55, b = 0.820 for Fe(II)
a = 5.18, b = 0.717 for Fe(III)
a = 1.68, b = 0.284 for Mn(II)

These equations are valid, respectively, from 10^{-8} to $10^{-5.3}$, $10^{-7.2}$ to $10^{-3.3}$, and $10^{-5.9}$ to $10^{-3.3}$ M.

The larger effect of Fe^{2+} is probably related to the formation of dissolved Fe^{3+} from the rapid oxidation of Fe^{2+} with oxygen. The oxidation of Fe^{2+} provides a higher initial concentration of Fe^{3+} than can be added from a stock solution of Fe^{3+} (which may be locally supersaturated). The peroxide generated by the oxidation of Fe^{2+},

$$O_2^- + H^+ = HO_2 \quad (10.83)$$

$$HO_2 + HO_2 = H_2O_2 + O_2 \quad (10.84)$$

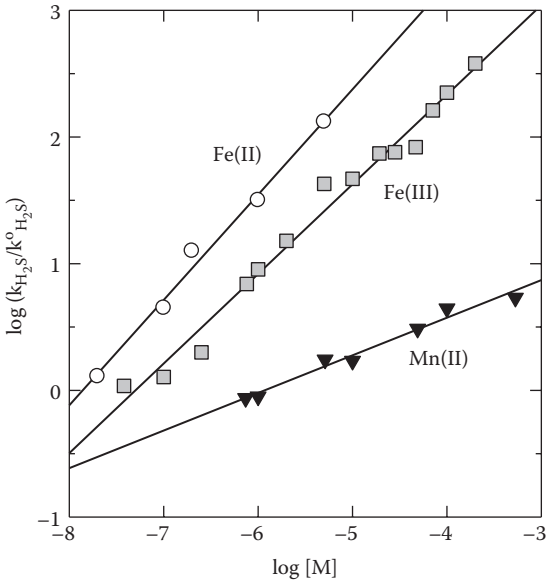

FIGURE 10.85
The effect of Fe and Mn on the rate of oxidation of H_2S in seawater at 25°C and pH 8.1.

can also increase the rates since it has a higher rate of oxidation with sulfide than oxygen. The Fe^{2+} formed from the reaction of dissolved or particulate Fe^{3+} can regenerate Fe^{2+} to complete the catalytic cycle. The effect of Fe^{3+} on the rates at low concentrations may be related to the reduction of Fe^{3+} to Fe^{2+} with HS^- and resultant oxidation of Fe^{2+} and generation of O_2^-. The effect of the metals on the rates of oxidation of H_2S below the observable precipitation of metal sulfides (which may be a slow process) can be attributed to the formation of ion pairs:

$$M^{2+} + HS^- \rightarrow MHS^+ \tag{10.85}$$

The overall rate constant is given by

$$k[HS^-]_T = k_{HS}[HS^-] + k_{MHS}[MHS^+] \tag{10.86}$$

where k_{HS} and k_{MHS} are the rate constants for the oxidation of HS^- and MHS^+, respectively. If k_{MHS} is greater than k_{HS}, the rate can be increased with the addition of the metal.

The presence of Fe and Mn in natural waters not only increases the rate of oxidation of sulfide but also can have an effect on the oxidation of intermediates such as sulfite. This can change the distribution of the products formed during the oxidation.

The final product of the oxidation of sulfide is sulfate, the sulfur compound with the highest oxidation state and the most stable compound in oxic waters. Various intermediates, such as sulfite and thiosulfate, also can be formed during the course of the reaction. The products formed from the oxidation of H_2S in seawater have been studied as a function of pH, temperature, salinity, and reactant concentration. To examine the mass balance of sulfur compounds during the oxidation, the experiments were made in pure water where SO_4^{2-} formed from oxidation could be measured by an ion chromatographic technique (Figure 10.86). The major products formed were SO_4^{2-}, SO_3^{2-}, and $S_2O_3^{2-}$. Elemental sulfur

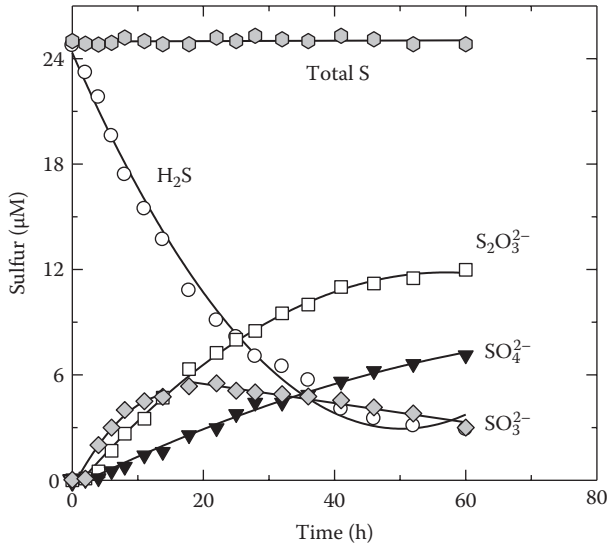

FIGURE 10.86
The various sulfur species form during the oxidation of H_2S in water at 50°C and pH 8.2. The smooth curves were calculated from the model.

or polysulfides were not found by spectroscopic techniques. The total equivalent sulfur of the products and reactants was constant, indicating that SO_4^{2-}, SO_3^{2-}, and $S_2O_3^{2-}$ were the main products. The distribution of products from the oxidation of H_2S in seawater was similar to the results in water (see Figure 10.86).

The concentration of thiosulfate increased slowly throughout the reaction after an initial lag period. This suggests that thiosulfate was not the initial product of the oxidation. Thiosulfate is a stable product in the absence of bacteria, and little oxidation occurs over 80 h. The effect of pH on the distribution of products has also been examined, and the results have been attributed to changes in the rates of the individual reaction steps. The effect of metals (Fe^{2+}, Fe^{3+}, Mn^{2+}, Cu^{2+}, and Pb^{2+}) and solids (FeOOH and MnO_2) on the distribution of products has also been studied. The intermediates formed during the oxidation of Cariaco Trench waters (350 n*M* Fe^{2+}) clearly show that metals not only increase the rate of oxidation of H_2S but also change the distribution of products.

A kinetic model was formulated based on the concentration–time dependence of the reactants (sulfide and oxygen) and products (sulfite, thiosulfate, and sulfate). The validity of the model was evaluated by comparing the model predictions with the experimental measurements of reactants and products. At low concentrations, the overall oxidation of HS^- with O_2 is given by

$$H_2S + O_2 \xrightarrow{k_1} \text{Products } (SO_3) \tag{10.87}$$

$$H_2SO_3 + O_2 \xrightarrow{k_2} \text{Products } (SO_4) \tag{10.88}$$

$$H_2S + H_2SO_3 + O_2 \xrightarrow{k_3} \text{Products } (S_2O_3) \tag{10.89}$$

The overall rate equations for H_2S, SO_3^{2-}, $S_2O_3^{2-}$, and SO_4^{2-} are given by

$$d[H_2S]/dt = -k_1[H_2S][O_2] - k_3[H_2S][SO_3^{2-}][O_2] \quad (10.90)$$

$$d[SO_3^{2-}]/dt = k_1[H_2S][O_2] - k_2[SO_3^{2-}]^2\,[O_2]^{1/2} - k_3[H_2S][SO_3^{2-}][O_2] \quad (10.91)$$

$$d[S_2O_3^{2-}]/dt = k_3[H_2S][SO_3^{2-}][O_2] \quad (10.92)$$

$$d[SO_4^{2-}]/dt = k_2[SO_3^{2-}]^2\,[O_2]^{1/2} \quad (10.93)$$

where [i] is the total concentration of i.

These rate equations have been integrated simultaneously to evaluate the values of k_1, k_2, and k_3 using the experimental time dependence concentrations of all the reactants and products. The experimentally measured concentrations of H_2S, SO_3^{2-}, $S_2O_3^{2-}$, and SO_4^{2-} were found to be in good agreement with the model predictions up to reaction times of 80 h (Figure 10.87). The values of k_2 in seawater needed to fit the data were slightly smaller than the values determined in our previous study, especially at higher temperatures. This was probably because of the inhibition of the oxidation of sulfite in the presence of sulfide. This finding is supported by the previous observations that sulfite in the presence of H_2S is more stable in seawater than predicted by its rate of oxidation.

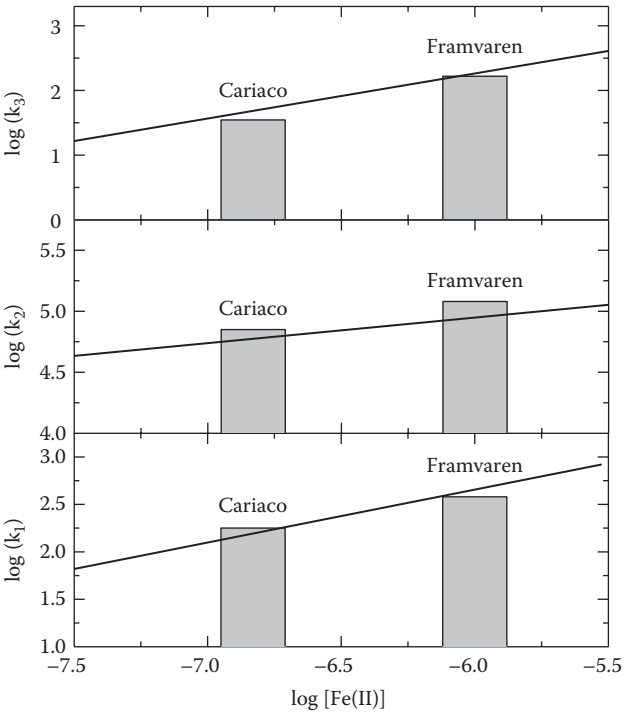

FIGURE 10.87
Comparison of the rate constants for the oxidation of H_2S (k_1) and H_2SO_3 (k_2) and formation of S_2O_3 (k_3) in the Cariaco Trench and Framvaren Fjord and those produced at the same levels of Fe. The lines are the rate constants predicted from laboratory measurements at various concentrations of Fe(II).

The values of k_1, k_2, and k_3 as a function of salinity (S) and temperature (T K) have been fitted to the equations (pH = 8.2):

$$\ln k_1 = 26.90 + 0.0322\ S - 8123.21/T \tag{10.94}$$

$$\ln k_2 = 14.91 + 0.0524\ S - 1764.68/T \tag{10.95}$$

$$\ln k_3 = 28.92 + 0.0369\ S - 8032.68/T \tag{10.96}$$

These equations should be valid for estuarine and seawaters over a wide range of salinity and temperature. This kinetic model can be used to predict the product distribution for the oxidation of sulfide in natural waters with low concentrations of trace metals. The agreement between the model and the observed distribution of reaction products does not provide conclusive proof that the reaction pathways of the overall model actually describe the series of elemental reactions that occur. The detailed mechanisms might involve many elemental reaction steps.

The rates of oxidation of hydrogen sulfide, the effect of metals, and the intermediates formed have been examined in a number of natural anoxic basins, such as the Black Sea, the Cariaco Trench, the Chesapeake Bay, and the Framvaren Fjord. The field measurements of the rates of oxidation of H_2S were found (Figure 10.86) to be in good agreement with those estimated from laboratory studies at the same concentration of Fe^{2+}. The levels of Fe^{2+} are high enough in most anoxic environments to increase the rates of oxidation of H_2S. A kinetic model has been used to analyze the distribution of products (SO_3^{2-}, $S_2O_3^{2-}$, SO_4^{2-}) formed during the oxidation in the Framvaren Fjord and the Cariaco Trench. The rate constants for the production of SO_3^{2-} (k_1), SO_4^{2-} (k_2), and S_2O_3 (k_3) estimated for these waters were in reasonable agreement with the predicted values at the same level of Fe^{2+}.

The values of k_2 estimated for the Framvaren Fjord and Cariaco Trench were slightly higher than the predicted values. This could have been due to errors in our estimation of the concentration and form of iron in these waters. Direct measurements of iron and manganese in anoxic waters should be made in all future kinetic studies to avoid this problem. The estimates based on only the concentration of iron may also lead to some errors. The concentrations of Mn^{2+} below the oxic–anoxic interface reached levels of 0.5 and 15 μ*M* in the Cariaco Trench and Framvaren Fjord, respectively. This Mn^{2+} came from reduction of MnO_2 sinking from above the oxic–anoxic interface. Reoxidation of Mn^{2+} to MnO_2 by bacteria occurs when Mn^{2+} diffuses up to the oxic layer. This cycling of manganese between Mn^{2+} and MnO_2 is an important feature of the oxic–anoxic interface and probably affects the distribution of products in the field. The products ($S_2O_3^{2-}$, SO_3^{2-}, and SO_4^{2-}) formed during the oxidation in the Framvaren also have been examined and used to determine k_1, k_2, and k_3 (Table 10.12). The measured results are compared in Figure 10.86, with the estimated values at the same level of Fe. The agreement is quite good.

TABLE 10.12

Comparison of the Rate Constants for the Oxidation of Hydrogen Sulfide in Different Waters

Rate Constant	Gulf Stream	Cariaco Trench		
		Surface	Mixed	Deep
k_1	1.7	3.1	18.4	36.3
k_2	48,000	48,000	72,000	240,000
k_3	30	15	180	360

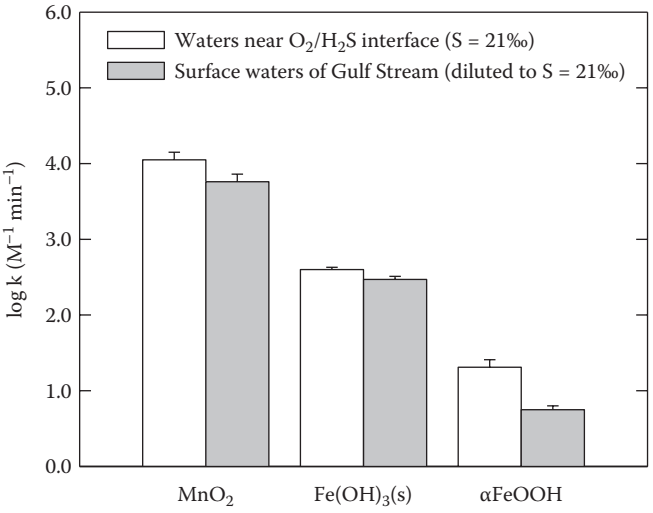

FIGURE 10.88
Comparison of the rates of oxidation of H_2S by Mn(IV) and Fe(III) (hydr)oxides in the Framvaren Fjord and laboratory measurements.

Yao and Millero (1995) examined how the oxidized products of Fe^{2+} and Mn^{2+} that occur above the anoxic–oxic interface can oxidize hydrogen sulfide and complete the redox cycle of these metals in anoxic waters (Figure 10.87). These reactions are much more complicated since they occur on the surfaces of the oxide minerals. The rates of oxidation of H_2S by Mn(IV) and Fe(III) (hydr)oxides in the water near the interface (~21 m) were determined and compared with the values obtained in the surface waters of the Gulf Stream (Figure 10.88) in the laboratory. The agreement is quite good. The slightly higher oxidation rates observed in the field might be related to the microbiological activities near the interface.

References and Further Reading

Photochemistry

Bielski, B.H.J., Re-evaluation of the spectra and kinetics properties of HO_2 and O_2^- free radicals, *Photochem. Photobiol.*, 38, 450 (1978).

Heltz, G.R., Zepp, R.G., and Crosby, D.G., *Aquatic and Surface Photochemistry*, Lewis, Boca Raton, FL (1994).

King, D.W., Lounsbury, H.A., and Millero, F.J., Rates and mechanism of Fe(II) oxidation at nanomolar total iron concentrations, *Environ. Sci. Technol.*, 29, 818 (1995).

Millero, F.J., Estimate of the life time of superoxide in seawater, *Geochim. Cosmochim. Acta*, 51, 351 (1987).

Moffett J.W., and Zafiriou, O.C., An investigation of hydrogen peroxide chemistry in surface waters of Vineyard Sound with $H_2{}^{18}O_2$ and $^{18}O_2$, *Limnol. Oceanogr.*, 35, 1221 (1990).

Moffett, J.W., and Zika, R.G., Measurement of copper (I) in surface waters of the subtropical Atlantic and Gulf of Mexico, *Geochim. Cosmochim. Acta*, 52, 1849 (1988).

Mopper, K., and Zhou, Z., Hydroxyl radical photoproduction in the sea and its potential impact on marine processes, *Science*, 250, 661 (1990).

Palenik, B., and Morel, F.F.M., Dark production of H_2O_2 in the Sargasso Sea, *Limnol Oceanogr*., 33, 1606 (1988).
Petasne, R.G., and Zika, R.G., Fate of superoxide in coastal waters, *Nature,* 325, 516 (1988).
Rush, J.D., and Bielski, B.H.J., Pulse radiolysis studies of the reactions of HO_2/O_2^- with ferric ions and its implication on the occurrence of the Haber–Weiss reaction, *J. Phys. Chem*., 89, 5062 (1985).
Sharma, V.K., and Millero, F.J., Oxidation of copper(I) in seawater, *Environ. Sci. Technol.*, 22, 768 (1988).
True, M., and Zafiriou, O.C., Reaction of Br_2^- by flash photolysis of seawater, in *Photochemistry of Environmental Aquatic System,* ACS Symp. Ser. 327, ACS, Washington, DC, pp. 166–170 (1987).
Zafiriou, O.C., Natural water photochemistry, Chapter 48, *Chemical Oceanography*, Vol. 8, 2nd ed., Riley, J.P., and Chester, R., Eds., Academic Press, New York, 339–379 (1983).
Zafiriou, O.C., Chemistry of superoxide ion-radical (O_2^-) in seawater. I. pK^*_{ASW}(HOO) and uncatalyzed dismutation kinetics studied by pulse radiolysis, *Mar. Chem*., 30, 31 (1990).
Zika, R.G. Marine organic photochemistry, in *Marine Organic Chemistry,* Duursma, E.K., and Dawson, R., Eds., Elsevier, Amsterdam, The Netherlands, 299–325 (1981).
Zika, R.G., and Cooper, W.J., *Photochemistry of Environmental Aquatic Systems,* ACS Symp. Ser. 327, ACS, Washington, DC (1987).
Zika, R.G., et al., H_2O_2 levels in rainwater collected in South Florida and the Bahamas Islands, *J. Geophys. Res*., 87, 5015 (1982).
Zika, R.G., Saltzman, E., and Cooper, W.J., Hydrogen peroxide concentrations in the Peru upwelling area, *Mar. Chem*., 17, 265 (1985).

Hydrothermal Vents

Bonatti, E., and Joensuu, O., Deep sea iron deposits from the South Pacific, *Science*, 154, 643 (1966).
Bostrom, K., and Peterson, M.N.A., Precipitates from hydrothermal exhalations on the East Pacific rise, *Econ. Geol*., 61, 1258–1265 (1966).
Childress, J.J., Ed., Hydrothermal vents (special issue), *Deep-Sea Res*., 35, (1988).
Coale, K.H., Chin, C.S., Massoth, G.J., Johnson, K.S., and Baker, E.T., In situ chemical mapping of dissolved iron and manganese in hydrothermal plumes, *Nature,* 352, 325 (1991).
Foustoukos, D.I., and Seyfried, W.E., Jr., Hydrocarbons in hydrothermal vent fluids: the role of chromium-bearing catalysts, *Science,* 304, 1002 (2004).
German, C.R., et al., Hydrothermal scavenging at the Mid-Atlantic Ridge: modification of trace element dissolved fluxes, *Earth Planet Sci. Lett*., 107, 101 (1991).
Johnson, K.S., Beehler, C.L., and Sakamoto-Arnold, C.M., A submersible flow analysis system, *Anal. Chim. Acta,* 179, 245 (1986).
Jones, E.J.W., Sea-floor spreading and the evolution of the ocean basins, Chapter 35, *Chemical Oceanography,* Vol. 7, 2nd ed., Riley, J.P., and Chester, R., Eds., Academic Press, New York, 1–74 (1978).
Karl, D.M., Ed., *The Microbiology of Deep-Sea Hydrothermal Vents,* CRC Press, Boca Raton, FL (1995).
Noble, A.E., et al., Basin-scale inputs of cobalt, iron, and manganese from the Benguela-Angola front to the South Atlantic Ocean, *Limnol. Oceanogr*., 57, 989–1010 (2012).
Rona, P.A., Bostrom, K., Lanbier, L., and Smith, K.L., Jr., *Hydrothermal Processes at Seafloor Spreading Centers,* NATO Conf. Ser. IV, Mar. Sci., Plenum Press, New York (1983).
Thompson, G., Hydothermal fluxes in the oceans, Chapter 47, *Chemical Oceanography,* Vol. 8, 2nd ed., Riley, J.P., and Chester, R., Eds., Academic Press, New York, 272–337 (1983).

Anoxic Basins

Broecker, W.S., and Peng, T.H., *Tracers in the Sea*, ELDIGO Press, New York (1982).
Deuser, W.G., Reducing environments, Chapter 16, *Chemical Oceanography,* Vol. 3, 2nd ed., Riley, J.P., and Skirrow, G., Eds., Academic Press, New York, 1–37 (1975).

Edmond, J.M., Measures, C., Mangum, B., Grant, B., Sclater, F.R., Collier, R., Hudson, A., Gordon, L.I., and Corliss, J.B. On the formation of metal-rich deposits at ridge crests, *Earth Planet. Sci. Ltrs*, 46, 1–8 (1979b).

Edmond, J.M., Measures, C., McDuff, R.E., Chan, L.H., Collier, R., Grant, B. Gordon, L.I., and Corliss, J.B. Ridgecrest hydrothermal activity and the balances of the major and minor elements in the ocean: The Galapagos data, *Earth Planet. Sci. Ltrs*, 46, 1–8 (1979a).

Friederich, G.E., et al., Tech. Rept. No. 90-3. Monterey Bay Aquarium Research Institute (1988).

Grasshoff, K., The hydrochemistry of landlocked basins and fjords, Chapter 15, *Chemical Oceanography,* Vol. 2, 2nd ed., Riley, J.P., and Skirrow, G., Eds., Academic Press, New York, 456–597 (1975).

Richards, F.A., Anoxic basins and fjords, Chapter 13, *Chemical Oceanography,* Vol. 1, Riley, J.P., and Skirrow, G., Eds., Academic Press, New York, 611–645 (1965).

Black Sea

Dyrssen, D., Some calculations on Black Sea chemical data, *Chemical Scripta*, 5, 199 (1985).

Goyet, C., Bradshaw, A.L., and Brewer, P.G., The carbonate system in the Black Sea, *Deep-Sea Res. A,* 38, S1049 (1991).

Grasshoff, K., The hydrochemistry of landlocked basins and fjords, Chapter 15, *Chemical Oceanography,* Vol. 2, 2nd ed., Riley, J.P., and Skirrow, G., Eds., Academic Press, New York, 456–597 (1975).

Haraldsson, C., and Westerlund, S., Trace metals in the water columns of the Black Sea and Framvaren Fjord, *Mar. Chem*., 23, 417 (1988).

Hiscock, W., and Millero, F.J., Alkalinity of the anoxic waters in the Western Black Sea, *Deep-Sea Res. II*, 53, 1787–1801 (2006).

Izdar, E., and Murray, J., Eds., *Black Sea Oceanography,* NATO ASI SERIES, Kluwer Academic, Dordrecht, The Netherlands (1991).

Millero, F.J., The oxidation of H_2S in Black Sea waters, *Deep-Sea Res*., 38, S1139 (1991).

Murray, J.M., Codispoti, L.A., and Friederich, G.E., Oxidation–reduction environments: the suboxic zone in the Black Sea, in *Aquatic Chemistry; Interfacial and Interspecies Processes,* Huang, C.P., O'Melia, C.R., and Morgan, J.J., Eds., Adv. Chem. Ser. 244, Am. Chem. Soc., New York, 157–176 (1995).

Schijf, J., De Baar, H.J.W., Wijbrans, J.R., and Landing, W.M., Dissolved rare earths in the Black Sea, *Deep-Sea Res*., 38, 805 (1991).

Cariaco Trench

Bacon, M.P., Brewer, P.G., Spencer, D.W., Murray, J.W., and Goddard, J., Lead-210, polonium-210, manganese and ion in the Cariaco Trench, *Deep-Sea Res.,* 27, 119 (1980).

Fanning, K.A., and Pilson, M.E.Q., A model for the anoxic zone of the Cariaco Trench, *Deep-Sea Res.,* 19, 847 (1972).

Holmen, K.J., and Rooth, C.G.H., Ventilation of the Cariaco Trench, a case of multiple source competition? *Deep-Sea Res.,* 37, 203 (1991).

Hughen, K., Overpeck, J.T., Peterson, L.C., and Anderson, R.F., The nature of varved sedimentation in the Cariaco Basin, Venezuela, and its paleoclimatic significance, in *Palaeoclimatology and Palaeoceanography from Laminated Sediments,* Kemp, A.E.S., Ed., Geol. Soc. Special Publ., 116, 171–183 (1996).

Scranton, M.I., Scales, F.L., Bacon, M.P., and Brewer, P.G., Temporal changes in the hydrography and chemistry of the Cariaco Trench, *Deep-Sea Res.,* 34, 945 (1987).

Zhang, J.-Z., and Millero, F.J., The chemistry of the anoxic waters in the Cariaco Trench, *Deep-Sea Res.,* 40, 1023 (1993).

Framvaren Fjord

Anderson, L.G., Dyrssen, D., and Hall, P.O.J., On the sulfur chemistry of a super-anoxic fjord, Framvaren, South Norway, *Mar. Chem.*, 23, 283 (1988).

Brewer, P.G., and Murray, J.M., Carbon, nitrogen and phosphorus in the Black Sea, *Deep-Sea Res.*, 20, 803 (1973).

Dyrssen, D., Stagnant sulphidic basin waters, *Sci. Total Environ.*, 5, 199 (1986).

Dyrssen, D., Biogenic sulfur in two different marine environments, *Mar. Chem.*, 28, 241 (1989).

Dyrssen, D., Hall, P., Haraldsson, C., Iverfeldt, A., and Westerlund, S., Trace metal concentrations in the anoxic bottom water of Framvaren, in *Complexation of Trace Metals in Natural Waters,* Kramer, C.J.M., and Duinker, J.C., Eds., Martinus Nijhoff/W. Junk, The Hague, 239–245 (1984).

Grasshoff, K., The hydrochemistry of landlocked basins and fjords, Chapter 15, *Chemical Oceanography,* Vol. 2, 2nd ed., Riley, J.P., and Skirrow, G., Eds., Academic Press, New York, 456–597 (1975).

Haraldsson, C., and Westerlund, S., Trace metals in the water columns of the Black Sea and Framvaren Fjord, *Mar. Chem.*, 23, 417 (1988).

Jacobs, L., Emerson, S., and Skei, J.M., Partitioning and transport of metals across the O_2/H_2S interface in a permanently anoxic basin: Framvaren Fjord, Norway, *Geochim. Cosmochim. Acta,* 49, 1433 (1985).

Landing, W.M., and Westerlund, S., The solution chemistry of iron (II) in Framvaren Fjord, *Mar. Chem.*, 23, 329 (1988).

McKee, B., and Skei, J.M., Framvaren Fjord as a natural laboratory for examining biogeochemical processes in anoxic environments., *Mar. Chem.*, 67, 147 (1999).

Millero, F.J., The oxidation of H_2S in Framvaren Fjord, *Limnol. Oceanogr.*, 36, 1007 (1991).

Naes, K., and Skei, J.M., Total particulate and organic fluxes in anoxic Framvaren waters, *Mar. Chem.*, 23, 257 (1988).

Redfield, A.C., Ketchum, B.H., and Richards, F.A., The influence of organisms on the composition of seawater, in *The Sea,* Vol. 2, Hill, M.N., Ed., Interscience, New York, 26–77 (1963).

Skei, J.M., *Geochemical and Sedimentological Considerations of a Permanent Anoxic Fjord—South Norway*, Data Report 1931-1985, Norwegian Institute for Water Research, Oslo, Norway (1983).

Skei, J.M., Formation of framboidal iron sulfide in the water of a permanently anoxic fjord—Framvaren, south Norway, *Mar. Chem.*, 23, 345 (1988a).

Skei, J.M., Framvaren—environmental setting, *Mar. Chem.*, 23, 209 (1988b).

Sørensen, K., The distribution and biomass of phytoplankton and phototrophic bacteria in Framvaren, a permanently anoxic fjord in Norway, *Mar. Chem.*, 23, 229 (1988).

Takahashi, T., Broecker, W.S., and Langer, S., Redfield ratio based on chemical data from isopycnal surfaces, *J. Geophys. Res.*, 90, 6907 (1985).

Wangerski, P.J., Ed., Framvaren Fjord (special issue), *Mar. Chem.*, 23 (1988).

Yao, W., and Millero, F.J., The chemistry of the anoxic waters in the Framvaren Fjord, Norway, *Aquatic Geochem.*, 1, 53–88 (1995).

Kinetics Oxidation of Hydrogen Sulfide in Natural Waters

Millero, F.J., The thermodynamics and kinetics of the hydrogen sulfide system in natural waters, *Mar. Chem.*, 18, 121 (1986).

Millero, F.J., The oxidation of H_2S in Black Sea waters, *Deep-Sea Res.*, 38, S1139 (1991a).

Millero, F.J., The oxidation of H_2S in Chesapeake Bay, Estuarine, *Coastal Shelf Sci.*, 33, 21 (1991b).

Millero, F.J., The oxidation of H_2S in Framvaren Fjord, *Limnol. Oceanogr.*, 36, 1007 (1991c).

Millero, F.J., and Hershey, J.P., Thermodynamics and kinetics of hydrogen sulfide in natural waters, in *Biogenic Sulfur in the Environment*, Saltzman, E., and Cooper, W.J., Eds., ACS Press, Washington, DC, 282–313 (1989).

Millero, F.J., Hubinger, S., Fernandez, M., and Garnett, S., The oxidation of H_2S in seawater as a function of temperature, pH and ionic strength, *Environ. Sci. Technol.*, 21, 439 (1987).

Peng, T.H., and Broecker, W.S., C/P ratios in marine detritus, *Global Biogeochem. Cycles*, 1, 155 (1987).

Vazquez, F., Zhang, J.-Z., and Millero, F.J., Effect of trace metals on the oxidation rates of H_2S in seawater, *Geophys. Res. Lett.*, 16, 1363 (1989).

Yao, W., and Millero, F.J., The rate of sulfide oxidation by δMnO_2 in seawater, *Geochim. Cosmochim. Acta*, 57, 3359 (1993).

Yao, W., and Millero, F.J., Oxidation of hydrogen sulfide by Mn(IV) and Fe(III) (hydr)oxides in seawater, Chapter 14, *Geochemical Transformation of Sedimentary Sulfur*, Vairavamurthy, M.A., and Schoonen, M.A., Eds., ACS Press, Washington, DC, 260–279 (1995).

Zhang, J.-Z., and Millero, F.J., The rate of sulfite oxidation in seawater, *Geochim. Cosmochim. Acta*, 55, 677 (1991).

Zhang, J.-Z., and Millero, F.J., The chemistry of the anoxic waters in the Cariaco Trench, *Deep-Sea Res.*, 40, 1023 (1993a).

Zhang, J.-Z., and Millero, F.J., The products from the oxidation of H_2S in seawater, *Geochim. Cosmochim. Acta*, 57, 1705 (1993b).

Glossary of Chemical Oceanography Terms

I. Descriptive Oceanography

Adiabatic: A process occurring without exchange of heat with the surroundings.

Adiabatic Temperature: The change in temperature of seawater due to the effect of pressure.

Agulhas Current: An Indian Ocean current that flows south along the southeastern coast of Africa.

Alaska Current: Flows northward from the coast of Alaska to the Bering Strait.

Antarctic Bottom Water (AABW): Formed in the Weddell and Ross Seas. A mixture of circumpolar and shelf water. Formed due to its high density.

Antarctic Convergence Zone: Where Antarctic intermediate water forms, the surface temperature rapidly increases 2–3°C (50° S in Atlantic and Indian, 60° S in the Pacific).

Antarctic Intermediate Water (AAIW): Forms at the Antarctic convergence. Includes Antarctic surface water and circumpolar water. Salinities less than 34.5 are found due to the melting of ice.

Antarctic Surface Water: Water that forms the Antarctic intermediate waters from the circumpolar waters.

Antarctic Zone: Area from the continent to the Antarctic convergence. Surface temperature of the water is –2 to 1°C in winter and –1 to 4°C in the summer.

Antilles Current: Flows northward from northern South America on the northern side of the Antilles to join the Florida Current, composed mostly of North Atlantic water (125 Sv).

Aragonite: Crystalline form of calcium carbonate, formed by pteropods (Bahama Banks).

Bar Built Estuary: An estuary that has a narrow channel between the shore and a bar built as a result of waves and sedimentation.

Basin: Relatively flat area; a large portion of the deep-sea bottom.

Benguilla Current: A continuation of the Brazil current with a lower salinity that flows north and northwest along the western coast of Africa and contains cold waters.

Bering Seawater: Warmer and denser water than the water in the Canadian Basin. Has a higher salinity and leads to the halocline in the Canadian Basin as it flows inward.

Biogenous: One of the four sediment types; formed by biological processes (e.g., shells of calcite).

Brazil Current: A current of warm, saline water that is a southern continuation of the South Equatorial Current and becomes part of the Circumpolar Current after flowing southward along the eastern coast of South America.

Break in Slope: The outer limit of the shelf with a slope of 1 to 20 and an average depth of 130 m.

Calcite: Crystalline form of calcium carbonate (rhombohedral form) that formed foraminifera and cocoliths—an example of biogenous sediment.

California Current: Flows south along the western United States and Peru; results in coastal upwelling and lower water temperatures.

Canadian Basin: Basin in the Arctic Sea; contains waters that move in a clockwise gyre that flow out to become the East Greenland Current (depth of 3800 m).

Canary Current: A current flowing south from the North Atlantic Current along the northwestern coast of Africa. Continues south to join the North Equatorial Current.

Circumpolar Current: Flows clockwise around the South Pole. Has a northerly component and the largest volume flow rate (150–190 Sv) in the ocean.

Clay: Product of the weathering of rocks. Fine particles of hydrous aluminum silicates and other minerals. An example of a lithogenous sediment. Clay is transported to the oceans by rivers, wind, volcanic action, and glacial waters.

Coastal Plain Estuary: An estuary that results from land subsidence or a rise of sea level.

Cold Core Rings: Gulf Stream eddies formed in the northern part of the Gulf Stream Current. The rings flow as a counterclockwise gyre and move to the south. They carry cold, high-nutrient water from the coastal water north of the Gulf Stream to the south. Rings can exist 2 to 4 yr, but most rejoin the Gulf Stream after 1/2 or 1 yr.

Continent: One of the six great divisions of land masses on the globe.

Continental Slope: Averages 4000 m from shelf to sea bottom, sometimes as much as 9000 m.

Convergence Zones: Area where ocean characteristics (T, S) change rapidly (e.g., subtropical convergence).

Cosmogenous: One of the four types of sediment; of cosmic or extraterrestrial origin (meteorites).

Cromwell Current: A current in Equatorial Pacific once found and forgotten until it was rediscovered by Cromwell. It was not predicted by theory. It is an undercurrent at the equator with an average transport of 40 Sv and speeds up to 170 cm s^{-1}.

Deep-Basin Estuary: An estuary that has a sill toward the sea that is shallower than the basin and the outside sea.

Deep-Sea Bottom: Represents the most extensive area of the ocean; from 3 to 6 km in depth.

Deep Water: Water located below the intermediate waters. Generally has very low temperature (2°C) and high salinity (34.9), yielding a high density.

Dicothermal Layer: A layer in ocean waters at high latitudes where cold waters are sandwiched between two warmer layers; stability is maintained by an increase in salinity through the layer.

Drake Passage: Area between the southern tip of South America and Antarctica, connecting the Atlantic and Pacific Oceans. The Circumpolar Current passes through this region.

East Australian Current: Southward-flowing water along the eastern coast of Australia.

East Greenland Current: Flows south with a transport of 7.5 Sv along eastern coast of Greenland. Carries ice and waters from the Arctic Sea into the North Atlantic.

East Wind Drift: The current that flows counterclockwise around Antarctica, driving surface water circulation.

Equation of State: An equation that describes the volume properties of seawater as a function of salinity, temperature, and pressure.

Equator: The dividing boundary between the Northern and Southern Hemispheres formed by the intersection of a plane passing through the earth's center perpendicular to its axis of rotation.

Equatorial Countercurrent: Flows southeast between the west-moving North Equatorial Current and the South Equatorial Current. The current speed slows in the spring,

separating the main gyres in the Atlantic and Pacific. The current flows in a direction opposite to the Equatorial Current.

Equatorial Current: Waters that move westward along or near the equator.

Estuary: A semienclosed body of coastal water formed by the mixing of river waters with seawaters.

Eurasian Basin: Basin in the Arctic Sea; contains waters that move with a countergyre (depth of 4200 m).

Evaporation: Process of conversion of liquid to vapor. Causes an increase in the salinity.

Falkland Current: Flows north off the eastern coast of South America from the Drake Passage up the eastern coast of South America.

Ferrel Cells: Midlatitude air circulation due to rising air at northern midlatitudes and sinking air at southern midlatitudes.

Florida Current: Formed from the waters that go through the Yucatan and the Gulf of Mexico. Flows between South Florida and Cuba (26 Sv).

Gulf Stream: A strong (80-Sv) current in the western North Atlantic that is a northern extension of the Florida Current and flows northeast to the Grand Banks off Newfoundland.

Hadley Cells: Circular air circulation in the tropics caused by rising air at the equator and sinking air in the high-latitude tropics (0–30° latitude).

Halocline: Steep vertical gradient of salinity in ocean waters.

Head: The portion of an estuary where the river water enters.

Highly Stratified Estuary: An estuary where the upper layer increases in salinity from zero at the head to close to that of seawater at the mouth. The deep water has an almost-uniform salinity. Outflow occurs in the surface layer and inflow in the deeper water. This results in the formation of a strong halocline. The circulation is dependent on the sill depth.

Horizontal Circulation: Transverse circulation; primarily a result of wind flowing across the ocean surface.

Hydrogenous: One of the four sediment types; formed by reactions such as precipitation and adsorption in the ocean water.

Intermediate Water: Water located between upper and deep waters. Sinks because of higher density caused mainly by cold temperatures.

Island Arc: An island created through uplifting of the earth's crystal layer. Island arcs are usually located in areas of intense volcanic activity, such as a subduction zone.

Isotherm: Lines connecting depths or locations of constant temperature in the oceans.

Kuroshio Current: Analogous to the Atlantic's Gulf Stream (65 Sv). It flows along the eastern coast of Asia.

Kuroshio Extension: Extension of the Kuroshio Current northward in the North Pacific.

Labrador Current: A low-salinity and -temperature current that flows south between North America and Greenland out of the Labrador Sea.

Latitude: Angular distance north or south of the equator; measured in degrees.

Lithogenous: One of the four sediment types; formed from rocks or weathered rock fragments (e.g., clays).

Longitude: Angular distance on the earth, east or west of the prime meridian at Greenwich, England, to the point on the earth's surface being determined. Expressed in degrees. The axis runs through both poles.

Mediterranean Water: High-salinity (39) intermediate water formed in the Mediterranean Sea. Enters the Atlantic as an overflow at Gibraltar (15°C and S = 37.3).

Meteorites: Extraterrestrial material that reaches the earth from outer space; forms cosmogenous sediment.

Mixed Estuary: An estuary with a shallow basin where the water is well mixed. This leads to similar salinities throughout the water column. The salinity increases as the water flows from the head to the mouth.

Mixed Layer: Upper layer of ocean surface waters (5 to 200 m) where the properties are homogenous because of mixing caused by wind stress.

Monsoon Current: Replaces the North Equatorial Current during monsoon season (May–September); driven by the monsoon winds. The current also causes the Equatorial Countercurrent to disappear.

Mouth: The portion of an estuary closest to the sea.

Negative Estuary: An estuary of high salinity caused by evaporation greater than precipitation and river runoff.

North Atlantic Current: A warm current that is a continuation of the Gulf Stream; high-salinity waters that flow northeasterly in the North Atlantic. It divides into the Norwegian Current going north and the Canary Current going south.

North Atlantic Deep Water (NADW): Major water mass in the Atlantic Ocean. Formed in the Norwegian Sea and flows in pulses over sills between Scotland, Iceland, and Greenland (S = 34.9, t = 2 to 3°C).

North Equatorial Current: Flows westward from North Africa to the Gulf Stream driven by northeast trade winds (45 Sv, with surface speeds of 25 to 30 cm s^{-1}).

Norwegian Current: Continuation of a portion of the North Atlantic Current flowing between the Shetland and Farrel Islands northward into the Norwegian Sea.

Oyashio Current: A cold current that flows northeast along the eastern Asia coast.

Peru Current: A cold, slow, and shallow water current flowing north off the west coast of South America.

Polar Cells: Air circulation caused by sinking air at the poles and rising air at high latitudes (60 to 90° latitude).

Polar Front: An area characterized by strong temperature gradients. Warm and cold air converge in the Polar Front Zone (approximately 55 to 60° N and further north).

Positive Estuary: An estuary of low salinity caused by precipitation and river runoff greater than evaporation.

Potential Temperature: Temperature of seawater corrected for the effects of pressure. The application of pressure (depth) to seawater causes the temperature to increase.

Practical Salinity: The salinity determined from conductivity measurements. It has no units since it is a ratio of conductance of an unknown and a standard. It has and still is denoted as S and should be denoted as S_P. For average seawater, S_P = 35.00, and the reference or absolute salinity is 35.16504 g/kg for surface water with little silica.

Precipitation: Formation of a solid from solution by physical or chemical processes. Formation of rain, hail, snow, or mist from cloud water. Causes the salinity to decrease and accounts for the lower salinities near the equator.

Profile: The plot of a physical or chemical property (S, O_2) as a function of depth.

Pycnocline: A depth layer of ocean where density increases rapidly, preventing vertical mixing because of rapid changes in temperature or salinity.

Red Sea Water: Warm, saline (S = 42.5) water that flows from the Red Sea into the northern, western Indian Ocean. Flows to a depth of 1000 to 1500 m. Lower salinity and temperature are found once the water exits the Red Sea due to mixing.

Ridge: An elongated elevation on the ocean bottom resembling a mountain range; prime example is the Mid-Atlantic Ridge.

Ross Sea: Located near the southern extension of the Pacific Ocean around Antarctica, west of the Weddell Sea near 73° S. Formation of some bottom water occurs in this region.

Salinity: The total grams of salts in 1 kg of seawater.

Salt Wedge Estuary: An estuary where saline water intrudes from the sea as a wedge below the surface river water. This occurs in estuaries formed by high-volume rivers. A strong horizontal salinity gradient occurs.

Sargasso Sea: Central North Atlantic waters. Called the "desert" of the North Atlantic. Very clear, nonproductive waters. 20 to 35° N latitude, 30 to 70° E longitude.

Sea Mount: An undersea mountain, usually of volcanic origin; some rise to the ocean surface and form islands.

Section: A slice of the ocean waters showing the contours of a physical or chemical property as a function of depth. Formed by combining a number of profiles from nearby stations.

Shelf: The zone extending from the line of permanent immersion to the depth, usually about 120 m, where there is a marked or rather steep descent toward the great depths. Average slope of 1 to 500 and average width of 65 km.

Shelf Water: Waters surrounding Antarctica. Very cold and dense.

Shore: The area of land close to the sea that has been modified by sea action.

Sigma-Θ: A term used to examine the density of seawater at the adiabatic temperature. It is defined as $\sigma_\theta = (\rho - 1)\ 1000$, where ρ is the density at the adiabatic temperature θ.

Sigma-T: A term used to examine the density of ocean waters at a given temperature. It is defined as $\sigma_T = (\rho - 1)\ 1000$, where ρ is the relative density at temperature T.

Slope: The declivity from the outer edge of the shelf into deeper water.

Somali Current: Flows north along the west coast of Africa during monsoon season. Supplied by the South Equatorial Current.

South Atlantic Central Waters: Upper waters below the surface in the South Atlantic. The waters extend to depths of 300 m on the equator and deeper further south.

South Equatorial Current: Flows west along the equator and northwest along northern South America, driven by southeast trade winds toward Central America.

Station: The location of a place where water samples are taken to determine physical or chemical properties.

Stratified Estuary: A shallow estuary where the salinity increases from the head to the mouth. The water is made up of two layers. The upper layer is less saline than the deep water; the upper layer flows seaward, and the deep layer flows inward.

Subantarctic Zone: Area from 40° S to 50° S, Antarctic and subtropical convergence.

Subtropical Convergence: A region of semipermanent high pressure at 35° latitude in both hemispheres caused by subsiding air.

Subtropical Convergence Zone: Area around Antarctica from the land to 40° N. Region where the water temperature rises approximately 4°C and salinity increases about 0.5. Occurs around Antarctica; is poorly defined in the eastern South Pacific. Salinity is as low as 33 in the summer.

Subtropical Zone: Area from 40° S to 24° S; subantarctic and subtropical convergence.

Sverdrup: A measure of the volume of flow of a given current or water mass ($S_V = 106\ cm^3\ s^{-1}$). Named after a famous oceanographer.

Thermocline: A thermally stratified layer of surface water that separates the upper, warmer, less-dense zone from the lower, colder, denser zone. It is the depth zone with the largest decrease in temperature in the water column and sometimes changes seasonally.

Thermohaline Circulation: Vertical and deep seawater circulation resulting from density differences caused by changes in T and S.

Tidal Currents: The currents produced by daily changes in the tides.

Trades: Airflow from the east to the west in the tropics. Surface winds forming part of Hadley cell.

Trench: A long, narrow depression with relatively steep sides; often is the deepest portion of the ocean.

Tropics: Region of the earth's surface lying between 23°27′ N and 23°27′ S; the Tropics of Capricorn and Cancer are the northern and southern boundaries, respectively.

T–S Diagram: A diagram plotting the temperature (T) versus salinity (S) of ocean waters; used to characterize water masses.

Upper Water: Area of water generally in the upper 1000 m.

Upwelling: The rising of cold, nutrient-rich bottom waters. Occurs near the western coast of South America and Africa as the result of offshore winds.

Vertical Circulation: Positive and negative circulation with respect to the vertical axis. Caused by density gradients as a result of differences in T and S.

Warm Core Rings: Formed in the Sargasso Sea due to Gulf Stream meandering. They are made up of low-nutrient waters that move north.

Water Mass: A parcel of seawater that has similar properties (T-S). Each water mass type is formed through surface climatic processes. Example: the North Atlantic Deep Water formed in the North Atlantic.

Weathering Products: Products formed as a result of weathering from wind, ice, rainfall, and the like at or near the earth's surface.

Weddell Sea: Southeast of Drake Pass and the tip of South America. Site of Antarctic bottom water formation.

West Australian Current: Waters that move north, along western coast of Australia.

West Greenland Current: Flows north, along western coast of Greenland (low salinity and temperature).

Westerlies: Airflow at midlatitudes from the west to the east. Produced by the temperature/pressure gradient. Surface winds form part of Ferrel cells.

Wind-Driven Circulation: Circulation caused by wind blowing over the surface of the ocean waters. Affects the upper few hundred meters of ocean.

II. Major Components of Seawater

Absolute Salinity, S_T: The salinity that represents the true amounts of salts in seawater. It can be determined by measuring all the individual major components of seawater. It is about 0.0165 g/kg higher than the practical salinity S_P for average seawater.

Alkalinity: The concentration of all the bases that can accept a proton when seawater is titrated with acid to a pH of 4.0.

Anoxic Basins: Basins that contain no O_2 below a given depth. Examples include the Black Sea and Cariaco Trench.

Artificial Seawater: A mixture of the major components of seawater that closely approximates the concentrations of real seawater.

Baltic Sea: A stratified positive estuary marked with large salinity and temperature gradients.

Brines: Water with extremely high salinities (greater than 200).

Chlorinity: The chloride equivalents (Cl + Br) in seawater (grams/kilogram). Defined by the mass in grams of pure silver needed to precipitate the halogens in 328.523 g of seawater.

Colloids: The dispersion of small particles (<500 nm in diameter) in solution. They are aggregates of numerous atoms or molecules. Most pass through a 0.45-μm filter but are not truly dissolved.

Conductance Cell: A glass or plastic cell that is used to measure the conductance of a solution.

Conductivity Ratio: The ratio of the specific conductivity of a seawater sample to that of standard seawater.

Conductivity Salinity, S_{COND}: The salinity of seawater determined from the measurement of conductivity. Determined from a measurement of the conductivity relative to a standard.

Conservative Element: An element whose concentration shows little or no variation in the ocean because it is unreactive or has a low crustal abundance. Most major ocean components of seawater are conservative.

Density Salinity, S_{DENS}: The salinity determined from the measurement of density.

Deuterium: An isotope of hydrogen (^2H) used to examine the effects of precipitation and evaporation in natural waters.

Equivalent Weight: The sum of the atomic weight corrected for the ionic charges (Σ = MW/charge).

Evaporation Salinity, S_{EVAP}: The salinity determined by the evaporation of seawater to dryness.

Gulf of Mexico: The areas located south of the United States bordered by Texas, Mexico, and the western coast of Florida.

Inductance Conductance Cell: Uses a transformer bridge to measure the resistance or conductance of seawater.

***In Situ* Pressure:** The measured pressure at a given depth.

***In Situ* Temperature:** The measured temperature at a given depth. Can be higher than expected for deep waters because of the adiabatic heating caused by pressure effects.

Interstitial Waters: The water present in the pores of sediments.

Ionic Strength (I): $I = 0.5\, Z_i^2\, m_i$, where Z is the charge and m is the molality of an ion.

Isotopes: Atoms that have the same atomic number but different mass numbers (i.e., equal number of protons but different numbers of neutrons).

Liquid: A state of matter in which a substance exhibits readiness to flow, little or no tendency to disperse, and relatively high compressibility.

Major Components: The major solutes in seawater (Na^+, Mg^{2+}, Ca^{2+}, K^+, Sr^{2+}, Cl^-, SO_4^{2-}, HCO_3^-, Br^-, CO_3^{2-}, $B(OH)_4^-$, F^-, $B(OH)_3$); concentrations from 0.05 to 750 m*M*.

Marcet Principle: The relative composition of seawater is the same for all ocean waters.

Minor Components: The components of seawater with concentrations of 0.05 to 50 μ*M*.

Molality (m): The moles of a solute per kilogram of solvent.

Molarity (M): The moles of a solute per liter of solution.

Mole Fraction (N): The fraction of the moles of a substance in a mixture ($N = n_i/\Sigma n_i$).

Molecular Weight: The sum of the atomic weights of a compound.

Nonconservative Element: An element whose concentration varies from place to place in the oceans. The variations are caused by variable inputs or reactivity (e.g., uptake by organisms or inputs from hydrothermal vents).

Normality (N): The equivalents of a solute per liter of solution.

Orca Basin: A deep basin located in the Gulf of Mexico south of Louisiana. Contains high-salinity and anoxic brines formed from the dissolution of evaporites.

Oscillator: An instrument used to measure the frequency.

Particulate Material: Solid material that does not pass through a 0.45-μm filter. Can be either organic or inorganic material.

Phase: The different physical states of a compound or element.

Practical Salinity Scale: The salinity defined by the conductivity ratio of seawater relative to a given mass of KCl. Salinity is a ratio or fraction of masses and does not have a scale.

Refractive Index: A dimension quantity that is related to how much light is reflected by a substance. A method used for determining salinity.

Resistance: The resistance R = V/i where V = potential (volts) and i = current (amps).

Salinity/Chlorinity Relations: A relationship between salinity and chlorinity. Different for various estuaries. For open ocean waters, it is assumed to be S = 1.80655 Cl.

Salinometer: An instrument used to measure salinity.

Sea Salt: The inorganic salts found in seawater; primarily NaCl and $MgSO_4$.

Solid: The material that does not pass through a 0.45-μm filter.

Solute: A molecule or compound that is dissolved in solution.

Specific Conductance: Defined as Lsp = k/R = l/AR, where R is the cell resistance, the cell constant = k distance (l) between electrodes/cross-sectional area (A).

Standard Mean Ocean Water (SMOW): Water collected in the deep ocean used as a reference sample for the isotope determination of the D:H and ^{18}O:^{16}O ratios in natural waters. Used to determine $\delta = [(R_{sample}/R_{SMOW}) - 1]1000$ where R gives the relative isotopic ratios of a sample, which can be used to examine changes in isotopes of H and O.

Submarine Volcanism: Undersea volcanoes that occur at ridge areas. The vent water coming from these systems has a composition different from seawater due to reactions occurring between seawater and molten basalts.

Trace Components: The components of seawater with concentrations 0.05 to 50 n*M*.

Tritium: An isotope of hydrogen (^3H) that is used as a tracer in water. It is radioactive with a half-life of 12.5 yr.

Weight Fraction (X): The fraction of the mass of a substance in a mixture ($X = g_i/\Sigma g_i$).

Wheatstone Bridge: Used to measure the resistance of a solution in a conductivity cell.

World River Water: The composition of waters representative of the average river water entering the oceans.

III. Minor Elements in Seawater

Active Uptake: The uptake of elements by organisms that need them (NO_3, PO_4).

Adsorption: The formation of a thin layer of a substance that is held on the surface of a solid because of a combination of physical and weak chemical forces.

Alkali Metals: Group IA elements (H, Li, Na, K, Rb, Cs, Fr).
Alkaline Earth Metals: Group IIA elements (Be, Mg, Ca, Sr, Ba, Ra).
Amorphous Silica: Silica (SiO_2) without crystalline shape.
Amphibolite: A group of metamorphic rocks that consist primarily of hornblende.
Andesite: A fine-grain intermediate rock formed when magma of dioritic composition is erupted as lava flows or is injected into fractures of volcanic vents.
Arkose: Pertains to rocks containing appreciable amounts of feldspar.
Atmospheric Input: The input of elements (Pb, Al) from the atmosphere to the oceans.
Atomic Number: The number of protons in an atomic nucleus.
Basalt: Occurs particularly in massive lava flows. Forms when gabbroic magma erupts at the earth's surface as lava. Fine-grain extrusive rock that covers much of the ocean floor beneath the sediments.
Chlorite: $(Mg, Fe)_6(AlSi_3)O_{10}(OH)_8$. A clay mineral.
Complexes: The formation of species from the interaction of a metal ion with one or more ligands, usually by the formation of covalent bonds.
Conservative Type Profile: The concentration shows little or no change with depth (constant ratio of concentration/salinity) due to low reactivity.
d0 Cations: The metallic elements with rare gas configurations; alkali metals, alkaline earth, and lanthanide series elements.
d10 Cations: The metallic elements with an outer shell of 18 d electrons (Ag^+, Zn^{2+}, Ga^{3+}, Sc^{4+}). Form strong halide complexes increasing in stability with increasing atom mass or ligand size.
Detrital Carbonate Rock: A rock formed by the accumulation of fragments derived from preexisting rocks and minerals by mechanical weathering and transported to their place of deposition by purely mechanical agents (water, wind, ice, and gravity).
Dolomite: $CaMg(CO_3)_2$. Calcium carbonate containing more than 50% Mg in place of Ca.
ECF(50): The concentration of a substance required to halt growth in 50% of the test organisms.
EDTA (ethylenediamine N,N,N,N′ tetraacetic acid): An organic ligand that forms strong complexes with metal ions.
Electronic Configuration of Atoms: A list of occupied orbitals in an atom.
Electrostatic Contribution: The measurement of the electrostatic contribution to the bond energy or a measure of the attraction of an element for an oxide-based mineral.
Evaporites: The resultant salt precipitates following the slow evaporation of seawater (gypsum and halite).
Gabbro: An igneous-plutonic rock (75% is dark ferromagnesian minerals and contains plagioclase feldspar, olivine, pyroxene, and hornblende).
Geochemical Balance: The balance of inputs (rivers, atmosphere) and outputs (sediments, vents) of elements in the marine environment. The balance is vital in the study of the evolution of seawater, sedimentary cycling, and the controls on the composition of the oceans.
Gneiss: A metamorphic rock. Parent rocks are commonly igneous-plutonic (granite, syenite, diorite, gabbro) and sedimentary rocks (sandstones and shales).
Granite: A coarse-grain, igneous-plutonic rock that is high in Si, K, and Na but low in Ca, Fe, and Mg.
Graywacke: An impure form of sandstone. Composed of rounded to angular fragments of shale, slate, chert, granite, basalt, in addition to quartz.
Gypsum: A white mineral composed of $CaSO_4 \cdot 2\,H_2O$ (hydrated calcium sulfate).

Halite: A rock salt (NaCl). One of the evaporites of the third stage of evaporation.

Heavy Metals: Metals that generally pose risk to living creatures in low concentrations by concentrating in the digestive organs (Pb, Hg, Cd).

Hydrothermal Input: The input of elements (Mn, Si) from hydrothermal vents to the oceans.

Igneous Rocks: Rocks formed directly from molten lava that cooled quickly on or near the earth's surface.

Illite: $K_2Al_4[Si_6Al_2O_{20}](OH)_4$. A group of clay minerals.

Irving–Williams Order: The order of complex stability of transition metals with organic ligands ($Mn^{2+} < Fe^{2+} < Co^{2+} < Ni^{2+} < Cu^{2+} > Zn^{2+}$).

Kaolinite: $Al_2Si_2O_5(OH)_4$. A clay mineral.

K-mica: $KAl_3Si_3O_{10}(OH)_2$. An original constituent of igneous rocks.

Lanthanides: The 14 elements with similar properties formed by filling the 5 f-orbitals of an atom (frequently called the rare earths and with atomic numbers 57–70).

Limestone: A shale-like or sandy sedimentary rock, chiefly composed of calcium carbonate, containing arable quantities of magnesium carbonate and quartz; chemical or organic in origin.

Major Elements: The elements in seawater with concentrations of 0.05–750 m*M*.

Marble: A metamorphic rock. Primary components are calcite and dolomite (calcium carbonate and magnesium carbonate).

Metamorphic Rocks: Rocks formed under conditions of intense heat, pressure, or both, at considerable depths within the earth, from older rocks (gneiss, schist, quartz).

Mica-Schist: A metamorphic rock formed from sedimentary rocks, volcanic igneous rocks, or other metamorphic rocks. *Schist* is a descriptive term only, and specific schist rocks are named after the principal band producing minerals in the rock.

Middepth Maximum Type Profile: The high values in deep water may result from a hydrothermal input from the midocean ridge system (e.g., Mn and ^3He).

Middepth Minimum Type Profile: The high surface concentrations result from an atmospheric or land input; the high deep-water values are caused by regeneration at or near the bottom (e.g., Al).

Minor Elements: The elements in seawater with concentrations of 0.05–50 μ*M*.

Montmorillonite: A clay mineral formed as an alteration product of aluminum silicates.

NTA (Nitrilotriacetic acid): An organic ligand that forms strong complexes with metal ions.

Nutrient Type Profile: The depth profile of an element that is similar to that of a nutrient (low in surface waters and an enrichment with depth). The element is removed from the surface waters by biological activity and is regenerated at depth by oxidizing bacteria. Shallow-water regeneration like NO_3^- and PO_4^{3-} in the soft parts and deep-water regeneration like SiO_2 in hard parts.

Ocean–Rock Partition Coefficient: The partitioning of that element between rocks and seawater.

Passive Uptake: The uptake of an element by organisms due to adsorption onto surface caused by chemical interactions with surface groups (carboxylic, phenolic).

Peridotite: An igneous-plutonic rock (high MgO and FeO/Fe_2O_3 content).

Phillipsite: A hydrous silicate of aluminum, iron, and magnesium.

Plutonic Rocks: The rocks formed directly from molten rock that cooled slowly at considerable depth beneath the earth's surface, which allows the mineral crystals to grow to visible size (granite, syenite, gabbro, peridotite).

Quartz: A common form of silica (SiO_2) resulting from the weathering of igneous rocks.

Quartzite: A sandstone with its primary component being quartz. A sedimentary rock with no porosity.

Quartzose Sandstone: A well-sorted sandstone that contains (if pure) more than 95% clear quartz grains and 5% or less of matrix and cement.

Rare Earths: The 14 elements with similar properties formed by filling the 5 f-orbitals of an atom (frequently called the lanthanides and with atomic numbers 57–70).

Rare Gas: The noble gases (He, Ne, Ar, Kr, Xe, Rn).

Residence Time: The average time that a substance remains in seawater before removal by some precipitation or adsorption process.

Rhyolyte: Formed when magma of granitic composition erupts at the earth's surface and intrudes the crust at shallow depths. Because of the rapid cooling, only small crystals are able to form. Equivalent to plutonic granite, with excess silica.

River Input: The input of elements (N, P) from rivers to the oceans.

Rock Salt: A common form of NaCl occurring in large masses; formed by evaporative processes.

Sandstone: The sedimentary rocks containing more than 50% fine-/medium-grain sand (quartz, greywacke).

Saturation Concentration: The maximum equilibrium concentration at which any additional increase in concentration would result in precipitation.

Scavenging: The removal of an element from the water column by adsorption, absorption, biological uptake, precipitation, and so on.

Sedimentary Rocks: Rocks formed under moderate pressure from layers of accumulated sediments (shale).

Sedimentation: The deposition of biogenic, authogenic, hydrogenic, and cosmogenic particles on the bottom of the ocean over a period of many years.

Shale: An easily split sedimentary rock having laminated layers of fine clay-like particles (70 to 80% argillaceous minerals; the remainder is silt).

Stability Constants: The thermodynamic constant for formation of an ion pair or complex ($K = \prod[P]/\prod[R]$ where $\prod[P]$ and $\prod[R]$ are the product of the activities or concentrations of the products P and reactants R, respectively).

Suboxic Layer: A depth layer of low oxygen that exists in some regions of the Pacific and Indian oceans.

Surface Enrichment and Depletion Type Profile: The high values in the surface are related to inputs from land or the atmosphere, while the low values in deep waters are related to a rapid removal caused by adsorption, precipitation, and the like (e.g., Pb).

Trace Elements: The elements in seawater with concentrations of 0.05–50 n*M*.

Transition Metals: Metallic elements with an outer d shell greater than zero and less than 10 electrons (Mn^{2+}, Fe^{2+}, Co^{2+}, Ni^{2+}).

Volatiles: Compounds that are easily transformed from the liquid to vapor phase (HBr).

Volcanic Rocks: Rocks formed directly from molten rock that cooled quickly at or near the earth's surface (basalt, andestite, and rhyolite).

Volume Concentration Factor: The concentration of an element in an organism relative to the concentration in a given volume of seawater.

Weathering of Rocks: The breakdown in the structure of rocks caused by rain, temperature changes, wind, and chemical reactions at or near the earth's surface (elements found in rocks are transported to the oceans via rivers and winds).

IV. Ionic Interactions in Seawater

Activity: The effective concentration of a given solute. Thermodynamically, it is related to the product of the concentration and an activity coefficient that describes the magnitude of the nonideal behavior of the solute with the solvent (it is defined as 1 for an ideal solution, with activity = concentration).

Activity Coefficient: The quantity that accounts for the nonideal behavior of a solute in solution. It is defined as 1 when the concentration approaches 0.

Association Constant: The thermodynamic constant for the formation of an ion pair or complex ($A + B \rightarrow AB$, $K_A = [AB]/[A][B]$).

Baseline Study: A study to determine the concentration or state of a system before it is affected by the influence of humans.

Bioavailability: The availability of an element needed by an organism for its growth or well-being.

Boiling Point Elevation: The increase in the boiling point temperature as the result of the presence of a solute.

Boiling Point Temperature: The temperature at which the vapor pressure of a liquid is equal to the atmospheric pressure or other external pressure.

Born–Haber Cycle: The cycle of the changes in energy that occur when a crystalline substance is formed from the constituent elements (considers the heat of sublimation, heat of ionization, electron affinity, heat of formation, and lattice energy).

Boyle's Law: The pressure of a given mass of a gas is inversely proportional to the volume.

Charles Law: The volume of a given mass of a gas is directly proportional to the absolute temperature.

Clathrate Water Structure Model: Originally postulated by Linus Pauling. The model suggests that the structure of water is an equilibrium between monomers in a clathrate hydrate cage. The discrete sites inside of the clathrate can serve as a host for individual water molecules.

Cluster Expansion Model: This model attempts to account for all the possible interactions that can occur between ions in solution (plus–minus, plus–plus, and minus–minus) and makes no attempt to separate coulombic and noncoulombic terms.

Cluster Water Structure Model: The model assumes that the structured form of water is a group of hydrogen-bonded water clusters in equilibrium with monomers (i.e., Frank and Wen model).

Complexed Ions: Ions that interact covalently with ligands (e.g., a metallic cation interacting with EDTA).

Compressibility: The change in the volume (V) of a substance from the application of pressure ($\beta = -(1/V)(\partial V/\partial P)$).

Contact Ion Pair: When the ions in an ion pair are in contact and linked electrostatically (little or no covalent bonding).

Continuum Model: The model that assumes that water is a continuous dielectric medium with no structure.

Covalent-Bonded Ion Pair: When the ions of an ion pair in contact share electrons (covalent character).

Cross-Square Rule: $\Sigma \square = \Sigma X$. The sum of the excess mixing properties around the sides of the diagram is equal to the sum of the excess properties of the cross mixtures.

Dalton's Law: The total pressure of a mixture of gases is equal to the sum of the partial pressure of the components of the mixture.

Debye–Hückel Equation: An equation that describes the theoretical concentration behavior of electrolytes in dilute solutions. For the activity coefficient of an electrolyte, the Debye-Hückel limiting law is given by $\ln \gamma = -0.509\ I_{0.5}/(1 + 0.33\ I^{0.5})$, where I is the ionic strength.

Dielectric Constant: The ratio of the capacitance of a solution to a vacuum.

Dipole/Dipole Interactions: The interaction between adjacent molecules caused by the attraction of the areas of charge separation (dipoles).

Dipole Moment: A measure of the charge separation in a molecule. It is defined as the product of the electrostatic charge times the distance between the two charges. Dipole moments are measured in units of Debye (1×10^{-8} esu cm).

Dissociation Constant: The thermodynamic constant for the dissociation of an ion pair, complex, or acid ($AB \rightarrow A + B$, $K_D = [A][B]/[AB]$).

E_h–pH Diagrams: The diagrams showing the relation of pH and E_h (oxidation potential) of species.

Electrical Conductance: The ability of a solution to carry an electrical current (conductance = 1/resistance; measured in ohm^{-1}).

Electrical Potential, E_h: The electrical potential generated for a oxidation–reduction reaction (related to the Nernst equation, $E_h = E_h^\circ + (RT/nF)\ln a_{ox}/a_{red,}$ where a is the activity).

Electrostriction: The decrease in the volume due the interactions of a solute with a solvent. The water molecules near an ion have a higher density than the bulk water.

Entropy of Hydration: The change in the amount of order or disorder in a system as a result of hydration.

Equilibrium: A state when the forward and backward reactions are equal. The rate of the products being formed is equal to the rate of the reactants being used.

Fraction of Free Ions: The fraction of ions that are not in a complex or ion pair ($\alpha_{MX} = [M]_F/[M]_T$).

Free Energy of Hydration: The free energy involved in the interaction of water with a solute.

Free Ions: Ions in solution that are only hydrated by water molecules (no interactions with other ions).

Freezing Point Depression: The decrease in the freezing temperature of a liquid as the result of the presence of a solute.

Heat Capacity: The amount of heat (calories or joules) needed to raise the temperature of a solid or liquid substance by 1 K.

Heat Conduction: The ability of a substance to transport heat.

Heat of Crystal Lattice Formation: The energy involved in the formation of a crystal lattice.

Heat of Dissociation: The energy involved in dissociation of a molecule into ions.

Heat of Evaporation: The amount of heat (calories or joules) released or taken up on the change of state of a liquid–vapor or vapor–liquid.

Heat of Formation: The energy involved in the formation of a compound formed from its constituent elements.

Heat of Fusion: The amount of heat (calories or joules) released or taken up on the change of state of a solid–liquid or liquid–solid.

Heat of Hydration: The energy involved in hydrating ions.

Heat of Ionization: The energy involved in the dissociation of a molecule into ions.

Heat of Solution: The energy change produced when a substance dissolves in a solvent.

Heat of Sublimation: The energy involved in the conversion of a solid to a gas.

Henry's Law: The partial pressure of a gas is directly proportional to the concentration ($P_A = k\ m_A$ or $k'\ X_A$, where m is the molality and X is the mole fraction).

Hydration: Results from the electrostatic attraction between a solute and a water molecule.
Hydration Number: The number of water molecules associated with a solute in solution.
Hydrogen Bond: A weak bond formed between hydrogen atoms in compounds and strong electronegative atoms in other molecules.
Ice-Like Model: The model assumes that the structure of liquid water is similar to the structure of the ice lattice.
Ideal Gas Equation: The pressure (P) times the volume (V) of a mole of an ideal gas is equal to the gas constant (R) times the absolute temperature, T ($PV = RT$).
Infinite Dilution: An ideal state in which a solute is surrounded by a large reservoir of water (ions cannot interact with each other).
Ion–Ion Interactions: The electrostatic interactions between ions.
Ion Pairing: The electrostatic attraction between ions of opposite charge.
Ion-Pairing Model: A model that accounts for the changes in the activities of ions in solution by assuming that ion pairs or complexes are formed.
Ion–Water Interactions: The interactions between charged ions and water molecules. The interactions are electrostatic between ions and water molecules treated as a continuous dielectric medium, ion–dipole, or ion–quadrupole.
Ligand: A molecule that can form a coordinate covalent chemical bond with a metal ion.
Maximum Density: The maximum density of a liquid. It normally occurs at the melting point. For water, it occurs at 4°C.
Melting Point: The temperature at which the solid and liquid phases of a substance can exist together at atmospheric pressure.
Mixture Water Structure Model: The model that assumes that two different species of water exist, a bulky species and a dense species. There are four general mixture model categories: broken-down ice lattice models, cluster models, clathrate models, and significant structure models.
Monomer: A simple molecule (H_2O) that is not interacting with other molecules.
Oxidation: The loss of an electron by an atom or molecule.
Partial Molal Compressibility: The effect of pressure on the volume that a solute occupies in solution.
Partial Molal Volume: The volume that a solute occupies in solution.
pE: The negative log of the activity of an electron.
pH: The negative log of the activity or concentration of the hydrogen ion.
Phase Diagram: A diagram that shows the relationship of the phases (liquid, solid, gas) of a system as a function of variables such as temperature and pressure.
Photochemical Processes: Processes that result from the absorption of light.
Plus–Minus Interactions: The interactions between ions of opposite charge.
Plus–Plus and Minus–Minus Interactions: The interactions between ions of the same charge.
Quadrupole Moment: Results from the intermolecular forces in a molecule caused by the unsymmetrical separation of four charges.
Raoult's Law: The partial pressure of a gas in an ideal mixture is equal to the partial pressure of the pure gas times the mole fraction ($P_A = X_A P_A^0$).
Redox Reactions: The reactions involving oxidation and reduction (loss and gain of electrons).
Reduction: The gain of an electron by an atom or molecule.
Significant Structure Model: Assumes that bulky species are not necessarily a monomer but another ice-like species of higher density.
Solvent-Separated Ion Pair: The ions of an ion pair are separated by more than one water molecule.

Solvent-Shared Ion Pair: The ions of an ion pair are separated by a single water molecule.
Speciation: The determination of the form of a given element.
Specific Interaction Model: A model that accounts for the changes in the activities of ions in solution by assuming that the interactions are mainly between specific ions (considers the interactions of ions of the same and opposite signs).
Structure-Breaking Ions: The addition of ions to water results in less structure than in pure water.
Structure-Making Ions: The addition of ions to water results in more structure than in pure water.
Surface Tension: The tangential forces acting at right angles at the surfaces of a liquid. Surface tension has the units of dynes cm^{-1}.
Thermal Expansion: The change in the volume (V) as a result of a change in temperature, $\alpha = (1/V)(\partial V/\partial T)$.
Toxicity: The ability of a certain chemical compound or element to be toxic to an organism.
Transparency: The ability of a substance to transmit a certain wavelength or band of wavelength of light or energy.
Uniformist Water Structure Model: The model that assumes that no unique local domains of structures exist in water. Also known as the average model.
Viscosity: The resistance of a liquid to motion or flow. Viscosity is caused by cohesive forces between molecules of a liquid. The viscosity is measured in poise (dynes cm^{-2}).
Water Structure: Structure models proposed to explain the unique properties of water. They are divided into two categories: the uniformist, or average, models and the mixture models.
Young's Rules: Three simple rules proposed by T. F. Young as a result of studying the properties of mixed electrolyte solutions: (1) The excess properties of mixing (ΔP_{ex}) are not very large and can be assumed to be zero in dilute solutions; (2) the values of ΔP_{ex} of mixtures with a common anion or cation are not strongly affected by the common ion; and (3) the sum of the excess mixing properties of ions with a common ion (the sides of the cross-square diagram) are equal to the sum of the mixing properties of the uncommon ions (the cross mixtures).

V. Atmospheric Chemistry

Acid Rain: The oxidation of NO_X and SO_2 results in the formation of HNO_3 and H_2SO_4 in the atmosphere and thus the acidification of precipitation. This is a result of industrial emissions and primarily affects the northeastern area of the United States and many areas in Europe.
Aerosols: A suspension of solid or liquid matter in a gaseous medium; range in size from about 10^{-4} μm to tens of micrometers; are a result of combustion, volcanoes, gas-to-particle conversion, dust, pollen, and spores.
Air Pollution: The addition of toxic or undesirable gases to the atmosphere, mostly from the burning of fossil fuels.
Biogenic Gases: Gases related to biological activities (CH_4, NH_3, N_2O, H_2, CS_2).
Boundary Layer: Also known as the mixed layer. Depth of the boundary layer is determined by thermodynamic processes. Typical depths are on the order of 1 km.

Chlorofluorocarbons: CFC compounds used primarily in the blowing of foams and as refrigerants. They have a long lifetime and can penetrate into the stratosphere, where they are photochemically broken down to produce Cl, which can react with ozone. The CFCs can also act as greenhouse gases.

Dobson Unit: A unit of measurement of stratospheric ozone. Regarded as a thickness of the ozone layer if brought to standard temperature and pressure (1 Dobson unit equals 0.1 cm of ozone).

Greenhouse Effect: The result of certain gases absorbing infrared (IR) radiative energy and increasing the temperature of the atmosphere like a "greenhouse." Water vapor, CO_2, and methane are the primary greenhouse gases.

Greenhouse Gases: Gases that absorb infrared energy in the troposphere and thus cause an increase in the temperature of the troposphere. Examples are H_2O, O_2, CO_2, freons, and CH_4.

Hydrogen Peroxide, H_2O_2: Occurs in the atmosphere as a result of two hydroperoxyl radicals reacting and in the ocean as a result of photochemical reactions of organic carbon. Unstable, colorless, heavy liquid; soluble in water and alcohol. Used as a bleach.

Hydroperoxyl Radical, HO_2: Formed from the photochemical reactions of the H radical with O_2. The hydroperoxyl radical can regenerate OH radicals and can lead to the chain termination.

Interhemispheric Mixing: Time it takes for a species to be mixed in the atmosphere between hemispheres (1–2 yr).

Intertropical Convergence Zone (ITCZ): Area close to the equator surrounding the earth where the northeast and the southeast trade winds flow together. Characterized by strong upward motion and heavy rainfall. Affects the transport of species from the Northern to Southern Hemispheres and vice versa.

Intrahemispheric Mixing: Time it takes for a species to be mixed in the atmosphere within the hemisphere (months).

Mesopause: The interface between the thermosphere and the mesosphere (100 km).

Mesosphere: The layer of the atmosphere below the thermosphere (50 to 100 km).

Mixing Time: The time it takes for a species to be mixed in the oceans or atmosphere. Intrahemispheric tropospheric mixing generally takes on the order of weeks to months. Interhemispheric tropospheric mixing takes on the order of years, usually less than 10. Stratospheric mixing is generally a longer time frame activity due to the stability of the stratosphere.

Nitrogen Cycle: The chemical cycling of nitrogen in the natural environment.

Ozone Formation: The photons with wavelengths shorter than 240 nm are absorbed by O_2 and N_2 molecules in the upper atmosphere, which results in the formation of O_3 by the chemical equations $O_2 + hn \rightarrow 2O$ and $O_2 + O + M \rightarrow O_3 + M$. The production is at a maximum in the lower stratosphere.

Ozone Hole: A hole that is found in the stratospheric levels of ozone above Antarctica and to a lesser extent above the Arctic. It is a result of heterogeneous reactions of chlorine with ozone in polar stratospheric clouds and a polar vortex that occurs during certain times of the year.

Photochemical Gases: Gases involved in the photochemistry of the atmosphere (CO, O_3, NO_2, HNO_3, H_2, OH, OH_2, H_2O_2, H_2CO).

Singlet Oxygen: Molecular oxygen in which all the electrons are paired.

Solar Radiation: The flux of solar photons is a function of wavelength.

Stratopause: The interface between the mesosphere and stratosphere (50 km).
Stratosphere: The layer of the atmosphere below the mesosphere and above the troposphere (10 to 50 km). Location of the ozone layer.
Sulfur Cycle: The chemical cycling of sulfur in the natural environment.
Superoxide Anion, O_2^-: The anion formed from the dissociation of HO_2. It is a key intermediate in the formation of hydrogen peroxide.
Thermosphere: The upper layer of the earth's atmosphere (100 km to approximately 1000 km).
Trace Gas: Gaseous compounds that are in relatively low concentrations in the atmosphere. Examples are OH, HO_2, CS_2, OCS, N_2O.
Triplet Oxygen: Molecular oxygen in which two electrons are unpaired with parallel spins.
Tropopause: The interface between the troposphere and the stratosphere (10 km).
Troposphere: The layer of the atmosphere from the surface to a height of 10 km.
Ultraviolet Radiation: The wavelengths of light less than 400 nm.

VI. Dissolved Gases Other than CO_2

Differential Heat Exchange: When the heat exchange is more rapid than gas exchange.
Fick's First Law: The flux of diffusion is proportional to the concentration gradient ($J = -D\,\partial c/\partial x$, where D is the diffusion coefficient, c is concentration, and x is the distance).
Fick's Second Law: The rate of change of the concentration of diffusion is related to the derivative of the diffusion coefficient time of the gradient $(\partial c/\partial t) = (\partial/\partial x)[D(\partial c/\partial t)]$.
Nernst Slope: The theoretical slope of the electrode potential E as a function of concentration in the Nernst equation, $E = E^0 + k \log c$, where $k = RT/F = 0.0591$ at 25°C.
pH Glass Electrode: An electrode can be used to determine the activity or concentration of hydrogen ions. The potential across the glass membrane is related to the concentration of the hydrogen ions in solution.
Reference Electrode: An electrode that is used along with a glass pH electrode to measure the concentration of the hydrogen ion (e.g., Ag, AgCl).
Scale Particle Theory: A theory that is used to account for the salting in and out of gases in solution.
Stoichiometric Constant: (K*), an equilibrium constant expressed in terms of the total concentration of the species.
Thermodynamic Constant: An equilibrium constant expressed in terms of the activities of the species.

VII. The Carbonate System

Acid: A substance that gives a pH less than 7 when added to water.
Alkalinity: The concentration of bases in a solution that can be titrated with acid to a fixed pH (4.0).
Aragonite: A form of calcium carbonate. Less common than calcite and less stable.
Base: A substance that gives a pH greater than 7 when added to water.

Bjerrum Diagram: Plots of the speciation of a substance as a function of pH.

Buffer: A solution that minimizes changes in pH on the addition of acids or bases (e.g., a weak acid and sodium salt of the acid).

Buffer Capacity: The ability of a buffer solution to resist changes in pH on addition of an acid or base.

$CaCO_3$ Compensation Depth: The depth at which the solid $CaCO_3$ is above 5% of the sediment composition.

$CaCO_3$ Saturation Depth: The depth at which solid $CaCO_3$ is in equilibrium with the solution.

Calcite: A hexagonal-rhombohedral form of calcium carbonate.

Carbonate Alkalinity, CA: The amount of carbonate bases in a solution that can titrate the carbonic acid end point with an acid, $CA = [HCO_3^-] + 2[CO_3^{2-}]$.

Coccolithifera: A type of marine phytoflagellates (i.e., protozoans) composed of calcite.

Coulometry: A determination of the amount of an electrolyte released during electrolysis by measuring the number of coulombs used.

Dehydration: The removal of water molecules from a hydrated solute.

Dibasic Acid: An acid that has two hydrogen atoms (H_2A).

Foraminifera: Marine protozoans that have a secreted shell enclosing the ameboid body made of calcite.

Fossil Fuel: Any hydrocarbon deposit that may be used for fuel (e.g., petroleum, coal, and natural gas).

Free pH Scale (pH_F): The pH scale defined as $pH_F = -\log[H^+]_F$ where $[H^+]_F$ is the free proton concentration.

Gas Chromatography: A separation technique involving the passage of a gaseous moving phase through a column containing a fixed adsorbent phase and subsequent detection after passage through the column. Used principally to determine the concentration of volatile compounds.

Greenhouse Effect: The maintenance of temperatures on earth by the passage through of UV radiation but the absorbance of outgoing IR radiation by H_2O, CO_2, and other greenhouse gases.

Hydration: The strong attraction of water molecules in a region around a solute.

Infrared Energy: Electromagnetic radiation with wavelengths from 0.75 to 0.8 μm.

Infrared Spectroscopy: The study of the properties of material by means of their interactions with infrared radiation; radiation is dispersed into a spectrum after passing through the material.

Lysocline: The depth at which the rate of dissolution of solid $CaCO_3$ is dramatically increased.

Monobasic Acid: An acid that has only one hydrogen atom (HA).

National Bureau of Standards Buffers: Buffers developed in the determination of the pH_{NBS} that had fixed values of pH at a given temperature. Name changed to NIST (National Institute of Science and Technology).

NBS pH Scale (pH_{NBS}): The practical pH scale developed by Bates at the National Bureau of Standards (now the National Institute of Science and Technology) based on conventional definitions of activity coefficients and dilute solution buffers.

Nernst Equation: The relationship between the electromotive force, the temperature, and the standard free energy change for an electrode reaction.

Normalized Alkalinity: The total alkalinity normalized to a salinity of 35 (Normalized total alkalinity [NTA] = Total alkalinity [TA] × 35/S).

Partial Pressure of CO_2: The partial pressure exerted by CO_2 in an inert gas like nitrogen that is in equilibrium with a solution.

pK of Acids: The logarithm to base 10 of the reciprocal of the dissociation constant for an acid ($pK = -\log K$).

Pteropods: Marine pelagic gastropod mollusks with a shell made of aragonite.

Revelle Factor: The ratio of the changes in the partial pressure of CO_2 to those in the TCO_2 (total CO_2) [$R = (\Delta pCO_2/pCO_2)/(\Delta TCO_2/TCO_2)$].

Saturation State: The equilibrium state of a solution relative to the solubility of a given solid (Ω = concentration product/Ksp, where Ksp is the equilibrium solubility).

Solubility Product: The equilibrium constant defined for formation of a solid from its components, $A + B \rightarrow AB(s)$, $Ksp = [A][B]$.

Specific Alkalinity: The total alkalinity corrected for differences in salinity (SA = TA/Cl).

Total CO_2: The total concentration of inorganic carbon dioxide in a system or sample ($[CO_2] + [HCO_3] + [CO_3]$).

Total pH Scale, pH_T: The pH scale defined as $pH_T = -\log[H^+]_T$, where $[H^+]_T$ is the total proton concentration. It is determined using buffer solutions of ionic strength similar to those being measured.

Tribasic Acid: An acid that has three hydrogen atoms (H_3A).

TRIS Buffer: Buffer made up in a seawater medium that is used to calibrate pH electrodes.

Ultraviolet Energy: Electromagnetic radiation with wavelength 4 to 400 nm.

Whitings of $CaCO_3$: Area where $CaCO_3$ appears to be precipitated from solution in the oceans (e.g., Bahama Banks).

VIII. Micronutrients in the Oceans

Amino Acid: An acid in which a portion of the nonacid hydrogen has been replaced by an amino group.

Ammonium: The nutrient NH_3 or NH_4^+.

Ammonium Oxidation: Oxidation of NH_3 to NO_2^- or NO_3^-. This process is thought to be responsible for the nitrite maximum immediately below the photosynthetic compensation depth.

Autoanalyzer: A device that automatically measures the nutrients in seawater.

Denitrification: Conversion of NO_3^- to N_2 or N_2O. This process occurs largely because of the use of nitrate for the growth of bacteria in anoxic waters.

Nitrate: The nutrient NO_3^-.

Nitrification: The oxidation of NH_3 to NO_3^-. This oxidation yields nitrite as an intermediate. The reaction takes place in the water column and in the sediments by bacteria.

Nitrite: The nutrient NO_2^-.

Nitrogen Dioxide: NO_2, a component of the atmosphere resulting from the oxidation of NO or nitrogen fixation.

Nitrogen/Phosphorus Ratio: A comparison of the levels of N to P in the oceans (N:P = 15 to 16).

NO: Used as a conservative NO_3 tracer in seawater, equal to $9[NO_3] + [O_2]_{meas}$.

Nutrient: Trace elements that marine phytoplankton require for growth (N, P, Si).

Phosphate: The different species of the nutrient phosphate found in seawater (H_3PO_4, $H_2PO_4^-$, HPO_4^{2-}, PO_4^{3-}).

Phytoplankton: Free-floating microscopic plants moving mostly in the confines of the water column. They are responsible for the greatest amount of primary production in the sea.

PO: Used as a conservative PO_4 tracer in seawater, equal to $35[PO_4]_{meas} + [O_2]_{meas}$.

Redfield Model: Redfield found the ratio N:O:C:P in phytoplankton was relatively constant. The model assumes that this is the same ratio needed for plants to grow and is released to solution when they die.

Silicate: SiO_2. A micronutrient found in the skeletal material of diatoms and radiolarians.

IX. Primary Production in the Oceans

Adenosine Diphosphate (ADP): Used in the production of ATP through a cyclical series of enzymatic reactions.

Adenosine Triphosphate (ATP): ADP + orthophosphate (P) → ATP. The phosphorylating power of ATP is used in the assimilation of carbon dioxide.

Adsorption: Adherence of solids, liquids, or gaseous atoms, ions, or molecules to liquid or solid surfaces.

Algae: Green plants that utilize photosynthesis to obtain energy.

Biomass: Another term for the standing crop. The amount of cells or phytoplankton in a given amount of seawater (10^6 cells/cm^3).

Chlorophyll: A principal pigment found in many plants and used in photosynthesis to absorb photons of light.

Chromatophores: Cells that contain the photosynthetic pigments.

Compensation Depth: The depth at which the amount of photosynthesis equals the amount of respiration (AOU = 0).

Exponential Death Phase: The phase when cells die at an exponential rate.

Exponential Growth Phase: The growth phase of an organism in which the number of cells (N) increases in an exponential manner, $\ln(N/N_0) = k\,t$, where N_0 is the initial number of cells, and k is a constant dependent on the organism and conditions of growth.

Extracellular Products: Metabolites formed outside the cell; 30% are often not retained when filtering seawater to measure the uptake of carbon dioxide.

Lag Phase: Delay of the growth of an organism; thought to be due to a lack of balance in the enzymatic reactions in the cell caused by growth promoters.

Light Intensity: The amount of light reaching the surface of the oceans. The amount is controlled by the altitude of the sun, the cloud cover, the wavelength of radiation, absorption, and scattering.

Light Saturation: The point at which the photosynthetic rate does not increase with an increased light intensity. After this point, inhibition of growth occurs because of high light levels.

Micronutrients: Trace elements that marine phytoplankton requires for growth. The most important are nitrogen, phosphorous, and silicate.

Microplankton: Phytoplankton ranging in size between 50 and 100 μm.

Nanoplankton: Phytoplankton ranging in size between 10 and 50 μm.

Photons: The packets of light energy emitted by the sun or the quantum of electromagnetic radiation.

Photosynthetic Pigments: Pigments that absorb the photons contained in the chromatophores (i.e., chlorophyll).

Photosynthetic Quotient (PQ): Molecules of oxygen liberated/molecules of carbon dioxide assimilated.

Photosynthetic Zone: The portion of the water column in which there is adequate light penetration for photosynthesis to occur. Usually, 100 m is the maximum depth.

Phototrophic Organisms: Organisms whose primary form of obtaining energy is photosynthesis.

Phytoplankton: Free-floating microscopic animals moving mostly in the confines of the water column. They are responsible for the greatest amount of primary production in the sea.

Primary Productivity: Rate of inorganic carbon fixed photosynthetically per unit time per unit volume or unit surface area. It is the result of the growth of organisms from photosynthesis.

Productive Waters: Waters found in areas of high primary productivity; often highest in coastal upwelling areas.

Radiant Energy: The energy produced by the sun's light (measured in cal cm^{-2} min^{-1}).

Reflection: One of the controlling factors in the amount of light that reaches the surface of the earth. It involves a beam hitting a surface and being bounced back at a different angle, not adsorbed.

Respiration: The process by which energy required for metabolic process is obtained by the oxidation of the photosynthesized organic compounds.

Respiration Quotient (RQ): Molecules of carbon dioxide liberated/molecules of oxygen assimilated.

Retardation Phase: The phase in the life cycle of an organism when a reduction occurs in the growth rate because of depletion of nutrients, the presence of growth inhibitors, and reduction of photosynthesis brought about by shading.

Scattering: The diffusion of light in the ocean produced by particulate matter.

Solar Energy: Radiant energy in the form of photons obtained from the sun.

Spectral Composition: The wavelengths of the light present in the atmosphere.

Standing Crop: The amount of cells or phytoplankton in a given amount of seawater (10^6 cells/cm^3).

Stationary Phase: The phase in which metabolic activity is maintained yet there is no net increase in living cells.

Ultraplankton: Phytoplankton ranging in size between 0.5 and 10 μm.

Upwelling: The process that brings nutrient-rich waters to the surface. The areas where this occurs usually have the highest primary productivity.

Organic Compounds

Alcohols: Compounds with a hydroxyl group on a nonaromatic carbon atom. Low molecular weight alcohols are found in natural waters because of their large solubility. Isoprenoid alcohols such as phytol are also widespread in marine waters.

Aldehydes: Contain the carbonyl group (H-C = O). Are very easily oxidized. Both aliphatic and aromatic aldehydes have been isolated from seawater and marine sediments. Biogenic and photochemical oxidations of humic substances are the primary origins of this class of organic compounds.

Amino Acids: The building blocks of proteins.

Aromatic Acids: Compounds that contain at least one benzene ring in addition to the carboxylic acid group. Aromatic acids are found in combination with humic substances.

Carbohydrates: A polyhydroxy carbonyl compound. The general formula for a carbohydrate is $C_n(H_2O)_m$.

Carboxylic Acids: Compounds that contain at least one carboxyl group (–COOH): fatty acids, humic and fulvic acids, hydroxy acids, and aromatic acids.

Cyclic Alkanes: Most found in marine areas are isoprenoids. Excellent biomarkers.

Cyclic Alkenes: Mostly of isoprenoid nature, are found in the marine environment.

Dissolved Organic Carbon (DOC): The concentration of dissolved organic carbon in seawater (passing through a 0.45-μm filter). Typical concentration ranges found in the oceans are 25 to 200 μ*M*.

Dissolved Organic Nitrogen (DON): The concentration of dissolved organic nitrogen in seawater (passing through a 0.45-μm filter).

Dissolved Organic Phosphorous (DOP): The concentration of dissolved organic phosphorous in seawater (passing through a 0.45-μm filter).

Fatty Acids: Compounds that consist of a carboxyl group attached to a long hydrocarbon chain. Major components of most organisms. Found as fats in animals and waxes in plants.

Fulvic Acids: Humic acids that are also soluble in acids.

Humic Acids: Base-soluble organic material. Humic acids from aquatic sources are more aliphatic than their terrestrial counterparts. The H:C ratio of a sample may be indicative of its major source of origin.

Humic Substances: Major organic component of seawater. Consist of 40 to 60% carbon, 30 to 45% oxygen, 1 to 5% nitrogen, and 2% or less sulfur. Major structural components include aromatic rings and phenolic, hydroxyl, methoxyl, and carboxylic acid groups. Concentrations in seawater range from 5 to 50 μ*M* as C.

Hydrocarbons: Organic compounds that contain hydrogen and carbon.

Kerogen: Organic matter of sedimentary rocks that is not extractable with organic solvents, mineral acids, or bases.

Ketones: General formula is RCOR′. Marine organisms can biosynthesize ketones in trace amounts. There has been very little research into this area.

Normal Alkanes: The dominant natural hydrocarbons in the marine environment; are the most abundant in organisms. Straight-chain alkanes; all single bonds.

Normal Alkenes: Straight-chain alkenes. Have been isolated from marine phytoplankton, zooplankton, benthic algae, and bacteria as well as from terrestrial sources. More reactive than alkanes.

Nucleic Acids: Polymers of the nucleotides (purines and pyridines) when the nucleotides are bound to a pentose sugar and a phosphate group and connected by phosphate ester bonds.

Organosulfur Compounds: Wide variety found in marine systems. Dimethylsulfide is emitted by oceanic biota and plays an important role in atmospheric chemistry. Many thiols (R-SH) are found in marine sediments as a result of biological degradation of organic matter.

Particulate Organics: The organic material that is collected on a 0.45-μm filter. It consists of a mixture of living and dead phytoplankton and zooplankton, bacteria, and the degradation and exudates of these biota.

Porphyrins: Consist of four nitrogen-containing pyrrole rings linked by methane groups to form a resonating ring system. This ring system can stabilize a central metal ion. Important in the biochemistry of living systems. Account for less than 1% of the DOC in the water column because of their extremely low solubilities.
Proteins: Polymeric amino acids linked by amide bonds.
Purines: A type of nucleotide. Adenine and guanine are the purines.
Pyridines: Same as purines, but pyridine base instead of purine. Cytosine, thymine, and uracil are the pyridines.
Saturated Hydrocarbons: Hydrocarbons with no double or triple bonds. Saturated hydrocarbons are primarily isoprenoids, normal paraffins, and steranes.
Steroids: Closely related structurally and biochemically to terpenes. All have the same basic carbon skeleton and are unique in the position of double bonds and functional groups. Cholesterol is the most abundant animal sterol, while ergosterol is the principal plant sterol.
Terpenoids: Natural products built of five-carbon atom isoprene units. Most are biosynthesized by plants. Characterized by a wide variety of oxygen-containing functional groups; may either be found as oxygen-deficient hydrocarbons or as oxygen-containing esters, aldehydes, ketones, alcohols, carboxylic acids, etc.
Wax Esters: Formed by the reaction of a carboxylic acid with an alcohol. They are simple esters of long-chain fatty alcohols with long-chain fatty acids. They are important cell wall components of many higher plants and comprise a significant fraction of soil lipids.

X. Processes in the Oceans

Photochemical Processes

Absorption: The loss of energy from radiation by the medium through which the radiation is passing.
Chromophore: An atom or molecule that can absorb light.
Competitive Reactions: When two or more reactions may take place at the same time.
Dark Reaction: A reaction that occurs in the dark to reverse the reaction that takes place in the presence of light.
Electromagnetic Radiation: Electromagnetic waves and, especially, the associated electromagnetic energy (i.e., the energy associated with electric or magnetic fields).
Emission: The loss of radiation of energy by means of electromagnetic waves.
Excitation: The process in which an atom or molecule gains energy from electromagnetic radiation or by collision, raising it to an excited state.
Excited State: When the light energy absorbed by an atom or molecule raises the electrons to a higher rotational or vibrational energy state.
Fluorescence: The emission of electromagnetic radiation from an excited molecule from a singlet state to the ground state.
Grotthus–Draper Law: Only light that is absorbed can cause a photochemical effect.
Ground State: The stationary state of lowest energy of an atom or molecule.
Hydrogen Peroxide (H_2O_2): Unstable, colorless, heavy liquid. Soluble in water and alcohol. Used as a bleach.

Ionization: The process by which a neutral atom or molecule loses or gains electrons, thereby acquiring a net charge and becoming an ion.

Phosphorescence: The emission of electromagnetic radiation from an excited molecule from a triplet state to the ground state.

Photochemical Effect: A chemical reaction that takes place in the presence of light.

Photon: A massless particle, the quantum of the electromagnetic field, carrying energy, momentum, and angular momentum (light quantum).

Photoreactions: Reactions that only take place in the presence of light.

Primary Photochemical Reaction: Reaction of a chromophore directly with light ($M + hv \rightarrow M^*$).

Quantum Yield: The number of moles of a reactant disappearing or product produced per photon of light absorbed for a photochemical reaction.

Redox Transients: States of an atom or molecule that are temporary and usually quickly converted back to their original state, although conversion to a new state is possible.

Rotational States: The energy levels of an atom or molecule due to the spinning or rotation of the molecule around a preferred axis.

Secondary Photochemical Reaction: Reactions that result from the formation of a radical ($e^- + O_2 \rightarrow O_2^-$).

Singlet State: Spin paired state of an atom or molecule.

Spectra of Light: The wavelength or frequency of visible light.

Stark–Einstein Law: The second law of photochemistry, which states that an atom or molecule undergoing a photochemical process absorbs only a single photon.

Superoxide Radical (O_2^-): An intermediate in the formation of hydrogen peroxide. A strong reducer that can result in the formation of reduced metals.

Triplet State: The state of an atom or molecule in which the spins of the electrons are unpaired or are parallel.

Vibration States: The energy levels of an atom or molecule due to vibrations.

Wave Number: The reciprocal of the wavelength of light, or sometimes 2π divided by the wavelength.

Hydrothermal Vent Chemistry

Black Smoker: Type of hot hydrothermal vent waters with an exit temperature of 350°C and a flow rate of 1 to 2 m/s.

Chemolithotrophy: Aerobic or anaerobic process whereby bacteria use reduced inorganic compounds as a source of energy.

Chemosynthesis: Biosynthesis of organic compounds from carbon dioxide using energy derived through chemical oxidation.

Hydrothermal Vents: Areas on the seafloor where active volcanism is found near areas of continental rifts. The hot water coming out of these systems is formed by the reactions of seawater with molten lava.

Photoautolithotropy: A type of photosynthesis used by green and purple bacteria and green plants. The bacteria make usage of a nonoxygenic pathway while green plants use oxygenic photoautolithotropy.

White Smoker: Type of hot hydrothermal vent waters with an exit temperature of 300°C and a flow rate of 1 to 2 m/s.

Anoxic Waters

Aerobic Respiration: Bacterial oxidation of organic matter using oxygen.

Anaerobic Respiration: Bacterial oxidation that occurs without oxygen. Other sources of electron acceptors are used, such as NO_3^-, MnO_2, and SO_4^{2-}.

Anoxic: Devoid of oxygen.

Anoxic Interface: The interface between waters with and without oxygen. It is normally controlled by the advection of oxygen into deep waters. This advection is limited by a salinity gradient or a sill that separates the deep waters from outside deep waters with oxygen.

Black Sea: The largest anoxic basin in the world. The waters below a depth of 200 m have no oxygen, while the levels of hydrogen sulfide can be as high as 400 μ*M*.

Cariaco Trench: An anoxic basin off the coast of Venezuela. The waters below a depth of 250 m are devoid of oxygen and have levels of hydrogen sulfide of 60 μ*M*.

Electron Acceptor: A molecule or atom that can accept electrons.

Framvaren Fjord: An anoxic fjord in the south of Norway. The waters below 20 m are devoid of oxygen and have hydrogen sulfide levels as high as 6 m*M* (the highest recorded levels).

Goteland Deep: A deep basin in the Baltic Sea that has become anoxic over the years.

Hydrogen Sulfide: The common form of reduced sulfur present in waters devoid of oxygen. It is formed by the reduction of sulfate by bacteria.

Iron Reduction: The formation of Fe(II) from the reduction of the oxides of Fe(III) by photochemical reactions or by bacteria.

Manganese Reduction: The formation of Mn(II) from the reduction of the oxides of Mn(IV) by bacteria.

Saanich Inlet: A fjord near Seattle, Washington, that becomes anoxic from time to time.

Sulfate Reduction: The formation of H_2S from the reduction of SO_4^{2-}, normally by bacteria in waters that are devoid of oxygen.

Sulfur Oxidation: The oxidation of H_2S with oxygen yields products such as polysulfides, SO_4^{2-}, SO_3^{2-}, and $S_2O_3^{2-}$.

Appendix 1

Atomic Weights of Elements (Based on $^{12}C = 12.000$)

Atomic Number	Name	Symbol	Atomic Weight
1	Hydrogen	H	1.0079
2	Helium	He	4.0026
3	Lithium	Li	6.941
4	Beryllium	Be	9.0122
5	Boron	B	10.811
6	Carbon	C	12.011
7	Nitrogen	N	14.007
8	Oxygen	O	15.999
9	Fluorine	F	18.998
10	Neon	Ne	20.180
11	Sodium	Na	22.990
12	Magnesium	Mg	24.305
13	Aluminum	Al	26.982
14	Silicon	Si	28.086
15	Phosphorus	P	30.974
16	Sulfur	S	32.066
17	Chlorine	Cl	35.453
18	Argon	A	39.948
19	Potassium	K	39.098
20	Calcium	Ca	40.078
21	Scandium	Sc	44.956
22	Titanium	Ti	47.867
23	Vanadium	V	50.942
24	Chromium	Cr	51.996
25	Manganese	Mn	54.938
26	Iron	Fe	55.845
27	Cobalt	Co	58.933
28	Nickel	Ni	58.693
29	Copper	Cu	63.546
30	Zinc	Zn	65.392
31	Gallium	Ga	69.723
32	Germanium	Ge	72.612
33	Arsenic	As	74.922
34	Selenium	Se	78.963
35	Bromine	Br	79.904
36	Krypton	Kr	83.80
37	Rubidium	Rb	85.468
38	Strontium	Sr	87.52
39	Yttrium	Y	88.906
40	Zirconium	Zr	91.224

continued

Atomic Weights of Elements (Based on $^{12}C = 12.000$)

Atomic Number	Name	Symbol	Atomic Weight
41	Niobium	Nb	92.906
42	Molybdenum	Mo	95.94
43	Technetium	Tc	98.906
44	Ruthenium	Ru	101.07
45	Rhodium	Rh	102.91
46	Palladium	Pd	106.42
47	Silver	Ag	107.87
48	Cadmium	Cd	112.41
49	Indium	In	114.82
50	Tin	Sn	118.71
51	Antimony	Sb	121.76
52	Tellurium	Te	127.60
53	Iodine	I	126.90
54	Xenon	Xe	131.29
55	Cesium	Cs	132.91
56	Barium	Ba	137.33
57	Lanthanum	La	138.91
58	Cerium	Ce	140.12
59	Prasodymium	Pr	140.91
60	Neodymium	Nd	144.24
61	Promethium	Pm	146.92
62	Samarium	Sm	150.36
63	Europium	Eu	151.96
64	Gadolinium	Gd	157.25
65	Terbium	Tb	158.93
66	Dysprosium	Dy	162.50
67	Holmium	Ho	164.93
68	Erbium	Er	167.26
69	Thulium	Tm	168.93
70	Ytterbium	Yb	173.04
71	Lutetium	Lu	174.97
72	Hafnium	Hf	178.49
73	Tantalum	Ta	180.95
74	Tungsten	W	183.84
75	Rhenium	Re	186.21
76	Osmium	Os	190.23
77	Iridium	Ir	192.22
78	Platinum	Pt	195.08
79	Gold	Au	196.97
80	Mercury	Hg	200.59
81	Thallium	Tl	204.38
82	Lead	Pb	207.20
83	Bismuth	Bi	208.98
84	Polonium	Po	209.98
85	Astatine	At	209.99
86	Radon	Rn	222.02

Atomic Weights of Elements (Based on $^{12}C = 12.000$)

Atomic Number	Name	Symbol	Atomic Weight
87	Francium	Fr	223.02
88	Radium	Ra	226.03
89	Actinium	Ac	227.03
90	Thorium	Th	232.04
91	Protoactinium	Pa	231.04
92	Uranium	U	238.03
93	Neptunium	Np	237.05
94	Plutonium	Pu	239.05
95	Americium	Am	241.06
96	Curium	Cm	244.06
97	Berkelium	Bk	249.08
98	Californium	Cf	251.07
99	Einsteinium	Es	252.08
100	Fermium	Fm	257.10
101	Mendelevium	Md	258.10
102	Nobelium	No	259.10
103	Lawrencium	Lr	262.11

Appendix 2

Useful Physical Constants

Symbol	Name	Value
F	Faraday	96,494 coulombs mol^{-1}
		23,062 cal $volt^{-1}$ eq^{-1}
R	Gas constant	8.3145 J mol^{-1} K^{-1}
		82.060 cm^3 atm mol^{-1}
N_0	Avogadro's number	6.023×10^{23} mol^{-1}
k	Boltzmann constant	1.38045×10^{-16} erg deg^{-1}
e	Electrostatic charge	4.8029×10^{-10} esu
		1.60206×10^{-19} coulomb
h	Planck's constant	6.6252×10^{-27} erg s^{-1}
c	Velocity of light	2.9979×10^{10} cm s^{-1}
g	Standard gravity	980.665 cm s^{-2}
atm	One standard atmosphere	1.01325×10^5 Pa
bar	One bar	10^5 Pa
cal	Calorie	4.184 J

Energy Conversion Factors: 1 cal mol^{-1}; 4.184 J mol^{-1}; 41.292 cm^3 atm mol^{-1}; 4.3361 10^{-5} ev; 6.9465 10^{-17} erg mol^{-1}; 1 J mol^{-1}; 0.23901 cal mol^{-1}; 9.8692 cm^3 atm mol^{-1}.

Appendix 3

Volumetric Properties of Seawater (S = 35) at One Atmosphere

Temperature (°C)	**ρ (g cm^{-1})**	**v (m^3 kg^{-1})**	**$10^6\alpha$ (deg^{-1})**	**$10^6\beta$ (bar^{-1})**	**$10^6\beta_S$ (bar^{-1})**
0	1.028103	972.665	53.49	46.341	46.322
5	1.027673	973.072	113.43	45.075	44.988
10	1.026950	973.757	166.38	44.061	43.869
15	1.025971	974.687	213.90	43.254	42.932
20	1.024761	975.837	257.14	42.624	42.150
25	1.023342	977.190	296.93	42.145	41.502
30	1.021729	978.733	333.93	41.797	40.969
35	1.019936	980.453	368.62	41.565	40.539
40	1.017974	982.343	401.36	41.437	40.199

Appendix 4

Effect of Pressure on the Volumetric Properties of Seawater (S = 35)

	0°C			25°C		
Pressure (b)	**v (m^3 kg^{-1})**	**$10^6\alpha$ (deg^{-1})**	**$10^6\beta$ (bar^{-1})**	**v (m^3 kg^{-1})**	**$10^6\alpha$ (deg^{-1})**	**$10^6\beta$ (bar^{-1})**
0	972.662	52.55	46.334	977.189	296.98	42.147
100	968.224	79.90	45.128	973.129	305.07	41.132
200	963.921	105.81	43.962	969.182	312.86	40.157
300	959.748	130.30	42.835	965.344	320.36	39.220
400	955.698	153.38	41.746	961.609	327.57	38.318
500	951.767	175.08	40.692	957.973	334.50	37.451
600	947.950	195.40	39.673	954.432	341.15	36.615
700	944.244	214.36	38.686	950.982	347.52	35.811
800	940.643	231.99	37.731	947.620	353.62	35.035
900	937.144	248.30	36.806	944.341	359.46	34.288
1000	933.743	263.31	35.910	941.143	365.04	33.566

Appendix 5

The Thermochemical Properties of Seawater (S = 35) at One Atmosphere

Temperature (°C)	Cp (J g^{-1} K^{-1})	C_V (J g^{-1} K^{-1})	10^3h (J g^{-1})	–g (J g^{-1})	10^6s (J $g^{-1}K^{-1}$)
0	3.9996	3.9979	–30.59	5.01	1.718
5	3.9932	3.9862	–17.18	5.10	1.735
10	3.9906	3.9736	–4.73	5.19	1.815
15	3.9906	3.9593	6.88	5.28	1.858
20	3.9921	3.9476	17.86	5.37	1.897
25	3.9945	3.9349	28.30	5.47	1.933
30	3.9973	3.9177	38.42	5.57	1.968
35	4.0002	3.9008	48.35	5.66	2.001
40	4.0031	3.8821	58.27	5.76	2.035

Note: Cp = specific heat capacity at constant pressure; C_V = specific heat capacity at constant volume; h = specific enthalpy; g = specific free energy; s = specific entropy.

Appendix 6

The Colligative Properties of Seawater (S = 35) at One Atmosphere

Salinity	$-T_f$ (°C)	Temp (°C)	φ	a	p (mm Hg)	π (bar)
0	0	0	0.8925	0.9815	4.496	23.54
5	0.274	5	0.8954	0.9814	6.419	24.05
10	0.542	10	0.8978	0.9814	9.036	24.54
15	0.811	15	0.8996	0.9814	12.551	25.02
20	1.083	20	0.9009	0.9813	17.213	25.46
25	1.358	25	0.9017	0.9813	23.323	25.90
30	1.637	30	0.9023	0.9813	31.245	26.31
35	1.922	35	0.9025	0.9813	41.412	26.70
40	2.211	40	0.9025	0.9813	54.329	27.09

Note: T_f = freezing point; φ = osmotic coefficient; a = activity of water; p = vapor pressure; π = osmotic pressure.

Index

F

I

N

O

P

Q

R

S

T

U

V

W

X

Y

Z

Environmental Science & Technology

Chemical Oceanography

FOURTH EDITION

Over the past ten years, a number of new large-scale oceanographic programs have been initiated. These include the Climate Variability Program (CLIVAR) and the recent initiation of the Geochemical Trace Metal Program (GEOTRACES). These studies and future projects will produce a wealth of information on the biogeochemistry of the world oceans. Authored by Frank J. Millero, an acknowledged international authority in the field, the fourth edition of **Chemical Oceanography** maintains the stellar insight that has made it a favorite of students, instructors, researchers, and other professionals in marine science, geochemistry, and environmental chemistry. Reflecting the latest updates on issues affecting the health of our environment, this text

- Supplies an in-depth treatment of ocean acidification, a key emerging environmental problem
- Provides updated coverage on the carbonate system in the ocean
- Presents expanded information on oceanic organic compounds
- Contains updates on dissolved organic carbon, phosphate, nitrogen, and metals in the ocean
- Offers a new definition of salinity and a new equation of the state of seawater based on recent, original research
- Describes the new thermodynamic equation of the state of seawater
- Includes full-color graphs and photographs to assist readers in visualizing the concepts presented

For more than two decades, this book has served as the "classic" textbook for students and a valuable reference for researchers in the fields of oceanography, environmental chemistry, and geochemistry. Designed for both classroom use and self-study, this comprehensive survey of essential concepts incorporates a wealth of state-of-the-art reference data discovered on large-scale oceanographic studies sponsored by the National Science Foundation and the National Oceanographic and Atmospheric Administration.

K14907

CRC Press
Taylor & Francis Group
an informa business

www.taylorandfrancisgroup.com

6000 Broken Sound Parkway, NW
Suite 300, Boca Raton, FL 33487
711 Third Avenue
New York, NY 10017
2 Park Square, Milton Park
Abingdon, Oxon OX14 4RN, UK

ISBN: 978-1-4665-1249-8
90000
9 781466 512498

www.crcpress.com